University of Southampton
Faculty of Physical Sciences and Engineering
School of Electronics and Computer Science

Quantum-Assisted Multi-User Wireless Systems

by

Panagiotis Botsinis
MEng, MSc

A thesis submitted in partial fulfilment for the degree of Doctor of Philosophy

March 2015

SUPERVISORS:
Professor Lajos Hanzo
and Dr Soon Xin Ng

UNIVERSITY OF SOUTHAMPTON

ABSTRACT

FACULTY OF PHYSICAL SCIENCES AND ENGINEERING
SCHOOL OF ELECTRONICS AND COMPUTER SCIENCE

Doctor of Philosophy

Quantum-Assisted Multi-Used Wireless Systems

by
Panagiotis Botsinis

The high complexity of numerous optimal classical communication schemes, such as the Maximum Likelihood (ML) and Maximum *A posteriori* Probability (MAP) Multi-User Detector (MUD) designed for coherent detection or the ML and MAP Multiple-Symbol Differential Detectors (MSDD) conceived for non-coherent receivers often prevents their practical implementation. In this thesis we commence with a review and tutorial on Quantum Search Algorithms (QSA) and propose a number of hard-output and iterative Quantum-assisted MUDs (QMUD) and MSDDs (QMSDD).

We employ a QSA, termed as the Dürr-Høyer Algorithm (DHA) that finds the minimum of a function in order to perform near-optimal detection with quadratic reduction in the computational complexity, when compared to that of the ML MUD / MSDD. Two further techniques conceived for reducing the complexity of the DHA-based Quantum-assisted MUD (QMUD) are also proposed. These novel QMUDs / QMSDDs are employed in the uplink of various multiple access systems, such as Direct-Sequence Code Division Multiple Access systems, Space Division Multiple Access systems as well as in Direct-Sequence Spreading and Slow Subcarrier Hopping SDMA systems amalgamated with Orthogonal Frequency Division Multiplexing and Interleave Division Multiple Access systems.

Furthermore, we follow a quantum approach to achieve the same performance as the optimal Soft-Input Soft-Output (SISO) classical detectors by replacing them with a quantum algorithm, which estimates the weighted sum of all the evaluations of a function. We propose a SISO QMUD / QMSDD scheme, which is the quantum-domain equivalent of the MAP MUD / MSDD. Both our EXtrinsic Information Transfer (EXIT) charts and Bit Error Ratio (BER) curves show that the computational complexity of the proposed QMUD / QMSDD is significantly lower than that of the MAP MUD / MSDD, whilst their performance remains equivalent. Moreover, we propose two additional families of iterative DHA-based QMUD / QMSDDs for performing near-optimal MAP detection exhibiting an even lower tunable complexity than the QWSA QMUD. Several variations of the proposed QMUD / QMSDDs have been developed and they are shown to perform better than the state-of-the-art low-complexity MUDs / MSDDs at a given complexity. Their iterative decoding performance is investigated with the aid of non-Gaussian EXIT charts.

Acknowledgements

By completing this Ph.D. thesis, I would like to thank the persons who supported and helped me throughout the completion of this work.
I would sincerely like to thank my supervisors on this project, Professor Lajos Hanzo and Dr. Soon Xin Ng for their continuous and valuable help and discussions, as well as their mental support and trust. Moreover, I feel grateful to Zunaira Babar and Dimitrios Alanis for their insightful comments.
I would also like to thank and dedicate this work to my family, my parents Dimosthenis and Magdalini, my brother Marinos - Damianos, to Agnieszka and to my friends, who are always standing by me, helping, caring, supporting and tolerating me.

DECLARATION OF AUTHORSHIP

I, **Panagiotis Botsinis**,

declare that the thesis entitled

Quantum-Assisted Multi-User Wireless Systems

and the work presented in the thesis are both my own, and have been generated by me as the result of my own original research. I confirm that:

- this work was done wholly or mainly while in candidature for a research degree at this University;
- where any part of this thesis has previously been submitted for a degree or any other qualification at this University or any other institution, this has been clearly stated;
- where I have consulted the published work of others, this is always clearly attributed;
- where I have quoted from the work of others, the source is always given. With the exception of such quotations, this thesis is entirely my own work;
- I have acknowledged all main sources of help;
- where the thesis is based on work done by myself jointly with others, I have made clear exactly what was done by others and what I have contributed myself;
- parts of this work have been published as: [1–6].

Signed:.....
Date:.....

List of Publications

Journal Papers:

1. D. Alanis, **P. Botsinis**, Z. Babar, S. X. Ng, and L. Hanzo, "Non-Dominated Quantum Iterative Routing Optimization for Wireless Multihop Networks," *IEEE Access*, *(in preparation)*

2. Z. Babar, **P. Botsinis**, D. Alanis, S. X. Ng, and L. Hanzo, "The Realm of Quantum LDPC Codes: A Survey & Improved Decoding Strategies," *IEEE Access*, *(in preparation)*

3. **P. Botsinis**, D. Alanis, Z. Babar, S. X. Ng, and L. Hanzo, "Iterative Quantum-Assisted Multi-User Detection for Multi-Carrier Interleave Division Multiple Access Systems," *IEEE Transactions on Communications*, *(submitted)*

4. **P. Botsinis**, D. Alanis, Z. Babar, S. X. Ng, and L. Hanzo, "Non-Coherent Quantum Multiple Symbol Differential Detection for Wireless Systems," *IEEE Access*, vol. 3, pp. 569–598, 2015

5. Z. Babar, **P. Botsinis**, D. Alanis, S. X. Ng, and L. Hanzo, "The Road From Near-Capacity Classical to Quantum Concatenated Code Design," *IEEE Access*, vol. 3, pp. 146–176, 2015

6. D. Alanis, **P. Botsinis**, S. X. Ng, and L. Hanzo, "Quantum-Assisted Routing Optimization for Self-Organizing Networks," *IEEE Access*, vol. 2, pp. 614–632, 2014

7. **P. Botsinis**, D. Alanis, S. X. Ng, and L. Hanzo, "Low-Complexity Soft-Output Quantum-Assisted Multi-User Detection for Direct-Sequence Spreading and Slow Subcarrier-Hopping Aided SDMA-OFDM Systems," *IEEE Access*, vol. 2, pp. 451–472, 2014

8. **P. Botsinis**, S. X. Ng, and L. Hanzo, "Fixed-Complexity Quantum-Assisted Multi-User Detection for CDMA and SDMA," *IEEE Transactions on Communications*, vol. 62, no. 3, pp. 990–1000, 2014

9. **P. Botsinis**, S. X. Ng, and L. Hanzo, "Quantum Search Algorithms, Quantum Wireless, and a Low-Complexity Maximum Likelihood Iterative Quantum Multi-User Detector Design," *IEEE Access*, vol. 1, pp. 94–122, 2013

Conference Papers:

1. **P. Botsinis**, S. X. Ng, and L. Hanzo, "Low-Complexity Iterative Quantum Multi-User Detection in SDMA Systems," *IEEE International Conference on Communications (ICC)*, June 2014

Contents

List of Symbols

$(E_b/N_0)^*$	Auxiliary E_b/N_0 value selected during the initialization stage of the non-Gaussian EXIT charts
A	Unitary operator that creates the state $\|\Psi\rangle$ of Equation 3.33
B	Bandwidth
$CCNOT$	Controlled-Controlled-NOT unitary gate, termed as the Toffoli gate
$CNOT$	Controlled-NOT unitary operator
C	Capacity
E_b	Energy per bit
F_d	Effective normalized Doppler frequency
G_q	Number of unique spreading codes present on the qth subcarrier
G	Number of spreading codes
H	Unitary Hadamard operator
$I_{DEC,a}$	Mutual *a priori* information at the output of the decoder
$I_{DEC,e}$	Mutual extrinsic information at the output of the decoder
$I_{MUD,a}$	Mutual *a priori* information at the input of the multi-user detector

$I_{MUD,e}$	Mutual extrinsic information at the input of the multi-user detector
I_{inner}	Number of decoding iterations between the component codes of a turbo code
J_0	Zeroth-order Bessel function
J	Number of iterations between the multi-user detector and the channel decoder
$L_{m,apr}$	*A priori* bit-based LLR of the MUD
$L_{m,e}$	Extrinsic bit-based LLR of the MUD
$L_{m,po}$	*A posteriori* bit-based LLR of the MUD
L_{stop}	Number of applications of the Grover operator before the algorithm is stopped
L	Number of applications of the Grover operator, or, equivalently, number of cost function evaluations
M	Constellation size of the user modulation scheme
N_0	Noise variance
N_w	Number of symbols for which the multiple symbol differential detector is employed
N_{T_x}	Number of transmit antennas per mobile station
N	Number of entries in a database
O	Oracle operator
$P(\mathbf{x})$	Probability of $\mathbf{x}$
P_0	Controlled phase shift gate that inverts the sign of all the input states except for the $\|0\rangle^{\otimes n}$ state when applied to n qubits.

P	Number of receive antenna elements at the base station
Q	Unitary operator, considered as a generalized Grover operator
R_θ	Unitary rotation operator with rotation angle θ
R	Coding rate
SB	Number of subcarriers in each subband
$S_{\min}$	Minimum non-zero detectable sum in the quantum weighted sum algorithm
S	Number of solutions in a search problem
T_h	Number of OFDM symbol periods between two consecutive applications of the subcarrier allocation algorithms
T_s	Symbol period
Tr	Trace of a square matrix
T	Number of time slots required for the transmission of a frame
U_L	Normalized user load
U_f	Unitary operator that performs function f
U_q	Number of users allocated to the qth subcarrier
U	Number of Users in a multiple access system
W	Number of subcarriers per user
Z	Number of classical or quantum bits used for representing a value of a function
Γ	Length of each user's symbol stream
Ψ	$(N_w \times N_w)$-element conditional autocorrelation matrix of the Rayleigh channel

Σ_h	Covariance matrix of the channel in the time domain
Ξ	Number of generations in the ant colony optimization algorithm
$\bar{\mathcal{X}}_{q,g}^{u,m,\nu}$	Subset of $\mathcal{X}_{q,g}^{u,m,\nu}$ that includes its best $\min\{\lvert\mathcal{X}_{q,g}^{u,m,0}\rvert, \lvert\mathcal{X}_{q,g}^{u,m,1}\rvert\}$ number of symbols with respect to their cost function value
$\chi(u, m, v)$	Set of multi-level symbols for which the $(u \log_2(M) + m)$th bits is equal to v
$\dagger$	$A^\dagger$ is the conjugate transpose of A
δ	The number we are searching for in a database
γ_c	Average channel power
$\hat{\mathcal{X}}_{q,g}^{u,m,\mathrm{v}}$	Subset of $\bar{\mathcal{X}}_{q,g}^{u,m,\nu}$ that includes its specific symbols that satisfy Equation 3.102
$\hat{\mathbf{x}}$	Detected symbol vector
$\hat{a}$	Estimated weighted sum of a function
$\lvert+\rangle$	Qubit in the $(\lvert0\rangle + \lvert1\rangle)/sqrt2$ state
$\lvert-\rangle$	Qubit in the $(\lvert0\rangle - \lvert1\rangle)/sqrt2$ state
$\lvert\Psi\rangle$	The main quantum state of the quantum function register in the quantum weighted sum algorithm, described in Equation 3.33
λ	Parameter in the BBHT quantum search algorithm chosen in the set $(1, 4/3)$
$\langle q\rvert$	Bra representation of the quantum bit (qubit) q. The Hermitian counterpart of the ket
$\mathcal{C}$	Complexity
$\mathcal{G}$	Grover operator

$\mathcal{M}$	Set of symbols in the constellation
$\mathcal{Q}$	Number of subcarriers
$\mathcal{X}_{q,g}^{u,m,\nu}$	Subset of $\mathcal{X}$ that includes the particular symbols for which the $[(u-1)\cdot \log_2 M + m]$th bit of the corresponding binary representation is equal to ν
$\mathcal{X}$	Set of the unique symbols that were evaluated during the Durr-Hoyer algorithm
ν	AWGN noise variable with variance N_ν
ϕ_{hh}^t	Autocorrelation function of the channel states in the time domain
σ	It is equal to $\sigma = \sqrt{N_0/2}$, where N_0 is the noise variance
$\mathbf{C}$	Codebook that contains the used direct sequence spreading codes
$\mathbf{H}$	Channel transfer matrix that contains the channel coefficients in the time domain in single-carrier systems or in the frequency domain in multi-carrier systems
$\mathbf{W}$	Complex-valued equalizer matrix
$\mathbf{Y}$	$(N_w \times P)$-element matrix that contains the P number of received symbol vectors $\mathbf{y}_p$, $p \in \{1, 2, \ldots, P\}$ in non-coherent multiple symbol differential detection
$\mathbf{c}_u$	Direct sequence spreading code of the uth user having a length equal to the employed spreading factor
$\mathbf{n}$	Additive white Gaussian noise vector
$\mathbf{r}$	Received signal vector before the application of an equalizer
$\mathbf{x}$	Symbol vector that contains the symbol of each user
$\mathbf{y}$	Received signal vector after the application of an equalizer

$\tilde{h}$	complex-valued channel coefficient corrupted by noise
$\varsigma_{u,m}$	Sign of the $[(u-1)\cdot \log_2 M + m]$th bit's LLR
ζ	Number of ants in the ant colony optimization algorithm
$\{\hat{b}_u\}$	Estimated bit stream of the uth user
$\{b_u\}$	Information bit stream of the uth user
$\{c_u\}$	Channel encoded bit stream of the uth user
$\{i_u\}$	Interleaved bit stream of the uth user
$\{s_u\}$	Encoded and spread bit stream of the uth user
$\{x_u\}$	Symbol stream of the uth user, which is transmitted in coherent systems, or differential encoded in non-coherent systems
a	Weighted sum of a function
$b_u^{(m)}$	The uth user's mth bit
f_c	Carrier frequency
f_d	Normalized Doppler frequency
f_s	Sampling frequency
g	Index for the direct sequence spreading codes
h	complex-valued channel coefficient
l	Number of quantum bits in the quantum control register of the quantum weighted sum algorithm
m	Index for the bits in a M-ary symbol
nb	Subscript which declares that the $x_{nb}^{u,m}$ is the neighbour of $x^{u,m}$ by having different values only at the $[(u-1)\cdot \log_2 M + m]$th bit

n	Number of quantum bits, equal to $\log_2(N)$
$p(\mathbf{y})$	Probability density function of $\mathbf{y}$
p_{fw}	Free will probability in the ant colony optimization algorithm
q	Index for the subcarriers
s	Differentially encoded symbol
u	Index for the users
v	Velocity of each mobile user
x_I	Initial input index to the DHA
x_s	Index that is a solution of the search problem
$x_{\min}$	Index x that corresponds to the minimum entry of a database
$\lvert\mathcal{X}\rvert$	Size of the set $\mathcal{X}$
$\lvert q\rangle$	Ket represenation of the quantum bit (qubit) q

Chapter 1

Introduction

1.1 Motivation

The history of wireless communications, the evolution of standards and a host of popular enabling techniques was detailed in [7]. These solutions paved the way for inching closer to the Shannonian channel capacity limits. However, these ultimate limits may only be approached for a single user link subjected to pure Additive White Gaussian-distributed Noise (AWGN) under Shannon's idealized simplifying assumptions of using random Gaussian transmit signals. By contrast, in practical state-of-the-art systems we employ digital, rather than Gaussian transmit signals. Furthermore, no quantitative statements were made by Shannon as regards to the system's delay and complexity, whilst in practice only the family of powerful and hence high-complexity, high-delay channel coded systems might be capable of approaching these limits and even then only under perfectly synchronized conditions. Regretfully however, perfect synchronization at near-capacity Signal-to-Noise Ratios (SNR) is again, a real challenge. Moreover, the near-perfect estimation of the Channel State Information (CSI) required for approaching the capacity limits imposes additional complexity. Hence the myth of operating in the vicinity of Shannon's capacity limit in practical systems was dispelled in [8], where it was quantitatively demonstrated with the aid of painstakingly meticulous measurements that only a fraction of the theoretically attainable capacity is actually achieved by the standardized systems.

Another limitation imposed on the operational standard systems is that a single link's Shannonian capacity is limited by the logarithmic Bit/Hz normalized capacity formula of $C/B = \log_2(1 + \text{SNR})$, which only allows the capacity to be increased logarithmically with the SNR, i.e. with the transmit power, where B is the available bandwidth. Nonetheless, we hasten to add that when B tends to infinity, like in Ultra-Wide Band (UWB) systems for example, this capacity formula also tends to a linearly increasing function of the SNR, at the low SNR region. By contrast, provided that we can construct a sufficiently high number of parallel streams and additionally, we are capable of conceiving low-complexity full-search-based detection techniques, the throughput of wireless systems may be increased

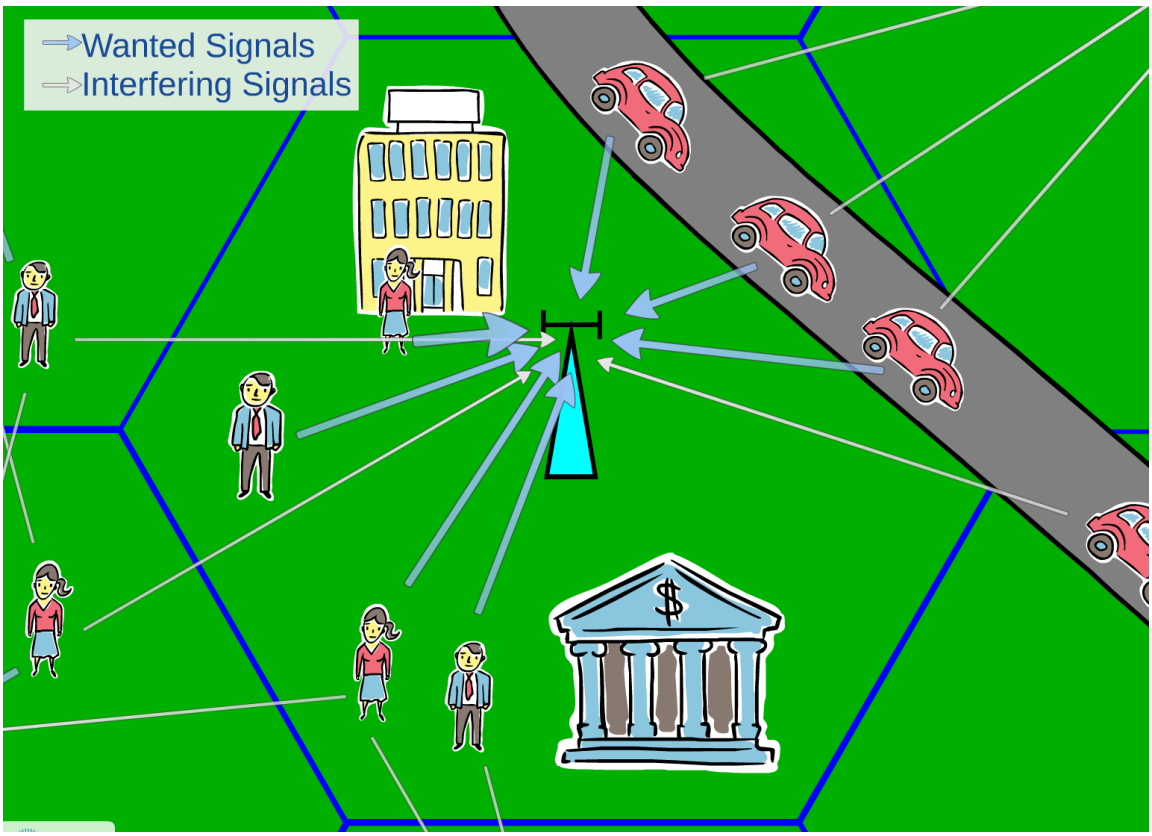

Figure 1.1: Uplink communication in a single cell, where the signals of users who transmit from within the cell represent the desired information, while those of the users who are in a different cell are treated as interference.

linearly, rather than logarithmically with the transmit power, leading to the concept of power-efficient "green" communications systems, which was the motto of the book [9].

Given this motivation, let us briefly elaborate on the potential techniques of creating parallel streams in wireless systems and then embark on conceiving high-efficiency quantum-processing techniques for creating powerful detectors for them!

1.1.1 Large-Dimensional Holistic Optimization in Wireless Systems

Figure 1.1 presents the uplink of a wireless communication system in a single cell, where any signals received from other cells are considered as interfering signals. The U useful information signals transmitted from within the serving cell by each user have to be detected and separated at the Base Station (BS), before they are independently decoded. Let us proceed by considering a number of schemes that may be used for accurately detecting the multiple streams at the BS.

1. The family of multi-stream wireless systems, such as for example the single-carrier Direct-Sequence Code Division Multiple Access (DS-CDMA) [10, 11] scheme of the operational third-generation Wideband-CDMA systems are capable of increasing the throughput linearly with the transmit power - provided that we assign multiple superimposed spreading codes to each of the U users supported.

2. Similarly, the pan-American Multi-Carrier (MC) DS-CDMA [11–13] cdma2000 system supports a multiplicity of users by allocating unique, user-specific spreading codes to them, which are also often referred to as user signatures. The throughput of MC-CDMA may also be increased linearly with the transmit power, since we can create superimposed parallel streams in both the time-domain and frequency-domain. Hence it may be anticipated that MC-CDMA systems will play a prominent role in future generations of wireless systems.

3. As a further dimension for creating superimposed parallel streams, the spatial domain of parallel transmit and receive antennas was proposed in the context of Multi-Functional Antenna Arrays (MFAA) [7]:

   - To elaborate a little further, firstly, MFAAs are capable of achieving a multiplexing gain by transmitting independent parallel streams, which may be separated at the receiver, provided that we can estimate the unique, antenna-specific Channel Impulse Responses (CIR) sufficiently accurately at the receiver. This scheme is termed as Spatial Multiplexing (SM).
   - Secondly, the MFAAs are also capable of supporting the uplink transmissions of multiple users instead of transmitting multiple streams for a single user, which is referred to as Spatial Division Multiple Access (SDMA) [14–16]. Similarly to separating multiple streams in spatial multiplexing, in SDMA the separation of users is achieved with the aid of the accurately estimated unique, user-specific CIRs.
   - The third key function of MFAAs is the provision of diversity gain for the sake of mitigating the deleterious effects of the wireless channel's fading imposed by the sometimes constructively, sometimes destructively superimposed multiple propagation paths. Naturally, the multiplicity of propagation paths contributes further towards the gradually escalating number of parallel streams, which may be coherently combined with the aid of maximal ratio combining for the sake of mitigating the effects of fading. It is important to note however that in order to achieve the maximum attainable diversity gain, the MFAA elements have to be sufficiently far apart for experiencing independent fading.
   - The MFAAs are also capable of attaining angular selectivity, hence potentially mitigating the effects of interference amongst the users, which is termed as co-channel or Multi-User Interference (MUI) - provided that the interfering signals arrive from angles outside the beamformer's main transmit/receive beam. These beamformers typically employ MFAA elements, which are half-the-wavelength apart, because in contrast to the independently fading signal components of the transmit diversity schemes, they aim for transmitting/receiving appropriately phase-combined signal components for creating maxima in the desired user's direction and minima towards the interferers. This feature of the MFAAs is very useful in the context of Millimiter Wave (mm-Wave) communications, where the wavelength is on the order of millimeters [17]. For example, at 60 GHz the

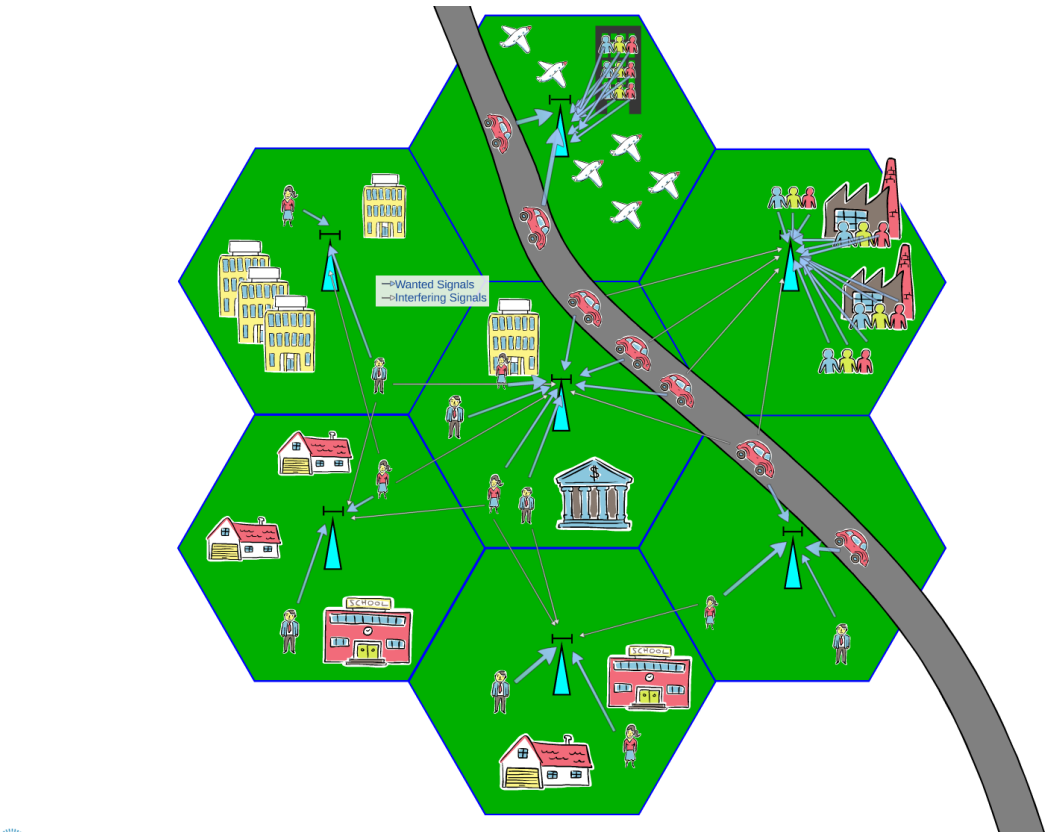

Figure 1.2: Uplink communication in seven neighbouring cells, where the signals of users who transmit from within a cell represent the desired information of that cell, while contributing to the interference power level of their adjacent cells.

wavelength is 5 mm, hence the beamforming elements could be placed at 2.5 mm spacing. Therefore, multiple transmit antennas may fit on the back plane of a laptop or a mobile phone for creating a beamformer.

- Finally, all the above-mentioned design objectives of MFAAs may be combined in the interest of benefiting from all of these desirable performance improvements - again, provided that low-complexity multi-stream detectors may be conceived.

4. A multiple access scheme similar to the CDMA system is constituted by the Interleave Division Multiple Access (IDMA) scheme [5, 18–20], where the users are separated with the aid of their user-specific interleaving sequences. More specifically, the channel coding and direct sequence spreading procedures are combined in an IDMA system and each user employs the same channel code and direct sequence. After channel coding and spreading the information bit sequence, each user interleaves his / her own chip sequence with a unique, user-specific interleaving sequence. Hence IDMA may also be viewed as chip-interleaved CDMA, because instead of the bits spread, the chips are interleaved by swapping the position of the interleaver and the spreading scheme. At the receiver, the multi-stream detection is performed on a chip-by-chip basis by exploiting the user-specific CIRs. Iterations between the multiple stream detector and the despreader-decoder may be performed for providing a better final estimate.

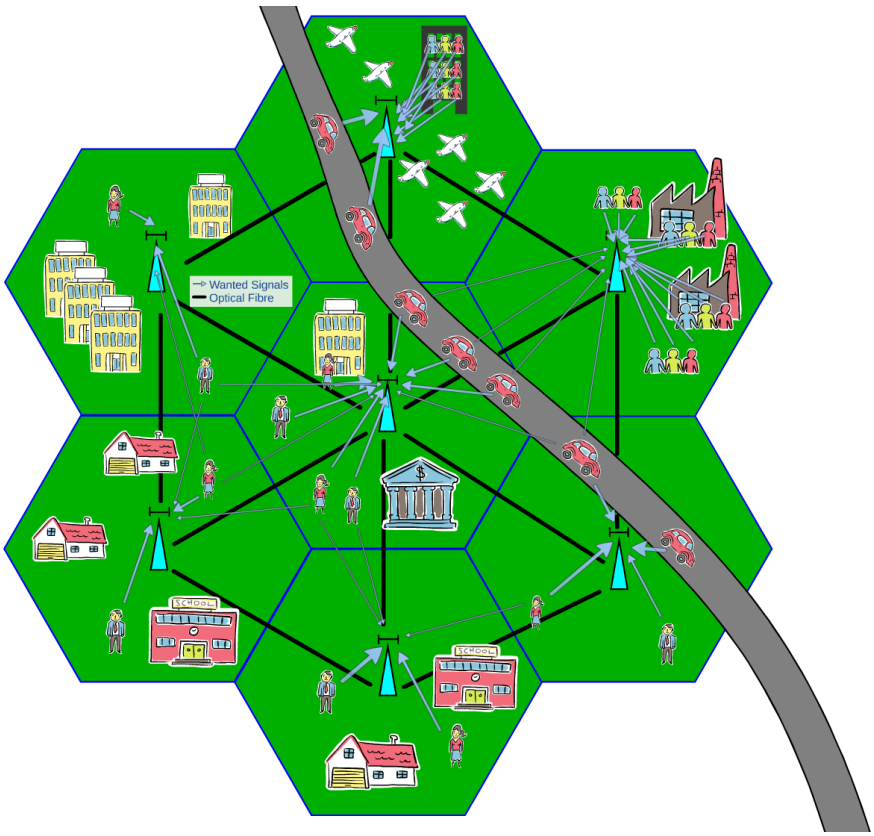

Figure 1.3: Uplink communication with the aid of Cooperative Multi-Cell Processing in seven neighbouring cells, where the seven base stations are connected with their neighbouring base stations via optical fibre. Another approach to CoMP-aided communications connects the base stations to a common central processing unit, instead of each other. In contrast to Figure 1.1 and Figure 1.2, all the signals are considered to be desired in CoMP-aided communication scenarios.

5. Similarly to MC-CDMA, all the above-mentioned concepts are also applicable to the fourth-generation Multiple-Input Multiple-Output (MIMO) aided Orthogonal Frequency-Division Multiplexing (OFDM) systems [3, 6, 21–23], where the users convey their information to and from the BS over multiple subcarriers.

6. However, so far we have only alluded to the multiple streams generated by multiple users and the MFAAs within a single cell. In reality one of the most severe performance limitations of wireless systems is constituted by the MUI imposed by the adjacent cells as presented in Figure 1.1 and Figure 1.2, because this can only be mitigated with the aid of Cooperative Multi-cell Processing (COMP), illustrated in Figure 1.3. More explicitly, the basic philosophy of COMP is that the base-stations are linked with the aid of either optical fibre or by a point-to-point microwave link and this way they exchange all their information, including all the uplink and downlink data of all the users, as well as their CIRs.

7. Albeit the COMP concept imposes a huge amount of data exchange amongst the BSs, as a benefit, no MUI is experienced, because all the energy received by all receivers is useful signal energy and hence directly contributes towards achieving the best possible holistic system performance, by exploiting the fast optical back-bone connecting the

cooperating BSs, as seen in Figure 1.3. As a result, the theoretically best possible multi-user, multi-cell performance constituted by an idealized system, where the only performance impairment is the AWGN may be asymptotically approached - again, provided that low-complexity parallel processing aided receivers may be constructed.

Expanding the multi-cell, multi-user optimization concept [24, 25] yet another step further, accurate near-instantaneous power control is required at the COMP-aided BSs in order to minimize the transmit power, while maintaining the required Quality of Service (QoS) constraints for each of the U users [26, 27]. In the operational standardized systems this is achieved by carefully optimizing both the step-size and the instants of power-updates as a function of the vehicular speed, but these step-by-step sequential power-adjustments do not necessarily approach the optimum, especially not for high velocities. *Hence a near-instantaneous "direct-dial-style" parallel power-adjustment of all transmitters would be desirable across the entire system.*

8. In large-dimensional COMP systems, relying on large-scale MIMOs, or in cells supporting a very high user density, such as airports, train stations and metropolitan areas, the sufficiently accurate estimation of all the channel gains required for performing coherent detection and therefore achieving near-capacity performance may impose an excessive complexity. The employment of differential encoded modulation relying on non-coherent detection imposes a performance degradation, but dispenses with the requirement of channel estimation at the BS [6, 21, 28, 29]. Furthermore, in a scenario where the users are separated in the frequency domain by transmitting on different orthogonal subcarriers, or in the time domain by using orthogonal DSS codes, the employment of Multiple Symbol Differential Detection (MSDD) [6, 21, 29] becomes attractive. Explicitly, with the aid of the MSDD, the detection of a user's symbols is performed over extended multiple-symbol windows of differentially modulated symbols, hence increasing the complexity of conventional non-coherent detection, while simultaneously improving the performance of the system.

   Additional large-dimensional optimization algorithms processing numerous parallel streams in wireless communication systems involve message-routing across large cooperative and multi-hop networks [30–35], where the specific multi-hop routing path having the minimum overall length, or the minimum number of hops or alternatively, the maximum received power between two predetermined nodes has to be found. These techniques may be readily combined with sophisticated message-scheduling and resource allocation [36, 37], as well as with cognitive radio techniques relying on efficient channel- and power-allocation designed for the primary user [38, 39]. Moreover, soft information exchange between the signal detector and the channel-decoding stages is required in the green communication systems of the future, where holistic optimization is pursued [40] as well as in massive MIMO systems [8, 21, 41, 42] where the computational complexity of the optimal full-search-based algorithms is potentially excessive. *As a remedy, in this thesis we propose quantum-domain parallel processing techniques for carrying out the above-mentioned massive parallel processing tasks.*

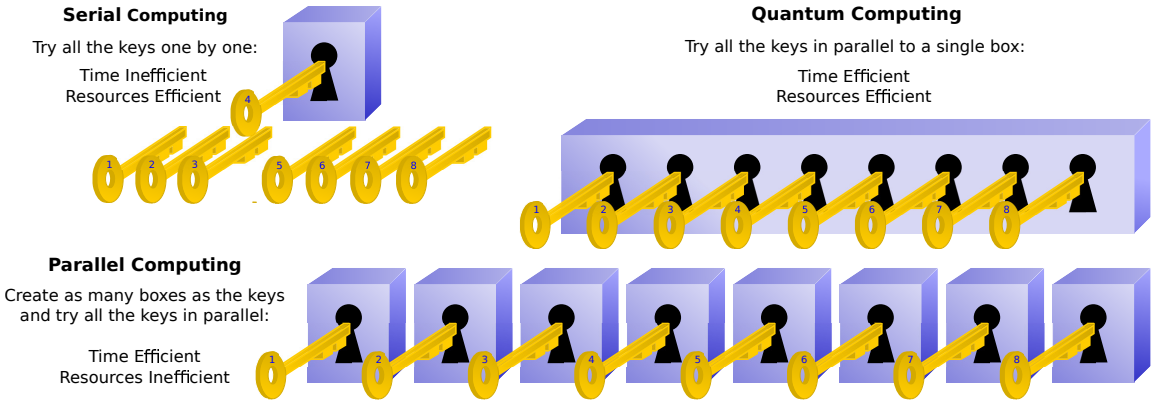

Figure 1.4: Comparison between classical serial, parallel and quantum computing. Assuming that only one of the eight keys unlocks the box, by employing serial computing we have to try each of the keys sequentially until one succeeds to unlock it. Classical parallel computing creates as many boxes as the available keys and tries all of them at once, requiring a large amount of resources. With quantum computing we are able to try all the keys in parallel on a single box. The box corresponds to a function, while the keys represent the legitimate inputs of the function. The key that unlocks the box is the input of the function which will lead to a desired output. By employing quantum computing, the function may be evaluated for the inputs in parallel, as in parallel computing, with the computational cost of a single evaluation, as in serial computing.

1.1.2 Multi-Stream Detection in Large-Dimensional Wireless Systems

As argued above, the employment of algorithms imposing a low computational complexity is essential, since low-complexity algorithms impose a low power-dissipation, which hence requires desirably low-weight, potentially solar-charged or kinetically-charged batteries for the shirt-pocket-sized wireless handsets.

A plethora of both Multi-User Detection (MUD) and multi-stream detections techniques has been proposed in the literature, as detailed for example in [10, 11]. In simple physically tangible terms we may argue that provided all the U users' signals in the above-mentioned holistically optimized system arrive at the base-station synchronously and they transmit M-ary signals, then the optimum full-search-based receiver has to tentatively check all the M^U symbol combinations, in order to reliably detect each of the U users' symbols. More specifically, this is achieved by identifying the most likely transmitted M-ary symbol of all the U users of the entire multi-user, multi-cell system by evaluating a carefully chosen Cost Function (CF), which may be the Mean Squared Error (MSE) or the Bit Error Ratio (BER), etc. *Suffice to say, however, that when using 64-level Quadrature Amplitude Modulation (QAM) for example at an airport, where say* $10\,000$ *users would like to use their phones, tablet computers or laptops, it is entirely unrealistic to evaluate the CF* $64^{10\,000}$ *times...*

This is where Quantum Computing may be employed in the above-mentioned systems for reducing the complexity of the above-mentioned processes by exploiting its inherent parallelism as illustrated in Figure 1.4. Assuming that only one of the eight keys unlocks the box in Figure 1.4, serial computing would have to perform consecutive trials (maximum eight; average four or five) until the correct key is found, requiring a long time for solving this problem. By contrast, parallel computing would recreate the box eight times and try

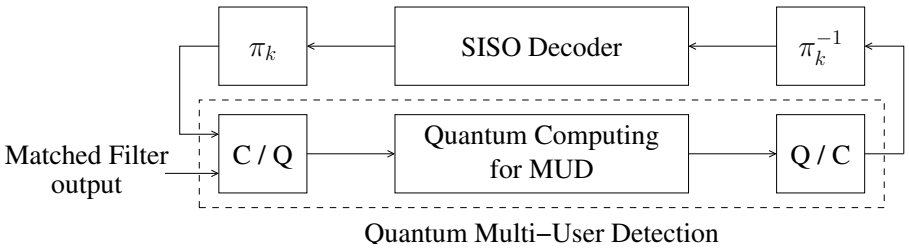

Figure 1.5: Block diagram of soft-input soft-output quantum-assisted multi-user detection, where the input/output signals are converted from/to the classical domain (CD) to/from the quantum domain (QD), while the inner operations are performed in the quantum domain.

all the keys in parallel, which is more efficient as far as the required time is concerned, but it relies on more hardware resources and it still requires a search afterwards. Quantum computing on the other hand is capable of trying all the keys at the same time, in the context of a single box.

Following the above low-paced tutorial exposure, in the rest of this treatise we will develop our ideas. In Section 1.2 we continue by formulating the signal detection problem, as well as reviewing the family of Quantum Search Algorithms (QSA) that may be used in the above-mentioned large-dimensional wireless systems. Specifically, we proceed by presenting the origins of quantum computation and their applications in wireless communication systems in Section 1.3. Finally, the relevant theoretical background on quantum computing is provided in Section 1.4 and the structure of the thesis is discussed in Section 1.5.

1.2 Signal Detection Meets Quantum Computing

With the size of a single transistor constantly shrinking according to Moore's law, it is expected to reach the atomic scale in a few years, where the postulates of quantum mechanics replace the laws of classical physics. The transition to quantum computing will unlock capabilities that a conventional classical computer is inherently incapable of [43–47]. For instance, quantum computing allows parallel evaluations of a function at a complexity equivalent to that of a single classical evaluation. An astonishing example of the power of quantum computing is the Quantum Amplitude Amplification (QAA) algorithm analysed in [48] employed in Grover's QSA [49, 50], which performs search in an unsorted database having N elements and finds a single *solution*[1] at a complexity order of $O(\sqrt{N})$, in contrast to its classical optimal counterpart imposing $O(N)$ operations. Boyer *et al.* [51] proposed the so-called Boyer-Brassard-Høyer-Tapp (BBHT) QSA, which is also based on quantum amplitude amplification and manages to perform search in an unsorted database even when the number of solutions is higher than one and even if the exact number is not known *a priori*. The Dürr-Høyer algorithm (DHA) presented in [52] manages to find the index of the minimum entry in a database by activating the BBHT QSA multiple times.

In addition to the breakthroughs in quantum error correction [53, 54] and quantum

[1] A solution is a specific index of the database, which holds the entry that satisfies the search problem.

cryptography [55, 56], a substantial amount of research has been devoted to the quantum search-based MUD field by creating quantum-assisted MUDs (QMUD) [44, 57], where classical algorithms are combined with quantum processes. It should be noted that the communication systems we investigate operate in the classical domain and only the QMUD processes are performed in the Quantum Domain (QD). The inputs and outputs of the QMUD are in the classical domain, as presented in Figure 1.5. A representative example of a quantum-assisted MUD was proposed in [57, 58], where the Quantum Counting Algorithm (QCA) of [59] is employed. The QCA exploits the Quantum Phase Estimation Algorithm (PEA) [60], which estimates the eigenvalues of unitary operators. In 2012, Zhou *et al.* [61] proposed a practical implementation of the PEA for single qubit unitary gates[2].

In this treatise, our novel contributions are:

1. *We have proposed a Maximum Likelihood Quantum-assisted Multi-User Detector (ML QMUD), where all the legitimate combinations of the users' transmitted symbols are taken into consideration at the receiver. The ML QMUD matches the performance of the classical ML MUD, while achieving a quadratic reduction in computational complexity. The ML QMUD is based on the DHA, hence it is termed as DHA-based QMUD [1, 2].*

2. *We have created an Early Stopping (ES)-aided DHA-based MUD [2], which reduces the computational complexity required by the DHA in terms of the number of the Cost Function Evaluations (CFEs). By exploiting the Matched Filter (MF) output, or the outputs of the Zero Forcing (ZF) or Minimum Mean Square Error (MMSE) detectors, we demonstrate the impact of the initial point on the DHA's complexity [2]. We have also removed the constraint of minimum required number of CFEs for the DHA in our MUD application [2].*

3. *Furthermore, even though both the ES-DHA QMUD and the DHA QMUD have a complexity of $O(\sqrt{M^U})$, the ES-DHA QMUD performs a fixed number of CFEs in contrast to the DHA QMUD where the number of CFEs follow a specific distribution depending on the system's size and power [2]. We have investigated the behaviour of the two algorithms and exploited the results to tune the ES-DHA QMUD according the near-optimum performance versus complexity requirements.*

4. *Based on the QD algorithm of estimating the mean of a function [62], also termed as the Quantum Mean Algorithm (QMA), we conceived an algorithm for estimating the weighted sum of a function. Explicitly, we propose an algorithm termed as the Quantum Weighted Sum Algorithm (QWSA) for estimating the LLRs [1]. This is achieved by computing the numerators and denominators of the LLRs, which involve the summations of conditional probabilities. These operations represent the CF evaluations,*

[2]The terms "operator" and "gate" are equivalent and interchangeable.

while the corresponding a priori probabilities act as the weights of the conditional probabilities.

5. *We have designed the first Soft-Input Soft-Output Quantum-assisted MUD (SISO QMUD) [1] for forwarding the bit LLRs to the decoding stage in the classical domain and for processing the decoder's soft outputs as a priori information also in the classical domain, making it eminently eligible for integration into an iterative receiver. The proposed SISO QMUD is termed as the DHA-QWSA QMUD, since it employs the DHA and the QWSA [1].*

6. *We have also proposed a Soft-Output (SO) QMUD relying solely on the DHA [3]. We have created two versions of the SO-DHA QMUD relying on the MAximum Approximation (MAA) [13] and on the MUlti-input Approximation (MUA) [63], based on the corresponding SO Ant Colony Optimization (ACO) MUD philosophy [13, 63]. We have demonstrated that the complexity of the SO-DHA QMUD is lower than that of the DHA-QWSA QMUD [1], while their performance is similar, provided that a sufficiently high complexity is affordable for the QWSA.*

7. *We have presented and investigated three variants of the MAA-based and MUA-based MUDs [3], where information is exchanged amongst the different detector components for the sake of improving the performance of both the SO-DHA QMUD and of the SO-ACO MUD, while keeping the per iteration complexity the same. The proposed MUDs have higher memory requirements and in some cases a delay is introduced between the MUD and the channel decoders.*

8. *We have applied a mutation probability in the ACO algorithm similar to the mutation probability of [64], termed as the "free will" (FW) of the ants, that never allows them to converge to a local minimum or maximum point, which is otherwise a potential problem in rank-deficient systems. Moreover, the information represented by the best so-far found symbol is exploited for further reducing the complexity of both the SO-DHA QMUDs and SO-ACO MUDs.*

9. *In the context of subcarrier allocation methodologies in multi-carrier multiple access systems, where DSS codes are allocated to users, such as in MC-CDMA systems, we have presented a novel DSS-based Uniform SSCH (USSCH) algorithm, which takes into consideration the DSS codes available for mapping the users to the subcarriers. We have shown that a better performance is achieved than that of the USSCH [21], whilst requiring a lower complexity.*

10. *Inspired by the Soft-Output (SO) QMUDs of [3], we propose the family of SISO DHA-MUA-aided QMUDs [5], which achieve a near-optimal performance even in rank-deficient systems with the aid of multiple MUD-decoder iterations, whilst imposing a*

lower complexity than the SISO DHA-QWSA-aided QMUD of [1, 4]. We also show that the family of DHA-MUA-aided QMUDs performs better than the DHA-MAA-assisted QMUDs in MC-IDMA systems relying on iterative receivers.

11. *In the context of non-coherent detection, we have designed a SISO Quantum Multiple Symbol Differential Detector (QMSDD) [6], based on the DHA and on the above-mentioned MAA, MUA approximations, which were previously employed for iterative detection in coherent receivers. The SISO-DHA QMSDDs perform similarly to the optimal MAP MSDD, while requiring much fewer CFEs. As in the case of coherent detection, the MUA-aided SISO-DHA QMSDDs experience a better performance than the MAA-aided SISO-DHA QMSDDs, but their complexity, memory requirements and potential delay are higher.*

12. *We use EXtrinsic Information Transfer (EXIT) charts [10, 65–67] charts for designing the proposed QMUDs [1, 3, 5, 6]. When we use EXIT charts relying on the assumption that the MUD's output is Gaussian distributed [10], different conclusions are arrived at, depending on the associated simplifying assumptions.*

1.3 Origins of Quantum Computing

Research on Quantum Mechanics initiated in 1923 by the renown physicists Planck, Bohr, Heisenberg, Einstein and Schrödinger. Even though arguments have been arisen against quantum mechanics being a compact and complete theory of describing nature, quantum mechanics is considered to be the superset of physical theories describing both the microscopic and macroscopic worlds, while abiding by the laws of the Newtonian theory.

By using the principles of quantum mechanics in order to improve intelligent computational systems, the field of Quantum Computing emerged. In 1981, Feynman introduced the concept of a quantum computer, which would be able to accurately simulate the evolution of a quantum system [68]. It was only a year later when Benioff presented a complete theoretical framework of the quantum computer concept [69]. The structural element of a quantum computer is a quantum bit, or *qubit*, that, in comparison to the classical bit, has values that are not limited to 0 and 1. Quite the contrary, it can have both of these two values simultaneously, like a spinning coin in a box, which will only assume the value of "Heads" or "Tails" upon observing it when it stops. This phenomenon is also often referred to as being in a superposition of the two orthogonal states, 0 and 1 [43]. The reason for this superposition of states being seemingly absent in the macroscopic world is related to the observation of the qubit. When a qubit is observed or "measured", any superposition of states that it might have assumed "collapses" to the classical states of 0 or 1 if the *computational basis* [44] is used for the measurement, as stated by the so-called Copenhagen interpretation [70], introduced by Bohr and Heisenberg in 1924. As a further terminology, Everett in 1957 proposed the "Many-World" or "Parallel-Universes" interpretation [71],

where an observation of a quantum state creates parallel universes that carry on with a different observation outcome taking place in each.

Quantum computing exploits a range of astonishing, non-intuitive characteristics of quantum mechanics, such as quantum parallelism, a term coined by Deutsch in 1985 [72], and entanglement [76] to accomplish computational tasks of stunningly high complexity, which would be deemed excessive in the classical computing world. Entanglement is a mysterious connection that can be established between qubits, where the observation of one of the entangled qubits allows instantaneous knowledge to be obtained for the other qubit. Einstein, Podolsky and Rosen challenged the validity of using quantum mechanics for describing nature by presenting a thought experiment which leads to a paradox (EPR paradox) [77]. Their thought experiment is based on the entanglement between particles. Assume that there are two particles, A and B, which interact with each other and then they are moved to different locations. Quantum theory and Heisenberg's uncertainty principle state that it is impossible to have knowledge of both the position and the momentum of a particle. According to the EPR thought experiment, if a measurement of A's position is made, then the position of B can be calculated. Similarly, the same statement can be made for B's momentum, and hence A's momentum can be calculated. Therefore, both the position and the momentum of particle B become known, resulting in a paradox. Hence Einstein's belief was that quantum mechanics was not a complete theory of nature. As a further advance, in 1966 Bell showed that at least one of the initial assumptions of Einstein, Podolsky and Rosen, namely locality and reality, was flawed, which was encapsulated in Bell's inequalities in [76].

Quantum parallelism is the ability to evolve the qubits of a quantum system in parallel, saving a large amount of computational complexity, when compared to classical computing. Quantum parallelism was first exploited by Deutsch in 1985, who proposed a quantum algorithm [72] based on the principles of quantum parallelism and quantum interference,

Table 1.1: Origins of Quantum Computing

Year	Author(s)	Contribution
1981	Feynman [68]	Proposed the basic model of a quantum computer, which was capable of simulating the sequence of quantum states in a quantum system.
1982	Benioff [69]	Proposed a theoretical framework for a quantum computer.
1985	Deutsch [72]	Deutch's Algorithm: A global property of a function $f : \{0,1\} \rightarrow \{0,1\}$ can be determined by using only a single evaluation of f.
1992	Deutsch and Jozsa [73]	Deutsch-Jozsa Algorithm: Succeeds to determine whether a function $f : \{0, 2^n - 1\} \rightarrow \{0,1\}$ is balanced or constant with one function evaluation.
1994	Shor [74, 75]	Shor's Algorithm: Proposed a quantum algorithm for integer factorization and introduced the concept of the Quantum Fourier Transform (QFT).
	Cleve *et al.* [60]	Proposed improvements to the Deutsch-Josza algorithm and introduced the phase estimation algorithm.

which is also part of quantum mechanics. By applying Deutsch's algorithm to a function $f : \{0, 1\} \rightarrow \{0, 1\}$, a global property can be determined by relying on a single evaluation of f. This property is the determination of whether the function f is an one-to-one mapping function, hence whether $f(0) \oplus f(1) = 1$, or not, resulting in $f(0) \oplus f(1) = 0$. In the context of a classical apparatus two evaluations of f would be required, one for each legitimate input.

In 1992, Deutsch and Jozsa [73] generalized Deutsch's algorithm of [72]. This algorithm was used to solve the so-called generalized Deutsch problem [73]. Converted into a real life scenario for better intuition, two persons are considered, Alice and Bob, with Alice classically transmitting a number x to Bob with $x \in \{0, 2^n - 1\}$ and $n \in \mathbb{N}$. When Bob receives this number, he evaluates a function $f(x)$ and sends the resultant value back to Alice, which may be either 0 or 1. The function that was used by Bob is either a constant function, in which case the output is fixed to a single value, namely to 0 or 1, regardless of the input, or balanced, which means that for half the possible inputs the outcome is 0 and for the other half it is 1. Alice's goal is to determine whether the function that was used by Bob is a constant or balanced, which she intends to find out by iterating the above procedure. More explicitly, by applying the Deutsch-Jozsa algorithm [73], Alice could achieve her goal in a single correspondence, while in classical computing $2^{n-1} + 1$ enquiries would be required in the worst case scenario, which includes f being a constant and hence reaching this conclusion after evaluating just over half of the legitimate inputs. The best case scenario in classical computing may occur when f is balanced and its first two evaluations output different values. The Deutsch-Josza algorithm was further improved by Cleve, Ekert, Macchiavello and Mosca in [60], by having a 100% probability of success. The same authors introduced the quantum phase estimation algorithm in [60], which was experimentally implemented by Zhou *et al.* [61] in 2012.

In 1994 Shor proposed a number of algorithms for quantum computation [74], such as for example a quantum algorithm conceived for integer factorization [75]. Furthermore, Shor introduced the concept of the Quantum Fourier Transform (QFT) [74]. A range of techniques for constructing unitary transformations in the form of matrices, which are used for describing the time-domain evolution of any quantum system, i.e. its consecutive states as a function of time were also presented. In 2012, Martín-López *et al.* managed to experimentally implement Shor's factoring algorithm designed for factoring the number 21 [78]. During the same year, Xu *et al.* by following a different approach of realizing a quantum system succeeded in factoring the number 143 [79].

Going back to 1994 once again, Simon managed to solve a black-box problem by using on the order of $O(n)$ queries to the black box, compared to the optimal classic algorithm, which uses $\Omega(2^{n/2})$ queries for the same task [80]. The black box U_f implements a function $f : \{0, 1\}^n \rightarrow \{0, 1\}^n$, which constitutes the input to the problem and has the property that $f(x) = f(y)$ if and only if $x = y$ or $x \oplus y = s$, for some $s \in \{0, 1\}^n$, where $x, y \in \{0, 1\}^n$. Simon's algorithm succeeds in finding this s that satisfies the function's above-mentioned property.

In the mid 1990's the field of quantum-domain search and quantum-assisted optimiza-

tion of intelligent computational systems started gaining substantial momentum based on the Deutsch-Jozsa algorithm [73] and Shor's factoring algorithm [74]. The quantum algorithms touched upon are summarized in Table 1.1. The rest of this section continues by introducing the quantum search algorithms along with their applications in the field of wireless communications. Nevertheless, this does not limit the applications of the quantum algorithms, since at the time of writing substantial research efforts are devoted into quantum-based communications, where quantum information is conveyed over quantum channels [81–83], with particularly attractive applications in the field of optical communications [84, 85].

1.3.1 Origins and Applications of Quantum Search Algorithms

In 1996 Grover proposed a quantum mechanical algorithm for performing quantum search in an unsorted classical database [49, 50]. Grover's QSA finds the index of the desired entry in the classical database, assuming that the desired value appears only once in the classical database, or, in other words, when there is only one solution in the classical database. During the same year, Boyer, Brassard, Høyer and Tapp (BBHT) in [51] generalized Grover's QSA to the case, where the desired value appears in more than one entry in the classical database. In the same paper, they proposed the BBHT algorithm, which yields the index of an entry having the desired value, provided that the number of identical desired entries is unknown *a priori*. Furthermore, they derived a closed-form mathematical expression for quantifying the success probability of Grover's QSA in identifying the desired entry. Grover's QSA is essentially an amplitude amplification process that allows the retrieval of the desired search outcome after a specific number L of tentative evaluations in the classical database [48]. The computational complexity of searching an unsorted classical database of size N by employing classical computing is $O(N)$, whereas by using Grover's QSA is $O(\sqrt{N})$.

In July of 1996 Dürr and Høyer proposed the DHA for finding the minimum entry in a classical database with ∼100% success probability, based on the BBHT QSA [52]. Furthermore, Bennett *et al.* in [86] proved that Grover's QSA is asymptotically optimal, by formally showing that there exists no quantum algorithm that can satisfy the search problem in fewer than $O(\sqrt{N})$ computational steps. In 1997, Zalka provided the mathematical proof that Grover's QSA is optimal in terms of maximizing the success probability of obtaining the index pointing to an entry having the desired value [87].

In 1998, Brassard, Høyer and Tapp proposed the Quantum Counting Algorithm (QCA) based on Grover's QSA and Shor's quantum algorithms in [59]. The concept of QCA was conceived by the same authors in [51]. The QCA is capable of providing the number of entries in a classical database that are equal to the desired value, or, in other words, the number of solutions in the database. The QCA may be viewed as an amplitude estimation process, which is capable of estimating the number of desired entries in the classical database [48].

In 1999, Ahuja and Kappor also presented a similar QSA to the DHA that was capable of

Table 1.2: Major contributions to Quantum Search Algorithms (QSA) with their applications

Year	Author(s)	Contribution
1996	Grover [49, 50]	Grover's Quantum Search Algorithm (QSA): A quantum mechanical algortihm performing quantum search in an unsorted classical database.
	Boyer *et al.* [51]	Showed a closed form for calculating the success probability of Grover's QSA and proposed an algorithm based on Grover's QSA where the wanted searched number appears more than once and also an unknown number of times in the database.
	Dürr and Høyer [52]	Dürr-Høyer Algorithm (DHA): Proposed a quantum algorithm for finding the minimum entry in an unsorted database.
	Bennett *et al.* [86]	Showed that Grover's QSA is asymptotically optimal.
1997	Zalka [87]	Proved that Grover's QSA is exactly optimal, in terms of providing the maximum possible probability of obtaining the solution.
1998	Ventura and Martinez [88]	Presented the concept of Quantum Associative Memory based on Grover's QSA.
	Brassard *et al.* [59]	Proposed the Quantum Counting Algorithm (QCA) based on Grover's QSA and Shor's factoring algorithm.
1999	Long *et al.* [89]	Proposed a generalized Grover's QSA by replacing the quantum circuit's unitary operators with arbitrary ones.
	Ahuja and Kapoor [90]	Presented a QSA similar to the DHA of [52] for finding the maximum entry in a database.
2000	Hogg [91]	Presented a heuristic quantum algorithm that finds the minimum by exploiting the correlation of the database entries.
	Brassard *et al.* [48]	Introduced the Quantum Amplitude Amplification (QAA) and Quantum Amplitude Estimation (QAE) concepts, along with a modified Grover's QSA that finds the solution with 100% probability.
2002	Imre and Balázs [57, 58]	Proposed a Quantum Multi-User Detector (QMUD) employing the QCA of [59].
2003	Shenvi *et al.* [92]	Proposed a quantum random walk search algorithm on graphs, having a similar approach as Grover's QSA [50].
2004	Imre and Balázs [93]	Presented a generalized Grover's QSA with a single application of the generalized Grover's operator.
2006	Zhao *et al.* [94]	Suggested improvements to the Grover's QSA-based MUD of [57].
2007	Imre [95]	Introduced Quantum Existence Testing (QET) based on QCA of [59] and proposed an algorithm searching for extreme values in an unsorted database based on QET.
2008	Malossini *et al.* [96]	Presented a Quantum Genetic Optimization Algorithm (QGOA) where the parent selection is based on the DHA of [52].
2011	Li [97]	Proposed a detection scheme for MIMO-OFDM systems based on the QCA of [59].
	Brassard *et al.* [62]	Proposed a quantum algorithm that finds the mean of a function inspired by the QCA of [59] and presented an application of it which finds the median of a function.

finding the maximum entry in a database [90]. During the same year, Long *et al.* introduced the generalized version of Grover's QSA by using arbitrary unitary operators and phase rotations in Grover's quantum circuit [89], replacing Grover's proposed operators [49]

When considering applications, where the entries of the database are related to each other, Hogg presented a heuristic QSA [91], which manages to find the specific index that corresponds to the minimum entry. Since this quantum algorithm is heuristic and application-based, no theoretical limits were provided. Then, Brassard *et al.* proposed a modification in the last part of Grover's QSA in order to successfully conclude the search with 100% probability [48]. In 2002, Imre and Balázs proposed an MUD scheme for a DS-CDMA system employing the QCA [57, 58]. The main process relies on creating symbol-specific quantum databases containing all the potential faded and noise – as well as interference – contaminated received signals corresponding to each user's hypothesized transmitted symbol and then aims for finding the transmitted symbol of each user relying on the QCA. If the faded and noise – as well as interference – contaminated received signal appeared in one of the symbol-specific databases, then the specific information symbol this database was constructed on is the most likely symbol to have been transmitted by the corresponding user.

In 2003, Shenvi *et al.* proposed a quantum random-walk search algorithm applied on graphs [92]. In 2004, Imre and Balázs generalized Grover's QSA, where arbitrary unitary operators are employed and only a single iteration of the Grover operator is applied [93]. Furthermore, Imre proposed the Quantum Existence Testing (QET) algorithm [44, 95] for replacing the QCA in the above-mentioned QMUD algorithm. The difference between the QCA and the QET algorithm is that the QET shows whether the faded and noise – as well as interference – contaminated received signal associated with a specific legitimate transmitted symbol does or does not exist in the quantum database. However, this is achieved without providing any information about the number of occurrences. By contrast, the QCA provides an estimate of the number of solutions in the database. Since in the QMUD proposed in [57] the knowledge required is the existence or non-existence of a solution in the databases, the QET is sufficient and less computationally complex. Moreover, Imre proposed a quantum algorithm for finding an extrinsic value in an unsorted database in [95], provided that the desired value was an integer number and that its approximate range was known *a priori*. In [94], Zhao *et al.* proposed the concept of a QMUD based on Grover's QSA [50] and Imre's previously proposed QMUD [57]. The main concept was to create a single quantum database for all users, containing the CF evaluations of all the legitimate multi-level symbols that might have been transmitted, and then to perform quantum search for finding the minimum entry in it.

Malossini *et al.* employed the DHA for creating a Quantum-assisted Genetic Optimization Algorithm (QGOA) [96] that has a performance similar to that of the classical GA, but this is achieved at a lower computational complexity. Briefly, the GAs typically carry out a random-guided search across a large search-space with the goal of finding the desired entry associated with a CF maximum/minimum, while visiting only a fraction of the legitimate entries. In 2011, Li *et al.* proposed a quantum detection scheme for MIMO-OFDM systems

Figure 1.6: Selected contributions in the field of quantum search algorithms and applications of quantum computing in wireless systems.

by employing Grover's QSA [97]. Similarly to the QMUD algorithm proposed in [94], a quantum database is created by including evaluations of the CF used for classical detection in MIMO systems for all the possible legitimate inputs. A quantum algorithm based on Grover's QSA is then employed for finding the minimum of the CF in the resultant quantum database. Brassard *et al.* proposed in [62] the QMA, which finds the mean of a function with a predefined precision. In the same paper the authors presented an application of the QMA for approximating the median of a function. The major contributions in the field of quantum search along with their applications are summarized in Table 1.2. Figure 1.6 summarizes the main contributions in quantum search algorithms, including their applications in the detection problems of wireless systems.

1.4 Fundamentals of Quantum Computing

In classical communications the smallest unit of information is the *bit*, which assumes binary values from the set $\{0, 1\}$. Its quantum-domain counterpart is the quantum bit or *qubit*, which is denoted as $|q\rangle$, where $|\cdot\rangle$ is termed as a *ket* [100]. A unique and rather unusual feature of the qubit is that apart from assuming the classical $\{0, 1\}$ states, it may also assume the superposition of them, as encapsulated in:

$$|q\rangle = a|0\rangle + b|1\rangle, \tag{1.1}$$

where we have $|a|^2 + |b|^2 = 1$, with $a, b \in \mathbb{C}$. If either $a = 0$ or $b = 0$, then we have $|q\rangle = |1\rangle$ or $|q\rangle = |0\rangle$, respectively. If neither a nor b is equal to 0, then the qubit is in a superposition of states, implying that it is in both states at the same time, until this somewhat strange state is perturbed by external interference, such as an attempt to "measure" or observe it. The probability of finding a qubit being in the state $|0\rangle$ after observing it is $|a|^2$ and in state $|1\rangle$ is $|b|^2$. One of the physical interpretations of a qubit was elegantly illustrated by Brassard in [101] by presenting a scenario where an atom with an electron orbiting on the ground state receives half the needed energy to excite it to a higher energy level orbit.

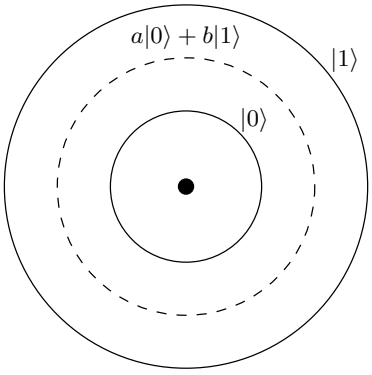

Figure 1.7: An atom with one electron orbiting around the nucleus having two legitimate energy levels (solid orbits). Quantum mechanics allow the electron to be in an arbitrary superposition of these two energy levels (dashed orbit), but when it is observed it may only be found in one of the two legitimate orbits.

The atom with the two allowed energy levels that the electron can occupy is presented in Figure 1.7. Quantum mechanics do not allow the electron to be observed in an intermediate state, even though it is simultaneously in both the excited and ground state.

The non-intuitive phenomenon of quantum mechanics may be better appreciated by imagining a coin spinning within a black box. Until it settles down and someone opens the box to observe it, it is considered as being 50% "Heads" and 50% "Tails", simultaneously. Hence the state of a spinning coin may indeed be deemed to be a superposition of states and its state may be described by

$$|q\rangle = a|0\rangle + b|1\rangle = \frac{1}{\sqrt{2}}|0\rangle + \frac{1}{\sqrt{2}}|1\rangle, \tag{1.2}$$

where $|0\rangle$ = "Heads" and $|1\rangle$ = "Tails", while $|a|^2 + |b|^2 = 0.5 + 0.5 = 1$.

When the spinning coin settles down and an observer approaches it, there is an $|a|^2 = 0.5$ probability of observing the "Heads" side of it and $|b|^2 = 0.5$ probability of observing its "Tails" side. When an "observation" reminiscent of observing the spinning coin takes place in a quantum system, the observed qubits "collapse" to a classical state according to the so-called Copenhagen interpretation [70], where this classical state is the observed one. In our example, if the coin is observed to be in the $|0\rangle$ state, naturally it will remain in this state, until an operation is applied to it. In a quantum communication system, a qubit's state is *decided* to be in a specific classical state upon its observation. According to the No-Cloning Theorem [43], a qubit being in an unknown, unobserved state cannot be copied, which is in contrast to the case of classical bits, which represent known, observed states.

A qubit $|x\rangle = a_x|0\rangle + b_x|1\rangle$ may also be interpreted as a vector on a unit sphere, termed as the Bloch sphere [43], where the positive z-axis represents the state $|0\rangle$ and the state $|1\rangle$ is mapped to the negative z-axis, as depicted in Figure 1.8. The relationship between the angles ϑ_x, φ_x and the quantum state's amplitudes a_x and b_x is

$$a_x = \cos\left(\frac{\vartheta_x}{2}\right), \quad b_x = e^{i\varphi_x}\sin\left(\frac{\vartheta_x}{2}\right), \tag{1.3}$$

where $0 \leq \vartheta_x \leq \pi$ and $0 \leq \varphi_x < 2\pi$. From Equation 1.3, we may conclude that $a_x \in \mathbb{R}_0^+$ and $b_x \in \mathbb{C}$. The quantum amplitude a_x of $|0\rangle$ may always be made real by applying a global phase rotation to the qubit, without essentially changing its quantum state [43]. A qubit in the quantum state $|q\rangle = a|0\rangle + b|1\rangle$ with $a, b \in \mathbb{R}$ has $\varphi_q = 0$ and $\vartheta_q = 2\cos^{-1}(a) = 2\sin^{-1}(b)$, as illustrated in Figure 1.8.

1.4.1 Composite Quantum Systems

Naturally, a quantum system may involve several qubits. For instance, a two-qubit state in a superposition of equiprobable states is described by

$$|q\rangle = a_0|00\rangle + a_1|01\rangle + a_2|10\rangle + a_3|11\rangle, \quad \sum_{i=0}^{3}|a_i|^2 = 1 \tag{1.4}$$

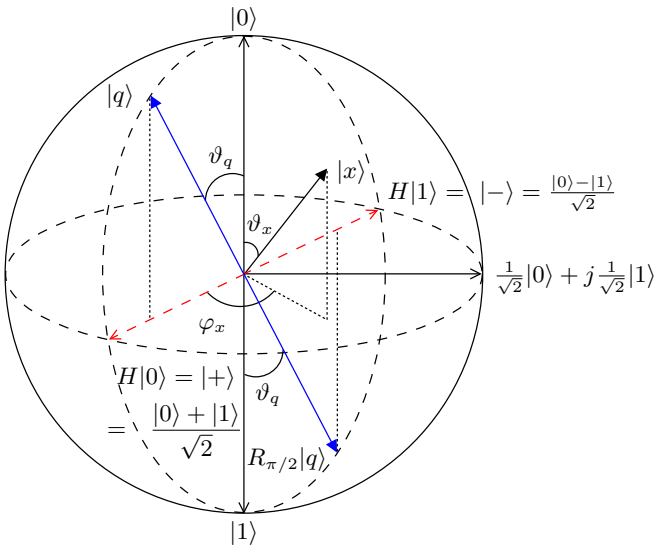

Figure 1.8: Geometrical representation of a qubit $|x\rangle = a_x|0\rangle + b_x|1\rangle = \cos\left(\frac{\vartheta_x}{2}\right)|0\rangle + e^{j\varphi_x}\sin\left(\frac{\vartheta_x}{2}\right)|1\rangle$ with $a_x \in \mathbb{R}$, $b_x \in \mathbb{C}$, $0 \leq \vartheta \leq \pi$ and $0 \leq \varphi < 2\pi$ on the Bloch sphere, along with the computational basis $\{|0\rangle, |1\rangle\}$, the sign basis $\{|+\rangle, |-\rangle\}$ and the Hadamard H operator. The rotation $R_{\pi/2}$ operator is applied on a qubit $|q\rangle = a|0\rangle + b|1\rangle = \cos\left(\frac{\vartheta_q}{2}\right)|0\rangle + e^{j\varphi_q}\sin\left(\frac{\vartheta_q}{2}\right)|1\rangle$ with $\varphi_q = 0$ and hence $a, b \in \mathbb{R}$.

where again, the square of the coefficients represents the probability of finding the two-qubit register in the corresponding state upon its observation.

A 3-qubit quantum system in a superposition of states may be described as

$$|q\rangle = \frac{1}{2\sqrt{2}}|000\rangle + \frac{1}{2\sqrt{2}}|001\rangle + \frac{\sqrt{3}}{2\sqrt{2}}|100\rangle + \frac{\sqrt{3}}{2\sqrt{2}}|101\rangle, \tag{1.5}$$

where we have $a_2 = a_3 = a_6 = a_7 = 0$ and $\sum_{i=0}^{2^3-1} |a_i|^2 = 1$. In practice, a specific scenario where this system may be found in this particular superposition of states is when unitary operators have been applied to the three qubits, which alter their state.

In this example, the second qubit is in the state $|0\rangle$, since the probability of finding it in $|1\rangle$ is zero. The third qubit can be considered to be in the superposition of equiprobable states, i.e. $|q_3\rangle = \frac{1}{\sqrt{2}}|0\rangle + \frac{1}{\sqrt{2}}|1\rangle$, since the probability of observing it in either of the states is the same according to Equation 1.5. Finally, the first qubit may be considered to be in the state of $|q_1\rangle = \frac{1}{2}|0\rangle + \frac{\sqrt{3}}{2}|1\rangle$, indicating a probability of 75% to retrieve $|0\rangle$ and 25% to observe $|1\rangle$. Hence, Equation 1.5 is derived by

$$\begin{aligned} |q\rangle =& |q_1\rangle|q_2\rangle|q_3\rangle \\ =& \left(\frac{1}{2}|0\rangle + \frac{\sqrt{3}}{2}|1\rangle\right)|0\rangle\left(\frac{1}{\sqrt{2}}|0\rangle + \frac{1}{\sqrt{2}}|1\rangle\right) \end{aligned}$$

$$=\frac{1}{2\sqrt{2}}|000\rangle + \frac{1}{2\sqrt{2}}|001\rangle + 0|010\rangle + 0|011\rangle + \frac{\sqrt{3}}{2\sqrt{2}}|100\rangle + \frac{\sqrt{3}}{2\sqrt{2}}|101\rangle + 0|110\rangle + 0|111\rangle. \quad (1.6)$$

This system's state can be equivalently represented in a vectorial form as

$$|q\rangle = \left[\frac{1}{2\sqrt{2}}, \frac{1}{2\sqrt{2}}, 0, 0, \frac{\sqrt{3}}{2\sqrt{2}}, \frac{\sqrt{3}}{2\sqrt{2}}, 0, 0\right]^T. \quad (1.7)$$

For an arbitrary n-qubit register, its state may be denoted as

$$|q\rangle = [a_0, a_1, a_2, \ldots, a_{2^n-2}, a_{2^n-1}]^T, \ \sum_{i=0}^{2^n-1} a_i^2 = 1, \quad (1.8)$$

where $|a_2|^2$ is the probability of observing the system in the state $|2\rangle = |010\rangle$ and $|a_j|^2$ is the probability of observing the system in the state $|j\rangle$, with $j = 0, 1, \ldots, 2^n - 1$. The formulation in Equation 1.8 will be used in algebraic manipulations in the following discussions. The states $|0\rangle$ and $|1\rangle$, that an 1-qubit system can be found in, may be represented in vectorial form as

$$|0\rangle = \begin{bmatrix} 1 \\ 0 \end{bmatrix}, \quad |1\rangle = \begin{bmatrix} 0 \\ 1 \end{bmatrix}. \quad (1.9)$$

The Hermitian counterpart of Equation 1.8 is referred to as a *bra* [100] and it is denoted as

$$\langle q| = |q\rangle^\dagger = [a_0^* \ a_1^* \ a_2^* \ \ldots \ a_{2^n-2}^* \ a_{2^n-1}^*], \ \sum_{i=0}^{2^n-1} |a_i^*|^2 = 1, \quad (1.10)$$

where the superscript † denotes the conjugate transpose of $|q\rangle$. It may be readily verified that the inner product obeys $\langle q||q\rangle = \langle q|q\rangle = 1$ and the outer product becomes:

$$|q\rangle\langle q| = \begin{bmatrix} |a_0|^2 & a_0 a_1^* & \cdots & a_0 a_{2^n-1}^* \\ a_1 a_0^* & |a_1|^2 & \cdots & a_1 a_{2^n-1}^* \\ \vdots & \vdots & \ddots & \vdots \\ a_{2^n-1} a_0^* & a_{2^n-1} a_1^* & \cdots & |a_{2^n-1}|^2 \end{bmatrix}. \quad (1.11)$$

1.4.2 Evolution of Quantum Systems

Unitary operators are employed to evolve a quantum system, altering the amplitude of its superposition of states a_i, but keeping the sum of the probabilities for the system to be observed to one of the superimposed states, to unity. An operator U is a unitary operator if it obeys $U^{-1} = U^\dagger$, where the superscript † denotes the conjugate transpose or the Hermitian adjoint matrix of U. Since a quantum system may be described by its quantum

state $|q\rangle$, the application of a unitary operator will transform it into the quantum state $|q'\rangle$ as in

$$|q'\rangle = U|q\rangle. \tag{1.12}$$

Two unitary operators that will be employed in our QMUD are the Hadamard operator H and the Rotation operator R_θ [43], with their one-qubit matrix representations being [43]:

$$H = \frac{1}{\sqrt{2}} \begin{bmatrix} 1 & 1 \\ 1 & -1 \end{bmatrix}, \; R_\theta = \begin{bmatrix} \cos\theta & -\sin\theta \\ \sin\theta & \cos\theta \end{bmatrix}. \tag{1.13}$$

Their effect may be interpreted as in Figure 1.9, where R_θ rotates $|q\rangle$ by θ anti-clockwise on the unit circle, while H creates an equiprobable superposition of the computational basis states, as encapsulated in

$$|0\rangle \xrightarrow{H} \frac{1}{\sqrt{2}}(|0\rangle + |1\rangle) \tag{1.14}$$

$$|1\rangle \xrightarrow{H} \frac{1}{\sqrt{2}}(|0\rangle - |1\rangle). \tag{1.15}$$

The representation of a quantum state portrayed in Figure 1.9 is only applicable when $b \in \mathbb{R}$. Comparing it to the portrayal of the quantum state as a vector on the Bloch sphere, we may conclude that the plane consisting of the computational basis $\{|0\rangle, |1\rangle\}$ and the sign basis $\{|+\rangle, |-\rangle\}$ on the Bloch sphere is mapped to the right half circle of Figure 1.9. In the case where a rotation operator R_θ results in the quantum state's vector lying on the left-hand plane in Figure 1.9, the resultant quantum state may be equivalently represented by applying a rotation gate associated with $\theta = \pi$. The application of a rotation gate with $\theta = \pi$ does not affect a quantum state, since it may be considered as applying a global phase to it, which is unobservable [43]. For example, the unitary rotation gate $R_{\pi/2}$ applied to $|q\rangle = a|0\rangle + b|1\rangle$ in Figure 1.8 and Figure 1.9 results in the state $R_{\pi/2} = -b|0\rangle + a|1\rangle$, which is equivalent to the state $|q'\rangle = -(b|0\rangle - a|1\rangle) = e^{j\pi}(b|0\rangle - a|1\rangle)$. The quantum states

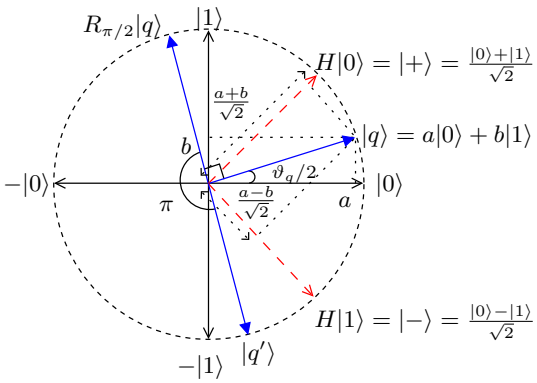

Figure 1.9: Geometrical interpretation of a qubit $|q\rangle = a|0\rangle + b|1\rangle$ with $a, b \in \mathbb{R}$, on the computational basis $\{|0\rangle, |1\rangle\}$ and the sign basis $\{|+\rangle, |-\rangle\}$, along with the Hadamard H and rotation $R_{\pi/2}$ operators.

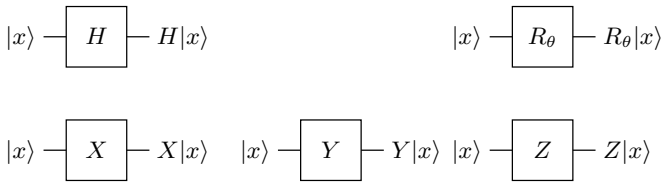

Figure 1.10: The circuit representation of the Hadamard operator, the rotation operator, the Pauli-X (NOT) gate, the Pauli-Y gate and the Pauli-Z gate.

$R_{\pi/2}|q\rangle$ and $|q'\rangle$ on the Bloch sphere of Figure 1.8 are represented by the same vector, since the amplitude of $|0\rangle$ has to be real and non-negative.

The Pauli-X, Pauli-Y and Pauli-Z operators, commonly referred to as Pauli matrices [43], are popularly used single-qubit operators. More precisely, the Pauli-X gate is the equivalent operator of the NOT gate and rotates the qubit around the X-axis of the Bloch sphere by π radians. Similarly, the Pauli-Y and Pauli-Z operators rotate the input qubit with respect to the Y-axis and Z-axis, respectively, by π radians. The matrix representations of the Pauli gates are

$$X = \begin{bmatrix} 0 & 1 \\ 1 & 0 \end{bmatrix}, \; Y = \begin{bmatrix} 0 & -i \\ i & 0 \end{bmatrix}, \; Z = \begin{bmatrix} 1 & 0 \\ 0 & -1 \end{bmatrix}. \tag{1.16}$$

The block representation of the Hadamard gate, the rotation operator and the Pauli gates is presented in Figure 1.10.

In contrast to H, R_θ and the Pauli gates, the Controlled-NOT ($CNOT$) operator [43] acts on two qubits jointly forming a Quantum Register (QR)[3], with the first qubit $|c\rangle$ being the control qubit and the second qubit $|t\rangle$ the target one. More specifically, if $|c\rangle = |1\rangle$, then the state of $|t\rangle$ is flipped, otherwise it remains intact, as encapsulated in

$$|c\rangle|t\rangle \xrightarrow{CNOT} |c\rangle|c \oplus t\rangle. \tag{1.17}$$

The circuit representation of the $CNOT$ operator is depicted in Figure 1.11. The truth table of the $CNOT$ operator is presented in Table 1.3 and its matrix representation is

$$CNOT = \begin{bmatrix} 1 & 0 & 0 & 0 \\ 0 & 1 & 0 & 0 \\ 0 & 0 & 0 & 1 \\ 0 & 0 & 1 & 0 \end{bmatrix}. \tag{1.18}$$

The QD unitary operator U_f does not have a classical counterpart and it is capable of evaluating the function f with the input qubits simultaneously representing multiple

[3] A QR is formed by any number of qubits and it exists only to underline the purpose of a set of qubits. The state of a two-qubit QR may be equivalently represented as $|q_1\rangle \otimes |q_2\rangle \equiv |q_1\rangle|q_2\rangle \equiv |q_1 q_2\rangle$.

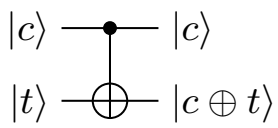

Figure 1.11: The circuit representation of the $CNOT$ gate.

Table 1.3: Truth table of the $CNOT$ gate

Input		**Output**	
c	t	c	t
0	0	0	0
0	1	0	1
1	0	1	1
1	1	1	0

arguments of the function, which is achieved by taking advantage of the superposition of states. More explicitly, it accepts two QRs as inputs, with the first QR $|x\rangle$ containing the argument, while the second QR is formed by the specific number of bits Z that we desire the function's evaluation to be approximated in. This second QR is initialized to the all-zero state $|0\rangle^{\otimes Z}$[4], as depicted in Figure 1.12, where the numeric kets subscripts distinguish the QRs employed. Assuming n qubits in the QR $|x\rangle_1 = H|0\rangle_1^{\otimes n}$ and having initialized it in an equiprobable superposition of states by applying a Hadamard gate, the system's quantum state before the application of U_f would be

$$\begin{aligned} |\psi_1\rangle &= |x\rangle_1|0\rangle_2^{\otimes Z} = H|0\rangle_1^{\otimes n}|0\rangle_2^{\otimes Z} \\ &= \left(\sum_{q=0}^{2^n-1} \frac{1}{\sqrt{2^n}}|q\rangle_1\right)|0\rangle_2^{\otimes Z} \\ &= \sum_{q=0}^{2^n-1}\left(\frac{1}{\sqrt{2^n}}|q\rangle_1|0\rangle_2^{\otimes Z}\right), \end{aligned} \tag{1.19}$$

where the integer values in q correspond to their respective binary values as for example in $|q\rangle = |5\rangle = |101\rangle$. The unitary operator U_f will evolve the system into

$$\begin{aligned} |\psi_2\rangle &= U_f \sum_{q=0}^{2^n-1}\left(\frac{1}{\sqrt{2^n}}|q\rangle_1|0\rangle_2^{\otimes Z}\right) \\ &= \sum_{q=0}^{2^n-1}\left(\frac{1}{\sqrt{2^n}}|q\rangle_1|f(q)\rangle_2\right). \end{aligned} \tag{1.20}$$

The U_f operator creates a strange connection between the two QRs. If only the first QR shown in Figure 1.12 is observed in the QD and $|x\rangle_1 = |0\rangle_1$ is obtained, then the second QR seen in Figure 1.12 will be in the $|f(0)\rangle_2$ state with 100% probability. Similarly, if we

[4]The Z-element tensor product is defined as: $|0\rangle^{\otimes Z} = \underbrace{|0\rangle \otimes |0\rangle \otimes \cdots \otimes |0\rangle}_{Z} = \underbrace{|0\rangle|0\rangle \ldots |0\rangle}_{Z} = \underbrace{|00\ldots0\rangle}_{Z}$

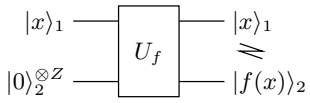

Figure 1.12: Unitary operator U_f entangling the f evaluations with the corresponding input argument. The subscripts of the kets are used to distinguish the QRs throughout a circuit analysis.

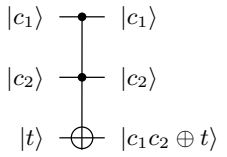

Figure 1.13: The circuit representation of the Tofffoli gate.

have $|f(x)\rangle_2 = |f(1)\rangle_2$ after an act of QD observation, then we have $|x\rangle_1 = |1\rangle_1$ with 100% probability. This peculiar connection is referred to as entanglement, as detailed in [43].

Any classical circuit may be converted to an equivalent circuit in the QD by using the unitary operators H, R_θ and $CNOT$ [43]. Additionally, any classical circuit may become reversible in the QD in the sense defined in [43] with the aid of the Toffoli gate, or equivalently by using the Controlled-Controlled-NOT ($CCNOT$) gate, and auxiliary qubits [43]. The circuit representation of the Toffoli gate is presented in Figure 1.13, which accepts two control qubits and flips the state of the target qubit, if and only if both control qubits are in the state $|1\rangle$. The matrix representation of the Toffoli gate is [43]:

$$CCNOT = \begin{bmatrix} 1 & 0 & 0 & 0 & 0 & 0 & 0 & 0 \\ 0 & 1 & 0 & 0 & 0 & 0 & 0 & 0 \\ 0 & 0 & 1 & 0 & 0 & 0 & 0 & 0 \\ 0 & 0 & 0 & 1 & 0 & 0 & 0 & 0 \\ 0 & 0 & 0 & 0 & 1 & 0 & 0 & 0 \\ 0 & 0 & 0 & 0 & 0 & 1 & 0 & 0 \\ 0 & 0 & 0 & 0 & 0 & 0 & 0 & 1 \\ 0 & 0 & 0 & 0 & 0 & 0 & 1 & 0 \end{bmatrix}. \tag{1.21}$$

Figure 1.14 shows a variation of the $CNOT$ and the Toffoli gates, where the controlled operation is performed on the target qubit if the control qubits are in the $|0\rangle$ state. This variation is equivalent to passing the control qubits through a NOT gate before performing the original CNOT or Toffoli gate operation, as presented in Figure 1.14.

The implementation of U_f will be based on the QD equivalent of the classical circuit that computes $f : \{0,1\}^{\otimes n} \rightarrow \{0,1\}^{\otimes Z}$. The time required for a single application of U_f compared to that for a single classical evaluation of f will depend on the technology used for creating U_f. In our analysis we will assume that these times are equal, since the same

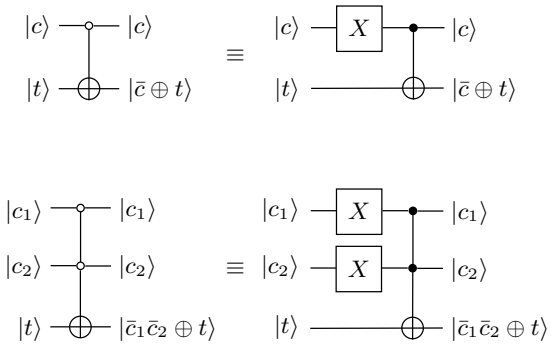

Figure 1.14: Variation of the *CNOT* and Toffoli gates, where the controlled operation is performed if the control qubits are in the $|0\rangle$ state.

has been assumed in the literature [49, 51, 52].

1.4.3 Measurement of Quantum States

When stating the terms of "measurement" or "observation", so far we have been referring to measurements with respect to the computational or standard basis $\{|0\rangle, |1\rangle\}$. If an 1-qubit quantum system is observed, its state after the measurement would be either $|0\rangle$ or $|1\rangle$, depending on the observation's result. However, measurements may be performed in a diverse base. In fact, the number of different bases that a qubit may be observed in is infinite [43]. A commonly used alternative basis the qubit may be measured in is the Hadamard or sign basis $\{|+\rangle, |-\rangle\}$ portrayed in Figure 1.8 and Figure 1.9, where we have:

$$|+\rangle = \frac{1}{\sqrt{2}}|0\rangle + \frac{1}{\sqrt{2}}|1\rangle \tag{1.22}$$

$$|-\rangle = \frac{1}{\sqrt{2}}|0\rangle - \frac{1}{\sqrt{2}}|1\rangle. \tag{1.23}$$

The specific reason for using a particular basis depends on the application. For example, if the intention of the observation is to determine which specific part of the Cartesian plane the qubit $|q\rangle = a|0\rangle + b|1\rangle$ lies on, then a measurement on the Hadamard basis would resolve whether we have $a \cdot b > 0$ or $a \cdot b < 0$, hence again determining the particular part of the plane the qubit exists on. By contrast, if an observation was made on the computational basis for the same purpose, then the resultant state would be mapped to one of the coordinate axes seen in Figure 1.8 and Figure 1.9, hence providing us with no particular clue as to its quadrant.

The representation of a qubit $|q\rangle$ on the computational basis is $|q\rangle = a|0\rangle + b|1\rangle$. In order to convert its representation to the sign basis, we exploit the fact that

$$|0\rangle = \frac{|+\rangle + |-\rangle}{\sqrt{2}} \tag{1.24}$$

$$|1\rangle = \frac{|+\rangle - |-\rangle}{\sqrt{2}}. \tag{1.25}$$

Hence, the same qubit may be represented in the sign basis as

$$|q\rangle = \frac{a+b}{\sqrt{2}}|+\rangle + \frac{a-b}{\sqrt{2}}|-\rangle \tag{1.26}$$

and the probability of getting the state $|+\rangle$ or $|-\rangle$ after a potential observation on the Hadamard basis is $\frac{|a+b|^2}{2}$ and $\frac{|a-b|^2}{2}$, respectively. If the observation's outcome is $|+\rangle$, then the state of the system after the observation will be $|+\rangle = \frac{1}{\sqrt{2}}(|0\rangle + |1\rangle)$. Similarly, if the observation's outcome is $|-\rangle$, then the resultant system's state will be $|-\rangle = \frac{1}{\sqrt{2}}(|0\rangle - |1\rangle)$.

1.4.3.1 Partial Measurement of Quantum States

As far as a multiple-qubit system is concerned, the measurement procedure is similar to the one analysed for a single-qubit system. For example, when considering a 2-qubit system, its general quantum state is presented in Equation 1.4. As in any quantum system, a potential measurement will only be able to reveal as many bits of information as the number of qubits in the system. In the 2-qubit system considered a measurement of the two qubits would yield the result $|00\rangle$ with probability $|a_{00}|^2$, or the state $|01\rangle$ with probability $|a_{01}|^2$ or in general the bit string $s \in \{0,1\}^2$ with probability $|a_s|^2$. The state of the quantum system after the measurement would be $|s\rangle$.

However, it is possible to measure only a subset of the qubits that a quantum system consists of by performing a *partial measurement*. Let us assume that in our example of a 2-qubit system we intend to observe only the second qubit. The probabilities of obtaining the second qubit in the state of $|0\rangle$ or $|1\rangle$ are

$$P_q(\text{x0}) = P_q(00) + P_q(10) = |a_{00}|^2 + |a_{10}|^2 \tag{1.27}$$

$$P_q(\text{x1}) = P_q(01) + P_q(11) = |a_{01}|^2 + |a_{11}|^2. \tag{1.28}$$

In other words, the probability of obtaining the second qubit in the state of $|0\rangle$ upon its measurement is equal to the probability of observing the full system in the states that have the second qubit equal to $|0\rangle$.

The main difference of the partial measurement compared to the full measurement of a quantum system lies in the gravity of the perturbation imposed on the system's original state and the resultant state. Following the same example, let us assume that the result of the second qubit's observation was $|0\rangle$. The new state of the system after the partial measurement will include all the states that are consistent with the measurement's specific outcome. Hence we have

$$|q_{\text{new}}\rangle = a_{00,\text{new}}|00\rangle + a_{10,\text{new}}|10\rangle, \tag{1.29}$$

where $a_{00,\text{new}}$ and $a_{10,\text{new}}$ are the new amplitudes of the legitimate remaining states. The new amplitudes will be the normalized versions of the corresponding amplitudes of the

original states before the measurement, resulting in

$$|q_{\text{new}}\rangle = \frac{a_{00}|00\rangle + a_{10}|10\rangle}{\sqrt{|a_{00}|^2 + |a_{10}|^2}}. \tag{1.30}$$

Any following measurement of the second qubit in the new quantum state $|q_{\text{new}}\rangle$ will result in the state $|0\rangle$ with 100% probability.

1.4.4 Entanglement

The new state after the partial measurement may be written as

$$\begin{aligned} |q_{\text{new}}\rangle &= \left(\frac{a_{00}}{\sqrt{|a_{00}|^2 + |a_{10}|^2}}|0\rangle + \frac{a_{10}}{\sqrt{|a_{00}|^2 + |a_{10}|^2}}|1\rangle \right) |0\rangle \\ &= (a_{00,\text{new}}|0\rangle + a_{10,\text{new}}|1\rangle) \otimes |0\rangle. \end{aligned} \tag{1.31}$$

As seen in Equation 1.31, the resultant quantum system consisting of two qubits may be decomposed in a way, where the composite quantum states are represented by the tensor products of the qubits. Another example is the 3-qubit quantum state presented in Equation 1.5 which may be decomposed as seen in Equation 1.6. The information that can be gained by the decomposition of Equation 1.6 is that the first qubit of the system is in the state $\frac{1}{2}|0\rangle + \frac{\sqrt{3}}{2}|1\rangle$, regardless of the states the rest of the qubits are in. Similar knowledge may be obtained for the second and third qubit. The quantum system is referred to as being "unentangled", if it is able to be decomposed i.e. it is decomposable.

However, this decomposition is not possible for every quantum state. Let us consider for example the quantum state of a 2-qubit system, which is initially in the state $|\psi_0\rangle = |00\rangle$, as seen in Figure 1.15. Once the first qubit passes through the Hadamard gate, the system's state becomes

$$\begin{aligned} |\psi_1\rangle &= (H|0\rangle_1)|0\rangle_2 \\ &= \left(\frac{1}{\sqrt{2}}|0\rangle_1 + \frac{1}{\sqrt{2}}|1\rangle_1 \right) |0\rangle_2 \\ &= \frac{1}{\sqrt{2}} \left(|00\rangle + |10\rangle \right). \end{aligned} \tag{1.32}$$

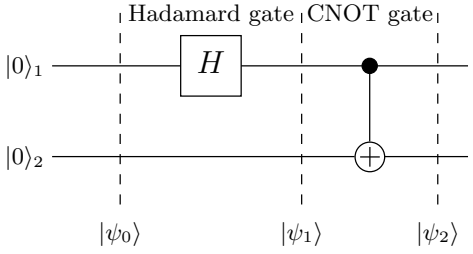

Figure 1.15: Quantum circuit for generating the entnagled Bell state $\frac{1}{\sqrt{2}}(|00\rangle + |11\rangle)$.

When the two qubits pass through the $CNOT$ gate, the first qubit $|\psi_1\rangle_1 = \frac{1}{\sqrt{2}}(|0\rangle + |1\rangle)$ acts as the control qubit to the second qubit $|\psi_1\rangle_2 = |0\rangle$, which is the target qubit. The transfer matrix of the $CNOT$ gate relying on the first qubit acting as the control qubit and the second qubit as the target qubit may be formulated as

$$CNOT = \begin{bmatrix} 1 & 0 & 0 & 0 \\ 0 & 1 & 0 & 0 \\ 0 & 0 & 0 & 1 \\ 0 & 0 & 1 & 0 \end{bmatrix}. \tag{1.33}$$

The final state of the system after passing it through the $CNOT$ gate becomes:

$$\begin{aligned} |\psi_2\rangle &= CNOT \cdot |\psi_1\rangle \\ &= \begin{bmatrix} 1 & 0 & 0 & 0 \\ 0 & 1 & 0 & 0 \\ 0 & 0 & 0 & 1 \\ 0 & 0 & 1 & 0 \end{bmatrix} \cdot \frac{1}{\sqrt{2}} \begin{bmatrix} 1 \\ 0 \\ 1 \\ 0 \end{bmatrix} \\ &= \frac{1}{\sqrt{2}} \begin{bmatrix} 1 & 0 & 0 & 1 \end{bmatrix}^T \\ &= \frac{1}{\sqrt{2}} (|00\rangle + |11\rangle). \end{aligned} \tag{1.34}$$

The resultant state $|\psi_2\rangle = \frac{1}{\sqrt{2}}(|00\rangle + |11\rangle)$ cannot be decomposed into a state representing the first qubit and a state corresponding to the second qubit. This may be readily shown by attempting to decompose $|\psi_2\rangle$ into separate states. Let us assume that the state of the first qubit is $|\psi_2\rangle_1 = a_{10}|0\rangle + a_{11}|1\rangle$ and the state of the second qubit is $|\psi_2\rangle_2 = a_{20}|0\rangle + a_{21}|1\rangle$. The resultant composite system of these two qubits would become:

$$\begin{aligned} |\psi_2\rangle_1 \otimes |\psi_2\rangle_2 &= (a_{10}|0\rangle + a_{11}|1\rangle)(a_{20}|0\rangle + a_{21}|1\rangle) \\ &= a_{10}a_{20}|00\rangle + a_{10}a_{21}|01\rangle + \\ &+ a_{11}a_{20}|10\rangle + a_{11}a_{21}|11\rangle. \end{aligned} \tag{1.35}$$

In order for the state in Equation 1.35 to be equal to $|\psi_2\rangle$, the amplitudes of $|00\rangle$ and $|11\rangle$ should be non-zero. This leads to $a_{10}, a_{11}, a_{20}, a_{21} \neq 0$. At the same time, the amplitudes of $|01\rangle$ and $|10\rangle$ should be equal to 0, leading to either $a_{10} = 0$ or $a_{21} = 0$ and at the same time $a_{11} = 0$ or $a_{20} = 0$. The latter constraints contradict the former ones, making it impossible for the quantum state $|\psi_2\rangle$ to be decomposed.

A system that is not possible to decompose to separate states corresponding to its constituent qubits is termed as "entangled". When one of the two qubits of the state $|\psi_2\rangle$

is observed, the outcome might be $|0\rangle$ with a probability of 1/2 or $|1\rangle$ with a probability of 1/2. If the outcome is 0, then a potential measurement of the second qubit will yield 0 with a probability of 1. Symmetrically, if the outcome of the first qubit's observation is 1, then a measurement of the second qubit will surely result in 1. It seems that a connection exists between these two qubits, relating them to each other, regardless of their spatial distance. This non-intuitive relationship between two entangled qubits was referred to by Einstein as a "spooky action in a distance" [102].

In fact, the state $|\psi_2\rangle$ is one of the four Bell basis states, named after John S. Bell [43], which are constituted by the following four entangled states

$$|\Phi^+\rangle = \frac{1}{\sqrt{2}}(|00\rangle + |11\rangle) \tag{1.36}$$

$$|\Phi^-\rangle = \frac{1}{\sqrt{2}}(|00\rangle - |11\rangle) \tag{1.37}$$

$$|\Psi^+\rangle = \frac{1}{\sqrt{2}}(|01\rangle + |10\rangle) \tag{1.38}$$

$$|\Psi^-\rangle = \frac{1}{\sqrt{2}}(|01\rangle - |10\rangle). \tag{1.39}$$

As for any other orthonormal basis defined over $\mathbb{C}^4$, a 2-qubit system may be measured on the Bell basis. None of the states of the Bell basis can be decomposed to the separate states constituted by each qubit.

1.5 Thesis Structure

Three quantum search algorithms that we will employ in our systems are investigated at a tutorial-based pace in the context of their application as coherent hard-output QMUDs in CDMA and SDMA communication systems in Chapter 2. The novel quantum weighted sum algorithm is investigated in Section 3.4, while in Section 3.5 we present soft-input soft-output QMUDs, which may be integrated in iterative receivers based on the quantum algorithms considered. Furthermore, we evaluate their performance in DSS-aided Slow SubCarrier Hopping (SSCH) SDMA-OFDM and MC-IDMA systems. Chapter 4 includes novel quantum-assisted MSDDs designed for performing non-coherent multi-stream detection, where the knowledge of the CIRs is no longer required at the BS, albeit this imposes a performance degradation. Finally, our conclusions are offered in Chapter 5. The flow chart of the treatise's structure is presented in Figure 1.16, and describes the quantum algorithms that will be analysed, the QMUDs that are conceived by using these algorithms, as well as the multiple access systems they are evaluated on.

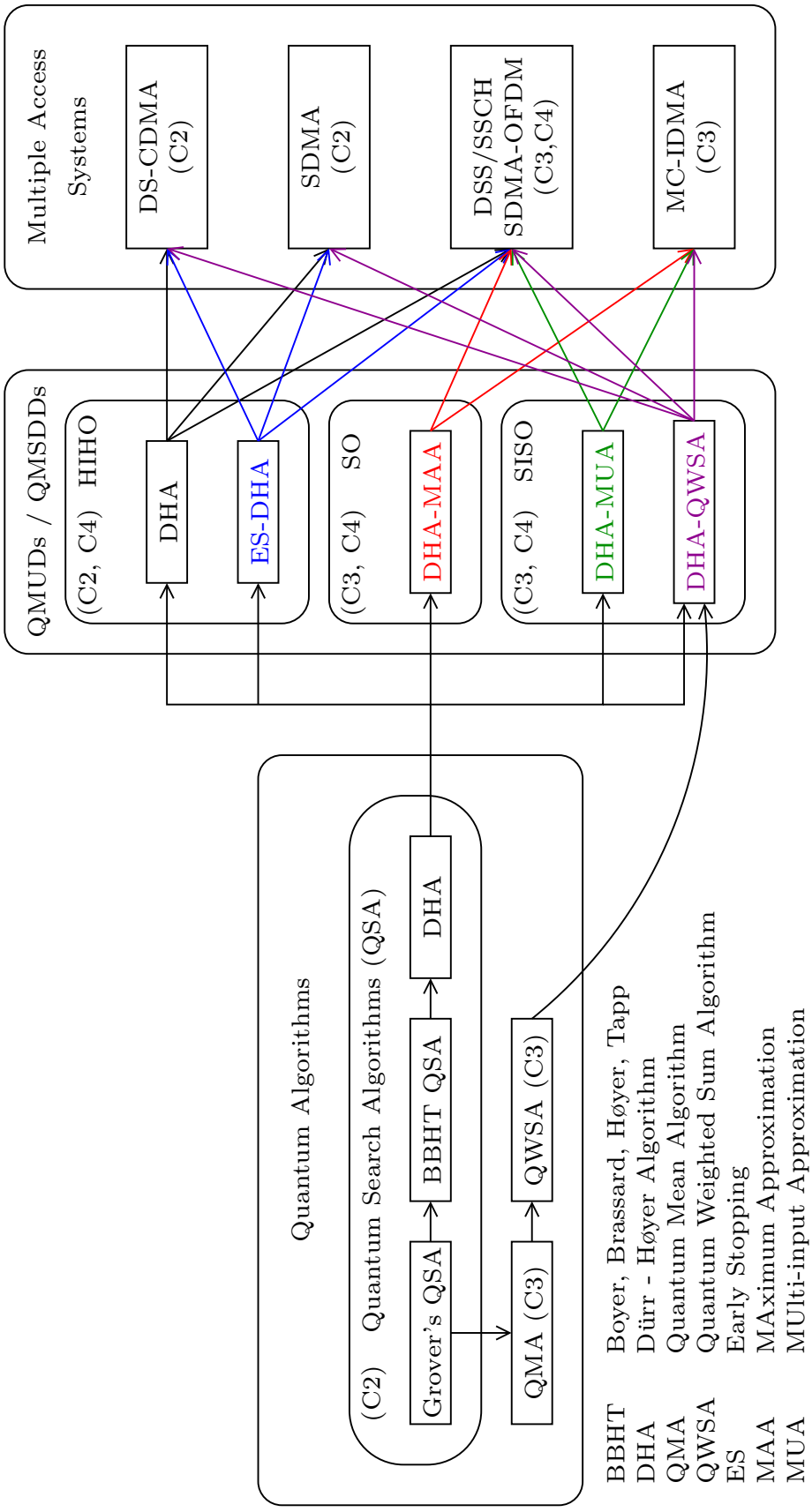

Figure 1.16: The quantum algorithms, QMUDs / QMSDDs and multiple access systems that will be investigated in this treatise, in the respective chapters included in the parentheses. The connections between the quantum algorithms and the quantum-assisted detectors indicate that these specific algorithms are the construction blocks of the corresponding detectors. The QMUDs and QMSDDs are employed and tested in the specific multiple access systems with which they are connected.

Chapter 2

Hard-Output Quantum-Assisted Multi-User Detection

2.1 Introduction

In this Chapter, several quantum search algorithms will be investigated in the context of Hard-Input Hard-Output (HIHO) multi-user detection in DS-CDMA and SDMA systems. The minimization of a CF is frequently required in diverse sections of a communication system, such as in detection and decoding at the receiver, in resource and power allocation, as well as when determining the optimal routing path in large multi-hop networks. A specific optimal HIHO MUD is constituted by the Maximum Likelihood (ML) MUD [103]. At the same time, when iterative receivers are used, the definition of an optimization CF requires further in-depth discussions. Specifically, in these cases, the summation of multiple CF evaluations (CFE) is required for approaching the ultimate performance limit constituted by the Soft-Input Soft-Output (SISO) Maximum *A posteriori* Probability (MAP) MUD.

The complexity of the optimal ML MUD [103] exhibits an exponential increase with the number of users, which prohibits its employment when many simultaneous users are supported by the system. Based on the superimposed constellations, the ML MUD exploits the Euclidean distance of the legitimate multi-level symbols with respect to the received multi-level symbol. Explicitly, the Euclidean distance is considered as the CF. In a system supporting U users employing M-ary modulation, the ML MUD uses M^U CFEs per time slot, which become excessive when U and M are large. Hence reduced-complexity solutions have been developed, such as the decorrelating and the Minimum Mean-Square Error (MMSE) MUDs [104], the iterative linear MMSE MUD [105], as well as the successive interference cancellation aided detector [106] and the family of iterative interference cancellers [107]. Following an approach, where the aim is to directly minimize the system's BER, the Minimum BER (MBER) detector was conceived [108, 109]. MUDs that can be integrated into an iterative receiver, providing soft decisions for the decoder, while accepting soft estimates from the decoder, have also been proposed [12, 110, 111].

Even though the concept of the MUD was introduced due to the suppression of the MUI in CDMA systems, it may be also applied in the uplink Multi-User Multiple-Input Multiple-Output (MU-MIMO) systems, where multiple users transmit to a BS with MFAAs [7, 9]. When the separation of the users' signals is performed depending on their unique, user-specific Channel Impulse Responses (CIR), we refer to SDMA schemes [14–16]. Because of the similarity between the CDMA uplink's system model and that of the Space Division Multiplexing (SDM)-aided uplink [41], the MUDs employed in the CDMA systems may also be applied in the SDMA systems. The main difference is that in SDMA systems the users are only separated by their CIR, in contrast to the CDMA systems where the users were also separated according to a user-specific spreading code, but requiring more bandwidth.

Linear MIMO detectors include the Zero-Forcing (ZF) [112] and the MMSE [113] detectors, which are less computationally complex than their non-linear counterparts but experience a worse performance especially when the number of users supported is larger than the number of antennas at the BS. Another example of linear MIMO detector is the MBER detector [14, 109] employing the Least BER (LBER) algorithm [114] which selects the multi-level symbols that minimize the system's BER rather than the MMSE criterion. The optimal non-linear HIHO MIMO detector is the ML MUD as in the case of CDMA systems. The extremely high computational complexity required by the ML MUD has resulted in the invention of less complex near-optimal and sub-optimal non-linear detectors. An example of a near-optimal detector is the tree search-based Sphere Detector (SD) [115–117] which limits the search space based on a user-defined parameter –for example a maximum value of a metric– and performs brute-force search at the remaining multi-level symbols like the ML MUD. The Fixed-Complexity Sphere Decoder (FCSD) [118] employs the SD up to a predetermined level and then the ZF detector takes over and determines the multi-level symbol.

Bio-inspired heuristic algorithms have also been conceived for shrinking the search space by performing a random-guided search, and are capable of near-optimal MUD. For example, Genetic Algorithm (GA)-based MUDs have been proposed in [23, 111, 119–122]. Furthermore, an Ant Colony Optimization (ACO) algorithm-based MUD was proposed for the uplink of a synchronous MFAA-assisted MC DS-CDMA system in [13], while its soft-output version, termed as the multi-input-approximation (MUA)-assisted soft output-ACO MUD, was presented in [63]. By exploiting the sheer power of Particle Swarm Optimization (PSO) algorithms, PSO-based MUDs were proposed in [123–125], while further low-complexity suboptimal MUDs were presented in [126, 127]. Quantum-inspired MUDs have also been proposed, adopting quantum-domain attributes in the classical domain. Representative examples of quantum-inspired MUDs are the combinations of the heuristic algorithms combined with quantum principles, such as the quantum PSO-based MUDs of [128–131], the quantum GA-optimized neural network employed for signal detection in [132], and the quantum GA-based MUDs of [128, 133, 134].

With the emergence of large-scale MIMO schemes [135–137] in combination with the millimeter wave transmissions [17], which allows numerous antennas to be installed in a compact space, we need yet optimal low-complexity detectors. The computational com-

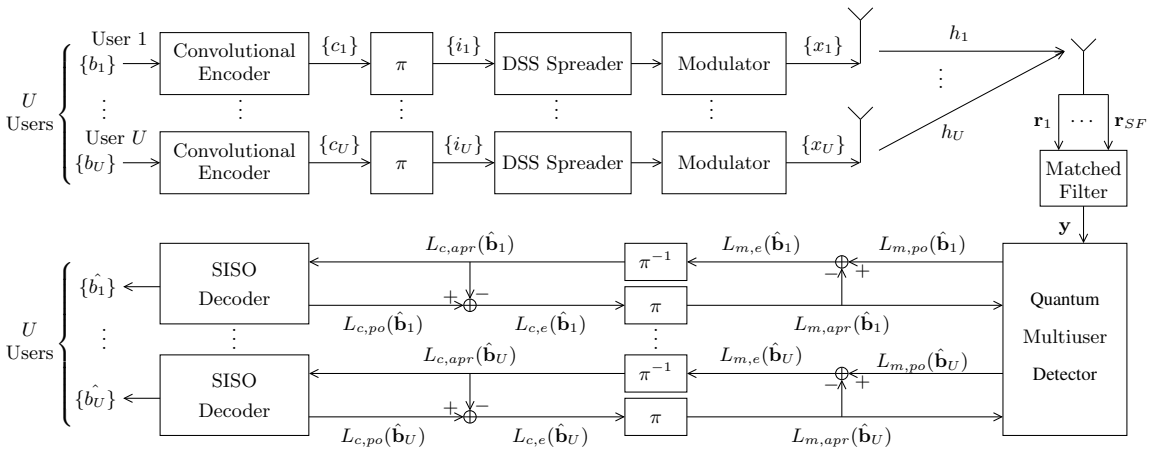

Figure 2.1: DS-CDMA system's block diagram with BICM-ID, U users and quantum-assisted multi-user detection in an iterative receiver. The matched filter provides an initial estimate of the transmitted multi-level symbol.

plexity of the optimal ML MUD might be excessive for its implementation, while the low-complexity MUDs tend to be suboptimal. For the sake of circumventing this design-dilemma, low-complexity optimal QMUDs may be designed by exploiting the inherent parallelism of quantum computing. In this chapter, as well as in the following one, we conceive coherent QMUDs, therefore it is assumed that channel state estimation is taking place; an assumption that may prove impractical in large-scale MIMO systems relying on millimeter wave mobile communications. As a further advance, Chapter 4 presents non-coherent HIHO and SISO QMUDs, for the sake of circumventing the problem of channel state estimation in systems associated with hundreds of channels.

The communication systems, namely the DS-CDMA and SDMA systems, we will apply the proposed HIHO QMUD schemes in are presented in Section 2.2 and Section 2.3. Section 2.4 introduces Grover's Quantum Search Algorithm (QSA), the Boyer-Brassard-Høyer-Tapp (BBHT) QSA and the Dürr-Høyer Algorithm (DHA), which are exploited in our proposed QMUDs. The resultant computational complexity of the proposed QMUDs applied to our DS-CDMA and SDMA systems are presented in their corresponding Section. The design methodology of the HIHO DHA-aided QMUDs is analysed in Section 2.5. Various DS-CDMA and SDMA systems are investigated in Section 2.6, where the achieved performance of the proposed QMUDs is stated and the trade-off between performance and computational complexity is investigated. Finally, our conclusions are offered in Section 2.7.

2.2 DS-CDMA System Overview

Bit-Interleaved Coded Modulation (BICM) with Iterative Decoding (ID) will be used in our uplink communications system presented in Figure 2.1. The information bit stream $\{b_u\}$ of each user is encoded into the stream $\{c_u\}$ by a convolutional encoder, which is passed through pseudo-random bit-based interleavers. Then, the interleaved bits $\{i_u\}$ are spread by the user-specific DS-CDMA sequences of the codebook $\mathbf{C}$ and are modulated onto the symbols $\{x_u\}$, which are transmitted over uncorrelated Rayleigh channels over T time slots.

The channel matrix $\mathbf{H}$ is assumed to be perfectly estimated at the BS. Moreover, the DS-CDMA codebook $\mathbf{C} = [\mathbf{c}_1, \ldots, \mathbf{c}_U]$ storing $\mathbf{c}_u = [c_{u,1} \ldots c_{u,SF}]^T$ employed by the individual users having a specific Spreading Factor (SF) is known at the BS. On the other hand, the thermal noise imposed at the receiver, along with the time delay introduced during the propagation is unknown. However, since we assume non-dispersive Rayleigh fading, only the noise levels are unknown.

The classical optimal MUD that accepts soft inputs and provides soft outputs is the one that computes the bit Log-Likelihood Ratios (LLR) of every bit of every symbol of each user. Let us consider a multi-user system supporting U users and employing an M-ary modulation scheme. Omitting the time superscript, the Matched Filter's (MF) outputs during a single time slot are described by

$$\begin{aligned} \mathbf{y} &= \mathbf{C}^H \mathbf{C}\mathbf{H}\mathbf{x} + \mathbf{C}^H \mathbf{n} \\ &= \mathbf{R}\mathbf{x} + \tilde{\mathbf{n}}, \end{aligned} \tag{2.1}$$

where $\mathbf{y} = [y_1, \ldots, y_U]^T$ includes each user's MF output during the same time slot, $\mathbf{x} = [x_1, \ldots, x_U]^T$ is the multi-level symbol, $\mathbf{n} = [n_1, \ldots, n_{SF}]^T$ contains the complex-valued thermal noise at the BS, where we have $\mathbf{R} = \mathbf{C}^H\mathbf{C}\mathbf{H}$ and $\tilde{\mathbf{n}} = \mathbf{C}^H\mathbf{n} = [\tilde{n}_1, \ldots, \tilde{n}_U]^T$.

2.2.1 Maximum *A posteriori* Probability MUD

The bit-based soft-metric computed by the MAP MUD is the *a posteriori* information of the encoded, interleaved bits, which is presented in terms of the LLRs as [10]:

$$\begin{aligned} L_{m,po}\left(b_u^{(m)}\right) &= \ln \frac{P\left(b_u^{(m)} = 0|\mathbf{y}\right)}{P\left(b_u^{(m)} = 1|\mathbf{y}\right)} \\ &= \ln \frac{\left[\sum\limits_{\mathbf{x}\in\chi(u,m,0)} p\left(\mathbf{y}|\mathbf{x}\right) P(\mathbf{x})\right] / p(\mathbf{y})}{\left[\sum\limits_{\mathbf{x}\in\chi(u,m,1)} p\left(\mathbf{y}|\mathbf{x}\right) P(\mathbf{x})\right] / p(\mathbf{y})}, \end{aligned} \tag{2.2}$$

where the subscript u is the index of the specific user $u \in \{1, \ldots, U\}$ the bit belongs to, the superscript $m \in \{1, \ldots, \log_2(M)\}$ denotes the index of the particular bit for which the LLR is computed in the current symbol of the uth user, M is the size of the modulation constellation, $\chi(u, m, v)$ is the set of multi-level symbols for which the $[u\log_2(M) + m]$th bit is equal to v, $P(\mathbf{x})$ is the *a priori* probability of the multi-level symbol $\mathbf{x}$, $p(\mathbf{y})$ is the model's likelihood, which reflects the Probability Density Function (PDF) of receiving $\mathbf{y}$ as [10]:

$$p(\mathbf{y}) = \sum_{\mathbf{x}} p\left(\mathbf{y}|\mathbf{x}\right) P(\mathbf{x}), \tag{2.3}$$

and finally, $p(\mathbf{y}|\mathbf{x})$ is the CF, which represents the PDF of having received $\mathbf{y}$, given that the multi-level symbol $\mathbf{x}$ was transmitted [10]:

$$f(\mathbf{x}) = p(\mathbf{y}|\mathbf{x}) = \frac{1}{\sigma\sqrt{2\pi}} \exp\left(-\left\|\mathbf{y} - \mathbf{R}\mathbf{x}\right\|^2 / 2\sigma^2\right), \tag{2.4}$$

where $2\sigma^2$ is the noise variance. Assuming the independence of the bits in a symbol, the *a priori* symbol probability is equal to the product of the *a priori* bit probabilities that the symbol was created from, i.e. we have

$$P(\mathbf{x}) = P\left(b_1^{(1)}\right) \cdot \ldots P\left(b_1^{(\log_2(M))}\right) \cdot \ldots P\left(b_U^{(\log_2(M))}\right). \tag{2.5}$$

It should be noted that $M^U/2$ CF evaluations are required in the summation in each of the numerator and denominator of Equation 2.2.

The extrinsic LLRs are passed to the U Max-Log *A Posteriori Probability* (APP) decoders [10], which in turn feed the QMUD with symbol probabilities, given the received channel-encoded soft sequence. These iterations are continued for a specific number of iterations. During the first iteration, or if the MUD is not part of an iterative procedure, as in non-iterative BICM, all the symbols have equal *a priori* probabilities, since no extrinsic information is available.

2.2.2 Maximum Likelihood MUD

When a HIHO MUD is employed, there are no iterations between the MUD and the U Max-Log APP decoders. The optimal ML MUD finds the specific multi-level symbol $\mathbf{x}_{\max}$ that maximizes the CF in Equation 2.4 after

$$\mathcal{C}_{MAP} = \mathcal{C}_{ML} = \frac{M^U}{U \cdot \log_2(M)} \tag{2.6}$$

CFEs per bit and forwards it to the Max-Log APP decoders. Note that the number of CFEs per bit is the same in the ML and MAP MUDs, when the CF values are stored and reused during each MUD-decoder iteration. In this chapter we will propose HIHO QMUDs and compare their performance to the ML MUD, as well as the MF, ZF and MMSE detectors. In Chapter 3 we present SISO QMUDs that perform equivalently to the optimal SISO MAP MUD, while requiring fewer cost function evaluations.

2.3 Spatial Division Multiple Access System Overview with Multiple Antennas

The system model of an SDMA-MIMO system's uplink is presented in Figure 2.2. Initially, the information bit stream $\{b_u\}$, $u \in \{1, 2, \ldots, U\}$, of each user is encoded into the bit stream $\{c_u\}$. After interleaving, the resultant bit stream $\{i_u\}$ is modulated in the symbol

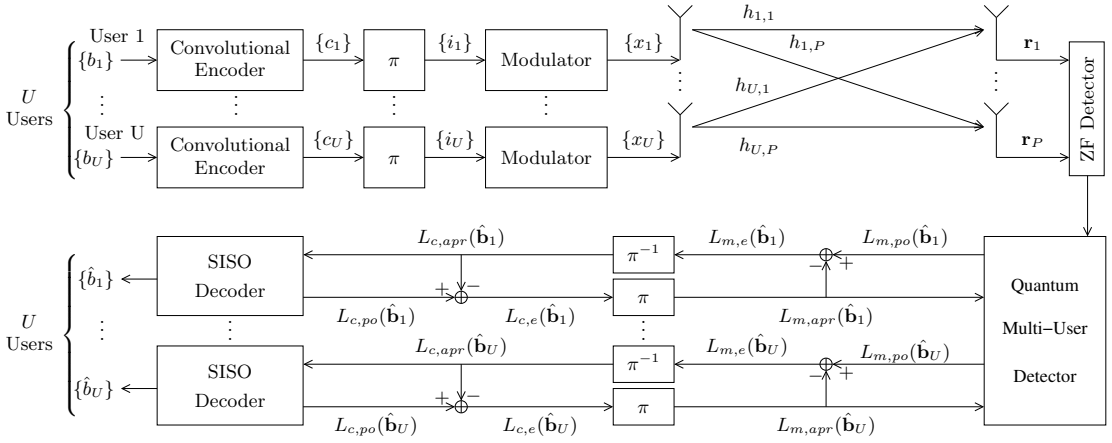

Figure 2.2: Block diagram of an SDMA-MIMO system's uplink supporting U users with a single antenna each and P antennas at the BS. Quantum-assisted multi-user detection is employed at the iterative receiver of the BS. The ZF detector provides an initial estimate of the transmitted multi-level symbol and it may be replaced by the MMSE detector for the same purpose.

stream $\{x_u\}$. The users transmit their respective symbol stream simultaneously, each using a single antenna. The users are also assumed to be physically separated, therefore the non-dispersive uncorrelated Rayleigh channels initiating from different transmitting antennas are assumed not to be correlated. At the BS, the received signal during a single time slot may be described as

$$\mathbf{r} = \mathbf{H}\mathbf{x} + \mathbf{n}, \tag{2.7}$$

where $r = [r_1, r_2, \ldots, r_P]^T$ includes the received signal at each of the receiver antennas, $\mathbf{H} \in \mathbb{C}^{P \times U}$ is the channel matrix containing the CSI of every channel, $\mathbf{x} = [x_1, x_2, \ldots, x_U]^T$ is the transmitted multi-level symbol vector and $\mathbf{n} = [n_1, n_2, \ldots, n_P]^T$ contains the AWGN imposed at each of the P antennas at the BS. The channel matrix $\mathbf{H}$ is assumed to be perfectly estimated at the BS. Please note the similarity of the received signal at the SDMA system with respect to that of the DS-CDMA system, where the only difference lies on the DS-CDMA codebook $\mathbf{C}$.

2.3.1 Maximum *A posteriori* Probability MUD

As in the case of MUDs in CDMA systems, the soft-input soft-output MUDs in the SDMA scenario will calculate the *a posteriori* information of the encoded, interleaved bits presented in terms of the LLRs as [10]

$$\begin{aligned} L_{m,po}\left(b_u^{(m)}\right) &= \ln \frac{P\left(b_u^{(m)} = 0|\mathbf{r}\right)}{P\left(b_u^{(m)} = 1|\mathbf{r}\right)} \\ &= \ln \frac{\left[\sum_{\mathbf{x} \in \chi(u,m,0)} p\left(\mathbf{r}|\mathbf{x}\right) P(\mathbf{x})\right] / p(\mathbf{r})}{\left[\sum_{\mathbf{x} \in \chi(u,m,1)} p\left(\mathbf{r}|\mathbf{x}\right) P(\mathbf{x})\right] / p(\mathbf{r})}, \end{aligned} \tag{2.8}$$

where the subscript u is the index of the specific user $u \in \{1, 2, \ldots, U\}$ the bit belongs to, the superscript $m \in \{1, 2, \ldots, \log_2(M)\}$ is the index of the particular bit the LLR is computed for in the symbol of the uth user, M is the size of the modulation constellation and $\chi(u, m, v)$ is the set of multi-level symbols $\mathbf{x}$ belongs to where the mth bit of the uth user's symbol is equal to v. Moreover, $P(\mathbf{x})$ is the *a priori* probability of the multi-level symbol $\mathbf{x}$, which is equal to

$$P(\mathbf{x}) = P\left(b_1^{(1)}\right) \cdot \ldots P\left(b_1^{(\log_2(M))}\right) \cdot \ldots P\left(b_U^{(\log_2(M))}\right) \tag{2.9}$$

when the bits in a symbol are assumed to be independent, and $p(\mathbf{r})$ is the model's likelihood, or, in other words, the PDF of receiving $\mathbf{r}$ which is equal to [10]

$$p(\mathbf{r}) = \sum_{\mathbf{x}} p(\mathbf{r}|\mathbf{x})P(\mathbf{x}). \tag{2.10}$$

Finally, $p(\mathbf{r}|\mathbf{x})$ represents the multi-level symbol-based CF, which in the SDMA-MIMO system describes the PDF of receiving $\mathbf{r}$ given that the multi-level symbol $\mathbf{x}$ was transmitted [10]

$$f(\mathbf{x}) = p(\mathbf{r}|\mathbf{x}) = \frac{1}{\left(\sigma\sqrt{2\pi}\right)^P} \exp\left(-\left\|\mathbf{r} - \mathbf{H}\mathbf{x}\right\|^2 / 2\sigma^2\right), \tag{2.11}$$

where $2\sigma^2$ is the noise variance.

The extrinsic LLRs of each user's bit stream are deinterleaved and passed to their corresponding Max-Log APP decoder [10] where a soft estimate of the information bit stream of each user is generated. If the number of iterations between the MUD and the SISO decoder is greater than one, then the SISO decoder feeds the MUD with symbol probabilities given the received soft sequence. The extrinsic LLRs provided by the decoder become the *a priori* symbol probabilities for the MUD for the next MUD-decoder iteration.

2.3.2 Maximum Likelihood MUD

The optimal hard-output classical MUD is the ML MUD, which finds the multi-level symbol $\mathbf{x}_{\max}$ that maximizes the conditional PDF of Equation 2.11. The number of CFEs required by the ML MUD is the same as the number of CFEs performed by the MAP MUD during the first iteration and is equal to

$$\mathcal{C}_{MAP} = \mathcal{C}_{ML} = \frac{M^U}{U \cdot \log_2(M)}. \tag{2.12}$$

By comparing Equation 2.6 and Equation 2.12 we may conclude that the complexity of the ML and MAP MUDs is independent of the multiple access system used. In fact, the number of CFEs performed by the ML and MAP MUDs depends on the size of the search space, which in turn depends on the constellation size M and exponentially increases with the number of users U.

The QMUD in Figure 2.2 may receive as an input the signals of each receiver antenna

and an initial guess which may be random or provided by a simple linear detector, such as the ZF or the MMSE detector, where the estimation of the multi-level symbol is performed by multiplying the received signals $\mathbf{r}$ by a complex-valued weight matrix $\mathbf{W}$ as in

$$\hat{\mathbf{x}} = \mathbf{W}^H \mathbf{r}. \tag{2.13}$$

Let us proceed by presenting the ZF and the MMSE detectors.

2.3.3 Zero-Forcing Detector

The ZF detector uses the inverse channel matrix $\mathbf{W}^H = \mathbf{H}^{-1}$ to detect the most likely multi-level transmitted symbol $\hat{\mathbf{x}}$ as in

$$\begin{aligned} \hat{\mathbf{x}}_{ZF} &= \mathbf{H}^{-1}\mathbf{r} \\ &= \mathbf{H}^{-1}\mathbf{H}\mathbf{x} + \mathbf{H}^{-1}\mathbf{n} \\ &= \mathbf{x} + \mathbf{H}^{-1}\mathbf{n}. \end{aligned} \tag{2.14}$$

Since the computation of the inverse of a complex-valued matrix may be computationally complex, the pseudo-inverse channel matrix $\mathbf{W}^H = \mathbf{H}^+$ [138] may be used instead. More precisely, depending on whether the number of receiver antennas is smaller or not than the number of supported users in the system, the pseudo-inverse channel matrix may be computed as in

$$\mathbf{H}^+ = \begin{cases} \left(\mathbf{H}^H\mathbf{H}\right)^{-1}\mathbf{H}^H & U \leq P \\ \mathbf{H}^H\left(\mathbf{H}\mathbf{H}^H\right)^{-1} & U > P \end{cases}. \tag{2.15}$$

The ZF detector ignores the effects of the amplified AWGN in Equation 2.14 hence its performance is degraded. Nevertheless, it may serve as an initial input in our QMUD which in many cases will be better than choosing a random one.

2.3.4 Minimum Mean Square Error Detector

The complex-valued weight matrix of the MMSE detector is chosen according to

$$\mathbf{W} = \left(\mathbf{H}\mathbf{H}^H + N_0\mathbf{I}\right)^{-1}\mathbf{H}, \tag{2.16}$$

where $N_0 = 2\sigma^2$ is the noise power spectral density. It is applied to the received signals according to

$$\hat{\mathbf{x}}_{MMSE} = \left(\mathbf{H}^H\mathbf{H} + N_0\mathbf{I}\right)^{-1}\mathbf{H}^H\mathbf{r}. \tag{2.17}$$

The MMSE detector is expected to provide a better performance than the ZF detector since it takes into account the noise statistics. However, in a rank-deficient scenario where more users are supported in the system than the number of receiver antennas $U > P$, the channel matrix $\mathbf{H}$ is rank-deficient and the presented linear detectors will fail to accurately

estimate the multi-level symbol since they will try to estimate U streams by exploiting only P equations. Once again, the MMSE detector's estimate may be exploited by the proposed QMUDs as an initial point for detecting the transmitted multi-level symbol.

2.4 Quantum Search Algorithms

For the case of providing further in-depth intuition we will proceed by investigating Grover's QSA [50], the BBHT QSA [51], the DHA [52] and the novel Early-Stopping DHA [2] in the context of a simple DS-CDMA scenario supporting $U = 2$ users employing the Binary Phase Shift Keying (BPSK) modulation scheme associated with $M = 2$ states. The channel coefficients are assumed to be perfectly estimated and Gold spreading codes [11] are used which have a spreading factor of $SF = 31$ chips. The CF evaluations in Equation 2.4 would be $f : \{0, 1, 2, 3\} \rightarrow [0, 1]$ and the size of the search space is $N = M^U = 4$, since we have four possible two-bit combinations at the BS's receiver. Let us assume that the CF outputs are

$$[f(0),\ f(1),\ f(2),\ f(3)] = [0.24,\ 0.16,\ 0.38,\ 0.27]\,, \tag{2.18}$$

which represent the PDF $p(\mathbf{y}|\mathbf{x})$ of receiving the signal $\mathbf{y}$ in Equation 2.1, given that the 4-level two-user signal $\mathbf{x}$ was transmitted. Due to the nature of the CF in Equation 2.4, the smaller the Euclidean distance of a legitimate noise-free 4-level symbol from the actually received faded and noise-contaminated signal $\mathbf{y}$ is, the higher its CF value. Hence, in our scenario we may conclude that the 4-level symbol $\mathbf{x} = [1,\ 0]^T$ is the most probable to have been transmitted. Naturally, in real applications we can only draw this conclusion, once we have computed all the possible CF values, hence facilitating an ML decision.

During our analysis of the QSAs, we will refer to the Quantum Register (QR) which will contain the indices of our search problems as the Quantum Index Register (QIR). In our scenario the QIR will consist of $n = \log_2 N = 2$ qubits forming the four states $|0\rangle$, $|1\rangle$, $|2\rangle$ and $|3\rangle$, corresponding to the legitimate 4-level symbols

$$\mathbf{x} \in \left\{[0,\ 0]^T,\ [0,\ 1]^T,\ [1,\ 0]^T,\ [1,\ 1]^T\right\} \equiv x \in \{0, 1, 2, 3\}\,, \tag{2.19}$$

respectively. The probabilities of observing each of these states will be evolving and changing as the QSAs proceed, as it will be detailed in Sections 2.4.1, 2.4.2, 2.4.3 and 2.4.4. The parameters of the system considered are displayed in Table 2.1. An intuitive way of illustrating the employment of the quantum search algorithms in our QMUDs is depicted in Figure 2.3, where the BBHT QSA and Grover's QSA are also included as a reference for the DHA.

2.4.1 Grover's Quantum Search Algorithm

The goal of Grover's QSA is exactly the same as that of any classical search algorithm's, namely that of finding the index of the desired entries, provided of course that the desired

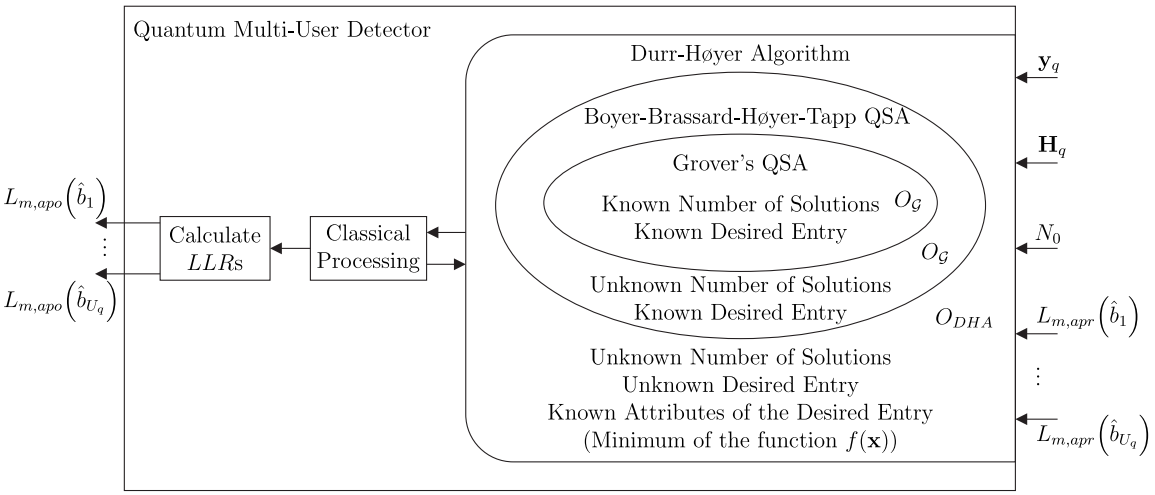

Figure 2.3: The DHA employed in our QMUDs makes multiple calls to the BBHT QSA. Grover's QSA is not used, but it is included for completeness, since the BBHT QSA uses the same Oracle O, but may even be capable of finding a solution with a ∼100% probability, when the number of solutions is unknown. The QMUD is performed on a subcarrier basis. The DHA processes the signals received at all the receive AEs on the qth subcarrier, along with the channel estimates, the noise's variance and the *a priori* LLRs. After it completes its initial procedure, the DHA exchanges information with a classical processing unit, which determines whether the DHA should or should not be called again, while additionally determining its search space. Finally, the QMUD outputs the calculated *a posteriori* LLRs.

Table 2.1: Parameters of the 2-User DS-CDMA System

Number of Users	$U = 2$
Number of AEs per User	$N_{T_x} = 1$
Number of AEs at the BS	$P = 1$
Modulation	BPSK $M = 2$
Channel Code	Turbo Code, $R = 1/2$, 8 Trellis states
Spreading Codes	Gold codes
Spreading Factor	$SF = 31$
Normalized User Load	$U_L = U \cdot N_{T_x}/SF = 2/31$
Channel Estimation	Perfect
CF outputs for the first symbol	$[f(0), f(1), f(2), f(3)] = [0.24, 0.16, 0.38, 0.27]$

entry is indeed part of the database. It was shown in [50] that it succeeds in finding the solution after $O(\sqrt{N})$ CF evaluations, in contrast to the optimal classical full-search algorithms which succeed after $O(N)$ calculations. Let us commence with an unrealistic version of our scenario, namely where we assume that we *know* that $\delta = 0.38$ appears in the database as one of the CF evaluations and also that it is unique. In practice this is unrealistic, because the CF value depends on the contaminating effects of random fading, noise and interference. Employing Grover's QSA we will determine the index x_s that corresponds to $f(x_s) = \delta$. Hence, we have $S = 1$ solution and $N = 4$ database indices. In classical search algorithms, once the desired entry associated with the lowest Euclidean distance was found, its index is readily observed and retrieved. In Grover's QSA on the

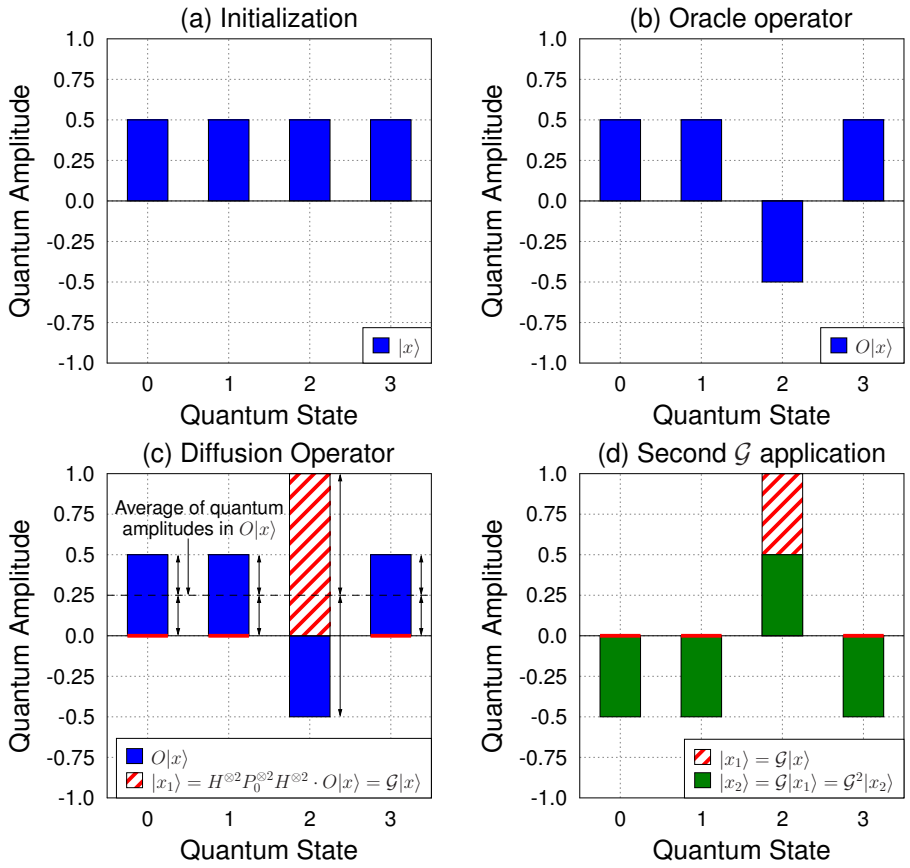

Figure 2.4: Graphical representation of Grover operator's $\mathcal{G}$ applications in our $U = 2$, $M = 2$ scenario with a unique solution $S = 1$ and $N = M^U = 4$ entries. The colours correspond to the rotations in Figure 2.8.

other hand, the process aims for maximizing the probability of observing the index in the QIR x_s. Each of the N indices is treated as a legitimate solution to the search problem. The QIR should be initialized in a superposition of N equiprobable states, which is formulated as:

$$|x\rangle = \sum_{q=0}^{N-1} a_q|q\rangle = \sum_{q=0}^{N-1} \frac{1}{\sqrt{N}}|q\rangle = \sum_{q=0}^{3} \frac{1}{2}|q\rangle, \tag{2.20}$$

since there is no *a priori* "preference" for any of the legitimate solutions. The initialization is performed with the aid of a two-qubit Hadamard gate $H^{\otimes 2}$ and two qubits in the $|00\rangle$ state which may be described based on Equation 1.15 as:

$$\begin{aligned} |x\rangle &= H^{\otimes 2}|00\rangle = H|0\rangle H|0\rangle \\ &= \frac{1}{\sqrt{2}}\left(|0\rangle + |1\rangle\right)\frac{1}{\sqrt{2}}\left(|0\rangle + |1\rangle\right) \\ &= \frac{1}{2}|00\rangle + \frac{1}{2}|01\rangle + \frac{1}{2}|10\rangle + \frac{1}{2}|11\rangle \\ &= \frac{1}{2}|0\rangle + \frac{1}{2}|1\rangle + \frac{1}{2}|2\rangle + \frac{1}{2}|3\rangle. \end{aligned} \tag{2.21}$$

The initial quantum amplitudes of the QIR $|x\rangle$ are depicted in Figure 2.4a which shows the evolution of the quantum states in our scenario.

Finding the highest-probability solution in the QIR is accomplished by the iterations of Grover's QSA as detailed below. A single iteration of Grover's QSA is carried out by applying a unitary operator $\mathcal{G}$, referred to as the *Grover operator* to the QIR $|x\rangle$. The operator's circuit-based representation is shown in Figure 2.5, which consists of a unitary operator termed as the *Oracle*, two Hadamard gates H exemplified in Equation 1.15, and a controlled phase shift gate P_0. The Hadamard gate creates a superposition of equiprobable states, when applied to a state of the computational basis, $|0\rangle$ or $|1\rangle$. The controlled phase shift gate P_0 inverts the sign of all the input states except for the $|0\rangle^{\otimes n}$ one. The Hadamard gate, $H^{\otimes n} = H^{\otimes 2}$, and the controlled phase shifter gate $P_0^{\otimes 2}$ of Figure 2.5 obey the following format

$$H^{\otimes n} = \frac{1}{\sqrt{2}} \begin{bmatrix} H^{\otimes(n-1)} & H^{\otimes(n-1)} \\ H^{\otimes(n-1)} & -H^{\otimes(n-1)} \end{bmatrix}, H^{\otimes 0} = 1 \tag{2.22}$$

$$P_0^{\otimes n} = \left.\begin{bmatrix} 1 & 0 & \cdots & 0 \\ 0 & -1 & \cdots & 0 \\ \vdots & \vdots & \ddots & \vdots \\ 0 & 0 & \cdots & -1 \end{bmatrix}\right\} (2^n \times 2^n). \tag{2.23}$$

In our scenario we have $n = 2$, hence the matrix representations of the Hadamard gate $H^{\otimes 2}$ and the controlled phase shift gate $P_0^{\otimes 2}$ are:

$$H^{\otimes 2} = \frac{1}{2} \begin{bmatrix} 1 & 1 & 1 & 1 \\ 1 & -1 & 1 & -1 \\ 1 & 1 & -1 & -1 \\ 1 & -1 & -1 & 1 \end{bmatrix} \tag{2.24}$$

$$P_0^{\otimes 2} = \begin{bmatrix} 1 & 0 & 0 & 0 \\ 0 & -1 & 0 & 0 \\ 0 & 0 & -1 & 0 \\ 0 & 0 & 0 & -1 \end{bmatrix}, \tag{2.25}$$

respectively.

2.4.1.1 The Oracle

The Oracle is capable of recognizing the legitimate solutions in the QIR by evaluating the CF at this input. More explicitly, the Oracle's task in Grover's QSA is that of finding

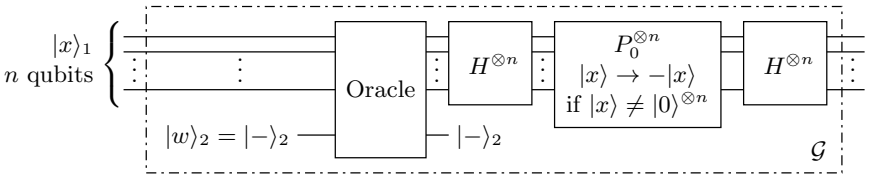

Figure 2.5: Grover operator's quantum circuit including an Oracle, two n-qubit Hadamard gates H and a controlled n-qubit phase shift gate P_0.

and marking the specific index sought. The Oracle may be described algebraically by an $(N \times N)$-element matrix with all the non-zero elements lying on its diagonal. Each of the N elements on the diagonal of the Oracle-matrix represents a specific cell of the QIR. The diagonal elements may assume the values of -1 or $+1$, depending on whether their corresponding CF evaluation is deemed to be a legitimate solution or not, respectively. Hence the format of the Oracle-matrix obeys

$$O = \begin{bmatrix} \pm 1 & 0 & \cdots & 0 \\ 0 & \pm 1 & \cdots & 0 \\ \vdots & \vdots & \ddots & \vdots \\ 0 & 0 & \cdots & \pm 1 \end{bmatrix}. \tag{2.26}$$

In our scenario, since the third index of the QIR, namely $x = 2$ is a solution to the search problem, the Oracle will recognize this by comparing the corresponding entry $f(2) = 0.38$ to the desired value $\delta = 0.38$ and the third element of the Oracle-matrix diagonal will be set to -1. On the other hand, since the first state $|0\rangle$ is not deemed to be a solution, because $f(0) = 0.24 \neq \delta = 0.38$, the first element of the Oracle's diagonal is set to $+1$. The second index $x = 1$ as well as the fourth index $x = 3$ are also not deemed to be solutions since $f(1) = 0.16 \neq \delta = 0.38$ and $f(3) = 0.27 \neq \delta = 0.38$, respectively, resulting to their corresponding positions on the diagonal of the Oracle-matrix to be set to $+1$ as encapsulated in

$$O = \begin{bmatrix} +1 & 0 & 0 & 0 \\ 0 & +1 & 0 & 0 \\ 0 & 0 & -1 & 0 \\ 0 & 0 & 0 & +1 \end{bmatrix}. \tag{2.27}$$

Moving deeper into the Oracle's operation, the Oracle's workspace is described by a single qubit, $|w\rangle$, initialized to the superposition of equiprobable states $|w\rangle = |-\rangle = \frac{|0\rangle - |1\rangle}{\sqrt{2}}$. This superposition of states is acquired by applying the Hadamard gate H to the state $|1\rangle$

as described in

$$|w\rangle = H|1\rangle = \frac{1}{\sqrt{2}} \begin{bmatrix} 1 & 1 \\ 1 & -1 \end{bmatrix} \cdot \begin{bmatrix} 0 \\ 1 \end{bmatrix} = \frac{1}{\sqrt{2}} \begin{bmatrix} 1 \\ -1 \end{bmatrix} = \frac{1}{\sqrt{2}} (|0\rangle - |1\rangle) = |-\rangle. \tag{2.28}$$

The Oracle will then map the N input states of the QIR $|x\rangle$ to

$$|x\rangle|w\rangle \xrightarrow{O} |x\rangle|w \oplus g(x)\rangle, \tag{2.29}$$

where we have

$$g(x) = \begin{cases} 1 & \text{if } f(x) = \delta \\ 0 & \text{otherwise} \end{cases}. \tag{2.30}$$

Since we have $|w\rangle = |-\rangle$, the operations encapsulated in Equation 2.29 may be expanded as:

$$|x\rangle \frac{|0\rangle - |1\rangle}{\sqrt{2}} \xrightarrow{O} (-1)^{g(x)} |x\rangle \frac{|0\rangle - |1\rangle}{\sqrt{2}}. \tag{2.31}$$

The function $g(x)$ of Equation 2.30 in our scenario is

$$g(x) = \begin{cases} 0 & x = 0, \text{ since } f(0) = 0.24 \neq \delta = 0.38 \\ 0 & x = 1, \text{ since } f(1) = 0.16 \neq \delta = 0.38 \\ 1 & x = 2, \text{ since } f(2) = 0.38 = \delta = 0.38 \\ 0 & x = 3, \text{ since } f(3) = 0.27 \neq \delta = 0.38 \end{cases} \tag{2.32}$$

and according to Equation 2.29 and Equation 2.31 the Oracle operation in our scenario is

$$\begin{aligned} |x\rangle|-\rangle =& \frac{1}{2} (|00\rangle + |01\rangle + |10\rangle + |11\rangle) |-\rangle \\ =& \frac{1}{2} (|0\rangle + |1\rangle + |2\rangle + |3\rangle) |-\rangle \\ =& \frac{1}{2}|0\rangle \frac{1}{\sqrt{2}}(|0\rangle - |1\rangle) + \frac{1}{2}|1\rangle \frac{1}{\sqrt{2}}(|0\rangle - |1\rangle) + \\ & \frac{1}{2}|2\rangle \frac{1}{\sqrt{2}}(|0\rangle - |1\rangle) + \frac{1}{2}|3\rangle \frac{1}{\sqrt{2}}(|0\rangle - |1\rangle) \end{aligned}$$

$$
\begin{aligned}
\xrightarrow{O} & \frac{1}{2}|0\rangle\left(\frac{1}{\sqrt{2}}(|0\rangle-|1\rangle)\oplus g(0)\right)+\\
& \frac{1}{2}|1\rangle\left(\frac{1}{\sqrt{2}}(|0\rangle-|1\rangle)\oplus g(1)\right)+\\
& \frac{1}{2}|2\rangle\left(\frac{1}{\sqrt{2}}(|0\rangle-|1\rangle)\oplus g(2)\right)+\\
& \frac{1}{2}|3\rangle\left(\frac{1}{\sqrt{2}}(|0\rangle-|1\rangle)\oplus g(3)\right)\\
= & \frac{1}{2}|0\rangle\left(\frac{1}{\sqrt{2}}(|0\rangle\oplus g(0)-|1\rangle\oplus g(0))\right)+\\
& \frac{1}{2}|1\rangle\left(\frac{1}{\sqrt{2}}(|0\rangle\oplus g(1)-|1\rangle\oplus g(1))\right)+\\
& \frac{1}{2}|2\rangle\left(\frac{1}{\sqrt{2}}(|0\rangle\oplus g(2)-|1\rangle\oplus g(2))\right)+\\
& \frac{1}{2}|3\rangle\left(\frac{1}{\sqrt{2}}(|0\rangle\oplus g(3)-|1\rangle\oplus g(3))\right)+\\
= & \frac{1}{2}|0\rangle\frac{1}{\sqrt{2}}(|0\rangle-|1\rangle)+\frac{1}{2}|1\rangle\frac{1}{\sqrt{2}}(|0\rangle-|1\rangle)+\\
& \frac{1}{2}|2\rangle\frac{1}{\sqrt{2}}(|1\rangle-|0\rangle)+\frac{1}{2}|3\rangle\frac{1}{\sqrt{2}}(|0\rangle-|1\rangle)\\
= & \frac{1}{2}|0\rangle|-\rangle+\frac{1}{2}|1\rangle|-\rangle+\frac{1}{2}|2\rangle\left(-|-\rangle\right)+\frac{1}{2}|3\rangle|-\rangle\\
= & \frac{1}{2}\left(|0\rangle+|1\rangle-|2\rangle+|3\rangle\right)|-\rangle\\
= & \frac{1}{2}\left(|00\rangle+|01\rangle-|10\rangle+|11\rangle\right)|-\rangle. \qquad (2.33)
\end{aligned}
$$

The Oracle generates the function g by evaluating f in parallel, thus a single Oracle operation will be considered to have the computational complexity of one CF evaluation.

The quantum circuit of the Oracle in Grover's Quantum Search Algorithm is presented in Figure 2.6. After the n qubits in the first quantum register of Figure 2.6 pass through the Hadamard gate, an equiprobable superposition of the 2^n legitimate quantum states is created. The U_f gate in Figure 2.6 is the U_f gate analysed in Figure 1.12, where Z qubits are employed for representing the value $f(x)$, similarly to the classical computing where Z bits would be used for describing a real number. More specifically, we have

$$f(x_j) \equiv |f(x_j)_1\rangle|f(x_j)_2\rangle\ldots|f(x_j)_Z\rangle,\ j=1,2,\ldots,2^n, \qquad (2.34)$$

$$f(x_j)_i \in \{|0\rangle,|1\rangle\},\ i=1,2,\ldots,Z. \qquad (2.35)$$

It is worth mentioning that the Z qubits of the second quantum register at the output of the U_f gate are entangled with the n qubits of the first register and represent simultaneously all the possible outputs of $f(x)$.

The third quantum register $|\delta\rangle$ seen in Figure 2.6 also consists of Z qubits and represents

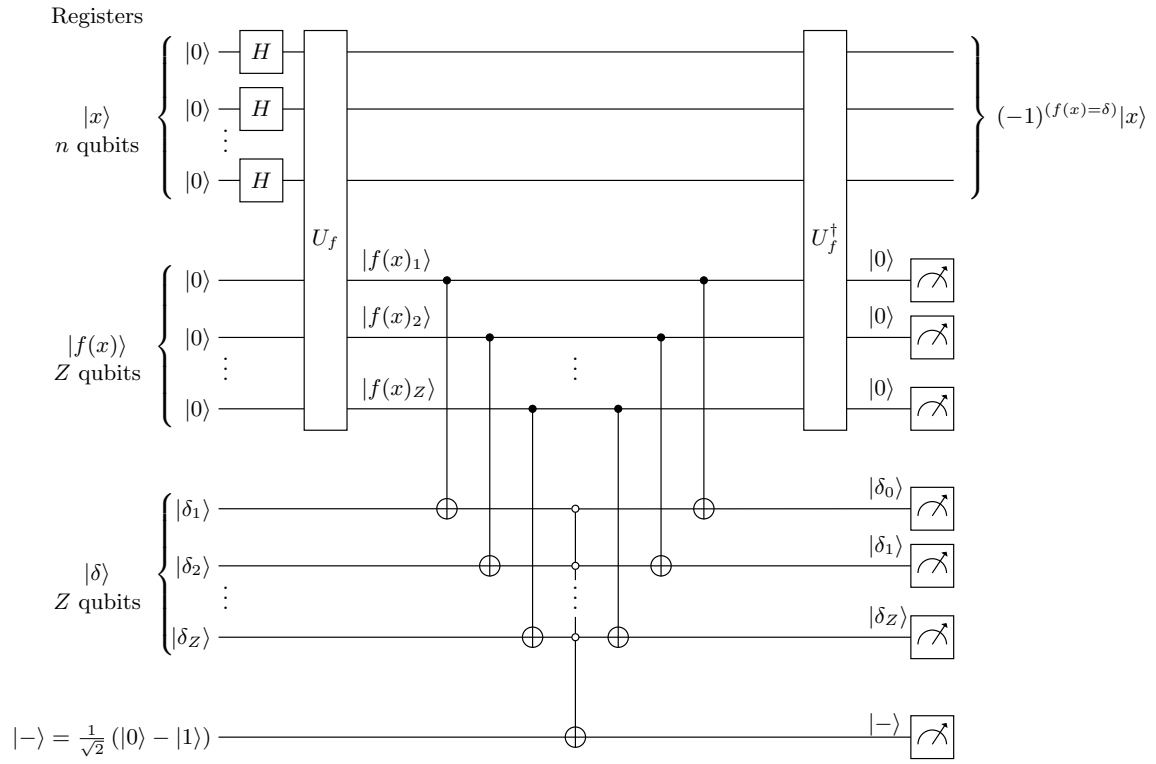

Figure 2.6: Quantum circuit of the Oracle in Grover's quantum search algorithm. Z qubits are employed for representing the outputs of the function $f(x) \equiv |f(x)_1\rangle|f(x)_2\rangle \dots |f(x)_Z\rangle$, with $|f(x)_i\rangle \in \{|0\rangle, |1\rangle\}$, $i = 1, 2, \dots, Z$, and Z more qubits are used for representing the value $\delta \equiv |\delta_1\rangle|\delta_2\rangle ... |\delta_Z\rangle$, with $|\delta_i\rangle \in \{|0\rangle, |1\rangle\}$ and $i = 1, 2, \dots, Z$.

the desired value δ as

$$\delta \equiv |\delta_1\rangle|\delta_2\rangle \dots |\delta_Z\rangle, \tag{2.36}$$

$$\delta_i \in \{|0\rangle, |1\rangle\}, \ i = 1, 2, \dots, Z. \tag{2.37}$$

The Oracle has to check if $f(x_j) = \delta$, for $j = 1, 2, \dots, 2^n$. The Z number of $CNOT$ gates appearing after the U_f gate in Figure 2.6, with the $f(x)$ (second) quantum register's qubits acting as control qubits and the δ (third) register's respective qubits acting as target qubits serve this purpose of checking whether the condition of $f(x_j) = \delta$ is satisfied, by checking if we have $f(x_j)_i = \delta_i$, for every $i = 1, 2, \dots, Z$. In more detail, the truth table of each of the Z number of $CNOT$ gates is given in Table 2.2. We may observe in Table 2.2 that if we have $f(x_j)_i = \delta_i$ before the $CNOT$ operation, then after the $CNOT$ operation the state of δ_i is always $|0\rangle$.

The operation of the Oracle in Grover's QSA according to Equation 2.31 is to flip the sign of a single qubit found in the $|-\rangle$ state, for marking a solution. The Z-times controlled gate seen in Figure 2.6 performs the NOT operation on the target qubit, if all the control qubits are in the $|0\rangle$ state [43]. As it was previously mentioned, the qubits in the δ register will be in the $|0\rangle$ state, if they initially had the same value as their respective $f(x_j)$ quantum register's qubit. Therefore, if all the qubits in the δ quantum register are in the $|0\rangle$ state after the $CNOT$ gates, then we have $f(x_j) = \delta$ and the NOT operation is performed on the last qubit of the circuit which was in the $|-\rangle$ state, essentially evolving into the $-|-\rangle$

Table 2.2: Truth table of the ith $CNOT$ gate in Figure 2.6

Input		**Output**	
$f(x_j)_i$	δ_i	$f(x_j)_i$	δ_i
0	0	0	0
0	1	0	1
1	0	1	1
1	1	1	0

state, as required by Equation 2.31.

The inverse operations are performed after the Z-times controlled NOT gate, for the sake of removing the entanglement of the $f(x)$ quantum register and the δ quantum register from both the x quantum register and from the last qubit, finally resulting in Equation 2.31. For removing the entanglement of the quantum registers seen in Figure 2.6, we use the same $CNOT$ gates as in the first part of the circuit and $U_f^\dagger$ for performing the inverse operation of the U_f. Finally, the $2Z$ number of qubits in the second and third quantum registers of Figure 2.6 will be in the same states for all the different 2^n quantum states as the first register will be in. Hence, we are ready to observe them for the sake of removing their effect from the quantum system's description. The first quantum register and the last qubit in Figure 2.6 will still be entangled with each other, as seen in Equation 2.31.

2.4.1.2 Grover's Operator

By combining Equation 2.22, Equation 2.23 and Equation 2.26, the algebraic description of the Grover operator may be constructed with the aid of Figure 2.5 as:

$$\mathcal{G} = H^{\otimes n} P_0^{\otimes n} H^{\otimes n} \cdot O. \tag{2.38}$$

Since in our scenario we have $n = \log_2 N = 2$, by substituting $H^{\otimes 2}$ from Equation 2.24, $P_0^{\otimes 2}$ from Equation 2.25 and the Oracle from Equation 2.27, the Grover operator in our scenario becomes equal to

$$\mathcal{G} = H^{\otimes 2} P_0^{\otimes 2} H^{\otimes 2} \cdot O = \frac{1}{2} \begin{bmatrix} -1 & 1 & -1 & 1 \\ 1 & -1 & -1 & 1 \\ 1 & 1 & 1 & 1 \\ 1 & 1 & -1 & -1 \end{bmatrix}. \tag{2.39}$$

The effect of the operation $\mathcal{G}$ on $|x\rangle$ may be seen in Figure 2.7, where the y-axis represents the superposition of states that are solutions – which are given by $|s\rangle = \sqrt{\frac{1}{S}}|2\rangle = |2\rangle$ in our scenario – while the x-axis represents the set of states that are not solutions, which

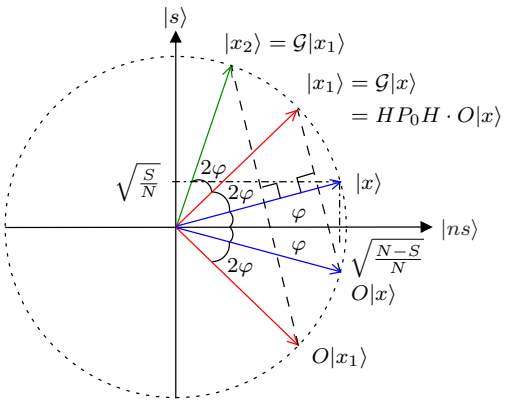

Figure 2.7: Geometrical interpretation of Grover's Quantum Search Algorithm.

are given by $|ns\rangle = \sqrt{\frac{1}{N-S}}\left(|0\rangle + |1\rangle + |3\rangle\right) = \sqrt{\frac{1}{3}}\left(|0\rangle + |1\rangle + |3\rangle\right)$. It should be noted that this is a geometrical representation, which explains the operation of $\mathcal{G}$ and that the states $|s\rangle$ and $|ns\rangle$ are not physically created. The initial state $|x\rangle$ may be represented as

$$\begin{aligned}
|x\rangle &= \sqrt{\frac{S}{N}}|s\rangle + \sqrt{\frac{N-S}{N}}|ns\rangle \\
&= \sqrt{\frac{1}{4}}|s\rangle + \sqrt{\frac{3}{4}}|ns\rangle \\
&= \frac{1}{2}|2\rangle + \frac{\sqrt{3}}{2}\left(\frac{1}{\sqrt{3}}\left(|0\rangle + |1\rangle + |3\rangle\right)\right) \\
&= \frac{1}{2}\left(|0\rangle + |1\rangle + |2\rangle + |3\rangle\right) \qquad (2.40) \\
&= \frac{1}{2}\left(|00\rangle + |01\rangle + |10\rangle + |11\rangle\right) \qquad (2.41)
\end{aligned}$$

The Oracle reflects $|x\rangle$ with respect to $|s\rangle$, since it marks the solution in $|x\rangle$ by transforming $|s\rangle$ to $-|s\rangle$ and leaving $|ns\rangle$ unaltered as in Equation 2.33. The HP_0H operator of Figure 2.7 reflects $O|x\rangle$ with respect to the input state $|x\rangle$, as it may be seen in Figure 2.7. More explicitly, the resultant state $|x_1\rangle = HP_0H \cdot O|x\rangle$ may be considered as a anti-clockwise rotation by 2φ with respect to $|x\rangle$, while the quantum state $O|x\rangle$ before HP_0H was applied may be considered as a clockwise rotation by 2φ with respect to the initial state $|x\rangle$, as illustrated in Figure 2.7. The HP_0H operator is considered to perform inversion about the average, as depicted in Figure 2.4c. Hence, $\mathcal{G}$ results in a total anti-clockwise rotation of the input state by 2φ, where we have [51]

$$\varphi = \arcsin\sqrt{S/N}. \qquad (2.42)$$

It should be noted that φ is the angle that the initial state $|x\rangle$ had with respect to the x-axis, which corresponds to $|ns\rangle$, and its value depends on the number of solutions S in the database, in addition to the size of the database N. If there was no solution in our problem $S = 0$, then $|ns\rangle = \sqrt{\frac{1}{N}}(|0\rangle + |1\rangle + |2\rangle + |3\rangle) = \frac{1}{2}(|0\rangle + |1\rangle + |2\rangle + |3\rangle)$ and $\varphi = 0$ from Equation 2.42, resulting in $|x\rangle = |ns\rangle$. In other words, the initial quantum state in Figure 2.7 would be on the x-axis and any application of $\mathcal{G}$ would have no effect on it, since

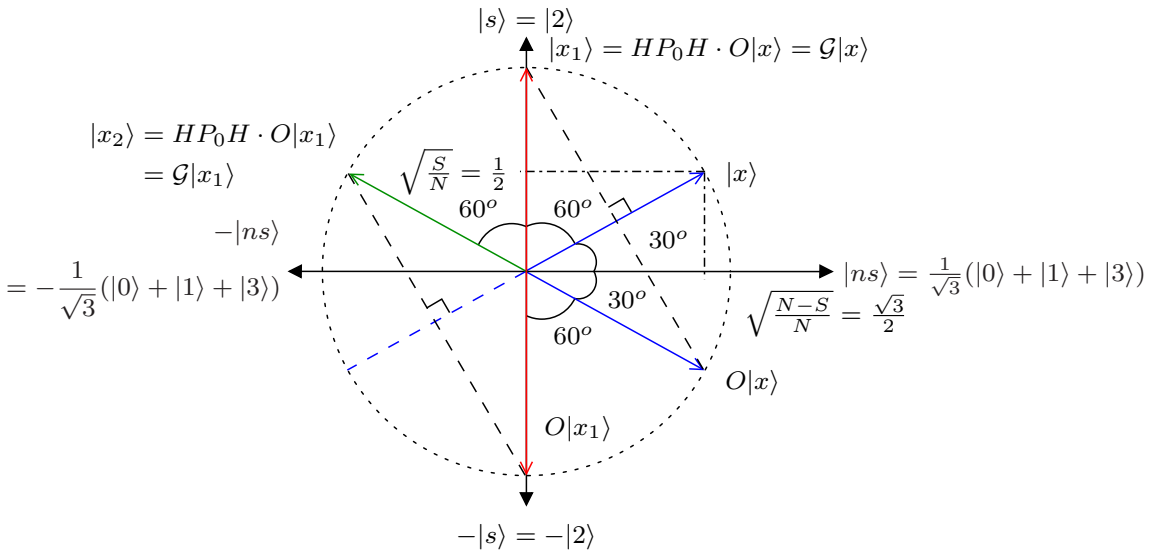

Figure 2.8: Geometrical interpretation of Grover's Quantum Search Algorithm applied in our $K = 2$, $M = 2$ scenario, where we have a unique solution $S = 1$ and $N = 4$ legitimate entries.

it would rotate it by $2\varphi = 0$.

The same process is repeated, if subsequent Grover operators are applied, with the initial state of the next iteration being the final state of the previous iteration. The target is for $\mathcal{G}^L|x\rangle$ to approach $|s\rangle$ as closely as possible so that when we observe the QIR, we will have the maximum possible probability of obtaining a state of the solutions set $|s\rangle$. This occurs the earliest after [51]

$$L_{opt} = \left\lfloor \frac{\pi}{4}\sqrt{\frac{N}{S}} \right\rfloor \tag{2.43}$$

consecutive applications of the $\mathcal{G}$ operator of Figure 2.5. This process is the Quantum Amplitude Amplification [48]. If we observe the resultant state in the QD, the probability of obtaining the correct answer is

$$P_{success} = \sin^2\left[(2L_{opt} + 1)\varphi\right]. \tag{2.44}$$

In our scenario, we have $\varphi = 30^o$ and $L_{opt} = 1$ according to Equation 2.42 and Equation 2.43, respectively. The geometric representation of the evolution of our scenario's QIR with respect to the applications of Grover operators may be seen in Figure 2.8. The application of the Oracle to the initial QIR state $|x\rangle$ in Equation 2.20 would result into

$$O|x\rangle = \begin{bmatrix} +1 & 0 & 0 & 0 \\ 0 & +1 & 0 & 0 \\ 0 & 0 & -1 & 0 \\ 0 & 0 & 0 & +1 \end{bmatrix} \cdot \frac{1}{2} \begin{bmatrix} 1 \\ 1 \\ 1 \\ 1 \end{bmatrix} = \frac{1}{2} \begin{bmatrix} 1 \\ 1 \\ -1 \\ 1 \end{bmatrix}, \tag{2.45}$$

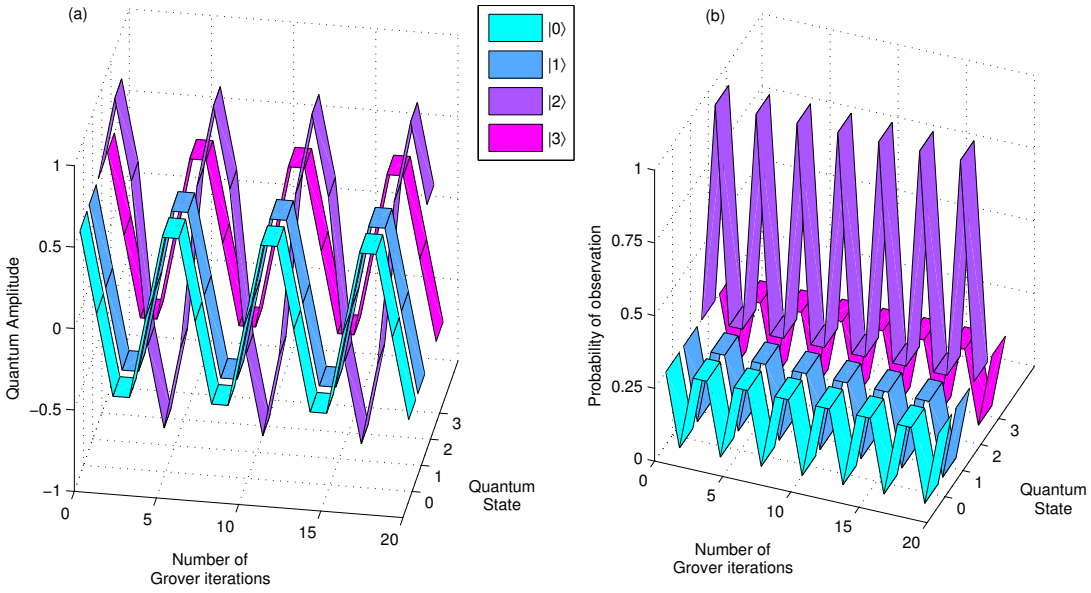

Figure 2.9: (a) Quantum amplitudes of the QIR $|x\rangle$ with respect to the number of Grover operators $\mathcal{G}$ applied to it. (b) Probability of obtaining a quantum state after applying the corresponding number of Grover operators $\mathcal{G}$. The minimum optimal number of Grover operations is one, which in our scenario is also the global optimal number of Grover operations, since the marked state reaches 100% probability to be observed.

and its graphical and geometrical representation may be seen in Figure 2.4b and Figure 2.8, respectively. If we applied the operators $H^{\otimes 2}P_0^{\otimes 2}H^{\otimes 2}$ on $O|x\rangle$ we would obtain

$$
\begin{aligned}
|x_1\rangle &= H^{\otimes 2}P_0^{\otimes 2}H^{\otimes 2}\cdot O|x\rangle = \mathcal{G}|x\rangle \\
&= \frac{1}{2}\begin{bmatrix} 1 & 1 & 1 & 1 \\ 1 & -1 & 1 & -1 \\ 1 & 1 & -1 & -1 \\ 1 & -1 & -1 & 1 \end{bmatrix} \cdot \begin{bmatrix} 1 & 0 & 0 & 0 \\ 0 & -1 & 0 & 0 \\ 0 & 0 & -1 & 0 \\ 0 & 0 & 0 & -1 \end{bmatrix} \cdot \frac{1}{2}\begin{bmatrix} 1 & 1 & 1 & 1 \\ 1 & -1 & 1 & -1 \\ 1 & 1 & -1 & -1 \\ 1 & -1 & -1 & 1 \end{bmatrix} \cdot \frac{1}{2}\begin{bmatrix} 1 \\ 1 \\ -1 \\ 1 \end{bmatrix} \\
&= \frac{1}{2}\begin{bmatrix} -1 & 1 & 1 & 1 \\ 1 & -1 & 1 & 1 \\ 1 & 1 & -1 & 1 \\ 1 & 1 & 1 & -1 \end{bmatrix} \cdot \frac{1}{2}\begin{bmatrix} 1 \\ 1 \\ -1 \\ 1 \end{bmatrix} = \begin{bmatrix} 0 \\ 0 \\ 1 \\ 0 \end{bmatrix}. \qquad (2.46)
\end{aligned}
$$

The sequence of the operators HP_0H is termed as the *diffusion operator*, since it reflects the amplitudes of the quantum states in $O|x\rangle$ with respect to the average of their amplitudes, as illustrated in Figure 2.4c, where the average of the amplitudes in our scenario's $O|x\rangle$ is $(3 \cdot 0.5 - 0.5)/4 = 0.25$ as it may be verified from Equation 2.45. At the same time, when considering the QIR as the superposition of the states $|s\rangle$ and $|ns\rangle$, the reflection with respect to the initial state $|x\rangle$ may be seen in Figure 2.8. Hence, a single application

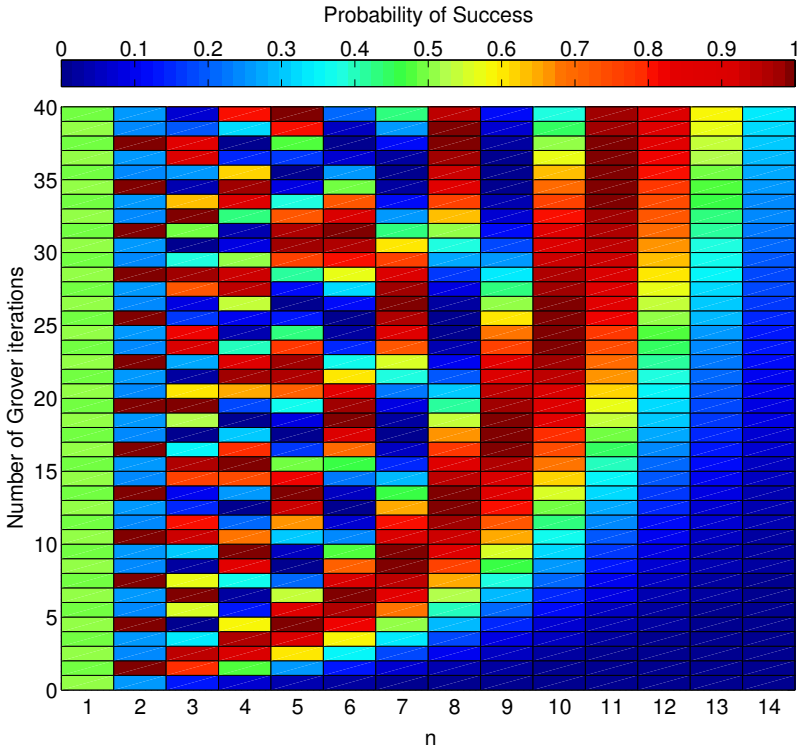

Figure 2.10: Probability of obtaining the solution when observing a QIR with $N = 2^n$ quantum states after having applied a specific number of Grover operators $\mathcal{G}$. The periodical nature of Grover's QSA is evident.

of $\mathcal{G}$ to the initial QIR state $|x\rangle$ verifies that it succeeds in maximizing the probability of obtaining the solution upon a potential observation of the QIR, since we have $|x_1\rangle = 0 \cdot |0\rangle + 0 \cdot |1\rangle + 1 \cdot |2\rangle + 0 \cdot |3\rangle$ in Equation 2.46. It should be noted that in different systems, the probability of finding the solution might not become equal to 100%, but it may be close to it. In fact, the probability of obtaining a solution is equal to 100% only when the number of solutions S is 25% of all the entries N, or, equivalently, when we have the ratio $S/N = 1/4$ [51]. If we apply $\mathcal{G}$ one more time, we arrive at

$$|x_2\rangle = \mathcal{G}|x_1\rangle = \mathcal{G}^2|x\rangle = \frac{1}{2}\begin{bmatrix} -1 \\ -1 \\ 1 \\ -1 \end{bmatrix}, \tag{2.47}$$

which is translated to another equiprobable superposition of all states, as presented in Figure 2.4d, verifying the rotation that $\mathcal{G}$ imposes on $|x\rangle$ with respect to the states $|s\rangle$ and $|ns\rangle$, as depicted in Figure 2.8. The periodicity imposed on the quantum amplitudes of the states in the QIR due to the consecutive applications of $\mathcal{G}$ is illustrated in Figure 2.9. The probability of success in finding the unique solution by applying the same number of $\mathcal{G}$ operators in systems having a different search space size N will vary. There is a

non-negligible probability that applying the same number of $\mathcal{G}$ operators to a search space having a size of $N = 2^n$ would provide an almost 100% probability of finding the unique solution, while applying the same number of $\mathcal{G}$ operators to a search space having a size of $N = 2^{n+1}$ would result in a probability of obtaining the unique solution which is close to zero. This phenomenon is depicted in Figure 2.10 in quantitative terms.

2.4.2 BBHT Quantum Search Algorithm

In many practical applications the number of solutions is higher than one and the exact number of solutions is not known beforehand. Grover's QSA would most probably fail, or, more precisely, we would have a successful detection probability of

$$P_{success} = \sin^2\left[(2L_{opt} + 1)\varphi\right] \approx 0, \tag{2.48}$$

if the same number of L_{opt} was used in diverse systems having different number of solutions, since φ of Equation 2.42 would have changed. The BBHT QSA of [51] circumvents this problem by applying $\mathcal{G}$ of Figure 2.5 a pseudo-random consecutive number of times to the initial system, observing the resultant state in the QD and then repeating it until a solution is obtained after the observation. Assuming $0 \leq S \leq 3N/4$, as it is the case in our scenario, the steps of the BBHT algorithm are summarized as in Algorithm 1 [2].

Algorithm 1 BBHT Quantum Search Algorithm [3]

1: Set $m \leftarrow 1$, $\lambda \leftarrow 6/5$ and $L^{QD}_{BBHT} \leftarrow 0$, $L^{CD}_{BBHT} \leftarrow 0$.
2: Choose L uniformly from the set $\{0, \ldots, \lfloor m \rfloor\}$.
3: Apply the $\mathcal{G}$ operator L times starting from the initial state $|x\rangle$ in Equation 2.20, resulting in the final state $|x_f\rangle = \mathcal{G}^L|x\rangle$.
4: Observe $|x_f\rangle$ in the QD and obtain $|j\rangle$.
5: Compute $f(j)$ in the CD.
6: Update $L^{CD}_{BBHT} \leftarrow L^{CD}_{BBHT} + 1$ and $L^{QD}_{BBHT} \leftarrow L^{QD}_{BBHT} + L$.
7: **if** $f(j) = \delta$ or $L^{QD}_{BBHT} \geq L^{QD,\,\max}_{BBHT}$ **then**
8: Set $x_s \leftarrow j$, output x_s, L^{CD}_{BBHT}, L^{QD}_{BBHT} and exit.
9: **else**
10: Set $m \leftarrow \min\left\{\lambda m, \sqrt{N}\right\}$ and go to Step 2.
11: **end if**

The counter L^{QD}_{BBHT} corresponds to the number of Grover iterations, or, equivalently, CFEs performed in the quantum domain, while L^{CD}_{BBHT} keeps track of the number of CFEs performed in the classical domain. Since we have assumed that a single CFE in the quantum domain has equal complexity to a single CFE in the classical domain, we should take into account the total number of CFEs in both domains for providing accurate comparisons with the classical MUDs. The BBHT QSA [51] manages to find a solution after $L^{QD,\,\max}_{BBHT} = 4.5\sqrt{N/S}$ $\mathcal{G}$ operations, or, equivalently, Oracle calls in the worst case as formally proved in [51]. It should be noted at this point that the total number of CFEs during a BBHT iteration is equal to the number of Oracle calls, plus an additional CFE

in the CD required for determining whether the obtained value j is a solution or not. The number of CFEs in the classical domain during a single run of the BBHT QSA is equal to the number of times we visited Step 5 and it may change during different runs of the BBHT QSA. If no solution is found after $L_{BBHT}^{QD,\max}$ Grover iterations, it may be concluded that we have $S = 0$. The parameter λ may be chosen in the set $(1, 4/3)$ and the evaluation of $f(j)$ at Step 5 is performed in the classical domain. If there is no solution for the search problem, i.e. we have $S = 0$, the BBHT QSA will realize this fact after $L_{BBHT}^{QD,\max} = 4.5\sqrt{N}$ Oracle operations by delivering a final output of x_f for which we have $f(x_f) \neq \delta$.

The value of $\lambda = 6/5$ in Step 1 of Algorithm 1 is not the only value λ may assume for ensuring that the BBHT succeeds. It should be noted that λ should be greater than 1, since if $\lambda < 1$, then m in Step 10 of Algorithm 1 would eventually be almost zero, resulting in applying no Grover iterations. At the same time, λ should be smaller than $4/3$ for ensuring that the BBHT succeeds with a probability of $\sim$100% after $L_{BBHT}^{QD,\max} = O(\sqrt{N/S})$ CFEs in the QD [51]. This is true even in the worst-case scenario, where the maximum allowed value of $L = \lfloor m \rfloor = \left\lfloor \lambda^{u+\lceil \log_\lambda m_c \rceil} \right\rfloor$ is chosen during the $(u + \lceil \log_\lambda m_c \rceil)$th BBHT iteration associated with $u \geq 0$.

For $1 < \lambda < 4/3$, the BBHT will find a solution, if it does exist, and this is accomplished in the worst-case scenario at the cost of fewer CFEs in the QD than [51]

$$L_{BBHT}^{QD,\max} = \left(\frac{\lambda}{\lambda - 1} + \frac{\lambda}{4 - 3\lambda} \right) \cdot \frac{1}{2} \sqrt{\frac{N}{S}}. \tag{2.49}$$

Let us continue by using $\lambda = 6/5$ in Algorithm 1, for the reason that this value of λ minimizes the $L_{BBHT}^{QD,\max}$ in Equation 2.49 and it corresponds to the minimum value of $L_{BBHT}^{QD,\max} = 4.5\sqrt{N/S}$.

Let us proceed by applying the BBHT QSA in our scenario described in Table 2.1 for finding the index x_s such that $f(x_s) = 0.38 = \delta$, assuming that we do not know that $\delta = f(2) = 0.38$ appears only once as a result of the CF evaluations. Assuming uniqueness of our solution, which is the worst case scenario, the BBHT QSA has to find it after a maximum of $L_{BBHT}^{QD,\max} = 4.5\sqrt{N} = 9$ $\mathcal{G}$ / Oracle calls and we choose $\lambda = 6/5$. Since the BBHT QSA includes randomly generated parameters, we offer one of the possible outcomes in Table 2.3, where the steps visited by the BBHT QSA are also given. The probabilities included in the parentheses denote the probability of observing the obtained state before the measurement, but naturally, these probabilities are not available in real applications. The total number of CFEs was $L_{BBHT}^{total} = L_{BBHT}^{CD} + L_{BBHT}^{QD} = 2 + 1 = 3$.

2.4.3 Dürr-Høyer Algorithm

The DHA [52] finds the solution $x_{\min} = \arg\min_{\forall x} \{f(x)\}$ that minimizes $f(x)$ by employing the BBHT QSA. The only modification in the BBHT QSA is that the Oracle in $\mathcal{G}$ of Figure 2.5 will mark as solutions those particular states x that satisfy $f(x) < \delta$. Since the Oracle no longer searches for the specific solutions that satisfy $f(x) = \delta$, the circuit introduced in Figure 2.6 cannot be used for the DHA.

Table 2.3: BBHT QSA Scenario's Instance

Step	Process
1	Set $m \leftarrow 1$, $\lambda \leftarrow 6/5$ and $L^{QD}_{BBHT} \leftarrow 0$, $L^{CD}_{BBHT} \leftarrow 0$
2	Since $m = 1$, we have $L \in \{0, 1\}$ and we randomly choose $L \leftarrow 0$
3	After $L = 0$ $\mathcal{G}$ operations: $\|x_f\rangle = \mathcal{G}^L\|x\rangle = \mathcal{G}^0\|x\rangle = \|x\rangle$
4	We observe $\|x_f\rangle$ and obtain $\|1\rangle$ (25% probability)
5	We compute $f(1) = 0.16$ in the classical domain.
6	Update $L^{CD}_{BBHT} \leftarrow L^{CD}_{BBHT} + 1 = 1$ and $L^{QD}_{BBHT} \leftarrow L^{QD}_{BBHT} + L = 0$
7	We check that $f(1) \neq \delta$
9-10	$L^{QD}_{BBHT} < L^{QD,\ \max}_{BBHT} = 9$, thus $m \leftarrow \min\{\lambda m, \sqrt{N}\} = \lambda m = 6/5 = 1.2$
2	Since $m = 1.2$, we have $L \in \{0, 1\}$ and we randomly choose $L = 1$
3	After $L = 1$ $\mathcal{G}$ operations: $\|x_f\rangle = \mathcal{G}^L\|x\rangle = \mathcal{G}^1\|x\rangle = \|x_1\rangle$, where $\|x_1\rangle$ is in Equation 2.46
4	We observe $\|x_f\rangle$ and obtain $\|2\rangle$ (100% probability)
5	We compute $f(2) = 0.38$ in the classical domain.
6	Update $L^{CD}_{BBHT} \leftarrow L^{CD}_{BBHT} \leftarrow L^{CD}_{BBHT} + 1 = 2$ and $L^{QD}_{BBHT} \leftarrow L^{QD}_{BBHT} + L = 1$
7-8	Since $f(2) = 0.38 = \delta$, we conclude $x_s \leftarrow 2$. Output x_s, L^{CD}_{BBHT}, L^{QD}_{BBHT} and exit.

2.4.3.1 Quantum Bit String Comparator

For the sake of marking the states x which satisfy $f(x) < \delta$ by passing an entangled qubit in the $|-\rangle$ state through a NOT gate as in Grover's QSA, we may use an alternative version of the Quantum Bit String Comparator (QBSC) introduced in [139] and depicted in Figure 2.11. Without loss of generality, we assume that Z qubits are employed for representing $f(x_j)$, $j = 1, 2, \ldots, 2^n$, and δ as in Equation 2.34, Equation 2.35, Equation 2.36 and Equation 2.37, and that the most significant qubits are $|f(x_j)_1\rangle$ and $|\delta_1\rangle$, respectively. Based on Figure 2.11, three auxiliary qubits are invoked for comparing each pair of $\{|f(x_j)_i\rangle, |\delta_i\rangle\}$, all initialised in the $|0\rangle$ state. After the operation of the three NOT gates and the three Toffoli gates of Figure 2.11, the first auxiliary qubit of each $\{|f(x_j)_i\rangle, |\delta_i\rangle\}$ pair will be found in the $|1\rangle$ state if $f(x_j)_i > \delta_i$, or, equivalently, if $f(x_j)_i = 1$ and $\delta_i = 0$. Similarly, the second auxiliary qubit of each $\{|f(x_j)_i\rangle, |\delta_i\rangle\}$ pair will be in the $|1\rangle$ state after the first five time steps if $f(x_j)_i = 0$ and $\delta_i = 1$, while the third auxiliary qubit will be in the $|1\rangle$ state if $f(x_j)_i = \delta_i$. Given that if $k < l$ then $|f(x_j)_k\rangle$ is a more significant qubit than $|f(x_j)_l\rangle$, we may observe in Figure 2.11 the order of influence for the less significant bit, which is illustrated by the Toffoli gates controlled by the more significant qubits. More specifically, the comparison of the kth pair of bits influences the total output of the circuit, if all the $\{|f(x_j)_i\rangle, |\delta_i\rangle\}$ pairs with $i = 1, 2, \ldots, k-1$ satisfy $f(x_j)_i = \delta_i$, or, in other words, if all the bits that are more significant than the kth bit in $f(x_j)$ have the same value as their respective bits in δ_j.

The output of the QBSC depends on the measurements of the first two auxiliary qubits, $|b_{1,>}\rangle$ and $|b_{1,<}\rangle$, of the most significant $\{|f(x_j)_i\rangle, |\delta_i\rangle\}$ pair. In more detail, if we observe

$|b_{1,>}\rangle = |1\rangle$ and $|b_{1,<}\rangle = |0\rangle$, then $f(x_j) > \delta$. Similarly, if we obtain $|b_{1,>}\rangle = |0\rangle$ and $|b_{1,<}\rangle = |1\rangle$, then $f(x_j) < \delta$. Finally, if we measure $|b_{1,>}\rangle = |b_{1,<}\rangle = |0\rangle$ then $f(x_j) = \delta$.

2.4.3.2 The Dürr-Høyer Oracle

The DHA aims for marking the state x_j if $f(x_j) < \delta$. The proposed circuit of the Oracle in the DHA is presented in Figure 2.12. An alternative version of the QBSC is used, where the least significant bits are checked only for the case, where $f(x_j)_Z < \delta_Z$. Moreover, instead of observing $|b_{1,>}\rangle$ and $|b_{1,<}\rangle$, we use $|b_{1,<}\rangle$ as the control qubit of a *CNOT* gate, where the Oracle's auxiliary qubit that is initially in the $|-\rangle$ state acts as the target qubit. Following the operation of the *CNOT* gate we perform the inverse operations, as in Figure 2.6, for ensuring that the Oracle is a unitary operator. Finally, the $|x\rangle$ quantum register is only entangled with the last qubit.

Algorithm 2 Dürr-Høyer Algorithm [3]

1: Choose i uniformly from the set $\{0, \ldots, N-1\}$ and set $L^{QD}_{DHA} \leftarrow 0$, $L^{CD}_{DHA} \leftarrow 0$.
2: The BBHT QSA is employed with $\delta \leftarrow f(i)$ and an Oracle that marks as solutions the states $|x\rangle$ that obey $f(x) < \delta$. Obtain x_s, L^{CD}_{BBHT} and L^{QD}_{BBHT} from the BBHT QSA.
3: $L^{CD}_{DHA} \leftarrow L^{CD}_{DHA} + L^{CD}_{BBHT}$ and $L^{QD}_{DHA} \leftarrow L^{QD}_{DHA} + L^{QD}_{BBHT}$.
4: **if** $f(x_s) \geq f(i)$ or $L^{QD}_{DHA} \geq L^{QD,\,\max}_{DHA}$ **then**
5: Set $x_{\min} \leftarrow i$, output $x_{\min}$ and exit.
6: **else**
7: Set $i \leftarrow x_s$ and go to Step 2.
8: **end if**

2.4.3.3 Methodology

The steps of the DHA are stated in Algorithm 2 [52]. It was formally shown in [52] that $x_{\min}$ is found with 100% probability after $L^{QD,\,\max}_{DHA} = 22.5\sqrt{N}$ applications of the $\mathcal{G}$ operator of Figure 2.5 in the worst-case scenario and from Section 2.4.2 we may conclude that the best case scenario includes as few as $4.5\sqrt{N}$ Grover iterations, if the initial i is chosen to be equal to $x_{\min}$ and thus $S = 0$. Hence, the DHA may be carried out in $22.5\sqrt{N}$ and $4.5\sqrt{N}$ Oracle operations in the worst-case and best-case scenario, respectively. It should be noted that in contrast to Grover's QSA [50] and the BBHT QSA [51], the DHA [52] does not assume any *a priori* knowledge of the values of the CF evaluations, making it applicable in a broad range of applications, where low-cost optimization is desired.

The CF evaluations in Step 4 of Algorithm 2 have already been realized in the BBHT QSA in the classical domain, therefore they do not contribute in the complexity. Since the number of CF evaluations performed by the BBHT QSA in the classical domain depend on the behaviour of the CFEs in the quantum domain, we are only able to predict with certainty only the minimum number of CFEs performed in the classical domain, which correspond to the $L^{QD}_{DHA} = 4.5\sqrt{N}$. The scenario which gives the lowest number of CFEs in the classical domain assumes that the initial input i is equal to the solution $x_{\min}$. Hence,

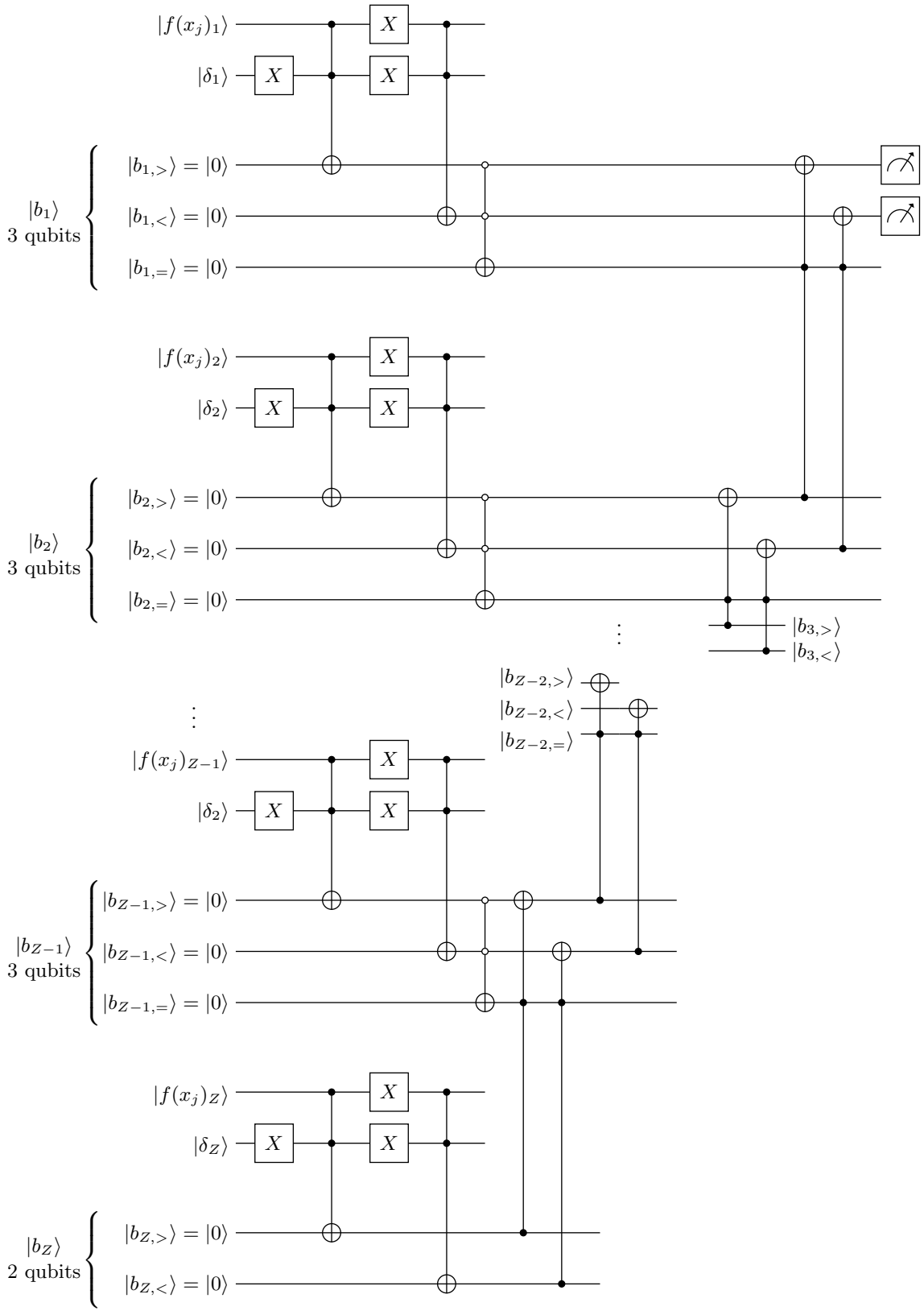

Figure 2.11: Quantum circuit of the Quantum Bit String Comparator presented in [139].

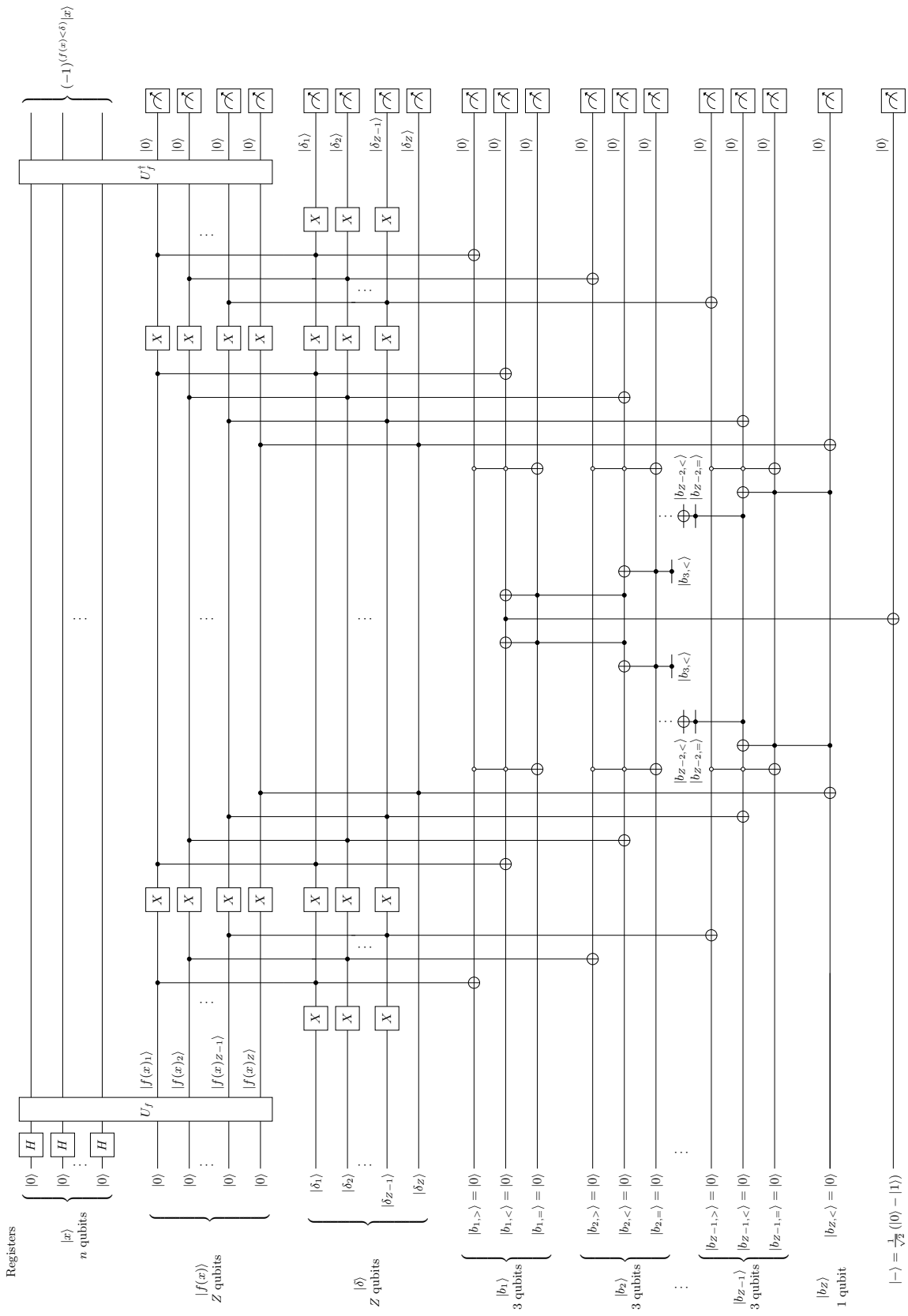

Figure 2.12: Quantum circuit of the proposed Oracle in the Dürr-Høyer algorithm, by using an alternate version of the Quantum Bit String Comparator.

the BBHT QSA employed by the DHA will stop after $L_{DHA}^{QD} = 4.5\sqrt{N}$ Oracle operations, which is the minimum possible number of CFEs in the quantum domain for the DHA. According to Step 2 of Algorithm 1, the number of Grover iterations L is uniformly chosen from the set $\{0, \ldots, \lfloor m \rfloor\}$ at the beginning of each BBHT iteration, where m is updated according to $m \leftarrow \min\{\lambda m, \sqrt{N}\}$ and it initially is equal to $m = 1$. A solution will not be found, since $i = x_{\min}$, hence the faster we reach $L_{BBHT}^{QD} = L_{BBHT}^{QD,\,\max} = 4.5\sqrt{N}$, the fewer CFEs we will need to perform in the classical domain after each "guess" of the BBHT QSA at Steps 4 and 5 of Algorithm 1. The scenario that includes the minimum number of CFEs in the classical domain is the one where L is chosen equal to $\lfloor m \rfloor$ during each BBHT iteration. Therefore, the minimum number of CFEs in the classical domain $L_{DHA}^{CD,\,\min}$ for the DHA is

$$L_{DHA}^{CD,\,\min} = \min\left\{ \arg_{L_{DHA}^{CD}} \left\{ \left[\sum_{j=0}^{L_{DHA}^{CD}-1} \min\left(\left\lfloor \lambda^j m \right\rfloor, \sqrt{N} \right) \right] \geq 4.5\sqrt{N} \right\} \right\}. \tag{2.50}$$

The scenario that includes the total minimum number of CFEs in the classical and the quantum domain, is the one where $L_{DHA}^{CD,\,\min}$ iterations of the BBHT are performed and the total number of Grover iterations applied in these BBHT iterations is equal to $L_{BBHT}^{QD,\,\max} = 4.5\sqrt{N}$. For example, in a system where $N = 4$ and $\lambda = 6/5$, the minimum number of CFEs in the classical domain in the DHA is performed when $x_{\min}$ is our initial guess and also when $L_{DHA}^{CD,\,\min} = 7$ according to Equation 2.50. The minimum total number of CFEs is achieved when at the same time we had $L_{DHA}^{QD} = L_{BBHT}^{QD,\,\max} = 4.5\sqrt{N} = 9$ Oracle operations. This may occur if L is chosen to be equal to 1 during the first 5 BBHT iterations, and then equal to 2 for the last two BBHT iterations. In general, the lower bound of the number of CFEs in the DHA is

$$L_{DHA}^{\min} = L_{DHA}^{QD,\,\min} + L_{DHA}^{CD,\,\min} = L_{BBHT}^{QD,\,\max} + L_{DHA}^{CD,\,\min}. \tag{2.51}$$

2.4.3.4 Dürr-Høyer based MUD in a DS-CDMA scenario

The DHA-based MUD may be employed in hard-input hard-output receivers, where channel coding has not been used, or no iterations between the channel decoder and the MUD are required. The DHA relies on a range of randomly generated variables, as exemplified in Algorithm 1 and Algorithm 2, hence resulting into different sequences of steps, even if we employ it in the same scenario. In our DS-CDMA scenario, the most likely 4-level symbol to have been transmitted is the one that maximizes the CF in Equation 2.18. Hence, we employ the DHA to find the minimum of the function $-f(x)$. An instance where the DHA is employed to find $x_{\min}$ such that $-f(x_{\min}) \leq -f(x)$, where $x = 0, 1, 2, 3$ in our DS-CDMA MUD scenario of Equation 2.18 is presented in Table 2.4, where we have $\lambda = 6/5$, $L_{BBHT}^{QD,\,\max} = 4.5\sqrt{N} = 9$ and $L_{DHA}^{QD,\,\max} = 22.5\sqrt{N} = 45$ Grover iterations. The acronym BBHT refers to the numbered step in the BBHT QSA. Even though the total number of CF evaluations in this scenario turns out to be higher than $N = 4$, which is the complexity in the optimal classical algorithm, its computational power is revealed in systems associated

with a large N.

Let us proceed by stating some insightful comments on the instance of the DHA's application in our scenario. For deeper intuition of the processes, let us assume that we knew *a priori* the CF evaluations of Equation 2.18. The first time when we visit Step 2 in Table 2.4, it may be concluded that we found a solution in the BBHT QSA without applying Grover operators of Figure 2.5 at all. This is very likely since all the CF evaluations of $-f(x)$ for $x = 0, 2, 3$ are smaller than $\delta = -f(1)$ and hence there are $S = 3$ solutions amongst the $N = 4$ entries, resulting in 75% probability of obtaining a solution by simply observing the equiprobable initialized superposition of states, with 25% probability of obtaining each of the four states. When the BBHT QSA of Algorithm 1 is employed for the second time, we have $S = 1$ solution and that solution is $|x_s\rangle = |2\rangle$. Since there are $N = 4$ entries, if $L = 1$ was chosen in the BBHT QSA we would obtain $|x_f\rangle = |2\rangle$ with 100% probability, as it was the case in our instance. Finally, when the BBHT QSA was employed for the last time, there were $S = 0$ solutions, since $x_{\min}$ had already been found. Naturally, this knowledge is unavailable to the BBHT QSA, which hence performed the maximum number of $\mathcal{G}$ operations, namely $L_{BBHT}^{QD,\,\max} = 9$, finally yielding $x_{new} = 0$ and allowing us to conclude that we have $x_{\min} = 2$, since $-f(2) < -f(0)$. The number of CFEs performed in the classical domain is equal to 12, which is larger than the Grover iterations. In larger systems, the number of CFEs in the classical domain is a small fraction of the CFEs performed in the quantum domain as it will be demonstrated in Section 2.6.

Algorithm 3 Deterministically-initialized, ES-aided Dürr-Høyer Algorithm [2]

1: Set the maximum allowed number of total CFEs L_{stop}. Furthermore, set $i \leftarrow x_I$ and $L_{DHA} \leftarrow 0$, $L_{DHA}^{CD} \leftarrow 0$, $L_{DHA}^{QD} \leftarrow 0$.
2: The BBHT QSA is employed with $\delta \leftarrow f(i)$, an Oracle that marks as solutions the states $|x\rangle$ that obey $f(x) < \delta$ and $L_{BBHT}^{\max} \leftarrow \min\{4.5\sqrt{N}, L_{stop} - L_{DHA}\}$, where $L_{BBHT}^{\max}$ refers to the total allowed number of CFEs in both the classical and the quantum domains. Obtain x_s, L_{BBHT}^{CD} and L_{BBHT}^{QD} from the BBHT QSA.
3: $L_{DHA}^{CD} \leftarrow L_{DHA}^{CD} + L_{BBHT}^{CD}$, $L_{DHA}^{QD} \leftarrow L_{DHA}^{QD} + L_{BBHT}^{QD}$ and $L_{DHA} \leftarrow L_{DHA} + L_{DHA}^{CD} + L_{DHA}^{QD}$.
4: **if** $f(x_s) \geq f(i)$ or $L_{DHA} \geq L_{stop}$, **then**
5: Set $x_{\min} \leftarrow i$, output $x_{\min}$ and exit.
6: **else**
7: Set $i \leftarrow x_s$ and go to Step 2.
8: **end if**

2.4.4 Deterministically-initialized Early-Stopping Dürr-Høyer Algorithm

The proposed Early-Stopping (ES) DHA is summarized in Algorithm 3. The differences with respect to the original DHA are two-fold. Firstly, a previously obtained value x_I, for example the MF output x_{MF} in CDMA communication systems or the ZF output x_{ZF} in SDMA communications systems, the CFE of which is considered to be closer to that of $x_{\min}$, is used as the initial input i in Step 1 of Algorithm 2 instead of i being randomly chosen from the set $\{0, \ldots, N-1\}$ with a probability of $1/N$. Secondly, a specific stopping condition is used in Step 6, which has to satisfy $L'_{stop} \geq L_{DHA}^{\min}$ which is the user-defined

Table 2.4: DHA in the DS-CDMA MUD Scenario

Step	**Process**
1	We randomly choose $i \leftarrow 1$ from the set $\{0, 1, 2, 3\}$ and set $L_{DHA}^{CD} \leftarrow 0$, $L_{DHA}^{QD} \leftarrow 0$
2	Set $\delta \leftarrow -f(1) = -0.16$ and employ the BBHT QSA
BBHT 1	Set $m \leftarrow 1$, $\lambda \leftarrow 6/5$ and $L_{BBHT}^{CD} \leftarrow 0$, $L_{BBHT}^{QD} \leftarrow 0$
BBHT 2	Since $m = 1$, $L \in \{0, 1\}$ and we randomly choose $L \leftarrow 0$
BBHT 3	After $L = 0$ $\mathcal{G}$ operations: $\|x_f\rangle = \mathcal{G}^L\|x\rangle = \mathcal{G}^0\|x\rangle = \|x\rangle$
BBHT 4-5	We observe $\|x_f\rangle$ and obtain $\|3\rangle$ (25% probability). We compute $-f(3) = -0.27$ in the classical domain.
BBHT 6	We set $L_{BBHT}^{CD} \leftarrow 1$ and $L_{BBHT}^{QD} \leftarrow 0$
BBHT 7-8	We check that $-f(3) < \delta$. Hence, set $x_s \leftarrow 3$ and exit
3	Set $L_{DHA}^{CD} \leftarrow L_{DHA}^{CD} + L_{BBHT}^{CD} = 1$ and $L_{DHA}^{QD} \leftarrow L_{DHA}^{QD} + L_{BBHT}^{QD} = 0$
4	$-f(3) < -f(1)$ and $L_{DHA}^{QD} < L_{DHA}^{QD,\,\max} = 45$
6-7	Set $i \leftarrow x_s = 3$
2	Set $\delta \leftarrow -f(3) = -0.27$ and employ the BBHT QSA
BBHT 1	Set $m \leftarrow 1$, $\lambda \leftarrow 6/5$ and $L_{BBHT}^{CD} \leftarrow 0$, $L_{BBHT}^{QD} \leftarrow 0$
BBHT 2	Since $m = 1$, $L \in \{0, 1\}$ and we randomly choose $L \leftarrow 1$
BBHT 3	After $L = 1$ $\mathcal{G}$ operations: $\|x_f\rangle = \mathcal{G}^L\|x\rangle = \mathcal{G}^1\|x\rangle = \|x_1\rangle$, where $\|x_1\rangle$ is in Equation 2.46
BBHT 4-5	We observe $\|x_f\rangle$ and obtain $\|2\rangle$ (100% probability). We compute $-f(2) = -0.38$ in the classical domain
BBHT 6	Set $L_{BBHT}^{CD} \leftarrow 1$ and $L_{BBHT}^{QD} \leftarrow 1$
BBHT 7-8	We check that $-f(2) < \delta$. Hence, set $x_s \leftarrow 2$ and exit
3	Set $L_{DHA}^{CD} \leftarrow L_{total}^{CD} + L_{BBHT}^{CD} = 2$ and $L_{DHA}^{QD} \leftarrow L_{total}^{QD} + L_{BBHT}^{QD} = 1$
4	$-f(2) < -f(3)$ and $L_{total}^{QD} < L_{DHA}^{QD,\,\max} = 45$
6-7	Set $i \leftarrow x_s = 2$
2 & BBHT	Set $\delta \leftarrow -f(2) = -0.38$ and the BBHT QSA outputs $x_s = 0$ with $L_{BBHT}^{QD} = 9$ and $L_{BBHT}^{CD} = 10$
3	$L_{DHA}^{QD} \leftarrow L_{DHA}^{QD} + L_{BBHT}^{QD} = 1 + 9 = 10$ and $L_{DHA}^{CD} \leftarrow L_{DHA}^{CD} + L_{BBHT}^{CD} = 2 + 10 = 12$
4-5	Since $-f(0) > -f(2)$, set $x_{\min} \leftarrow 2$, as well as $L_{DHA} = L_{DHA}^{CD} + L_{DHA}^{QD} = 22$, output $x_{\min}$ and exit

Table 2.5: MF-initiated, ES-aided DHA in the DS-CDMA MUD Scenario

Step	Process
1	We set $L_{stop} = 4$, $i \leftarrow x_{MF} = 2$ and also set $L_{total} \leftarrow 0$, $L_{total}^{CD} \leftarrow 0$, $L_{total}^{QD} \leftarrow 0$
2	Set $\delta \leftarrow -f(2) = -0.38$ and employ the BBHT QSA with $L_{BBHT}^{\max} \leftarrow \min\{4.5\sqrt{N}, L_{stop} - L_{total}\} = \min\{9, 3\} = 3$
BBHT 1	Set $m \leftarrow 1$, $\lambda \leftarrow 6/5$ and $L_{BBHT} \leftarrow 0$
BBHT 2	Since $m = 1$, $L \in \{0, 1\}$ and we randomly choose $L \leftarrow 1$
BBHT 3	After $L = 1$ $\mathcal{G}$ operations: $\|x_f\rangle = \mathcal{G}^L\|x\rangle = \mathcal{G}\|x\rangle = \|x\rangle$, since no solutions exist
BBHT 4-5	We observe $\|x_f\rangle$ and obtain $\|1\rangle$ (25% probability). We compute $-f(1) = -0.16$ in the classical domain.
BBHT 6	Set $L_{BBHT}^{CD} \leftarrow 1$ and $L_{BBHT}^{QD} \leftarrow 1$. Hence, $L_{BBHT} \leftarrow L_{BBHT}^{CD} + L_{BBHT}^{QD} = 2$
BBHT 9-10	We check that $-f(1) > \delta$ and $L_{BBHT} < L_{BBHT}^{\max} = 3$ and $L_{BBHT}^{QD} < L_{BBHT}^{QD,\,\max} = 4.5\sqrt{N} = 9$. Hence, $m \leftarrow \min\{\lambda m, \sqrt{N}\} = \min\{6/5, 2\} = 6/5$. Go to Step BBHT 2
BBHT 2	Since $m = 6/5$, $L \in \{0, 1\}$ and we randomly choose $L \leftarrow 1$
BBHT 3	After $K = 1$ $\mathcal{G}$ operations: $\|x_f\rangle = \mathcal{G}^L\|x\rangle = \mathcal{G}\|x\rangle = \|x\rangle$, since no solutions exist
BBHT 4-5	We observe $\|x_f\rangle$ and obtain $\|2\rangle$ (25% probability). We compute $-f(2) = -0.38$ in the classical domain
BBHT 6	Set $L_{BBHT}^{CD} \leftarrow 2$, $L_{BBHT}^{QD} \leftarrow 2$ while $L_{BBHT} \leftarrow 4$
BBHT 9-10	We check that $-f(2) = \delta$. However, since $L_{BBHT} = L_{BBHT}^{\max} = 4$, we set $x_s \leftarrow 2$, output x_s and exit the BBHT QSA
3	$L_{total} \leftarrow L_{total} + L_{BBHT} = 0 + 4 = 4$
4-5	Since $-f(1) > -f(2)$, set $x_{\min} \leftarrow 2$, output $x_{\min}$ and exit

number of CFEs, instead of naturally stopping when $x_{\min}$ was found. In Step 4, we have proposed the subtraction of $L_{DHA}^{\min} = L_{DHA}^{CD,\,\min} + L_{DHA}^{QD,\,\min} = 4.5\sqrt{N} + L_{DHA}^{CD,\,\min}$ CFEs, where $L_{DHA}^{CD,\,\min}$ is given in Equation 2.50, due to their redundancy in detecting $x_{\min}$, since they are employed only to determine that the optimal point has been already found and not to actually find it. Hence, $L'_{stop} \geq L_{DHA}^{\min}$ may be selected according to acquired statistics, such as the Cumulative Density Function (CDF) of the CFEs required to achieve a certain probability of success. For example, L'_{stop} may be equal to the total number of CFEs required in both the classical and the quantum domain for the DHA to succeed in finding $x_{\min}$ in 60% of the time. In this scenario, if we allow only $L_{stop} = L'_{stop} - L_{DHA}^{\min}$ CFEs instead, we should expect the same 60% probability of success since the last $L_{DHA}^{\min}$ CFEs were only employed for the DHA to realize that the solution has already been found. Based on the application-based proposed techniques which will be analysed in the following, at least $L_{DHA}^{\min} = L_{DHA}^{QD,\,\min} + L_{DHA}^{CD,\,\min} = 4.5\sqrt{N} + L_{DHA}^{CD,\,\min}$ CFEs may be avoided, which greatly reduces the computational complexity in large systems. Further explanation and more examples are presented in Section 2.6.

Let us proceed by employing the proposed ES-aided DHA in our DS-CDMA scenario. The initial input will be the MF output, which was $x_{MF} = 2$. It should be noticed that $x_{MF} = x_{\min}$, but this cannot be known in a real application before evaluating the CFE of every legitimate multi-level symbol. In addition, let us fix $L_{stop} = 3$ CFEs. The value of

L_{stop} may be the upper available limit of CFEs, representing the affordable computational complexity. Hence, the fixed computational complexity of the ES-aided DHA is another advantage when compared to the optimal DHA where the number of CFEs in the quantum domain varies from $4.5\sqrt{N}$ up to $22.5\sqrt{N}$. An instance of our scenario when $x_{MF} = 2$ and $L_{stop} = 4$ is provided in Table 2.5. Even though $x_{\min}$ had been already found, the ES-aided DHA was not aware of it. By fixing $L_{stop} = 3$ CFEs, we managed to stop the DHA and determine $x_{\min} = 2$, even though the probability of success is not 100%. It should be noted that we would obtain the same result even if $0 \leq L_{stop} \leq 4.5\sqrt{N} + L_{DHA}^{CD,\,\min} = 9 + 7 = 16$, since we already own $x_{\min}$. The total number of CFEs was smaller than the lower bound of the DHA. In larger systems the choice of x_I and L_{stop} have a great impact on the performance of the algorithm. The choice of x_I will be made depending on the application, while L_{stop} will be determined according to offline simulations of the CDF of the frequency of total CFEs in the optimal DHA in every application.

2.5 Design Methodology

In this section we present the design methodology of our proposed ES-aided DHA QMUD by employing it in both full-rank and in challenging rank-deficient DS-CDMA and SDMA systems, both having the same user load. In this context it is of paramount importance that conventional MUDs tend to exhibit a high residual BER in rank-deficient scenarios, even though these often occur in practice, unless the upper layers simply block or drop users requesting access in scenarios of $U > SF$ and $U > P$. Quantitatively, our full-rank DS-CDMA system supports $U = 15$ users in conjunction with Gold codes having $SF = 15$ chips, while the SDMA system supports $U = 15$ users with the aid of $P = 15$ receive antennas at the BS, resulting in a user load of $U/SF = U/P = 1$. By contrast, our rank-deficient DS-CDMA system supports $U = 14$ users employing m-sequences having $SF = 7$ chips, while $U = 14$ users are supported in the SDMA system using $P = 7$ receive antennas installed at the BS. Hence the normalized user load in the rank-deficient systems is $U_L = U/SF = U/P = 2$. In all four systems BPSK symbols associated with $M = 2$ were transmitted and Turbo Convolutional Codes (TCC) having a rate of R=1/2, 8 trellis states and 4 inner decoding iterations were used. The bit-based interleavers have a length of 40 000 bits and 42 000 bits in the full-rank and the rank-deficient systems, respectively. The specific E_b/N_0 values we will refer to are the E_b/N_0 values per receive antenna. Table 2.6 summarizes the parameters of these four systems.

The BER performance of the [U=15, SF=15], [U=15, P=15], [U=14, SF=7] and [U=14, P=7] systems relying on the classical ML MUD and on the optimal DHA QMUD is presented in Figure 2.13. The BER of the optimal DHA QMUD is equivalent to that of the ML MUD, but this is achieved at fewer CFEs, as seen in Table 2.7. The DHA QMUD is deterministically-initialized, where the MF output was used as the initial input of the DHA in the DS-CDMA systems, while the ZF and MMSE detectors' outputs were used in the SDMA system for the rank-deficient and the full-rank scenarios, respectively. The full-rank [U=15, SF=15] system performs by 1.87 dB better than the rank-deficient [U=14, SF=7]

Table 2.6: Parameters of the four DS-CDMA and SDMA systems

	System 1	System 2	System 3	System 4
Number of Users	$U = 14$	$U = 14$	$U = 15$	$U = 15$
Multiple Access Scheme	DS-CDMA	SDMA	DS-CDMA	SDMA
Number of AEs at the BS	$P = 1$	$P = 7$	$P = 1$	$P = 15$
Spreading Factor	$SF = 7$	N/A	$SF = 15$	N/A
Spreading Codes	m-sequences	N/A	Gold Codes	N/A
Normalized User Load	$U_L = 2$	$U_L = 2$	$U_L = 1$	$U_L = 1$
Bit-based Interleaver Length	42 000	42 000	40 000	40 000
Number of AEs per User	$N_{T_x} = 1$			
Modulation	BPSK $M = 2$			
Channel Code	Turbo Code, $R = 1/2$, 8 Trellis states $I_{inner} = 4$ iterations			
Channel	Uncorrelated Rayleigh Channel			
Channel Estimation	Perfect			

system. This was indeed expected, since the Multi-User Interference (MUI) in the former system is lower owing to its lower normalized user-load of $U/SF = 1$, instead of $U/SF = 2$. A similar conclusion may be drawn for the full-rank and rank-deficient SDMA systems. As seen in Figure 2.13, the full-rank SDMA system requires approximately 3.04 dB lower bit-energy per receive antenna than the full-rank DS-CDMA system supporting $U = 15$ users for achieving a BER of 10^{-5}. Please note again that the [U=14, SF=7] and the [U=14, P=7] scenarios are highly rank-deficient, hence conventional MMSE-style MUDs would result in a high residual BER.

In our proposed MUD application, the M^U-ary symbol x_{MF} at the MF output of the DS-CDMA systems will be the initial value of $i = x_{MF}$ in Step 1 of the ES-DHA, since the MF output has on average a lower Euclidean distance from the optimal M^U-ary symbol $x_{\min}$ than a randomly chosen one, hence requiring fewer iterations for both the

Table 2.7: Number of CFEs of the systems in Figure 2.13 at the E_b/N_0 values per receive antenna corresponding to a BER of $\sim 10^{-5}$

	ML MUD	**DHA QMUD**	DS-CDMA	SDMA
$U = 14$	16 384	$SF = P = 7$	10 dB	6.65 dB
		Minimum	604	604
		Average	967.26	914.72
		Maximum	2238	2181
$U = 15$	32 768	$SF = P = 15$	8 dB	4.96 dB
		Minimum	844	844
		Average	1016.1	1286.6
		Maximum	2352	2763

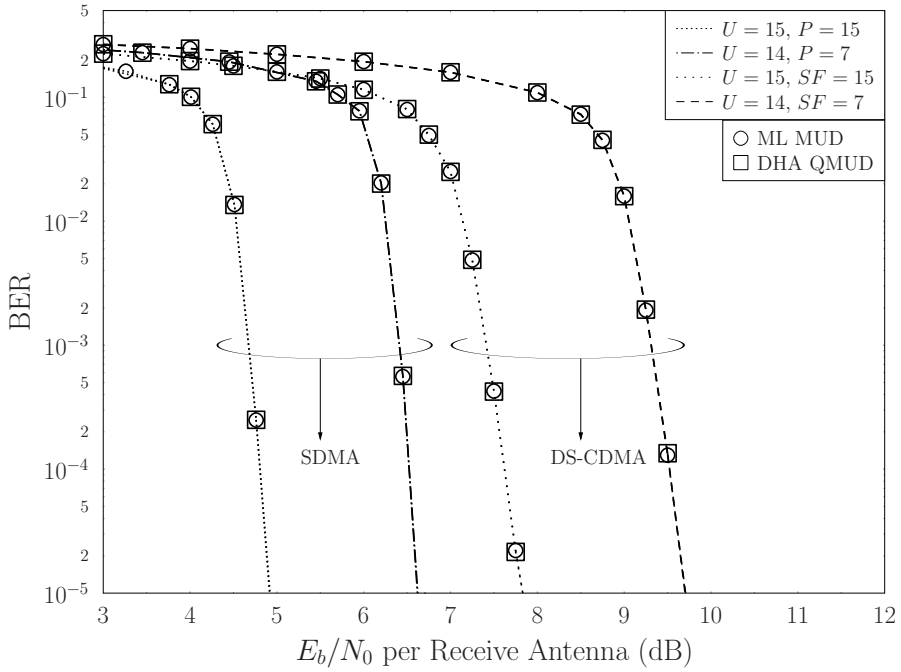

Figure 2.13: BER performance with respect to the E_b/N_0 per receive antenna of DS-CDMA and SDMA systems of Figure 2.1 and Figure 2.2, respectively, using the parameters of Table 2.6 supporting U users with SF chips in the spreading codes of the DS-CDMA systems and P receive antennas in the SDMA systems, employing BPSK modulation. The DHA is employed for performing optimal MUD. The bit-based interleavers' length is equal to 40 000 and 42 000 bits in the full-rank and the rank-deficient systems, respectively.

DHA and therefore also for the BBHT QSA to reach $x_{\min}$. The dependence of the DHA's complexity on the initial value i chosen at its first step is illustrated in Figure 2.14a, Figure 2.14b, Figure 2.14g and Figure 2.14h, where both the simulation-based experimental histogram approximating the PDF and the corresponding CDF of the DHA's total CFEs are presented for the investigated systems. Moreover, the PDF and CDF curves of the CFEs performed in the quantum and classical domains are also given for the rank-deficient systems in Figure 2.14c, Figure 2.14d, Figure 2.14e and Figure 2.14f. The randomly-initialized DHA QMUD has a similar PDF and CDF for the DS-CDMA and SDMA systems for the same search space size, verifying that the randomly-initialized DHA's complexity depends solely on the number of users and on the number of bits / symbol used, but not on the operating E_b/N_0 value or on the multiple access scheme used, in terms of the SF value, or the number of receive antennas P employed. The CDF curves of the randomly-initialized DHA provide the upper limit for the complexity of the QMUD, since in the worst-case scenario the conventional detectors will output random symbols. The complexity reduction achieved by the deterministically-initialized DHA with respect to the complexity of the randomly-initialized DHA varies as a function of the SF, E_b/N_0, the number of receive antennas P, as well as the channel, but it is almost always non-negligible, as illustrated in Figure 2.14, except when the conditions are so severe that essentially turn the conventional detector into a random symbol generator. Moreover, the PDF of the total number of CFEs performed in both the CD and QD in the DHA is the convolution of the number of CFEs performed in the CD and the number of Grover iterations, as it may be seen in

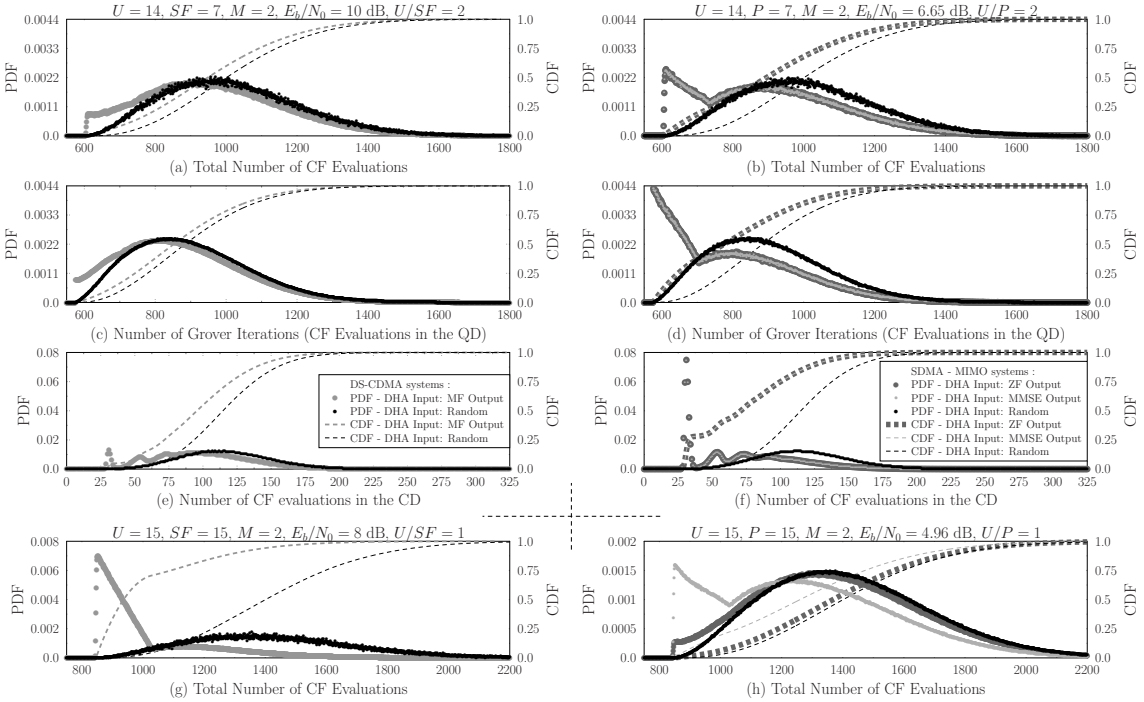

Figure 2.14: Simulated PDF and CDF of the total number of CFEs in the DHA employed in the (a) $[U{=}14, SF{=}7]$ DS-CDMA system of Figure 2.1, (b) $[U{=}14, P{=}7]$ SDMA system of Figure 2.2. The parameters of both systems are summarized in Table 2.6. The corresponding PDF and CDF curves of the number of CFEs performed in the quantum domain are presented in (c) and (d) for the $[U{=}14, SF{=}7]$ DS-CDMA system and the $[U{=}14, P{=}7]$ SDMA system, respectively, while the PDF and CDF curves of the number of CFEs performed in the classical domain are illustrated in (e) and (f) for the two systems, respectively. The PDF and CDF curves of the total number of CFEs in the DHA employed in the $[U{=}15, SF{=}15]$ DS-CDMA system and the $[U{=}15, P{=}15]$ SDMA system are depicted in (g) and (h), respectively. The chosen E_b/N_0 per receive antenna values correspond to a BER of $\sim 10^{-5}$.

Figure 2.14b, Figure 2.14d and Figure 2.14f for the rank-deficient SDMA system.

Again, the last $L_{DHA}^{QD,\,\min}{=}4.5\sqrt{M^U}$ Grover operations in the DHA are purely required by the DHA in order to realize that $x_{\min}$ has already been found, rather than to actually find it. Hence, if we have $i = x_{\min}$, then only $L_{DHA}^{\min}$ CFEs of Equation 2.51 will be performed, representing the lower limit in the DHA and explaining the reason that the probability of finding $x_{\min}$ with less than $L_{DHA}^{\min} = 604$ CFEs in the simulated PDF curves seen in Figure 2.14a, Figure 2.14b is equal to zero. The same applies for the full-rank systems of Figure 2.14g and Figure 2.14h, where $L_{DHA}^{\min} = 844$ CFEs are required according to Equation 2.51. Since $x_{MF} = x_{\min}$ is a common occurrence in full-rank DS-CDMA systems [11], such as the fully-loaded system of Figure 2.14g associated with $U/SF = 1$, we observe a peak in its PDF at $L_{DHA} = L_{DHA}^{\min}$ CFEs for $i = x_{MF}$. On the other hand, for the rank-deficient systems, such as the ones characterized in Figure 2.14a and Figure 2.14b, where we have $U/SF > 1$ and $U/P > 1$, respectively, we may observe that the MF, ZF and MMSE outputs are closer to a random guess of the transmitted M^U-ary symbol.

The CDF curves seen in Figure 2.14 are also shifted towards the lower CFE limit of the DHA, when we have deterministically-initialized i, indicating the complexity reduction

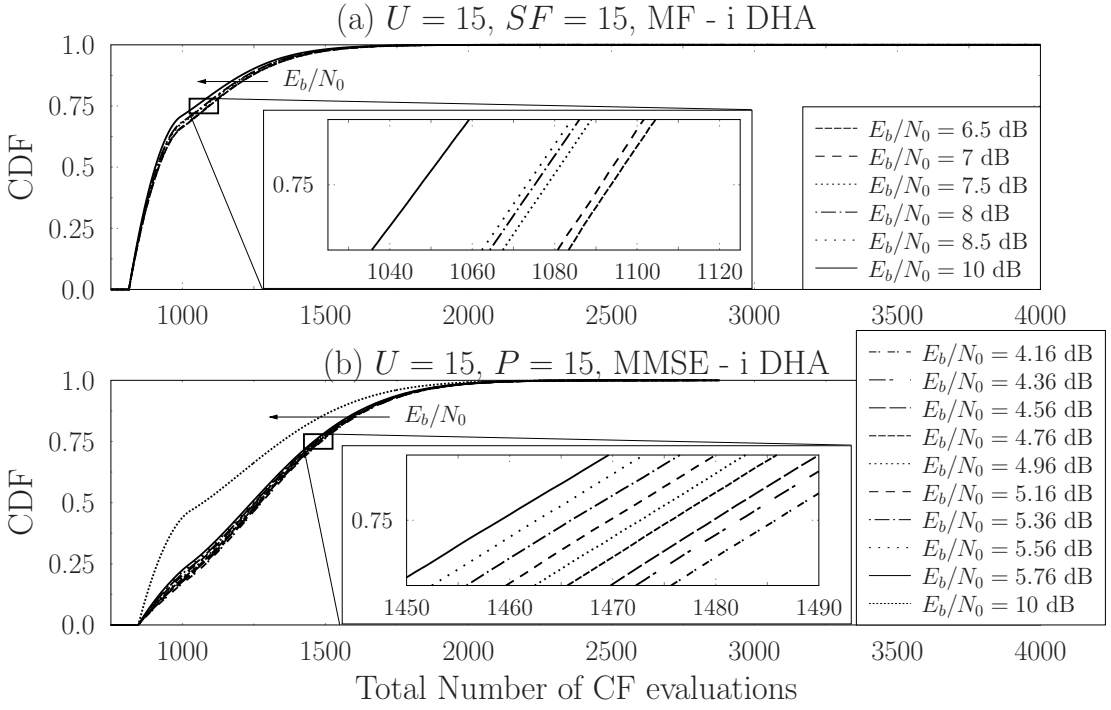

Figure 2.15: Simulated CDF curves of the number of CFEs in the DHA employed in the (a) [U=15, SF=15] and (b) [U=15, P=15] systems of Figure 2.1 and Figure 2.2, respectively, using the parameters of Table 2.6 for various values of E_b/N_0 per receive antenna.

achieved. Observe that in the full-rank scenario of Figure 2.14g, the shift of the MF-initialized system's CDF is more substantial than that of the MF-initialized rank-deficient DS-CDMA scenario. The specific E_b/N_0 per receive antenna value, where each system was investigated in Figure 2.14 corresponds to a BER of $\sim 10^{-5}$, since practical systems are desired to operate in that region. It is expected that the PDF and CDF curves will be further shifted towards fewer CFEs, when the E_b/N_0 is increased, since the event of $i = x_{MF} = x_{\min}$ in the DS-CDMA and $i = x_{MMSE} = x_{\min}$ in the SDMA systems will become more frequent even in rank-deficient systems. The CDF curves recorded for the [U=15, SF=15] and [U=15, P=15] systems in Figure 2.15 verify our expectations. According to the CDF curves seen in Figure 2.15, given at the same bit power per receive antenna of 10 dB, namely when an SDMA and a DS-CDMA system supporting the same number of users and employing the same modulation scheme operate at the same power level, the deterministically-initialized DHA used in the DS-CDMA system would require fewer CFEs to find $x_{\min}$. For example, for the sake of achieving 75% detection success probability, when the DS-CDMA and the SDMA systems support $U = 15$ users associated with $SF = 15$ chips and $P = 15$ receive antennas, respectively, at an E_b/N_0 per receive antenna value of 10 dB, the DHA requires 1047 CFEs in the DS-CDMA systems and 1347 CFEs in the SDMA system according to Figure 2.15a and Figure 2.15b, respectively.

The CDF shift seen in Figure 2.15a is small, when operating in the desired power region of the [U=15, SF=15] system, where the BER is sufficiently low. Similarly, the CDF shift seen in Figure 2.15b is also low – approximately 10 CFEs per 0.6 dB power

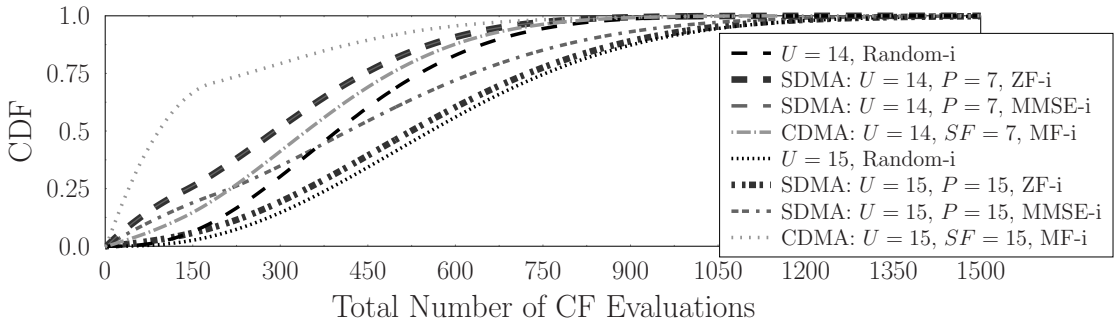

Figure 2.16: Simulated CDF curves of the number of CFEs in the DHA employed in the [U=14, SF=7], [U=15, SF=15] DS-CDMA systems of Figure 2.1 and [U=14, P=7], [U=15, P=15] SDMA systems of Figure 2.2, using the parameters summarized in Table 2.6, employing BPSK modulation for E_b/N_0 per receive antenna equal to 10 dB, 6.65 dB, 8 dB and 4.96 dB, respectively, where $L_{DHA}^{\min} = 604$ CFEs and 844 CFEs have been subtracted from the systems supporting $U = 14$ and $U = 15$ users, respectively.

increase. Based on the gradually-shifting nature of the CDFs with respect to power, we can benefit from an early stopping of the DHA. For example, if we stop the MMSE-initialized DHA of the [U=15, P=15] system after $L_{stop} = 1473$ CFEs, we will expect the DHA to find $x_{\min}$ in 75% of the instances for $E_b/N_0 = 4.96$ dB according to the CDF of Figure 2.15b. Furthermore, we may eliminate the redundant $L_{DHA}^{\min}$ number of CFEs without any degradation of the BER performance. The maximum number of CFEs required for achieving a specific probability of success may be visually presented as in Figure 2.16, where the CDF point corresponding to $L_{DHA}^{\min}$ CFEs in Figure 2.14 is mapped to 0 CFEs in Figure 2.16 and the rest of the points are mapped accordingly. Hence, if say 75% of detection success is desired at an E_b/N_0 per receive antenna of 4.96 dB in the system of Figure 2.15b, this may be achieved by employing the ES-DHA at the expense of $L_{DHA}^{75\%,10\text{ dB}} - L_{DHA}^{\min} = 1473 - 844 = 629$ CFEs, as illustrated in Figure 2.16. If the different CDF curves associated with each operating E_b/N_0 value are available, the probability of achieving the target BER may be estimated. In our simulations we will only rely on the CDFs of the systems evaluated at the power levels corresponding to a BER of $\sim 10^{-5}$, which are presented in Figure 2.14. Again, the SDMA systems operate at a lower power level than the DS-CDMA systems supporting the same user-load ratios.

The design procedure of the proposed ES-DHA QMUD may commence by generating the CDF curves of the randomly-initialized DHA, which do not depend on the channel, on the number of receive antennas, the value of SF, or the E_b/N_0 value, but only on the number of users U and on the specific choice of the M-ary modulation employed, which determine the size M^U of the search problem. Therefore, the CDF curve obtained by employing the randomly-initialized DHA for finding the index of the minimum entry in a database having M^U randomly generated entries is the same as if the CDF curve of the randomly-initialized DHA was generated based on the channel probabilities of the communication system. Moreover, the complexity of determining the CDFs of the randomly-initialized DHA when invoked for a database having randomly generated entries is much lower, since there is no need for employing U encoding and decoding procedures, as well as U bit

stream generations, symbol mapping and transmissions over fading channels. The CDF of the randomly-initialized DHA provides an upper limit for the complexity of the QMUD.

The design methodology is straightforward, since the ES-DHA QMUD may be flexibly set to the required number of CFEs. When approaching the optimal ML performance is the ultimate target, the design may commence by deciding upon the power levels the system's power control will have to operate at. Subsequently, the CDF curve of the deterministically-initialized DHA should be determined by off-line simulations at a power close to the chosen one. By observing the CDF curve generated after subtracting the number of CFEs $L_{DHA}^{\min}$ required by the DHA for realizing that the solution has already been found in Equation 2.51, the maximum number of CFEs L_{stop} corresponding to the desired point of the CDF may be extracted. Employing the ES-DHA QMUD and stopping it after the predetermined number of L_{stop} CFEs statistically-speaking guarantees the required performance at a low and fixed complexity even in highly rank-deficient systems, when powerful turbo codes are used for correcting the majority of the remaining detection errors.

The design methodology would depend on the maximum tolerable complexity quantified in terms of the maximum number of CFEs. By examining the pre-stored CDF of the randomly-initialized DHA, the expected probability of success may be found. If the probability of success is unsatisfactory, we may employ deterministically-initialized DHA. Consulting a pre-stored CDF curve for a specific operational E_b/N_0 value will lead us to conclusions regarding the probability of success, which will be higher than that of the randomly-initialized DHA. If the updated probability of success remains unsatisfactory, we may increase the power level. If the probability of success exceeds the design specifications, we may either choose to operate at a lower power, or reduce the complexity invested, in order to "just" satisfy our desired probability of success.

2.6 Simulation Results and Discussions

2.6.1 Full-Rank and Rank-Deficient DS-CDMA Versus SDMA Systems

Based on the previous observations and the CDF curves of Figure 2.16, in Table 2.8 we have gathered the maximum number of CFEs required by each investigated system for achieving a certain probability of success in finding $x_{\min}$ using the proposed deterministically-initialized ES-DHA. In Figure 2.17 and Figure 2.18 we considered the BER performance of both the rank-deficient and full-rank systems, respectively, where the ES-DHA was stopped after L_{stop} iterations appropriately chosen from Table 2.8. More precisely, according to Table 2.8, for the [U=15, SF=15] system we may infer that 99% of the instances require less than $L_{DHA}^{99\%,8\text{ dB}} = 827$ CFEs. Hence we expect the performance associated with $L_{stop} = 827$ CFEs to be the same as that of the optimal DHA QMUD, where we have $L_{stop} = 22.5\sqrt{M^U} = 4072$ Grover iterations and the maximum number of CFEs required for the detection of an M^U-ary symbol in our simulations was 2 352 CFEs. Therefore, by using the proposed ES-aided DHA we match the performance of the ML MUD, as seen in Figure 2.18, while eliminating the randomly appearing high peaks in its search-complexity.

Table 2.8: Number of CFEs of the systems in Figure 2.17 and Figure 2.18 required for achieving a specific success probability in the DHA.

CDF %	$U = 14$ $SF = 7$ @ 10 dB	$U = 15$ $SF = 15$ @ 8 dB	$U = 14$ $P = 7$ @ 6.65 dB	$U = 15$ $P = 15$ @ 4.96 dB
99%	881	827	854	1200
90%	628	461	590	832
80%	527	310	484	685
70%	456	175	410	175
60%	397	122	348	496
50%	345	93	292	418

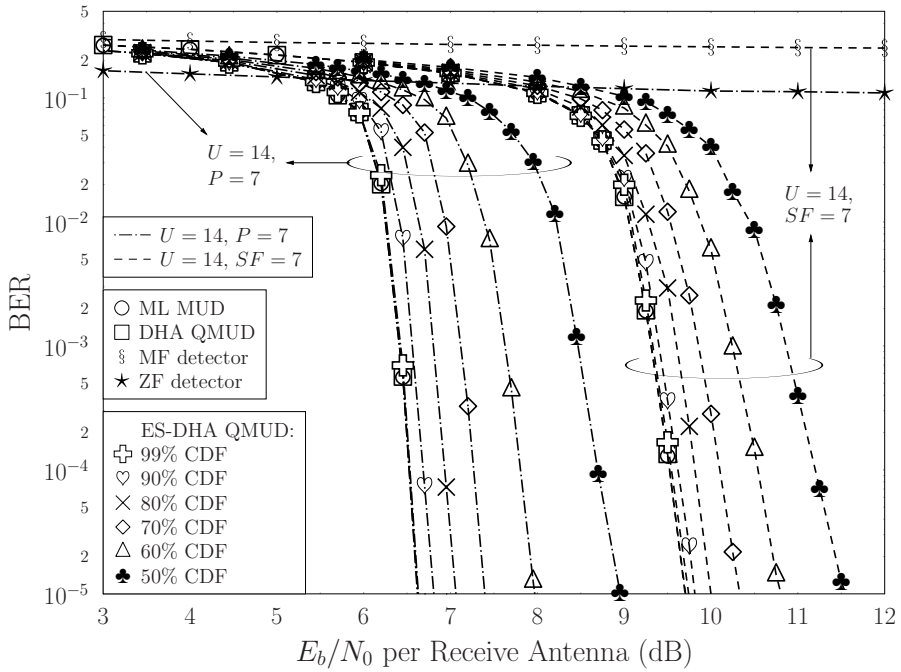

Figure 2.17: BER performance with respect to the E_b/N_0 per receive antenna of the rank-deficient DS-CDMA system of Figure 2.1 supporting $U = 14$ users with $SF = 7$ chips and the rank-deficient SDMA system of Figure 2.2 supporting $U = 14$ users with $P = 7$ receive antennas, with the stopping points of the ES-aided DHA QMUD having been chosen based on the fractions of the corresponding CDFs of Figure 2.14 and they are given in Table 2.8. The parameters of the systems are summarized in Table 2.6. The [U=14, P=7] system employs ZF-initialized ES-DHA QMUD while the MF-initialized ES-DHA QMUD is applied in the rank-deficient DS-CDMA system. Both systems employ a turbo convolutional code with rate R=1/2, relying on 8 trellis states, 4 inner decoding iterations and the bit-based interleavers have a length of 42 000 bits.

In fact, in the [U=15, SF=15] system we achieve the optimal ML performance at a complexity below the lower limit of the optimal DHA. The optimal ML performance is also achieved in the rank-deficient systems of Figure 2.17, provided that their specific numbers of CFEs associated with 99% detection success probability are used from Table 2.8.

Following the same methodology, in Figure 2.17 and Figure 2.18 we have also evaluated

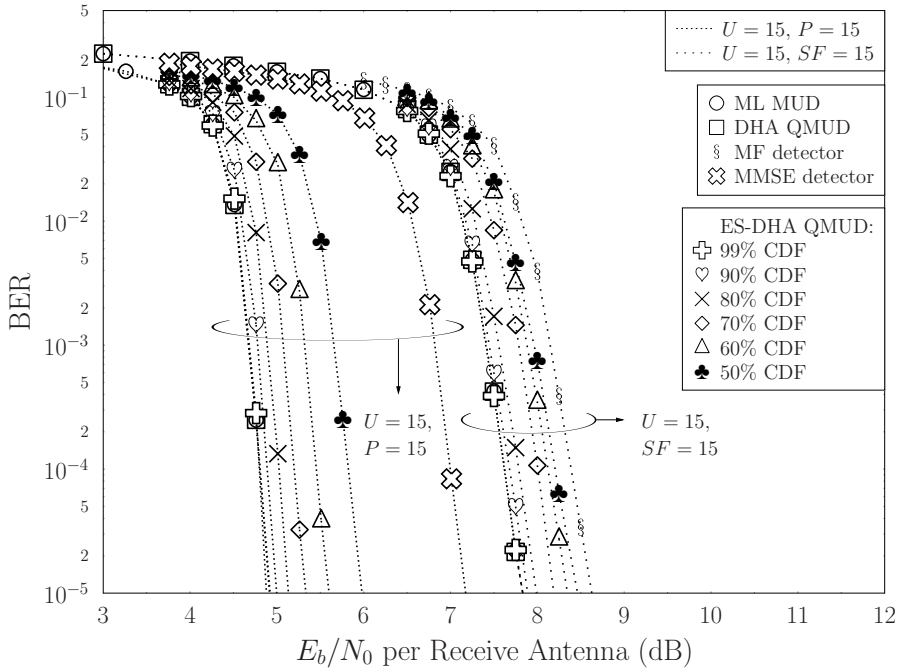

Figure 2.18: BER performance with respect to the E_b/N_0 per receive antenna of the full-rank DS-CDMA system of Figure 2.1 supporting $U = 15$ users with $SF = 15$ chips and the full-rank SDMA system of Figure 2.2 supporting $U = 15$ users with $P = 15$ receive antennas, with the stopping points of the ES-aided DHA QMUD having been chosen based on the fractions of the corresponding CDFs of Figure 2.14 and they are given in Table 2.8. The parameters of the systems are summarized in Table 2.6. The [U=15, P=15] system employs MMSE-initialized ES-DHA QMUD while the MF-initialized ES-DHA QMUD is applied in the full-rank DS-CDMA system. Both systems employ a turbo convolutional code with rate R=1/2, relying on 8 trellis states, 4 inner decoding iterations and the bit-based interleavers have a length of 40 000 bits.

the BER performance of both the fully-loaded and of the rank-deficient DS-CDMA and SDMA systems, respectively, while imposing specific complexity limits on the DHA. The ES-DHA QMUD was MMSE-initialized in the full-rank SDMA system of Figure 2.18, since this was found to provide a better initial estimate according to Figure 2.14h, while the ES-DHA QMUD of the rank-deficient SDMA system of Figure 2.17 was ZF-initialized. Both DS-CDMA systems employ MF-initialized ES-DHA QMUDs. As expected, the achievable performance degrades, when the DHA is stopped earlier than it naturally would, because in some of the cases only a sub-optimal solution will have been found. Comparing Figure 2.17 to Figure 2.18, the degradation experienced is higher for the rank-deficient systems. Furthermore, the DS-CDMA systems experience a lower degradation, when operating at the same success probability point of their respective CDF curves in both full-rank and rank-deficient systems. When operating at lower CDF points, the BER performance approaches that of the initial detector, since the 0% point of the CDF corresponds to having an output constituted by the initial "guess". It may be verified by the full-rank systems characterized in Figure 2.18 that indeed this is the case, while the performance of the rank-deficient systems in Figure 2.17 operating at the 50% points of their respective CDF curves is still adequate, when compared to the conventional detectors' performance, both of which have a high residual BER. If an even lower CDF point was chosen in a rank-deficient system, a

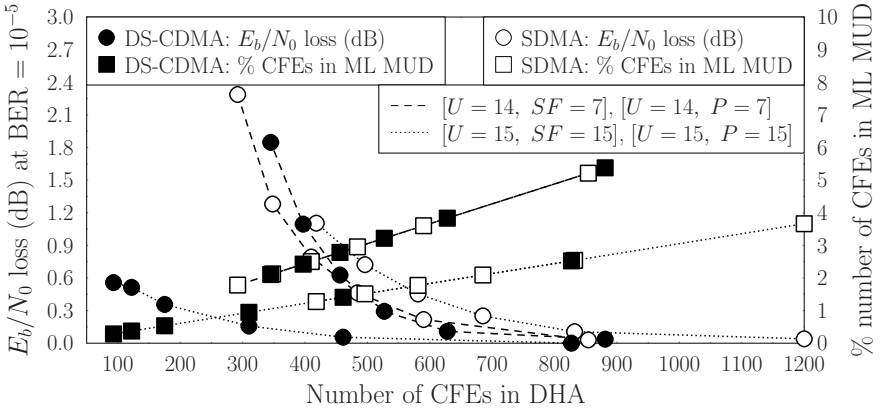

Figure 2.19: Illustration of the power loss and the simultaneous reduction in complexity in the full-rank and rank-deficient DS-CDMA and SDMA systems of Figure 2.1 and Figure 2.2, respectively, with respect to the maximum allowed CFEs in the ES-aided DHA QMUD when compared to that of the ML MUD, and when a turbo convolutional code associated with R=1/2, relying on 8 trellis states and 4 inner iterations is used. The bit-based interleavers have a length of 40 000 and 42 000 bits each for the systems supporting $U = 15$ and $U = 14$ users, respectively. The parameters of the systems are summarized in Table 2.6.

high residual BER would also appear.

The E_b/N_0 loss versus the reduction in complexity is illustrated in Figure 2.19. As the number of CFEs increases, the performance loss diminishes. The SDMA systems may require more CFEs for approaching their optimal performance, especially when they operate at a low power, as observed in Figure 2.19 for our full-rank SDMA scenario, because at low SNRs the conventional detectors fail to provide an accurate initial estimate of the M^K-ary symbol. Hence, depending both on the specific applications considered and on the computational power available, an adaptive strategy of choosing L_{stop} may be conceived.

2.6.2 Under-Loaded DS-CDMA Systems

When the multiple access systems are under-loaded, the expected reduction in computational complexity becomes higher, since the linear detectors provide a better initial symbol for the DHA than when they are employed in full-rank or rank-deficient systems. This is demonstrated in Figure 2.20, Figure 2.21 and Figure 2.22, where the PDF and CDF curves of three additional under-loaded systems supporting $U = 4, 6, 8$ users with $SF = 31$ employing QPSK ($M = 4$) modulation are shown, respectively, with their optimal BER performance presented in Figure 2.23. The E_b/N_0 value where each system was simulated at corresponds to the 10^{-4} BER point when TCC with rate $R = 1/2$, 8 trellis states and 4 inner iterations were used for transmission over uncorrelated Rayleigh channel. The parameters are summarized in Table 2.9. The shape of the PDF when the MF output is used for initializing the DHA declares that for many of the simulation instances the MF output was equal or very close to x_{MF}, in contrast to the MF output of rank-deficient systems which were closer to a randomly chosen symbol. The CDFs follow the trend of the corresponding PDFs by reaching their 50% point with 41, 167 and 586 fewer CFEs than the number of

CFEs required by the randomly-initialized DHA QMUD to reach the 50% CDF point in the systems supporting $U = 4, 6, 8$ users, respectively.

Let us proceed by presenting the simulated CDF curves of the system supporting $U = 8$ users using the QPSK modulation and $SF = 31$ for different power levels in Figure 2.24. More specifically, the chosen E_b/N_0 values range from the beginning of the BER turbo cliff (∼6.5 dB), up to power values beyond the point where BER= 10^{-5} (∼8.16 dB) when transmitting over uncorrelated Rayleigh channel employing turbo convolutional codes with rate $R = 1/2$, 8 trellis states and 4 iterations between the convolutional codes have been performed. The resultant CDF curves indicate a weak power sensitivity for the chosen E_b/N_0 range since we need approximately 5–10 fewer CFEs to reach the 65% point of the CDF when increasing the power by 0.5 dB. Therefore, a CDF curve simulated for a single E_b/N_0 value may be used for determining the maximum allowed number of CFEs L_{stop} in our simulations. In the following simulations, we have chosen the CDF corresponding to $E_b/N_0 = 7.78$ dB for determining L_{stop} for the system supporting $U = 6$ users. It should be noted though that better performance is expected when we use the CDF curve that corresponds to the power level we operate at. This would be translated in a pre-computed collection of CDF curves for various E_b/N_0 values for a specific system.

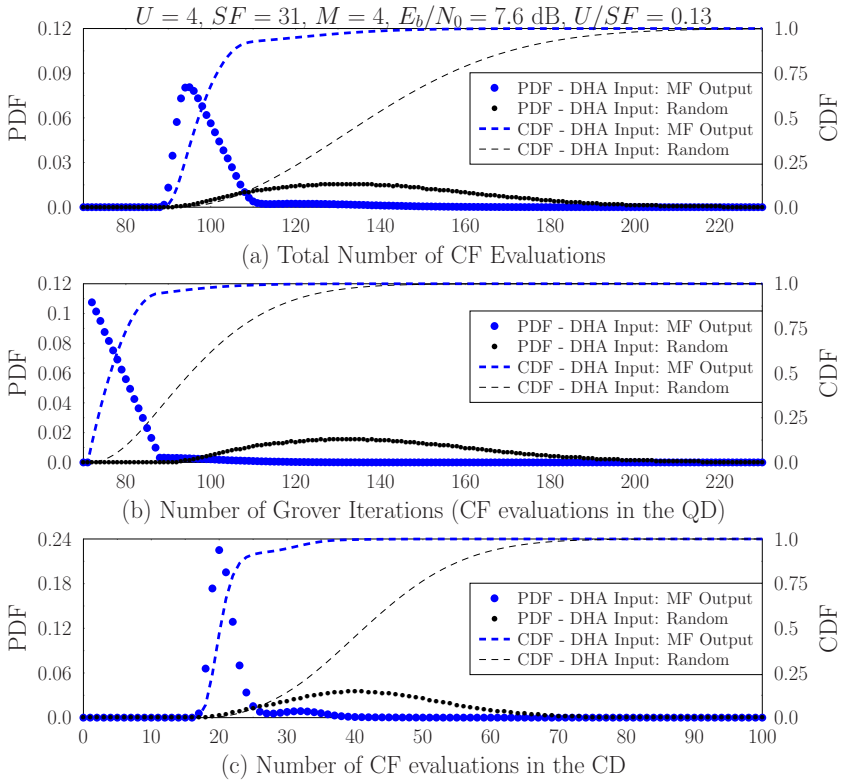

Figure 2.20: Simulated PDF and CDF of (a) the total number of CFEs in both the classical and the quantum domain, (b) the number of CFEs in terms of Grover iterations in the quantum domain, (c) the number of CFEs in the classical domain, in the DHA employed in the DS-CDMA system of Figure 2.1, using QPSK modulation and supporting $U = 4$ users with $SF = 31$. The parameters of the system are summarized in Table 2.9. The chosen $E_b/N_0 = 7.6$ dB value corresponds to a BER performance of $\sim 10^{-4}$ of the system depicted in Figure 2.23.

Table 2.9: Parameters of the three underloaded DS-CDMA systems

	System 1	System 2	System 3
Number of Users	$U = 4$	$U = 6$	$U = 8$
Normalized User Load	$U_L = 4/31$	$U_L = 6/31$	$U_L = 8/31$
Multiple Access Scheme			DS-CDMA
Number of AEs at the BS			$P = 1$
Spreading Factor			$SF = 31$
Spreading Codes			Gold Codes
Bit-based Interleaver Length			20 000
Number of AEs per User			$N_{T_x} = 1$
Modulation			QPSK $M = 4$
Channel Code			Turbo Code, $R = 1/2$, 8 Trellis states $I_{inner} = 4$ iterations
Channel			Uncorrelated Rayleigh Channel
Channel Estimation			Perfect

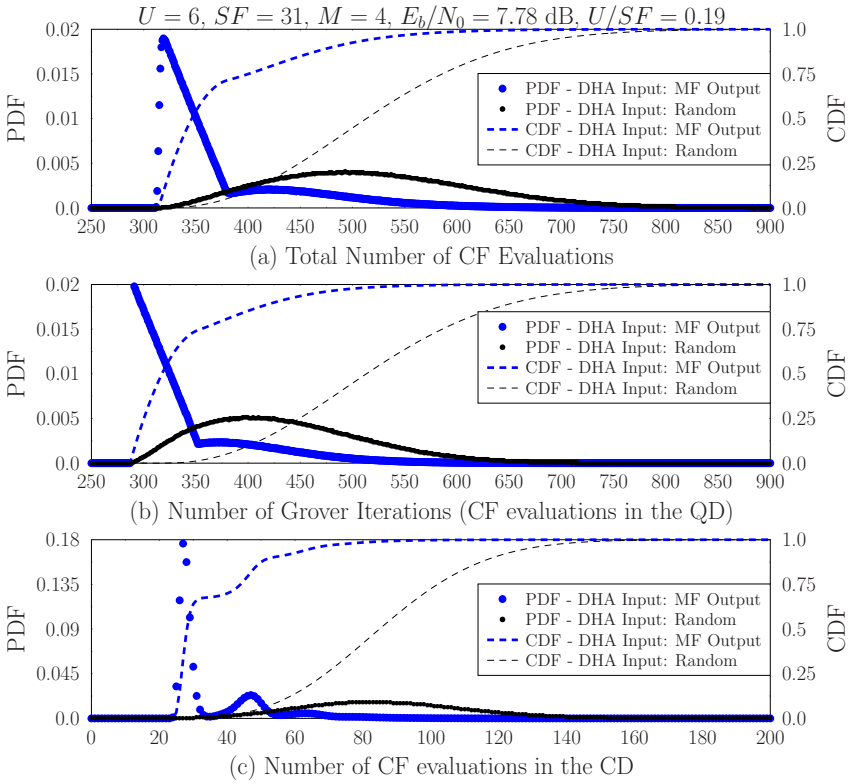

Figure 2.21: Simulated PDF and CDF of (a) the total number of CFEs in both the classical and the quantum domain, (b) the number of CFEs in terms of Grover iterations in the quantum domain, (c) the number of CFEs in the classical domain, in the DHA employed in the DS-CDMA system of Figure 2.1, using QPSK modulation and supporting $U = 6$ users with $SF = 31$. The parameters of the system are summarized in Table 2.9. The chosen $E_b/N_0 = 7.78$ dB value corresponds to a BER performance of $\sim 10^{-4}$ of the system depicted in Figure 2.23.

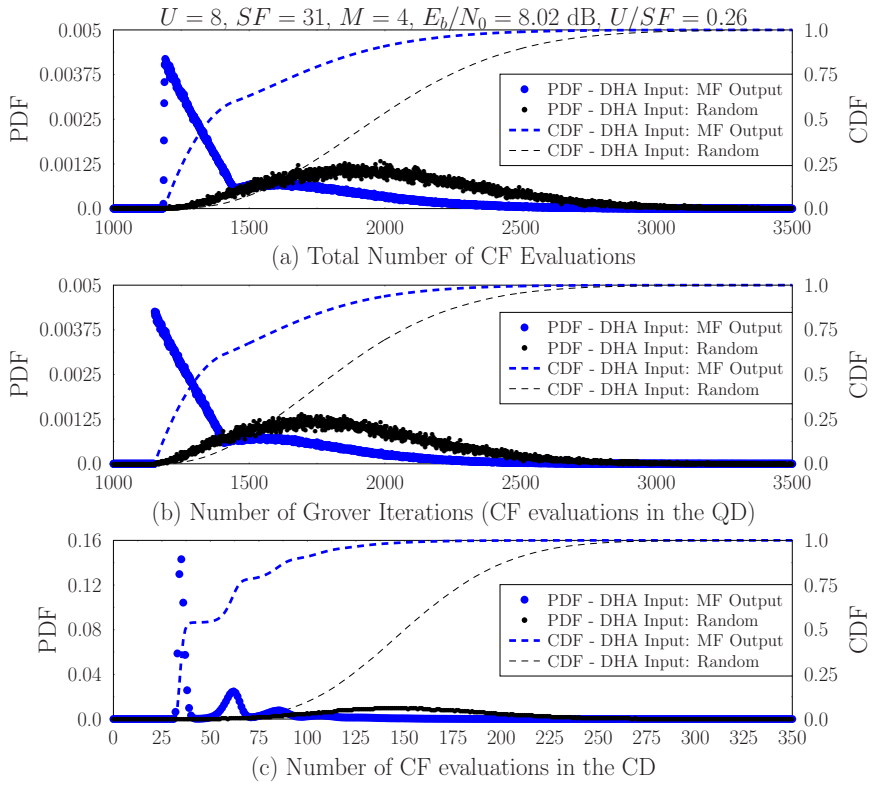

Figure 2.22: Simulated PDF and CDF of (a) the total number of CFEs in both the classical and the quantum domain, (b) the number of CFEs in terms of Grover iterations in the quantum domain, (c) the number of CFEs in the classical domain, in the DHA employed in the DS-CDMA system of Figure 2.1, using QPSK modulation and supporting $U = 8$ users with $SF = 31$. The parameters of the system are summarized in Table 2.9. The chosen $E_b/N_0 = 8.02$ dB value corresponds to a BER performance of $\sim 10^{-4}$ of the system depicted in Figure 2.23.

Based on the previous observations, the BER performance of the ES-DHA QMUD in the under-loaded system supporting $U = 8$ users employing QPSK modulation and $SF = 31$, as well as turbo convolutional codes with rate $R = 1/2$, 8 trellis states and 4 inner iterations when transmitting over uncorrelated Rayleigh channels is depicted in Figure 2.25. The performance of the systems supporting $U = 4, 6$ users is the same as in Figure 2.23. In Figure 2.25 we may observe that when L_{stop} is chosen to be the 99% point of the CDF in Figure 2.22c corresponding to 2519 CFEs minus the minimum number of CFEs needed by the DHA $L_{DHA}^{\min} = 1182$, leading to $L_{stop} = 2519 - 1182 = 1337$ CFEs, the performance of the ES-aided DHA QMUD is optimal and equal to that of the DHA QMUD and ML MUD. As in the case of the full-rank and rank-deficient systems, the BER performance also worsens when L_{stop} becomes smaller in under-loaded systems.

The main difference of the employment of the ES-aided DHA QMUD in rank-deficient and under-loaded systems is the much larger relevant computational complexity reduction achieved in the latter systems. It is verified by Figure 2.26, where the E_b/N_0 loss is plotted with respect to the number of CFEs in the DHA and a "cliff" is formed as U/SF becomes smaller, followed by a floor when the power loss is already too small. Such an indication of a rapid improvement in performance when allowing a few more CFEs in the lower regions

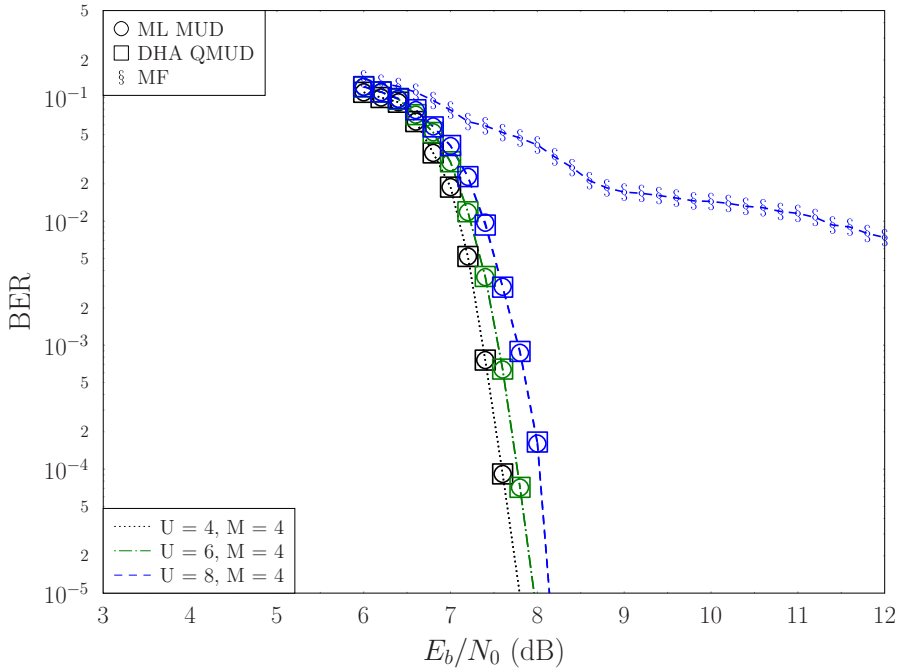

Figure 2.23: BER performance of BICM-ID DS-CDMA systems of Figure 2.1, supporting $U = 4, 6, 8$ users transmitting QPSK $M = 4$ symbols. The parameters of the systems are summarized in Table 2.9. The DHA QMUD is compared to the ML MUD and the MF detector, verifying its optimality in finding the minimum of a function. Turbo coding is used relying on 8 trellis states at a rate of $R = 1/2$ and $I_{inner} = 4$ iterations between the component codes. The interleaver length is equal to 20 000 bits.

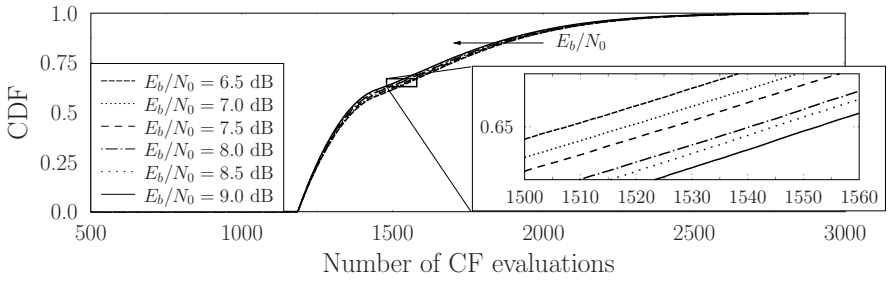

Figure 2.24: Simulated CDFs of the number of CFEs in the DHA employed in the DS-CDMA system of Figure 2.1 and Figure 2.23 using QPSK modulation and supporting $U = 6$ users with $SF = 31$, for various values of E_b/N_0. The parameters of the system are summarized in Table 2.9.

of the CDF enables a fine tuning between the available computational resources and the required performance.

The BER performance of the $U = 4$, $M = 4$ and $U = 6$, $M = 4$ systems is characterized in Figure 2.27, where the DHA is stopped after 11 and 45 CFEs, respectively. Figure 2.27 demonstrates the dependence of the proposed ES-aided DHA-based QMUD on the channel code used. More specifically, when the turbo convolutional codes associated with a rate of $R = 1/2$, 8 trellis states and $I = 4$ inner decoding iterations is used, both systems operate closer to the respective ML performance than the Non-Systematic Convolutional Code (NSCC) having a rate of $R = 1/2$ and 8 trellis states or when no coding is used. Hence, our proposed ES DHA-based MUD is only suitable for powerful channel codes, since they will

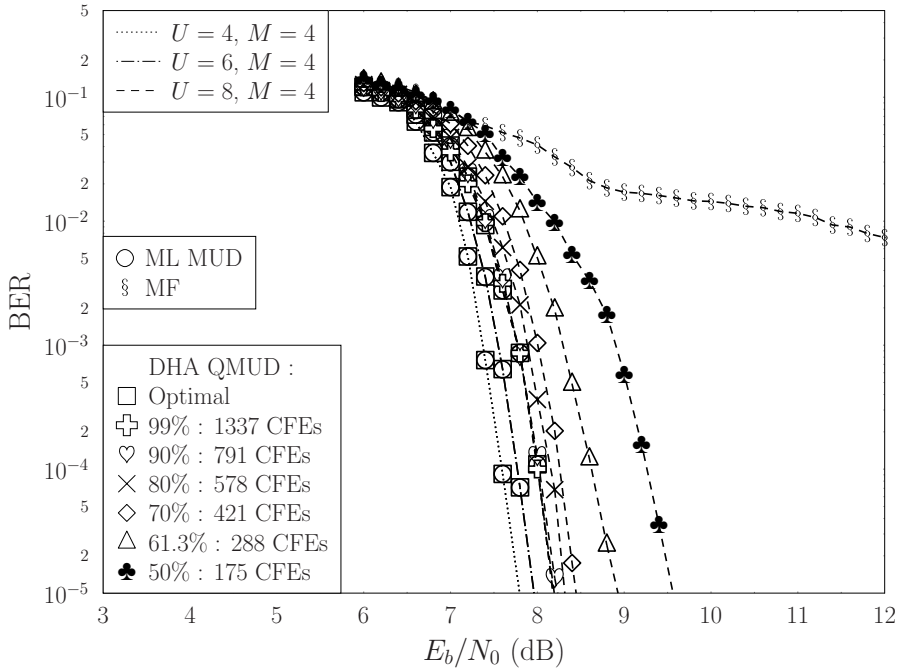

Figure 2.25: BER performance of DS-CDMA systems of Figure 2.1 supporting $U = 4, 6, 8$ users with $SF = 31$ chips, employing QPSK modulation, a turbo convolutional code with rate $R = 1/2$, 8 trellis states, 4 inner iterations as well as the DHA QMUD and the ES-aided DHA QMUD for the system supporting $U = 8$ users. The bit-based interleavers have a length of 20000 bits each and the transmission takes place over an uncorrelated Rayleigh channel. The parameters of the systems are summarized in Table 2.9.

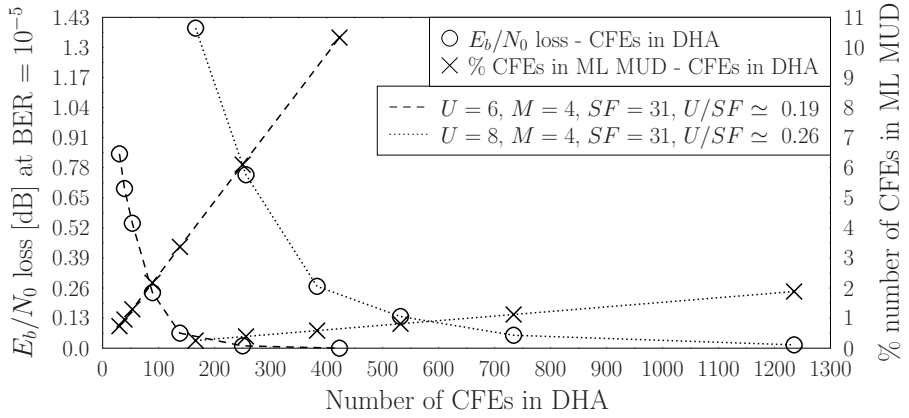

Figure 2.26: Illustration of the power loss and the simultaneous reduction in complexity with respect to the maximum allowed CFEs in the ES-aided DHA QMUD when compared to that of the ML MUD in under-loaded DS-CDMA systems of Figure 2.1, when a turbo convolutional code associated with R=1/2, relying on 8 trellis states and 4 inner iterations is used. The bit-based interleavers have a length of 20 000 bits each. The parameters of the systems are summarized in Table 2.9.

not be severely affected by an erroneous decision at the detector, but instead succeed in correcting the bit errors. The chosen $L_{stop} = 11$ CFEs for the [U=4, SF=31] system and $L_{stop} = 45$ CFEs for the [U=6, SF=31] system correspond to the 60% point of the CDF in Figure 2.20a and Figure 2.21a, respectively, minus $L_{DHA}^{\min} = L_{DHA}^{QD,\,\min} + L_{DHA}^{CD\,\min} = 88$ CFEs for [U=4, SF=31] and $L_{DHA}^{\min} = 311$ CFEs for [U=6, SF=31]. By comparing the

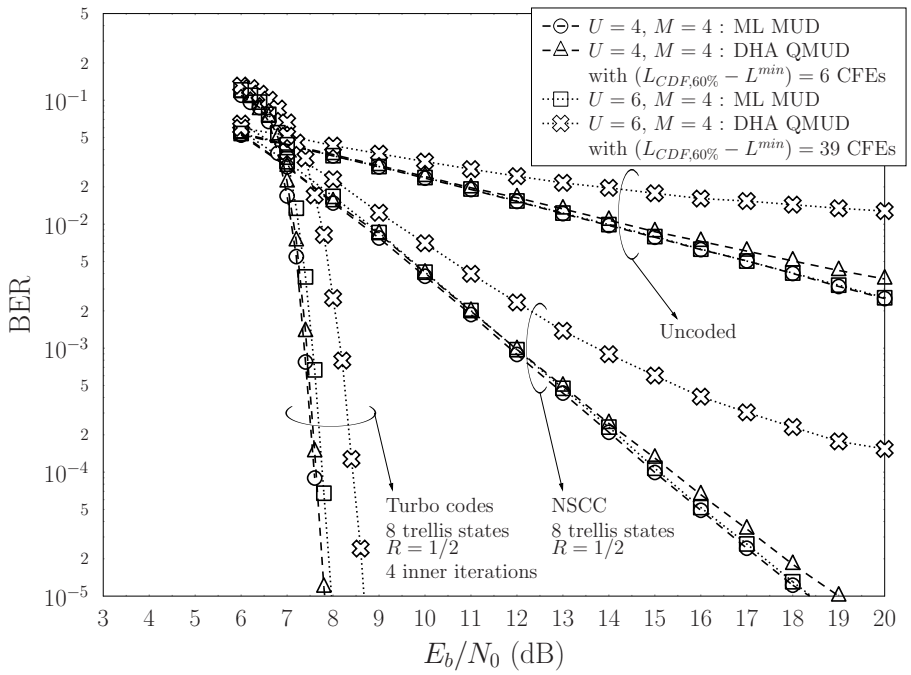

Figure 2.27: BER performance of the DS-CDMA systems of Figure 2.1 supporting $U = 4, 6$ users in conjunction with QPSK modulation and $SF = 31$ in the cases where either no channel coding is employed, or a turbo convolutional code associated with $R = 1/2$, 8 trellis states and 4 inner iterations is employed, or alternatively, NSCC with $R = 1/2$, 8 trellis states is used. The bit-based interleavers have a length of 20 000 bits each. The parameters of the systems are summarized in Table 2.9.

Table 2.10: Parameters of the three SDMA systems

	System 1	System 2	System 3
Number of AEs at the BS	$P = 20$	$P = 10$	$P = 5$
Normalized User Load	$U_L = 0.5$	$U_L = 1$	$U_L = 2$
Number of Users			$U = 10$
Multiple Access Scheme			SDMA
Bit-based Interleaver Length			20 000
Number of AEs per User			$N_{T_x} = 1$
Modulation			BPSK $M = 2$
Channel Code			Turbo Code, $R = 1/2$
			8 Trellis states
			$I_{inner} = 4$ iterations
Channel			Uncorrelated Rayleigh Channel
Channel Estimation			Perfect

resultant BER curves when 61.3% of the DHA CFEs are performed in the $U = 8$, $M = 4$ system in Figure 2.25 to those where 60% of the CFEs are allowed in Figure 2.27, we may also conclude that the power-loss increases when the system's dimensionality grows and the percentage of the included instances remains the same.

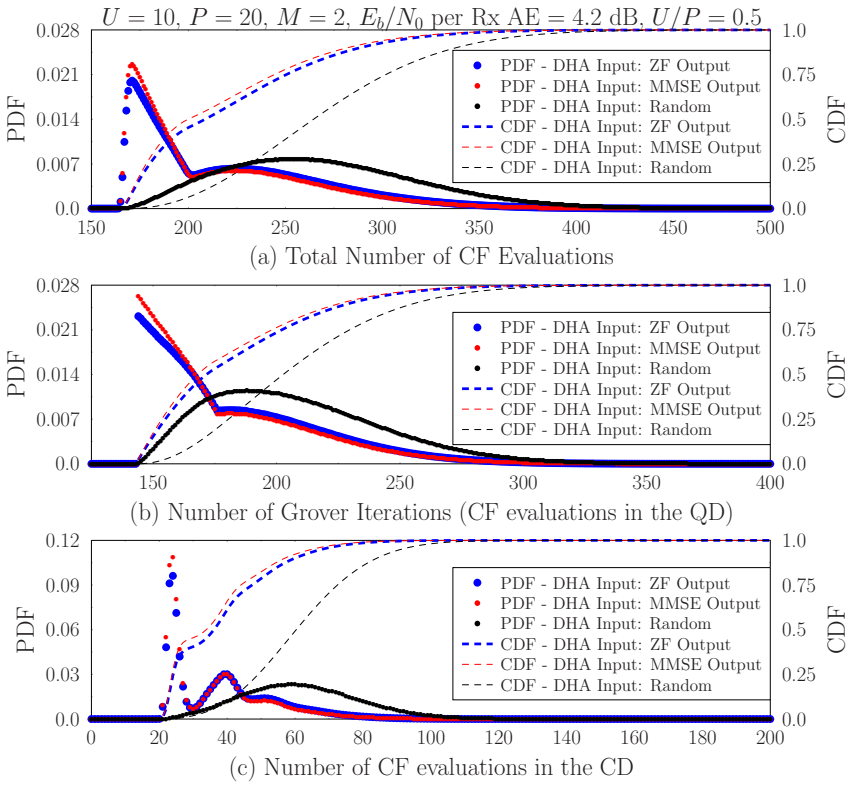

Figure 2.28: Simulated PDF and CDF of (a) the total number of CFEs performed both in the classical and the quantum domain, (b) the number of CFEs in the quantum domain and (c) the number of CFEs in the classical domain in the DHA employed in an under-loaded SDMA system of Figure 2.2 using BPSK modulation and supporting $U = 10$ users with $P = 20$ receiver antennas. The DHA's initial input was either randomly generated, or equal to the ZF or the MMSE detector's output. The chosen E_b/N_0 per receive antenna value of 4.2 dB that the system has been simulated at corresponds to $BER = 10^{-5}$ when a turbo convolutional code with $R = 1/2$, 8 trellis states and 4 inner iterations, as well as bit-based interleavers with a length of 20 000 bits are employed. The parameters of the system are summarized in Table 2.10.

2.6.3 Effect of the Number of Receive Antennas in SDMA systems

Let us continue by investigating three SDMA systems supporting $U = 10$ single-antenna users, employing BPSK associated with $M = 2$, while $P = 5, 10, 20$ receiver antennas are installed at the BS, respectively. By fixing the number of users to $U = 10$ we are able to observe the effect that the number of receive antenna elements has on the DHA QMUD's performance. The $[U = 10,\ P = 20]$ scenario represents an under-loaded system, while the $[U = 10,\ P = 10]$ and $[U = 10,\ P = 5]$ scenarios correspond to a full-rank and to a rank-deficient system, respectively. The parameters of the systems investigated are summarized in Table 2.10.

The simulated PDFs associated with the corresponding CDFs are presented in Figure 2.28, Figure 2.29 and Figure 2.30 for the under-loaded, full-rank and rank-deficient systems, respectively. The E_b/N_0 values chosen correspond to a BER performance of 10^{-5}, when turbo convolutional codes associated with a rate of $R = 1/2$, 8 trellis states and 4 inner iterations were employed, along with bit-based interleavers having a length of 20 000

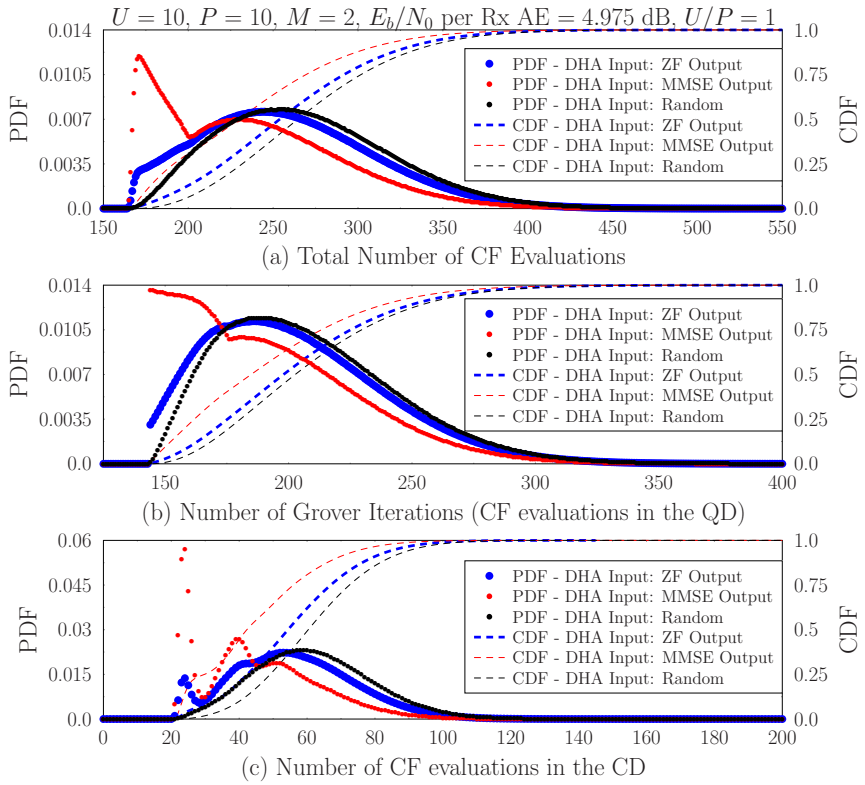

Figure 2.29: Simulated PDF and CDF of (a) the total number of CFEs performed both in the classical and the quantum domain, (b) the number of CFEs in the quantum domain and (c) the number of CFEs in the classical domain in the DHA employed in a full-rank SDMA system of Figure 2.2 using BPSK modulation and supporting $U = 10$ users with $P = 10$ receiver antennas. The DHA's initial input was either randomly generated, or equal to the ZF or the MMSE detector's output. The chosen E_b/N_0 per receive antenna value of 4.975 dB that the system has been simulated at corresponds to $BER = 10^{-5}$ when a turbo convolutional code with $R = 1/2$, 8 trellis states and 4 inner iterations, as well as bit-based interleavers with a length of 20 000 bits are employed. The parameters of the system are summarized in Table 2.10.

bits. All of the investigated systems indicate an improvement in the average complexity of the DHA, when the ZF or MMSE detector's output are exploited as its initial input, rather than using a random value. Observing the under-loaded and full-rank SDMA systems in Figure 2.28a and Figure 2.29a, respectively, we may infer that the MMSE-initialized DHA requires fewer CFEs than the ZF-initialized DHA for detecting $\mathbf{x}_{\text{min}}$. On the other hand, for the rank-deficient system of Figure 2.30a we may conclude that the MMSE-initialized DHA is equivalent to the ZF-initialized DHA, both achieving an improvement of 33 CFEs at the 50% point of their CDF.

For deeper intuition, in Figure 2.31, Figure 2.32 and Figure 2.33 we have recorded the PDF and CDF curves of the above-mentioned systems when fixing the power to $E_b/N_0 = -3$ dB corresponding to the E_b/N_0 values per receive antenna of 10 dB, 7 dB and 4 dB for the $[U = 10, P = 20]$, $[U = 10, P = 10]$ and $[U = 10, P = 5]$ systems, respectively. For the under-loaded and full-rank systems, it is expected that the average complexity imposed by the ZF-initialized and MMSE-initialized DHA is lower when operating at $E_b/N_0 = -3$ dB compared to their corresponding power that results in a BER of 10^{-5}, since the power is

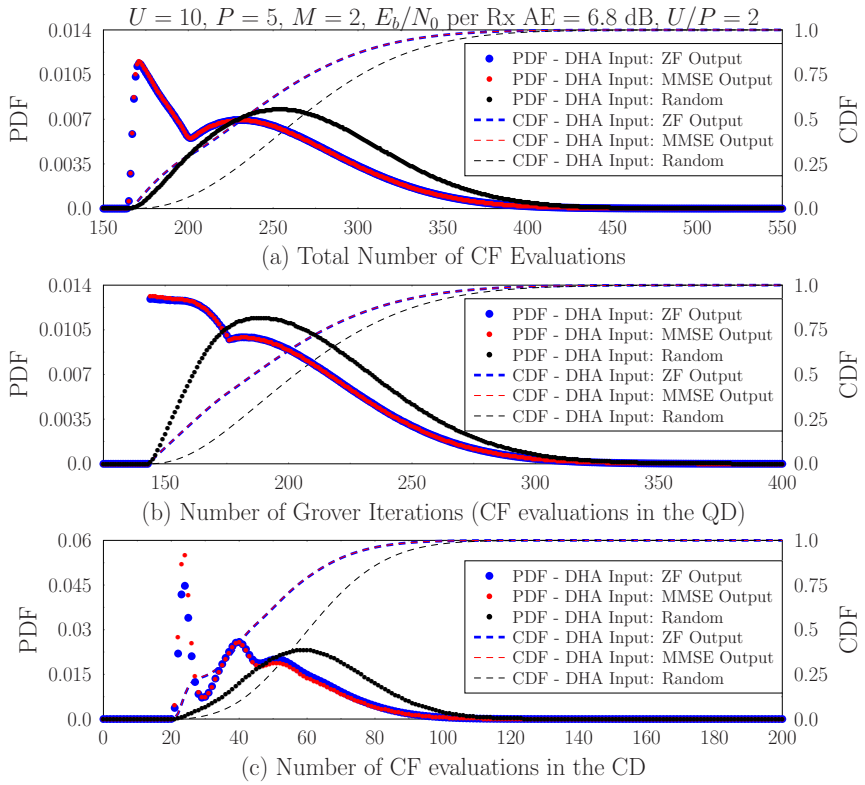

Figure 2.30: Simulated PDF and CDF of (a) the total number of CFEs performed both in the classical and the quantum domain, (b) the number of CFEs in the quantum domain and (c) the number of CFEs in the classical domain in the DHA employed in a rank-deficient SDMA system of Figure 2.2 using BPSK modulation and supporting $U = 10$ users with $P = 5$ receiver antennas. The DHA's initial input was either randomly generated, or equal to the ZF or the MMSE detector's output. The chosen E_b/N_0 per receive antenna value of 6.8 dB that the system has been simulated at corresponds to $BER = 10^{-5}$ when a turbo convolutional code with $R = 1/2$, 8 trellis states and 4 inner iterations, as well as bit-based interleavers with a length of 20 000 bits are employed. The parameters of the system are summarized in Table 2.10.

higher. The reason behind this expectation is that the MMSE and ZF detectors perform better when the power increases, hence their initial guess of the multi-level symbol will have a lower Euclidean distance from the actually transmitted multi-level symbol. This is verified by the resultant shift of the CDF curves to the left in Figure 2.31a and Figure 2.32a with respect to the same CDF curves in Figure 2.28a and Figure 2.29a, respectively. On the other hand, the complexity of the randomly initialized DHA remains the same, since in this case the power level does not affect the quantum algorithm. As far as the rank-deficient system is considered, the ZF-initialized and MMSE-initialized DHA provide equivalent CDF curves – with the MMSE-initialized DHA resulting in a slightly lower complexity – which are shifted to the right compared to the respective CDF curves seen in Figure 2.30, since they operate at a lower power level.

Based on the previous observations, let us proceed by investigating the dependency of the DHA's CDF curves on the power levels. The resultant CDF curves of the under-loaded $[U = 10,\ P = 20]$ system when varying the E_b/N_0 value per receive antenna value in the range of $[3.4, 5]$ dB is presented in Figure 2.34. We may note that the reduction in

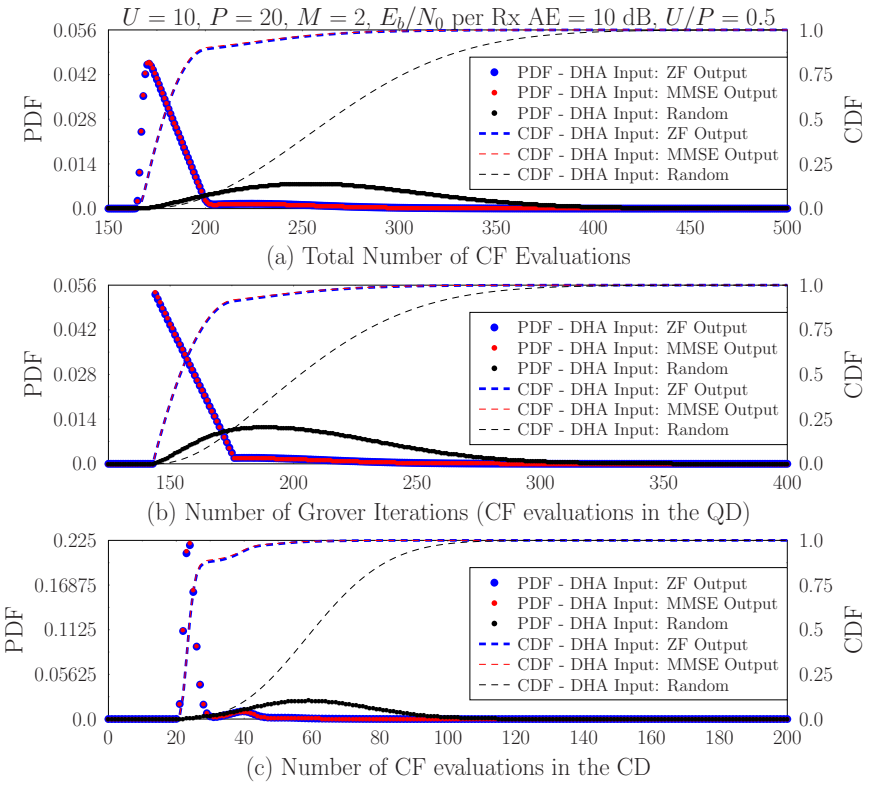

Figure 2.31: Simulated PDF and CDF of (a) the total number of CFEs performed both in the classical and the quantum domain, (b) the number of CFEs in the quantum domain and (c) the number of CFEs in the classical domain in the DHA employed in an under-loaded SDMA system of Figure 2.2 using BPSK modulation and supporting $U = 10$ users with $P = 20$ receiver antennas. The DHA's initial input was either randomly generated, or equal to the ZF or the MMSE detector's output. The selected E_b/N_0 value is -3 dB, which corresponds to an E_b/N_0 per receive antenna value of 10 dB. The parameters of the system are summarized in Table 2.10.

the number of CFEs needed to reach the same probability of success in the DHA when increasing the power is roughly 1 CFE per 0.2 dB in both the ZF-initialized and MMSE-initialized DHA QMUD in the under-loaded SDMA system. Similarly, the resultant CDF curves when we vary the E_b/N_0 value per receive antenna in the full-rank $[U = 10,\ P = 10]$ system are illustrated in Figure 2.35. The CDF curves of the ZF-initialized DHA in the full-rank system are shifted towards lower CFEs by 1 CFE per 1.6 dB, while the shift of the MMSE-initialized DHA's CDF curves to the left is approximately 1 CFE per 1 dB. The ZF-initialized and MMSE-initialized DHA QMUDs have a similar complexity in the context of rank-deficient systems. Hence, we simulated the CDF curves when varying the power level only for the ZF-initialized DHA in Figure 2.36. The improvement in the complexity is approximately 1 CFE per 1 dB, as in the full-rank system.

The shifts of the CDF curves towards lower number of CFEs when increasing the power in our systems is so small that it may be considered negligible. Therefore, the CDF generated at a single E_b/N_0 value may be considered sufficient for characterizing the CDF curves of all the power levels. The BER performance results presented in the following section are related to the CDF curves presented in Figure 2.28, Figure 2.29 and Figure 2.30 for each system for all the E_b/N_0 values. In other words, operating at the 60% point of

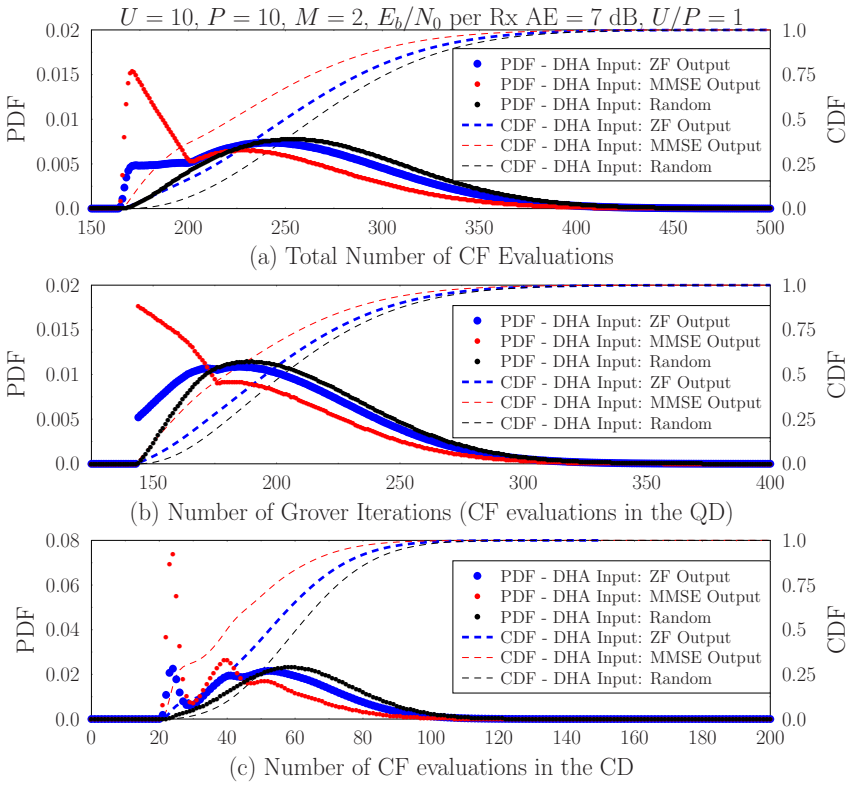

Figure 2.32: Simulated PDF and CDF of (a) the total number of CFEs performed both in the classical and the quantum domain, (b) the number of CFEs in the quantum domain and (c) the number of CFEs in the classical domain in the DHA employed in a full-rank SDMA system of Figure 2.2 using BPSK modulation and supporting $U = 10$ users with $P = 10$ receiver antennas. The DHA's initial input was either randomly generated, or equal to the ZF or the MMSE detector's output. The selected E_b/N_0 value is -3 dB, which corresponds to an E_b/N_0 per receive antenna value of 7 dB. The parameters of the system are summarized in Table 2.10.

the CDF in the under-loaded $[U = 10,\ P = 20]$ system while using the CDF generated at $E_b/N_0 = -8.8$ dB, corresponding to an E_b/N_0 per receive antenna value of 4.2 dB, will result in stopping the MMSE-initialized ES-DHA after $L_{stop} = 182 - L_{DHA}^{\min}$, regardless of the E_b/N_0 value the system is operating at. According to Equation 2.50 for $N = M^U = 2^{10} = 1024$ and $\lambda = 6/5 = 1.2$ we have $L_{DHA}^{CD,\ \min} = 20$ CFEs and the maximum number of Grover iterations in the BBHT when $N = 1024$ is $L_{DHA}^{QD,\ \min} = L_{BBHT}^{QD,\ \max} = 4.5\sqrt{N} = 144$. Hence, we may conclude that in the systems examined we require $L_{DHA}^{\min} = L_{DHA}^{CD,\ \min} + L_{DHA}^{QD,\ \min} = 164$ CFEs and $L_{stop} = 182 - 164 = 18$ for the 60% point of the MMSE-initialized ES-DHA in the under-loaded system, when the E_b/N_0 value per receive antenna is 4.2 dB.

2.6.3.1 Under-Loaded Scenario: $U = 10$ Users - $P = 20$ Receiver Antennas

The BER performances of the under-loaded SDMA system supporting $U = 10$ users with the aid of $P = 20$ receiver antennas, where the ZF-initialized and MMSE-initialized DHA QMUD has been used are given in Figure 2.37 and Figure 2.38, respectively. In both cases the points of the CDF seen in Figure 2.28a corresponding to the E_b/N_0 value per receive antenna of 4.2 dB were used for determining the maximum number of CFEs L_{stop}. Turbo

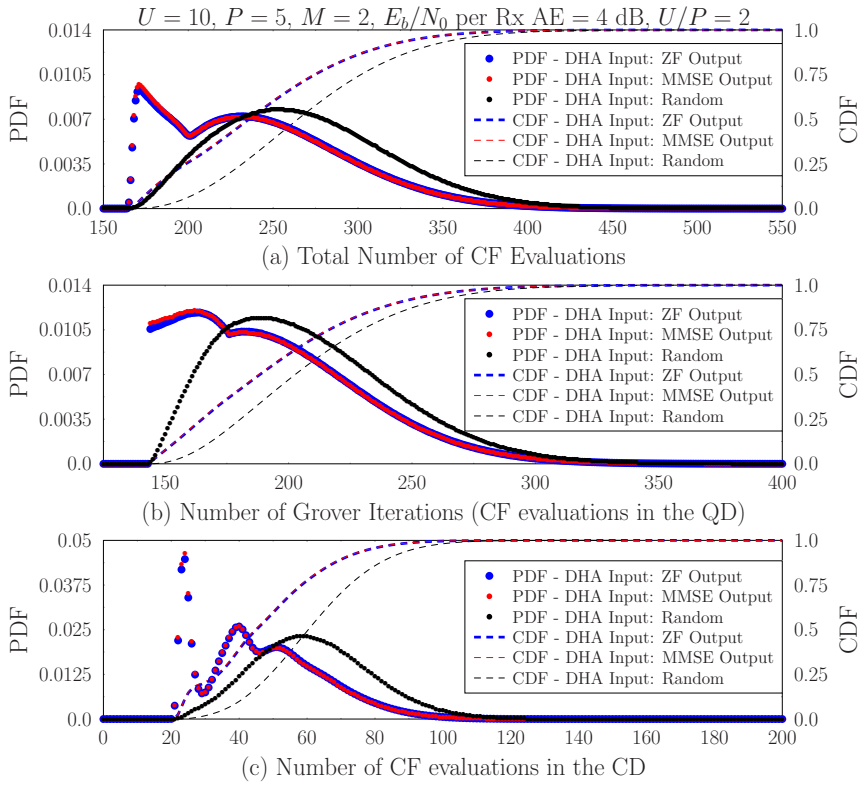

Figure 2.33: Simulated PDF and CDF of (a) the total number of CFEs performed both in the classical and the quantum domain, (b) the number of CFEs in the quantum domain and (c) the number of CFEs in the classical domain in the DHA employed in a rank-deficient SDMA system of Figure 2.2 using BPSK modulation and supporting $U = 10$ users with $P = 5$ receiver antennas. The DHA's initial input was either randomly generated, or equal to the ZF or the MMSE detector's output. The selected E_b/N_0 value is -3 dB, which corresponds to an E_b/N_0 per receive antenna value of 4 dB. The parameters of the system are summarized in Table 2.10.

convolutional codes associated with rate $R = 1/2$, 8 trellis states and 4 inner iterations between the convolutional codes were used and the bit interleavers' length was 20 000 bits. The performance of the DHA-based QMUD matches that of the ML MUD. The ZF-initialized and MMSE-initialized ES-DHA QMUDs improve their performance, when they operate closer to the 100% point of their respective CDF curve, while the degradation in the BER performance when they operate at the 60% point of their CDF is approximately 0.7 dB in both cases. The "turbo cliff" ends at a BER value of $8 \cdot 10^{-7}$, while the residual BER is 10^{-7}.

In Figure 2.39 we have plotted together the BER curves of the ZF-initialized and the MMSE-initialized ES-DHA QMUDs shown in Figure 2.37 and Figure 2.38, respectively. The MMSE-initialized ES-DHA QMUD performs slightly better than the ZF-initialized ES-DHA QMUD, when they both operate at the same low point of their respective CDF curve. It should be made clear that the number of CFEs is different in these two cases, hence the MMSE-initialized ES-DHA QMUD performs better, while also using fewer CFEs. If both QMUDs were allowed to perform the same number of CFEs, then the MMSE-initialized ES-DHA QMUD would outperform the ZF-initialized ES-DHA QMUD by a greater margin. Nevertheless, their performance when operating at the same CDF point

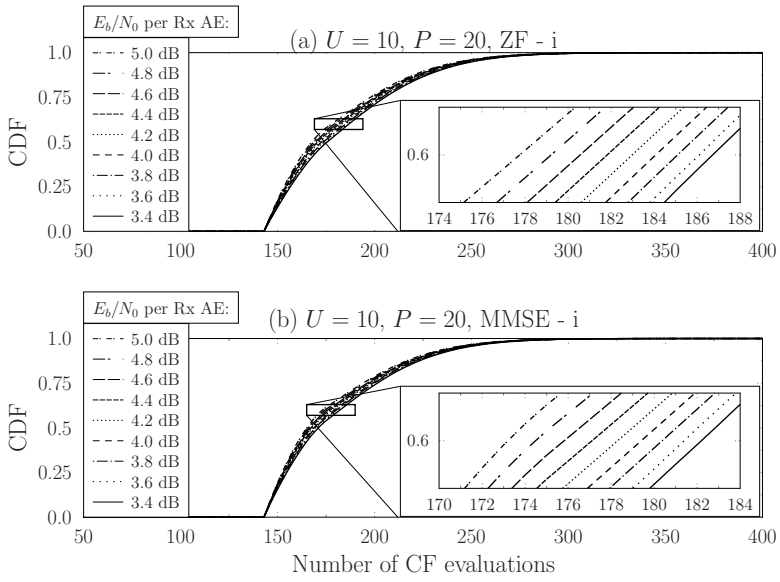

Figure 2.34: Simulated CDF curves of the number of CFEs in the a) ZF-initialized and the b) MMSE-initialized DHA employed in the under-loaded [$U = 10,\ P = 20$] SDMA system of Figure 2.2 for various values of E_b/N_0 per receive antenna. The parameters of the system are summarized in Table 2.10.

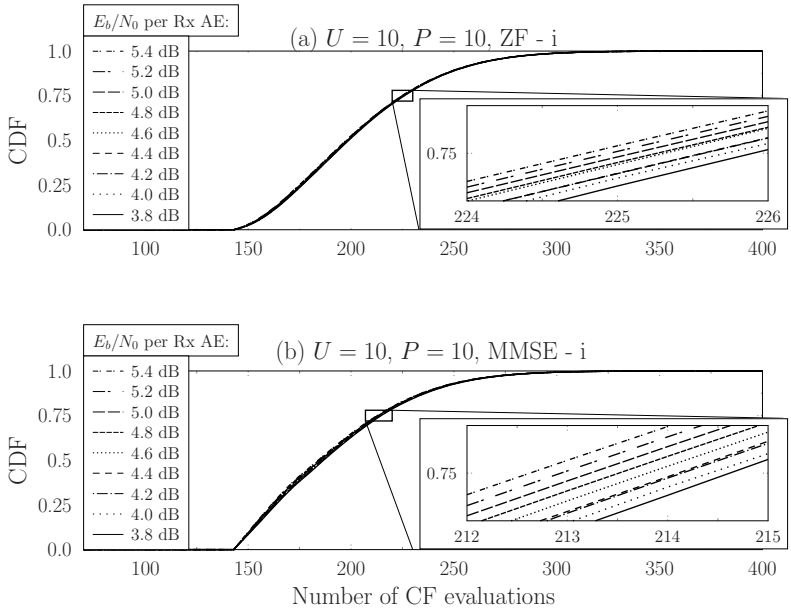

Figure 2.35: Simulated CDF curves of the number of CFEs in the a) ZF-initialized and the b) MMSE-initialized DHA employed in the full-rank [$U = 10,\ P = 10$] SDMA system of Figure 2.2 for various values of E_b/N_0 per receive antenna. The parameters of the system are summarized in Table 2.10.

may be considered equivalent due to the nature of the under-loaded systems, which allow the ZF and MMSE detectors to provide a satisfactory estimate of the multi-level symbol.

2.6.3.2 Full-Rank Scenario: $U = 10$ Users - $P = 10$ Receiver Antennas

The full-rank SDMA system investigated has the same format as the previously analysed under-loaded SDMA system, with the slight difference that there are $P = 10$ receiver

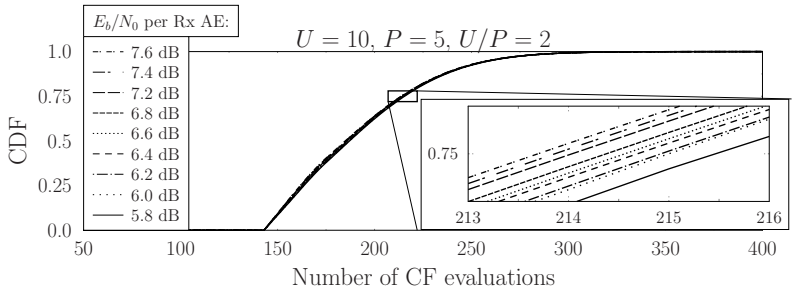

Figure 2.36: Simulated CDF curves of the number of CFEs in the ZF-initialized DHA employed in the rank-deficient [$U = 10,\ P = 5$] SDMA system of Figure 2.2 for various values of E_b/N_0 per receive antenna. The parameters of the system are summarized in Table 2.10.

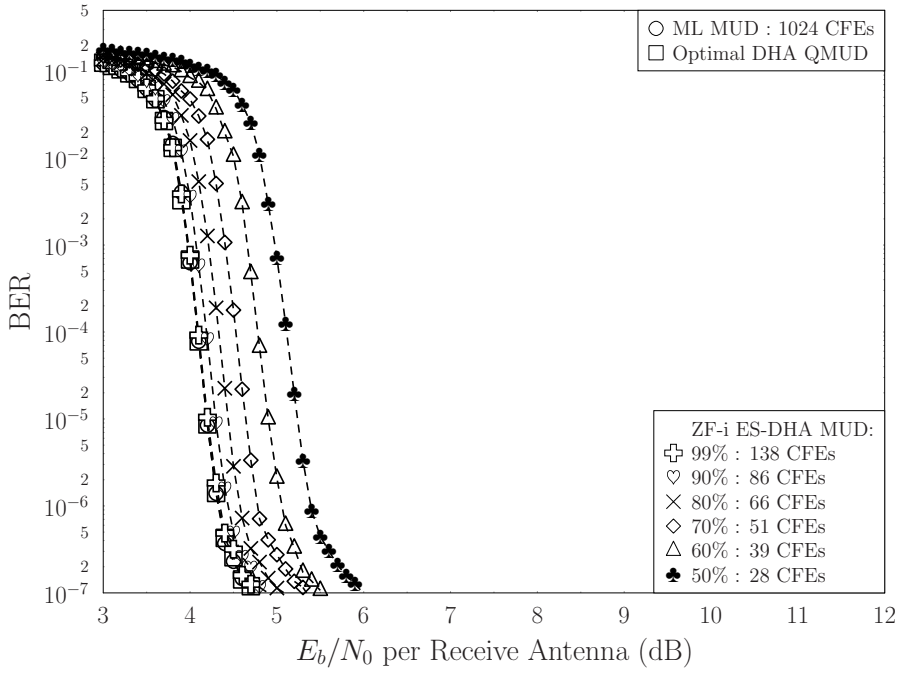

Figure 2.37: BER performance of an under-loaded SDMA system of Figure 2.2 supporting $U = 10$ users, $P = 20$ receiver antennas, employing BPSK and a turbo convolutional code with rate $R = 1/2$, 8 trellis states and $I_{inner} = 4$ iterations, along with ML-based, ZF-initialized DHA-based and ZF-initialized ES-aided DHA-based MUD for various maximum allowed number of CFEs extracted by the CDF in Figure 2.28a. The interleaver length is equal to 20 000 bits. The parameters of the system are summarized in Table 2.10.

antennas at the BS. More precisely, $U = 10$ users encode their information bits using a turbo convolutional code associated with rate $R = 1/2$, 8 trellis states and 4 inner iterations. They interleaved the coded bits using bit-based interleavers having a length of 20 000 bits and finally mapped their interleaved bit stream to BPSK symbols using Gray coding, before transmitting them to the BS. The resultant BER versus E_b/N_0 curves when ZF-initialized and MMSE-initialized ES-DHA QMUD are used at the BS are offered in Figure 2.40 and Figure 2.41, respectively. The CDF curves exploited by the QMUDs were generated at an E_b/N_0 value per receive antenna of 4.975 dB and they are presented in Figure 2.29a. The performance of both proposed systems matches that of the ML MUD,

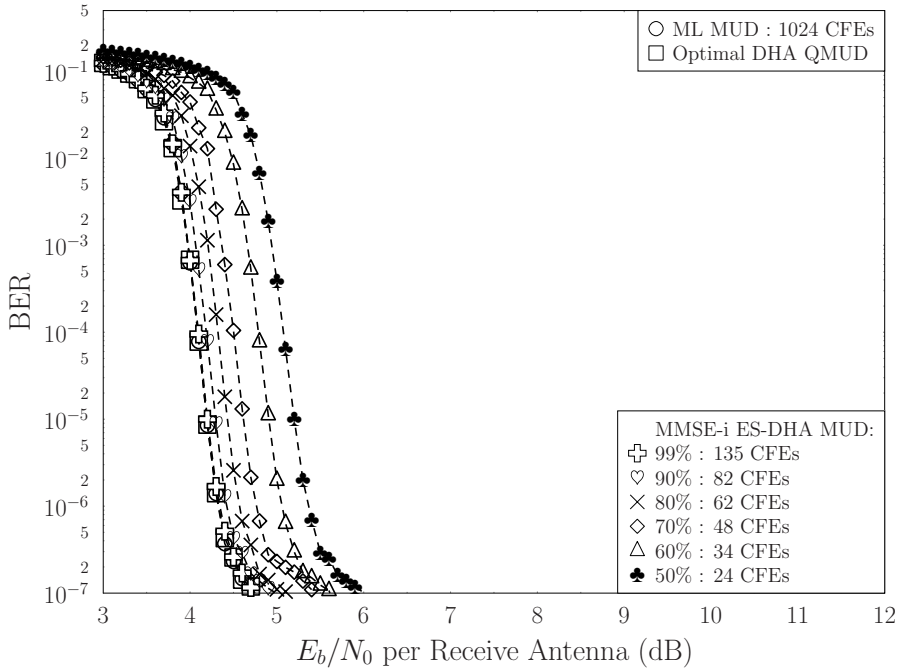

Figure 2.38: BER performance of an under-loaded SDMA system of Figure 2.2 supporting $U = 10$ users, $P = 20$ receiver antennas, employing BPSK and a turbo convolutional code with rate $R = 1/2$, 8 trellis states and $I_{inner} = 4$ iterations, along with ML-based, MMSE-initialized DHA-based and MMSE-initialized ES-aided DHA-based MUD for various maximum allowed number of CFEs extracted by the CDF in Figure 2.28a. The interleaver length is equal to 20 000 bits. The parameters of the system are summarized in Table 2.10.

when they operate at high points at their CDF curves. Furthermore, we may observe that as we reduce the maximum number of CFEs in both ES-DHA QMUDs, the rate of the performance degradation increases.

The MMSE-initialized ES-DHA QMUD used in full-rank systems performs equivalently to the ZF-initialized ES-DHA QMUD, when they both operate at the same low points of their CDF, as it may be observed in Figure 2.42, where the curves observed in Figure 2.40 and Figure 2.41 have been plotted together. Since the available resources are represented by the maximum number of CFEs, the MMSE-initialized ES-DHA QMUD performs better than the ZF-initialized ES-DHA QMUD in full-rank SDMA systems. This may be verified by observing Figure 2.42 and specifically the curves that correspond to the 80% point of the CDF of the MMSE-initialized ES-DHA QMUD and that of the 70% point of the CDF corresponding to the ZF-initialized ES-DHA QMUD, which use 77 CFEs and 75 CFEs, respectively. The performance of the MMSE-initialized ES-DHA QMUD is 0.3 dB better, leading to the conclusion that when the same number of CFEs is available, the MMSE-initialized ES-DHA QMUD should be used.

2.6.3.3 Rank-Deficient Scenario: $U = 10$ Users - $P = 5$ Receiver Antennas

Since the CDF curves of the ZF-initialized and the MMSE-initialized DHA QMUDs used in the rank-deficient scenario of Figure 2.30a are the same, their BER performances are

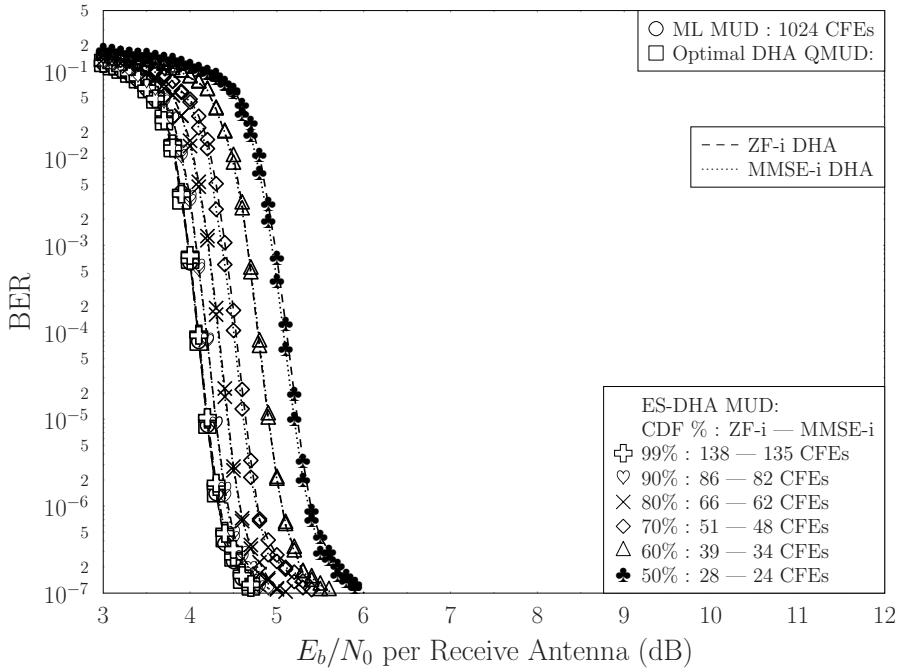

Figure 2.39: Comparison between the BER performance of an under-loaded SDMA system of Figure 2.2 supporting $U = 10$ users, $P = 20$ receiver antennas, when ZF-initialized and MMSE-initialized ES-aided DHA-based MUDs are used for various maximum allowed number of CFEs extracted by the CDF in Figure 2.28a. The used modulation is BPSK and a turbo convolutional code with $R = 1/2$, 8 trellis states and $I_{inner} = 4$ iterations is selected. The interleaver length is equal to 20 000 bits. The parameters of the system are summarized in Table 2.10.

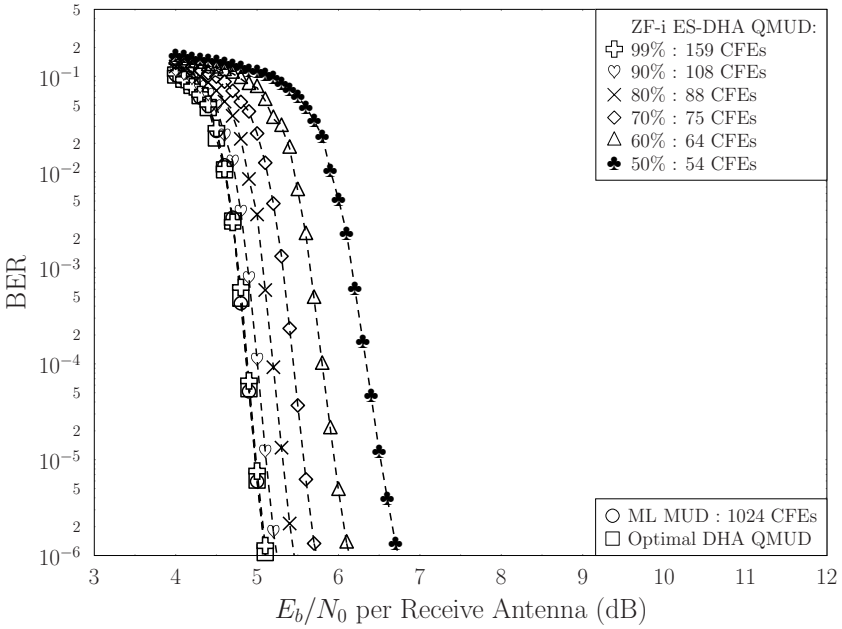

Figure 2.40: BER performance of a full-rank SDMA system of Figure 2.2 supporting $U = 10$ users, $P = 10$ receiver antennas, employing BPSK and a turbo convolutional code with rate $R = 1/2$, 8 trellis states and $I_{inner} = 4$ iterations, along with ML-based, ZF-initialized DHA-based and ZF-initialized ES-aided DHA-based MUD for various maximum allowed number of CFEs extracted by the CDF in Figure 2.29a. The interleaver length is equal to 20 000 bits. The parameters of the system are summarized in Table 2.10.

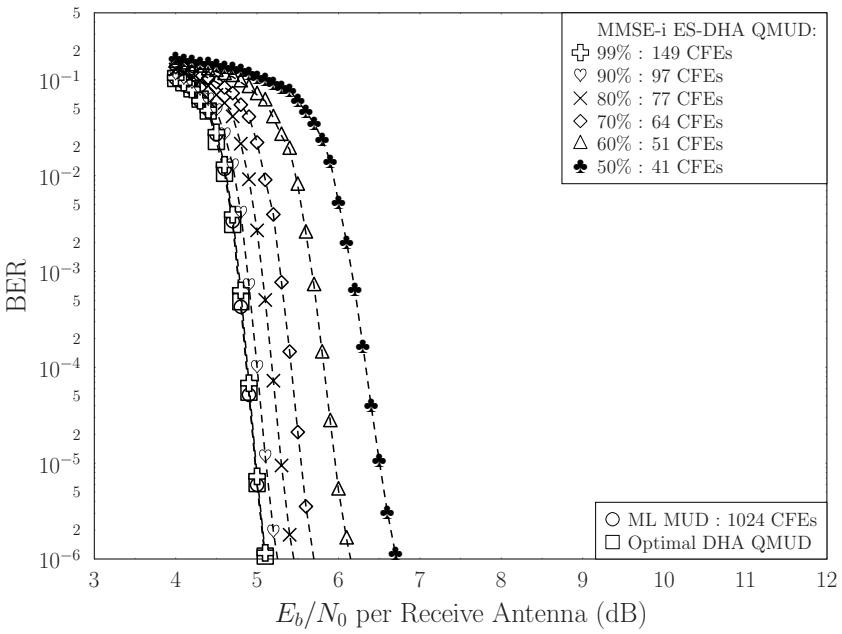

Figure 2.41: BER performance of a full-rank SDMA system of Figure 2.2 supporting $U = 10$ users, $P = 10$ receiver antennas, employing BPSK and a turbo convolutional code with rate $R = 1/2$, 8 trellis states and $I_{inner} = 4$ iterations, along with ML-based, MMSE-initialized DHA-based and MMSE-initialized ES-aided DHA-based MUD for various maximum allowed number of CFEs extracted by the CDF in Figure 2.29a. The interleaver length is equal to 20 000 bits. The parameters of the system are summarized in Table 2.10.

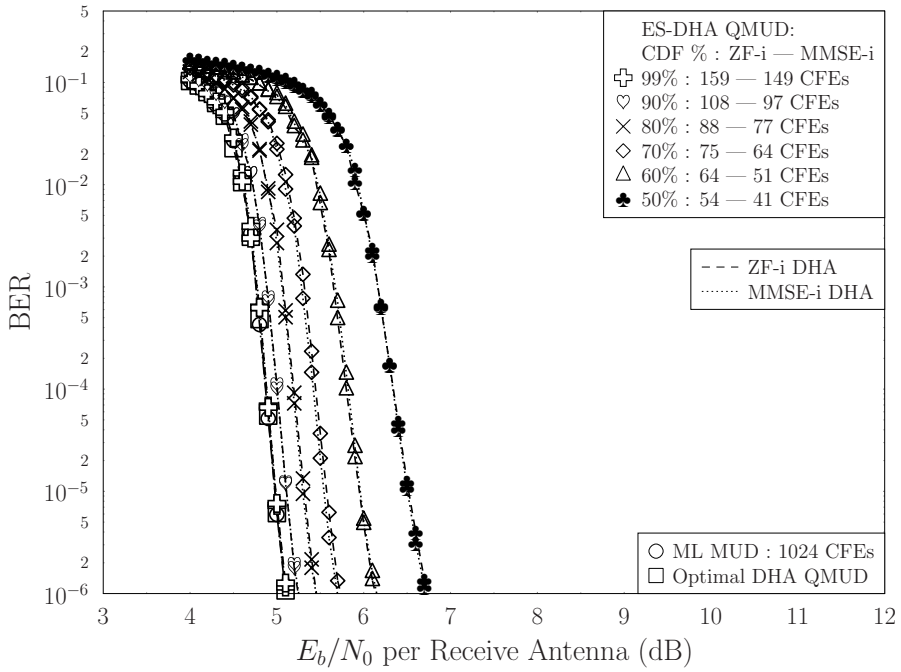

Figure 2.42: Comparison between the BER performance of a full-rank SDMA system of Figure 2.2 supporting $U = 10$ users, $P = 10$ receiver antennas, when ZF-initialized and MMSE-initialized ES-aided DHA-based MUDs are used for various maximum allowed number of CFEs extracted by the CDF in Figure 2.29a. The used modulation is BPSK and a turbo convolutional code with $R = 1/2$, 8 trellis states and $I_{inner} = 4$ iterations is selected. The interleaver length is equal to 20 000 bits. The parameters of the system are summarized in Table 2.10.

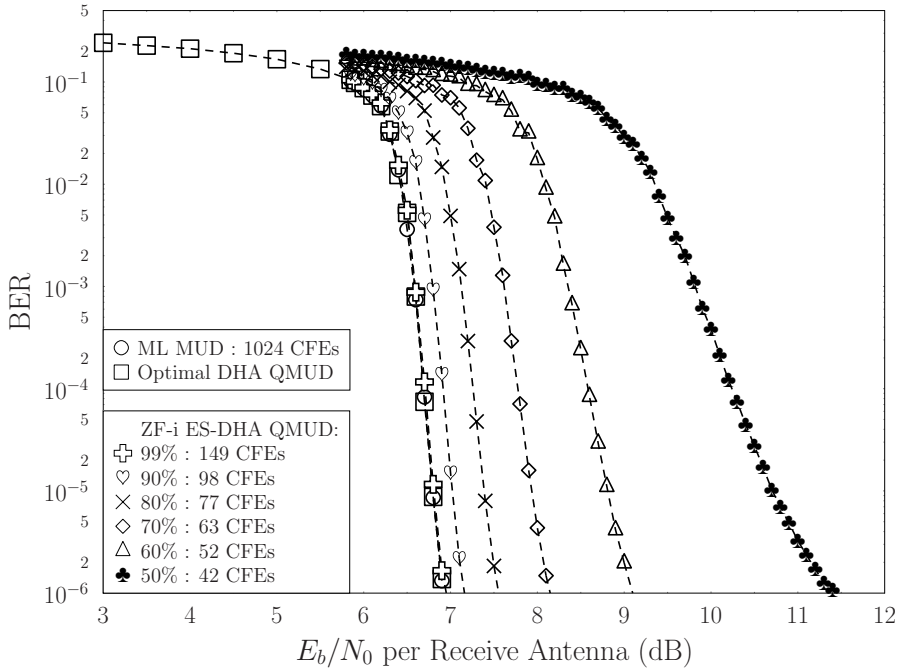

Figure 2.43: BER performance of a rank-deficient SDMA system of Figure 2.2 supporting $U = 10$ users, $P = 5$ receiver antennas, employing BPSK and a turbo convolutional code with $R = 1/2$, 8 trellis states and $I_{inner} = 4$ iterations, along with ML-based, ZF-initialized DHA-based and ZF-initialized ES-aided DHA-based MUD for various maximum allowed number of CFEs extracted by the CDF in Figure 2.30a. The interleaver length is equal to 20 000 bits. The parameters of the system are summarized in Table 2.10.

also expected to be identical since the maximum number of CFEs and the initial guess of the multi-level symbol will not be different. Therefore, let us proceed by examining the BER performance of the ZF-initialized ES-aided DHA-based QMUD and the ML MUD in the rank-deficient SDMA system supporting $U = 10$ users and employing $P = 5$ receiver antennas, as depicted in Figure 2.43. Once again, turbo convolutional codes with rate $R = 1/2$, 8 trellis states and 4 inner iterations are used, in conjunction with BPSK modulation and a 20 000 bit interleaver length. The maximum numbers of CFEs are based on the CDF curves plotted in Figure 2.30a.

The main difference between the ES-aided DHA-based QMUD performance in this rank-deficient scenario compared to the under-loaded and full-rank scenarios is the larger performance degradation, when operating at lower CDF points. More specifically, when the 60% point is chosen in the ZF-initialized ES-DHA QMUDs, the resultant BER is 1.9 dB away from the optimal limit, while the power loss when operating at the 80% CDF point is approximately 0.6 dB with respect to the ML MUD performance. Furthermore, the power gain achieved by switching from the 80% CDF point to the 90% point is 0.35 dB, whilst a shift from the 50% point to the 60% point would result in a power gain of at least 0.8 dB, with the same gain exceeding 2 dB when a BER value of 10^{-5} is targeted. Operating at the 90% CDF point results in performing 0.5 dB away from the optimal limit for both systems, but if the 99% CDF point is chosen, the BER performance becomes similar to that of the optimal DHA-based QMUD and of the ML-based MUD.

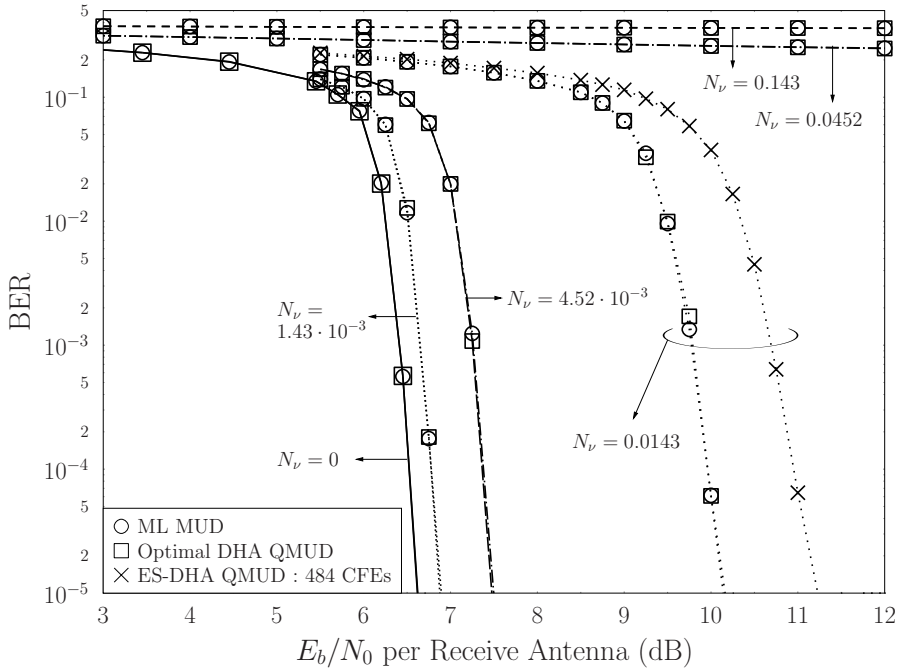

Figure 2.44: BER performance with respect to the E_b/N_0 per receive antenna of the rank-deficient SDMA system of Figure 2.2 supporting $U = 14$ users associated with $P = 7$ receive antennas when imperfect channel estimation is available. The CSI estimation noise variance N_ν describes the channel estimation error with $N_\nu = 0$ corresponding to perfect CSI estimation. The ML MUD, DHA QMUD and ES-aided DHA QMUD are employed and a turbo convolutional code associated with R=1/2, relying on 8 trellis states and 4 inner iterations is used. The bit-based interleavers have a length of 42 000 bits each. The parameters of the system are summarized in Table 2.6.

2.6.4 Effect of the Imperfect Channel Estimation

In Figure 2.44 we also considered the rank-deficient SDMA system in the realistic scenario where perfect estimation of the CSI is unavailable. We corrupted the perfect CSI with AWGN as in

$$\tilde{h}_{u,p} = h_{u,p} + \nu, \tag{2.52}$$

where h is the complex-valued channel coefficient depicted in Figure 2.1b, with $u \in \{1, \ldots, U\}$, $p \in \{1, \ldots, P\}$, and ν is the zero-mean and N_ν-variance AWGN noise. The imperfect channel estimation's error is described by the associated noise variance, where $N_\nu = 0$ denotes perfect channel estimation. The average channel power is the inverse of the number of the receive antennas $\gamma_c = 1/P$. According to Figure 2.44, the DHA QMUD continues to have optimal ML performance even with imperfect channel estimation. On the other hand, when the ES-DHA QMUD is stopped after 484 CFEs, which corresponds to the 80% CDF point of the same system at an E_b/N_0 per receive antenna value of 6.65 dB and using perfect channel estimation based on Table 2.8, the performance is approximately 1.1 dB away from that of the ML MUD. By contrast, in the [U=14, P=7] system relying on perfect channel estimation shown in Figure 2.19 the degradation was just 0.45 dB. This was expected, since imperfect channel estimation results in a worse initial guess from the ZF detector, therefore requiring more CFEs in the DHA to find the optimum M^U-ary symbol. In other words, the CDF is shifted to the right and the simulated curve at 484

Table 2.11: Summary of the presented QMUDs for the DS-CDMA system of Figure 2.1 and Table 2.6 with $U = 14$ and $SF = 7$

MUD	Complexity (CFEs / bit)	% complexity of the ML MUD	E_b/N_0 (dB)	E_b/N_0 difference from the ML MUD (dB)	BER Figure
MF-i ES-DHA (50% CDF)	24.6	2.1%	11.5	1.8	2.17
MF-i ES-DHA (99% CDF)	62.9	5.4%	9.72	0.02	2.17
MF-i DHA	63.9	5.5%	9.7	0	2.17
Random-i DHA	69.1	5.9%	9.7	0	2.13, 2.17
ML	1170.3	100%	9.7	0	2.13, 2.17

CFEs corresponds to a success probability below 80%. We may conclude that our proposed ES-DHA QMUD depends on the accuracy of the channel estimation.

2.7 Conclusions

In Section 2.4 we investigated the quantum search algorithms, which may be exploited for hard-output signal detection, in the context of both DS-CDMA and SDMA communication systems, which were presented in Section 2.2 and Section 2.3, respectively. More precisely, starting from Grover's QSA of Section 2.4.1 we moved to the BBHT algorithm, which is employed in the DHA. In Figure 2.13 we demonstrated that the DHA-based QMUD results in a performance equivalent to that of the classical hard-input hard-output ML MUD. In Section 2.5 we showed that the exploitation of the MF output in DS-CDMA systems and the ZF or the MMSE output in SDMA systems as the DHA's initial point beneficially reduces the complexity of the DHA-based MUD by allowing it to find $x_{\min}$ using fewer CFEs than those required, when choosing a random initial point, having been based on Figure 2.14. Moreover, in the same section we lifted the lower complexity bound of the optimal DHA and proposed an ES-aided DHA-based MUD, which is sub-optimal but has lower complexity than the DHA-based MUD, which is also fixed, as it was demonstrated in Figures 2.16, 2.17 and 2.18.

The ES-DHA QMUD operating at a sufficiently high number of CFEs, which is still lower than the average – or even lower than the minimum in some scenarios – number of CFEs in the DHA QMUD, achieves the optimal ML performance. When the maximum affordable number of CFEs carried out by the ES-DHA QMUD is reduced, the resultant performance becomes sub-optimal, but it remains close to the ML limit. We proposed a design methodology for operating the ES-DHA QMUDs by taking into consideration a predetermined complexity budget, or target BER value, based on the statistics of the DHA, which may be acquired in practice by off-line simulations.

The investigation of the ES-DHA QMUD in under-loaded, full-rank and rank-deficient

scenarios carried out in Section 2.6 concluded that the MMSE-initialized ES-DHA QMUD performs better than the ZF-initialized ES-DHA QMUD in both under-loaded and full-rank systems, when the same maximum number of CFEs is allowed in both systems, as verified by Figure 2.39 and Figure 2.42. In the rank-deficient scenarios, the ZF and MMSE detectors may be considered equivalent according to Figure 2.30 and Figure 2.33, hence the pair of proposed ES-DHA QMUDs have the same performance, when the same computational complexity is available. Table 2.11 characterizes the QMUDs for the DS-CDMA system of Figure 2.1 supporting $U = 14$ users with the aid of $SF = 7$ and using the parameters of Table 2.6. Finally, based on Figure 2.44, we may conclude that imperfect channel estimation results both in a degraded performance for the proposed QMUDs and in a higher complexity, since the conventional coherent detectors, which generate the initial deterministic input for the QMUDs also experience a degraded performance. However, the performance of the DHA-based QMUD is still equivalent to that of the ML MUD according to Figure 2.44.

In Chapter 4 we present quantum-assisted detectors for non-coherent systems, which do not depend on the accuracy of channel estimation. Even though the performance of the proposed coherent QMUDs matches that of the ML MUD, the decoder's potential error correction capability is not fully exploited, since only hard outputs are provided by the MUDs. In Chapter 3 we proceed by introducing QMUDs that not only provide soft estimates for the decoders, but also accept soft inputs from the decoders, resulting in an enhanced overall system performance by facilitating iterations between the MUD and the channel decoders.

Chapter 3

Iterative Quantum-Assisted Multi-User Detection

3.1 Introduction

In Chapter 2 we have investigated hard-output quantum-assisted detectors, which provide the channel decoders with hard estimates of the transmitted bits. The detection and decoding performance of a receiver is substantially improved, when the Multi-User Detector (MUD) and the channel decoder are allowed to exchange extrinsic information. The employment of MUD facilitates achieving a near-single-user performance with the aid of joint iterative detection and decoding by exchanging extrinsic information in the form of Log-Likelihood Ratios (LLR) between the receiver components. Even if an MUD is not eligible to exploit information received by the channel decoder, it is beneficial to provide the decoder with soft estimates of the symbol or bit values, for enhancing the decoding procedure [21].

The Maximum *A posteriori* Probability (MAP) detector constitutes the optimal Soft-Input Soft-Output (SISO) detector in terms of maximizing the *a posteriori* probability, but requires an excessive number of Cost Function Evaluations (CFE). The Soft-Output (SO) Ant Colony Optimization (ACO) MUDs relying on the MAximum Approximation (MAA) [13] and the MUlti-input Approximation (MUA) [63] have been employed for low-complexity detection, but their performance in rank-deficient systems is unsatisfactory.

In this chapter we investigate a number of quantum-assisted SISO and SO Quantum-assisted MUDs (QMUD). Initially, the Quantum Mean Algorithm (QMA) [62] is presented. The QMA succeeds in finding the mean of a function $f(x)$, where $f : \{0, 1 \ldots, N-1\} \rightarrow [0, 1]$, while requiring a lower number of evaluations of f than the size of the search space N. Based on the QMA, we then propose the novel Quantum Weighted Sum Algorithm (QWSA) [1], which calculates the weighted sum of the values returned by the same function f. Naturally, the QMA constitutes a special case of the QWSA, where all

the weights are equiprobable. By invoking the QWSA we will be able to compute the necessary summations in the numerator and denominator of the bit-based LLRs [1]. The Dürr-Høyer Algorithm (DHA) presented in Section 2.4.3 is also employed in the QWSA QMUD for applying a necessary normalization.

Moreover, in Section 3.5 we present the DHA-aided QMUDs relying on the MAximum Approximation (DHA-MAA QMUD) [3] as well as on the MUlti-input Approximation (DHA-MUA QMUD) [3] and show that they outperform their ACO counterparts and indeed they perform close to the optimal MAP MUD, while requiring a lower complexity than the classical MUDs employed. Furthermore, we investigate their employment in iterative receivers, concluding with their EXtrinsic Information Transfer (EXIT) chart analysis [21] and with the Probability Density Functions (PDF) of the bit-based LLRs. We demonstrate that the family of DHA-MAA QMUDs may only be used for soft-output detection, while the DHA-MUA QMUDs may be integrated into iterative receivers.

The DHA-QWSA QMUD is initially introduced with the aid of a Direct Sequence Code Division Multiple Access (DS-CDMA) system. An efficient multiple access scheme that combines the principles of DS-CDMA, Spatial Division Multiple Access (SDMA) and Multiple Input Multiple Output (MIMO) Orthogonal Frequency Division Multiplexing (OFDM) [21–23] is constituted by the Direct Sequence Spreading (DSS) and Slow Subcarrier-Hopping aided (SSCH) SDMA-OFDM system of [21]. More specifically, each user has been assigned a DSS code, which may or may not be unique among the supported users. Moreover, each user transmits on an identical fraction of the number of available subcarriers, while the specific subcarriers each user transmits on are allocated via a predetermined subcarrier allocation algorithm. Therefore, if two users transmit on different orthogonal subcarriers, their signals are separated in the Frequency Domain (FD). At the same time, when using orthogonal Walsh-Hadamard (WH) codes [11], provided that two users transmitting on the same subcarrier have been allocated different WH codes, their signals are separated in the Time Domain (TD). Finally, if two users transmit on the same subcarrier and have been allocated the same DSS code, they will be separated in the spatial domain by exploiting their channel knowledge obtained with the aid of pilot signals [21].

The presented SISO QMUDs will also be employed in Multi-Carrier Interleave Division Multiple Access (MC-IDMA). The Interleave Division Multiple Access (IDMA) scheme of [5, 18–20, 140–143] distinguishes the users supported with the aid of their unique, user-specific interleaving sequence, whilst each user employs the same channel code and the same Direct Sequence Spreader (DSS). These two procedures are combined in an IDMA system, which is achieved by swapping the position of the DSS and the interleaver of a classic CDMA system [11], which has the advantage of potentially increasing the performance of a CDMA system as a benefit of its increased diversity gain gleaned from the independently fading chips. After channel coding and spreading the information bit sequence, the users interleave their own resultant chip sequence with the aid of a uniquely allocated interleaving sequence. At the receiver, the MUD is invoked on a chip-by-chip basis by exploiting the user-specific channel impulse responses. Iterations between the MUD and the despreader-decoder (DES-DEC) may be performed for providing a better final estimate [9]. Finally, we consider

Multi-Carrier (MC) IDMA owing to its increased flexibility, as detailed in [5, 11, 21].

The rest of this Chapter is structured as follows. The DSS/SSCH SDMA-OFDM system is described in Section 3.2, along with the novel DSS-based Uniform SSCH methodology. In Section 3.3 our MC-IDMA system is investigated. Furthermore, Section 3.4 introduces the QMA and proposes the specific measures required for the transfiguration of the QMA into the QWSA. In the same section, we present a design example of the QWSA QMUD in the context of a DS-CDMA system. The Dürr-Høyer Algorithm-based QMUDs relying on the Maximum Approximation and Multi-input Approximation techniques are presented in Section 3.5, while a soft-output Ant Colony Optimization (ACO) detector using the *free will* modification is investigated in Section 3.6. In Section 3.7 we characterize the soft-output performance of our proposed QMUDs in the context of DSS/SSCH SDMA-OFDM systems and in Section 3.8 we compare the performance of the systems presented when the Uniform SSCH (USCCH) or the novel DSS-based USSCH subcarrier allocation methodologies are employed. The simulation results and the discussions regarding the comparisons of the soft-input soft-output QMUDs with respect to the classical MUDs in MC-IDMA systems, as well as the description of non-Gaussian EXIT charts [144] are offered in Section 3.9. Our conclusions are formulated in Section 3.10.

3.2 DSS/SSCH SDMA-OFDM System Overview

The block diagram of a DSS/SSCH SDMA-OFDM system supporting U geographically separated users and Bit Interleaved Coded Modulation (BICM) is given in Figure 3.1. The information bit stream $\{b_u\}$ of the uth user is encoded by using Turbo Convolutional Codes (TCC) and the encoded bit stream $\{c_u\}$ is then interleaved. The interleaved encoded bit stream of the uth user $\{i_u\}$ is mapped onto the symbol stream $\{x_u\}$. Let us assume that there are $\mathcal{Q}$ available subcarriers, that the length of each user's symbol stream is Γ and that each user occupies W subcarriers during a time frame, where we have $W \leq \mathcal{Q}$, $W \leq \Gamma$ and $\mod(\Gamma, W) = 0$. The user-specific subcarrier mapping pattern is periodically generated based on an appropriately selected approach. The SSCH mapper then maps the $\mathcal{Q}$ available subcarriers to the users, before the OFDM modulator converts the mapped symbols to OFDM symbols by applying the $\mathcal{Q}$-point Inverse Fast Fourier Transform (IFFT)

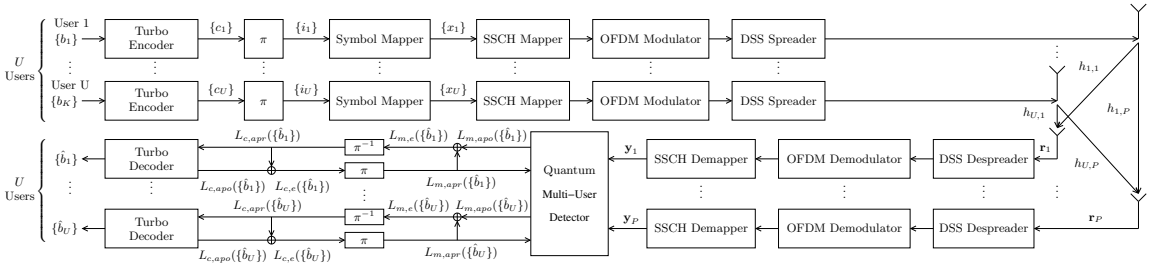

Figure 3.1: Direct Sequence Spreading and Slow Subcarrier-Hopping aided SDMA-OFDM uplink communication system's block diagram supporting U users employing turbo encoding using two convolutional codes as well as non-iterative, soft-output QMUD at the base station.

algorithm. The OFDM symbols are then spread in the time domain based on the user-specific spreading sequences. The Spreading Factor (SF) of the DSS code defines the number of chips used in a spreading sequence. In our scenario we will assume that each user is allocated one of the $G = SF$ available Walsh-Hadamard (WH) spreading codes, which are orthogonal to each other. Without any loss of generality, the number of users employing the gth DSS code, with $g = 1, 2, \ldots, G$, is equal to

$$\left\lfloor \frac{U}{G} \right\rfloor + \begin{cases} 1 & \text{if } g < \text{mod}(U, G) \\ 0 & \text{if } g \geq \text{mod}(U, G) \end{cases} . \tag{3.1}$$

The spread signal is then transmitted over multipath channels and it is received by the P receive Antenna Elements (AE), where the signals of all the users are added together, assuming the employment of a synchronous system, and Additive White Gaussian Noise (AWGN) is added. At the pth receive AE's chain, with $p = 1, 2, \ldots, P$, the received signal $\mathbf{r}_p$ is despread in the time domain and the users employing orthogonal spreading codes are separated. The Fast Fourier Transform (FFT) algorithm is then employed at the OFDM Demodulator. After the OFDM demodulated signal is dehopped on the pth receive AE's chain, it is fed to the QMUD along with the signals of the other receive AEs.

Let us focus on the discrete description of the signals that arrived at the pth receive AE on the qth subcarrier. Let us also assume that $1 \leq U_q \leq U$ users have been allocated to the qth subcarrier, while G_q different DSS codes are present on the qth subcarrier, where $1 \leq G_q \leq G$. Two users may or may not have been allocated the same DSS code. For the gth DSS code of the G_q number of present DSS codes on the qth subcarrier, there is a group of $U_{q,g}$ users who have been allocated the gth DSS code, where

$$U_q = \sum_{g=1}^{G_q} U_{q,g}. \tag{3.2}$$

The signal $\mathbf{r}_{p,q}$ received at the pth received AE, transmitted over the qth subcarrier, $q = 1, 2, \ldots, \mathcal{Q}$, during an OFDM symbol duration is [21]

$$\mathbf{r}_{p,q} = \bar{\mathbf{c}}_{G_q} \bar{\mathbf{H}}_{p,q} \bar{\mathbf{x}}_q + \mathbf{n}_{p,q}, \tag{3.3}$$

where $p = 1, 2, \ldots, P$, $\bar{\mathbf{c}}_{G_q}$ is the $(SF \times U_q)$-element matrix that contains the DSS of each user as in [21]

$$\bar{\mathbf{c}}_{G_q} = [\underbrace{\mathbf{c}_1, \ldots, \mathbf{c}_1}_{U_{q,1}}, \underbrace{\mathbf{c}_2, \ldots, \mathbf{c}_2}_{U_{q,2}}, \ldots, \underbrace{\mathbf{c}_{G_q}, \ldots, \mathbf{c}_{G_q}}_{U_{q,G_q}}], \tag{3.4}$$

where $\mathbf{c}_g = [c_g[1], c_g[2], \ldots, c_g[SF]]^T$ is the gth DSS code and $c_g[k]$ is the value of the kth chip of the gth DSS code. In (3.3), the Frequency-Domain CHannel Transfer Function (FD-CHTF) of the pth receive AE and on the qth subcarrier $\bar{\mathbf{H}}_{p,q}$ is a $(U_q \times U_q)$-element

diagonal matrix, as encapsulated in [21]

$$\bar{\mathbf{H}}_{p,q} = \text{ diag}[h^{(1)}_{p,1,q}, \ldots, h^{(u_1)}_{p,1,q}, h^{(1)}_{p,2,q}, \ldots, h^{(u_2)}_{p,2,q}, h^{(1)}_{p,G_q,q}, \ldots, h^{(u_{G_q})}_{p,G_q,q}], \tag{3.5}$$

where $h^{(i)}_{p,g,q}$ is the complex-valued channel coefficient of the ith user in the gth DSS code group transmitting at the qth subcarrier and received by the pth receive AE. Finally, the $(1\times U_q)$-element vector $\bar{\mathbf{x}}_q$ in Equation 3.3 represents the signal vector on the qth subcarrier and its structure is

$$\bar{\mathbf{x}}_q = [x^{(1)}_{1,q}, \ldots, x^{(u_1)}_{1,q}, x^{(1)}_{2,q}, \ldots, x^{(u_2)}_{2,q}, x^{(1)}_{G_q,q}, \ldots, x^{(u_{G_q})}_{G_q,q}]^T, \tag{3.6}$$

while $\mathbf{n}_{p,q} = [n_{p,q}[1], \ldots, n_{p,q}[SF]]$ is the $(1\times SF)$-element complex-valued thermal noise vector at the pth receive AE added to the signal received on the qth subcarrier with zero mean and σ^2 variance.

The $(G_q\times 1)$-element despread signal $\bar{\mathbf{y}}_{p,q} = [y_{p,1,q}, \ldots, y_{p,G_q,q}]^T$ at the pth receive AE from the qth subcarrier is [21]

$$\bar{\mathbf{y}}_{p,q} = \check{\mathbf{c}}_{G_q}\mathbf{r}_{p,q} = \bar{\mathbf{R}}_{G_q}\bar{\mathbf{H}}_{p,q}\bar{\mathbf{x}}_q + \bar{\mathbf{n}}_{p,q}, \tag{3.7}$$

where $\bar{\mathbf{n}}_{p,q} = [n_{p,1,q}, n_{p,2,q}, \ldots, n_{p,G_q,q}]^T$ is the effective noise vector, $\check{\mathbf{c}}_{G_q}$ is the DSS codebook that includes the DSS codes that appeared on the qth subcarrier as described in

$$\check{\mathbf{c}}_{G_q} = [\mathbf{c}_1, \mathbf{c}_2, \ldots, \mathbf{c}_{G_q}]^T, \tag{3.8}$$

and $\bar{\mathbf{R}}_{G_q}$ is the $(SF\times U_q)$-element cross-correlation matrix of the G_q DSS codes that were employed by the U_q users on the qth subcarrier, as given in

$$\bar{\mathbf{R}}_{G_q} = \begin{bmatrix} \omega_{11} \ldots \omega_{11} & \ldots & \omega_{1G_q} \ldots \omega_{1G_q} \\ \omega_{22} \ldots \omega_{22} & \ldots & \omega_{2G_q} \ldots \omega_{2G_q} \\ \vdots & \vdots & \vdots \\ \underbrace{\omega_{G_q1} \ldots \omega_{G_q1}}_{U_{q,1}} & \ldots & \underbrace{\omega_{G_qG_q} \ldots \omega_{G_qG_q}}_{U_{q,G_q}} \end{bmatrix}, \tag{3.9}$$

where $\omega_{i,j}$ is the cross-correlation between the ith and the jth DSS code [21].

3.2.1 Multi-User Detection

The QMUD will perform a subcarrier-based and DSS-code group-based detection of the users relying on the same DSS code and transmitting over the same subcarrier by combining the signals at the receive AEs, while outputting a soft estimate of each user's transmitted bit sequence in the form of Log-Likelihood Ratios. The hard output of the MMSE detector may be used as the initial input of the DHA in the SISO QMUDs, as well as for calculating

the initial intrinsic affinity in the SO-ACO MUDs. The $(1\times U_{q,g})$-element signal vector output of the MMSE detector at the qth subcarrier of the gth DSS group linearly combines the signals received by the P receive AEs $\mathbf{y}_{g,q} = [y_{1,g,q}, \ldots, y_{P,g,q}]^T$ as in

$$\mathbf{z}_{\mathrm{MMSE}_{g,q}} = \mathbf{W}^H_{\mathrm{MMSE}_{g,q}} \mathbf{y}_{g,q}, \tag{3.10}$$

where $\mathbf{z}_{\mathrm{MMSE}_{g,q}} = [z^{(1)}_{\mathrm{MMSE}_{g,q}}, \ldots, z^{(U_{q,g})}_{\mathrm{MMSE}_{g,q}}]^T$, $g = 1, \ldots, G_q$, and $\mathbf{W}^H_{\mathrm{MMSE}_{g,q}}$ is equal to

$$\mathbf{W}^H_{\mathrm{MMSE}_{g,q}} = \left(\mathbf{H}^H_{g,q}\mathbf{H}_{g,q} + N_0\mathbf{I}\right)^{-1} \mathbf{H}^H_{g,q}, \tag{3.11}$$

where N_0 is the noise's variance and $\mathbf{H}_{g,q}$ is the $(P\times U_{q,g})$-element FD-CHTF matrix of the users associated with the gth DSS code group at the qth subcarrier and is equal to

$$\mathbf{H}_{g,q} = \begin{bmatrix} h^{(1)}_{1,g,q} & h^{(2)}_{1,g,q} & \cdots & h^{(U_{q,g})}_{1,g,q} \\ \vdots & \vdots & \vdots & \vdots \\ h^{(1)}_{P,g,q} & h^{(2)}_{P,g,q} & \cdots & h^{(U_{q,g})}_{P,g,q} \end{bmatrix}. \tag{3.12}$$

The LLR of the mth bit of the uth user in the gth DSS code group at the qth subcarrier may be calculated as [10]

$$L_{m,po}\left(b^{(m)}_u\right) = \ln \frac{\sum\limits_{\mathbf{x}\in\chi_{g,q}(u_{q,g},m,0)} p\left(\mathbf{y}_{g,q}|\mathbf{x}\right) P(\mathbf{x})}{\sum\limits_{\mathbf{x}\in\chi_{g,q}(u_{q,g},m,1)} p\left(\mathbf{y}_{g,q}|\mathbf{x}\right) P(\mathbf{x})}, \tag{3.13}$$

where $\chi_{g,q}(u_{q,g}, m, \mathrm{v})$ is the set of multi-level symbols formed by the users in the gth DSS code group at the qth subcarrier, for which the $[(u_{q,g}-1)\log_2 M + m]$th bit's value is equal to v, with $u_{q,g} = 1, \ldots, U_{q,g}$ and $m = 1, \ldots, \log_2 M$. Furthermore, $P(\mathbf{x})$ is the *a priori* probability of the $U_{q,g}$ users transmitting $\mathbf{x}$ and $p(\mathbf{y}_{g,q}|\mathbf{x})$ is the conditional PDF of having obtained $\mathbf{y}_{g,q}$, given that $\mathbf{x}$ was transmitted by the $U_{q,g}$ users. The conditional PDF $p(\mathbf{y}_{g,q}|\mathbf{x})$ multiplied by the corresponding *a priori* LLRs describes our CF $f(\mathbf{x})$, as encapsulated in [10]

$$f(\mathbf{x}) = p\left(\mathbf{y}_{g,q}|\mathbf{x}\right) P(\mathbf{x}) = \frac{1}{\left(\sigma\sqrt{2\pi}\right)^P} \exp\left(\frac{-\left\|\mathbf{y}_{g,q} - \mathbf{H}_{g,q}\mathbf{x}\right\|^2}{2\sigma^2}\right) P(\mathbf{x}). \tag{3.14}$$

When the QMUD is invoked for the first time, the *a priori* probabilities $P(\mathbf{x})$ are equal for all possible vectors of $\mathbf{x}$. After the QMUD, the extrinsic LLR stream of each user is deinterleaved and then passed to the U Max-Log *A Posteriori* Probability (APP) decoders. By making a hard decision on the soft outputs of the uth decoder we may estimate the uth user's information bit stream $\{\hat{b}_u\}$.

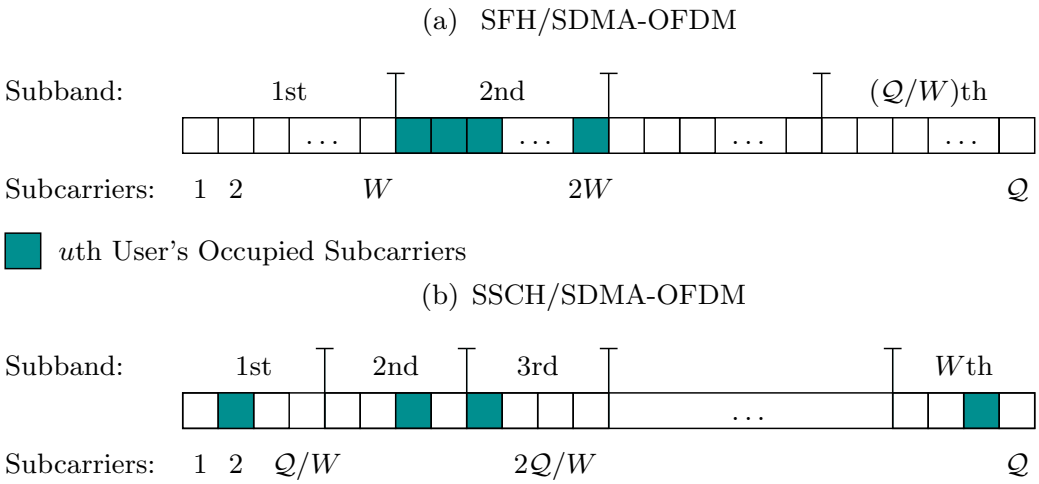

Figure 3.2: (a) The SFH methodology, which allocates one of the $\mathcal{Q}/W$ subbands, or, in other words, W adjacent subcarriers to each user. (b) The SSCH methodology, which allocates one subcarrier of each of the W formed subbands to each user. Hence, each user is allocated W non-adjacent subcarriers.

3.2.2 Slow Frequency Hopping

The Slow Frequency Hopping (SFH) methodology [21] divides the $\mathcal{Q}$ available subcarriers into $\mathcal{Q}/W$ number of subbands having W subcarriers in each subband, as illustrated in Figure 3.2a. Each of the U supported users is allocated the W subcarriers of a subband. A disadvantage of SFH is that if a subcarrier is deeply faded, there is a high probability that its adjacent subcarriers are also experiencing fading during the same OFDM frame. Therefore, the users allocated to that particular subband, which contains the fading subcarriers, experience fading on most of the subcarriers, resulting in a degraded performance. For circumventing this problem, we employ the SSCH methodology.

3.2.3 Slow Subcarrier Hopping

According to the SSCH specifications [21], the $\mathcal{Q}$ available subcarriers are divided into W subbands with $SB = \mathcal{Q}/W$ subcarriers in each subband, as shown in Figure 3.2b. The SSCH regime allocates a single subcarrier from each of the W subbands to the uth user. As in the SFH methodology, by employing the SSCH methodology each user transmits on W subcarriers, with the difference that the allocated subcarriers are no longer adjacent. Therefore, there is a low probability that most of the subcarriers of a user will be fading.

3.2.3.1 Random Slow Subcarrier Hopping

The Random SSCH (RSSCH) scheme allocates subcarriers to users on a subband basis, by allocating a random subcarrier of each subband to the uth user, with $u = 1, 2, \ldots, U$. By adopting the RSSCH methodology, we may encounter the incident where some subcarriers will be unnecessarily loaded with a high number of users, while others may support a single user or even no users at all.

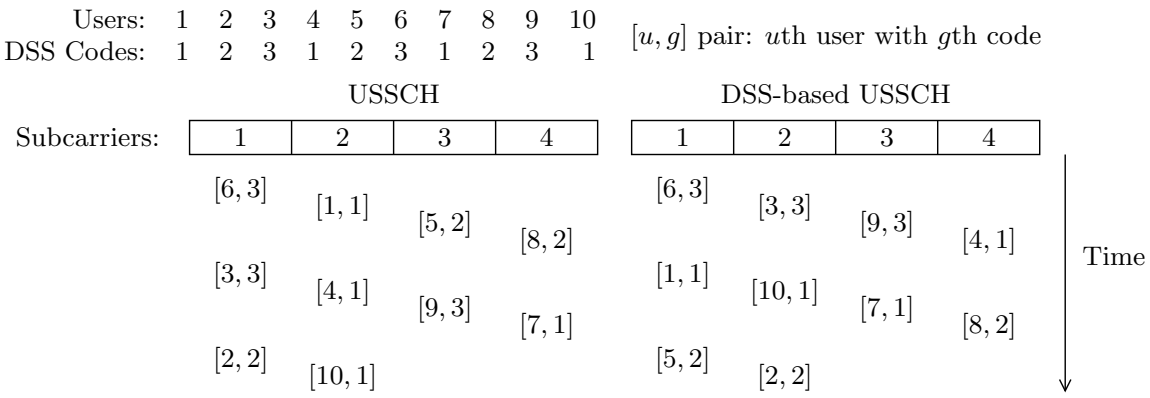

Figure 3.3: Comparison between the USSCH [21] and the proposed DSS-based USSCH in an example with $U = 10$ users, $\mathcal{Q}/W = 4$ subcarriers per subband and 3 DSS-codes. If USSCH is employed, the presented scenario may occur and we may have MUI by 2 users at the first subcarrier of that particular subband, as well as MUI by 3 users at the second subcarrier. It should be noted that employing USSCH may result in different distribution of users on each subband, and hence different amount of MUI. On the other hand, if DSS-based USSCH is followed in this scenario, there is no MUI at any of the subcarriers in all subbands with 100% probability, since its methodology keeps MUI to the smallest possible value by distributing users with the same DSS-code to different subcarriers.

3.2.3.2 Uniform Slow Subcarrier Hopping

The USSCH also performs subband-based subcarrier mapping by firstly allocating each subcarrier of the wth subband, $w = 1, 2, \ldots, W$, to a different, randomly selected user, until each of the subcarriers in the wth subband has been allocated to a user. Afterwards, restarting from the first subcarrier of the wth subband, a second user is allocated to each subcarrier. The above procedure is repeated until all the users have been allocated a subcarrier in the wth subband. The USSCH continues by allocating the subcarriers of the $(w + 1)$th subband to the users with the same procedure. The USSCH adopts a specific subcarrier mapping strategy, where the number of users on each subcarrier, and hence the Multi-User Interference (MUI), is similar.

3.2.3.3 DSS-based Uniform Slow Subcarrier Hopping

The DSS-based USSCH follows the methodology of the USSCH, apart from the difference that when a user is randomly allocated to a subcarrier, then the rest of the users who belong to the same DSS-code group as the already allocated user will be allocated to subcarriers, before the users who belong to a different DSS-code group. Once all the users of that particular DSS-code group have been allocated to a subcarrier of the current subband, the procedure continues with one of the remaining users being randomly selected to be allocated to the subsequent subcarrier. Afterwards, the rest of the users in the same DSS-code group as the last randomly selected user will be allocated to subcarriers, before a user from a different DSS-code group is randomly selected again. By following the DSS-based USSCH, the users who belong to the same DSS-code group are allocated to as many subcarriers as possible, hence reducing the MUI on each subcarrier. Figure 3.3 compares the USSCH to

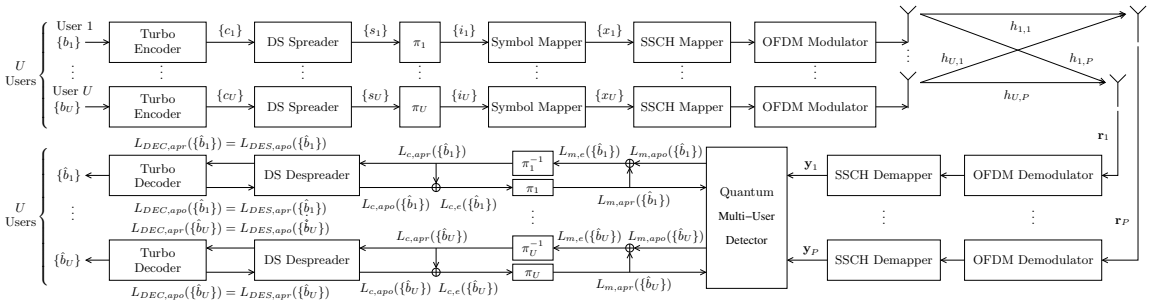

Figure 3.4: MC-IDMA uplink communication system's block diagram supporting U users employing non-systematic convolutional coding and direct sequence spreading as well as iterative, soft-input soft-output QMUD at the BS.

the DSS-based USSCH philosophy and shows the advantages of the DSS-based USSCH, such as the achievement of a better system performance, while supporting the same number of users or the capability of supporting more users at the same complexity in the MUD stage.

The USSCH, as well as the DSS-based USSCH, RSSCH and SFH are periodically performed with a period of T_h for making the communication fairer for the specific users who happen to transmit on deeply fading subcarriers. It is noted that T_h should be higher than the symbol period T_s, for coherent demodulation to be used at the receiver. In practice, T_h will be equal to an integer number of symbol periods.

3.3 MC-IDMA System Overview

Similarly to the analysis of the DSS/SSCH SDMA-OFDM systems, let us assume that U users are supported by our MC-IDMA system, as seen in Figure 3.4. The uth user, $u = 1, 2, \ldots, U$, initially encodes his / her information bit sequence $\{b_u\}$ by a turbo encoder having a code rate R. The coded bit sequence $\{c_u\}$ of Figure 3.4 is then spread using a DSS code having a spreading factor of SF. Since every user employs the same DSS code, this may be viewed as a repetition code having a code rate of $1/SF$ [10]. The turbo-encoded and DSS-spread bit sequence $\{s_u\}$ is then interleaved based on a user-specific interleaving sequence, resulting in the bit sequence $\{i_u\}$. Once the interleaved bit sequence of Fig. 3.4 has been mapped to symbols based on the M-ary modulation scheme selected and the symbol sequence $\{x_u\}$ has been obtained, it is mapped to the specific subcarriers that have been allocated to the uth user based on the Slow SubCarrier Hopping (SSCH) Mapper, followed by Orthogonal Frequency Division Multiplexing (OFDM) modulation by applying the classic $\mathcal{Q}$-point Inverse Fast Fourier Transform (IFFT) of Fig. 3.4.

Let us also assume as in the case of the DSS/SSCH SDMA-OFDM systems in Section 3.2 that the length of the symbol sequence $\{x_u\}$ is equal to Γ. Out of the $\mathcal{Q}$ available subcarriers of our system seen in Fig. 3.4 W subcarriers are allocated to each of the U users, obeying $W \leq \mathcal{Q}$, $W \leq \Gamma$, $\mod(\Gamma, W) = 0$ and $\mod(\mathcal{Q}, W) = 0$. In this treatise we apply the Uniform SSCH (USSCH) scheme [21] for allocating the subcarriers to the users.

The U transmitted signals are received by the P receive AEs at the BS at the same time, assuming a synchronous system [21]. Therefore, at the pth receive AE, p=1, 2, ..., P, the U received signals are superimposed on each other, along with the Additive White Gaussian Noise (AWGN) having a zero mean and a variance of N_0=$2\sigma^2$. The resultant signal $\mathbf{r}_p$=$[r_{p,1}, r_{p,2}, \ldots, r_{p,\mathcal{Q}}]^T$ is then OFDM demodulated by applying the $\mathcal{Q}$-point Fast Fourier Transform (FFT) and dehopped according to the SSCH demapper, before $\mathbf{y}_p$ is forwarded to the MUD along with the rest of the signals gleaned from the other receive AE chains. The MUD operates on a subcarrier-basis. Let us focus our attention on the qth subcarrier and assume that the qth subcarrier has been allocated to U_q users, associated with $U_q < U$. The signal entering the MUD on the qth subcarrier is

$$\mathbf{y}_q = \mathbf{H}_q \cdot \mathbf{x}_q + \mathbf{n}_q, \tag{3.15}$$

where $\mathbf{y}_q$=$[y_{1,q}, y_{2,q}, \ldots, y_{P,q}]^T$ is the (P×1)-element received signal vector and $\mathbf{H}_q$ is the Frequency-Domain CHannel Transfer Function (FD-CHTF) on the qth subcarrier, which may be represented by a (P×U_q)-element matrix as in

$$\mathbf{H}_q = \begin{bmatrix} h_{1,q}^{(1)} & h_{1,q}^{(2)} & \cdots & h_{1,q}^{(U_q)} \\ h_{2,q}^{(1)} & h_{2,q}^{(2)} & \cdots & h_{2,q}^{(U_q)} \\ \vdots & \vdots & \ddots & \vdots \\ h_{P,q}^{(1)} & h_{P,q}^{(2)} & \cdots & h_{P,q}^{(U_q)} \end{bmatrix}, \tag{3.16}$$

where $h_{p,q}^{(u_q)}$ is the complex-valued channel coefficient between the u_qth user and the pth receive AE on the qth subcarrier. Moreover, $\mathbf{x}_q$=$[x_q^{(1)}, x_q^{(2)}, \ldots, x_q^{(U_q)}]^T$ is the (U_q×1)-element symbol vector of the U_q users on the qth subcarrier and $\mathbf{n}$=$[n_{1,q}, n_{2,q}, \ldots, n_{P,q}]^T$ is the (P×1)-element noise vector.

The MAP MUD performs detection on a subcarrier basis by exploiting $\mathbf{y}_q$ from Equation 3.15 and generates bit-based LLRs. Focusing on the qth subcarrier supporting U_q users, the *a posteriori* bit based LLR of the u_qth user's mth bit at the output of the MAP MUD is formulated as

$$L_{m,po}\left(b_{u_q}^{(m)}\right) = \ln \frac{\sum_{\mathbf{x}\in\chi_q(u_q,m,0)} p\left(\mathbf{y}_q|\mathbf{x}\right) P(\mathbf{x})}{\sum_{\mathbf{x}\in\chi_q(u_q,m,1)} p\left(\mathbf{y}_q|\mathbf{x}\right) P(\mathbf{x})}, \tag{3.17}$$

where $\chi_q(u_q, m, \mathrm{v})$ is the set of legitimate multi-level symbols, which have the u_qth user's mth bit equal to v, with $u_q \in \{1, 2, \ldots, U_q\}$, $m \in \{1, 2, \ldots, \log_2(M)\}$ and $\mathrm{v} \in \{0, 1\}$. Furthermore, $p(\mathbf{y}_q|\mathbf{x})$ is the conditional probability of receiving the signal $\mathbf{y}_q$, given that $\mathbf{x}$ was transmitted. The product $f(\mathbf{x})$ of the channel and of the *a priori* symbol probabilities

$P(\mathbf{x})$ acts as our Cost Function (CF), which is equal to [10]

$$f(\mathbf{x}) = \frac{1}{\left(\sigma\sqrt{2\pi}\right)^P} \exp\left(-\frac{\left\|\mathbf{y}_q - \mathbf{H}_q\mathbf{x}\right\|^2}{2\sigma^2}\right) P(\mathbf{x}) = P\left(\mathbf{y}_q|\mathbf{x}\right) P(\mathbf{x}). \tag{3.18}$$

Finally, the *a priori* symbol probability $P(\mathbf{x})$ of Equation 3.17 is fed back by the DES/DEC of Fig. 3.4 after having been appropriately rearranged by the interleaver π to the MUD as its extrinsic information, which is initially identical for all legitimate symbols $\mathbf{x}$. The extrinsic LLR at the output of the MUD of Fig. 3.4 is

$$L_{m,e}\left(b_{u_q}^{(m)}\right) = L_{m,po}\left(b_{u_q}^{(m)}\right) - \ln\frac{P\left(b_{u_q}^{(m)}=0\right)}{P\left(b_{u_q}^{(m)}=1\right)}. \tag{3.19}$$

As seen in Fig. 3.4, the bit-based extrinsic LLR stream of the uth user gleaned from all the W allocated subcarriers is deinterleaved based on the user-specific interleaver and then despread in the time domain, before it is fed to the turbo decoder, which outputs its own bit-based *a posteriori* LLRs. After a sufficiently high number of iterations between the MUD and the DES/DEC, a hard decision is made on the LLRs at the output of the decoder of Fig. 3.4, yielding the estimated $\{\hat{b}_u\}$ bit sequence.

3.4 Quantum Weighted Sum Algorithm

In a DSS/SSCH SDMA-OFDM or MC-IDMA system, the MUDs search through a pool of $M^{U_{q,g}}$ legitimate inputs to the CF of Equation 3.14 and Equation 3.18, respectively. In DSS/SSCH SDMA-OFDM systems the symbol index $x \in \{0, \ldots, M^{U_{q,g}} - 1\}$ is the decimal representation of the $M^{U_{q,g}}$-ary symbols. For example, if $M = 4$ and $U_{q,g} = 2$, then $\mathbf{x} = [+1 - j, -1 + j]$ demodulates into $\left[b_{u=0}^{(m=0)}|b_{u=0}^{(m=1)}|b_{u=1}^{(m=0)}|b_{u=1}^{(m=1)}\right] = [01|10]$, which corresponds to the index of $x = 6$. The same description is applied for MC-IDMA systems, without the subscript g, which defines the group of users equipping different DSS codes, since all U users employ the same spreading code.

The QWSA is capable of estimating the weighted sum of the CF in both the numerator and denominator of the LLR expressed in Equation 3.13 and Equation 3.17 by using a fixed number of CF evaluations, regardless of the number of users U or of the modulation order M. Note that in a multi-carrier system the number of users interfering on the qth subcarrier is U_q. For the analysis of the QWSA we will assume that all the users' signals are spread across all the subcarriers and hence we have $U_q = U$ for $q \in \{1, 2, \ldots, Q\}$. The QWSA can be applied to any function $f : \{0, 1, \ldots, N-1\} \rightarrow [0, 1]$ including the CF of Equation 2.4 in conjunction with $N = M^U/2$. Where necessary, we will present application examples for a system supporting $U = 2$ users and QPSK modulation relying on $M = 4$. Furthermore, $N = 8$ CF evaluations contribute to each summation and the numerator ($b = 0$) of the first user's ($u = 1$) first bit ($m = 1$) LLR is estimated. The same process is also applied for the denominator of the same bit, as well as for the numerators and denominators of the rest of

the bits of the multi-level M^U-ary symbol.

The QWSA invoked for a user's bit value estimates the weighted sum of the evaluations of the function $f(x)$ in Equation 3.14 and Equation 3.18 for all the x values that contribute to that bit value. The process of the QWSA invoked for determining each user's bit value may be summarized in two steps:

1. Construct a quantum register associated with $(U \log_2 M)$ qubits in the state

$$|\Psi\rangle = \sum_{x \in \chi(0,0,0)} \left(\sqrt{P(x)(1-f(x))}|x\rangle \right) |0\rangle + \sum_{x \in \chi(0,0,0)} \left(\sqrt{P(x)f(x)}|x\rangle \right) |1\rangle. \tag{3.20}$$

   The number of qubits is one less than the number of bits in our M^U-ary symbols, $(U \cdot \log_2(M) - 1) = 3$, plus 1. The last qubit distinguishes between the states which have the probability of $P(x)(1-f(x))$ and those with a probability of $P(x)f(x)$, when the last qubit is $|0\rangle$ and $|1\rangle$, respectively. It should be noted that the probability of a state associated with the last qubit being $|1\rangle$ is one of the additive terms in our desired summation in the numerator of Equation 3.13 or Equation 3.17.

2. Employ l qubits and the Quantum Amplitude Estimation (QAE) algorithm [48] to estimate the probability of obtaining a state with the last qubit equal to $|1\rangle$, when observing $|\Psi\rangle$ in the Quantum Domain (QD). This probability is given by the sum of the square of the amplitudes of all the states for which the last qubit is $|1\rangle$, hence $\sum_{x \in \chi(1,1,0)} [P(x)f(x)]$ from Equation 3.20, which is the numerator of the first user's first bit as in Equation 3.13 or Equation 3.17.

The QWSA algorithm is summarized in Algorithm 4, and it will be thoroughly analysed in the following sections. The quantum circuit of the QWSA is given in Figure 3.5. The Quantum Control Register (QCR) and the Quantum Function Register (QFR) are the two quantum registers employed in the QWSA, as seen in Figure 3.5. After the theoretical analysis of the QWSA, the proposed algorithm is employed step-by-step in a simple single-carrier DS-CDMA scenario for providing deeper intuition of its operation, before employing it in the multi-carrier multiple access systems presented in the chapter.

3.4.1 Preparation of the quantum register $|\Psi\rangle$

Let us commence our analysis by introducing the unitary operator A, relying on the quantum circuit of Figure 3.6. We employ $n = \log_2 N$ qubits for representing all the input arguments of the CF evaluations included in the summation, Z qubits to store the CF evaluations and an additional auxiliary qubit, $|0\rangle_3$, all initialized to the $|0\rangle$ state. The first n qubits are rotated by a qubit-specific rotation operator R_i. The rotation angle of each qubit depends on the *a priori* probability of the specific classical bit being equal to 0, which the qubit corresponds to. If for example $P\left(b_u^{(m)} = 0\right)$ is the *a priori* probability of the uth

Algorithm 4 Quantum Weighted Sum Algorithm [1]

1: *Resources:* For estimating the weighted sum a of a function $f : \{0, 1, \ldots, 2^n - 1\} \rightarrow [0, 1]$, set l qubits for the QCR in the all-zero state $|t\rangle = |0\rangle^{\otimes l}$ and $n+1$ qubits for the QFR in the all-zero state $|0\rangle^{\otimes (n+1)}$.

2: *Initialization:* The QCR passes through a Hadamard gate $H^{\otimes l}$ as in Equation 3.53, while the A operator – Equation 3.31, Equation 3.24, Figure 3.6, Figure 3.7 – is applied on the QFR resulting in the state $|\Psi\rangle$ described in Equation 3.33. The wanted weighted sum a appears as the sum of the probabilities of observing half of the quantum states that $|\Psi\rangle$ is superimposed in, namely the probability of observing a state belonging to $|\Psi_1\rangle$ of Equation 3.36.

Quantum Amplitude Estimation

3: *Controlled Q operators:* The QCR controls a number of Q operators – Equation 3.39, Figure 3.8 – with the QFR acting as the target quantum register. The QCR's qubits determine the specific number of Q operators that are applied on the QFR each subsequent time. The resultant state of the system $|\phi_1\rangle$ in Figure 3.5 is presented in Equation 3.56.

4: *Inverse Quantum Fourier Transform:* The IQFT is applied on the QCR, yielding the quantum state $|\phi_2\rangle$ described in Equation 3.58.

5: *Observation of the QCR:* The QCR is observed and the state $|z_{obs}\rangle \in \{|0\rangle, |1\rangle, \ldots, |2^l - 1\rangle\}$ is obtained with the probability given in Equation 3.63.

6: *Estimation of θ:* Based on $|z_{obs}\rangle$ and Equation 3.64, θ is estimated by $\hat{\theta}$.

7: *Estimation of a:* Based on $\hat{\theta}$ and Equation 3.38, the weighted sum a of f is estimated.

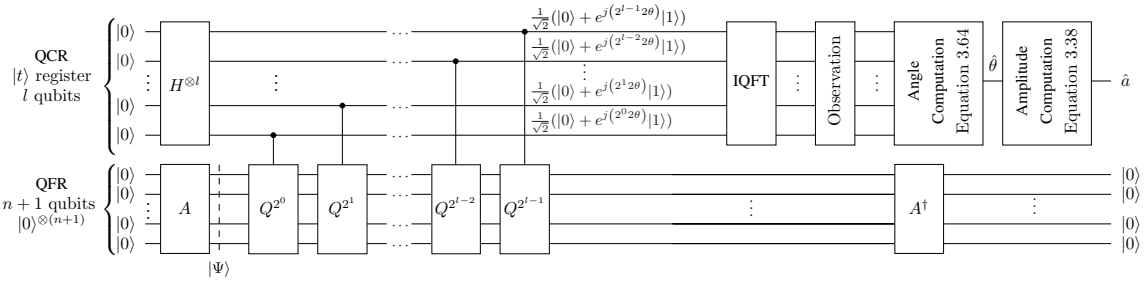

Figure 3.5: Quantum circuit of the QWSA, where the operators A and Q are depicted in Figure 3.6 and Figure 3.8, respectively. The superscripts of the Q operators signify the number of times the Q operator will be consecutively applied. The number of qubits in the QFR is $(n + 1) = (U \log_2 M - 1 + 1) = U \log_2 M$.

user's mth bit being 0, and the currently estimated LLR does not belong to it, then the $i = [(u - 1) \log_2 M + m]$th qubit's unitary rotation operator R_i would be equal to

$$R_i = \begin{bmatrix} \sqrt{P\left(b_u^{(m)} = 0\right)} & -\sqrt{P\left(b_u^{(m)} = 1\right)} \\ \sqrt{P\left(b_u^{(m)} = 1\right)} & \sqrt{P\left(b_u^{(m)} = 0\right)} \end{bmatrix}. \tag{3.21}$$

This is the only difference with respect to the QMA, which uses H operators instead of R_i, for creating an equiprobable superposition of all the input arguments at this point. It should be noted that if all the *a priori* bit probabilities are equal to 0.5, the QWSA transforms into the QMA, since the weights will be equal to each other and R_i will have the same effect as H. The state $|\xi\rangle$ in Figure 3.6 in our $U = 2$ user scenario with $M = 4$,

where we want to find the numerator of the first user's first bit's extrinsic $LLR\left(b_1^{(1)}\right)$ is

$$\begin{aligned}
|\xi\rangle &= \left(\sqrt{P\left(b_1^{(2)}=0\right)}|0\rangle_{1,1} + \sqrt{P\left(b_1^{(2)}=1\right)}|1\rangle_{1,1}\right) \otimes \\
&\quad \otimes \left(\sqrt{P\left(b_2^{(1)}=0\right)}|0\rangle_{1,2} + \sqrt{P\left(b_2^{(1)}=1\right)}|1\rangle_{1,2}\right) \otimes \\
&\quad \otimes \left(\sqrt{P\left(b_2^{(2)}=0\right)}|0\rangle_{1,3} + \sqrt{P\left(b_2^{(2)}=1\right)}|1\rangle_{1,3}\right) \otimes |0\rangle_2^{\otimes Z} \otimes |0\rangle_3 \\
&= \left(\sqrt{P\left(b_1^{(2)}=0\right)P\left(b_2^{(1)}=0\right)P\left(b_2^{(2)}=0\right)}|000\rangle_1 + \right. \\
&\quad + \sqrt{P\left(b_1^{(2)}=0\right)P\left(b_2^{(1)}=0\right)P\left(b_2^{(2)}=1\right)}|001\rangle_1 + \\
&\quad + \sqrt{P\left(b_1^{(2)}=0\right)P\left(b_2^{(1)}=1\right)P\left(b_2^{(2)}=0\right)}|010\rangle_1 + \\
&\quad + \sqrt{P\left(b_1^{(2)}=0\right)P\left(b_2^{(1)}=1\right)P\left(b_2^{(2)}=1\right)}|011\rangle_1 + \ldots \\
&\quad \left. \cdots + \sqrt{P\left(b_1^{(2)}=1\right)P\left(b_2^{(1)}=1\right)P\left(b_2^{(2)}=1\right)}|111\rangle_1\right) \otimes |0\rangle_2^{\otimes Z}|0\rangle_3 \\
&= \left(\sum_{x=0}^{7}\sqrt{P(x)}|x\rangle_1\right) \otimes |0\rangle_2^{\otimes Z} \otimes |0\rangle_3. \qquad (3.22)
\end{aligned}$$

This part of the QWSA describes the C/Q section of the QMUD of Figure 1.5, since classical information is encoded into the probabilities of quantum states. Therefore, the quantum state $|\xi\rangle$ at the input of the block A' in Figure 3.6 is equal to

$$|\xi\rangle = \sum_{x=0}^{N-1}\sqrt{P(x)}|x\rangle_1|0\rangle_2^{\otimes Z}|0\rangle_3, \qquad (3.23)$$

where $P(x)$ is the product of all the probabilities of the bits' values, which contribute to the evaluation of $f(x)$ presented in Equation 3.14 or Equation 3.18, except for the specific bit for which the LLR is estimated. In our scenario, for $x = 1$, we have $P(1) = P(\mathbf{0}001) = P\left(b_1^{(2)}=0\right)P\left(b_2^{(1)}=0\right)P\left(b_2^{(2)}=1\right)$.

The unitary operator A' is then applied to the state $|\xi\rangle$. The quantum circuit is presented in Figure 3.7 and its operation may be summarized as

$$|x\rangle|0^{\otimes Z}\rangle|0\rangle \xrightarrow{A'} |x\rangle|0^{\otimes Z}\rangle\left(\sqrt{1-f(x)}|0\rangle + \sqrt{f(x)}|1\rangle\right), \qquad (3.24)$$

where the controlled rotation gate R may be described as

$$R = \begin{bmatrix} \sqrt{1-f(x)} & -\sqrt{f(x)} \\ \sqrt{f(x)} & \sqrt{1-f(x)} \end{bmatrix}. \qquad (3.25)$$

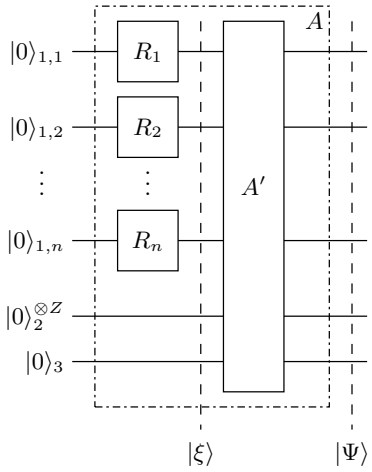

Figure 3.6: Quantum circuit of the unitary operator A. In the first quantum register, the $i = [(u-1)\log_2 M + m]s$th rotation gate R_i, $i = 0, 1, \ldots, n$ maps the ith qubit to the state $\sqrt{P\left(b_u^{(m)} = 0\right)}|0\rangle + \sqrt{P\left(b_u^{(m)} = 1\right)}|1\rangle$, where the resultant amplitudes are the *a priori* bit probabilities included in Equation 2.5. The A' operator illustrated in Figure 3.7 is then applied to the three quantum registers.

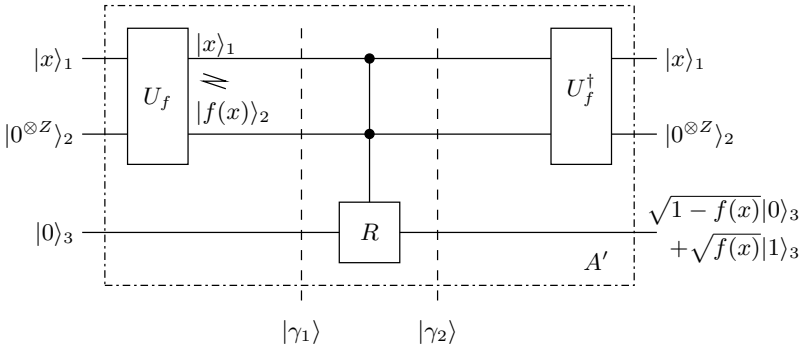

Figure 3.7: Quantum circuit of the unitary operator A'. The unitary operator U_f accepts as inputs a quantum state $|x\rangle$ and Z qubits in the zero state, where Z is the number of bits $f(x)$ is desired to be calculated in. After the controlled R operation, the inverse quantum circuit of U_f is applied in order to return the second quantum register to the all-zero state.

The rationale behind the constraint that only functions with evaluations between 0 and 1 are eligible to be inputs for the QMA and the QWSA becomes clear in Equation 3.24, where the probabilities of observing the last qubit in the state $|0\rangle$ or $|1\rangle$ while having already observed the first n qubits in the $|x\rangle$ state are $1 - f(x)$ and $f(x)$, respectively, emphasizing that $0 \leq f(x) \leq 1$ should be true for every x. The operator A' is unitary since it applies controlled rotations on the last qubit with the angle depending on the evaluation of $f(x)$. The evaluations of f will be represented in the Z qubits of the second quantum register, where the number of qubits Z depends on the allowed precision and the technology of U_f and it does not affect the algorithm's complexity. We will assume that Z is sufficiently large for our simulations, without any loss of generality.

In the context of the QWSA the quantum state $|\xi\rangle$ of Equation 3.23 will be the input

of the unitary operator A' yielding the quantum state $|\gamma_1\rangle$ as in:

$$\begin{aligned}|\gamma_1\rangle &= U_f \sum_{x=0}^{N-1} \sqrt{P(x)}|x\rangle_1|0\rangle_2^{\otimes Z}|0\rangle_3 \\ &= \sum_{x=0}^{N-1} \left(\sqrt{P(x)}U_f|x\rangle_1|0\rangle_2^{\otimes Z}\right)|0\rangle_3 \\ &= \sum_{x=0}^{N-1} \left(\sqrt{P(x)}|x\rangle_1|f(x)\rangle_2\right)|0\rangle_3. \end{aligned} \tag{3.26}$$

After the controlled rotation gate R is applied to the quantum state $|\gamma_1\rangle$, the resultant state $|\gamma_2\rangle$ will be equal to

$$\begin{aligned}|\gamma_2\rangle = R|\gamma_1\rangle &= R\left(\sum_{x=0}^{N-1} \left(\sqrt{P(x)}|x\rangle_1|f(x)\rangle_2\right)|0\rangle_3\right) \\ &= \sum_{x=0}^{N-1} \left(\sqrt{P(x)}R|x\rangle_1|f(x)\rangle_2|0\rangle_3\right) \\ &= \sum_{x=0}^{N-1} \left(\sqrt{P(x)}|x\rangle_1|f(x)\rangle_2\left(\sqrt{1-f(x)}|0\rangle_3 + \sqrt{f(x)}|1\rangle_3\right)\right). \end{aligned} \tag{3.27}$$

Finally, the conjugate transpose of the unitary operator U_f is applied to the first 2 quantum registers in order to reset the second quantum register to the all-zero state. The quantum state $|\Psi\rangle$ becomes:

$$|\Psi\rangle = \sum_{x=0}^{N-1} \left(\sqrt{P(x)}|x\rangle_1|0\rangle_2^{\otimes Z}\left(\sqrt{1-f(x)}|0\rangle_3 + \sqrt{f(x)}|1\rangle_3\right)\right). \tag{3.28}$$

Equation 3.24 and Equation 3.28 may be further simplified by removing the second quantum register $|0_2^{\otimes Z}\rangle$, since it is independent of $|x\rangle$ and the operation of the block A' in Figure 3.7 becomes:

$$|x\rangle|0\rangle \xrightarrow{A'} |x\rangle\left(\sqrt{1-f(x)}|0\rangle + \sqrt{f(x)}|1\rangle\right). \tag{3.29}$$

The matrix representation of the unitary operator A' for a function f with inputs $x = \{0, 1\}$, where $n = 1$ and $N = 2^1 = 2$, while ignoring the second quantum register, would be

$$A' = \begin{bmatrix} \sqrt{1-f(0)} & -\sqrt{f(0)} & 0 & 0 \\ \sqrt{f(0)} & \sqrt{1-f(0)} & 0 & 0 \\ 0 & 0 & \sqrt{1-f(1)} & -\sqrt{f(1)} \\ 0 & 0 & \sqrt{f(1)} & \sqrt{1-f(1)} \end{bmatrix}, \tag{3.30}$$

where it is straightforward that $A'^{\dagger}A' = A'A'^{\dagger} = I^{\otimes n}$. Similarly, when the second quantum register is ignored in the algebraic analysis, the operator A shown in Figure 3.6 is described

as:

$$A = A'(R_1 \otimes R_2 \otimes \cdots \otimes R_n \otimes I^{\otimes Z} \otimes I), \tag{3.31}$$

while if we ignore the second quantum register, it becomes

$$A = A'(R_1 \otimes R_2 \otimes \cdots \otimes R_n \otimes I). \tag{3.32}$$

The operator A uses 2 CF evaluations and its output state $|\Psi\rangle$ of Equation 3.28 may be described as

$$\begin{aligned}
|\Psi\rangle &= \sum_{x=0}^{N-1} \left(\sqrt{P(x)}|x\rangle_1 \left(\sqrt{1-f(x)}|0\rangle_3 + \sqrt{f(x)}|1\rangle_3 \right) \right) \\
&= \sum_{x=0}^{N-1} \left(\sqrt{P(x)}\sqrt{1-f(x)}|x\rangle_1|0\rangle_3 + \sqrt{P(x)}\sqrt{f(x)}|x\rangle_1|1\rangle_3 \right) \\
&= \underbrace{\sum_{x=0}^{N-1} \sqrt{P(x)(1-f(x))}|x\rangle_1|0\rangle_3}_{\sqrt{1-a}|\Psi_0\rangle} + \underbrace{\sum_{x=0}^{N-1} \sqrt{P(x)f(x)}|x\rangle_1|1\rangle_3}_{\sqrt{a}|\Psi_1\rangle}.
\end{aligned} \tag{3.33}$$

where a is the probability of arriving at the states belonging to the set $|\Psi_1\rangle$ when $|\Psi\rangle$ is observed, which is equal to the desired weighted sum

$$a = \sum_{x=0}^{N-1} P(x)f(x), \tag{3.34}$$

and the states $|\Psi_0\rangle$ and $|\Psi_1\rangle$ are equal to

$$|\Psi_0\rangle = \frac{1}{\sqrt{1 - \sum_{i=0}^{N-1} P(i)f(i)}} \sum_{x=0}^{N-1} \left(\sqrt{P(x)(1-f(x))}|x\rangle \right) |0\rangle \tag{3.35}$$

$$|\Psi_1\rangle = \frac{1}{\sqrt{\sum_{i=0}^{N-1} P(i)f(i)}} \sum_{x=0}^{N-1} \left(\sqrt{P(x)f(x)}|x\rangle \right) |1\rangle, \tag{3.36}$$

respectively. The probability of obtaining a quantum state $|\upsilon\rangle$ that belongs to the wanted

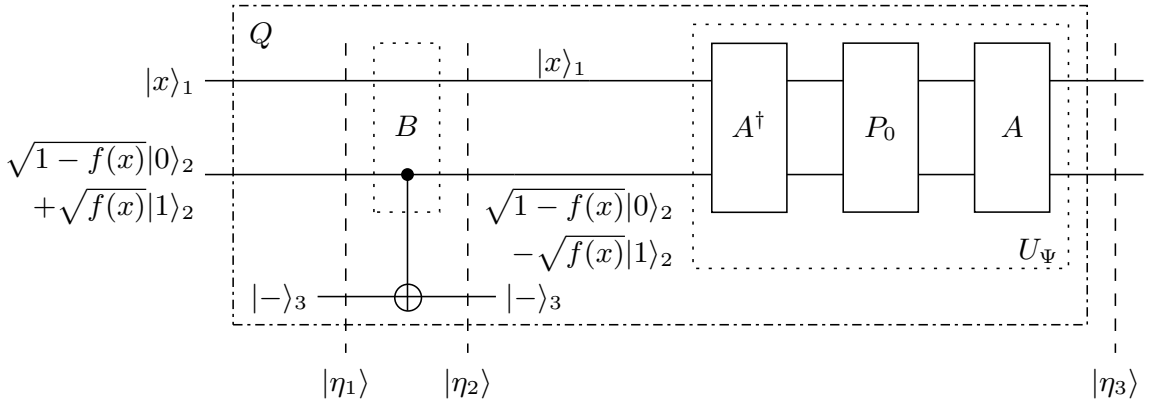

Figure 3.8: Quantum circuit of the unitary operator Q, where B consists of a CNOT gate, the quantum circuit of A is illustrated in Figure 3.6 and the controlled phase shift gate P_0 is stated in Equation 2.23.

set of states $\sqrt{a}|\Psi_1\rangle$ when $|\Psi\rangle$ is observed is equal to a as verified by

$$\begin{aligned}
P(|\upsilon\rangle \in |\Psi_1\rangle) &= a\langle\Psi_1|\Psi_1\rangle \\
&= \frac{\sum_{i=0}^{N-1} P(i)(1-f(i))}{\sum_{j=0}^{N-1} P(j)(1-f(j))} \sum_{x=0}^{N-1} \left(\sqrt{P(x)f(x)}\langle x|\langle 1|\right) \sum_{z=0}^{N-1} \left(\sqrt{P(z)f(z)}|z\rangle|1\rangle\right) \\
&= \left(\sqrt{P(0)f(0)}\langle 0|\langle 1| + \cdots + \sqrt{P(N-1)f(N-1)}\langle N-1|\langle 1|\right) \cdot \\
&\quad \cdot \left(\sqrt{P(0)f(0)}|0\rangle|1\rangle + \cdots + \sqrt{P(N-1)f(N-1)}|N-1\rangle|1\rangle\right) \\
&= P(0)f(0) + P(1)f(1) + P(2)f(2) + \cdots + P(N-1)f(N-1) \\
&= \sum_{x=0}^{N-1} P(x)f(x) = a. \qquad (3.37)
\end{aligned}$$

The states in $|\Psi_1\rangle$ are the wanted states, which differ from the unwanted states of $|\Psi_0\rangle$ only in terms of the last qubit being $|1\rangle$ and $|0\rangle$, respectively. In other words, the probability of obtaining one of the states that belong to $|\Psi_1\rangle$ when $|\Psi\rangle$ is observed, is the desired weighted sum of the function f that we want to estimate. The QMA, when all the weights are equiprobable, and the QWSA for the general case achieve this by creating the state $|\Psi\rangle$ and estimating the amplitude of $\sqrt{a}|\Psi_1\rangle$ by employing the QAE proposed in [48].

3.4.2 Quantum Amplitude Estimation

The QAE process of [48] is employed for estimating the amplitude $\sqrt{a}$ of $|\Psi_1\rangle$ in Equation 3.33. The quantum circuit of the QWSA integrating A and the QAE is illustrated in Figure 3.5. The superscript of the Q operator indicates the number of Q operator activations. Every time the unitary operator Q is applied, it rotates the QFR by 2θ, where we have:

$$\theta = \arcsin\sqrt{a} \Rightarrow a = \sin^2\theta. \qquad (3.38)$$

Therefore, an estimate of θ would also provide an estimate of a. More specifically, the quantum circuit of Q is shown in Figure 3.8 and its operation is formulated as:

$$Q = AP_0A^\dagger B, \tag{3.39}$$

where B is a unitary operator that "marks" the desired states by changing their sign and P_0 changes a state's sign if and only if that state is not the all-zero state as encapsulated in Equation 2.23, where the Grover operator was presented. Operator B may be implemented with the aid of a $CNOT$ gate as in Equation 1.17 controlled by the particular qubit that determines if a state is a wanted one or not, and by an auxiliary target qubit in the $|-\rangle = \frac{1}{\sqrt{2}}(|0\rangle - |1\rangle)$ state. The unitary operator Q may be considered as a generalized Grover operator, since it is constructed in a similar way as the generalized Grover operators in [89, 93], by replacing the Hadamard operators H with the unitary operators A, as well as the Oracle O by B and leaving the controlled phase shift operator P_0 unaltered. Geometrically, when B is applied to $|\Psi\rangle$, the input state $|\Psi\rangle$ is reflected with respect to the unwanted states $|\Psi_0\rangle$ and $U_\Psi = AP_0A^\dagger$ reflects the resultant state $B|\Psi\rangle$ with respect to the input state $|\Psi\rangle$, resulting in an anti-clockwise rotation by 2θ, as presented in Figure 3.9.

In the following subsections, we will verify that the unitary operator Q rotates the QFR by 2θ and that a in Equation 3.34 is eventually estimated, by following the evolution of our quantum system when the quantum circuit of Q and eventually that of the QWSA is applied to it.

3.4.2.1 Reflection with respect to the unwanted states

Let us follow the evolution of our quantum system as it passes through the unitary gates of the operator Q in Figure 3.8 in the context of the QWSA in Figure 3.5. Initially, following the lower part of Figure 3.5, the quantum state $|\Psi\rangle$ of Equation 3.33 is the input of the unitary operator Q the quantum circuit of which is depicted in Figure 3.8. Before the application of the gate B in Figure 3.8, the quantum state of the system is

$$\begin{aligned}
|\eta_1\rangle &= |\Psi\rangle_{12}|-\rangle_3 \\
&= \sum_{x=0}^{N-1} \left(\sqrt{P(x)(1-f(x))}|x\rangle_1\right)|0\rangle_2|-\rangle_3 + \sum_{x=0}^{N-1} \left(\sqrt{P(x)f(x)}|x\rangle_1\right)|1\rangle_2|-\rangle_3 \\
&= \sum_{x=0}^{N-1} \left(\sqrt{P(x)(1-f(x))}|x\rangle_1\right)|0\rangle_2 \frac{1}{\sqrt{2}}\left(|0\rangle_3 - |1\rangle_3\right) \\
&\quad + \sum_{x=0}^{N-1} \left(\sqrt{P(x)f(x)}|x\rangle_1\right)|1\rangle_2 \frac{1}{\sqrt{2}}\left(|0\rangle_3 - |1\rangle_3\right).
\end{aligned} \tag{3.40}$$

The distinction between the wanted and unwanted states may be done with the use of the unitary operator $B = I \otimes CNOT_{23}$ operating on the last two qubits of the quantum state $|\eta_0\rangle$, which constitute the second and third quantum register, respectively. The unitary operator $CNOT_{ij}$ is a $CNOT$ gate where the ith quantum register is the control

register and the jth quantum register is the target register. The resultant state $|\eta_2\rangle$ after the application of $CNOT_{23}$ on $|\eta_1\rangle$ may be described by:

$$
\begin{aligned}
|\eta_2\rangle &= (I \otimes CNOT_{23})|\eta_1\rangle \\
&= \sum_{x=0}^{N-1} \left(\sqrt{P(x)(1-f(x))}|x\rangle_1\right) CNOT_{23}|0\rangle_2 \frac{1}{\sqrt{2}}(|0\rangle_3 - |1\rangle_3) \\
&\quad + \sum_{x=0}^{N-1} \left(\sqrt{P(x)f(x)}|x\rangle_1\right) CNOT_{23}|1\rangle_2 \frac{1}{\sqrt{2}}(|0\rangle_3 - |1\rangle_3) \\
&= \sum_{x=0}^{N-1} \left(\sqrt{P(x)(1-f(x))}|x\rangle_1\right) |0\rangle_2 \frac{1}{\sqrt{2}}(|0\rangle_3 - |1\rangle_3) \\
&\quad + \sum_{x=0}^{N-1} \left(\sqrt{P(x)f(x)}|x\rangle_1\right) |1\rangle_2 \frac{1}{\sqrt{2}}(|1\rangle_3 - |0\rangle_3) \\
&= \sum_{x=0}^{N-1} \left(\sqrt{P(x)(1-f(x))}|x\rangle_1\right) |0\rangle_2|-\rangle_3 + \sum_{x=0}^{N-1} \left(\sqrt{P(x)f(x)}|x\rangle_1\right) |1\rangle_2(-|-\rangle_3) \\
&= \sum_{x=0}^{N-1} \left(\sqrt{P(x)(1-f(x))}|x\rangle_1\right) |0\rangle_2|-\rangle_3 - \sum_{x=0}^{N-1} \left(\sqrt{P(x)f(x)}|x\rangle_1\right) |1\rangle_2|-\rangle_3
\end{aligned} \tag{3.41}
$$

We may conclude that the $CNOT$ gate combined with the use of an auxiliary qubit in the $|-\rangle$ state changes only the sign of the wanted states' amplitudes, or, equivalently, marks the wanted states. The $B = I \otimes CNOT_{23}$ gate may be compared to the Oracle in Grover's QSA. Since the auxiliary qubit $|-\rangle_3$ remains unaltered and is not entangled with the rest of the qubits, it may be ignored for the rest of the analysis. In practice, the $CNOT$ gate and the auxiliary qubit will be employed, but for simplicity and clarity in the calculations after ignoring the third quantum register, we will use an equivalent unitary operator that acts only on the first 2 quantum registers. For example, in a system with $n = 2$ and $x \in \{0,1\}^{\otimes 2} = \{0,1,2,3\}$, the matrix representation of B is

$$
B = \begin{bmatrix}
1 & 0 & 0 & 0 & 0 & 0 & 0 & 0 \\
0 & -1 & 0 & 0 & 0 & 0 & 0 & 0 \\
0 & 0 & 1 & 0 & 0 & 0 & 0 & 0 \\
0 & 0 & 0 & -1 & 0 & 0 & 0 & 0 \\
0 & 0 & 0 & 0 & 1 & 0 & 0 & 0 \\
0 & 0 & 0 & 0 & 0 & -1 & 0 & 0 \\
0 & 0 & 0 & 0 & 0 & 0 & 1 & 0 \\
0 & 0 & 0 & 0 & 0 & 0 & 0 & -1
\end{bmatrix}, \tag{3.42}
$$

essentially flipping the signs of the amplitudes of the states of which the last qubit is $|1\rangle$. This may be seen in Figure 3.9 where the operator B reflects the input state $|\Psi\rangle$ with

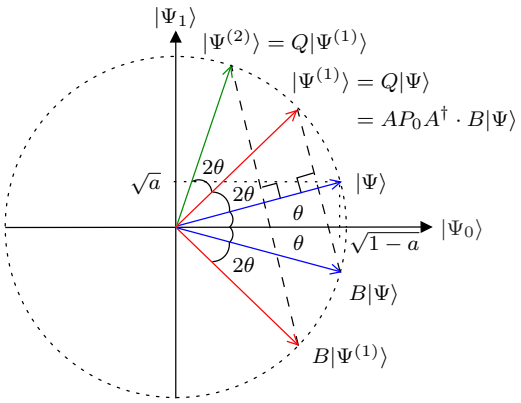

Figure 3.9: Geometrical interpretation of the operations of Q on $|\Psi\rangle$. The unitary operator B reflects the initial state $|\Psi\rangle$ with respect to $|\Psi_0\rangle$, while the unitary operator $AP_0A^\dagger$ reflects the state $B\cdot|\Psi\rangle$ with respect to $|\Psi\rangle$, resulting in the state $|\Psi^{(1)}\rangle = Q|\Psi\rangle$ and an overall counter-clockwise rotation of 2θ. The same process is repeated in subsequent applications of Q.

respect to the unwanted states included in $|\Psi_0\rangle$, changing the sign of the amplitudes of the set of wanted states $|\Psi_1\rangle$, resulting in

$$|\eta_2\rangle = B|\Psi\rangle = \sqrt{1-a}|\Psi_0\rangle - \sqrt{a}|\Psi_1\rangle. \tag{3.43}$$

3.4.2.2 Reflection with respect to the input state $|\Psi\rangle$

The quantum state $|\phi_1\rangle$ is then passed through the operator $U_\Psi = AP_0A^\dagger$, termed as the diffusion operator, which reflects it with respect to the input state $|\Psi\rangle$ as presented in Figure 3.9. The operator A is defined in Equation 3.32, while the operator P_0 which changes the sign of all but the all-zero states is the same as in Grover's QSA and is demonstrated in Equation 2.25 for $n = 2$. In the end, when the operator Q is applied on the state $|\Psi\rangle = A|0\rangle^{\otimes n+1}$, it rotates it by twice the angle the initial state $|\Psi\rangle$ had with the unwanted set of states $|\Psi_0\rangle$, as encapsulated in

$$|\eta_2\rangle = AP_0A^\dagger|\eta_1\rangle = AP_0A^\dagger B|\Psi\rangle = Q|\Psi\rangle = e^{j2\theta}|\Psi\rangle, \tag{3.44}$$

where θ is stated in Equation 3.38. The fact that the effect of Q on $|\Psi\rangle$ is a rotation, allows us to conclude that $|\Psi\rangle = \sqrt{1-a}|\Psi_0\rangle + \sqrt{a}|\Psi_1\rangle$ is a scaled version of an eigenvector of Q with eigenvalue $e^{j2\theta}$. In particular, since the sign of the unwanted states remains untouched, it is reasonable to also consider the state $-|\Psi_0\rangle + |\Psi_1\rangle$ as a scaled version of another eigenvector with eigenvalue $e^{-j2\theta}$. Since Q is unitary, its eigenvectors of

$$|\Psi_\pm\rangle = \frac{1}{\sqrt{2}}\left(\pm j|\Psi_0\rangle + |\Psi_1\rangle\right), \tag{3.45}$$

which are associated with the corresponding eigenvalues of

$$\lambda_\pm = e^{\pm j2\theta} \tag{3.46}$$

form an orthonormal basis. Every application of Q on $|\Psi\rangle$ results in a rotation, therefore an estimation of the angle θ would provide us with an estimation of the wanted amplitude a via Equation 3.38.

3.4.2.3 Phase Estimation Algorithm

Let us continue by changing the basis of the representation of $|\Psi\rangle$ to the eigenvector basis. From Equation 3.45 we may find that

$$|\Psi_0\rangle = -\frac{j}{\sqrt{2}}\left(|\Psi_+\rangle - |\Psi_-\rangle\right) \tag{3.47}$$

$$|\Psi_1\rangle = \frac{1}{\sqrt{2}}\left(|\Psi_+\rangle + |\Psi_-\rangle\right). \tag{3.48}$$

By substituting Equation 3.47 and Equation 3.48 into Equation 3.33 and exploiting the fact that from Equation 3.38 we have

$$e^{j\theta} = \sqrt{1-a} + j\sqrt{a}, \tag{3.49}$$

we are able to obtain

$$\begin{aligned} |\Psi\rangle &= -\frac{j}{\sqrt{2}}\left(\left(\sqrt{1-a}+j\sqrt{a}\right)|\Psi_+\rangle - \left(\sqrt{1-a}-j\sqrt{a}\right)|\Psi_-\rangle\right) \\ &= -\frac{j}{\sqrt{2}}\left(e^{j\theta}|\Psi_+\rangle - e^{-j\theta}|\Psi_-\rangle\right). \end{aligned} \tag{3.50}$$

Since $|\Psi_+\rangle$ and $|\Psi_-\rangle$ are eigenvectors of Q, a single application of the Q operator on $|\Psi\rangle$ would result in

$$\begin{aligned} Q|\Psi\rangle &= Q\left(-\frac{j}{\sqrt{2}}\left(e^{j\theta}|\Psi_+\rangle - e^{-j\theta}|\Psi_-\rangle\right)\right) \\ &= -\frac{j}{\sqrt{2}}\left(\lambda_+ e^{j\theta}|\Psi_+\rangle - \lambda_- e^{-j\theta}|\Psi_-\rangle\right) \\ &= -\frac{j}{\sqrt{2}}\left(e^{j2\theta}e^{j\theta}|\Psi_+\rangle - e^{-j2\theta}e^{-j\theta}|\Psi_-\rangle\right) \\ &= -\frac{j}{\sqrt{2}}\left(e^{j(2+1)\theta}|\Psi_+\rangle - e^{-j(2+1)\theta}|\Psi_-\rangle\right). \end{aligned} \tag{3.51}$$

A repeated application of the Q operator i times would yield

$$\begin{aligned} Q^i|\Psi\rangle &= -\frac{j}{\sqrt{2}}\left(e^{j(2i+1)\theta}|\Psi_+\rangle - e^{-j(2i+1)\theta}|\Psi_-\rangle\right) \\ &= \cos((2i+1)\theta)|\Psi_0\rangle + \sin((2i+1)\theta)|\Psi_1\rangle. \end{aligned} \tag{3.52}$$

The amplitudes of $|\Psi_0\rangle$ and $|\Psi_1\rangle$, with respect to the number of applications of the Q operator, are sinusoidal functions with a period of θ/π. The resemblance that the Q operator in Equation 3.39 has with the Grover operator $\mathcal{G}$ in Equation 2.38 may be seen by comparing their circuits in Figure 3.8 and Figure 2.5, respectively, as well as their

operations illustrated in Figure 3.9 and Figure 2.7, respectively. A QCR $|t\rangle$ containing l qubits will be initialized in an equiprobable superposition of states

$$|t\rangle = \frac{1}{\sqrt{2^l}} \sum_{q=0}^{2^l-1} |q\rangle, \tag{3.53}$$

and will encode the angle of θ/π into its phases by using controlled Q operators, as seen in Figure 3.5. Elaborating further, each of the QCR's qubits will apply a specific number of Q operators to the QFR, but only when its state is $|1\rangle$. The ith qubit of the QCR, where $0 \leq i \leq l-1$, controls 2^i consecutive Q operators.

For a scenario where $l = 1$, the state $|\phi_1\rangle$ shown in Figure 3.5 may be formulated after the controlled Q (CQ) operators as

$$\begin{aligned}
|\phi_1\rangle &= CQ^{2^{l-1}}|t\rangle|\Psi\rangle \\
&= CQ^{2^0}\left(\frac{|0\rangle+|1\rangle}{\sqrt{2}} \cdot \frac{-je^{j\theta}|\Psi_+\rangle + je^{-j\theta}|\Psi_-\rangle}{\sqrt{2}}\right) \\
&= -\frac{je^{j\theta}}{2}CQ|0\rangle|\Psi_+\rangle + \frac{je^{-j\theta}}{2}CQ|0\rangle|\Psi_-\rangle - \frac{je^{j\theta}}{2}CQ|1\rangle|\Psi_+\rangle + \frac{je^{j\theta}}{2}CQ|1\rangle|\Psi_-\rangle \\
&= -\frac{je^{j\theta}}{2}|0\rangle|\Psi_+\rangle + \frac{je^{-j\theta}}{2}|0\rangle|\Psi_-\rangle - \frac{je^{j\theta}}{2}|1\rangle e^{j2^0 2\theta}|\Psi_+\rangle + \frac{je^{-j\theta}}{2}|1\rangle e^{-j2^0 2\theta}|\Psi_-\rangle \\
&= -\frac{je^{j\theta}}{2}\left(|0\rangle + e^{j2^0 2\theta}|1\rangle\right)|\Psi_+\rangle + \frac{je^{-j\theta}}{2}\left(|0\rangle + e^{-j2^0 2\theta}|1\rangle\right)|\Psi_-\rangle,
\end{aligned} \tag{3.54}$$

where only one block of CQ operators were employed according to Figure 3.5 for $l = 1$. Similarly, if $l = 3$ was chosen, the quantum state $|\phi_1\rangle$ after the CQ operations would be

$$\begin{aligned}
|\phi_1\rangle = &-\frac{je^{j\theta}}{2}\left(\frac{1}{\sqrt{2}}\left(|0\rangle_1 + e^{j2^2 2\theta}|1\rangle_1\right) \otimes \frac{1}{\sqrt{2}}\left(|0\rangle_2 + e^{j2^1 2\theta}|1\rangle_2\right) \otimes \right. \\
&\left. \otimes\frac{1}{\sqrt{2}}\left(|0\rangle_3 + e^{j2^0 2\theta}|1\rangle_3\right)\right)|\Psi_+\rangle + \\
&+ \frac{j}{e^{-j\theta}}\left(\frac{1}{\sqrt{2}}\left(|0\rangle_1 + e^{-j2^2 2\theta}|1\rangle_1\right) \otimes \frac{1}{\sqrt{2}}\left(|0\rangle_2 + e^{-j2^1 2\theta}|1\rangle_2\right) \otimes \right. \\
&\left. \otimes\frac{1}{\sqrt{2}}\left(|0\rangle_3 + e^{-j2^0 2\theta}|1\rangle_3\right)\right)|\Psi_-\rangle \\
= &-\frac{je^{j\theta}}{\sqrt{2^4}}\left(|000\rangle + e^{j2^0 2\theta}|001\rangle + e^{j2^1 2\theta}|010\rangle + e^{j\left(2^1+2^0\right)2\theta}|011\rangle + e^{j2^2 2\theta}|100\rangle + \right. \\
&\left. + e^{j\left(2^2+2^0\right)2\theta}|101\rangle + e^{j\left(2^2+2^1\right)2\theta}|110\rangle + e^{j\left(2^2+2^1+2^0\right)2\theta}|111\rangle\right)|\Psi_+\rangle \\
&+ \frac{je^{-j\theta}}{\sqrt{2^4}}\left(|000\rangle + e^{-j2^0 2\theta}|001\rangle + e^{-j2^1 2\theta}|010\rangle + e^{-j\left(2^1+2^0\right)2\theta}|011\rangle + e^{-j2^2 2\theta}|100\rangle + \right. \\
&\left. + e^{-j\left(2^2+2^0\right)2\theta}|101\rangle + e^{-j\left(2^2+2^1\right)2\theta}|110\rangle + e^{-j\left(2^2+2^1+2^0\right)2\theta}|111\rangle\right)|\Psi_-\rangle \\
= &-\frac{je^{j\theta}}{4}\sum_{q=0}^{7} e^{jq2\theta}|q\rangle|\Psi_+\rangle + \frac{je^{-j\theta}}{4}\sum_{q=0}^{7} e^{jq2\theta}|q\rangle|\Psi_-\rangle.
\end{aligned} \tag{3.55}$$

In the general case of an arbitrary number of qubits l in the QCR, after ignoring the global phase $-j$ without any loss of generality [43], the quantum state $|\phi_1\rangle$ shown in Figure 3.5 may be described as

$$|\phi_1\rangle = \frac{e^{j\theta}}{\sqrt{2^{(l+1)}}} \sum_{q=0}^{2^l-1} e^{jq2\theta}|q\rangle|\Psi_+\rangle - \frac{e^{-j\theta}}{\sqrt{2^{(l+1)}}} \sum_{q=0}^{2^l-1} e^{-jq2\theta}|q\rangle|\Psi_-\rangle, \tag{3.56}$$

which may be interpreted as an encoding of θ into the phases of 2^l quantum states. By substituting Equation 3.47, Equation 3.48 and Equation 3.45 in Equation 3.56, we may express $|\phi_1\rangle$ in the computational basis as

$$\begin{aligned}|\phi_1\rangle =& \frac{e^{-j\theta}}{\sqrt{2^{l+2}(1-a)}} \sum_{q=0}^{2^l-1}\sum_{x=0}^{N-1} \left(e^{j(2q+1)\theta} + e^{-j(2q+1)\theta}\right) \sqrt{P(x)(1-f(x))}|q\rangle|x\rangle|0\rangle + \\ &+ \frac{e^{j\theta}}{\sqrt{2^{l+2}a}} \sum_{q=0}^{2^l-1}\sum_{x=0}^{N-1} \left(e^{j(2q+1)\theta} - e^{-j(2q+1)\theta}\right) \sqrt{P(x)f(x)}|q\rangle|x\rangle|1\rangle. \end{aligned} \tag{3.57}$$

The Inverse Quantum Fourier Transform (IQFT) [43] is applied to $|\phi_1\rangle$, resulting in

$$\begin{aligned}|\phi_2\rangle &= IQFT\left\{|\phi_1\rangle\right\} \\ &= IQFT\left\{\frac{e^{j\theta}}{\sqrt{2^{(l+1)}}} \sum_{q=0}^{2^l-1} e^{jq2\theta}|q\rangle|\Psi_+\rangle - \frac{e^{-j\theta}}{\sqrt{2^{(l+1)}}} \sum_{q=0}^{2^l-1} e^{-jq2\theta}|q\rangle|\Psi_-\rangle\right\} \\ &= \frac{e^{j\theta}}{\sqrt{2}}\left(\sum_{q=0}^{2^l-1} \frac{1}{2^{l/2}} e^{jq2\pi\frac{\theta}{\pi}} \frac{1}{2^{l/2}} \sum_{z=0}^{2^l-1} e^{-jq2\pi\frac{z}{2^l}}|z\rangle\right)|\Psi_+\rangle - \\ &\quad - \frac{e^{-j\theta}}{\sqrt{2}}\left(\sum_{q=0}^{2^l-1} \frac{1}{2^{l/2}} e^{-jq2\pi\frac{\theta}{\pi}} \frac{1}{2^{l/2}} \sum_{z=0}^{2^l-1} e^{-jq2\pi\frac{z}{2^l}}|z\rangle\right)|\Psi_-\rangle \\ &= \frac{e^{j\theta}}{\sqrt{2}}\left(\frac{1}{2^l}\sum_{z=0}^{2^l-1}\sum_{q=0}^{2^l-1}\left(e^{j2\pi\left(\frac{\theta}{\pi}-\frac{z}{2^l}\right)}\right)^q|z\rangle\right)|\Psi_+\rangle - \\ &\quad - \frac{e^{-j\theta}}{\sqrt{2}}\left(\frac{1}{2^l}\sum_{z=0}^{2^l-1}\sum_{q=0}^{2^l-1}\left(e^{j2\pi\left(-\frac{\theta}{\pi}-\frac{z}{2^l}\right)}\right)^q|z\rangle\right)|\Psi_-\rangle. \end{aligned} \tag{3.58}$$

An observation of the QCR, which consists of the first l qubits in Equation 3.58, will provide us with a quantum state $|z\rangle$. Let us compute the probability of observing each of these states. The amplitudes of the quantum states that $|\phi_2\rangle$ is superimposed in may be categorized in those belonging to $|\Psi_1\rangle$ and those that belong to $|\Psi_0\rangle$, depending on their last qubit of the QFR being $|1\rangle$ or $|0\rangle$, respectively. The amplitude of one of the states that the quantum system $|z\rangle|x\rangle$ is superimposed in may be derived by combining Equation 3.58, Equation 3.45, Equation 3.47 and Equation 3.48. When $|x_1\rangle$ is a wanted state, or, equivalently, it belongs to the set $|\Psi_1\rangle$, the amplitude of the quantum state $|z\rangle|x_1\rangle$

is

$$\beta_{zx_1} = \frac{1}{2^{l+1}\sqrt{a}} \left(e^{j\theta} \sum_{q=0}^{2^l-1} \left(e^{j2\pi\left(\frac{\theta}{\pi}-\frac{z}{2^l}\right)} \right)^q - e^{-j\theta} \sum_{q=0}^{2^l-1} \left(e^{j2\pi\left(-\frac{\theta}{\pi}-\frac{z}{2^l}\right)} \right)^q \right) \sqrt{P(x_1)f(x_1)} \tag{3.59}$$

$$= \frac{1}{2^{l+1}\sqrt{a}} \left(e^{j\theta} \frac{1-e^{j2\pi\left(2^l\frac{\theta}{\pi}-z\right)}}{1-e^{j2\pi\left(\frac{\theta}{\pi}-\frac{z}{2^l}\right)}} - e^{-j\theta} \frac{1-e^{j2\pi\left(-2^l\frac{\theta}{\pi}-z\right)}}{1-e^{j2\pi\left(-\frac{\theta}{\pi}-\frac{z}{2^l}\right)}} \right) \sqrt{P(x_1)f(x_1)}, \tag{3.60}$$

where the summations in Equation 3.60 were interpreted as the summations of geometric series with quotient $\exp\left[j2\pi\left(\frac{\theta}{\pi}-\frac{z}{2^l}\right)\right]$ and $\exp\left[j2\pi\left(-\frac{\theta}{\pi}-\frac{z}{2^l}\right)\right]$, respectively. Similarly, the amplitude of the state $|z\rangle|x_0\rangle$ in $|\phi_2\rangle$ with $|x_0\rangle$ being one of the states that $|\Psi_0\rangle$ is superimposed in, is equal to

$$\beta_{zx_0} = \frac{1}{2^{l+1}\sqrt{1-a}} \left(e^{j\theta} \sum_{q=0}^{2^l-1} \left(e^{j2\pi\left(\frac{\theta}{\pi}-\frac{z}{2^l}\right)} \right)^q + e^{-j\theta} \sum_{q=0}^{2^l-1} \left(e^{j2\pi\left(-\frac{\theta}{\pi}-\frac{z}{2^l}\right)} \right)^q \right) \cdot \sqrt{P(x_0)(1-f(x_0))} \tag{3.61}$$

$$= \frac{1}{2^{l+1}\sqrt{1-a}} \left(e^{j\theta} \frac{1-e^{j2\pi\left(2^l\frac{\theta}{\pi}-z\right)}}{1-e^{j2\pi\left(\frac{\theta}{\pi}-\frac{z}{2^l}\right)}} + e^{-j\theta} \frac{1-e^{j2\pi\left(-2^l\frac{\theta}{\pi}-z\right)}}{1-e^{j2\pi\left(-\frac{\theta}{\pi}-\frac{z}{2^l}\right)}} \right) \sqrt{P(x_0)(1-f(x_0))}. \tag{3.62}$$

Therefore, if we combine Equation 3.60 and Equation 3.62 we may conclude that the probability of obtaining the state $|z_{obs}\rangle$ after observing $|\phi_2\rangle$ is

$$P(|z_{obs}\rangle) = \sum_{|x_1\rangle\in|\Psi_1\rangle} |\beta_{z_{obs}x_1}|^2 + \sum_{|x_0\rangle\in|\Psi_0\rangle} |\beta_{z_{obs}x_0}|^2, \tag{3.63}$$

since the same state $|z_{obs}\rangle$ of the QCR is entangled with all the states in $|\Psi_1\rangle$ as well as with those in $|\Psi_0\rangle$. According to Equation 3.60, Equation 3.62 and Equation 3.63, a QCR's state $|z\rangle$ in $|\phi_2\rangle$ has the same probability to be observed in the QD as the state $|2^l - z\rangle$, with the maximum probability belonging to the states that minimize $z \pm 2^l\theta/\pi$. Once the QCR is observed and $|z_{obs}\rangle$ is obtained, θ is estimated as

$$\hat{\theta} = \pi\frac{z_{obs}}{2^l}. \tag{3.64}$$

The QD observation performed at this step of the QWSA is the Q/C conversion stage of the QMUD seen in Figure 1.5, since the quantum state of the system converts to a classical one. Finally, the weighted sum a is estimated from Equation 3.38 and the operator $A^\dagger$ returns the QFR of Figure 3.5 to the all-zero state.

3.4.3 Normalization and Computational Complexity

The operators A and $A^\dagger$ perform $\mathcal{C} = 2$ CF evaluations each. The QWSA repeatedly uses the Q operator $(2^l - 1)$ times, which in turn performs $\mathcal{C} = 4$ CF evaluations each,

resulting in a complexity of $\mathcal{C} = 4 \cdot 2^l = 2^{l+2}$ CF evaluations. It should be noted that the number of qubits employed in the QCR unambiguously determines the complexity of the algorithm, which is independent of the number of the additive terms [62], or, in other words, independent of both the number of users and of the modulation scheme employed. For example, a QWSA QMUD employing $l = 12$ qubits results in a complexity of 2^{14} CF evaluations for each user's each bit. According to our simulation results presented in the following sections, a choice of $l = 10$ qubits is sufficient in terms of balancing the performance versus complexity relationship. In the QWSA-based QMUD, the QWSA of Figure 3.5 is employed twice for each bit of every user, namely once for that bit's value being 0 and once for 1, during each MUD-decoder iteration.

The minimum non-zero detectable sum in Equation 3.34 is equal to $S_{\min} = \sin^2(\pi/2^l)$. The QWSA QMUD may deliver a zero output if the actual sum is smaller than $S_{\min}/2$. When many users are supported in the system, $f(\mathbf{x})$ in Equation 3.14 and Equation 3.18 becomes extremely small even for the $\mathbf{x}_{\max}$ that provides the maximum CF value, $f(\mathbf{x}_{\max}) < S_{\min}/2$. Hence, the QWSA will fail to estimate the summation of both the numerator and denominator of Equation 3.13 and Equation 3.17, mapping them to 0. In order to circumvent this problem, we normalize $f(x) = p(\mathbf{y}|\mathbf{x})$ with respect to the maximum value $f(\mathbf{x}_{\max})$ of the CF. This will result in the normalized $f(\mathbf{x})$ being equal to 1 at $\mathbf{x}_{\max}$ and will be lower for the remaining arguments. In order to determine the maximum value of $f(\mathbf{x})$ during each timeslot, various techniques may be employed, such as a quantum-inspired GA MUD, the classical ACO algorithm of [13], or the DHA that finds the minimum of a function [52], with the function in our case being $-f(\mathbf{x})$.

The classical ACO algorithm employs ζ ants in each of the Ξ generations and outputs the argument $\mathbf{x}_{\max}$ that maximizes the CF in the majority of the cases, while imposing a complexity of $(\zeta \times \Xi)$ CF evaluations. Each of the parameters ζ and Ξ may be chosen to be $\log_2(M^U)$, resulting in a total complexity of $\log_2^2(M^U)$ CF evaluations [13].

As analysed in Section 2.4.3, the DHA employs the BBHT QSA. The DHA is provided with a random initial argument $\mathbf{x}_{init}$ and finds $\mathbf{x}_{\max}$ with ∼100% probability after $22.5\sqrt{M^U}$ CF evaluations in the worst case [52]. In our multiple access systems we may have access to the output of the Matched Filter (MF), the Zero Forcing (ZF) detector or the Minimum Mean Square Error (MMSD) detector. Assuming our CDMA scenario where an MF equalizer is used, we may employ the deterministically-initialized DHA and choose $\mathbf{x}_{init} = \mathbf{x}_{MF}$ for avoiding this worst case scenario. Furthermore, in some of the cases we have $\mathbf{x}_{\max} = \mathbf{x}_{MF} = \mathbf{x}_{init}$, resulting in the lowest bound of $4.5\sqrt{M^U}$ CF evaluations per time slot [51] for finding $f(\mathbf{x}_{\max}) = p(\mathbf{y}|\mathbf{x}_{\max})$. The individual employment of the DHA provides a quantum-assisted optimal hard-output MUD, since it finds the argument $\mathbf{x}_{\max}$ that maximizes the CF at a complexity of $O(\sqrt{M^U})$. The Early Stopping-aided DHA may also be employed for finding $\mathbf{x}_{\max}$ with smaller computational complexity, by carefully choosing the maximum allowed number of CFEs so that we have 100% probability of success.

Hence, a QWSA QMUD relying on l qubits, M-ary modulation, U users and J MUD-

decoder iterations will have an overall complexity order of

$$\mathcal{C}_{DHA-QWSA} = 2^{l+3} \cdot J \cdot \log_2\left(M^U\right) + \begin{cases} 22.5\sqrt{M^U} & \text{upper bound} \\ 4.5\sqrt{M^U} & \text{lower bound} \end{cases} \tag{3.65}$$

CF evaluations when DHA is employed for normalization, compared to M^U for the classical MAP MUD. The factor $O\left(\sqrt{M^U}\right)$ becomes dominant in large-dimensional systems. If the ES-DHA of Section 2.4.4 is employed, the computational complexity of the normalization will be fixed and lower than $4.5\sqrt{M^U}$, but depending on the load of the system in terms of U users per code, it may still be on the order of $O\left(\sqrt{M^U}\right)$. If the ACO algorithm is used in order to find the maximum of $f(x)$, the complexity imposed will be lower, as illustrated in

$$\mathcal{C}_{ACO-QWSA} = 2^{l+3} \cdot J \cdot \log_2\left(M^U\right) + \log_2^2\left(M^U\right), \tag{3.66}$$

but the attainable performance would also be degraded, if an erroneous $\mathbf{x}_{\max}$ was chosen. If $l = 11$ is chosen and there are $J = 4$ iterations between the MUD and the decoder, the upper bound of the DHA-QWSA QMUD's complexity becomes $2^{16} \cdot U \log_2 M + 22.5\sqrt{M^U}$ CF evaluations, which is less complex than the MAP MUD for $U > 6$ users transmitting 8-PSK symbols or for $U > 10$ users employing QPSK modulation, as quantified in Figure 3.10. If

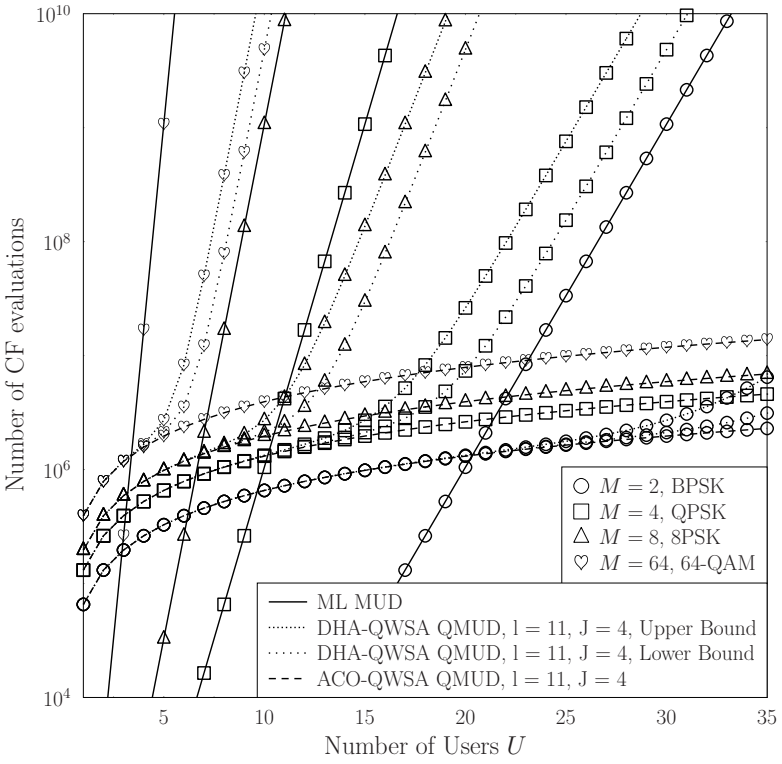

Figure 3.10: Complexity in terms of the number of CF evaluations for the proposed QWSA MUD with $l = 11$ qubits and the classic, optimal ML MUD, without MUD-decoder iterations ($J = 1$). The system schematic may be any multiple access system, where U users interfere with each other, while the rest of the system parameters do not affect the complexity of the QWSA QMUD.

the affordable complexity of our receiver processor is a maximum of $4 \cdot 10^6$ CF evaluations, a BPSK system will be able to support $U = 33$ users using the QWSA QMUD in contrast to $U = 22$ users, when the MAP MUD is employed. Similarly, in a 64-QAM system supporting $U = 5$ users, the complexity of the QWSA QMUD is 0.25% of that of the MAP MUD in the worst-case scenario. On the other hand, if the ACO-QWSA MUD is used, the complexity is always lower than that of the DHA-QWSA QMUD complexity's upper bound and also smaller than its lower bound in large-dimensional systems. In greater detail, for $U = 30$ users and QPSK symbols, the complexity of the ACO-QWSA is a fraction of 10^{-12} in comparison to that of the MAP MUD. It should be stated that the ACO-QWSA QMUD's performance is extremely dependent on the accuracy of the ACO algorithm involved for finding the maximum value of the CF. Comparing the proposed QWSA QMUD to the hard-output QMUD introduced in [57] that has a complexity of $O[2^{l+1} \log_2(M^U)]$ CF evaluations [57], for $l \geq \log_2\left(M^U\right)$ operating in a noiseless scenario [57], we may conclude that its complexity is lower, regardless of whether the DHA or ACO is used.

The simulation results of this treatise, where the QWSA is used in a QMUD, have been recorded for a DHA-QWSA QMUD, where the DHA offers ∼100% probability of success in finding the minimum of $-f(\mathbf{x})$. The reason behind our choice was to demonstrate the capabilities of the QWSA, providing it with perfect and error-free normalization of the CF, hence reaching the upper bound of the QWSA-based MUD's performance. It should be noted that the DHA-QWSA QMUD is a quantum-based MUD implementable in classical systems, whereas the ACO-QWSA QMUD is a hybrid of the classical- and the quantum-domain. After finding $f(\mathbf{x}_{\max})$ with the aid of the DHA, the CF is transformed into

$$f'(\mathbf{x}) = \frac{f(\mathbf{x})}{f(\mathbf{x}_{\max})} = \frac{p(\mathbf{y}|\mathbf{x})}{p(\mathbf{y}|\mathbf{x}_{\max})}. \tag{3.67}$$

The accuracy of the weighted sum's estimate according to [48, 62] is upper-bounded by

$$|\hat{a} - a| \leq 2\pi w \frac{\sqrt{a(1-a)}}{2^l} + w^2 \frac{\pi^2}{2^{2l}}, \quad w = 1, 2, \ldots \tag{3.68}$$

with a probability $8/\pi^2$ for $w = 1$ and at least $1 - 1/(2(w-1))$ for $w \geq 2$. The choice of the number of qubits l in the QCR depends on both the maximum tolerable probability of erroneously deciding θ and on the accuracy, expressed in terms of the number of bits that θ is represented by.

If during the calculation of the LLRs only one of the two bit's values turn out to be 0 according to the QWSA QMUD, then we assume maximum confidence and we map that bit's LLR to 20 or -20, where $\sum_{\mathbf{x}\in\chi(k,m,1)} p\left(\mathbf{y}|\mathbf{x}\right) P(\mathbf{x}) = 0$ or $\sum_{\mathbf{x}\in\chi(k,m,0)} p\left(\mathbf{y}|\mathbf{x}\right) P(\mathbf{x}) = 0$, respectively. If according to the QWSA QMUD the numerator and the denominator of a bit LLR turns out to be equal to each other, but not equal to 0 or $S_{\min}$, at low E_b/N_0, there is no significant error, since the actual LLR will also be close to 0. In this scenario, the dominant source of error may occur due to having an inadequate precision in terms of the number of qubits l.

3.4.4 Quantum Weighted Sum Algorithm QMUD in a DS-CDMA scenario

Let us proceed by applying the QWSA QMUD in a simple DS-CDMA scenario, where the DS-CDMA system was described in Section 2.2. Our system supports $U = 2$ users who employ Bit-Interleaved Coded Modulation (BICM) with the aid of Convolutional Codes (CC) with rate $R = 1/2$ and 8 trellis states. The chosen modulation is QPSK ($M = 4$) and DS-CDMA is used with a codebook $\mathbf{C}$ including Gold Codes with $SF = 31$ chips. In this example we will only focus on the QWSA QMUD, which depends on the symbols that were transmitted during a single time slot. Let us assume that during the present time slot and after the encoding procedure and the interleaver, the users modulate the bits $\mathbf{u}_1 = \left[u_1^{(1)}, u_1^{(2)}\right] = [0, 0]$ and $\mathbf{u}_2 = \left[u_2^{(1)}, u_2^{(2)}\right] = [1, 1]$. The interleaved coded bits are modulated in the QPSK symbols $x_1 = 1 + j0$ and $x_2 = -1 + j0$, where Gray mapping has been used since iterative decoding will not be employed. The energy per bit divided by the noise power spectral density is equal to $E_b/N_0 = 6$ dB and the symbols are transmitted over uncorrelated Rayleigh channels with the Channel State Information (CSI) equal to

$$\mathbf{H} = \begin{bmatrix} -0.95 + j0.88 & 0 \\ 0 & 0.55 - j0.20 \end{bmatrix}. \tag{3.69}$$

The system's parameters are summarized in Table 3.1. At the receiver side, at the output of the matched filter stage we have

$$\mathbf{y} = \mathbf{C}^H \mathbf{C}\mathbf{H}\mathbf{x} + \mathbf{C}^H \mathbf{n} = \mathbf{R}\mathbf{x} + \mathbf{C}^H \mathbf{n} \tag{3.70}$$

Table 3.1: Parameters of the QWSA MUD in the DS-CDMA scenario

Number of Users	$U = 2$
Modulation	QPSK
Modulation Mapping Type	Gray
Spreading Codes	Gold codes, $SF = 31$ chips
Channel Coding	Convolutional Code, $R = 1/2$, 8 trellis states
E_b/N_0	6 dB
CSI in the present symbol period	$h_{1,1} = -0.95 + j0.88$
	$h_{2,2} = 0.55 - j0.20$
Coded & Interleaved Bits	$\mathbf{u}_1 = \left[u_1^{(1)}, u_1^{(2)}\right] = [0, 0]$
in the present symbol period	$\mathbf{u}_2 = \left[u_2^{(1)}, u_2^{(2)}\right] = [1, 1]$
Number of qubits in the QCR	$l = 6$ qubits
Number of qubits in the QFR	$n + 1 = 4$ qubits

and we may derive that $\mathbf{R}$ is equal to

$$\mathbf{R} = \mathbf{C}^H\mathbf{C}\mathbf{H} = \begin{bmatrix} -0.95 + j0.88 & -0.018 + j0.0065 \\ 0.031 - j0.029 & 0.55 - j0.20 \end{bmatrix}, \tag{3.71}$$

and the output of the MF stage $\mathbf{y}$ is

$$\mathbf{y} = \mathbf{R}\mathbf{x} + \mathbf{C}^H\mathbf{n} = \begin{bmatrix} -0.45 + j0.37 \\ -0.27 + j0.09 \end{bmatrix}, \tag{3.72}$$

where $\mathbf{x} = [x_1, x_2]^T$ and $\mathbf{n}$ is the $SF \times 1$ noise vector. Let us focus on the first user's first bit and apply the optimal soft MAP MUD as well as the QWSA QMUD to compute its LLR. The extrinsic LLR of the first user's first bit will not include the *a priori* probabilities of that particular bit being equal to 0 or 1. We will follow the notation that $\mathbf{x} \in \{\mu([0,0,0,0]), \mu([0,0,0,1]), \mu([0,0,1,0]), \ldots, \mu([1,1,1,1])\}$ corresponds to indices $x \in \{0, 1, 2, \ldots, 15\}$, where $\mu(\cdot)$ describes the bits-to-symbol mapping procedure. Moreover, the model's likelihood $p(\mathbf{y})$ which normalizes the probabilities is replaced by $p(\mathbf{y}|x_{\max})$ in the QWSA QMUD for the same purpose. Therefore, the extrinsic LLR of the first user's first bit is

$$\begin{aligned} L_{m,e}\left(b_1^{(1)}\right) = \ln \frac{\left(p\left(\mathbf{y}|x=0\right) P\left(b_1^{(2)}=0\right) P\left(b_2^{(1)}=0\right) P\left(b_2^{(2)}=0\right) + \right.}{\left(p\left(\mathbf{y}|x=8\right) P\left(b_1^{(2)}=0\right) P\left(b_2^{(1)}=0\right) P\left(b_2^{(2)}=0\right) + \right.} \\ \frac{+p\left(\mathbf{y}|x=1\right) P\left(b_1^{(2)}=0\right) P\left(b_2^{(1)}=0\right) P\left(b_2^{(2)}=1\right) + \ldots}{+p\left(\mathbf{y}|x=9\right) P\left(b_1^{(2)}=0\right) P\left(b_2^{(1)}=0\right) P\left(b_2^{(2)}=1\right) + \ldots} \\ \frac{\cdots + p\left(\mathbf{y}|x=7\right) P\left(b_1^{(2)}=1\right) P\left(b_2^{(1)}=1\right) P\left(b_2^{(2)}=1\right)\right) / p(\mathbf{y}|x=x_{\max})}{\cdots + p\left(\mathbf{y}|x=15\right) P\left(b_1^{(2)}=1\right) P\left(b_2^{(1)}=1\right) P\left(b_2^{(2)}=1\right)\right) / p(\mathbf{y}|x=x_{\max})}, \end{aligned} \tag{3.73}$$

where $p(\mathbf{y}|x) = f(x)$ is our CF described in Equation 2.4 with $\sigma = \sqrt{N_0/2} = 0.39$ and $x_{\max}$ is the index of the symbol that maximizes the CF. Since we have no *a priori* knowledge about the bit probabilities,

$$P\left(b_1^{(1)}=0\right) = P\left(b_1^{(2)}=0\right) = P\left(b_2^{(1)}=0\right) = P\left(b_2^{(2)}=0\right) = 0.5. \tag{3.74}$$

Hence, the extrinsic LLR in Equation 3.73 becomes

$$L_{m,e}\left(b_1^{(1)}\right) = \log \frac{\frac{1}{2^3}\left(f(x=0) + f(x=1) + \cdots + f(x=7)\right) / f(x=x_{\max})}{\frac{1}{2^3}\left(f(x=8) + f(x=9) + \cdots + f(x=15)\right) / f(x=x_{\max})}. \tag{3.75}$$

Table 3.2: Cost Function evaluations

x_i	$p(\mathbf{y}\|x = x_i) = f(x_i)$	x_i	$p(\mathbf{y}\|x = x_i) = f(x_i)$
$x_0 = \mu([0000])$	0.0045	$x_8 = \mu([1000])$	$2.04 \cdot 10^{-5}$
$x_1 = \mu([0001])$	0.024	$x_9 = \mu([1001])$	$5.42 \cdot 10^{-5}$
$x_2 = \mu([0010])$	0.020	$x_{10} = \mu([1010])$	0.00013
$x_3 = \mu([0011])$	0.11	$x_{11} = \mu([1011])$	0.00033
$x_4 = \mu([0100])$	$1.35 \cdot 10^{-5}$	$x_{12} = \mu([1100])$	$6.19 \cdot 10^{-8}$
$x_5 = \mu([0101])$	$5.47 \cdot 10^{-5}$	$x_{13} = \mu([1101])$	$1.22 \cdot 10^{-8}$
$x_6 = \mu([0110])$	$2.99 \cdot 10^{-5}$	$x_{14} = \mu([1110])$	$1.84 \cdot 10^{-7}$
$x_7 = \mu([0111])$	0.00012	$x_{15} = \mu([1111])$	$3.63 \cdot 10^{-7}$

Table 3.3: Log Likelihood Ratios

User k	Bit m	$P\left(b_k^{(m)} = 0\|y_k\right)$	$P\left(b_k^{(m)} = 1\|y_k\right)$	$L\left(b_k^{(m)}\right)$
0	0	0.02	$2.75 \cdot 10^{-5}$	5.71
0	1	$0.01\bar{9}$	$6.66 \cdot 10^{-5}$	6.59
1	0	0.0036	0.016	-1.69
1	1	0.0031	0.017	-1.51

3.4.4.1 Soft-Input Soft-Output Maximum *A posteriori* Probability MUD

The SISO MAP MUD will calculate the $M^U = 16$ CFEs for every possible x and substitute them in the numerator and denominator of Equation 3.75, ignoring the normalization factor $f(x = x_{\max})$. Even though the 16 CFEs of the SISO MAP MUD in our scenario will be proved that are fewer than the corresponding CFEs performed by the QWSA QMUD, this is not the case in larger systems as it may be seen in Figure 3.10. The CFEs as well as the LLRs computed for all the bits of every user by following the classical optimal method in our scenario may be found in Tables 3.2 and 3.3, respectively. It should be noted that the normalization factor $f(x = x_{\max}) = 0.11$ corresponds to $x_{\max} = 3$ even though it was not used by the classical SISO MAP MUD, therefore it was not included in the calculations of the probabilities in Table 3.2 and 3.3.

3.4.4.2 Dürr-Høyer Algorithm-based MUD / Normalization Factor

Let us proceed by applying the QWSA QMUD for estimating the numerator and denominator of the first user's first bit in Equation 3.75. Firstly, the DHA will be employed for finding $x_{\max}$ by finding the index that minimizes $-f(x)$. The MF output in Equation 3.72 would make the decision that the transmitted symbol was $\mathbf{x}_{MF} = \mu([0011])$ which corre-

sponds to the index $x_{MF} = 3$. From Table 3.2 we may conclude that $x_{MF} = x_{\max}$, but in practice there is no way to have this knowledge unless all the CFEs have been obtained. The employment of the DHA with initial input $x_{MF} = 3$ would output $x_{\max} = 3$ after the minimum number of CFEs, equal to $L_{DHA}^{\min} = L_{DHA}^{QD,\,\min} + L_{DHA}^{CD} = 4.5\sqrt{M^U} + 10 = 28$, according to Algorithm 2, where $L_{DHA}^{CD} = L_{DHA}^{CD,\,\min}$ was used from Equation 2.50 even though in practice L_{DHA}^{CD} may be larger than $L_{DHA}^{CD,\,\min}$. As explained in Section 2.4.3, since the initial input is the wanted one, the DHA will perform the minimum possible number of Oracle operations which is equal to the maximum number of Grover iterations performed by the BBHT algorithm when there is no solution –an index with a smaller CFE than that of the initial input– in the search problem, plus a number of CFEs in the classical domain equal to the number of BBHT iterations.

3.4.4.3 Quantum Weighted Sum Algorithm Analysis

In our QWSA QMUD scenario, we will estimate the numerator of the first user's first bit's LLR given in Equation 3.75. Since the bit that we desire to compute the LLR for is not included in the QFR, we need $n = U \cdot \log_2(M) - 1 = 3$ qubits to represent all the CFEs that exist in the numerator. More specifically, we need $n = 3$ qubits to create all the $N = 2^n = 8$ different x that appear at the numerator of Equation 3.75. From this point onwards, the problem is transformed into estimating the weighted sum $\hat{a}$ of the CFEs that appear in the left column in Table 3.2. Since all the probabilities are equiprobable according to Equation 3.74, the QWSA may be considered as the QMA. Therefore, according to Equation 3.37, Equation 3.74, Table 3.2 and the fact that $f(x = x_{\max}) = f(x = 3) = 0.11$, we may conclude that

$$\begin{aligned} a &= \frac{1}{8}\left(\frac{f(x=0)}{f(x=3)} + \frac{f(x=1)}{f(x=3)} + \cdots + \frac{f(x=7)}{f(x=3)}\right) \\ &= \frac{1}{8}\left(0.041 + 0.22 + 0.18 + 1 + 0.00012 + 0.0005 + 0.00027 + 0.0011\right) \\ &= 0.18. \end{aligned} \tag{3.76}$$

The following steps are summarized in Algorithm 4.

1) Resources: We will employ $l = 6$ qubits in the QCR and $n + 1 = 4$ qubits in the QFT, initially in the all-zero states $|t\rangle = |0\rangle^{\otimes 6}$ and $|0000\rangle$, respectively.

2) Initialization: A Hadamard gate is applied to the QCR, evolving its state into

$$|t\rangle = H^{\otimes 6}|0\rangle^{\otimes 6} = \frac{1}{2^3}\sum_{q=0}^{2^6-1}|q\rangle. \tag{3.77}$$

At the same time, the operator $A = A'(H^{\otimes n} \otimes I)$ in Equation 3.32 is used on the QFR. In our scenario where the CF is $f'(x) = f(x)/f(x_{\max})$ as described in Equation 3.67, the

matrix representation of the operator A' described in Equation 3.24 and Equation 3.30 is

$$A' = \begin{bmatrix} \sqrt{1-f'(0)} & -\sqrt{f'(0)} & \cdots & 0 & 0 \\ \sqrt{f'(0)} & \sqrt{1-f'(0)} & \cdots & 0 & 0 \\ \vdots & \vdots & \ddots & \vdots & \vdots \\ 0 & 0 & \cdots & \sqrt{1-f'(N-1)} & -\sqrt{f'(N-1)} \\ 0 & 0 & \cdots & \sqrt{f'(N-1)} & \sqrt{1-f'(N-1)} \end{bmatrix}$$

$$= \begin{bmatrix} 0.98 & -0.20 & 0 & 0 & \cdots & 0 & 0 \\ 0.20 & 0.98 & 0 & 0 & \cdots & 0 & 0 \\ 0 & 0 & 0.88 & -0.47 & \cdots & 0 & 0 \\ 0 & 0 & 0.47 & 0.88 & \cdots & 0 & 0 \\ \vdots & \vdots & \vdots & \vdots & \ddots & \vdots & \vdots \\ 0 & 0 & 0 & 0 & \cdots & 0.99 & -0.033 \\ 0 & 0 & 0 & 0 & \cdots & 0.033 & 0.99 \end{bmatrix}, \tag{3.78}$$

while the rotation gate R_i, for $i = 1, 2 \ldots, n$ in Figure 3.6 will be equal to

$$R_i = \begin{bmatrix} 1/\sqrt{2} & -1/\sqrt{2} \\ 1/\sqrt{2} & 1/\sqrt{2} \end{bmatrix} \quad \forall\, i = 1, 2 \ldots, n, \tag{3.79}$$

since all the bits are considered equiprobable during the first outer iteration between the demapper and the decoder. The state of the QFT after the application of the operator A becomes $|\Psi\rangle = A|0\rangle^{\otimes(n+1)}$ as in Equation 3.33. Following the notation in Figure 3.6 and ignoring the auxiliary second quantum register, in our scenario we have

$$\begin{aligned} |\Psi\rangle &= \sum_{x=0}^{7} \left(\sqrt{P(x)(1-f'(x))}|x\rangle_1 \right) |0\rangle_3 + \sum_{x=0}^{7} \left(\sqrt{P(x)f'(x)}|x\rangle_1 \right) |1\rangle_3 \\ &= \frac{1}{2\sqrt{2}} \sum_{x=0}^{7} \left(\sqrt{1-f'(x)}|x\rangle_1 \right) |0\rangle_3 + \frac{1}{2\sqrt{2}} \sum_{x=0}^{7} \left(\sqrt{f'(x)}|x\rangle_1 \right) |1\rangle_3 \\ &= 0.35|000\rangle_1|0\rangle_3 + 0.072|000\rangle_1|1\rangle_3 + 0.31|001\rangle_1|0\rangle_3 + 0.17|001\rangle_1|1\rangle_3 + \\ &\quad + 0.32|010\rangle_1|0\rangle_3 + 0.15|010\rangle_1|1\rangle_3 + 0|011\rangle_1|0\rangle_3 + 0.35|011\rangle_1|1\rangle_3 + \\ &\quad + 0.35|100\rangle_1|0\rangle_3 + 0.0038|100\rangle_1|1\rangle_3 + 0.35|101\rangle_1|0\rangle_3 + 0.0079|101\rangle_1|1\rangle_3 + \\ &\quad + 0.35|110\rangle_1|0\rangle_3 + 0.0058|110\rangle_1|1\rangle_3 + 0.35|111\rangle_1|0\rangle_3 + 0.012|111\rangle_1|1\rangle_3 \end{aligned}$$

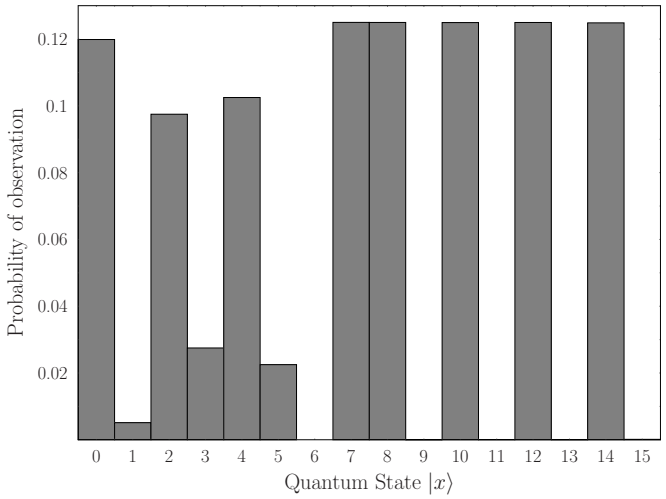

Figure 3.11: The probability of observing each of the states that $|\Psi\rangle$ is superimposed in. The odd states belong to $|\Psi_1\rangle$ while the even states belong to $|\Psi_0\rangle$ and $|\Psi\rangle = \sqrt{1-a}|\Psi_0\rangle + \sqrt{a}|\Psi_1\rangle$ for the DS-CDMA system of Figure 2.1, using the parameters summarized in Table 3.1.

$$= \Big[\; 0.35 \quad 0.072 \quad 0.31 \quad 0.17 \quad 0.32 \quad 0.15 \quad 0 \quad 0.35 \quad 0.35 \quad 0.0038 \quad 0.35 \quad 0.0079 \quad 0.35 \quad 0.0058 \quad 0.35 \quad 0.012 \; \Big]^T . \tag{3.80}$$

The probability of observing each of the computational basis's states that $|\Psi\rangle$ is superimposed in is

$$P(|\Psi\rangle) = \Big[\; 0.12 \quad 0.005 \quad 0.098 \quad 0.028 \quad 0.10 \quad 0.023 \quad 0 \quad 0.125 \quad 0.125 \quad 1.5 \cdot 10^{-5} \quad 0.125 \quad 6.25 \cdot 10^{-5} \quad 0.125 \quad 3.38 \cdot 10^{-5} \quad 0.125 \quad 0.00014 \; \Big]^T \tag{3.81}$$

and it is presented in Figure 3.11. The even states, or, equivalently, the states that have the last qubit equal to $|0\rangle$ form the set $|\Psi_0\rangle$ stated in Equation 3.35, while the odd states constitute $|\Psi_1\rangle$ as in Equation 3.36. In more detail, we have

$$|\Psi_0\rangle = \Big[\; 0.60 \quad 0 \quad 0.54 \quad 0 \quad 0.56 \quad 0 \quad 0 \quad 0 \quad 0.61 \quad 0 \quad 0.61 \quad 0 \quad 0.61 \quad 0 \quad 0.61 \; \Big]^T$$
$$|\Psi_1\rangle = \Big[\; 0 \quad 0.17 \quad 0 \quad 0.39 \quad 0 \quad 0.35 \quad 0 \quad 0.83 \quad 0 \quad 0.0091 \quad 0 \quad 0.019 \quad 0 \quad 0.014 \quad 0 \quad 0.028 \; \Big]^T . \tag{3.82}$$

The probability of observing a state that belongs to $|\Psi_1\rangle$ is equal to the sum of probabilities

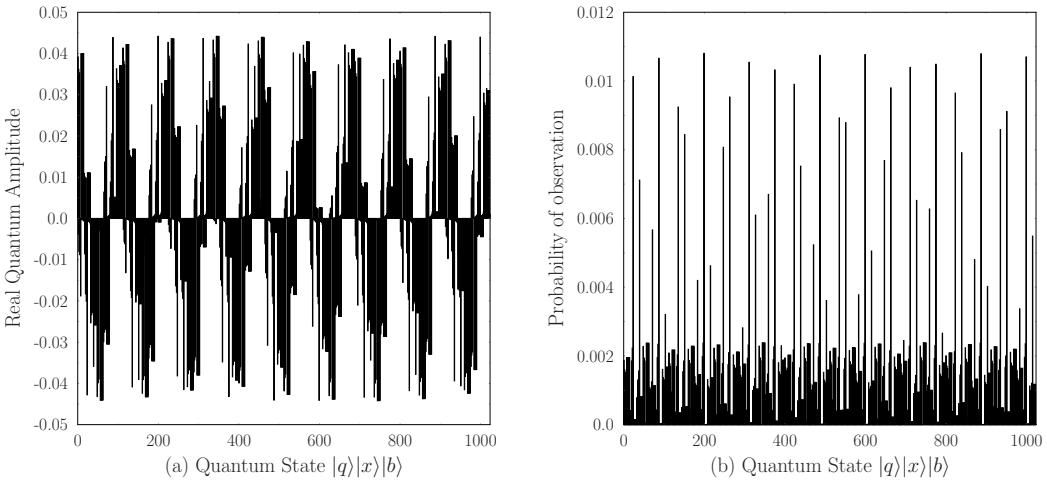

Figure 3.12: (a) The real part of the quantum amplitudes of the computational basis's states $|\phi_1\rangle$ is superimposed in. (b) The probability of obtaining each of the states when observing the quantum system. The QWSA is employed in the DS-CDMA system of Figure 2.1, using the parameters summarized in Table 3.1.

of all the odd states, as encapsulated in

$$\begin{aligned} P(|z_{obs}\rangle \in |\Psi_1\rangle) &= P\left(|z_{obs}\rangle = |0001\rangle\right) + P\left(|z_{obs}\rangle = |0011\rangle\right) + P\left(|z_{obs}\rangle = |0101\rangle\right) + \\ &\quad + P\left(|z_{obs}\rangle = |0111\rangle\right) + P\left(|z_{obs}\rangle = |1001\rangle\right) + P\left(|z_{obs}\rangle = |1011\rangle\right) + \\ &\quad + P\left(|z_{obs}\rangle = |1101\rangle\right) + P\left(|z_{obs}\rangle = |1111\rangle\right) \\ &= 0.005 + 0.028 + 0.023 + 0.125 + 1.5 \cdot 10^{-5} + \\ &\quad + 6.25 \cdot 10^{-5} + 3.38 \cdot 10^{-5} + 0.00014 \\ &= 0.18. \end{aligned} \tag{3.83}$$

As it was expected, the probability of obtaining a state that belongs to $|\Psi_1\rangle$ when the QFT is observed is equal to the desired weighted sum a of the CF. The problem now transforms into estimating the amplitude of the set of state in $|\Psi_1\rangle$ and therefore the numerator of Equation 3.75.

3) Controlled Q Operators: The QCR controls the Q operators that are applied to the QFR. The eigenvalues of Q that are not equal to 1 or -1 are $\lambda_\pm = 0.64 \pm j0.77$. From Equation 3.46 we have that $\lambda_\pm = e^{\pm j2\theta}$, hence we may derive that $\theta = -\frac{j}{2}\log(\lambda_+) = 0.44$. Obviously, this is unknown to the system and we may not exploit it but only for terms of comparison with the estimated value. The quantum system's state after the application of the controlled Q operators may be derived by Equation 3.56 and is

$$\begin{aligned} |\phi_1\rangle &= \frac{e^{j\theta}}{\sqrt{2^{(l+1)}}} \sum_{q=0}^{2^l-1} e^{jq2\theta}|q\rangle|\Psi_+\rangle - \frac{e^{-j\theta}}{\sqrt{2^{(l+1)}}} \sum_{q=0}^{2^l-1} e^{-jq2\theta}|q\rangle|\Psi_-\rangle \\ &= (0.08 + j0.038) \sum_{q=0}^{63} e^{jq0.88}|q\rangle|\Psi_+\rangle - (0.08 - j0.038) \sum_{q=0}^{63} e^{-jq0.88}|q\rangle|\Psi_-\rangle. \end{aligned} \tag{3.84}$$

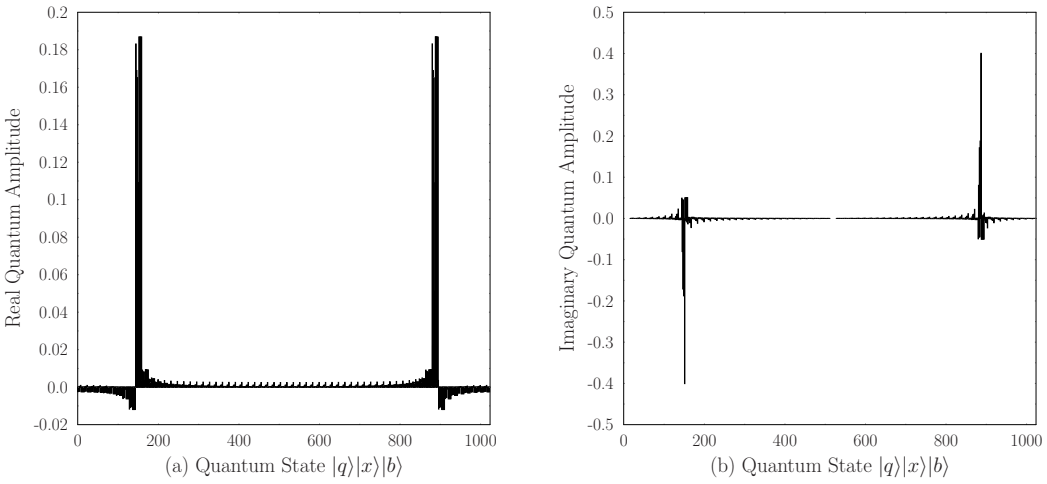

Figure 3.13: The (a) real and (b) imaginary part of the quantum amplitudes of the computational basis's states that $|\phi_2\rangle$ is superimposed in. The QWSA is employed in the DS-CDMA system of Figure 2.1, using the parameters summarized in Table 3.1.

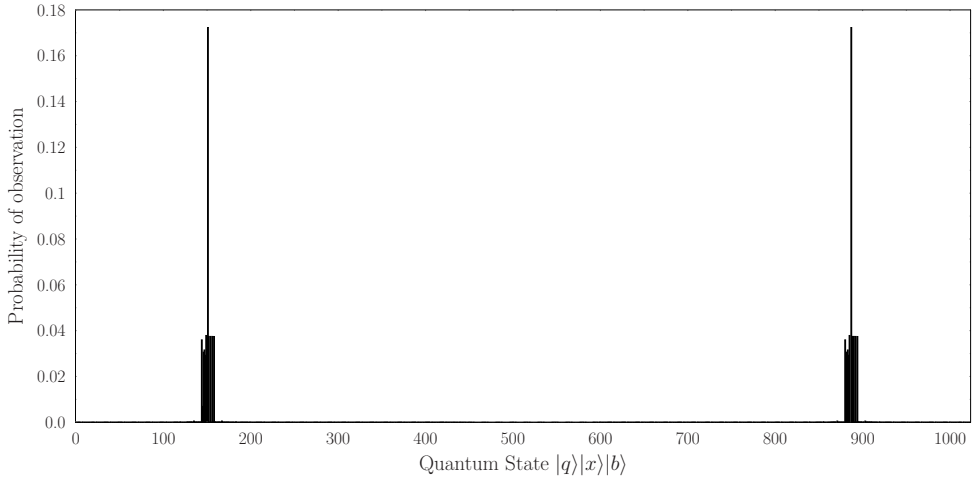

Figure 3.14: Probability of obtaining each of the computational basis's states when observing the quantum state $|\phi_2\rangle$. The QWSA is employed in the DS-CDMA system of Figure 2.1, using the parameters summarized in Table 3.1.

In the computational basis, $|\phi_1\rangle$ may be expressed as in Equation 3.57, resulting in

$$|\phi_1\rangle = (0.022 - j0.010) \sum_{q=0}^{63} \sum_{x=0}^{7} \left(e^{j(2q+1)0.44} + e^{-j(2q+1)0.44} \right) \sqrt{1 - f'(x)} |q\rangle|x\rangle|0\rangle + \\ + (0.047 + j0.022) \sum_{q=0}^{63} \sum_{x=0}^{7} \left(e^{j(2q+1)0.44} - e^{-j(2q+1)0.44} \right) \sqrt{f'(x)} |q\rangle|x\rangle|1\rangle, \quad (3.85)$$

as it may be seen in Figure 3.12 along with the probability of observing each of its states.

4) Inverse Quantum Fourier Transform: After the IQFT has been applied to $|\phi_1\rangle$ we expect $|\phi_2\rangle$ to be in a superposition of $2^l \times (N+1)$ states. By using Equation 3.62

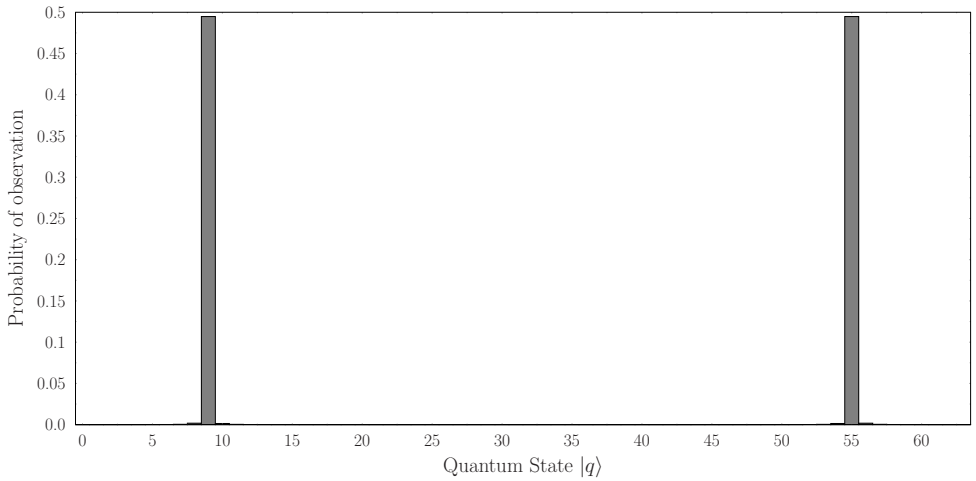

Figure 3.15: Probability of observing each of the states in the QCR after the application of the IQFT. The QWSA is employed in the DS-CDMA system of Figure 2.1, using the parameters summarized in Table 3.1.

and Equation 3.60, our scenario's quantum state at this point would be

$$|\phi_2\rangle = \sum_{z=0}^{63}\sum_{x=0}^{7}\beta_{zx_0}|z\rangle|x\rangle|0\rangle + \sum_{z=0}^{63}\sum_{x=0}^{7}\beta_{zx_1}|z\rangle|x\rangle|1\rangle. \tag{3.86}$$

Each state's quantum amplitude and probability of observation that $|\phi_2\rangle$ is superimposed in are presented in Figure 3.13 and Figure 3.14, respectively. It may be observed from Figure 3.14 that some of the states in $|\phi_2\rangle$ have a much larger probability to be observed, a fact that will be exploited in order to estimate θ accurately.

5) Observation of the QCR: Observing only the QCR in our quantum system's state $|\phi_2\rangle$ translates in observing only its first $l = 6$ qubits. This observation is a partial measurement and will leave the unobserved QFR in the superposition it was before the measurement, while the QCR will be in the observed state. Since the QFR was in the state $|\Psi\rangle$ before entangling it with the QCR through the controlled Q operators, the resultant system's state would be $|z_{obs}\rangle|\Psi\rangle$ after the observation of the QCR, where $|z_{obs}\rangle \in \{|0\rangle, |1\rangle, \ldots, |63\rangle\}$.

The probability of observing the state $|z_{obs}\rangle$ in the QCR during a partial measurement is the sum of the probabilities of observing the whole system in a state that has the first l qubits equal to $|z_{obs}\rangle$. More specifically, according to Equation 3.63 the probability of observing $|z_{obs}\rangle$ in our scenario is

$$P(|z_{obs}\rangle) = \sum_{x=0}^{7}|\beta_{z_{obs}x_1}|^2 + \sum_{x=0}^{7}|\beta_{z_{obs}x_0}|^2. \tag{3.87}$$

The probability of observing each of the 64 possible states is presented in Figure 3.15. It may be noticed that the probability of observing a state $|z_{obs}\rangle$ is equal to the probability of observing the state $|2^l - z_{obs}\rangle = |64 - z_{obs}\rangle$. This is one of the attributes introduced by the IQFT and will be exploited at the estimation of θ. By performing an observation of

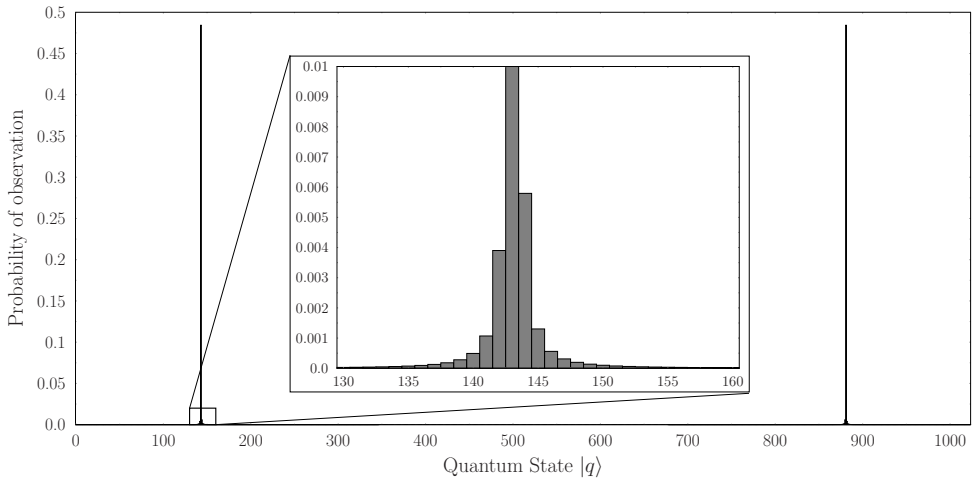

Figure 3.16: Probability of observing each of the states in the QCR after the application of the IQFT when $l = 10$ qubits exist in the QCR. The QWSA is employed in the DS-CDMA system of Figure 2.1, using the parameters summarized in Table 3.1.

the QCR we obtained

$$|z_{obs}\rangle = |9\rangle. \tag{3.88}$$

6) & 7) Estimation of θ and a: According to Equation 3.64 the observed state $|z_{obs}\rangle$ will provide an estimate of θ equal to

$$\hat{\theta}_{z_{obs}} = \pi \frac{z_{obs}}{2^l} = \pi \frac{z_{obs}}{64}, \tag{3.89}$$

while the observed state $|64 - z_{obs}\rangle$ would yield

$$\hat{\theta}_{z_{obs}} = \pi \frac{64 - z_{obs}}{64} = \pi - \theta_{z_{obs}}. \tag{3.90}$$

Hence, the symmetry of the probability of the QCR state with respect to the quantum state $|2^l - 1\rangle$ provides angles that have the same $\sin(\cdot)$ value. Since in Equation 3.38 we use the sine of θ to compute a, no further action regarding the observed state is required.

In our scenario where $|z_{obs}\rangle = |9\rangle$ we obtain

$$\hat{\theta} = \pi \frac{9}{64} = 0.44 \tag{3.91}$$

and finally the estimated value of the numerator of the LLR in Equation 3.75 is

$$\hat{a} = \sin^2 \hat{\theta} = 0.18. \tag{3.92}$$

We would have obtained exactly the same results if $|z_{obs}\rangle = |64 - 9\rangle = |55\rangle$. Even though the error between the actual value of a in Equation 3.76 and $\hat{a}$ in Equation 3.92 seems to be equal to zero, this is only due to the rounding operations. In fact, the error between the estimated and actual value is

$$|a - \hat{a}| = 0.0021, \tag{3.93}$$

and its magnitude is a result of the employment of $l = 6$ qubits in the QCR. If more qubits were used in the QCR, the precision would be better and the error would be closer to zero. Let us also emphasize the fact that the error in our scenario is the smallest possible we were able to have for $l = 6$, since we obtained one of the two most probable quantum states when we observed the QCR, which correspond to the closest estimate $\hat{a}$ to the correct value a. For example, if $|59\rangle$ was observed with probability 0.01%, the estimate of the numerator would be $\hat{a} = 0.059$ and the error equal to 0.12. If we increase the number of qubits l in the QCR the quantum states with non-negligible probability of observation will yield an estimate closer to a as described in Equation 3.68. Figure 3.16 demonstrates the probability of observing $|z_{obs}\rangle$ in our scenario when $l = 10$ qubits are used in the QCR. For the case where $l = 10$ qubits are employed, the state $|136\rangle$ has 0.01% probability to be observed and the resultant error would be 0.016, almost 10 times smaller than the respective error when $l = 6$. In the same example, if the most probable state $|143\rangle$ was obtained with 0.48 probability, the error would be $|a - \hat{a}| = 2.3 \cdot 10^{-4}$. The trade-off for this improvement in the estimation of the LLR when l becomes larger is the increased complexity of the QWSA.

3.4.5 Performance of the Quantum Weighted Sum Algorithm QMUD

Let us now proceed to the soft-input soft-output QMUD by introducing a CDMA system supporting $U = 2$ coexisting users, employing Gold codes having a spreading factor of $SF = 31$. Each of them uses BICM with Iterative Detection (ID) constructed by a non-systematic convolutional codes having a rate of $R = 2/3$ and 16 trellis states, 3 parallel bit interleavers and 8-PSK modulators. The system model may be found in Figure 2.1. The EXIT curves[1] of both the inner MUD and of the outer decoder are presented in Figure 3.17 for $E_b/N_0 = 6$ dB and 11 dB. It may be clearly observed that the EXIT curves of the QWSA QMUD match those of the MAP MUD, confirming that the two systems have the same performance. In Figure 3.17 we have also presented the EXIT curves of a system for $U = 2$ users and $M = 8$, but replacing the $R = 2/3$-rate NSCC by a Turbo Convolutional Code (TCC) having a rate of $R = 1/2$, relying on 8 trellis states and 4 iterations between the convolutional codes. It may be readily verified that the EXIT curve of the inner QWSA QMUD is identical to that of the MAP MUD.

The Monte-Carlo simulation based decoding trajectories of Figure 3.17 further justify that the proposed QWSA QMUD may be integrated into an iterative receiver. At $E_b/N_0 = 6$ dB and employing a $R = 2/3$ NSCC there is no open EXIT-tunnel leading to the $I_{DEC,e} = 1$ line, which is in contrast to the $E_b/N_0 = 11$ dB and $R = 2/3$ scenario, where we have $I_{DEC,e} \approx 1$ after $J = 2$ outer iterations between the MUD and the decoder. We may conclude that the extrinsic information at the NSCC decoder's output recorded at 6 dB and the rate $R = 2/3$ scheme will not exceed $I_{DEC,e} = 0.9$, even if an infinite number of MUD-decoder outer iterations are performed, while at 11 dB the maximum $I_{DEC,e} = 1$ is reached even with as few as $J = 2$ outer iterations. Furthermore, the system using TCC needs $J \approx 7$ outer iterations at $E_b/N_0 = 5$ dB in order to reach $I_{DEC,e} = 1$. The size of the

[1]For a tutorial on EXIT charts please refer to [10].

interleaver in the NSCC systems is 20 000 bits, while that in the TCC system is 21 000 bits. The reason why the decoding trajectories undershoot the NSCC curve for $I_{MUD,a} < 0.5$ is because the outputs of the MAP and QWSA MUDs are not perfectly modelled as a Gaussian distribution, whereas the outer EXIT curve was created assuming that the LLRs obey the Gaussian distribution.

Even though the complexity of the DHA-QWSA QMUD in this two-user scenario is higher than that of the MAP MUD, which are associated with 393 446 CF evaluations in the worst case and 64 CF evaluations per time slot, respectively, our objective was to demonstrate the match between the classical and quantum MUDs EXIT curves. The application area of our QWSA QMUD is in systems designed for numerous users and larger modem constellations, since its complexity is proportional to $O(\sqrt{M^U})$ when the DHA [52] is used and $O[2^{l+3} \log\left(M^U\right)]$ when the ACO is employed, while that of the classical MAP MUD is proportional to $O\left(M^U\right)$, as seen in Figure 3.10.

In a BICM-ID system using $R = 1/2$ TCC and supporting $U = 2$ users employing Gold codes associated with $SF = 31$ chips each, the performance of the QWSA QMUD again matches the MAP MUD's, as it may be concluded from the EXIT chart of Figure 3.18.

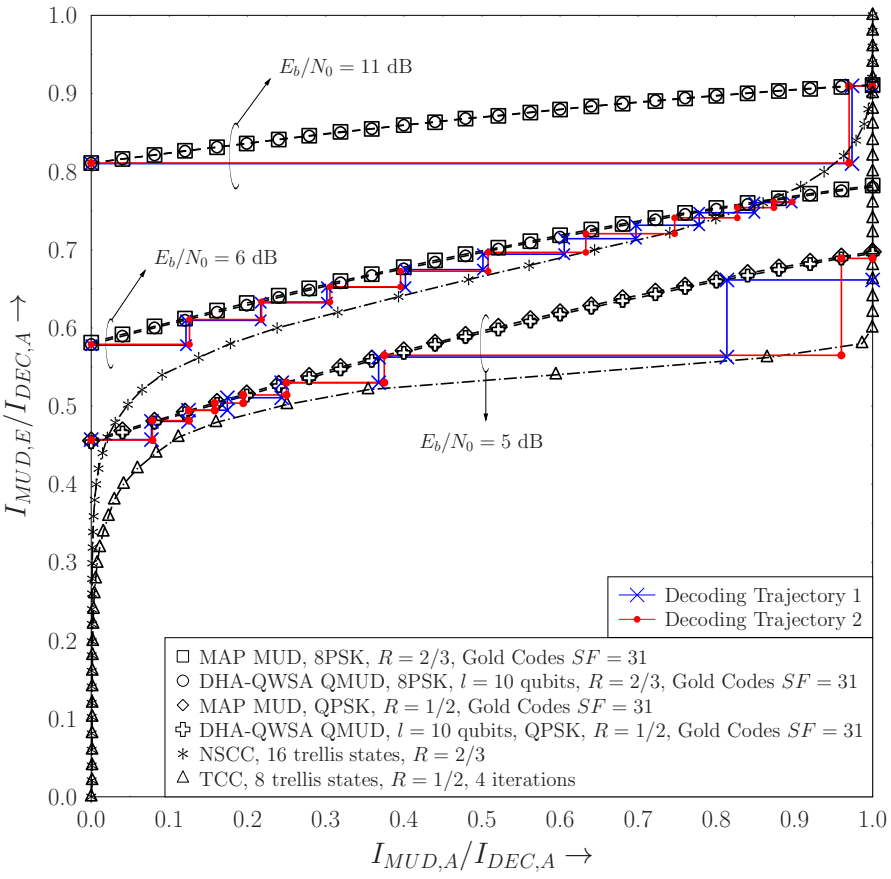

Figure 3.17: EXIT charts of a DS-CDMA system of Figure 2.1 with $U = 2$ users, $SF = 31$ chips, BICM-ID with $8PSK$ and Non-Systematic Convolutional Codes, $R = 2/3$, 16 trellis states as well as with $QPSK$ modulation and Turbo Convolutional Code, $R = 1/2$, 8 trellis states and $I_{inner} = 4$ inner iterations. DHA-QWSA-based QMUD is used with $l = 10$ qubits in the QCR of Figure 3.5.

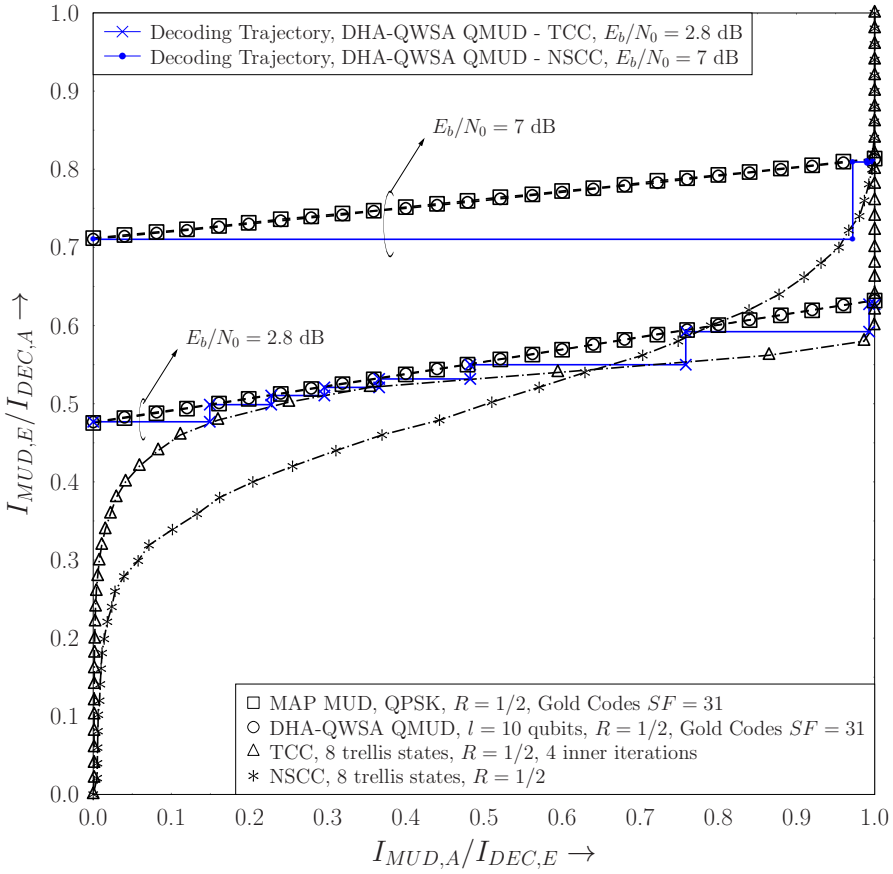

Figure 3.18: EXIT charts of two CDMA systems of Figure 2.1 with $U = 2$ users, $SF = 31$ chips, BICM-ID with $QPSK$ modulation and $R = 1/2$, Turbo Code relying on Convolutional Codes and Non-Systematic Convolutional Code, along with MAP-based and DHA-QWSA-based MUD with $l = 10$ qubits in the QCR of Figure 3.5.

Two encoders are compared, namely a TCC and an NSCC. The choice of $E_b/N_0 = 2.8$ dB for the TCC system was made with a value in mind, where the "turbo cliff" emerges, whereas in the NSCC system $I_{DEC,e}$ has exceeded 0.9 at $E_b/N_0 = 7$ dB. The similarity in the BER performance between the QWSA QMUD and the classical MAP MUD is seen in Figure 3.19. The size of the interleaver is 20 000 for each user, the number of inner iterations in the TCC is $I_{inner} = 4$, while the number of MUD-decoder outer iterations is also fixed to $J = 4$. The large size of the interleaver allows the BER floor of the TCC system to be lower than 10^{-5}. If more qubits are used in the QCR, the system's performance approaches that of the MAP MUD more closely. Furthermore, if more MUD-decoder outer iterations are performed, the overall QMUD system's BER becomes closer to that of the MAP MUD.

In order to further investigate the effect that the l QCR qubits have on the attainable performance, Figure 3.20 characterizes a BICM-ID system supporting $U = 4$ users with the aid of $SF = 7$ chips, TCC with $R = 1/2$, 8 trellis states and $I_{inner} = 4$. The DHA-QWSA QMUD is used in conjunction with l ranging from 9 to 12 qubits in the QCR and the number of MUD-decoder outer iterations considered are $J = 1$ and $J = 4$. The system characterized in Figure 3.20 has a higher complexity than that used in Figure 3.19. As the number of qubits l increases, the precision in the QWSA becomes better and $S_{\min}$

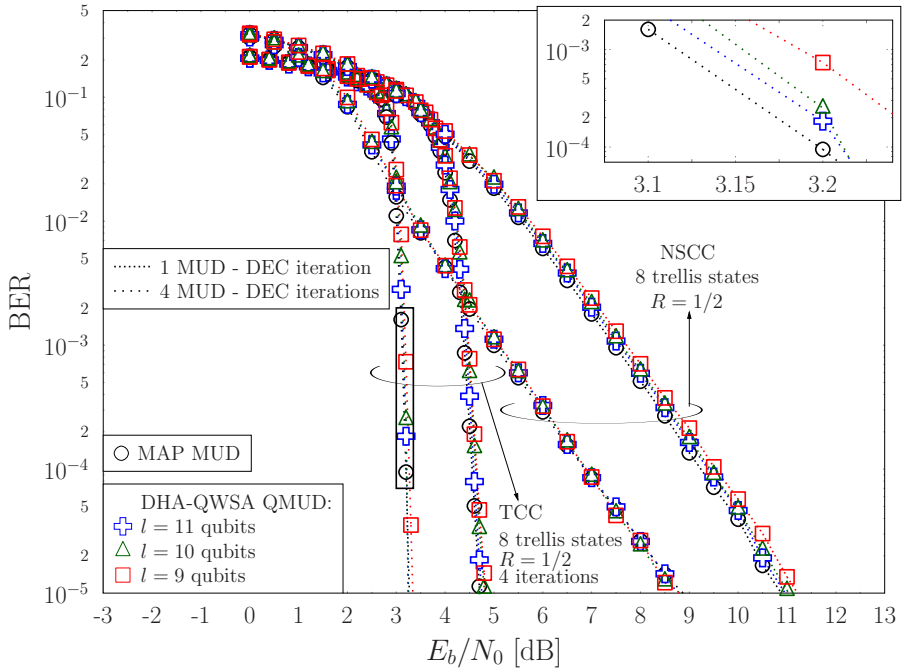

Figure 3.19: BER performance of two CDMA systems of Figure 2.1 with $U = 2$ users, $SF = 31$ chips, BICM-ID with QPSK modulation and $R = 1/2$, Turbo Code relying on Convolutional Codes and Non-Systematic Convolutional Code, along with MAP-based and QWSA-based MUD with $l = 9$, 10 and 11 qubits in the QCR of Figure 3.5. The interleaver length is equal to 20 000 bits and 4 MUD-decoder iterations have been applied.

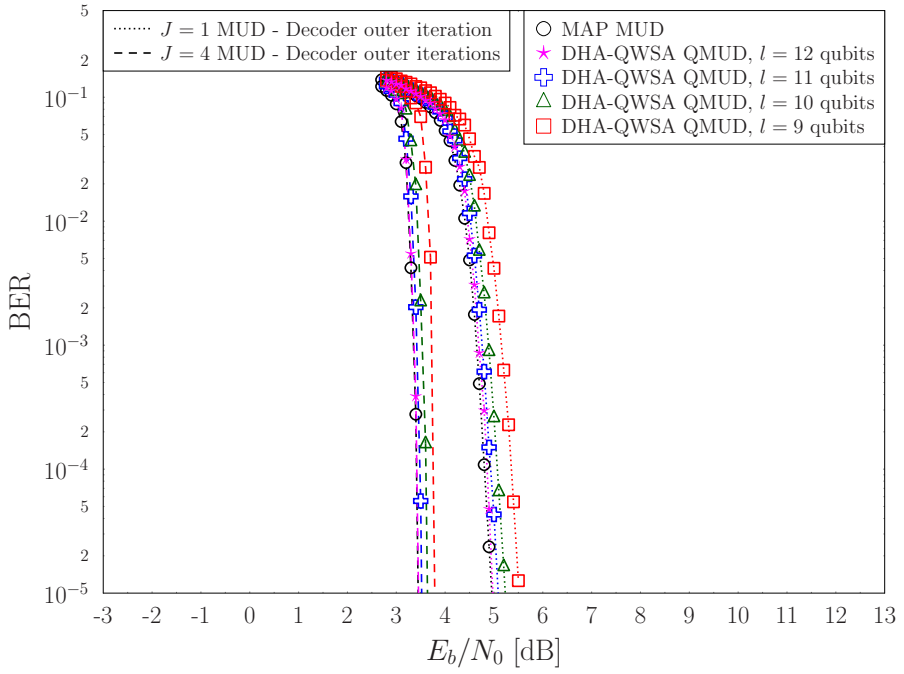

Figure 3.20: BER performance of a CDMA system of Figure 2.1 with $U = 4$ users, $SF = 7$ chips, BICM-ID employing QPSK and a Turbo Code relying on Convolutional Codes with $R = 1/2$, 8 trellis states and $I_{inner} = 5$ iterations, along with MAP-based and QWSA-based MUD for various number of qubits l in the QCR of Fig 3.5. The interleaver length is equal to 20 000 bits and the number of MUD-decoder outer iterations is $J = 1$ and $J = 4$.

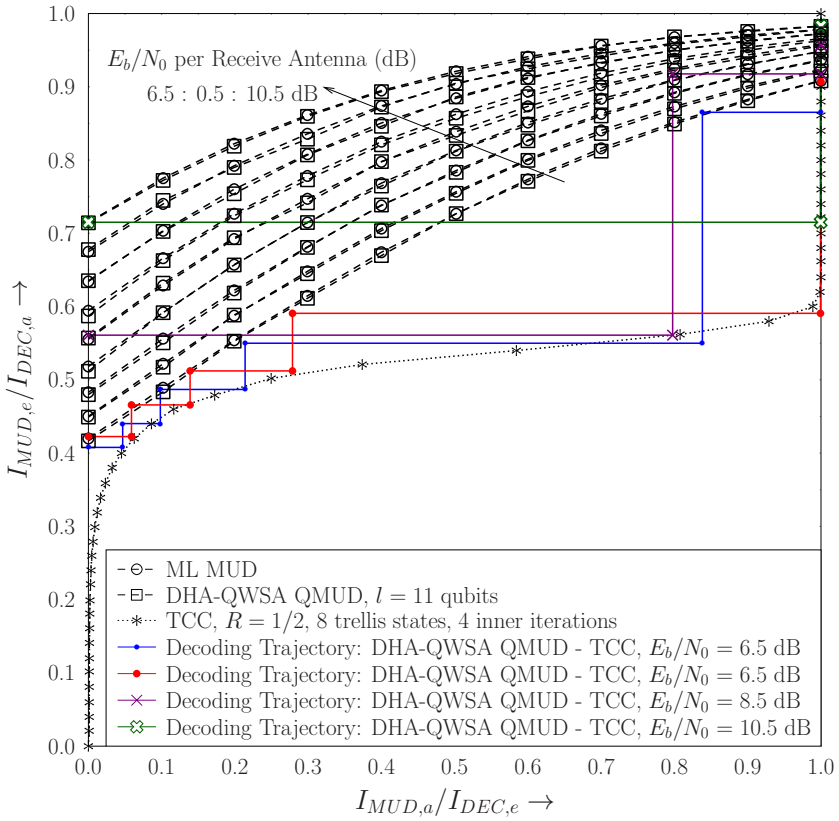

Figure 3.21: EXIT chart of an SDMA system supporting $U = 3$ users transmitting QPSK symbols with $N_{T_x} = 2$ transmit antennas each and $P = 3$ receive antennas, TCC with $R = 1/2$, 8 trellis states and $I_{inner} = 4$ inner iterations. DHA-QWSA QMUD is used with $l = 11$ qubits in the QCR of Figure 3.5.

becomes smaller. Hence, the performance is improved and it approaches that of the MAP MUD, as it is clearly seen in Figure 3.20. In more detail, for $J = 1$ the E_b/N_0 loss that is experienced when we have $l = 12$, $l = 11$, $l = 10$ and $l = 9$ compared to the optimal MAP MUD is approximately 0.05 dB, 0.1 dB, 0.2 dB and 0.5 dB, respectively. In all cases, the DHA-QWSA MUD performance has more closely approached that of the MAP MUD for $J = 4$, because the classical decoder assists in mitigating both the probabilistic nature of quantum computation and the errors due to the limited precision of the QWSA. If $l > 12$ qubits were to be used, the performance would be expected to be even closer to that of the MAP MUD. Once again, the trade-off between the performance attained and the complexity imposed becomes explicit.

Let us now proceed by applying the DHA-QWSA QMUD in an SDMA uplink scenario supporting $U = 3$ users, each having $N_{T_x} = 2$ TAs and transmitting QPSK ($M = 4$) symbols, while the BS has as few as $P = 3$ RAs. Hence the system is rank-deficient, since we have $(U \cdot N_{T_x})/P = 2 > 1$ and therefore conventional MUDs such as the MMSE MUD exhibit a high error-floor. A TCC associated with $R = 1/2$, having 8 trellis states and $I_{inner} = 4$ inner iterations is employed. The EXIT chart of our system employing $l = 11$ qubits in the QCR of the QWSA is depicted in Figure 3.21 for various values of E_b/N_0 per RA. It should be noted that the EXIT curves of the inner DHA-QWSA QMUD are identical to those of the ML MUD for all the E_b/N_0 per RA values. Furthermore,

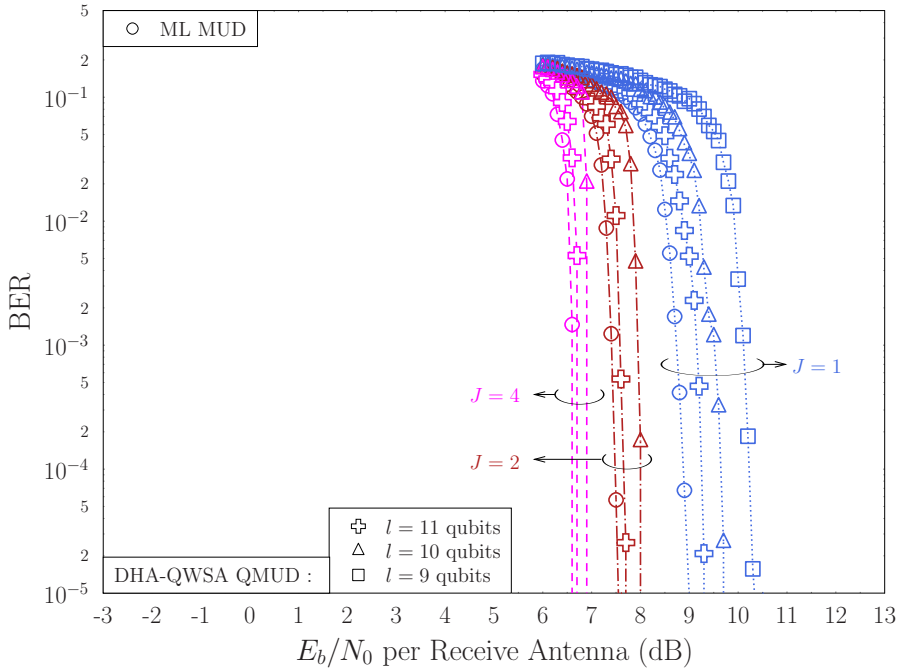

Figure 3.22: BER performance of an SDMA system supporting $U = 3$ users using QPSK with $N_{T_x} = 2$ transmit antennas each and $P = 3$ receive antennas, TCC with $R = 1/2$, 8 trellis states and $I = 4$ inner iterations for $J = 1, 2, 4$ MUD-Decoder iterations and $l = 9, 10, 11$ qubits in the QCR of Figure 3.5. The bit-based interleavers have a length of 10 000 bits each.

the stair-case-shaped Monte-Carlo simulation-based decoding trajectories verify that the DHA-QWSA QMUD may indeed be readily integrated with iterative receivers.

The BER performance of our SDMA uplink is shown in Figure 3.22. The number J of MUD-decoder iterations was varied for $J = 1, 2, 4$ and so was the number of qubits in the QCR for $l = 9, 10, 11$ for the sake of investigating their effect on the attained BER. Upon increasing the number of qubits l in the QCR, the BER performance of the DHA-QWSA QMUD approaches that of the classic ML MUD, since the accuracy of the QWSA in Equation 3.68 becomes better. At the same time, the complexity of the QWSA is increased. Moreover, if we increase J while considering l to be fixed, the E_b/N_0 power-loss of the DHA-QWSA QMUD with respect to the optimal ML MUD becomes smaller, since the powerful TCC corrects more errors at the output of the QMUD, when J is increased. For $l = 11$ qubits, the BER performance of the DHA-QWSA QMUD is just 0.15 dB away from the optimal limit. If a higher value of l was used, the performance would be expected to be even closer to that of the ML MUD.

The complexity of the ML MUD in our system is $M^{U \cdot N_{T_x}} = 4096$ CFEs per multi-level symbol. The complexity of the QWSA for $l = 11$ is equal to 8192 CFEs, hence the application of the QWSA $J \cdot 2 \cdot \log_2(M^{U \cdot N_{T_x}})$ times for $J = 4$ results in a complexity of 786 432 CFEs. The average complexity of the DHA in our system was found to be $533.52 = 8.3\sqrt{M^{U \cdot N_{T_x}}}$ CFEs. Therefore, the DHA-QWSA QMUD associated with $l = 11$ and $J = 4$ needed 786 966 CFEs for each multi-level symbol. Even though the complexity of the QMUD is higher than that of the ML MUD in this small-scale system, the proposed DHA-QWSA QMUD is designed for large-scale multi-user systems, as shown in [1]. For example,

in an SDMA system supporting $U = 6$ users transmitting QPSK symbols associated with $M = 4$, $N_{T_x} = 2$ transmit antennas per user as well as $J = 2$ MUD-decoder iterations, the complexity of the ML MUD is 16 777 216 CFEs. At the same time, the DHA-QWSA QMUD needs 878 592 CFEs, when $l = 11$ qubits are used in the QCR for the worst-case scenario, where the DHA finds $x_{\max}$ after $22.5\sqrt{M^{U \cdot N_{T_x}}} = 92\,160$ CFEs.

3.5 Iterative Dürr-Høyer Algorithm-based Quantum-assisted Multi-User Detection

In a DSS/SSCH SDMA-OFDM system, the iterative MAP MUD calculates the CF values of all the legitimate $M^{U_{q,g}}$-ary symbols of the interfering users in the gth DSS code group on the qth subcarrier, based on Equation 3.14 and uses them for calculating each bit's LLR according to Equation 3.13. It was proposed in [13, 63] that even if a reduced subset of the CFEs of all the legitimate $M^{U_{q,g}}$-ary symbols is used for the calculation of each bit's LLR, the performance would be near-optimal with respect to that of the MAP MUD, provided that the subset of CF values includes the maximum possible CF values of the numerator and the denominator of each bit's LLR. Hence in [13, 63] an ACO-based search was employed for selecting the particular symbol subset used for the calculation of the LLRs. The main challenges of the ACO invoked for the selection of the symbol subsets were identified in [13, 63] as being two fold. Firstly, when the ACO converges either to a local or to the global maximum, all the ants follow the same path with ∼100% probability, hence the search is converged and concluded. Moreover, in rank-deficient systems where there are more transmit AEs than receive AEs, the ACO rarely converges to the globally optimal symbol in that particular search space, which naturally leads to an erroneously calculated LLR, since the selected subset of symbols does not include the globally maximum values.

As a beneficial design alternative, the DHA may be employed for performing iterative detection by finding the specific symbol that minimizes $-f(x)$ of Equation 3.14, or, equivalently, maximizes $f(x)$ of Equation 3.14, where x is the decimal representation, or index, of $\mathbf{x}$ in Equation 3.14. Let us denote the true globally optimal symbol as $x_{\max}$ and the best symbol found by the DHA as $\hat{x}_{\max}$, even though we are aware that $\hat{x}_{\max} = x_{\max}$ with ∼100% probability. As illustrated in Figure 3.23 for a system associated with QPSK modulation ($M = 4$) and $U_{1,1} = 3$ users relying on the first DSS code on the first subcarrier, the DHA commences its search from an initial symbol and makes its way to the symbol that maximizes $f(x)$, while evaluating numerous other symbols due to the probabilistic nature of the BBHT QSA. Observe in the scenario of Figure 3.23, that the symbols with indices of 58, 57, 21, 17 and 61 have been evaluated after the point where the symbol with index 43 has been found, before finally symbol 8 is found, which has a higher CF value than that of symbol 43. The particular symbols that were evaluated during the BBHT QSA calls but were not found to be better than the "best-so-far" symbol may also be used for the calculation of the LLRs, since they have already been evaluated. Again, the DHA has ∼100% success probability in finding the maximum of the $f(x)$ CF of Equation 3.14

Symbol / Index	0	1	2	3	4	5	6	7
Cost Function Value	$9.6 \cdot 10^{-4}$	0.0059	0.086	0.53	$2.4 \cdot 10^{-5}$	$4.9 \cdot 10^{-7}$	0.034	$7 \cdot 10^{-4}$
Symbol / Index	8	9	10	11	12	13	14	15
Cost Function Value	0.76	0.29	0.23	0.087	0.019	$2.4 \cdot 10^{-5}$	0.092	$1.2 \cdot 10^{-4}$
Symbol / Index	16	17	18	19	20	21	22	23
Cost Function Value	0.0089	0.43	0.0082	0.39	0.064	0.01	0.95	0.16
Symbol / Index	24	25	26	27	28	29	30	31
Cost Function Value	0.065	0.19	$2 \cdot 10^{-4}$	$6 \cdot 10^{-4}$	0.46	0.0047	0.024	$2.4 \cdot 10^{-4}$
Symbol / Index	32	33	34	35	36	37	38	39
Cost Function Value	$3.2 \cdot 10^{-8}$	$1.9 \cdot 10^{-5}$	$2.3 \cdot 10^{-5}$	0.013	$8.5 \cdot 10^{-8}$	$1.7 \cdot 10^{-7}$	$9.7 \cdot 10^{-4}$	0.0019
Symbol / Index	40	41	42	43	44	45	46	47
Cost Function Value	0.0074	0.27	0.018	0.65	0.02	0.0025	0.77	0.095
Symbol / Index	48	49	50	51	52	53	54	55
Cost Function Value	$3 \cdot 10^{-7}$	0.0014	$2.2 \cdot 10^{-6}$	0.01	$2.3 \cdot 10^{-4}$	0.0037	0.027	0.43
Symbol / Index	56	57	58	59	60	61	62	63
Cost Function Value	$6.3 \cdot 10^{-4}$	0.18	$1.6 \cdot 10^{-5}$	0.0045	0.49	0.48	0.2	0.19

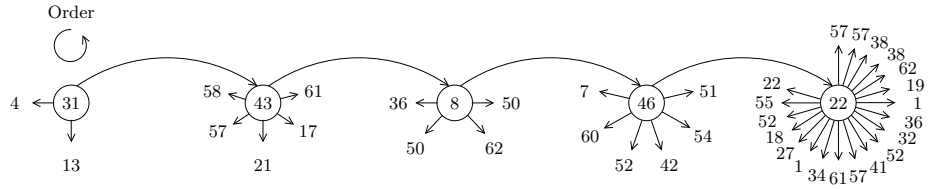

Unique Symbols Evaluated: 31, 4, 13, 43, 58, 57, 21, 17, 61, 8, 36, 50, 62, 46, 7, 60, 52, 42, 54, 51, 22, 55, 18, 27, 1, 34, 41, 32, 19, 38

Figure 3.23: Scenario of applying the DHA for finding the $M^{U_{q,g}}$-ary symbol that maximizes the CF in Equation 3.14 in a rank-deficient DSS / USSCH SDMA-OFDM system where $U_{q,g} = U_{1,1} = 3$ users coexist on the first subcarrier having been allocated the first DSS code and they transmit QPSK symbols associated with $M = 4$ to $P = 1$ receive AE. Top: The database of symbol indices and the corresponding CF values. The rectangular box indicates the optimal symbol index associated with the maximum CF value, while the ellipse encircles the MMSE detector's output which is used as the initial guess in the DHA. Bottom: The DHA process. The circles indicate the best so far found symbols. Starting from the leftmost circle and moving counter-clockwise, the BBHT QSA is invoked for finding a symbol that has a higher CF value than the symbol in that particular circle. Once a better symbol is found, the BBHT QSA is restarted for the new symbol. Once the global best symbol has been found, the BBHT QSA times out after $4.5\sqrt{M^{U_{q,g}}} = 36$ QD-CFEs. The number of QD-CFEs and CD-CFEs in the DHA in this small-scale system were 52 and 41, respectively. Therefore, the total number of CFEs was 93, which is greater than the total number of symbols. The SO-DHA QMUD is designed for large-scale systems where its complexity becomes much lower than that of the ML MUD.

even in rank deficient systems, since it is independent of both the actual CF values and of the "neighbourhood criterion"[2] of the evolutionary algorithms [21]. Furthermore, the probabilistic nature of the BBHT QSA provides the necessary candidate diversity for a potential iterative DHA QMUD.

Let us now proceed conceiving the SISO DHA QMUDs, which are less complex than those presented in [13, 63]. Moreover, let us assume that the discussions are based on performing MUD at the qth subcarrier, $q = 1, 2, \ldots, \mathcal{Q}$ of a DSS / USSCH SDMA-OFDM system, where $U_{q,g}$ users have been allocated the gth DSS code and they transmit M-ary symbols, implying that the database's size is $N_{q,g} = M^{U_{q,g}}$.

3.5.1 DHA QMUD Relying on Maximum Approximation

The DHA QMUD relying on MAximum Approximation (DHA-MAA QMUD) employs the DHA for finding the specific symbol that maximizes the CF $f(x)$ in Equation 3.14. Focusing on the mth bit of the $N_{q,g}$-ary symbol, only the pair of best symbols found for each of the mth bit's 0 and 1 logical values is included in the calculation of that bit's LLR. Since the DHA succeeds in finding the globally best symbol with ∼100% probability, that symbol's CF value will be included in all the LLR calculations, resulting in achieving the same LLR signs as the MAP MUD. The unique symbols that were evaluated during the DHA form the evaluated symbol set $\mathcal{X}$. Let us also define the sets $\mathcal{X}_{q,g}^{u,m,\nu}$, which are specific subsets of $\mathcal{X}$, namely those that include the particular symbols for which the $[(u-1)\cdot \log_2 M + m]$th bit of the corresponding binary representation is equal to v, as encapsulated in

$$x \in \mathcal{X}_{q,g}^{u,m,\mathrm{v}} \Leftrightarrow x \in \mathcal{X} \wedge x \in \chi_{q,g}(u, m, \mathrm{v}), \tag{3.94}$$

where $\wedge$ denotes logical conjunction. Therefore, in our example of Figure 3.23, the LLR of the first user's first bit using the MAA would be

$$L_{m,po}\left(b_{u=1}^{(m=1)}\right) = \ln \frac{\max\left(f(x)|x \in \mathcal{X}_{q,g}^{u,m,0}\right)}{\max\left(f(x)|x \in \mathcal{X}_{q,g}^{u,m,1}\right)} \tag{3.95}$$

$$= \ln \frac{f(22)}{f(46)}, \tag{3.96}$$

since the globally best symbol with index $22_{10} = [01|01|10]_2$ corresponds to $b_1^{(1)} = 0$ and the best symbol found with $b_1^{(1)} = 1$ is symbol 46. If the scenario is encountered, where the set $\mathcal{X}_{q,g}^{u,m,\mathrm{v}}$ is empty for a specific $[q, g, u, m, \mathrm{v}]$ value, then according to [13, 63] another search process should be initiated for finding the specific symbol that maximizes the CF having fixed the mth bit of the uth user associated with the gth DSS code at the qth subcarrier to the value v. Reasonably, the new search space has half the size compared to the one in the first DHA operation of the DHA-MAA QMUD, but the resultant complexity may prove to be severe, especially if more than one of the $\mathcal{X}_{q,g}^{u,m,\mathrm{v}}$ sets are found empty after the

[2]The evolutionary algorithms follow a "neighbourhood criterion", where the search space of each generation is created around the best-so-far found symbol.

first DHA call. Hence, for the sake of circumventing this problem, we propose a Neighbour Exploitation (NE) based complexity reduction technique.

Algorithm 5 DHA-MAA-NE QMUD [3]

1: $U_{q,g}$ users, M-ary modulation, $N_{q,g} \leftarrow M^{U_{q,g}}$.
2: $\mathcal{X}_{q,g}^{u,m,\mathrm{v}} \leftarrow \emptyset$, for $u = 1, 2, \ldots, U_{g,q}$, $m = 1, 2, \ldots, \log_2 M$ and $\mathrm{v} = 0, 1$.
3: The DHA is employed for finding the symbol $\hat{x}_{\max}$ that maximizes the CF in Equation 3.14 with $\sim$100% success probability after searching the whole search space $N_{q,g}$. Update the sets $\mathcal{X}$ and $\mathcal{X}_{q,g}^{u,m,\mathrm{v}}$, for $u = 1, \ldots, U_{g,q}$, $m = 1, \ldots, \log_2 M$, $\mathrm{v} = 0, 1$, when a unique symbol is evaluated by the DHA.
4: **for** $u = 1, 2, \ldots, U_{q,g}$ **do**
5: **for** $m = 1, 2, \ldots, \log_2 M$ **do**
6: **if** $\hat{x}_{\max} \in \mathcal{X}_{q,g}^{u,m,0}$ **then**
7: Include symbol x_{nb} in $\mathcal{X}_{q,g}^{u,m,1}$, where the binary representation of x_{nb} is the same as that of $\hat{x}_{\max}$ with the difference that the value of the $[(u-1)\cdot\log_2 M + m]$th bit is equal to 1.
8: **else if** $\hat{x}_{\max} \in \mathcal{X}_{q,g}^{u,m,1}$ **then**
9: Include symbol x_{nb} in $\mathcal{X}_{q,g}^{u,m,0}$, where the binary representation of x_{nb} is the same as that of $\hat{x}_{\max}$ with the difference that the value of the $[(u-1)\cdot\log_2 M + m]$th bit is equal to 0.
10: **end if**
11: Calculate the LLR of the $[(u-1)\cdot\log_2 M + m]$th bit according to Equation 3.95.
12: **end for**
13: **end for**

3.5.1.1 Neighbour Exploitation

If a set $\mathcal{X}_{q,g}^{u,m,\mathrm{v}}$ is empty, it means that the best symbol $\hat{x}_{\max}$ found by the DHA belongs to the set $\mathcal{X}_{q,g}^{u,m,\bar{\mathrm{v}}}$, where $\bar{\mathrm{v}} = \mathrm{v} \oplus 1$ and $\oplus$ denotes the modulo-2 addition. According to the proposed NE-based modification, the set $\mathcal{X}_{q,g}^{u,m,\mathrm{v}}$ will include the CF value of the neighbour of the globally best found symbol, where the uth user's mth bit will be equal to $\bar{\mathrm{v}}$. In our example of Figure 3.23, if the indices of all the symbols found by the DHA were smaller than 32, then the set $\mathcal{X}_{q,g}^{0,0,1}$ would be void. Since we have $\hat{x}_{\max} = 22 = [01|01|10]$, the symbol with index $[11|01|10] \Rightarrow x_{nb} = 54$, where nb stands for neighbour, would then be included in the set $\mathcal{X}_{q,g}^{0,0,1}$ according to the NE modification.

The NE contributes an additional CD-CFE to the MUD's complexity every time it is performed, since the new symbol's CF value has to be calculated. It may also be used for improving the MUD's performance even if the set that does not include $\hat{x}_{\max}$ is not empty. In that case x_{nb} is added to that set and it may be used for the calculation of that specific LLR provided that its CF value is the highest one in that set. The steps of the DHA-MAA-NE QMUD are stated in Algorithm 5 and the corresponding flow chart is given in Figure 3.24.

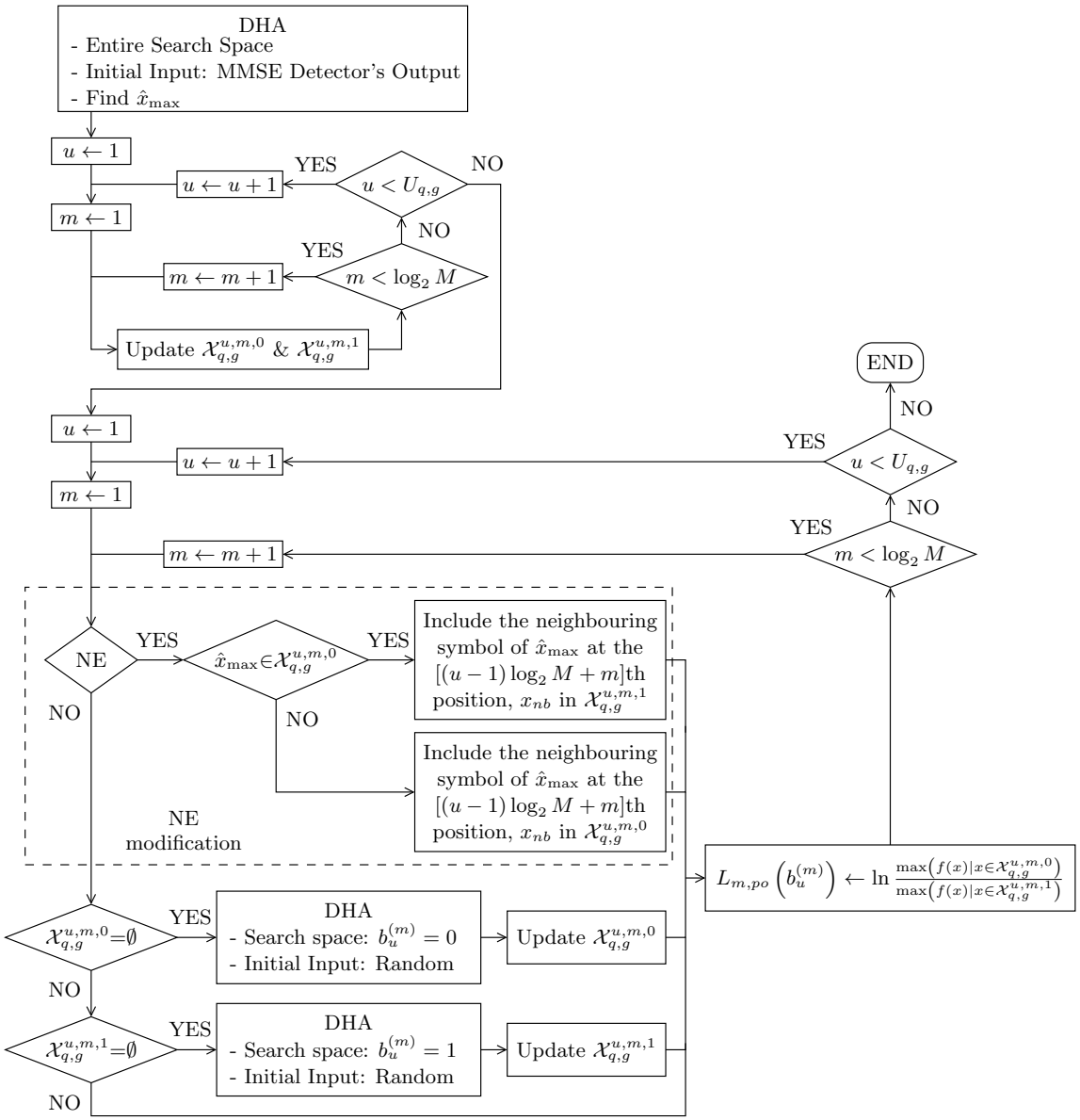

Figure 3.24: Flow Chart of the DHA-MAA QMUD with and without the NE modification.

3.5.1.2 Complexity

The complexity of the first DHA employment is $O(\sqrt{N_{q,g}})$, since it is applied to the entire available search space, while the complexity of any subsequent DHA employment is $O(\sqrt{N_{q,g}/2})$. More specifically, if the first DHA application encountered symbols for both values of each bit in the DHA-MAA QMUD, the minimum complexity per bit is

$$\begin{aligned} \mathcal{C}_{SO-DHA}^{MAA,\min} &= \frac{L_{DHA}^{QD,\min} + L_{DHA}^{CD,\min}}{U_{q,g} \cdot \log_2 M} = \\ &= \frac{4.5\sqrt{M^{U_{q,g}}} + L_{DHA}^{CD,\min}}{U_{q,g} \cdot \log_2 M} \end{aligned} \tag{3.97}$$

CFEs, where $L_{DHA}^{CD,\min}$ is given in Equation 2.50 in the specific scenario, where the MMSE detector's output is equal to $\hat{x}_{\max}$. Therefore the DHA will realize that the globally optimal

value has already been found after $4.5\sqrt{N_{q,g}}$ QD-CFEs. On the other hand, if no symbols were found for a specific bit's value, the DHA has to be called again for the respective search space, which has half the size of the total search space. The complexity per bit for the DHA-MAA QMUD, when there are two DHA calls in total is

$$\begin{aligned} \acute{\mathcal{C}}_{SO-DHA}^{MAA,\min} =& \frac{L_{1,DHA}^{QD,\min} + L_{1,DHA}^{CD,\min} + L_{2,DHA}^{QD,\min} + L_{2,DHA}^{CD,\min}}{U_{q,g} \cdot \log_2 M} = \\ =& \frac{7.682\sqrt{M^{U_{q,g}}} + L_{1,DHA}^{CD,\min} + L_{2,DHA}^{CD,\min}}{U_{q,g} \cdot \log_2 M} \end{aligned} \tag{3.98}$$

CFEs. The minimum complexity per bit of the DHA-MAA-NE QMUD is

$$\begin{aligned} \mathcal{C}_{SO-DHA}^{MAA,NE,\min} =& \frac{L_{DHA}^{QD,\min} + L_{DHA}^{CD,\min} + U_{q,g} \cdot \log_2 M}{U_{q,g} \cdot \log_2 M} = \\ =& \frac{4.5\sqrt{M^{U_{q,g}}} + L_{DHA}^{CD,\min}}{U_{q,g} \cdot \log_2 M} + 1 \end{aligned} \tag{3.99}$$

CFEs. The third term in Equation 3.99 corresponds to the CFEs required for finding the neighbours of $\hat{x}_{\max}$, once for each bit of the multi-level symbol and it is independent of the DHA. Note that the complexity per bit of the DHA-MAA-NE QMUD in Equation 3.99 includes one more CFE compared to the complexity of the DHA-MAA QMUD, if the DHA is applied only once. By contrast, if the DHA is called at least twice in the DHA-MAA QMUD, its complexity formulated in Equation 3.98 is significantly higher than that of the DHA-MAA-NE QMUD.

3.5.2 DHA QMUD Relying on Multi-Input Approximation

The main differences between the DHA-MAA QMUD and the DHA QMUD with MUlti-input Approximation (DHA-MUA QMUD) are that multiple symbols take part in the calculation of the LLRs in the MUA. More specifically, commencing from the first user's $u = 1$ first bit's $m = 1$ LLR calculation, the DHA is invoked for its numerator's search space, having fixed the $[(u-1) \cdot \log_2 M + m] = 1$st bit to v = 0, and then also for the denominator's search space, where only the specific symbols with the 1st bit being v = 1 are considered. The two sets $\mathcal{X}_{q,g}^{u,m,0}$ and $\mathcal{X}_{q,g}^{u,m,1}$ are filled by the DHAs' outputs in a sorted order. Since the two DHA activations have jointly searched the entire search space, the globally maximal symbol $\hat{x}_{\max}$ corresponds to the maximum CF valued entries $\hat{x}_{\max}^{u,m,0}$ and $\hat{x}_{\max}^{u,m,1}$ of the two sets $\mathcal{X}_{q,g}^{u,m,0}$ and $\mathcal{X}_{q,g}^{u,m,1}$, respectively. Therefore, by comparing the maximum CF valued entries of the two sets we may determine $\hat{x}_{\max}$ as in

$$\hat{x}_{\max} = \begin{cases} \hat{x}_{\max}^{u,m,0} & \text{if } f\left(\hat{x}_{\max}^{u,m,0}\right) > f\left(\hat{x}_{\max}^{u,m,1}\right) \\ \hat{x}_{\max}^{u,m,1} & \text{if } f\left(\hat{x}_{\max}^{u,m,0}\right) \leq f\left(\hat{x}_{\max}^{u,m,1}\right) \end{cases}, \tag{3.100}$$

$$\mathcal{X}_{q,g}^{1,1,0} = \left\{ \begin{array}{cccccccccc} 22, & 8, & 17, & 9, & 23, & 12, & 21, & 18, & 31, & 5 \\ 0.95 & 0.76 & 0.43 & 0.29 & 0.16 & 0.019 & 0.01 & 0.0082 & 2.4 \cdot 10^{-4} & 4.9 \cdot 10^{-7} \end{array} \right\}$$

$$\mathcal{X}_{q,g}^{1,1,1} = \left\{ \begin{array}{cccccc} 46, & 43, & 61, & 62, & 63, & 54 \\ 0.77 & 0.65 & 0.48 & 0.2 & 0.19 & 0.027 \end{array} \right\} \quad |\mathcal{X}_{q,g}^{1,1,0}| = 10 \quad |\mathcal{X}_{q,g}^{1,1,1}| = 6 \quad \varsigma_{1,1} = +1$$

$$\downarrow \text{ Best } \min\{|\mathcal{X}_{q,g}^{1,1,0}|, |\mathcal{X}_{q,g}^{1,1,1}|\} \text{ symbols}$$

$$\bar{\mathcal{X}}_{q,g}^{1,1,0} = \left\{ \begin{array}{cccccc} \boxed{22,} & \boxed{8,} & 17, & \boxed{9,} & 23, & 12 \\ \boxed{0.95} & \boxed{0.76} & 0.43 & \boxed{0.29} & 0.16 & 0.019 \end{array} \right\} \xrightarrow{\varsigma_{1,1}} \hat{\mathcal{X}}_{q,g}^{1,1,0} = \left\{ \begin{array}{ccc} 22, & 8, & 9 \\ 0.95 & 0.76 & 0.29 \end{array} \right\}$$

$$\bar{\mathcal{X}}_{q,g}^{1,1,1} = \left\{ \begin{array}{cccccc} \boxed{46,} & \boxed{43,} & 61, & \boxed{62,} & 63, & 54 \\ \boxed{0.77} & \boxed{0.65} & 0.48 & \boxed{0.2} & 0.19 & 0.027 \end{array} \right\} \qquad \hat{\mathcal{X}}_{q,g}^{1,1,1} = \left\{ \begin{array}{ccc} 46, & 43, & 62 \\ 0.77 & 0.65 & 0.2 \end{array} \right\}$$

$$i = \begin{array}{cccccc} 1 & 2 & 3 & 4 & 5 & 6 \end{array}$$

Figure 3.25: Scenario of the DHA QMUD with MUA. The set $\mathcal{X}_{q,g}^{1,1,0}$ was created based on the first DHA call with the MMSE detector's output 31 as the initial input, where only symbols with $b_1^{(1)} = 0$ were searched. The set $\mathcal{X}_{q,g}^{1,1,1}$ was constructed based on the second DHA call with the neighbour of $\hat{x}_{\max}^{1,1,0}$ at the first user's first bit's position $22 \rightarrow 54$ as initial input, where only symbols with $b_1^{(1)} = 1$ were searched. Top to bottom left: Formulation of the sets $\bar{\mathcal{X}}_{q,g}^{1,1,0}$ and $\bar{\mathcal{X}}_{q,g}^{1,1,1}$ based on the set sizes $|\mathcal{X}_{q,g}^{1,1,0}| = 10$ and $|\mathcal{X}_{q,g}^{1,1,1}| = 6$ of the sets $\mathcal{X}_{q,g}^{1,1,0}$ and $\mathcal{X}_{q,g}^{1,1,1}$, respectively. The last $|\mathcal{X}_{q,g}^{1,1,0}| - |\mathcal{X}_{q,g}^{1,1,1}| = 4$ symbols are deleted from $\bar{\mathcal{X}}_{q,g}^{1,1,0}$, since $|\mathcal{X}_{q,g}^{1,1,0}| > |\mathcal{X}_{q,g}^{1,1,1}|$. Bottom left to bottom right: Construction of the sets $\hat{\mathcal{X}}_{q,g}^{1,1,0}$ and $\hat{\mathcal{X}}_{q,g}^{1,1,1}$ based on the signs of the difference of the CF values of the sorted symbol pairs in $\bar{\mathcal{X}}_{q,g}^{1,1,0}$ and $\bar{\mathcal{X}}_{q,g}^{1,1,1}$. The symbols in the positions $i = 3, 5, 6$ are deleted since $\text{sign}(f(x_i^{1,1,0}) - f(x_i^{1,1,1})) \neq \varsigma_{1,1} = +1$ for $i = 3, 5, 6$.

and hence the sign of the $[(u-1) \cdot \log_2 M + m]$th bit's LLR is given by [63]

$$\varsigma_{u,m} = \text{sign}\left[L_{m,po}\left(b_u^{(m)}\right)\right] = \begin{cases} +1 & \text{if } \hat{x}_{\max} \in \mathcal{X}_{q,g}^{u,m,0} \\ -1 & \text{if } \hat{x}_{\max} \in \mathcal{X}_{q,g}^{u,m,1} \end{cases} . \tag{3.101}$$

The LLR sign $\varsigma_{u,m}$ will be exploited for selecting the specific entries in the sets $\mathcal{X}_{q,g}^{u,m,0}$ and $\mathcal{X}_{q,g}^{u,m,1}$ that will participate in the calculation of the LLR. Let us denote the size of $\mathcal{X}_{q,g}^{u,m,0}$ by $|\mathcal{X}_{q,g}^{u,m,0}|$ and that of $\mathcal{X}_{q,g}^{u,m,1}$ as $|\mathcal{X}_{q,g}^{u,m,1}|$. The two sets may consist of a different number of entries, therefore $|\mathcal{X}_{q,g}^{u,m,0}|$ may or may not be equal to $|\mathcal{X}_{q,g}^{u,m,1}|$. If $|\mathcal{X}_{q,g}^{u,m,0}| > |\mathcal{X}_{q,g}^{u,m,1}|$ is true, then the $|\mathcal{X}_{q,g}^{u,m,0}| - |\mathcal{X}_{q,g}^{u,m,1}|$ entries with the smallest CF value in $\mathcal{X}_{q,g}^{u,m,0}$ are excluded from the sum. Otherwise, if $|\mathcal{X}_{q,g}^{u,m,0}| < |\mathcal{X}_{q,g}^{u,m,1}|$ is true, then the $|\mathcal{X}_{q,g}^{u,m,1}| - |\mathcal{X}_{q,g}^{u,m,0}|$ symbols that correspond to the smallest CF values in $\mathcal{X}_{q,g}^{u,m,1}$ are deleted. The $\min\{|\mathcal{X}_{q,g}^{u,m,0}|, |\mathcal{X}_{q,g}^{u,m,1}|\}$ number of remaining symbols in $\mathcal{X}_{q,g}^{u,m,0}$ and $\mathcal{X}_{q,g}^{u,m,1}$ form the sets $\bar{\mathcal{X}}_{q,g}^{u,m,0}$ and $\bar{\mathcal{X}}_{q,g}^{u,m,1}$, respectively. Let us now consider the scenario described in Figure 3.25, where the above-mentioned two DHA calls created the sorted sets $\mathcal{X}_{q,g}^{u,m,0}$ and $\mathcal{X}_{q,g}^{u,m,1}$ for the calculation of the first user's $u = 1$ first bit's $m = 1$ LLR. The CF values of the symbols in the scenario of Figure 3.25 are the same as in Figure 3.23. Furthermore, the initial input of the DHA is the MMSE detector's output x_{MMSE}, when the first user's first bit's LLR has to be calculated and the search space does include the MMSE detector's output. By contrast, when the search space does not include x_{MMSE}, as in the second search of

Figure 3.25, where we want to construct $\mathcal{X}_{q,g}^{1,1,1}$, two options may be used, depending on whether the two DHA calls are running in parallel or consecutively:

1. If the two DHA calls are performed in parallel, the initial point may be the immediate neighbour of x_{MMSE} at the first user's first bit's location. In our scenario of Figure 3.25 this may lead to the symbol $x_{init}^{1,1,0} = x_{MMSE} = 31 = [01|11|11] \rightarrow [11|11|11] = 63 = x_{init}^{1,1,1}$.

2. If the two DHA calls are performed serially, we always activate the DHA first on the search space corresponding to $\mathcal{X}_{q,g}^{1,1,\mathrm{v}_0}$, where the MMSE detector's output is included in the search space as $\mathrm{v}_0 = b_{1,MMSE}^{(1)}$. The reason behind this choice is that there is a higher probability of finding the global maximum of $x_{\max} = \hat{x}_{\max}^{1,1,0}$ in the same search space that the MMSE detector's output belongs to [21]. After we have found the specific index that maximizes the CF in that search space, which is $\hat{x}_{\max}^{1,1,0} = 22$ in our scenario, we exploit its neighbour at the first user's first bit's location according to $\hat{x}_{\max}^{1,1,0} = 22 = [01|01|10] \rightarrow [11|01|10] = 54 = \hat{x}_{init}^{1,1,1}$ as the initial point of the second DHA activation employed in the search space, which corresponds to $\mathcal{X}_{q,g}^{1,1,\mathrm{v}_0 \oplus 1}$. The reason of choosing the neighbour of $\hat{x}_{\max}^{1,1,\mathrm{v}}$ as the initial point of the second DHA is that the neighbour of the "hitherto-optimal" symbol may also be close to the maximum value in that particular search space, especially if $\hat{x}_{\max}^{1,1,\mathrm{v}}$ turns out to be equal to the globally optimal symbol $x_{\max}$, since the values of the CF in Equation 3.14 are correlated with the bit locations [9, 21].

In our simulations we assume that the DHA operations are performed serially, therefore we follow the second method of selecting the initial points of the DHA calls.

Once the pair of sets $\bar{\mathcal{X}}_{q,g}^{u,m,0}$ and $\bar{\mathcal{X}}_{q,g}^{u,m,1}$ have been formulated depending on $|\mathcal{X}_{q,g}^{u,m,0}|$ and $|\mathcal{X}_{q,g}^{u,m,1}|$, it has to be ensured that the resultant sign of the LLR is the same as the value $\varsigma_{u,m}$ calculated in Equation 3.101. It is certain according to Equation 3.101, that the sign of the difference of the maximum CF values of the two sets, namely $\mathrm{sign}\left[f(x_1^{u,m,0}) - f(x_1^{u,m,1})\right]$ is equal to $\varsigma_{u,m}$ [63], where we have $x_1^{u,m,\mathrm{v}} = x_{\max}^{u,m,\mathrm{v}}$. For the sake of forcing the LLR to have the same sign as $\varsigma_{u,m}$ with 100% probability, we may only include the symbol pairs of the two sets of which the sign of the CF-difference is equal to $\varsigma_{u,m}$ of Equation 3.101, as encapsulated in

$$\begin{aligned} & x_i^{u,m,0} \in \hat{\mathcal{X}}_{q,g}^{u,m,0} \wedge x_i^{u,m,1} \in \hat{\mathcal{X}}_{q,g}^{u,m,1} \\ & \Leftrightarrow \mathrm{sign}\left[f\left(x_i^{u,m,0}\right) - f\left(x_i^{u,m,1}\right)\right] = \varsigma_{u,m} \wedge x_i^{u,m,0} \in \bar{\mathcal{X}}_{q,g}^{u,m,0} \wedge x_i^{u,m,1} \in \bar{\mathcal{X}}_{q,g}^{u,m,1} \\ & i = 2, \ldots, \min\{|\mathcal{X}_{q,g}^{1,1,0}|, |\mathcal{X}_{q,g}^{1,1,1}|\}, \end{aligned} \tag{3.102}$$

where the sets $\hat{\mathcal{X}}_{q,g}^{u,m,0}$ and $\hat{\mathcal{X}}_{q,g}^{u,m,1}$ consist of the filtered symbols. In our scenario of Figure 3.25, three of the symbol pairs in $\bar{\mathcal{X}}_{q,g}^{u,m,0}$ and $\bar{\mathcal{X}}_{q,g}^{u,m,1}$ satisfy the constraints introduced in Equation 3.102, therefore they are the specific symbols that will be included in the calculation of the LLR.

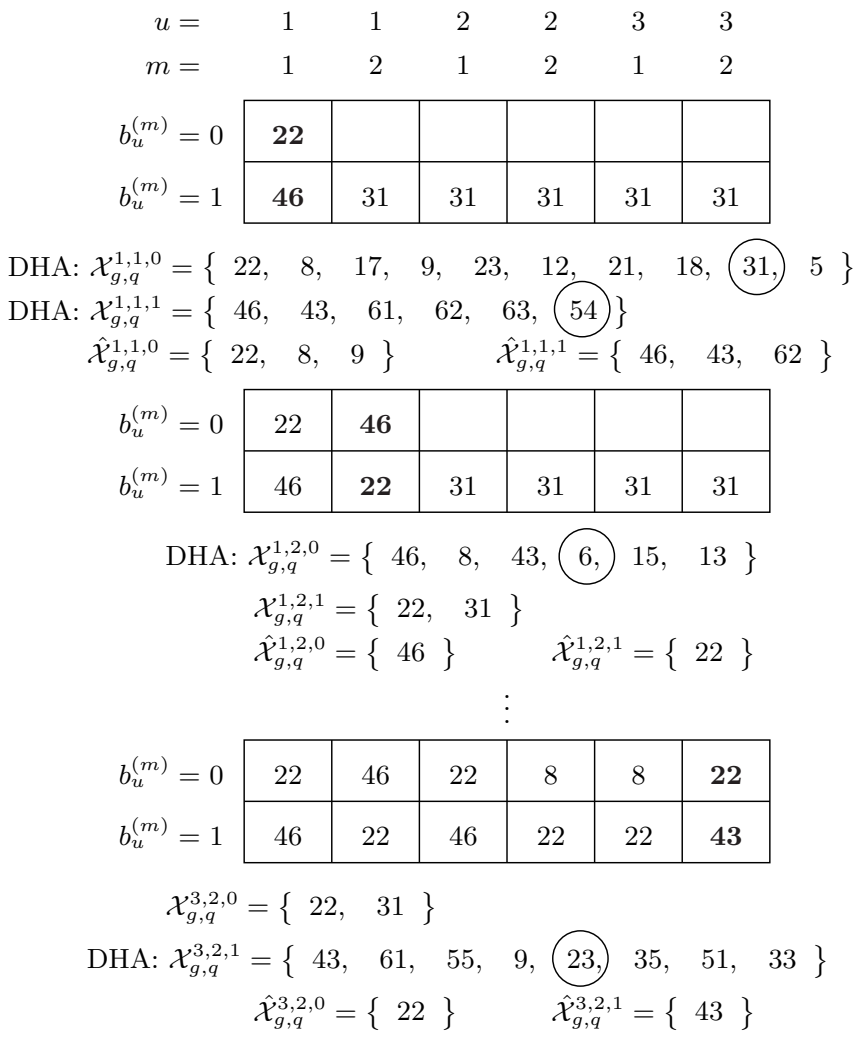

Figure 3.26: Construction of the sets $\hat{\mathcal{X}}_{q,g}^{u,m,\mathrm{v}}$ for $u = 1,2,3$, $m = 1,2$, $\mathrm{v} = 0,1$ in the DHA QMUD with MUA scenario described in Figure 3.23. The symbol indices in the boxes represent the best so far found symbols for that particular bit value, while the bold numbers indicate the bit of which the sets have just been constructed. The circled indices denote the initial point of a DHA procedure. Since we assume that the DHA calls are performed serially, the initial point will be the MMSE output for one of the first bit's values and the neighbours of the best found symbol for the other value of the first bit, as well as for the rest of the bits.

After the pair of sets $\hat{\mathcal{X}}_{q,g}^{u,m,0}$ and $\hat{\mathcal{X}}_{q,g}^{u,m,1}$ has been determined for the uth user's mth bit, its LLR in the DHA-MUA QMUD may be calculated according to

$$L_{m,po}\left(b_u^{(m)}\right) = \ln \frac{\sum\limits_{x \in \hat{\mathcal{X}}_{q,g}^{u,m,0}} f(x)}{\sum\limits_{x \in \hat{\mathcal{X}}_{q,g}^{u,m,1}} f(x)}. \tag{3.103}$$

In Figure 3.25 the first user's first bit's LLR would be equal to

$$L_{m,po}\left(b_1^{(1)}\right) = \ln \frac{f(22)+f(8)+f(9)}{f(46)+f(43)+f(62)} = 0.21. \tag{3.104}$$

Algorithm 6 DHA-MUA QMUD [3]

$U_{q,g}$ users, M-ary modulation, $N \leftarrow M^{U_{q,g}}$.
$\mathcal{X}_{q,g}^{u,m,\mathrm{v}} \leftarrow \emptyset$, $\bar{\mathcal{X}}_{q,g}^{u,m,\mathrm{v}} \leftarrow \emptyset$, $\hat{\mathcal{X}}_{q,g}^{u,m,\mathrm{v}} \leftarrow \emptyset$, for $u = 1, \ldots, U_{g,q}$, $m = 1, \ldots, \log_2 M$ and $\mathrm{v} = 0, 1$.
if $b_{1,\,MMSE}^{(1)} = 0$ **then**
    The DHA is employed for finding $\hat{x}_{\max}^{1,1,0}$ and for filling the set $\mathcal{X}_{q,g}^{1,1,0}$, by exploiting the search space where $b_1^{(1)} = 0$. Initial input: MMSE detector's output x_{MMSE}.
    The DHA is employed for finding $\hat{x}_{\max}^{1,1,1}$ and for filling the set $\mathcal{X}_{q,g}^{1,1,1}$, by exploiting the search space where $b_1^{(1)} = 1$. Initial input: neighbour of $\hat{x}_{\max}^{1,1,0}$ at the first bit.
else if $b_{1,\,MMSE}^{(1)} = 1$ **then**
    The DHA is employed for finding $\hat{x}_{\max}^{1,1,1}$ and for filling the set $\mathcal{X}_{q,g}^{1,1,1}$, by searching the search space where $b_1^{(1)} = 1$. Initial input: MMSE detector's output x_{MMSE}.
    The DHA is employed for finding $\hat{x}_{\max}^{1,1,0}$ and for filling the set $\mathcal{X}_{q,g}^{1,1,0}$, by searching the search space where $b_1^{(1)} = 0$. Initial input: neighbour of $\hat{x}_{\max}^{1,1,1}$ at the first bit.
end if
Determine $\hat{x}_{\max}$ according to Equation 3.100.
for $u = 1, 2, \ldots, U_{q,g}$ **do**
    for $m = 1, 2, \ldots, \log_2 M$ **do**
        if $u \neq 1$ or $m \neq 1$ **then**
            if $\hat{x}_{\max} \in \mathcal{X}_{q,g}^{u,m,0}$ **then**
                The DHA is employed for finding $\hat{x}_{\max}^{u,m,1}$ and for filling the set $\mathcal{X}_{q,g}^{u,m,1}$, by exploiting the search space where $b_u^{(m)} = 1$. Initial input: neighbour of $\hat{x}_{\max}$ at the $[(u-1) \cdot \log_2 M + m]$th bit.
            else if $\hat{x}_{\max} \in \mathcal{X}_{q,g}^{u,m,1}$ **then**
                The DHA is employed for finding $\hat{x}_{\max}^{u,m,0}$ and for filling the set $\mathcal{X}_{q,g}^{u,m,0}$, by exploiting the search space where $b_u^{(m)} = 0$. Initial input: neighbour of $\hat{x}_{\max}$ at the $[(u-1) \cdot \log_2 M + m]$th bit.
            end if
        end if
        Determine the sign of the LLR $\varsigma_{u,m}$ based on Equation 3.101.
        Create $\bar{\mathcal{X}}_{q,g}^{u,m,0}$ and $\bar{\mathcal{X}}_{q,g}^{u,m,1}$ depending on the sets' sizes $|\mathcal{X}_{q,g}^{u,m,0}|$ and $|\mathcal{X}_{q,g}^{u,m,1}|$, by keeping the best $\min\{|\mathcal{X}_{q,g}^{u,m,0}|, |\mathcal{X}_{q,g}^{u,m,1}|\}$ values from $\mathcal{X}_{q,g}^{u,m,0}$ and $\mathcal{X}_{q,g}^{u,m,1}$, respectively.
        Create $\hat{\mathcal{X}}_{q,g}^{u,m,0}$ and $\hat{\mathcal{X}}_{q,g}^{u,m,1}$ according to Equation 3.102.
        Calculate the $[(u-1) \cdot \log_2 M + m]$th bit's LLR based on Equation 3.103.
    end for
end for

Recall from [63] that when we proceed to the calculation of the second bit of the $M^{U_{q,g}}$-ary symbol, the ACO algorithm is called again for performing the same operation as for the first bit, since the true globally optimal symbol $x_{\max}$ may not have been found during the first two ACO operations, especially in rank-deficient systems. By contrast, this is unnecessary in the DHA-MUA QMUD, since we have $\hat{x}_{\max} = x_{\max}$ with $\sim$100% probability. Therefore, there is no need for calling the DHA for finding the best symbol in the subsequent search spaces where $\hat{x}_{\max}$ belongs to, resulting in a substantially reduced complexity. The DHA is called only for the particular bit value that is not the same as that bit's value in $\hat{x}_{\max}$. In our scenario of Figure 3.23 and Figure 3.25, the binary representation of the optimal symbol is $\hat{x}_{\max} = 22 = [01|01|10]$, therefore the set $\hat{\mathcal{X}}_{q,g}^{1,2,1}$ will only consist of $\hat{\mathcal{X}}_{q,g}^{1,2,1} = \{22, 31\}$. The MMSE detector's output of $x_{MMSE} = 31$ is also included in that set, since the second bit of its binary representation is equal to 1. For filling the set $\hat{\mathcal{X}}_{q,g}^{1,2,0}$, we employ the DHA for searching the symbols associated with $b_1^{(2)} = 0$, as in Figure 3.25. The same procedure applies for the rest of the bits in the $M^{U_{q,g}}$-ary symbol,

as described in the example of Figure 3.26, where the sets of the bits are presented along with their method of construction. The performance of the DHA-MUA QMUD will be shown to be substantially better than that of the DHA-MAA QMUD, since the maximum CF value of each LLR's numerator and denominator is found with a ∼100% probability. The DHA-MUA QMUD is described in Algorithm 6.

3.5.2.1 Complexity

The complexity of each DHA call in the DHA-MUA QMUD is $O(\sqrt{N_{q,g}/2})$, since the searched space is half of the total search space. Therefore, the minimum complexity per bit for the DHA-MUA-NE QMUD is

$$\begin{aligned}
&\mathcal{C}_{SO-DHA}^{MUA,NE,\min} = \\
&\Big[(U_{q,g}\cdot\log_2 M+1)\left(4.5\sqrt{M^{U_{q,g}}/2}+L_{DHA}^{CD,\min}\right) \\
&+U_{q,g}\cdot\log_2 M\Big]/\left(U_{q,g}\cdot\log_2 M\right) = \\
&=\left(4.5\sqrt{M^{U_{q,g}}/2}+L_{DHA}^{CD,\min}\right)\left(1+\frac{1}{U_{q,g}\cdot\log_2 M}\right)+1
\end{aligned} \tag{3.105}$$

CFEs, where $L_{DHA}^{CD,\min}$ is computed according to Equation 2.50. The first additive term of the lower complexity bound of the DHA-MUA-NE QMUD in Equation 3.105 corresponds to the scenario, where the initial inputs of all $(U_{q,g}\cdot\log_2 M+1)$ number of DHA calls are equal to the respective optimal symbols of the search space. The second additive term corresponds to the CFE of the neighbour of $\hat{x}_{\max}$ for each bit of the multi-level symbol. The complexity of the DHA-MUA-NE QMUD in Equation 3.105 is higher than that of the DHA-MAA-NE QMUD in Equation 3.99.

Let us now proceed by proposing two modifications to the DHA-MUA QMUD, which improve the attainable performance, while reducing the complexity even further, but may impose delay and additional memory requirements on our system.

3.5.2.2 Forward Knowledge Transfer

In the Forward Knowledge Transfer (FKT) based modification, the symbols evaluated by the DHA performed for the ith bit of the $N_{q,g}$-ary symbol, with $i = 1, 2, \ldots, N_{q,g}$, are included not only in the set $\mathcal{X}_{q,g}^{u,m,\mathrm{v}}$, for which set we have $i = (u-1)\cdot\log_2 M + m$, but also in the appropriate sets of the subsequent bits j, for $j = i+1, i+2, \ldots, N_{q,g}$. By invoking the proposed FKT the performance of the SO-DHA QMUD is expected to improve, since the sets that only consisted of $\hat{x}_{\max}$ and x_{MMSE} as in Figure 3.26 will now include more symbols, which will have been evaluated during previous calls of the DHA, leading to LLR values closer to those of the MAP MUD. No additional delay is introduced, because once the DHA has finished the search related to the ith bit, that bit's LLR is computed and passed to the deinterleaver. However, additional memory is required for storing the found

symbols in the multiple appropriate sets.

When the FKT is applied, the initial input of the DHA of the $i = [(u-1)\cdot\log_2 M+m]$th bit, with $i \geq 2$, is determined by a comparison between the "best-so-far" symbol included in $\mathcal{X}_{q,g}^{u,m,\mathrm{v}}$ by the previous DHA operations, and the specific neighbour of the globally optimal symbol $\hat{x}_{\max}$ at the ith bit position $x_{nb,\max}^{u,m}$, as formulated in

$$x_{init}^{u,m,\mathrm{v}} = \begin{cases} \hat{x}_{nb,\max}^{u,m}, & \text{if } f\left(\hat{x}_{nb,\max}^{u,m}\right) > f\left(\hat{x}_{\max}^{u,m,\mathrm{v}}\right) \\ \hat{x}_{\max}^{u,m,\mathrm{v}}, & \text{if } f\left(\hat{x}_{nb,\max}^{u,m}\right) \leq f\left(\hat{x}_{\max}^{u,m,\mathrm{v}}\right) \end{cases}. \tag{3.106}$$

By selecting $x_{init}^{u,m,\mathrm{v}}$ according to Equation 3.106 we introduce an extra CFE for calculating $f\left(\hat{x}_{nb,\max}^{u,m}\right)$, but the total complexity is expected to be reduced, since the initial point in the DHA will be closer to the symbol having the maximum CF value in that particular search space, hence saving multiple CFEs during the search. An example of the FKT is illustrated in Figure 3.27a and its operation is formally described in Algorithm 7.

Algorithm 7 Forward Knowledge Transfer &
Forward and Backward Knowledge Transfer [3]

1: Applicable immediately after the DHA application in steps 4, 5, 7, 8, 15 and 17 of Algorithm 6, or after any search algorithm used in the MUA. Let us assume the DHA was employed for the uth user's mth bit with i=$(u-1)\cdot\log_2 M+m$, u=$1,\ldots,U_{q,g}$ and m=$1,\ldots,\log_2 M$.
2: **if** Forward Knowledge Transfer **then**
3: $d \leftarrow i$
4: **else if** Forward and Backward Knowledge Transfer **then**
5: $d \leftarrow 0$
6: **end if**
7: **for** $j = d, d+1, \ldots, U_{q,g}\cdot\log_2 M$ **do**
8: Determine u' and m' from $u'\cdot\log_2 M + m' = j$ and $u', m' \in \mathbb{Z}$.
9: Update $\mathcal{X}_{q,g}^{u',m',\mathrm{v}}$ for $\mathrm{v} = 0, 1$ with the new symbols evaluated by the DHA for the ith bit of the $M^{U_{q,g}}$-ary symbol.
10: **end for**

3.5.2.3 Forward and Backward Knowledge Transfer

In the Forward and Backward Knowledge Transfer (FBKT) modification both sets of every bit of the $N_{q,g}$-ary symbol are updated after every DHA application, regardless of which user's bit's search space the DHA was employed for. The FBKT process is formally stated in Algorithm 7. When using the FBKT, all the LLR values will be calculated based on the same symbol pool containing all the symbols evaluated during the $(U_{q,g}\cdot\log_2 M+1)$ different DHA calls. For this reason an additional memory requirement and delay are imposed on the system, since the bits' LLRs are calculated after all the DHA activations have completed, which is in contrast to the FKT, where the LLR of a bit is calculated after the DHA has been applied to its own search spaces.

Furthermore, the FBKT is expected to have a substantial impact on sub-optimal heuristic search algorithms used in rank-deficient systems. For example, let us assume that the true global optimal symbol $x_{\max}$ is found during an ACO search in the search space of the

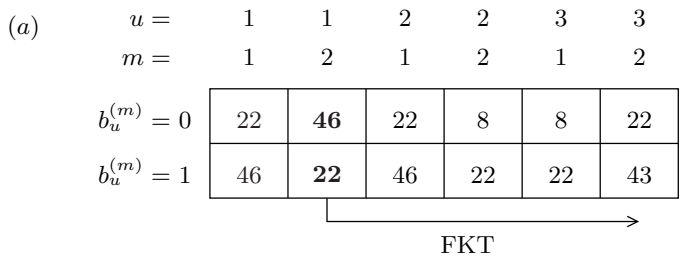

$\mathcal{X}_{g,q}^{1,1,0} = \{\ 22,\ 8,\ 17,\ 9,\ 23,\ 12,\ 21,\ 18,\ 31,\ 5\ \}$
$\mathcal{X}_{g,q}^{1,1,1} = \{\ 46,\ 43,\ 61,\ 62,\ 63,\ 54\ \}$
DHA: $\mathcal{X}_{g,q}^{1,2,0} = \{\ (46),\ 8,\ 43,\ 9,\ \underline{41},\ \underline{6},\ 12,\ \underline{15},\ \underline{13}\ \ 5\ \}$
$\mathcal{X}_{g,q}^{1,2,1} = \{\ 22,\ 61,\ 17,\ 62,\ 63,\ 23,\ 54,\ 21,\ 18,\ 31\ \}$
$\hat{\mathcal{X}}_{g,q}^{1,2,1} = \{\ 22,\ 23,\ 54,\ 21,\ 18,\ 31\ \}$
$\hat{\mathcal{X}}_{g,q}^{1,2,0} = \{\ 46,\ 6,\ 12,\ 15,\ 13,\ 5\ \}$

$\vdots$

$\mathcal{X}_{g,q}^{3,2,0} = \{\ 22,\ 46,\ 8,\ 62,\ \underline{6},\ 54,\ 12,\ 18\ \}$
$\mathcal{X}_{g,q}^{3,2,1} = \{\ 43,\ 61,\ 17,\ 9,\ \underline{41},\ 63,\ 23,\ 21,\ 31,\ \underline{15},\ \underline{13},\ 5\ \}$

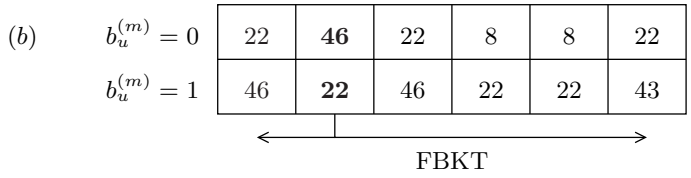

$\mathcal{X}_{g,q}^{1,1,0} = \{\ 22,\ 8,\ 17,\ 9,\ 23,\ \underline{6},\ 12,\ 21,\ 18,\ 31,\ \underline{15},\ \underline{13},\ 5\ \}$
$\mathcal{X}_{g,q}^{1,1,1} = \{\ 46,\ 43,\ 61,\ \underline{41},\ 62,\ 63,\ 54\ \}$

The rest of the sets are the same as in (a)

Figure 3.27: Scenario of the DHA-MUA QMUD and (a) Forward Knolwedge Transfer or (b) Forward & Backward Knowledge Transfer in the rank-deficient DSS / USSCH SDMA-OFDM system of Figure 3.23. Focusing on the DHA application for the $i = 2$nd bit, the underlined indices represent the new symbols found during the current DHA search. The circled index 46 is selected to be the initial input of the DHA, because it has a higher CF value than that of the neighbour of the optimal symbol at the $i = 2$nd bit, corresponding to the decimal index 6, according to Figure 3.23. When FKT is applied in (a) the sets of the subsequent bits $i = 3, 4, 5, 6$ are also updated with the new symbols found. Similarly, when FBKT is applied in (b), the sets of the preceding and the subsequent bits are updated along with the sets of the $i = 2$nd bit for which the search was performed.

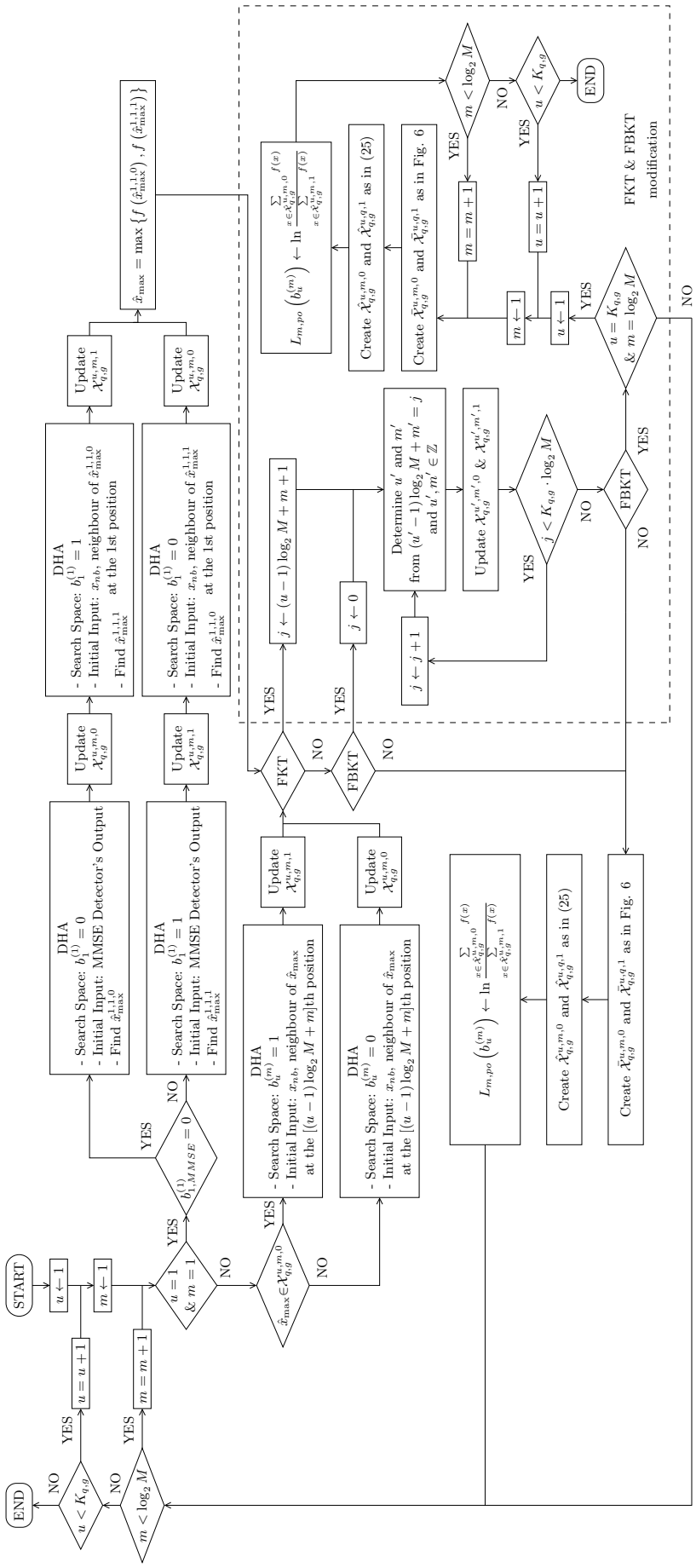

Figure 3.28: Flow Chart of the SO-DHA-MUA MUD with the NE modification, as well as the FKT and FBKT methodologies of Section 3.5.2.2 and Section 3.5.2.3.

last bit of the multi-level symbol $i = U_{q,g} \cdot \log_2 M$. Based on the FBKT, all the bit-based LLRs of that particular $N_{q,g}$-ary symbol will be computed based on $x_{\max}$, as if it was found during the first search. If no knowledge transfer was employed, or even if the above-mentioned FKT was used in the same scenario, only the last bit's LLR would exploit $x_{\max}$ and hence calculate an LLR close to that of the MAP MUD. An example of the FBKT is portrayed in Figure 3.27b. The flowchart of the DHA-MUA MUD with and without the aid of the FKT or the FBKT is depicted in Figure 3.28.

3.6 Soft-Output Ant Colony Optimization with Free Will

The ACO algorithm of [145] employs ζ ants during Ξ generations. In the ξth generation, with $\xi = 1, 2, \ldots, \Xi$, every ant chooses a $(U_{q,g} \cdot \log_2 M)$-bit long binary path, having a decimal representation corresponding to a specific symbol index. According to the ACO algorithm [145], if all ζ ants follow the same path during a single generation, the ACO algorithm is deemed to have converged and it is stopped at that particular generation. When the Soft-Output-ACO (SO-ACO) MUDs proposed in [13, 63] are employed in heavily rank-deficient systems, they may converge with a high probability to a local optimum, rather than to the globally optimal symbol $x_{\max}$. Therefore, the performance of the SO-ACO MUDs may be degraded in rank-deficient systems and its complexity may vary, depending on the number of generations that were evaluated before the ACO algorithm converged.

For the sake of circumventing these problems and for improving the performance, while fixing the complexity to a predetermined number of CFEs, we introduce a mutation probability [64], which may be interpreted as the *free will*[3] (FW) of the ants. According to the FW, after each ant has chosen its path for the current generation based on both the pheromone and on the intrinsic affinity [13], we introduce the concept of mutation probability, namely the probability that a bit of the selected path will change its value. For example, if an ant has chosen the [01|10|11] path in a system where $U_{q,g} = 3$ users transmit QPSK ($M = 4$) symbols, and the FW probability is chosen to be $p_{fw} = 0.1$, then there is a $0.1 \cdot 0.9^5 = 0.06$ probability of the final path to be [11|10|11]. Furthermore, there also is a 0.06 probability for the final path to be [01|10|01], while there is a $0.9^6 = 0.53$ probability of the selected path to remain unchanged.

By introducing the concept of FW, we deliberately expand the search space by introducing new symbols that might not have been visited otherwise, and the attainable performance is therefore expected to be improved. At the same time, the ACO algorithm has a modest, but non-negligible probability of convergence given by $(1 - p_{fw})^{\zeta \cdot U_{q,g} \cdot \log_2 M}$, which corresponds to the unlikely scenario, where none of the ants changed the initially selected paths. Therefore, the complexity may be considered as being fixed to $(\zeta \cdot \Xi)$ number of CFEs.

The NE modification proposed for the DHA-MAA and DHA-MUA QMUDs may also

[3]The free will probability of an ant in the ACO algorithm may be considered as the equivalent of the mutation probability of a chromosome in the genetic algorithm.

be used for the SO-ACO MUDs. More specifically, during the ACO-MAA-NE MUD the neighbours of the best found symbol $\hat{x}_{\max}$ of the first ACO search applied to the total search space are also considered as candidates for the calculations of the LLRs. Moreover, when the ACO is employed twice in the ACO-MUA-NE MUD for the ith bit, the neighbour of the best found symbol in these two ACO calls is included for the ith bit's LLR calculation. On the other hand, if the ACO-MUA-FKT-NE MUD is employed, the neighbour of the "best-so-far" symbol of all the ACO searches up to the ith bit's searches is included in the ith bit's LLR calculation. Finally, in the ACO-MUA-FBKT-NE MUD the neighbours of the best found symbol after all the ACO searches have been completed for the current multi-level symbol are included in all the LLR calculations.

The corresponding complexity of the ACO-MAA-NE-FW MUD becomes

$$\mathcal{C}_{SO-ACO}^{MAA,NE,FW,\min} = \frac{\zeta \cdot \Xi}{U_{q,g} \cdot \log_2 M} + 1 \tag{3.107}$$

CFEs per bit, where the first additive term corresponds to the number of CFEs of the sole ACO based search in the total search space divided by the number of bits in the $M^{U_{q,g}}$-ary symbol, while the second term represents the extra CFE required for the calculation of the best found symbol's neighbour for each bit. If no FW is used in the ACO, then the complexity of the ACO-MAA-NE is expected to be lower, since the ACO will converge sooner with a high probability. Nonetheless, it might converge to a local optimum. The total complexity of the ACO-MUA-NE-FW MUD is equal to

$$\mathcal{C}_{SO-ACO}^{MUA,NE,FW,\min} = 2 \cdot \zeta \cdot \Xi + 1 \tag{3.108}$$

CFEs per bit, since two ACO activations take place for each bit and a neighbour's CF value is calculated.

3.7 Soft-Output Detection Performance in DSS/SSCH SDMA-OFDM Systems

In this section we evaluate the soft-output BER performance versus complexity performance of our proposed families DHA QMUDs in the uplink of DSS/USSCH SDMA-OFDM systems. The first communication system investigated supports $U = 8$ users transmitting QPSK $M = 4$ symbols and the base station is equipped with $P = 4$ AEs. We adopt a channel model used in the Long Term Evolution (LTE) standard, termed as the Extended Vehicular A (EVA) model [146]. We assume an urban vehicular scenario, where the velocity of each mobile user is $v = 30$ km/h, the carrier frequency is $f_c = 2.5$ GHz, the sampling frequency is equal to $f_s = 15.36$ MHz and hence the Doppler frequency is $f_d \simeq 70$ Hz. The users transmit on $\mathcal{Q} = 1024$ OFDM subcarriers and the length of the cyclic prefix (CP) is 128. For comparison between the iterative DHA QMUDs and the SO-ACO MUDs, let us firstly investigate a scenario where all users transmit on all the subcarriers. Moreover, we will also temporarily assume that all the users have been allocated the same DSS

Table 3.4: Parameters of the SDMA-OFDM uplink scenario

Number of Users	$U = 8$
Number of AEs per User	$N_{T_x} = 1$
Number of AEs at the BS	$P = 4$
Normalized User-Load	$U_L = U_{q,g}/P = 2$
Modulation	QPSK $M = 4$
Channel Code	TCC, $R = 1/2$, 8 trellis states
	$I_{\text{inner}} = 4$ iterations
Mobile Velocity	$v = 30$ km/h
Carrier Frequency	$f_c = 2.5$ GHz
Sampling Frequency	$f_s = 15.36$ GHz
Doppler Frequency	$f_d = 70$ Hz
Channel Model	Extended Vehicular A [146]
Number of Subcarriers	$\mathcal{Q} = 1024$
Cyclic Prefix	CP = 128
Number of Subcarriers per User	$W = 1024$
Number of DSS codes	$G = 1$
Bit Interleaver Length	10 240 symbols per user

code, therefore they all interfere with each other, hence the resultant system becomes an SDMA-OFDM system. The interleaver length is equal to 10 240 symbols per user and turbo convolutional codes associated with a rate of $R = 1/2$, 8 trellis states and $I_{\text{inner}} = 4$ inner iterations are employed. The specifications of our SDMA-OFDM system are summarized in Table 3.4.

Observe in Figure 3.29, that the ACO-MAA MUD and ACO-MUA MUD are exactly as proposed in [13] and [63], respectively, when employed in the context of the SDMA-OFDM system of Table 3.4. These may be compared to the BER curves of the MAP MUD, as well as to those of the proposed ACO-MAA-FW, ACO-MAA-NE, ACO-MAA-NE-FW, ACO-MUA-NE-FW, ACO-MUA-FKT, ACO-MUA-FKT-NE-FW, ACO-MUA-FBKT and ACO-MUA-FBKT-NE-FW MUDs, which are gathered in Table 3.5. After appropriate tuning of the ACO for minimizing the BER, we have opted for the pheromone weight of $a = 1$, the intrinsic affinity weight of $\beta = 6$, while the weight of the elite ant was set to $\sigma = 8$ and the evaporation rate to $\rho = 0.5$ [63] for the ACO-aided searches in all the ACO-based MUDs. The number of ants in the ACO-MAA MUDs is equal to $\zeta = 44$, and the number of generations is also $\Xi = 44$. Similarly, in the ACO-MUA MUDs invoked for our SDMA-OFDM system of Figure 3.29 we employ $\zeta = 27$ ants during $\Xi = 27$ generations, while $\zeta = 25$ ants and $\Xi = 25$ generations are used in the ACO-MUA-FKT and ACO-MUA-FBKT MUDs. Explicitly, we have selected these values for achieving a similar average number of CFEs per bit between the ACO-FW-based MUDs and the DHA-based QMUDs. The FW probability, when used, is chosen to be equal to $p_{FW} = 0.1$. The parameters of the ACO instances are gathered in Table 3.6.

According to Figure 3.29, the BER curves of the ACO-MAA and ACO-MAA-NE MUDs

Table 3.5: Algorithmic elements of the prototype detectors

Search Algorithm:	• Dürr-Høyer Algorithm (DHA). • Ant Colony Optimization (ACO) Algorithm.
Approximation:	• MAximum Approximation (MAA): Each LLR is computed based on the pair of symbols that maximize the CF both in its numerator and denominator, respectively, as in Equation 3.95. • MUlti-input Approximation (MUA): Each LLR is computed based on a carefully selected subset of symbols, as in Equation 3.101, Equation 3.102 and Equation 3.103.
Knowledge Transfer:	After the completion of the selected search algorithm for the $i = [(u-1)\log_2 M + m]$th bit position • OFF: Only $\mathcal{X}_{q,g}^{u,m,0}$ and $\mathcal{X}_{q,g}^{u,m,1}$ are updated with the search results. • Forward Knowledge Transfer (FKT): The sets $\mathcal{X}_{q,g}^{u',m',0}$ and $\mathcal{X}_{q,g}^{u',m',1}$ are updated with the search results, for all $[u', m']$ values satisfying $(u'-1)\log_2 M + m' \geq i$ with $u' = 0, 1, \ldots, U_{q,g}$, $m' = 0, 1, \ldots, \log_2 M$. • Forward & Backward Knowledge Transfer (FBKT): All the sets $\mathcal{X}_{q,g}^{u,m,0}$ and $\mathcal{X}_{q,g}^{u,m,1}$ are updated with the search results, for $u = 0, 1, \ldots, U_{q,g}$, $m = 0, 1, \ldots, \log_2 M$.
Neighbour Exploitation (NE):	• OFF: If a set $\mathcal{X}_{q,g}^{u,m,\mathrm{v}}$ is empty for a specific $[u, m, \mathrm{v}]$ value, the search algorithm employed is initiated again for the search space corresponding to the $[u, m, \mathrm{v}]$ value. • ON: The neighbour x_{nb} of the best-so-far found symbol $\hat{x}_{\max}$ at each bit position is included as a candidate for the calculation of the respective LLR. If the DHA is used, x_{nb} is the initial input when possible. No set $\mathcal{X}_{q,g}^{u,m,\mathrm{v}}$, for $u = 1, 2, \ldots, U_{q,g}$, $m = 1, 2, \ldots, \log_2 M$, $\mathrm{v} = 0, 1$ will be empty with NE.
Free Will (FW):	Applicable only when the ACO algorithm is chosen as the search algorithm. • OFF: Conventional ACO algorithm employed in [13, 63]. • ON: After an ant has selected a step along its path, which corresponds to a specific bit position, during each generation, there is a predetermined FW mutation probability to flip that bit's value for that specific ant's path.

of Table 3.5 are approximately 7.25 dB and 8.25 dB away from the MAP MUD's limit for a BER of 10^{-1}, respectively. Furthermore, the ACO-MAA and ACO-MAA-NE MUDs reach a BER floor of $\sim 10^{-3}$, indicating that the ACO-MAA MUDs' performances are degraded in rank-deficient systems supporting a normalized user-load of $U_L = U/P = 2$. The ACO-MAA-NE MUDs attain a modest performance improvement in rank-deficient systems supporting $U_L = 2$ over the respective ACO-MAA MUDs, and they also have a lower complexity than the ACO-MAA MUD when no FW is enabled, since only a single ACO search is performed, when the NE modification is applied. In our scenario of Figure 3.29 the average number of CFEs per bit is approximately three times lower in the ACO-MAA-NE MUD compared to the ACO-MAA MUD.

When the FW-based mutation is enabled in the ACO-MAA-FW and ACO-MAA-NE-FW MUDs of Table 3.5, the BER performances become better than those of the ACO-MAA or ACO-MAA-NE MUDs. More precisely, the ACO-MAA-FW and ACO-MAA-NE-FW MUDs reach a BER of 10^{-5} when operating 4.9 dB and 4.85 dB away from the MAP MUD.

Table 3.6: Parameters of the ACO in the SDMA-OFDM scenario

Number of Ants	MAA:	$\zeta = 44$ ants
	MAA-NE:	$\zeta = 44$ ants
	MUA:	$\zeta = 27$ ants
	MUA-FKT:	$\zeta = 25$ ants
	MUA-FBKT:	$\zeta = 25$ ants
Number of Generations	MAA:	$\Xi = 44$ generations
	MAA-NE:	$\Xi = 44$ generations
	MUA:	$\Xi = 27$ generations
	MUA-FKT:	$\Xi = 25$ generations
	MUA-FBKT:	$\Xi = 25$ generations
Pheromone Weight	$a = 1$	
Intrinsic Affinity Weight	$\beta = 6$	
Weight of Elite Ant	$\sigma = 8$	
Evaporation Rate	$\rho = 0.5$	
Free Will Probability	$p_{FW} = 0.1$	

Still referring to Figure 3.29, the performances of the ACO-MUA and ACO-MUA-NE-FW MUDs of Table 3.5 are also seen to be close to those of the ACO-MAA and ACO-MAA-FW MUDs, respectively. This is because in rank-deficient systems the ACO algorithm fails in finding the true globally maximal symbol $x_{\max}$ for the numerator and the denominator of each bit of a multi-level symbol, even if FW-based mutation is adopted. Note that when the FW-based mutation is not used, the performance of the SO-ACO-MUA MUD becomes worse than those of the ACO-MAA and of the ACO-MAA-NE MUDs. The reason for this observation is that according to the MUA approach of [63], when $x_{\max}$ is found during the two ACO activations for the ith bit, it will only be used for the LLR calculation of the ith bit. This is in contrast to the MAA approach of [13], where $x_{\max}$ is exploited for the calculation of all the LLRs provided that it has been found. The search space of the first ACO employment in the MAA approach has twice the size with respect to the search spaces of the ACO calls in the MUA approach. However, even in conjunction with the provision of a larger number of ants and generations, $x_{\max}$ may not be found by the ACO search in the MAA approach. When FW-based mutation is used, the ant population does not converge, therefore the incident of evaluating $x_{\max}$ becomes more frequent in the FW-aided MUA approach. The increased probability of finding $x_{\max}$, in conjunction with the use of a subset of legitimate symbols for calculating the LLR in the ACO-MUA-NE-FW results in a better performance than that of the ACO-MAA-FW and ACO-MAA-NE-FW MUDs of Table 3.5.

When the proposed FKT of Section 3.5.2.2 is adopted in the MUA approach, the performance is improved, as it may be verified by observing the ACO-MUA-FKT MUD's and ACO-MUA-FKT-NE-FW MUD's curves in Figure 3.29. Upon invoking the FKT of Table 3.5 in the ACO, if $x_{\max}$ is found during one of the ith bit's ACO searches, then it will also be included in the LLR calculations of the subsequent bits, even if those bits' ACO calls

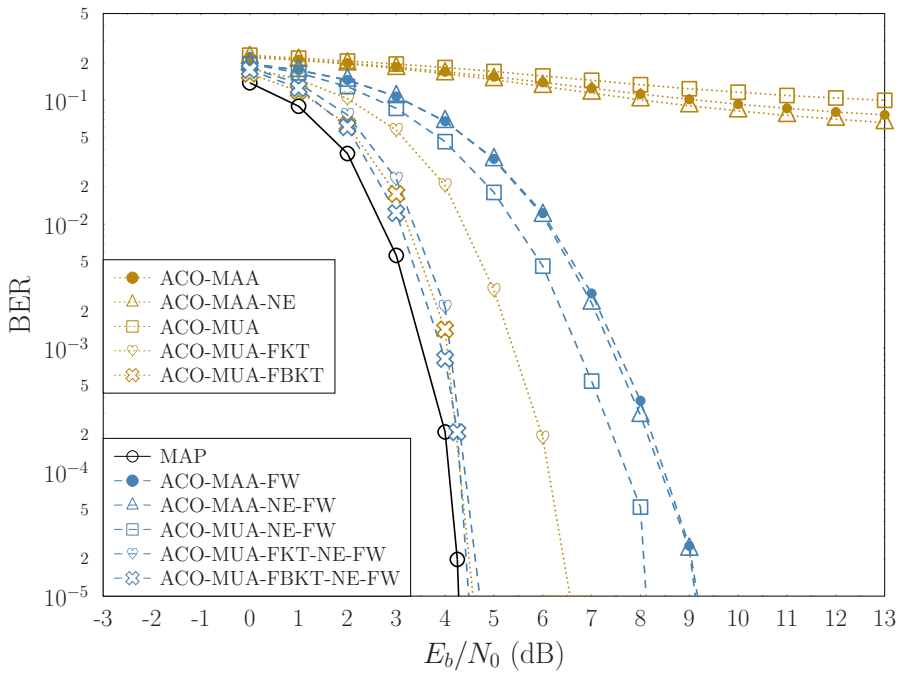

Figure 3.29: BER versus E_b/N_0 performance in the rank-deficient SDMA-OFDM system of Figure 3.1, using the parameters of Table 3.4, supporting a normalized user-load of $U_L = U/P = 2$ when the MAP MUD and various modifications of the ACO-MAA and ACO-MUA MUDs with neighbour exploitation, free will, forward knowledge transfer, as well as forward and backward knowledge transfer are employed. The algorithmic elements of the detectors are summarized in Table 3.5 and the parameters of the ACO are stated in Table 3.6. All the MUDs provide soft outputs and only one iteration is allowed between the MUD and the decoder.

failed to find $x_{\max}$ on their own. Hence, by using the FKT of Table 3.5, the accuracy of the LLR values is greatly improved provided that $x_{\max}$ is found, hence gradually approaching the LLR values of the SO-MAP MUD. Similarly, the BER performances of the ACO-MUA-FBKT and ACO-MUA-FBKT-NE-FW MUDs of Table 3.5 become even better than that when the FKT is used, since all the LLRs exploit $x_{\max}$, provided it is indeed found during any of the ACO searches employed for that particular $N_{q,g}$-ary symbol. Upon invoking the FBKT of Table 3.5 there is a trade-off between the attainable performance and the delay imposed, since the calculation of the LLR of each bit in a multi-level symbol has to be stalled until after all the searches have been completed. In all the ACO-based MUDs of Table 3.5 the performance is improved, when the FW-based mutation is adopted. When the FKT or the FBKT is used, the memory requirements are increased.

The SO-DHA QMUDs of Figure 3.24 and Figure 3.28, which are also summarized in Table 3.5, perform better than their classical ACO MUDs counterparts, as shown in Figure 3.30, where we compare the SO-DHA QMUDs to our novel SO-ACO MUDs using both the NE and FW, which outperform the ACO MUDs presented in [13, 63], as evidenced in Figure 3.29. Since the DHA succeeds in finding $x_{\max}$ with ∼100% probability, the DHA-MAA, DHA-MAA-NE and DHA-MUA QMUDs of Figure 3.24, Figure 3.28 and Table 3.5 experience improved BER curves in contrast to the ACO-MAA-FW, ACO-MAA-NE-FW and ACO-MUA-FW MUDs. The DHA-MAA and DHA-MAA-NE QMUDs perform within about 1.35 dB and 1.45 dB, respectively, of the MAP MUD's limit at a BER of 10^{-5}. The

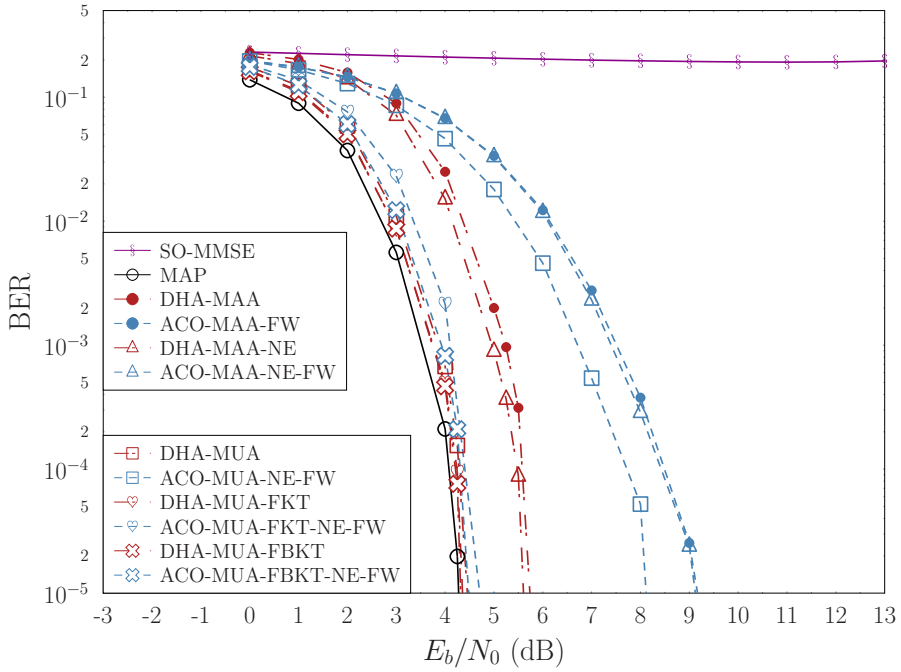

Figure 3.30: BER performance with respect to E_b/N_0 in the rank-deficient SDMA-OFDM system of Figure 3.1, using the parameters of Table 3.4 when the MAP MUD and various DHA QMUDs, as well as ACO MUDs with free will are employed. The effects of the modifications of neighbour exploitation, forward knowledge transfer, as well as forward and backward knowledge transfer on the BER of the ACO-FW MUDs and the DHA QMUDs are illustrated. The algorithmic elements of the detectors are summarized in Table 3.5 and the parameters of the ACO are stated in Table 3.6. All the MUDs provide soft outputs and only one iteration is allowed between the MUD and the decoder.

DHA-MUA QMUD performs better than the ACO-MUA-FBKT-NE-FW MUD, which is the best-performing MUD from the family of SO-ACO MUDs, demonstrating the attractive performance versus complexity potential of the QMUDs. As expected, the DHA-MUA-FKT and DHA-MUA-FBKT QMUDs have an improved performance, despite their lower complexity than that of the DHA-MUA QMUD. Since information about the searched symbols is transferred between the relevant bits after each DHA application in the FKT and FBKT, there is a higher probability that the next DHA call will have as an initial input a symbol with a closer CF value to that specific search space's optimal symbol's CF value. This leads to fewer CFEs before that optimal symbol is found by the DHA. The BER performances of the DHA-MUA QMUDs closely match the MAP limit of Figure 3.30. The specific effect that the FKT and FBKT modifications have on the DHA-MUA QMUD is minor compared to their effect on the ACO-MUA MUDs, since all the DHA-MUA QMUDs find $x_{\max}$ during the first two DHA calls.

The complexity expressed in terms of the total number of CFEs performed per bit both in the classical and the quantum domain of the analysed soft DHA QMUDs and SO-ACO MUDs is depicted in Figure 3.31 versus the E_b/N_0 values. The total number of CFEs of all the SO-ACO MUDs that use FW is fixed and independent of the E_b/N_0 values. More specifically, the exact number of CFEs per bit for the ACO-MAA-FW MUDs is 122 CFEs according to both Equation 3.107 and Figure 3.31, while the complexity

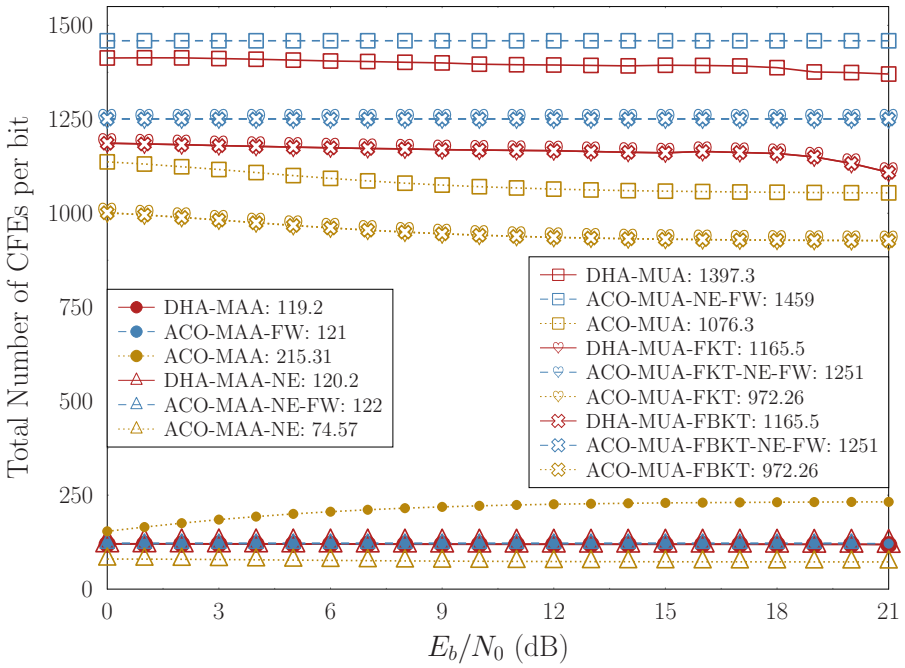

Figure 3.31: Complexity in terms of total number of CFEs per bit of each MUD and QMUD employed in the SDMA-OFDM system of Figure 3.1, using the parameters of Table 3.4 with respect to the E_b/N_0 values. The BER performances of the ACO-based MUDs and DHA-based QMUDs are depicted in Figure 3.29 and Figure 3.30, respectively. The average number of CFEs per bit of each MUD is stated at the legend. The complexity of the MAP MUD is 4096 CFEs per bit. The algorithmic elements of the detectors are summarized in Table 3.5 and the parameters of the ACO are stated in Table 3.6. All the MUDs provide soft outputs and only one iteration is allowed between the MUD and the decoder.

of the ACO-MUA-FW MUD is 1459 CFEs and that of both the ACO-MUA-FKT-NE-FW and ACO-MUA-FBKT-NE-FW MUDs is 1251 CFEs based on Equation 3.108 and Figure 3.31. The complexities of the SO-DHA QMUDs are reduced only marginally versus the transmit power. Therefore they may be practically considered as being fixed even in the context of rank-deficient systems. This phenomenon is observed due to the E_b/N_0-related improvement of the MMSE detector's output, which is the input of the first DHA call, as investigated in [2]. If the DHA-QWSA QMUD [1] was employed in our SDMA-OFDM system in conjunction with 11 qubits in the Quantum Control Register (QCR) of Figure 3.5, its minimum complexity would be 32 792 CFEs per bit for $U_{q,g} = 6$ and $M = 4$ [1], which is significantly higher than both that of the MAP MUD and the SO-DHA QMUDs. The DHA-QWSA QMUD aims to operate in systems supporting many users and multiple MUD-decoder iterations, while its performance matches that of the MAP MUD, provided that the number of qubits in the QCR is sufficiently high. Observe in Fig. 3.30 that the DHA QMUDs with no MUD-decoder iterations perform close to the MAP MUD's limit and they only impose a fraction of the complexity that DHA-QWSA QMUD does.

The specific choice of the number of ants ζ and generations Ξ in the SO-ACO MUDs was specifically arranged to make the complexities of the iterative DHA QMUDs and of the respective ACO-FW MUDs comparable. The MAP MUD performs 4096 CFEs per bit in our SDMA-OFDM system, which is higher than that of all the investigated MUDs. The

Table 3.7: Comparison of the MUDs in the SDMA-OFDM system of Table 3.4

MUD	Distance from MAP MUD at BER $= 10^{-5}$ (dB)	Complexity at BER $= 10^{-5}$ (CFEs / bit)	Increased Delay	Increased Memory Requirements
MAP	0	4096	✓	✓✓✓
DHA-MAA	1.46	119.4		
ACO-MAA-FW	4.90	121		
ACO-MAA	(BER $= 0.1$) 8.25	(BER $= 0.1$) 218.77		
DHA-MAA-NE	1.32	120.4		
ACO-MAA-NE-FW	4.85	122		
ACO-MAA-NE	(BER $= 0.1$) 7.25	(BER $= 0.1$) 75.06		
DHA-MUA	0.18	1409		
ACO-MUA-NE-FW	3.81	1459		
ACO-MUA	(BER $= 0.1$) 13.25	(BER $= 0.1$) 1060		
DHA-MUA-FKT	0.08	1176.8		✓
ACO-MUA-FKT-NE-FW	0.44	1251		✓
ACO-MUA-FKT	2.29	955.2		✓
DHA-MUA-FBKT	0.045	1177.42	✓	✓✓
ACO-MUA-FBKT-NE-FW	0.2	1251	✓	✓✓
ACO-MUA-FBKT	0.67	967.73	✓	✓✓

complexities of a system that employs FKT and one that uses FBKT are the same, since they have the same effect on the subsequent searches. Furthermore, the difference in the number of CFEs per bit between the DHA-MAA and the DHA-MAA-NE QMUDs is only 1 CFE, corresponding to the CFE of the best found symbol's neighbour for each bit.

The complexity of the ACO-MAA MUD is seen to be higher in Figure 3.31 than those of the ACO-MAA-NE, ACO-MAA-FW and ACO-MAA-NE-FW MUDs, as well as than those of the DHA-MAA QMUDs, since the ACO-aided search is re-employed, unless a symbol corresponding to each bit's value is found. This is not an issue in the ACO-MAA-NE MUD, where the ACO is called only once. Based on this fact, it may be observed in Figure 3.31 that the complexity of the ACO-MAA-NE MUD is the lowest of the MUDs based on MAA, as are the complexities of the ACO-MUA MUDs of Table 3.5 operating without FW and NE with respect to the rest of the MUDs based on MUA.

Table 3.7 summarizes both the performance and complexity, as well as the delay and memory requirements of the MUDs employed. The check mark (✓) in Table 3.7 indicates the existence of delay or increased memory requirement, when compared to the MAA and MUA methodologies. The number of check marks represents the size of the increase. Even though the ACO-MUA-FBKT needs fewer CFEs per bit on average than the DHA-MUA,

DHA-MUA-FKT and DHA-MUA-FBKT QMUDs according to Figure 3.31, its performance is slightly worse than that of the above-mentioned QMUDs according to Figure 3.29 and Figure 3.30. Furthermore, the comparison of the DHA-MUA-FKT and DHA-MUA-FBKT QMUDs indicates that there is no substantial benefit in tolerating an increased delay, since the performance of the higher-delay systems is almost identical. Finally, when we compare the DHA-MUA QMUD to the ACO-MUA-FBKT MUD, a trade-off between the complexity versus the extra delay - and memory - requirements has to be struck, with the DHA-MUA QMUD offering a better performance.

3.8 DSS-based Uniform Slow Subcarrier Hopping Versus Uniform Slow Subcarrier Hopping

Let us now proceed to the uplink scenario of the DSS/SSCH SDMA-OFDM system of Figure 3.1, where $U = 24$ users transmitting QPSK ($M = 4$) symbols are supported, there are $P = 2$ receive AEs at the BS and $G = 2$ WH DSS codes are allocated to the $U = 24$ users. Furthermore, each user transmits on $W = 512$ out of the $\mathcal{Q} = 1024$ subcarriers. The subcarrier allocation algorithm is performed every $T_h = 2$ OFDM frames. The new parameters are summarized in Table 3.8, while the rest of the parameters are the same as in Table 3.4. Since there are $U = 24$ users and $G = 2$ DSS codes, $U/G = 12$ users will be allocated the $g =$ 1st code and the remaining 12 users will have the code associated with $g = 2$. Similarly, since each user transmits on W subcarriers, the number of subbands is also $W = 512$. The number of subcarriers per subband is $SB = \mathcal{Q}/W = 2$. According to the DSS-based USSCH and the example presented in Figure 3.3, $U_1 = 6$ users with the $g =$ 1st code will be allocated to one of the $SB = 2$ subcarriers of a subband and the other $U_2 = 6$ users will be allocated to the remaining subcarrier in the same subband. Therefore, we expect to support $U_{q,g} = 6$ for $q = 1, 2, \ldots, 1024$ and $g = 1, 2$. Indeed, by observing Figure 3.32, where we compare the proposed DSS-based USSCH to the USSCH and the RSSCH [21] for the same DSS code allocated to the same subcarrier, it is verified that $U_{q,g} = 6$ can be supported for all values of q and g in the DSS-based USSCH. On the other hand, when the USSCH is used in our system supporting $U = 24$ users, the allocation of the $U_1 = 12$ users which have been allocated the same DSS code on the two subcarriers of each subband varies from 6 users to each subcarrier up to the rare incident, where all 12 users are allocated to one of the two subcarriers causing an excessive amount of unnecessary MUI and simultaneous increase in complexity, albeit this only occurs with a probability of 10^{-6}. Quantitatively, if the MAP MUD is employed in the DSS-based USSCH system the average complexity would be

$$C_{MAP}^{DSS/USSCH} = \sum_{U_{q,g}=1}^{\infty} \frac{p_{U_{q,g}} \cdot M^{U_{q,g}}}{U_{q,g} \cdot \log_2 M} = \frac{1 \cdot 4^6}{6 \cdot 2} = 341.33 \tag{3.109}$$

CFEs per bit, where $p_{U_{q,g}}$ is the probability of having $U_{q,g}$ users associated with the gth DSS code on the qth subcarrier. On the other hand, the average complexity in the USSCH

Table 3.8: Parameters of the DSS/USSCH SDMA-OFDM uplink scenario

Number of Users	$U = 24$
Number of AEs at the BS	$P = 2$
Number of Subcarriers per User	$W = 512$
Number of DSS codes	$G = 2$
Normalized User-Load	
$\hookrightarrow$ DSS-based USSCH	$U_L = U_{q,g}/P = 3$
$\hookrightarrow$ USSCH	$U_L = U_{q,g}/P \in \{0, 0.5, \ldots, 6\}$
Subcarrier Allocation Period	$T_h = 2$ OFDM frames

system would be 1135.3 CFEs per bit according to Figure 3.32, while the complexity of the RSSCH was 3188.3 CFEs per bit for the system supporting 24 users.

Let us now also investigate a system, where $SF = 4$ WH DSS codes are allocated to $U = 235$ users. Let us assume furthermore that each user transmits on half of the available subcarriers, hence we have $SB = \mathcal{Q}/W = 2$. Since there are $K = 235$ users and 4 DSS codes, 59 users will be allocated to the first 3 DSS codes and 58 will be allocated to the last one according to Equation 3.1. When the DSS-based USSCH is used, exploiting the fact that $SB = 2$, the first DSS code group's users will be split as uniformly as possible between the two subcarriers. In other words, for each of the first three DSS code groups 29 users will be allocated to one subcarrier and the remaining 30 users will be allocated to the other subcarrier. For the last DSS code group, 29 users will be allocated to each subcarrier. As a result, 5 out of 8 times, or 62.5% of the time, we will have 29 users of the same DSS code group on the same subcarrier and 37.5% of the instances 30 users of the same DSS code group will transmit on the same subcarrier. The simulations of Figure 3.32 verify these expectations, resulting in an average complexity for the DSS-based USSCH which is $\sim$736 times lower than that of the USSCH system, when the MAP MUD is used.

In Figure 3.33 the BER curves of the DSS/USSCH SDMA-OFDM system employing the USSCH and the DSS-based USSCH procedures of Section 3.2.3 are combined with different MUDs. More specifically, the MAP MUD is used in both scenarios and the BER performance is improved by the system employing DSS-based USSCH by approximately 0.5 dB, as a benefit of its reduced MUI. Moreover, the average complexity of the MAP MUD is reduced from 1494 CFEs per bit in the USSCH system to 341.33 CFEs per bit in the DSS-based USSCH system, which is due to the fact that we have $U_{q,g} = 6$ for all values of g and q. Furthermore, in Figure 3.33 we employ the DHA-MUA-FKT QMUD of Figure 3.28 and Table 3.5 in our DSS-based USSCH scenario achieving a near-optimal performance, which is also better than that of the MAP MUD, when USSCH is used. As an added benefit, it has a lower complexity than both the MAP MUDs investigated in the context of the DSS/USSCH SDMA-OFDM system.

In Figure 3.33 we also present a hybrid DHA-MUA-FKT / MAP MUD, when USSCH is employed. According to Figure 3.32, the value of $U_{q,g}$ varies with respect to the specific subcarrier and DSS code group when USSCH is used. The average complexity of the DHA-

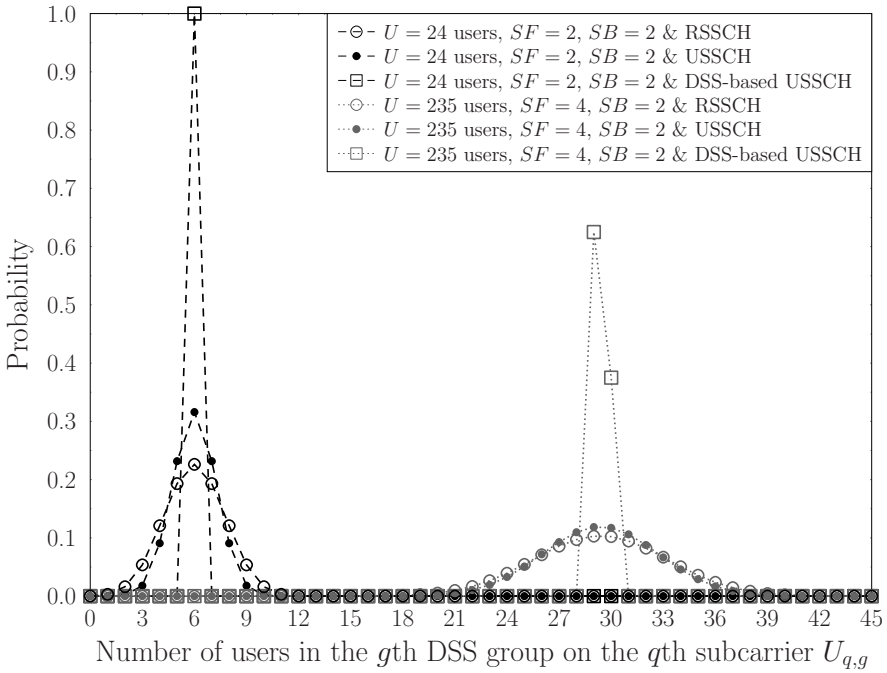

Figure 3.32: Histograms of the number of users who belong to the same gth DSS code group while transmitting on the qth subcarrier when the RSSCH, USSCH and the DSS-based USSCH are employed in the DSS/SSCH SDMA-OFDM system of Figure 3.1, using the parameters summarized in Table 3.8 and Table 3.4. The two subcarrier allocation schemes are compared in a system where $SF = 2$ WH DSS codes are allocated to $U = 24$ users who transmit on half of the available subcarriers $SB = \mathcal{Q}/W = 2$, as well as in a system where $SF = 4$ WH DSS codes are allocated to $U = 235$ users who also transmit on half of the available subcarriers.

MUA-FKT QMUD used by DSS-based USSCH system associated with $U_{q,g} = 6$ and $M = 4$ is 316.33 CFEs per bit. According to Equation 3.105, the minimum complexity of pure CFEs in the quantum domain employed in isolation if $U_{q,g} = 5$ and QPSK ($M = 4$) is used when the DHA-MUA-FKT QMUD is employed becomes

$$4.5 \cdot \sqrt{M^{U_{q,g}}/2} \cdot (U_{q,g} \log_2 M + 1)/(U_{q,g} \cdot \log_2 M) = 112.01$$

CFEs per bit, which is slightly higher than the MAP MUD's complexity of $4^5/10 = 102.4$ CD-CFEs per bit. Therefore, we introduce a threshold based on $U_{q,g}$ for activating either the use of the DHA-MUA-FKT QMUD or that of the MAP MUD. If $U_{q,g} \geq 6$ is true on the qth subcarrier, the DHA-MUA-FKT QMUD is employed, otherwise the MAP MUD performs the detection. The resultant SNR performance of the hybrid MUD is approximately 0.5 dB away from the MAP MUD's performance limit, while performing 34.1% of the CFEs that the MAP MUD requires.

3.9 Iterative Detection Performance in MC-IDMA Systems

In this section we investigate the behaviour, in the advanced context, when the system benefits from exchanging soft-information between the QMUD and the despreader / decoder

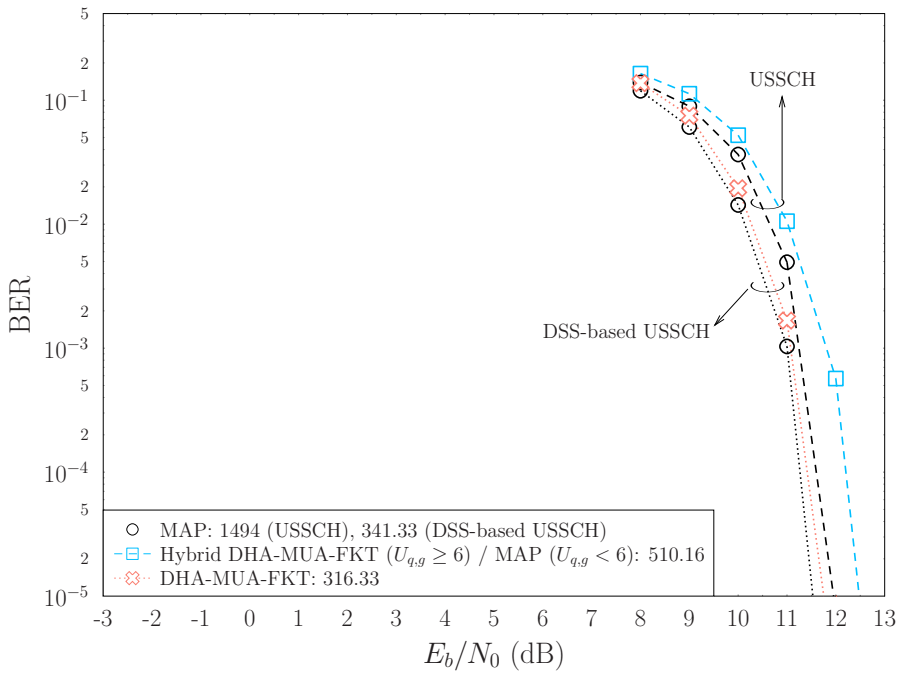

Figure 3.33: BER performance with respect to E_b/N_0 in the rank-deficient DSS/USSCH SDMA-OFDM system of Figure 3.1, using the parameters of Table 3.8, when the USSCH and DSS-based USSCH subcarrier allocation algorithms are used. The hybrid DHA-MUA-FKT / MAP MUD employs the DHA-MUA-FKT QMUD when the number of users on the qth subcarrier using the gth DSS code is higher than $U_{q,g} \geq 6$, otherwise the MAP MUD is employed. The numbers in the legend denote the average number of CFEs per bit for each MUD. Both MUDs provide soft outputs and only one iteration is allowed between the used MUD and the decoder.

(DES/DEC) in the context of an attractive MC-IDMA system [5] of Fig. 3.4, in contrast to Section 3.7, where we allowed only one MUD-DEC iteration in DSS/USSCH SDMA-OFDM systems. More specifically, the QMUDs perform approximations in the calculation of the bit-based LLRs of Equation 3.19 for the sake of avoiding all M^{U_q} CFEs of the classical MAP MUD. However, the specific values of the extrinsic LLRs calculated at the output of the QMUD affect both the decoding procedure and hence also the updated *a priori* probabilities $P(x)$. It is expected that if the QMUD outputs incorrect LLRs during the first QMUD-DES/DEC iteration, which we associate with erroneous signs or extremely high / low confidence, it will be difficult to correct them during the subsequent iterations, since the updated *a priori* LLRs will have been calculated based on these erroneous values. Therefore, we have to determine which approximations applied to the LLR calculations affect the suitability of the QMUDs to be implemented in iterative receivers and then compare the resultant QMUDs to the SISO DHA-QWSA QMUD, which was shown in Section 3.4.5 that it may be integrated in an iterative receiver.

Let us focus our investigations on the uplink of the sophisticated MC-IDMA system of Figure 3.4 supporting $U = 14$ users and transmitting QPSK symbols to $P = 4$ receive AEs. The system's parameters are summarized in Table 3.9. We have selected a half-rate non-systematic convolutional (NSC) code and $SF = 2$ for the repetition-spreading code, resulting in a total code rate of $R_{total} = R/SF = 1/4$. The Extended Typical Urban (ETU) channel model of [146] corresponds to a high-velocity scenario, of $v = 130$ km/h,

Table 3.9: Parameters of the 14-User MC-IDMA System

Number of Users	$U = 14$
Number of AEs per User	$N_{T_x} = 1$
Number of AEs at the BS	$P = 4$
Modulation	QPSK $M = 4$
Mapping Type	Gray for soft-output receivers & Set Partition for iterative receivers
Channel Code	Non-Systematic Convolutional Code, $R = 1/2$, 8 Trellis states
Spreading Factor	$SF = 2$
Number of Subcarriers	$\mathcal{Q} = 1024$
Cyclic Prefix	CP = 128
Number of Subcarriers per User	$W = 512$
Normalized User Load	$U_L = U \cdot N_{T_x} \cdot W/(P \cdot Q) = 7/4$
Subcarrier Allocation every	$T_h = 5$ OFDM symbol periods
Bit Interleaver Length	20 480 per User
Channel Model	Extended Typical Urban (ETU) [146]
Mobile Velocity	$v = 130$ km/h
Sampling Frequency	$f_s = 15.36$ MHz
Carrier Frequency	$f_c = 2.5$ GHz
Normalized Doppler Frequency	$f_d = 1.96 \cdot 10^{-5}$
Channel Estimation	Perfect, unless specified otherwise

which we use for representing the maximum Doppler frequency for this channel model. We assume practical scenarios, where we experience complex-valued continuously fluctuating Rayleigh-fading envelopes at the subcarriers. Since the normalized Doppler frequency of the independent Rayleigh fading channels on each tap of the ETU channel model is equal to f_d and we have $\mathcal{Q}$ subcarriers, the effective Doppler frequency F_d becomes

$$F_d = \mathcal{Q} \cdot f_d \simeq 0.02. \tag{3.110}$$

The normalized user load U_L is equal to 1.75, indicating a rank-deficient system, where conventional detectors would perform poorly. Since the $U = 14$ users transmit on half the subcarriers, we will have $U_q = 7$ for $q \in \{1, 2, \ldots, 1024\}$, allowing us to focus our discussions only on the qth subcarrier. Finally, the USSCH is applied every $T_h = 5$ OFDM symbol periods and every user transmits 20 480 bits per frame.

The BER performance of the DHA-MAA and DHA-MUA QMUDs employed in our MC-IDMA system described in Table 3.9 after $1, 2$ and 3 MUD-DES/DEC iterations is presented in Figure 3.34. The BER curves of the DHA-MUA QMUDs closely follow those of the MAP MUD, even when multiple MUD-DES/DEC iterations are employed, indicating that they are eminently suitable for iterative detection. On the other hand, we may observe that the performance of the DHA-MAA QMUDs is improved slower upon increas-

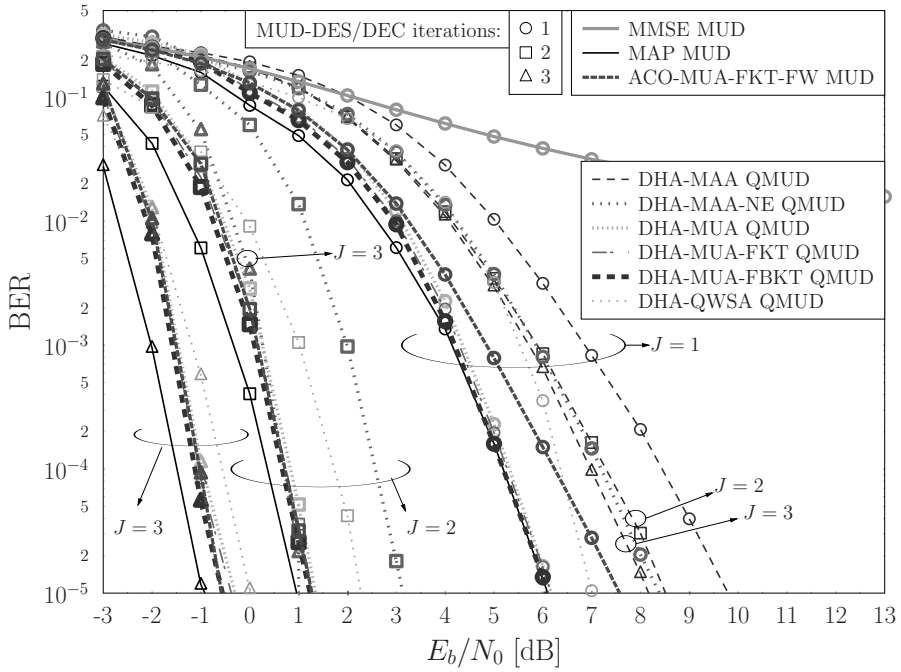

Figure 3.34: BER performance of the families of DHA-MAA QMUDs and DHA-MUA QMUDs, the DHA-QWSA QMUD, as well as the MAP MUD in the MC-IDMA system scenario of Figure 3.4, using the parameters of Table 3.9. The algorithmic elements of the detectors are summarized in Table 3.5.

ing the number of MUD-DES/DEC iterations. This is in contrast to the trend of both the MAP MUD and of the DHA-MUA QMUDs, both of which exhibit an approximately 5 dB improvement, when a second MUD-DES/DEC iteration is affordable. The DHA-MAA QMUD relying on Neighbour Exploitation (NE)[4] [3] performs better than the DHA-MAA QMUD. Quantitatively, it is only 2.1 dB away from the MAP MUD's curve at BER $= 10^{-5}$ after 3 MUD-DES/DEC iterations, compared to the 9 dB loss of the DHA-MAA QMUD. However, it still performs worse than the DHA-MUA QMUDs. Therefore, generating inflated LLRs based on the simplified LLR calculation of Equation 3.95 for the DHA-MAA methodology results in lower-quality *a priori* LLRs at the output of the DES/DEC of Figure 3.4. However, the DHA-MUA methodology, which uses the more accurate LLRs of Equation 3.103 exhibits an improved BER in Figure 3.34. The SISO DHA-MUA QMUDs also perform better than the DHA-QWSA QMUD with the aid of $l = 10$ control qubits, where the number of control qubits l in the DHA-QWSA QMUD determines both the precision of the LLRs' calculation, as well as the complexity of the QWSA as demonstrated in Section 3.4.5. Explicitly, if we use more control qubits in the DHA-QWSA QMUD, the extrinsic LLRs will become more accurate, but the complexity will be higher.

The complexities of the QMUDs employed are summarized in Table 3.10. As expected, the complexities per bit of the QMUDs are lower than that of the MAP MUD during the

[4]In the DHA-MAA QMUD, after the initial DHA search the sets $\mathcal{X}_q^{u,m,0}$ and $\mathcal{X}_q^{u,m,1}$ of each bit are updated with the search results. Naturally, one of the two sets of each bit will include the globally optimal symbol $x_{\max}$. When the Neighbour Exploitation modification is employed, the set of each bit that does not include the globally optimal symbol $x_{\max}$ will include its neighbour symbol x_{nb} at that specific bit position, as described in Steps 7 and 9 of Algorithm 3, regardless of whether it is among the DHA's search results or not.

Table 3.10: Complexity in terms of the number of CFEs / bit in Figure 3.34

E_b/N_0	6 dB	1 dB	−1 dB
MUD-DES/DEC Iterations	1	2	3
MAP	1170.30	1170.30	1170.30
DHA-MAA	67.40	139.27	210.65
DHA-MAA-NE	68.33	140.56	213.19
DHA-MUA	744.35	1390.24	1998.39
DHA-MUA-FKT	599.17	1204.95	1773.42
DHA-MUA-FBKT	599.17	1204.95	1773.42
DHA-QWSA	769.49	1472.09	2174.05

first MUD-DES/DEC iteration. When multiple MUD-DES/DEC iterations are used and we assume that perfect channel estimation is available before the first iteration with the aid of decision-directed channel estimation, then the complexity of the MAP MUD may remain constant, provided that we have sufficient memory for storing the CF values obtained during the first iteration. Naturally, in practical systems perfect channel estimation is unachievable, but a better channel estimate becomes available during each subsequent MUD-DES/DEC iteration, essentially forcing the MAP MUD to evaluate all the legitimate CF values again, hence resulting in 2340 and 3510 CFEs/bit after the second and third MUD-DES/DEC iteration, respectively. It is worth mentioning that according to Figure 3.34 the DHA-MUA QMUDs outperform the DHA-QWSA QMUD associated with $l = 10$, despite requiring fewer CFEs/bit, as seen in Table 3.10.

3.9.1 Gaussian Versus Non-Gaussian LLR Distributions and EXIT Chart Analysis

The effect that a simplified LLR calculation has on the MUD's performance may be observed on the inner EXIT curves, when they are generated under the Gaussian assumptions. Figure 3.35 shows the EXIT chart of our system under the assumption of having a Gaussian distribution at the output of the DHA-MAA and DHA-MAA-NE QMUDs, as well as for the MAP MUD at $E_b/N_0 = 0$ dB. The figure also includes the corresponding Monte-Carlo simulation based stair-case-shaped decoding trajectory, where each user has transmitted a frame of 20 480 bits. Similarly, Figure 3.36 depicts the EXIT chart relying on Gaussian assumptions for the DHA-MUA, DHA-MUA-FKT and DHA-MUA-FBKT QMUDs, as well as for the MAP MUD of the system described in Table 3.9.

According to Figure 3.35 and Figure 3.36, the QMUDs initially output a lower Mutual Information (MI) than the MAP MUD, but eventually "appear" to yield a higher MI, except for the DHA-MUA and DHA-QWSA QMUDs, which output smaller MI than the MAP MUD for any input. However, we will demonstrate that this fact does not represent the reality. To elaborate a little further, the investigated QMUDs always generate extrinsic LLRs, which have the same polarity as those of the MAP MUD. Due to the fact that the

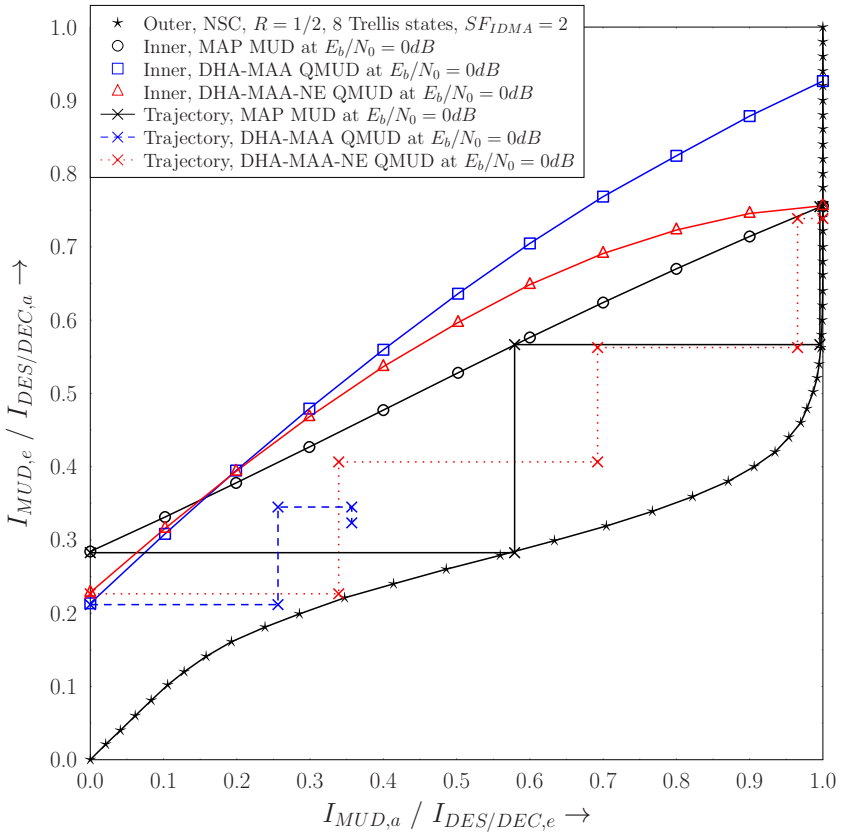

Figure 3.35: EXIT chart of the DHA-MAA and DHA-MAA-NE QMUDs in the MC-IDMA system scenario of Figure 3.4, using the parameters of Table 3.9. The algorithmic elements of the detectors are summarized in Table 3.5. The inner and outer average EXIT curves of the MI are presented, along with the inner EXIT curves that take into consideration the standard deviation. Moreover, a snapshot of the inner EXIT curves and the corresponding trajectories are shown.

DHA-MAA QMUDs generate their LLRs according to Equation 3.95 and that most of the time they do not use the optimal symbols - either for the numerator or for the denominator - we expected to obtain LLR values having the correct polarity, but a higher confidence than they should truly have. Therefore, their inner QMUD EXIT curves erroneously give the impression that the QMUDs outperform the MAP MUD.

The DHA-QWSA QMUD estimates the total sum in the numerator and denominator of every bit-based LLR, therefore its inner EXIT curve seen in Figure 3.36 is expected to have a lower MI at its output than the MAP MUD. The DHA-MUA QMUD may be considered as a special case of the DHA-MAA QMUD. In more detail, during the two DHA search processes of the first bit, the globally optimal symbol is found. This and only this globally optimal symbol is copied into the appropriate symbol sets of all the bits of the multi-level symbol. Note that no DHA search is performed for those sets, since the optimal symbol has already been found. According to the algorithm of Figure 3.28 and Algorithm 6, the LLR of each bit in the DHA-MUA will be calculated by using the same number of symbols in the numerator and the denominator. Therefore, the DHA-MUA QMUD will calculate each bit-based LLR using the globally optimal symbol and the best symbol found for that set's counterpart, which is the best symbol for that bit's value, because the DHA will have

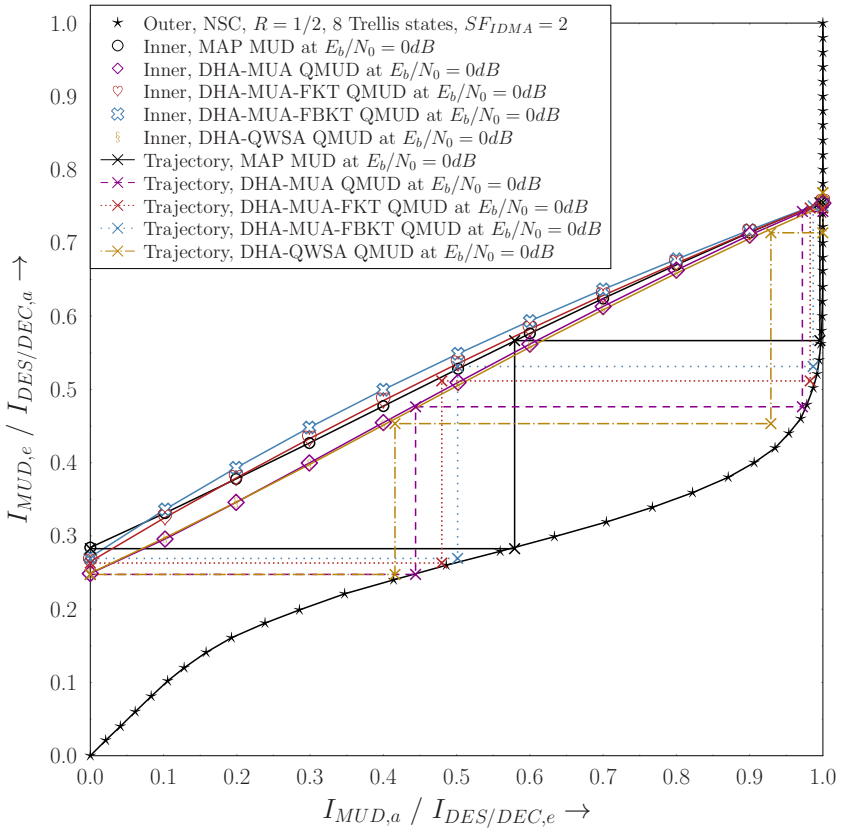

Figure 3.36: EXIT chart of the DHA-MUA, DHA-MUA-FKT, DHA-MUA-FBKT and DHA-QWSA QMUDs in the MC-IDMA system scenario of Figure 3.4, using the parameters of Table 3.9. The algorithmic elements of the detectors are summarized in Table 3.5. The inner and outer average EXIT curves of the MI are presented, along with the EXIT inner curves that take into consideration the standard deviation. Moreover, a snapshot of the inner EXIT curves and the corresponding trajectories are shown.

found it with ∼100% success probability. In a nutshell, the DHA-MUA QMUD calculates an LLR by using the single best symbols of each sets, achieving the correct polarity with the maximum possible confidence, when following our MUA algorithm of Algorithm 6. This is the reason why the output MI of the DHA-MUA QMUD is always lower than that of the optimal MAP MUD, except for the case of $I_{MUD,a} = 1$, when the MAP MUD is also using only the single best symbol of each set for calculating a bit's LLR.

Moreover, all the EXIT curves seen in Figure 3.35 and Figure 3.36 have been generated using Gaussian-distributed LLRs as their inputs, which is one of the necessary requirements to be satisfied for creating an accurate EXIT chart as a design tool [9]. In practice, this has been adopted because the outputs of both the widely used MUDs as well as of the channel decoders follow the Gaussian distribution, provided that their input is also Gaussian distributed. Since the initial input of the MUD obeys the Gaussian distribution with zero mean and zero standard deviation - this scenario corresponds to the $I_{MUD,\,a} = 0$ point - the generation of EXIT curves using input LLRs obeying the Gaussian distribution is indeed accurate.

The output of the DHA-MUA QMUDs is also approximately Gaussian, but the actual output values of the DHA-MUA-FKT and DHA-MUA-FBKT QMUDs are slightly higher

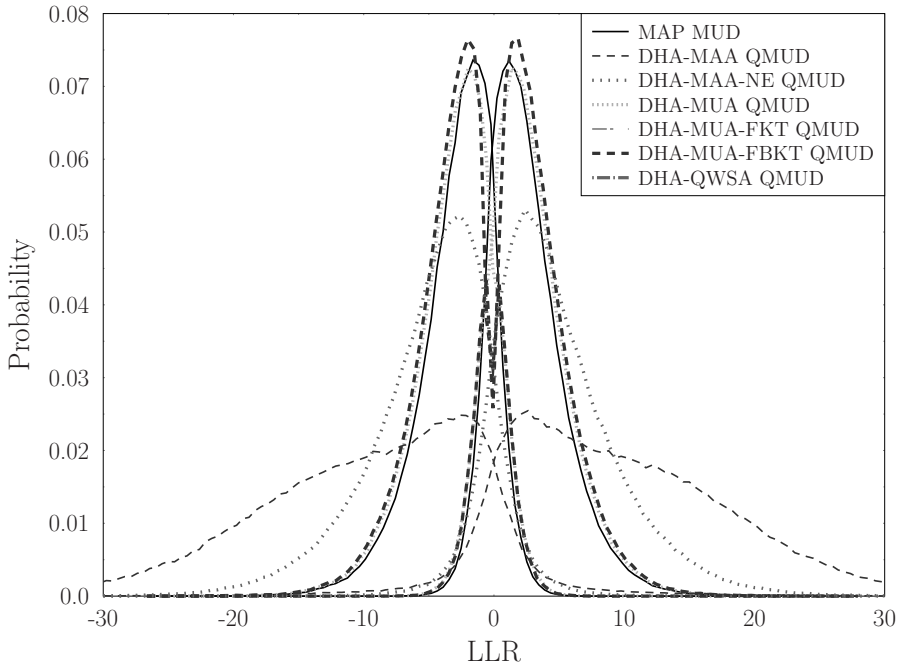

Figure 3.37: Histograms of the output LLRs of the MAP MUD, the DHA-MAA, DHA-MAA-NE, DHA-MUA, DHA-MUA-FKT, DHA-MUA-FBKT and DHA-QWSA QMUDs at $I_{MUD,\,a} = 0.5$ of a single frame of 20 480 bits per user in the MC-IDMA system of Figure 3.4, using the parameters of Table 3.9. The algorithmic elements of the detectors are summarized in Table 3.5. The histograms which have their main peak at a positive LLR value correspond to the LLRs of a bit equal to 0, while those which have their main peak at a negative LLR value correspond to the LLRs of a bit equal to 1.

than those of the MAP MUD, as it may be observed in Figure 3.37, where the PDF curves of the LLRs obtained for $I_{MUD,\,a} = 0.5$ are plotted. The DHA-MAA-NE QMUD mistakenly projects a higher confidence than that of the MAP MUD. By contrast, the DHA-MAA QMUD does not follow the Gaussian distribution and the probability of providing "over-confident" LLRs is expected to lead to a flawed design. More precisely, for $I_{MUD,\,a} = 0.5$ and for Gaussian distributed LLRs inputs to the MUDs, the probability of obtaining an LLR with an absolute value of $|L_{m,e}| \geq 5$ is 67.84% for the DHA-MAA QMUD, 21.98% for the DHA-MUA-FBKT QMUD and only 16.85% for the MAP MUD, indicating the excessive confidence exhibited by the QMUDs' outputs.

3.9.1.1 Consistency Condition of the DHA-MAA QMSDDs

As stated in Section 3.3, the *a posteriori* probability of the u_qth user's mth bit, where $u_q \in \{1, 2, \ldots, U_q\}$ and $m \in \{1, 2, \ldots, \log_2(M)\}$, at the output of the MUD on the qth subcarrier of an MC-IDMA system is equal to

$$P\left(b_{u_q}^{(m)}|\mathbf{y}_q\right) = \frac{p\left(\mathbf{y}_q|b_{u_q}^{(m)}\right) P\left(b_{u_q}^{(m)}\right)}{p\left(\mathbf{y}_q\right)} \tag{3.111}$$

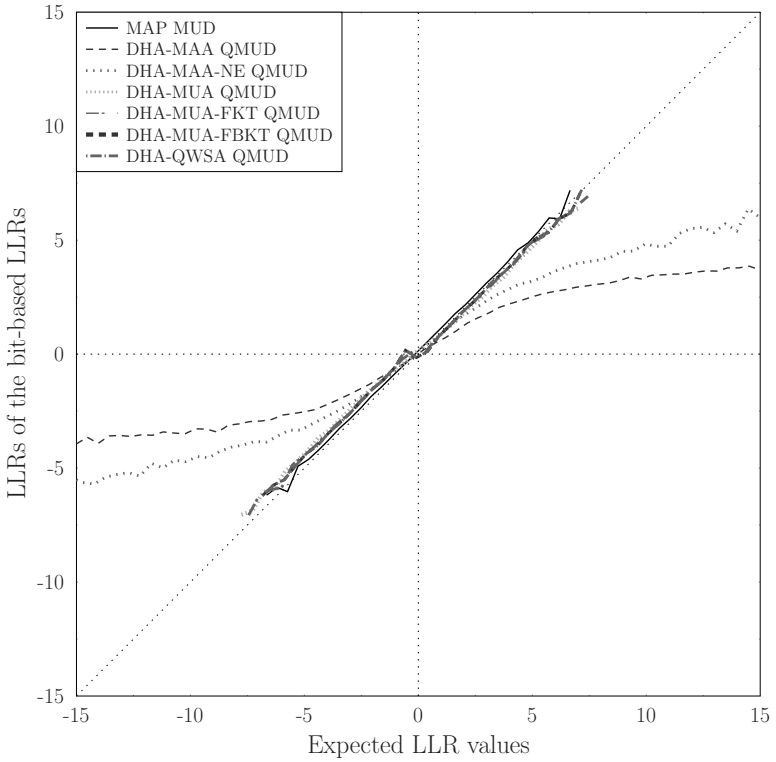

Figure 3.38: LLR values obtained by the MUDs with respect to the expected LLR values based on the histograms in Figure 3.37. The consistency condition for iterative detection for a particular MUD is satisfied if its corresponding curve is close to the main diagonal line. The frame length of each user is equal to 20 480 bits.

and its extrinsic LLR is equal to

$$L_{MUD,e}\left(b_{u_q}^{(m)}\right) = \ln \frac{P\left(b_{u_q}^{(m)}=0|\mathbf{y}_q\right)}{P\left(b_{u_q}^{(m)}=1|\mathbf{y}_q\right)} - L_{MUD,apr}\left(b_{u_q}^{(m)}\right) \tag{3.112}$$

$$= \ln \frac{P\left(b_{u_q}^{(m)}=0|\mathbf{y}_q\right)}{P\left(b_{u_q}^{(m)}=1|\mathbf{y}_q\right)} - \ln \frac{P\left(b_{u_q}^{(m)}=0\right)}{P\left(b_{u_q}^{(m)}=1\right)} \tag{3.113}$$

$$= \ln \frac{P\left(b_{u_q}^{(m)}=0|\mathbf{y}_q\right) \cdot P\left(b_{u_q}^{(m)}=1\right)}{P\left(b_{u_q}^{(m)}=1|\mathbf{y}_q\right) \cdot P\left(b_{u_q}^{(m)}=0\right)} \tag{3.114}$$

$$= \ln \frac{\frac{P\left(b_{u_q}^{(m)}=0|\mathbf{y}_q\right)\cdot P(\mathbf{y}_q)}{P\left(b_{u_q}^{(m)}=0\right)}}{\frac{P\left(b_{u_q}^{(m)}=1|\mathbf{y}_q\right)\cdot P(\mathbf{y}_q)}{P\left(b_{u_q}^{(m)}=1\right)}} \tag{3.115}$$

$$= \ln \frac{p\left(\mathbf{y}_q|b_{u_q}^{(m)}=0\right)}{p\left(\mathbf{y}_q|b_{u_q}^{(m)}=1\right)}, \tag{3.116}$$

where the channel PDF $p(\mathbf{y}_q|\mathbf{x})$ is given in Equation 3.18. Unless the MAP MUD is employed, in practice the extrinsic LLRs at the output of the QMUDs is not equal to the

value of Equation 3.116, due to the necessary simplifications that have been applied for lowering the computational complexity of the calculations.

Assuming a single-user, single-input single-output fading channel in a coherent example system, the channel PDF is equal to

$$p\left(y|x\right) = \frac{1}{\sqrt{2\pi\sigma^2}} \exp\left(-\frac{|y - h \cdot x|^2}{2\sigma^2}\right), \tag{3.117}$$

where $y = h \cdot x + n$ is the received signal, x is the transmitted BPSK symbol, σ^2 is the variance of the AWGN noise n and h is the channel state. The extrinsic LLR of the bit that corresponds to the symbol x, where $x \in \{-1, +1\}$ is equal to

$$L_e = L_c \cdot y, \tag{3.118}$$

where

$$L_c = \frac{2h}{\sigma^2} = 4 \cdot h \cdot E_s/N_0. \tag{3.119}$$

In order for the EXIT chart of an MUD to be useful as a design tool, the output LLRs of the MUD should satisfy the consistency condition [147]. In the case of the single user, single input single output scenario, this is verified by combining Equation 3.116 and Equation 3.118 as in

$$L_c \cdot y = \ln \frac{p\left(y|x = +1\right)}{p\left(y|x = -1\right)} \Rightarrow \tag{3.120}$$

$$p(y|x = -1) = \exp(-L_c \cdot y) \cdot p(y|x = +1). \tag{3.121}$$

A symmetrical probability density function $p(y|x)$ satisfies

$$p\left(-y|x = +1\right) = p\left(y|x = -1\right). \tag{3.122}$$

Therefore, by combining Equation 3.121 and Equation 3.122 we arrive at

$$\left.\begin{aligned} p(-y|x = +1) &= \exp(-L_c \cdot y) \cdot p(y|x = +1) \\ p(-y|x = -1) &= \exp(+L_c \cdot y) \cdot p(y|x = -1) \end{aligned}\right\} \Rightarrow \tag{3.123}$$

$$p(-y|x) = \exp(-x \cdot L_c \cdot y) \cdot p(y|x) \Rightarrow \tag{3.124}$$

$$L_c \cdot y = L_e = \ln \frac{p(y|x = +1)}{p(y|x = -1)}, \tag{3.125}$$

which is the consistency condition [147].

In order to check if the consistency condition is still true for an MUD after calculating $\hat{L}_e$ with the applied simplifications, we may observe its PDF described in Figure 3.37 and substitute the PDF of $\hat{L}_e$ in the right hand term of Equation 3.125. If the right hand term in Equation 3.125 turns out to be equal to the expected extrinsic LLR values, then the MUD satisfies the consistency condition. It should be noted that since we compare the calculated

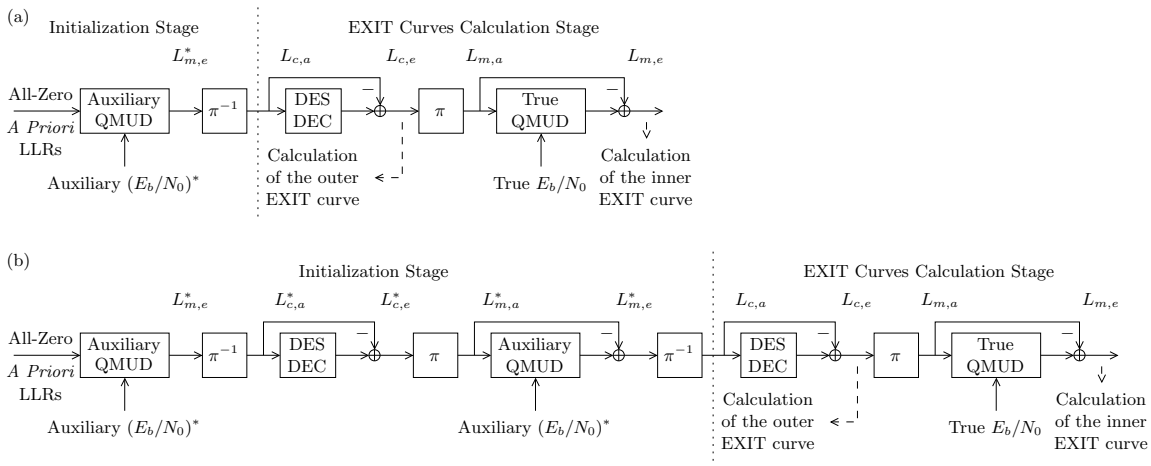

Figure 3.39: Methodology for the generation of inner and outer EXIT curves with non-Gaussian distributed inputs by using (a) one and (b) two auxiliary MSDD-DEC iterations.

LLR values to the expected LLR values, the consistency condition is satisfied if the equality in Equation 3.125 is held. If no approximations have been made in the calculations of the bit-based LLRs, we should expect the values of the LLRs of the bit-based LLRs to be equal to those of the bit-based LLRs, therefore the corresponding curves in Figure 3.38 should be on the main diagonal. Indeed, the MAP MUD's curve follows the main diagonal. Even though both families of DHA-MAA and DHA-MUA QMUDs have performed simplifications on the calculation of LLRs, the DHA-MAA QMUDs are far away from the main diagonal in Figure 3.38, due to their more simplified approximation, explaining the smaller gain in dB achieved by allowing additional MUD-DES/DEC iterations when compared to the rest of the MUDs.

The fact that the inner detector EXIT curves generated with the aid of Gaussian assumptions correspond to an unrealistic scenario may be verified by inspecting the Monte-Carlo simulation based decoding trajectories of the QMUDs in Figure 3.35 and Figure 3.36, which do not accurately match the inner and outer decoder EXIT curves. The mismatch becomes particularly grave for the DHA-MAA QMUD in Figure 3.35, which exhibits a closed EXIT tunnel. Although not visible in Figure 3.35, our investigations, which are included in the following figures, demonstrated that this mismatch occurs, because the inner and outer decoder EXIT curves that the system actually experiences during the second QMUD-DES/DEC iteration exhibit a lower MI than that shown by the EXIT curves generated with the aid of Gaussian assumptions, as a consequence of processing non-Gaussian distributed LLRs output by the previous MUD and DES/DEC processes. This is a result of the approximations applied in the calculations of the QMUD's LLRs in Equation 3.95 and Equation 3.103. The staircase-shaped Monte-Carlo simulation based decoding trajectories represent the simulation of an actual system, while the inner and outer decoder EXIT curves are generated separately without taking into consideration the specific outer and inner codes, respectively.

For verifying the aforementioned speculations concerning the iterative behaviour of our proposed SISO QMUDs, let us now dispense with the assumption of having non-Gaussian LLRs in order to generate accurate EXIT charts [144]. More specifically, the generation

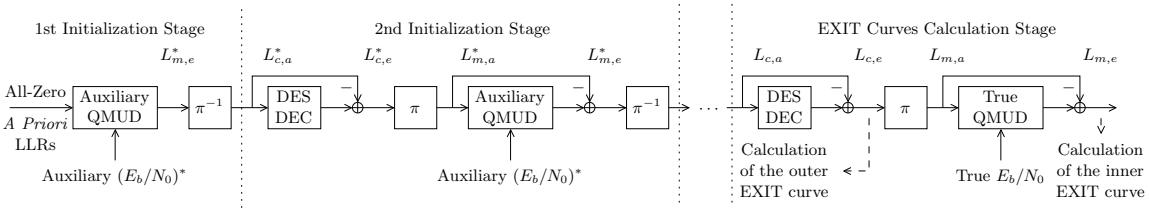

Figure 3.40: General Methodology for the generation of inner and outer EXIT curves with non-Gaussian distributed inputs by using multiple auxiliary MSDD-DEC iterations.

of the EXIT curves for the QMUDs and the decoders with non-Gaussian assumptions follows the methodology described in Figure 3.39 [144]. Following Figure 3.39a, an auxiliary $(E_b/N_0)^*$ value is selected during the initialization stage. This $(E_b/N_0)^*$ value acts as our control parameter and replaces the need for having Gaussian distributed input LLRs corresponding to a specific $I_{MUD,a}$ value. By feeding the auxiliary QMUD with an all-zero *a priori* LLR sequence and the auxiliary $(E_b/N_0)^*$ value, at its output we obtain the auxiliary extrinsic LLRs $L^*_{m,e}$. These extrinsic LLRs obey the specific distribution, which characterizes the outputs of the auxiliary QMUD employed, and by calculating their MI after deinterleaving them, we are able to determine the specific $I_{DES/DEC,\,a}$ value of our non-Gaussian assumption-based EXIT chart. Still following Figure 3.39a, at the output of the DES/DEC used during the EXIT curve calculation stage we may obtain the extrinsic LLRs $L_{c,e}$, generated by a non-Gaussian input. Once we have calculated the corresponding MI of $L_{c,e}$, we have found the specific point $\{I_{DES/DEC,a}, I_{DES/DEC,e}\}$ of the EXIT outer curve. Moreover, the $L_{c,e}$ stream of Figure 3.39a is interleaved and fed to the same QMUD, but operating at the true E_b/N_0 value we want to create the non-Gaussian inner EXIT curve for. At the output of the QMUD we may obtain the extrinsic LLRs, based on which we calculate $I_{MUD,e}$. By carefully tuning the auxiliary $(E_b/N_0)^*$ value, we are able to create the resultant inner and outer decoder EXIT curves.

Let us assume now that both initialization stages are invoked as in Figure 3.39b. We perform two MUD-DES/DEC iterations at the auxiliary $(E_b/N_0)^*$ value, commencing with an all-zero *a priori* LLR vector, before proceeding to the EXIT curve calculation stage, which is the same as in Figure 3.39a. If the QMUDs affect the distribution of the output extrinsic LLRs, it is expected for the MI of both the inner and outer EXIT curves to have smaller values than those of the corresponding curves generated with none or a single auxiliary MSDD-DEC iteration. This would result in a narrower constriction in the open tunnel for the trajectory and it may explain why the trajectory of the DHA-MAA QMSDD seen in Figure 3.35 gets stuck, despite having an open tunnel.

Figure 3.40 shows the general flow chart of creating a non-Gaussian EXIT chart. The number of initialization stages may be as high as required, with the first one being the same as the first stage in Figure 3.39 and the rest being the same as the second stage in Figure 3.39, added before the EXIT curves calculation stage. In this treatise we use up to 2 initialization stages for the non-Gaussian EXIT charts. Every initialization stage corresponds to an actual MUD-DES/DEC iteration of the decoding trajectory and an auxiliary MUD-DES/DEC iteration during the generation of the non-Gaussian PDF-based

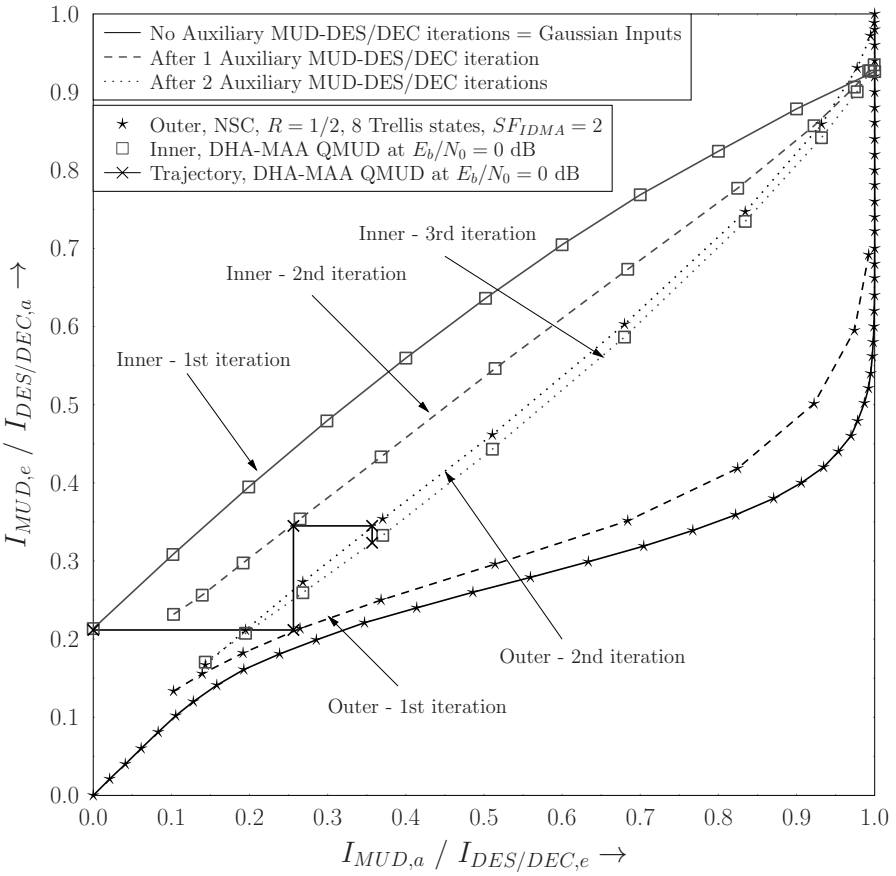

Figure 3.41: EXIT chart of the DHA-MAA QMUD in the MC-IDMA system of Figure 3.4, using the parameters of Table 3.9, as well as 0, 1 and 2 auxiliary QMUD-DES/DEC iterations for the generation of the inner and outer EXIT curves for $E_b/N_0 = 0$ dB and $(E_b/N_0)^* = -3, -2, \ldots, 7$ dB. The inner and outer curves corresponding to each iteration match the decoding trajectory. The algorithmic elements of the detector are summarized in Table 3.5.

inner and outer decoder EXIT curves. Therefore, the trajectory is expected to match with the inner decoder's EXIT curve generated using 0 initialization stages during its first iteration, with the inner and outer EXIT curves generated using 1 initialization stage during its second iteration and so on.

The inner and outer decoder EXIT curves of the DHA-MAA QMUD with none, a single and two auxiliary MUD-DEC iterations are plotted for $E_b/N_0 = 0$ dB in Figure 3.41. Similarly, the non-Gaussian EXIT charts of the DHA-MAA-NE, DHA-MUA, DHA-MUA-FKT and DHA-MUA-FBKT QMUDs are presented in Figure 3.42, Figure 3.43, Figure 3.44 and Figure 3.45, respectively. The non-Gaussian inner and outer decoder EXIT curves were generated for $(E_b/N_0)^* = -3, -2, \ldots, 7$ dB. By observing the inner decoder's EXIT curve in the aforementioned figures, we may conclude that for a fixed value of $I_{MUD,a}$, the output MI of the presented QMUDs becomes lower upon increasing the number of MUD-DES/DEC iterations, because the input and output LLRs do not obey the Gaussian distribution. Similarly, the same figures verify that the operation of the DES/DEC in Figure 3.4 is also affected by the non-Gaussian LLR inputs. More specifically, the DES/DEC perturbs the classic turbo effect and provides a reduced $I_{DES/DEC,e}$ for the same $I_{DES/DEC,a}$ upon

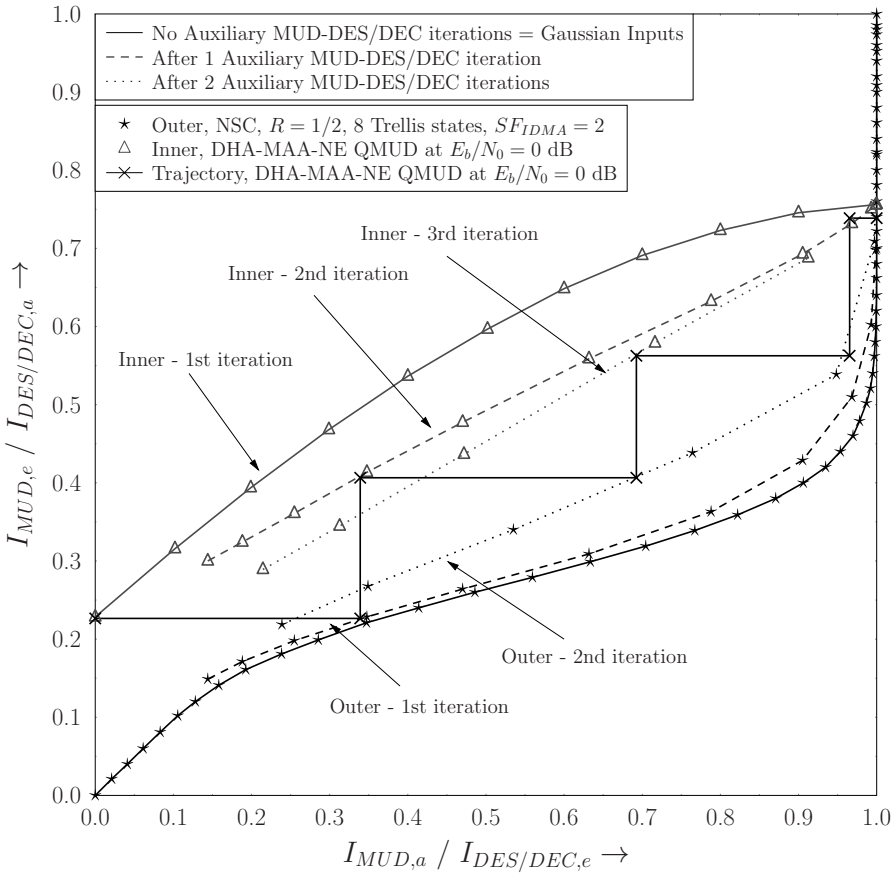

Figure 3.42: EXIT chart of the DHA-MAA-NE QMUD in the MC-IDMA system of Figure 3.4, using the parameters of Table 3.9, as well as 0, 1 and 2 auxiliary QMUD-DES/DEC iterations for the generation of the inner and outer EXIT curves for $E_b/N_0 = 0$ dB and $(E_b/N_0)^* = -3, -2, \ldots, 7$ dB. Only the parts of the inner and outer EXIT curves that are in the proximity of the trajectory are shown for clarity. The algorithmic elements of the detector are summarized in Table 3.5.

increasing the number of MUD-DES/DEC iterations. As expected for the DHA-MAA QMUD, the outer decoder's EXIT curve is above the inner decoder's EXIT curve after two MUD-DES/DEC iterations, essentially closing the tunnel. On the other hand, the trajectory of the DHA-MUA-FBKT QMUD shown in Figure 3.45 can still get through the open tunnel after two iterations and reaches the $I_{DES/DEC,e} = 1$ line.

3.9.2 Impact of the Coding Rate and Spreading Factor

The employment of non-Gaussian EXIT charts assists us in interpreting the exact behaviour of practical receivers, where approximations have been applied either at the MUDs or the decoders. However, since the DHA-MUA QMUDs are expected to have similar Gaussian and non-Gaussian EXIT charts, as shown in Figure 3.43, Figure 3.44 and Figure 3.45, in this section we will rely on Gaussian EXIT charts for characterizing the DHA-MUA-FKT QMUD.

Figure 3.46 presents the EXIT chart of three MC-IDMA systems having $[R_1 = 1, SF_1 =$

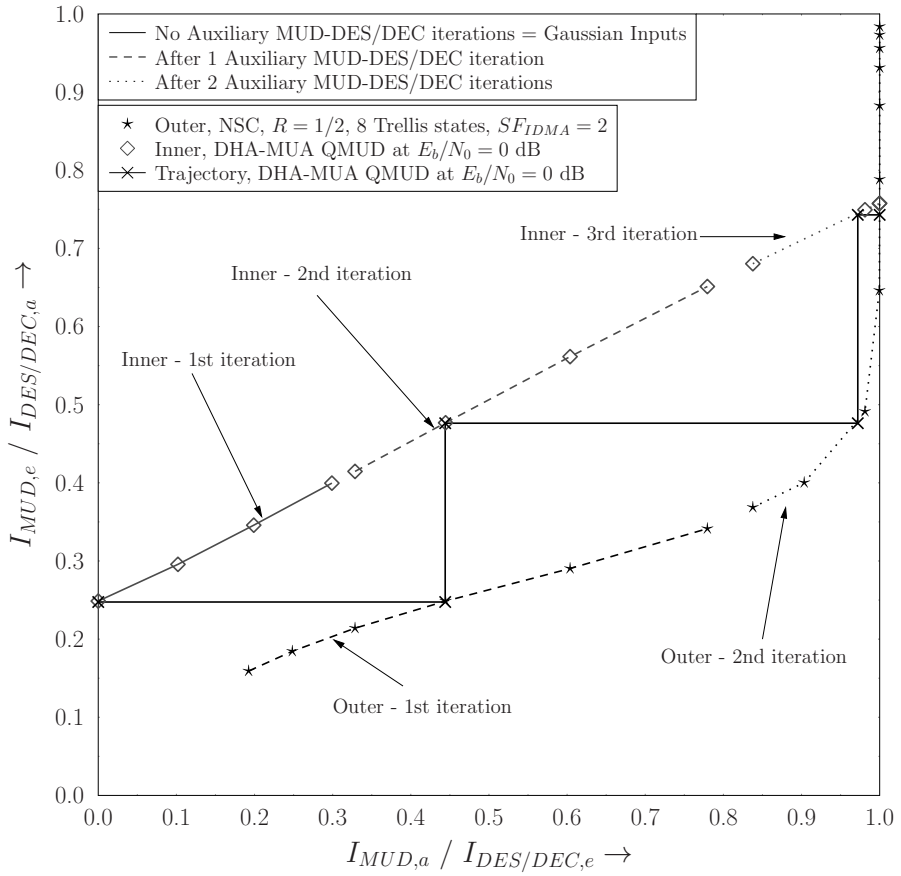

Figure 3.43: EXIT chart of the DHA-MUA QMUD in the MC-IDMA system of Figure 3.4, using the parameters of Table 3.9, as well as 0, 1 and 2 auxiliary QMUD-DES/DEC iterations for the generation of the inner and outer EXIT curves for $E_b/N_0 = 0$ dB and $(E_b/N_0)^* = -3, -2, \ldots, 7$ dB. Only the parts of the inner and outer EXIT curves that are in the proximity of the trajectory are shown for clarity. The algorithmic elements of the detector are summarized in Table 3.5.

4], $[R_2 = 1/2, SF_2 = 2]$ and $[R_3 = 1/4, SF_3 = 1]$ and the parameters summarized in Table 3.9. It should be noted that we have $R/SF = 1/4$ for all three systems, therefore they have an identical throughput, since we keep the frame length the same. As expected, the inner decoder's EXIT curves which correspond to the MUD procedure are the same in all three systems. Based on the outer decoder's EXIT curves, the $[R_3 = 1/4, SF_3 = 1]$ system does not spread the bits and provides error-free decoding with the fewest iterations, provided that a sufficiently high E_b/N_0 value is used. In the other extreme scenario, the $[R_1 = 1, SF_1 = 4]$ system employs only a repetition code and performs better than the rest, when the power is so low that the EXIT tunnel will be closed for the $[R_2 = 1/2, SF_2 = 2]$ and $[R_3 = 1/4, SF_3 = 1]$ systems, even though it will not reach the $I_{DEC,e} = 1$ line. We may observe that even for $E_b/N_0 = 0$ dB, it outputs a higher MI than the other two systems during the first iteration. The $[R_2 = 1/2, SF_2 = 2]$ system's performance lies between that of the other two systems, but it is more similar to that of the $[R_3 = 1/4, SF_3 = 1]$ system. Based on Figure 3.46, if the received power is high enough, we should expect a small difference between these two systems' performance. The conclusions we made based on the EXIT chart of Figure 3.46 are verified by inspecting the BER vs E_b/N_0 curves

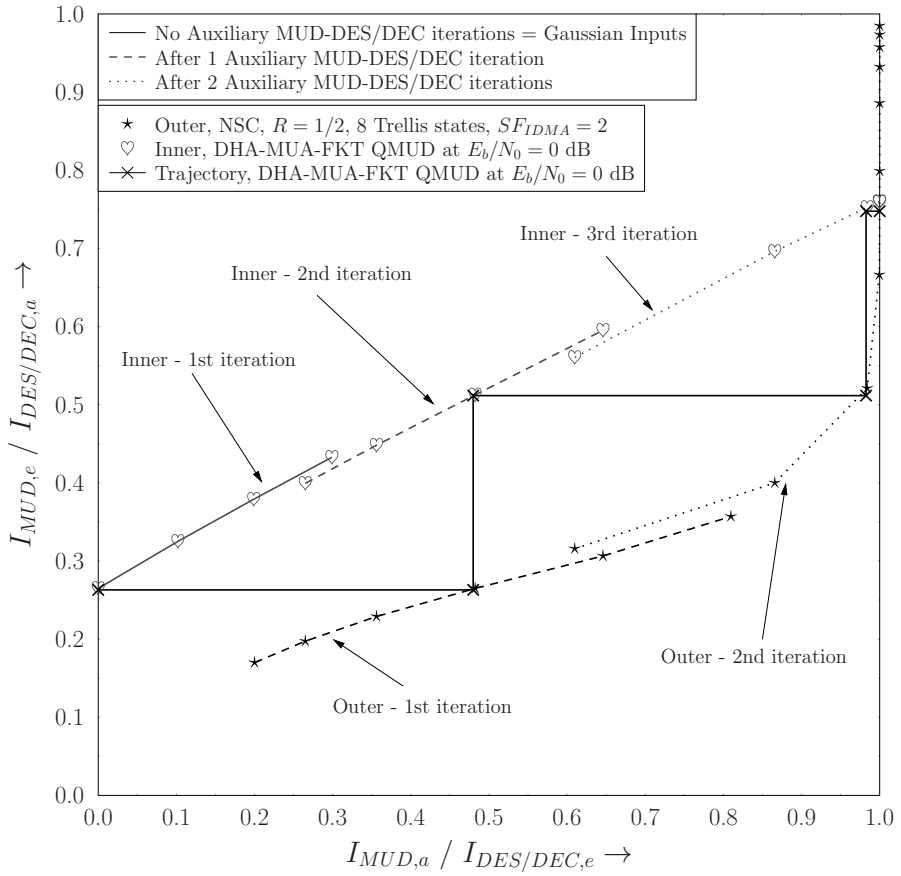

Figure 3.44: EXIT chart of the DHA-MUA-FKT QMUD in the MC-IDMA system of Figure 3.4, using the parameters of Table 3.9, as well as 0, 1 and 2 auxiliary QMUD-DES/DEC iterations for the generation of the inner and outer EXIT curves for $E_b/N_0 = 0$ dB and $(E_b/N_0)^* = -3, -2, \ldots, 7$ dB. Only the parts of the inner and outer EXIT curves that are in the proximity of the trajectory are shown for clarity. The algorithmic elements of the detector are summarized in Table 3.5.

encapsulated in Figure 3.47, where we have invoked $J = 3$ MUD-DES/DEC iterations. The $[R_1 = 1, SF_1 = 4]$ system offers a lower BER at low powers, while the $[R_2 = 1/2, SF_2 = 2]$ and $[R_3 = 1/4, SF_3 = 1]$ systems perform equally well. However, the DES/DEC complexity of the $[R_2 = 1/2, SF_2 = 2]$ system is lower than that of the $[R_3 = 1/4, SF_3 = 1]$ system, even though they both use the same constraint length. This observation is due to having fewer coded bits at the output of the NSC and hence a reduced number of branches in the decoding trellis diagram [10], assuming that having 12 additional branches in a trellis diagram contributes more to the DES/DEC complexity than a half-rate repetition code does [10] in terms of the classic Add-Compare-Select (ACS) arithmetic operations.

3.9.3 Effect of the Imperfect Channel Estimation

In practice perfect CSI is not available, especially during the first MUD-DES/DEC iteration. For characterizing the systems, when only realistic imperfect CSI is available, we contaminated the perfect CSI values $h_{p,q}^{(u_q)}$ of Equation 3.16 with AWGN, assuming that

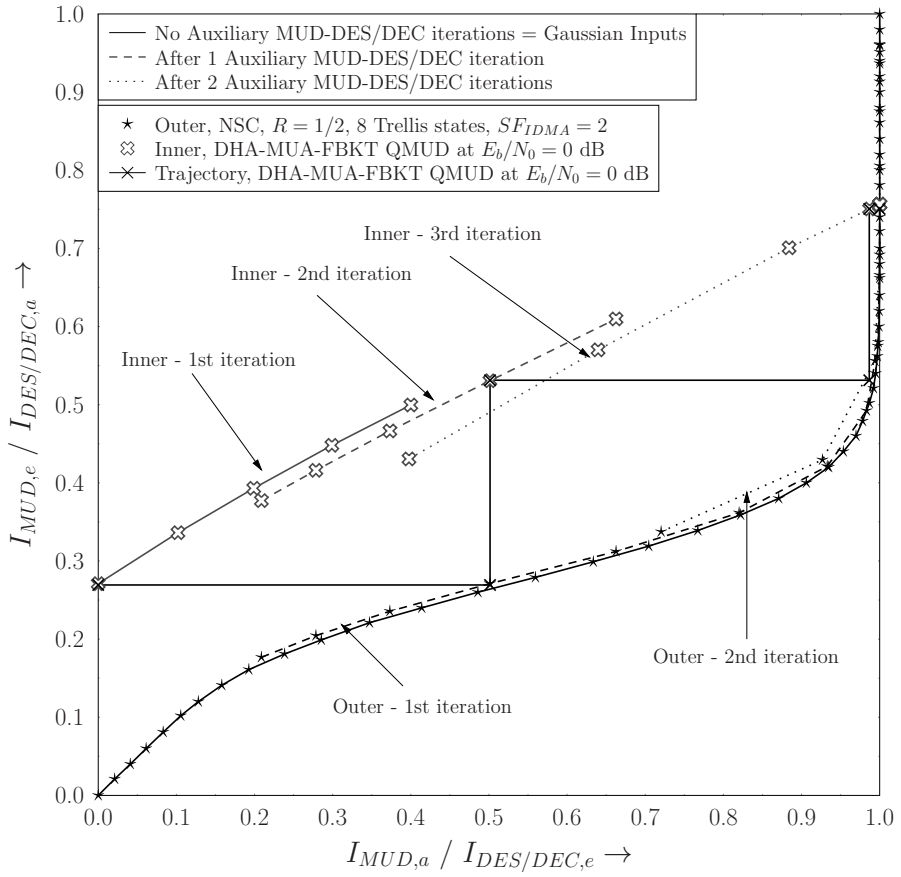

Figure 3.45: EXIT chart of the DHA-MUA-FBKT QMUD in the MC-IDMA system of Figure 3.4, using the parameters of Table 3.9, as well as 0, 1 and 2 auxiliary QMUD-DES/DEC iterations for the generation of the inner and outer EXIT curves for $E_b/N_0 = 0$ dB and $(E_b/N_0)^* = -3, -2, \ldots, 7$ dB. Only the parts of the inner and outer EXIT curves that are in the proximity of the trajectory are shown for clarity. The algorithmic elements of the detector are summarized in Table 3.5.

the CSI-estimation error is Gaussian, yielding

$$\tilde{h}_{p,q}^{(u_q)} = h_{p,q}^{(u_q)} + \nu, \tag{3.126}$$

where ν is an AWGN sample having a zero mean and a variance of N_ν, with $N_\nu = 0$ corresponding to the perfect CSI scenario. In our system we assume that the CSI noise power is halved during each MUD-DES/DEC iteration, modelling in this way the better CSI estimate that becomes available during each iteration. In Figure 3.48 we have plotted the BER performance of the system characterized in Table 3.9, when the MAP MUD and the DHA-MUA-FKT QMUD are employed in conjunction with $N_\nu = 0.0791, 0.0396, 0.0198$ during the first, second and third iteration, respectively. We may observe that the DHA-MUA-FKT QMUD's performance is within 0.7 dB of that of the MAP MUD, regardless of the accuracy of the channel estimates, even though they are 6.5 dB away from the MAP MUD's performance recovered with the aid of perfect CSI at BER = 0.0025 after a single MUD-DES/DEC iteration. An important observation is that with the aid of imperfect CSI, the MAP MUD has to repeat the CFEs during each MUD-DES/DEC iteration, in a similar

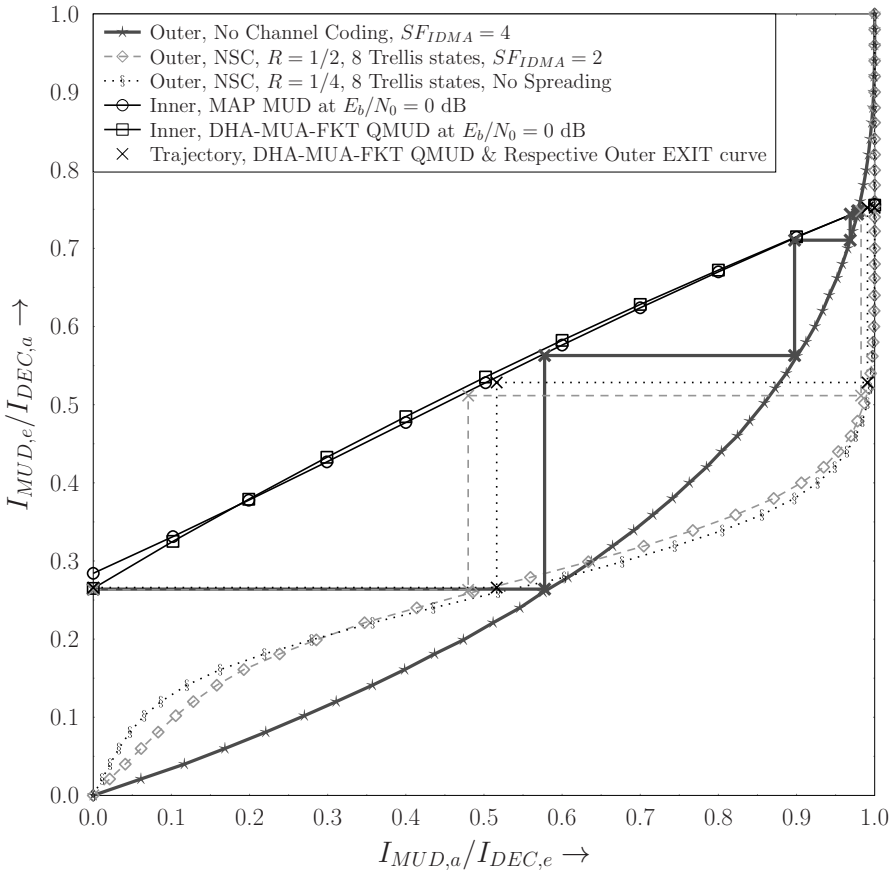

Figure 3.46: EXIT chart of the DHA-MUA-FKT QMUD in 3 MC-IDMA system scenarios of Figure 3.4 with $[R_1 = 1, SF_1 = 4]$, $[R_2 = 1/2, SF_2 = 2]$ and $[R_3 = 1/4, SF_3 = 1]$ and the rest of the parameters summarized in Table 3.9.

way as the DHA-MUA-FKT QMUD, hence having completed in total 1170, 2340 and 3510 CFEs / bit after the first, second and third MUD-DES/DEC iteration, respectively, regardless of the power level and N_ν. At the same time, the DHA-MUA-FKT QMUD's complexity depends on both E_b/N_0 and on N_ν due to its deterministic initialization with the aid of the MMSE detector [3]. Therefore, assuming operation at BER = 10^{-5} after $J = 3$ MUD-DES/DEC iterations, the DHA-MUA-FKT QMUD has carried out 600, 1226 and 1783 CFEs / bit, after the first, second and third MUD-DES/DEC iteration.

Therefore, since every multi-level symbol in our scenario includes 14 bits, we may conclude that when the MAP MUD is called during each MUD-DES/DEC iteration, its complexity is higher than those of the proposed SISO QMUDs in a system having 2^{14} entries in its database. In fact, based on our simulations, the proposed SISO DHA-MAA and DHA-MUA QMUDs have a lower complexity than the MAP MUD, even when the database's size is reduced to 2^{12} entries, which corresponds to a scenario where 12 (3) users transmitting BPSK (16-QAM) symbols interfere with each other.

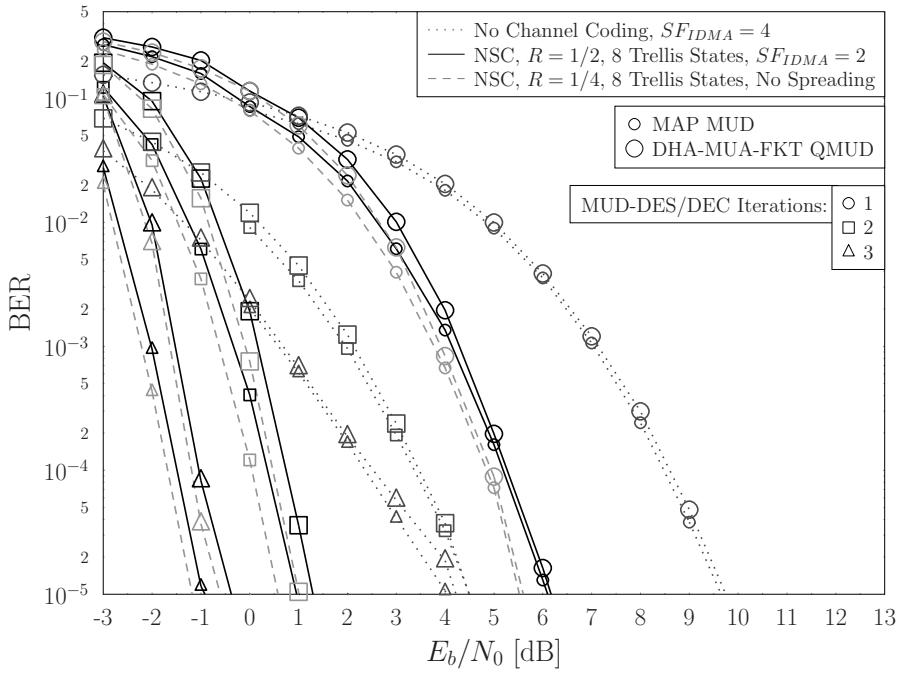

Figure 3.47: BER performance of the DHA-MUA-FKT QMUD in 3 MC-IDMA system scenarios of Figure 3.4 with $[R_1 = 1, SF_1 = 4]$, $[R_2 = 1/2, SF_2 = 2]$ and $[R_3 = 1/4, SF_3 = 1]$ and the rest of the parameters summarized in Table 3.9.

3.10 Conclusions

In Section 3.4 we presented a generalized version of the quantum mean algorithm [62] resulting in the quantum weighted sum algorithm [1], which is employed for designing a quantum-assisted MUD relying on soft inputs and providing soft outputs. The QWSA-based QMUD may be considered as the quantum-domain equivalent of the MAP MUD, since it aims for estimating the weighted sums that are present in the numerator and denominator of a bit's LLR. The process within the QWSA QMUD takes place in the quantum domain, while its inputs and outputs remain in the classical domain, hence allowing the quantum-assisted MUD to be integrated in a state-of-the-art iterative receiver of a classical communication system. The DHA is used prior to the QWSA in order to detect the specific multi-level symbol that maximizes the CF and for normalizing its outputs. The EXIT charts of Figure 3.17, Figure 3.18, Figure 3.36 and BER curves of Figure 3.20, Figure 3.34 presented for the DS-CDMA and MC-IDMA systems verify that the QWSA MUD has a performance equivalent to that of the classical optimal ML MUD, which is achieved at a reduced computational complexity, when compared to the MAP MUD supporting numerous users and high-order modulation schemes.

Diverse iterative DHA QMUDs [3] were designed in Section 3.5, which were applied in a rank-deficient vehicular DSS/SSCH SDMA-OFDM system in Section 3.7 and in MC-IDMA systems in Section 3.9, where the conventional detectors experience an error floor. A range of further measures were also applied for improving the SO-ACO MUDs of [13, 63] in Section 3.6, while introducing the free-will-based mutation. The BER performances of the soft-output DHA QMUDs were better than those of the corresponding SO-ACO

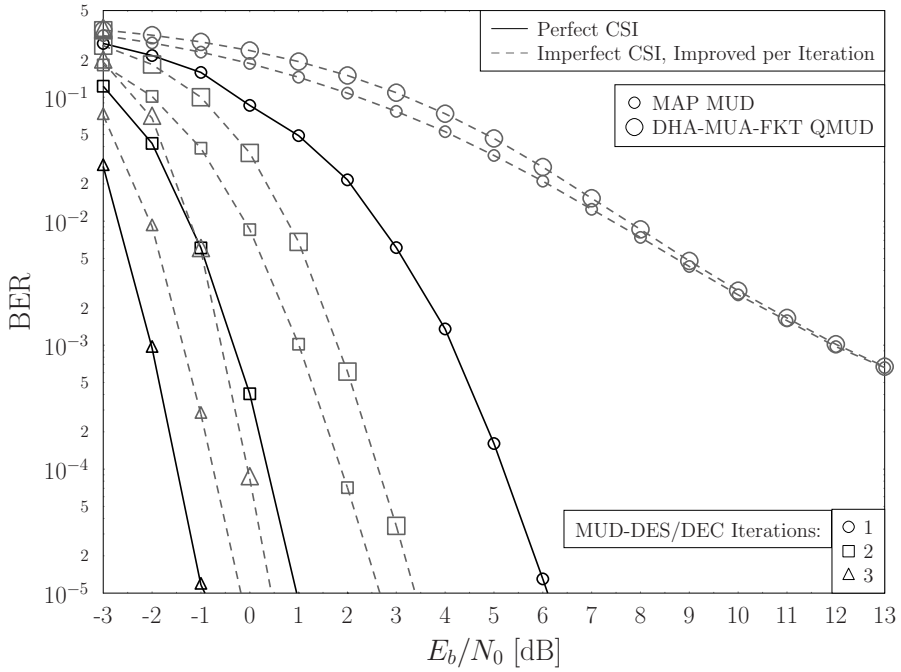

Figure 3.48: BER performance of the DHA-MUA-FKT QMUD in the MC-IDMA system of Figure 3.4, using the parameters of Table 3.9 with imperfect CSI, where $N_\nu = 0.0791, 0.0396, 0.0198$ during the first, second and third MUD-DES/DEC iteration.

MUDs according to Figure 3.30, while requiring fewer CFEs per bit than the DHA-QWSA QMUD of [1] based on Figure 3.34 and Table 3.10. Table 3.11 summarizes the performance and complexity of the proposed SISO QMUDs in the context of the MC-IDMA system of Figure 3.34 and Table 3.9 when perfect channel estimation is available.

A novel DSS-based USSCH was also proposed in Section 3.2.3.3 for both reducing the complexity of the MUD and for improving the BER performance of the system, when compared to a system where USSCH [21] is used. Finally, in Figure 3.33 a hybrid SO-DHA / SO-ML MUD was designed for the family of DSS/SSCH SDMA-OFDM systems.

In Section 3.9.1 we used non-Gaussian EXIT charts for explaining the behaviour of the iterative DHA-based as well as QWSA-based QMUDs and then highlighted the effects that the necessary simplifications of the SISO QMUDs have on the design of the systems. Moreover, in Figure 3.47 we compared an MC-IDMA system to two systems using either only convolutional channel coding or DSS with the same joint coding rate of R/SF and with the same throughput by keeping the frame length the same. Finally, in Figure 3.48 we evaluated the optimal MAP MUD and the DHA-MUA-FKT QMUD in an MC-IDMA system, where only imperfect CSI was available, hence degrading the performance and forcing the MAP MUD to be employed during each MUD-DES/DEC iteration for exploiting the improved channel estimates. Table 3.12 describes the performance of the optimal classical SISO MAP MUD, when compared to the DHA-MUA-FKT QMUD in the system context of Figure 3.48 and Table 3.9, where realistic imperfect channel estimation is used. The effect that the imperfect CSI has on the performance motivates us to investigate non-coherent receivers, where detection is successfully performed without the need for knowing the CSI, albeit at a performance penalty when compared to a coherent receiver with perfect

Table 3.11: Summary of the QMUDs designed for the MC-IDMA system of Figure 3.34 and Table 3.9 for BER = 10^{-5}

MUD	MUD-DEC iterations	Complexity (CFEs / bit)	% complexity of the MAP MUD	E_b/N_0 (dB)	E_b/N_0 difference from the MAP MUD (dB)	BER Figure
DHA-MAA	1	67.4	5.76%	9.8	3.7	3.34
	2	139.3	11.9%	8.5	7.55	
	3	210.7	18%	8.15	9.06	
DHA-MAA-NE	1	68.3	5.83%	8.39	2.29	3.34
	2	140.6	12%	3.135	2.185	
	3	213.2	18.2%	1	1.91	
DHA-MUA	1	744.4	63.6%	6.175	0.075	3.34
	2	1390.2	118.8%	1.135	0.185	
	3	1998.4	170.8%	−0.3	0.61	
DHA-MUA-FKT	1	599.2	51.2%	6.165	0.065	3.34
	2	1205.0	103%	1.29	0.34	
	3	1773.4	151.5%	−0.4	0.51	
DHA-MUA-FBKT	1	599.2	51.2%	6.1	0	3.34
	2	1205.0	103%	1.23	0.28	
	3	1773.4	151.5%	−0.56	0.35	
DHA-QWSA	1	769.5	65.75%	7	0.9	3.34
	2	1472.1	125.8%	2.28	1.33	
	3	2174.4	185.8%	0	0.91	
MAP	1	1170.3	100%	6.1	0	3.34
	2	1170.3	100%	0.95	0	
	3	1170.3	100%	−0.91	0	

CSI knowledge.

Table 3.12: Summary of the QMUDs designed for the MC-IDMA system of Figure 3.48 and Table 3.9 for BER = 10^{-5}

MUD	MUD-DEC iterations	Complexity (CFEs / bit)	% complexity of the MAP MUD	E_b/N_0 (dB)	E_b/N_0 difference from the MAP MUD (dB)	BER Figure
DHA-MUA-FKT	1	600.9	51.3%	18	0	3.48
	2	1226.1	52.4%	3.39	0.73	
	3	1783.6	50.8%	0.44	0.62	
MAP	1	1170.3	100%	18	0	3.48
	2	2340.6	100%	2.66	0	
	3	3510.9	100%	−0.18	0	

Chapter 4

Non-Coherent Quantum Multiple-Symbol Differential Detection in Multiple Access Systems

4.1 Introduction

The family of coherent MUDs and QMUDs that were investigated in Chapter 2 and in Chapter 3 perform optimally when there is perfect knowledge of all the channel states at the receiver. However, the potentially excessive additional complexity required for performing channel estimation [21, 29, 148] has not been included in the calculations of the complexity of the MUDs and QMUDs. Nonetheless, the comparison between the MUDs and QMUDs presented in Chapter 2 and in Chapter 3 remains valid if the complexity of the channel estimation procedure is also taken into account.

When a fading channel's state experiences small fluctuations over several transmission periods, it is typically termed as a quasi-static channel, which hence only has to be estimated infrequently, therefore imposing a moderate complexity. The channel estimation may be based on training by transmitting known pilot symbols to the receiver [149, 150]. Given the knowledge of the transmitted pilot symbol, the channel state may be estimated by comparing it to the noisy received pilot signal. In practice, the channel estimation does not offer perfect estimates of the channel states [21, 29, 148] due to a number of reasons, such as the limited number of pilots used, the dynamic nature of the channels and the noise. Semi-blind channel estimation [151, 152], which uses a reduced number of pilot signals, as well as totally blind channel estimation dispensing with pilots [153–155] may also be used for quasi-static channels.

When a fading channel's state changes rapidly between transmissions due to its high

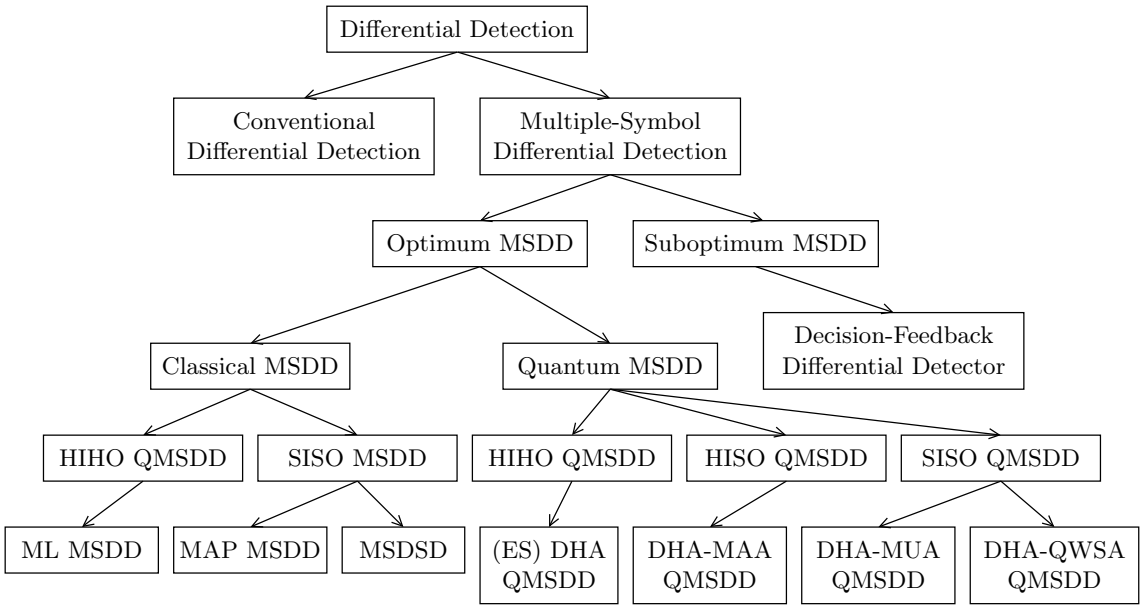

Figure 4.1: Classical and quantum-assisted non-coherent data detectors.

Doppler frequency, the density of pilot symbols in a Pilot Symbol Assisted Modulation (PSAM) frame [156] should be increased. When the density of the pilot symbols in a frame is increased, the effective throughput of the system is reduced. If the Doppler frequency of a fading channel is excessive, it may become infeasible to try and estimate the channel states, whilst simultaneously supporting an adequate throughput, since the density of pilot symbols required for performing accurate channel estimation will be too high.

As verified in Chapter 2 and Chapter 3, imperfect channel estimation in a multiple-access system results in a degradation of the performance of the Multi-User Detectors (MUD) [2], even though it gives a more realistic view of a practical system. In the emerging mm-Wave communication [17] and massive MIMO [8, 21, 41, 42] eras the number of transmit and receive antenna elements may be over 100 at each terminal, hence the total number of channels invoked in a single transmission may be over 10^4, essentially making the accurate estimation of their channel states impractical.

The family of non-coherent data detection schemes [21, 29, 148] presented in Figure 4.1 relies on no channel estimation, for the sake of avoiding the computational complexity imposed by the channel estimation algorithms. Furthermore, since channel estimation is not required, apart from a reference symbol for each detection window, there is no need for pilot signals to be transmitted for this purpose, hence actually resulting in a higher system throughput and more efficient channel usage. On the other hand, the performance of a system relying on a non-coherent detector is worse than that of a system using a coherent detector as detailed in [21].

In the multiple access systems considered in this Chapter, the users' transmissions are orthogonal to each other in either the time domain, the frequency domain or the code domain and hence they may be readily separated without estimating their Channel State Information (CSI). Hence in this treatise we will focus our attention on differential modulation [21] and more specifically on Differential Phase Shift Keying (DPSK) [157–160].

In DPSK, the symbol transmitted in the tth time slot depends on the symbol transmitted during the $(t-1)$st time slot. At the receiver side, the non-coherent Conventional Differential Detector (CDD) [157–159] performs the inverse procedure and extracts the transmitted symbol based on the previously detected, differentially modulated symbol. The Multiple Symbol Differential Detector (MSDD) [157, 161, 162] makes a decision concerning all the most recent $(N_w - 1)$ differentially modulated and transmitted symbols, based on the most recent N_w received signals, where N_w is the decision window width. If we have $N_w = 2$, then the MSDD becomes equivalent to the CDD. It is expected that the higher the value of N_w, the more computationally demanding the MSDD becomes, but at the same time the BER performance of the system is improved. The classical Maximum Likelihood (ML) MSDD [21] is considered as the optimal but high-complexity non-coherent Hard-Input Hard-Output (HIHO) MSDD. Both the Decision-Feedback Differential Detector (DFDD) [158, 163–165] and the Multiple Symbol Differential Sphere Detector (MSDSD) [166–168] are attractive non-coherent detectors, since they offer a near-optimal performance with respect to the MSDD whilst imposing a reduced complexity. The Soft-Input Soft-Output (SISO) versions of the MSDD [161], namely the DFDD [169–171] and the MSDSD [172] may be integrated into an iterative receiver, where extrinsic information is exchanged between the channel decoders and the multiple symbol detectors as detailed in [21].

In this Chapter we propose attractive low-complexity HIHO, Hard-Input Soft-Output (HISO) and SISO Quantum-assisted MSDDs [6], which require no knowledge of the CSI, hence eliminating the computational complexity that would be required by the channel estimation procedure for providing accurate channel estimates. More specifically, we conceive both the SISO DHA-aided QMSDD relying on MUlti-input Approximation (MUA) and the DHA-aided Quantum Weighted Sum Algorithm (QWSA) assisted QMSDD, both of which achieve a performance equivalent to that of the MAP MSDD, while requiring a substantially lower number of CFEs than the MAP MSDD. In addition, we design the DHA-aided MAximum Approximation (MAA) QMSDD, which may be used for non-iterative soft-output data detection and has a lower number of CFEs than the DHA-MUA QMSDD and the DHA-QWSA QMSDD. Furthermore, we propose the HIHO DHA-based and Early-Stopping-aided (ES) DHA QMSDD, followed by comparing their performances to that of the optimal HIHO ML MSDD.

The QMSDDs are employed in multi-user Direct Sequence Spreading (DSS) and Slow SubCarrier Hopping (SSCH)-aided Spatial Division Multiple Access (SDMA) systems intrinsically amalgamated with Orthogonal Frequency Domain Multiplexing (OFDM), where the users are separated in the frequency, time or code domain. The QMSDDs' performance is evaluated based on their Bit Error Ratio (BER) versus E_b/N_0 plots, as well as on EXtrinsic Information Transfer (EXIT) charts. Moreover, a novel methodology is designed for deterministically initializing the DHA for the proposed QMSDDs for the sake of reducing the receiver's complexity by exploiting the CDD. For further lowering the detector's complexity invoked in our iterative receivers, the SISO QMSDDs are not activated during every single MSDD - DECoder (DEC) iteration, whilst mitigating the resultant perfor-

mance degradation. Finally, the effect of the detection window length N_w employed in the QMSDDs, that of the interleaver length and of the SSCH period on the QMSDDs' performance is investigated.

The chapter is structured as follows. In Section 4.2 we will analyse the DPSK modulation scheme in the context of a Direct-Sequence and Slow Subcarrier-Hopping aided SDMA-OFDM system. In Section 4.3 we will present the classical CDD, while in Section 4.4 we will investigate the HIHO QMSDDs and compare them to the classical HIHO multiple symbol differential detectors. In Section 4.5 the SISO QMSDDs are analysed, along with the MAP MSDD. A novel methodology for deterministically initializing the DHA searches in the QMSDDs is proposed in Section 4.6, while in Section 4.7 we employ the QMSDD every IpS number of QMSDD-DEC iterations. The effect of the detection window length N_w, the interleaver length and the subcarrier hopping period on the QMSDDs' performance is stated in Section 4.8. Finally, our conclusions are offered in Section 4.9.

4.2 Direct-Sequence and Slow Subcarrier-Hopping aided SDMA-OFDM System Model With Non-Coherent Receiver

The DSS/SSCH SDMA-OFDM system model relying on non-coherent detection is presented in Figure 4.2. The system supports U users, each of whom encodes his / her information bits $\{b_u\}$, $u \in \{1, 2, \ldots, U\}$, using a turbo convolutional encoder, resulting in the encoded bit sequence $\{c_u\}$.

After the encoded bit sequence has been interleaved, the bit sequence $\{d_u\}$ is separated into W parallel streams, where W is the number of subcarriers associated to each user. Let us assume that $\mathcal{Q}$ subcarriers are available in our system and that the length of each user's symbol stream is equal to Γ symbols. Therefore, we have $W \leq \mathcal{Q}$, $W \leq \Gamma$ and $\mathrm{mod}\,(\Gamma, W) = 0$. It should be noted at this stage that the user-specific scheduling of the subcarrier allocation algorithm is assumed to change every T_h OFDM symbol periods. The subcarrier allocation procedure follows the DSS-aided Uniform SSCH (USSCH) [3] algorithm performed at the BS.

Each parallel stream is differentially encoded by the DMPSK Symbol Mapping block of Figure 4.2. The differentially encoding process for the DMPSK modulation scheme is described in Figure 4.3. Let us assume that conventional M-ary PSK modulation having a mapping set $\mathcal{M} = \{2\pi m/M;\ m = 0, 1, \ldots M-1\}$ is chosen. Furthermore, we omit the user subscript without any loss of generality, since the same procedure occurs at each user's terminal. The first transmitted symbol $s[0]$ is termed as the reference symbol, which is assumed to be known at the receiver. After $\log_2(M)$ bits have been mapped to an M-ary PSK symbol $x[t]$ during the tth time slot, the resultant symbol is multiplied by the symbol transmitted during the $(t-1)$st time slot $s[t-1]$, as encapsulated in

$$s[t] = s[t-1] \cdot x[t]. \tag{4.1}$$

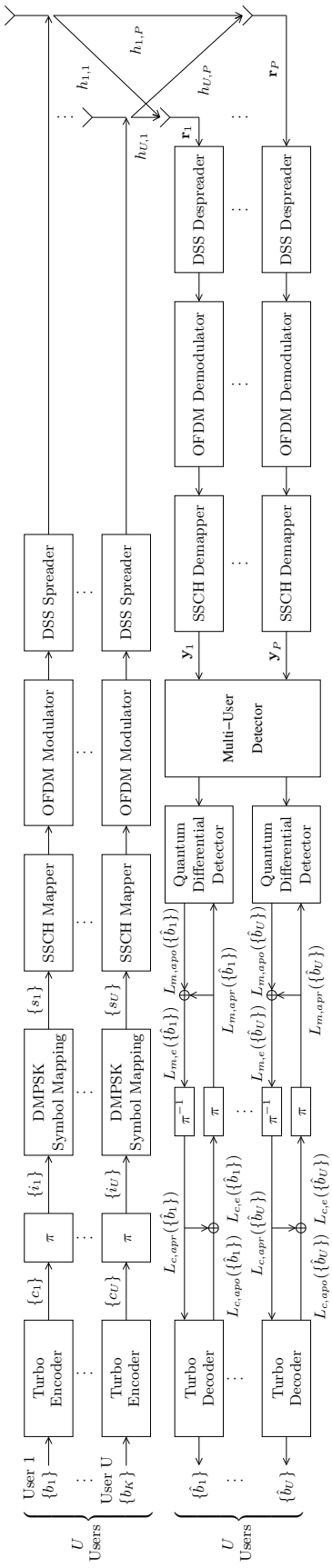

Figure 4.2: System model of a direct-sequence and slow subcarrier-hopping aided SDMA-OFDM system with a non-coherent receiver.

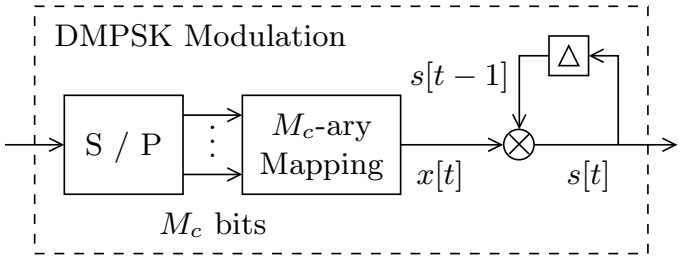

Figure 4.3: Mapping of the DPSK modulation scheme.

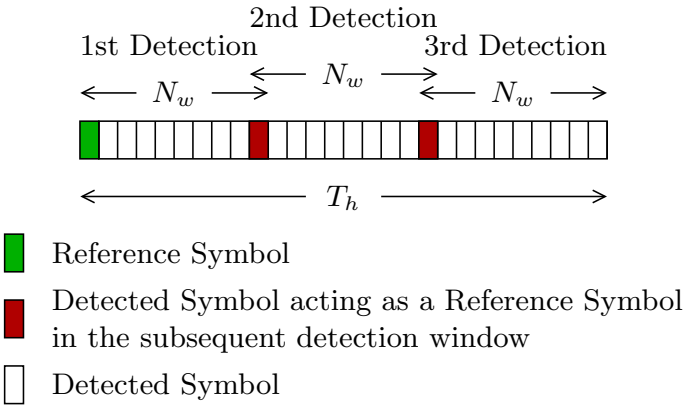

Figure 4.4: Visual representation of T_h and N_w for the uth user on the qth subcarrier.

Then, $s[t]$ is buffered at the transmitter for encoding $s[t+1]$, following Equation 4.1.

Each of the W differentially encoded symbol sequences $\{s_{u,w}\}$ of the uth user are then mapped to the respective subcarriers based on the schedule received by the BS. The differential detection carried out at the receiver is based on the assumption that the multipath Rayleigh channel states change very slowly in that specific domain where the differential encoding took place. In this treatise we have opted for the differential encoding to take place in the time domain, hence the channels are assumed to experience slow fading. Since the subcarrier allocation schedule changes every T_h OFDM symbol periods for each user, it is not reasonable to assume that the channel state of the uth user on the qth subcarrier will be similar to that of the same user on the jth subcarrier after a new subcarrier allocation schedule associated with $j \neq q$. Therefore, the differential encoding procedure of the DMPSK symbol mapping block seen in Figure 4.2 and Figure 4.3 occurs in blocks of T_h symbols on each of the W parallel streams of the uth user. This architecture ensures that a new reference symbol is transmitted every time the subcarriers the uth user transmits on are changed. A visual representation of N_w and T_h is depicted in Figure 4.4. It is logical to expect that when T_h is increased, the channel-correlation between the differentially encoded symbols is also increased. Therefore, if an MSDD is used in conjunction with $N_w = T_h$, the performance will be improved. However, at the same time, the complexity of the MSDD becomes higher. Furthermore, in the same scenario, the users who have been allocated gravely faded subcarriers suffer from prolonged frames, since the channel states vary slowly.

Following the SSCH mapper of Figure 4.2, the OFDM modulator modulates the symbols

of each user by performing a $\mathcal{Q}$-point Inverse Fast Fourier Transform (IFFT). The symbols are then spread in the time domain by a DSS spreader, using a user-specific spreading sequence associated with a spreading factor of SF. Let us use $G = SF$-chip Walsh-Hadamard spreading codes, which are orthogonal to each other. The allocation of the G number of WH spreading codes to the U users may be performed as in

$$\left\lfloor \frac{U}{G} \right\rfloor + \begin{cases} 1 & \text{if } g < \text{mod}(U, G) \\ 0 & \text{if } g \geq \text{mod}(U, G) \end{cases}, \tag{4.2}$$

where $g \in \{1, 2, \ldots, G\}$. Following the DSS spreading scheme in Figure 4.2 in the time domain, the symbols are transmitted over multipath Rayleigh channels to the BS.

Since we will focus our attention on the QMSDD performance rather than the MUD, let us proceed by separating the users in the frequency or the code domain in order to remove the need for an MUD. More precisely, in this Chapter the systems we investigate have users supported by the same DSS code allocated to different subcarriers. Therefore, there is no need to perform non-coherent multi-user detection in the spatial domain, since there will be no users who interfere with each other, because we use orthogonal WH codes. It should be noted that even though we use multipath channels, we transmit on narrowband subcarriers, which have smaller signal bandwidth than the coherence bandwidth of the channel. Therefore, each subcarrier experiences flat fading and the WH codes do not lose their orthogonality at the receiver. These scenarios assist us in focusing our attention on non-coherent MSDD, rather than on non-coherent MUD.

Still considering Figure 4.2, after the signals of the U users have been transmitted, they are received by the P receive AEs at the BS. Naturally, the users who transmit on different subcarriers do not interfere with each other, since they are separated in the frequency domain. In this treatise we assume the employment of a synchronous system, therefore all the received signals are synchronously superimposed at the pth receive AE, with $p \in \{1, 2, \ldots, P\}$. Furthermore, Additive White Gaussian Noise (AWGN) is added at each receive AE, having a zero mean and a variance of $N_0 = 2\sigma^2$. The DSS despreader of Figure 4.2 then despreads the signals received on each receive AE in the time domain. At this stage, the users who transmit on the same subcarrier and have been allocated different orthogonal DSS codes are separated. Afterwards, the received OFDM symbol is demodulated on the pth receive AE chain by using the $\mathcal{Q}$-point FFT. Finally, the demodulated symbols transmitted on different subcarriers are dehopped and fed to the MUD / Differential Detector.

For the analysis of differential detectors, let us focus our attention on the signal processing of the qth subcarrier and the pth receive AE chain. Let us assume that $U_{g,q}$ users have been allocated the gth DSS code on the qth subcarrier, U_q users transmit on the qth subcarrier, with $1 \leq U_q \leq U$, while G_q different DSS codes are present on the qth subcarrier, with $1 \leq G_q \leq G$. Since in our differential detection scenarios we allow at most one user belonging to a single DSS group to transmit on the qth subcarrier, we have $U_q = G_q$ and

$U_{q,g} = 1$. Therefore, the signal $\mathbf{r}_{p,q}$ received in our synchronous DSS/SSCH SDMA-OFDM system on the qth subcarrier at the pth receive AE is expressed as [21]

$$\mathbf{r}_{p,q} = \bar{\mathbf{c}}_{G_q} \bar{\mathbf{H}}_{p,q} \bar{\mathbf{s}}_q + \mathbf{n}_{p,q}, \tag{4.3}$$

where $\bar{\mathbf{c}}_{G_q}$ is the $(SF \times U_q) = (SF \times G_q)$-element matrix that contains the DSS codes of the U_q users on the qth subcarrier, as in [21]

$$\bar{\mathbf{c}}_{G_q} = [\underbrace{\mathbf{c}_1, \ldots, \mathbf{c}_1}_{U_{q,1}=1}, \underbrace{\mathbf{c}_2, \ldots, \mathbf{c}_2}_{U_{q,2}=1}, \ldots, \underbrace{\mathbf{c}_{G_q}, \ldots, \mathbf{c}_{G_q}}_{U_{q,G_q}=1}] \tag{4.4}$$

$$= [\mathbf{c}_1, \mathbf{c}_2, \ldots, \mathbf{c}_{G_q}], \tag{4.5}$$

where $\mathbf{c}_g$ is the gth DSS code, represented by a $(SF \times 1)$-element vector as in

$$\mathbf{c}_g = [\, c_g[1], c_g[2], \ldots, c_g[SF] \,]^T, \tag{4.6}$$

and $c_g[i]$ is the value of the ith chip of the gth DSS code, with $g \in \{1, 2, \ldots, G_q\}$ and $c_g[i] \in \{-\frac{1}{\sqrt{SF}}, +\frac{1}{\sqrt{SF}}\}$. Furthermore, the $\bar{\mathbf{H}}_{p,q}$ matrix in Equation 4.3 represents the $(U_q \times U_q)$-element FD-CHTF matrix of the channel states on the qth subcarrier between the U_q users and the pth receive AE, which is represented as [21]

$$\bar{\mathbf{H}}_{p,q} = \text{diag}\left[h^{(1)}_{p,1,q}, h^{(1)}_{p,2,q}, \ldots, h^{(1)}_{p,G_q,q}\right] \tag{4.7}$$

$$= \text{diag}\left[h_{p,1,q}, h_{p,2,q}, \ldots, h_{p,G_q,q}\right], \tag{4.8}$$

where $h^{(i)}_{p,g,q}$ is the complex-valued channel state in the frequency domain on the qth subcarrier between the ith user in the gth DSS code group and the pth receive AE, where the fact that we have $U_{q,g_q} = 1$ was exploited, with $g_q \in \{1, 2, \ldots, G_q\}$. Since in our non-coherent scenarios we have allowed only one user, if any, from a single DSS code group to be mapped to a subcarrier, we have $i = 1$ if the gth DSS code is present on the qth subcarrier. Therefore, we may omit the superscript (i) corresponding to the user index in the gth DSS code group. Moreover, the $(U_q \times 1)$-element symbol vector $\bar{\mathbf{s}}_q$ in Equation 4.3 represents the differentially encoded symbols of the U_q users who transmit on the qth subcarrier, as in [21]

$$\bar{\mathbf{s}}_q = \left[s^{(1)}_{1,q}, s^{(1)}_{2,q}, \ldots, s^{(1)}_{G_q,q}\right]^T \tag{4.9}$$

$$= \left[s_{1,q}, s_{2,q}, \ldots, s_{G_q,q}\right]^T, \tag{4.10}$$

where $s^{(i)}_{g,q}$ is the differentially encoded symbol transmitted by the ith user of the gth DSS group on the qth subcarrier. Once again, in our system we have $i \in \{0, 1\}$, therefore we may omit the superscript (i) as we did in Equation 4.10. Finally, the $(1 \times SF)$-element noise vector $n_{p,q}$ with zero mean and a variance equal to $N_0 = 2\sigma^2$ is represented as [21]

$$\mathbf{n}_{p,q} = [\, n_{p,q}[1], n_{p,q}[2], \ldots, n_{p,q}[SF] \,]^T. \tag{4.11}$$

After the DSS despreading procedure, the $(G_q \times 1)$-element symbol vector mapped to the qth subcarrier at the pth receive AE chain $\bar{\mathbf{y}}_{p,q}$ is equal to [21]

$$\bar{\mathbf{y}}_{p,q} = \check{\mathbf{c}}_{G_q} \mathbf{r}_{p,q} \tag{4.12}$$

$$= \bar{\mathbf{R}}_{G_q} \bar{\mathbf{H}}_{p,q} \bar{\mathbf{s}}_q + \bar{\mathbf{n}}_{p,q}, \tag{4.13}$$

where $\check{\mathbf{c}}_{G_q}$ is the $(SF \times G_q)$-element code book, containing all the different DSS codes that appear on the qth subcarrier, as in [21]

$$\check{\mathbf{c}}_{G_q} = \left[\mathbf{c}_1, \mathbf{c}_2, \ldots, \mathbf{c}_{G_q}\right]^T, \tag{4.14}$$

where $\mathbf{c}_g$ is the DSS code presented in Equation 4.6. In our system, where a maximum of one user of the gth DSS code group is allowed to transmit on the qth subcarrier, we have

$$\check{\mathbf{c}}_{G_q} = \left(\bar{\mathbf{c}}_{G_q}\right)^T, \tag{4.15}$$

where $\bar{\mathbf{c}}_{G_q}$ is given in Equation 4.5. In Equation 4.13, the $(G_q \times 1)$-element noise vector $\bar{\mathbf{n}}_{p,q}$ represents the effective noise and is given in

$$\bar{\mathbf{n}} = \check{\mathbf{c}}_{G_q} \mathbf{n}_{p,q} \tag{4.16}$$

$$= \left[n_{p,1,q}, n_{p,2,q}, \ldots, n_{p,G_q,q}\right]^T. \tag{4.17}$$

Finally, $\bar{\mathbf{R}}_{G_q}$ in Equation 4.13 is the $(SF \times U_q)$-element cross-correlation matrix of the G_q DSS codes that are present on the qth subcarrier, as formulated in

$$\bar{\mathbf{R}}_{G_q} = \begin{bmatrix} \omega_{11} \cdots \omega_{11} & \cdots & \omega_{1G_q} \cdots \omega_{1G_q} \\ \omega_{21} \cdots \omega_{21} & \cdots & \omega_{2G_q} \cdots \omega_{2G_q} \\ \vdots & \vdots & \vdots \\ \underbrace{\omega_{G_q1} \cdots \omega_{G_q1}}_{U_{q,1}} & \cdots & \underbrace{\omega_{G_qG_q} \cdots \omega_{G_qG_q}}_{U_{q,G_q}} \end{bmatrix} \tag{4.18}$$

$$= \begin{bmatrix} \omega_{11} & \omega_{12} & \cdots & \omega_{1G_q} \\ \omega_{21} & \omega_{22} & \cdots & \omega_{2G_q} \\ \vdots & \vdots & \ddots & \vdots \\ \omega_{G_q1} & \omega_{G_q2} & \cdots & \omega_{G_qG_q} \end{bmatrix}, \tag{4.19}$$

where $\omega_{i,j}$ is the cross-correlation between the ith and the jth DSS code, where $U_{q,i} = 1$ was exploited. Since we have chosen orthogonal WH codes in our system, the cross-correlation

matrix in Equation 4.19 is equal to the identity matrix, because we have:

$$\omega_{i,j} = \begin{cases} 1 & \text{if } i = j \\ 0 & \text{if } i \neq j \end{cases} . \tag{4.20}$$

In the end, the signal $\bar{\mathbf{y}}_{p,q}$ in Equation 4.13 becomes

$$\begin{bmatrix} y_{p,1,q} \\ y_{p,2,q} \\ \vdots \\ y_{p,G_q,q} \end{bmatrix} = \begin{bmatrix} 1 & 0 & \cdots & 0 \\ 0 & 1 & \cdots & 0 \\ \vdots & \vdots & \ddots & \vdots \\ 0 & 0 & \cdots & 1 \end{bmatrix} \cdot \begin{bmatrix} h_{p,1,q} & 0 & \cdots & 0 \\ 0 & h_{p,2,q} & \cdots & 0 \\ \vdots & \vdots & \ddots & \vdots \\ 0 & 0 & \cdots & h_{p,G_q,q} \end{bmatrix} \cdot \begin{bmatrix} s_{1,q} \\ s_{2,q} \\ \vdots \\ s_{G_q,q} \end{bmatrix} + \begin{bmatrix} n_{p,1,q} \\ n_{p,2,q} \\ \vdots \\ n_{p,G_q,q} \end{bmatrix} \tag{4.21}$$

$$= \begin{bmatrix} h_{p,1,q} & 0 & \cdots & 0 \\ 0 & h_{p,2,q} & \cdots & 0 \\ \vdots & \vdots & \ddots & \vdots \\ 0 & 0 & \cdots & h_{p,G_q,q} \end{bmatrix} \cdot \begin{bmatrix} s_{1,q} \\ s_{2,q} \\ \vdots \\ s_{G_q,q} \end{bmatrix} + \begin{bmatrix} n_{1,q} \\ n_{2,q} \\ \vdots \\ n_{G_q,q} \end{bmatrix} . \tag{4.22}$$

Therefore, a user transmitting on the qth subcarrier and having been allocated the gth DSS code is separated by the rest of the users. According to Equation 4.22, the resultant tth symbol of the uth user entering the quantum differential detector of Figure 4.2 is formulated as:

$$y_{p,g,q}[t] = h_{p,g,q}[t] \cdot s_{g,q}[t] + n_{g,q}[t] \tag{4.23}$$

$$\Rightarrow y_{p,u,q}[t] = h_{p,u,q}[t] \cdot s_{u,q}[t] + n_{u,q}[t], \tag{4.24}$$

since in our system there is an one-to-one correspondence between the user index and the DSS code index on every subcarrier. In the following sections the same differential detection process will be applied for every user's symbol stream, having been allocated a DSS code and transmitting on their allocated subcarriers, therefore we may omit the u, g and q subscripts without any loss of generality.

4.3 Conventional Differential Detector

In this section we will investigate the classic differential detector employed in the DSS/SSCH SDMA-OFDM system of Section 4.2. The procedures described in this section correspond to the Differential Detection block of Figure 4.2, therefore the symbols given in Equation 4.24 are assumed to be available. As mentioned in Section 4.2, the differential detec-

tion is performed on three parallel bases, hence we omit the subscripts corresponding to the specific user, subcarrier and DSS code indices.

The signals received during the $(t-1)$st and tth time slots at the pth receive AE are

$$y_p[t-1] = h_p[t-1] \cdot s[t-1] + n_p[t-1] \tag{4.25}$$

$$y_p[t] = h_p[t] \cdot s[t] + n_p[t], \tag{4.26}$$

respectively, where $h_p[t-1]$ and $h_p[t]$ denote the channel states at the $(t-1)$st and tth time slots, respectively, between the user and the pth receive AE, while $n_p[t-1]$ and $n_p[t]$ are the AWGN samples imposed on the pth receive AE at the $(t-1)$st and tth time slots, respectively. Each of the noise samples $n_p[t-1]$ and $n_p[t]$ have zero mean and a variance of $2\sigma^2$. Assuming that the transmissions occur over slow-fading channels, we have

$$h_p[t-1] = h_p[t], \ \forall p = 1, 2, \ldots, P \tag{4.27}$$

for every time slot that corresponds to the same transmitted frame after the most recent reference symbol was transmitted. It should be noted that Equation 4.27 represents the main assumption of non-coherent detection, but it does not imply that $h_p[t-1] = h_p[t]$ is necessarily true in the actual channel. Therefore, the more the channel varies in time, the more inaccurate the assumption in Equation 4.27 becomes, and hence the worse the performance of the non-coherent detector is expected to be. By substituting Equation 4.27 into Equation 4.25 and Equation 4.26, we arrive at:

$$y_p[t] = h_p[t-1] \cdot s[t-1] \cdot x[t] + n_p[t] \tag{4.28}$$

$$= y_p[t-1] \cdot x[t] + \underbrace{n_p[t] - n_p[t-1] \cdot x[t]}_{n'_p[t]}. \tag{4.29}$$

Therefore, the M-ary symbol $x[t]$ may be obtained by following the same procedure as in a single-input multiple-output channel, where $y_p[t-1]$ is the reference signal, or the "known" channel state, and $n'_p[t]$ is the effective noise with a variance of $4\sigma^2$, since $n_p[t]$ and $n_p[t-1]$ are added. The resultant decision concerning $x[t]$ is performed as in

$$x[t] = \sum_{p=1}^{P} \frac{y_p[t]}{y_p[t-1]}, \tag{4.30}$$

where $y_p[t-1]$ and $y_p[t]$ are described in Equation 4.25 and Equation 4.26, respectively.

The advantage of detecting the desired symbol without requiring an estimate of the channel state is gleaned at the cost of a 3 dB penalty due to the effects of noise [21]. This is verified in Figure 4.5, where we present the BER performance of both the conventional coherent detector and of the CDD in the uplink of a four-user $U = 4$ OFDM system having one transmit antenna each and $P = 2$ receive AEs at the BS, using QPSK modulation, no channel coding and $\mathcal{Q} = 1024$ subcarriers with a channel bandwidth of 10 MHz [146]. In contrast to the LTE standard, we will assume that all $\mathcal{Q} = 1024$ subcarriers are active.

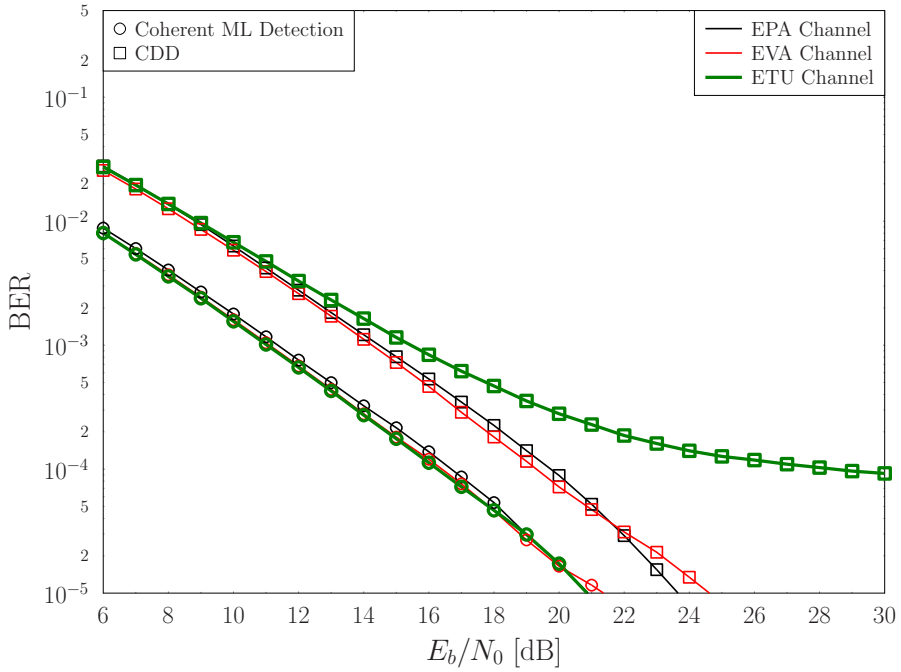

Figure 4.5: BER performance of a $U = 4$-user DSS/SSCH SDMA-OFDM system of Figure 4.2, with the parameters stated in Table 4.1. The EPA, EVA and ETU channel models of the LTE standard, which are summarized in Table 4.2, have been used and no channel coding has been applied. The frame length of each user is 12 288 bits. The conventional coherent and differential detectors are compared, with the CDD experiencing a 3 dB performance loss when the effective normalized Doppler frequency F_d is small enough, but not requiring channel estimation.

Moreover, each user transmits on $W = 512$ subcarriers out of the available $\mathcal{Q} = 1024$ subcarriers and is allocated one of the $G = 2$ available Walsh-Hadamard DSS codes. The schedule of the subcarrier allocation is generated by the DSS-based USSCH [3] and it changes every $T_h = 13$ OFDM symbol periods, while the length of a symbol frame is equal to 12 288 symbols. Let us use the Extended Pedestrian A (EPA), Extended Vehicular A (EVA) and Extended Typical Urban (ETU) LTE channel models for our example. The parameters of the system are described in Table 4.1, while those of the channel models are offered in Table 4.2. The sampling frequency is chosen according to the LTE standard [146], while a carrier frequency of $f_c = 2.5$ GHz is selected. The mobile velocity of the three channels is the one that corresponds to the maximum Doppler frequency of the channels, according to the LTE standard [146]. It should be noted that we assume a practical LTE system, where we experience continuous Rayleigh fading at the subcarriers. Therefore, if the normalized Doppler frequency of the independent Rayleigh channels on each tap of the multipath channel model is equal to f_d and we have $\mathcal{Q}$ subcarriers, the effective Doppler frequency between the channel states of two consecutively received symbols on the qth subcarrier is equal to

$$F_d = f_d \cdot \mathcal{Q}. \tag{4.31}$$

In other words, the effective channel that a subcarrier experiences in the time domain has a Doppler frequency of F_d in Equation 4.31. In this treatise, all the channels experience Rayleigh fading, unless specified otherwise. The Rayleigh fading is a complex-valued zero-

Table 4.1: Parameters of the 4-user OFDM system used for analysing differential detection

Number of Users	$U = 4$
Number of AEs per User	$N_{T_x} = 1$
Number of AEs at the BS	$P = 2$
Normalized User Load	$U_L = U \cdot N_{T_x}/P = 2$
Modulation	DQPSK in time domain
Mapping Type	Gray for soft-output receivers &
	Set Partition for iterative receivers
Channel Code (when used)	Turbo Code, $R = 1/2$, 8 Trellis states
	$I_{inner} = 4$ iterations
Number of Subcarriers	$\mathcal{Q} = 1024$
Cyclic Prefix	CP = 128
Number of Subcarriers per User	$W = 512$
Number of Walsh-Hadamard DSS Codes	$G = 2$
Subcarrier Allocation every	$T_h = 13$ OFDM symbol periods
Bit Interleaver Length	24 576 per User
Channel Models	Refer to Table 4.2

mean Gaussian process with a variance of σ_h^2 [21].

We may observe the 3 dB performance loss in Figure 4.5, when comparing the two BER curves that correspond to the CDD and the coherent ML detector when transmitting on the EPA and the EVA channels. No channel coding is employed. When we use the ETU channel model, the CDD experiences a BER floor at a BER of approximately 10^{-4}, due to the increased effective normalized Doppler frequency of the channel based on Table 4.2. At the same time, the coherent ML detection is affected less severely by the normalized Doppler frequency, resulting in an E_b/N_0 performance loss of 12 dB for the CDD at a BER of 10^{-4}. Therefore, we may conclude that the EPA and EVA channels, when we use the 10 MHz channel bandwidth, are suitable for the CDD, while the ETU channel varies far too rapidly for the CDD to perform well. Even though a higher transmission power is required in non-coherent systems for achieving the same performance as their coherent counterparts, the complexity of the non-coherent receivers is typically much lower.

4.3.1 Effect of Time-Selective Channels

The DPSK modulation may be performed for the consecutive symbols in the time domain, for consecutive OFDM symbols of the same subcarriers. It may also be carried out in the frequency domain, by differentially encoding the symbols of the adjacent subcarriers of the same OFDM symbol. In this treatise, we will proceed by applying differential modulation in the time domain. Therefore, according to the slow-fading assumption made in Equation 4.27 about the channels, time-selective channels are expected to impose a major effect on the differential detection in our systems. This is characterized by the

Table 4.2: Parameters of the LTE channel models

Sampling Frequency	$f_s = 15.36$ MHz
Carrier Frequency	$f_c = 2.5$ GHz
Extended Pedestrian A (EPA)	
Mobile Velocity	$v = 5$ km/h
Normalized Doppler Frequency	$f_d = 7.54 \cdot 10^{-7}$
Number of Taps	$N_{taps} = 5$
Power Profile	$[-2.392 \ -4.392 \ -12.931 \ -22.131 \ -25.731]$
Delay Profile	[0 1 2 3 6]
Extended Vehicular A (EVA)	
Mobile Velocity	$v = 30$ km/h
Normalized Doppler Frequency	$f_d = 4.52 \cdot 10^{-6}$
Number of Taps	$N_{taps} = 8$
Power Profile	$[-3.852 \ -7.576 \ -9.776 \ -6.776$ $-15.276 \ -13.176 \ -18.177 \ -23.076]$
Delay Profile	[0 2 5 6 11 17 27 39]
Extended Typical Urban (ETU)	
Mobile Velocity	$v = 130$ km/h
Normalized Doppler Frequency	$f_d = 1.96 \cdot 10^{-5}$
Number of Taps	$N_{taps} = 9$
Power Profile	$[-9.062 \ -9.062 \ -9.062 \ -8.062 \ -8.062$ $-8.062 \ -11.062 \ -13.062 \ -15.062]$
Delay Profile	[0 1 2 3 4 8 25 35 77]

autocorrelation function of the channel states between the uth user and the pth receive AE on the qth subcarrier, which is [21]

$$\phi^t_{hh}[\kappa] \triangleq \mathcal{E}\left\{h_p[t+\kappa] \cdot h^*_p[t]\right\} = J_0\left(2\pi F_d \kappa\right) = J_0\left(2\pi \mathcal{Q} f_d \kappa\right), \tag{4.32}$$

where $J_0(\cdot)$ is the zeroth-order Bessel function, f_d is the normalized Doppler frequency of the channels, while F_d is the effective normalized Doppler frequency of the channels as described in Equation 4.31.

Figure 4.6 demonstrates the effect of time-selectivity in the performance of differential detectors, by showing the BER curves of the system described in Table 4.1 when transmitting over EVA channels. The magnitude of the autocorrelation function given in Equation 4.32 is also shown in Figure 4.6 for various effective Doppler frequencies. Even though the maximum Doppler frequency in an EVA channel is equal to 70 Hz, corresponding to a normalized Doppler frequency of $f_d = 70/f_s = 4.52 \cdot 10^{-6}$, let us assume higher normalized Doppler frequencies for observing the CDD's performance. In Figure 4.6 we may observe that when the normalized Doppler frequency f_d is high enough, the system experiences an error floor in its BER performance, in addition to the 3 dB performance loss, when compared to the conventional coherent detection. Furthermore, the higher the

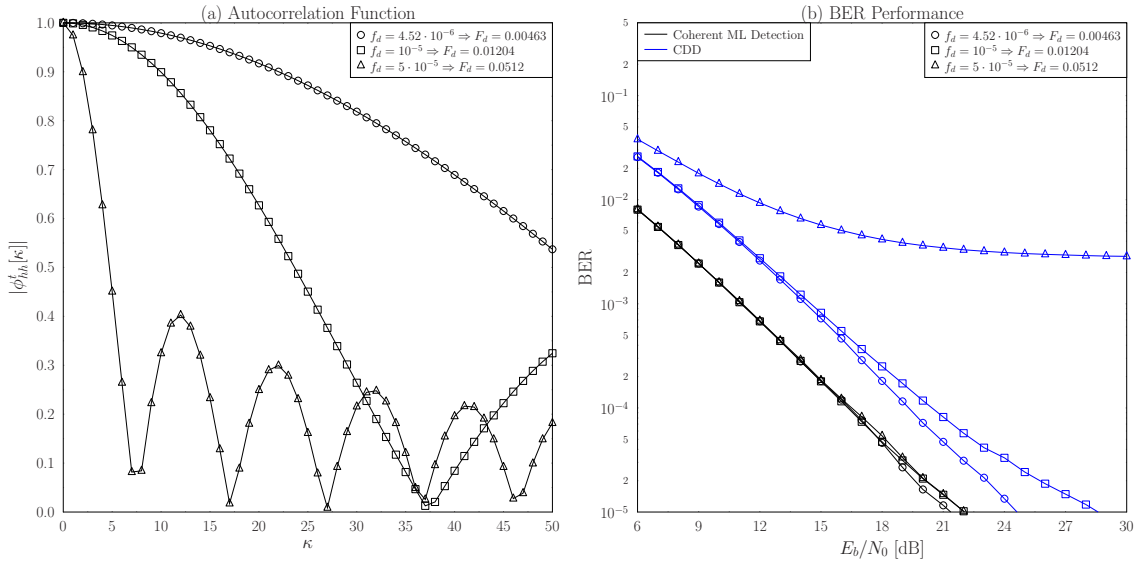

Figure 4.6: (a) Magnitude of the autocorrelation function in Equation 4.32 for different values of the effective normalized Doppler frequency F_d in Equation 4.31. (b) BER performance of the uncoded DSS/SSCH SDMA-OFDM system of Figure 4.2 with its parameters summarized in Table 4.1, in an EVA channel with different Doppler frequencies, as stated in Table 4.2. The frame length of each user is 12 288 bits.

normalized Doppler frequency of the channels, the higher the BER value that the error floor appears at.

The differential detectors exploit the correlation between the phase distortions of the consecutively received symbols in the time or the frequency domain. Since in our treatise we differentially encode the symbols in the time domain, we should exploit the correlation of the channels in the time domain. The CDD compares the signal received during the tth time slot to the signal received during the $(t-1)$th time slot. Since the detection of the CDD is based on two symbols, it may be viewed as detection using a sliding window of $N_w = 2$ symbols. In the first OFDM symbol on the qth subcarrier, $q \in \{1, 2, \ldots, \mathcal{Q}\}$, the reference symbol is transmitted. Afterwards, the first differentially encoded symbol is transmitted during the second OFDM symbol and the CDD estimates its value. Once the third OFDM symbol has been received, the previously detected symbol, which was transmitted during the second OFDM symbol, acts as the reference symbol. Explicitly, assuming that the previous detection was correct, the CDD makes a decision concerning the third symbol. This procedure is repeated, until the whole frame has been transmitted, or another reference symbol is transmitted.

4.4 Hard-Input Hard-Output Multiple Symbol Differential Detectors

The performance of the CDD mainly depends on the accuracy of the detection, since every decision made for the most recently received symbol affects the detection of the next symbol. The MSDD performs detection on N_w consecutively received symbols with $N_w > 2$. The

BER performance of the MSDDs is assumed to be better than that of the CDD, since the correlation between the phase distortions of symbols that were transmitted with more than one symbol period difference is also taken into consideration in the detection. On the other hand, the complexity of any MSDD is higher than that of the CDD, since the problem becomes a "shortest-vector" problem [21] and the pool of legitimate candidates increases exponentially with N_w. Since the reference symbol is known to the receiver, the MSDD performing detection over N_w received symbols determines the estimates of (N_w-1) symbols.

As in the CDD section, the following analysis takes place at the differential detection stage of Figure 4.2. We focus our attention on the uth user, having been assigned the gth DSS code and transmitting on the qth subcarrier, therefore we omit the subscripts u, g and q. Furthermore, the symbols described in Equation 4.24 are assumed to be available. The number of OFDM symbols transmitted between two reference symbols is equal to T_h.

Since the detection is performed in blocks of N_w symbols, with the consecutive blocks overlapping by one symbol, the ith received symbol vector, $i \in \{1, 2, \ldots, T_h/N_w\}$, at the pth receive AE consisting of N_w consecutively received symbols in the time domain is

$$\mathbf{y}_p[i] \triangleq [y_p[N_w \cdot i - (N_w - 1))],\ y_p[N_w \cdot i - (N_w - 2)], \ldots,\ y_p[N_w \cdot i]]^T. \tag{4.33}$$

The received symbol vector of Equation 4.33 is exploited by the MSDD for estimating the ith N_w-element transmitted symbol vector $\hat{\mathbf{s}}[i]$, which corresponds to the ith actually transmitted symbol vector

$$\mathbf{s}[i] \triangleq [s[N_w \cdot i - (N_w - 1))],\ s[N_w \cdot i - (N_w - 2)], \ldots,\ s[N_w \cdot i]]^T, \tag{4.34}$$

which in turn is the differentially encoded version of the $(N_w - 1)$-element symbol vector

$$\mathbf{x}[i] \triangleq [x[N_w \cdot i - (N_w - 2))],\ x[N_w \cdot i - (N_w - 3)], \ldots,\ x[N_w \cdot i]]^T. \tag{4.35}$$

The objective of the MSDD is to find the best estimate $\hat{\mathbf{x}}[i]$ of the symbol vector in Equation 4.35. The MSDD performs detection on a block-by-block basis, therefore we may omit the subscript i in Equation 4.33, Equation 4.34 and Equation 4.35 from our analysis, resulting in

$$\mathbf{y}_p \triangleq [\ y_p[1],\ y_p[2],\ \ldots\ ,\ y_p[N_w]\ ]^T, \tag{4.36}$$

$$\mathbf{s} \triangleq [\ s[1],\ s[2],\ \ldots\ ,\ s[N_w]\ ]^T, \tag{4.37}$$

$$\mathbf{x} \triangleq [\ x[2],\ x[3],\ \ldots\ ,\ x[N_w]\ ]^T. \tag{4.38}$$

The conditional PDF of the received symbol vector $\mathbf{y}$ of Equation 4.36 over N_w consecutive OFDM symbols, given that the symbol vector $\mathbf{s}$ of Equation 4.37 was transmitted, is [166]

$$p(\mathbf{Y}|\mathbf{s}) = \frac{\exp\left(-Tr\left\{\mathbf{Y}^H \Psi^{-1} \mathbf{Y}\right\}\right)}{\left(\det\left\{\pi\Psi\right\}\right)^P}, \tag{4.39}$$

where $\mathbf{Y}$ is the $(N_w \times P)$-element matrix that contains the P number of received symbol vectors $\mathbf{y}_p$, $p \in \{1, 2, \ldots, P\}$, as in

$$\mathbf{Y} = [\mathbf{y}_1, \mathbf{y}_2, \ldots, \mathbf{y}_P] \tag{4.40}$$

and $Tr\{\cdot\}$ yields the trace of a square matrix. Furthermore, $\Psi = \mathcal{E}\left\{\mathbf{y}_p \mathbf{y}_p^H | \mathbf{s}\right\}$ is the $(N_w \times N_w)$-element conditional autocorrelation matrix of the Rayleigh channel. The conditional autocorrelation matrix of the Rayleigh channel Ψ in Equation 4.39 depends on the transmitted symbol vector $\mathbf{s}$, the noise variance N_0 and the normalized Doppler frequency F_d, therefore it is the same for each of the P receive AEs, hence allowing us to omit the subscript p from the following discussion of Ψ. It may be expanded as

$$\begin{aligned}
\Psi &= \mathcal{E}\left\{\mathbf{y}\mathbf{y}^H | \mathbf{s}\right\} && (4.41)\\
&= \text{diag}(\mathbf{s}) \cdot \mathcal{E}\left\{\mathbf{h}\mathbf{h}^H\right\} \cdot \text{diag}(\mathbf{s}^H) + \mathcal{E}\left\{\mathbf{n}\mathbf{n}^H\right\} && (4.42)\\
&= \text{diag}(\mathbf{s}) \cdot \left(\mathcal{E}\left\{\mathbf{h}\mathbf{h}^H\right\} + 2\sigma^2 \cdot \mathbf{I}_{N_w}\right) \cdot \text{diag}(\mathbf{s}^H) && (4.43)\\
&= \text{diag}(\mathbf{s}) \cdot \mathbf{C} \cdot \text{diag}(\mathbf{s}^H), && (4.44)
\end{aligned}$$

where $\mathbf{C} \triangleq \mathcal{E}\left\{\mathbf{h}\mathbf{h}^H\right\} + 2\sigma^2 \cdot \mathbf{I}_{N_w}$ and $\text{diag}(\mathbf{s})$ is a diagonal matrix with the vector $\mathbf{s}$ on its diagonal as in

$$\text{diag}(\mathbf{s}) = \begin{bmatrix} s_1 & 0 & \cdots & 0 \\ 0 & s_2 & \cdots & 0 \\ \vdots & \vdots & \ddots & \vdots \\ 0 & 0 & \cdots & s_{N_w} \end{bmatrix}, \tag{4.45}$$

where we have $\text{diag}(\mathbf{s}^*) = \text{diag}(\mathbf{s})^H$ for any complex vector $\mathbf{s}$ and

$$\text{diag}(\mathbf{s})^{-1} = \text{diag}(\mathbf{s}^*) = \text{diag}(\mathbf{s})^H, \tag{4.46}$$

since $\mathbf{s} \in \mathcal{M}^{N_w}$. Moreover, $\Sigma_h = \mathcal{E}\left\{\mathbf{h}\mathbf{h}^H\right\}$ is the channel's covariance matrix in the time or frequency domain. Since we have opted for differentially encoding the symbols in the time domain, Σ_h may be represented as

$$\Sigma_h = \mathcal{E}\left\{\mathbf{h}\mathbf{h}^H\right\} \tag{4.47}$$

$$= \sigma_h^2 \cdot \begin{bmatrix} \phi_{hh}^t[0] & \phi_{hh}^t[1] & \cdots & \phi_{hh}^t[N_w - 1] \\ \phi_{hh}^t[1] & \phi_{hh}^t[0] & \cdots & \phi_{hh}^t[N_w - 2] \\ \vdots & \vdots & \ddots & \vdots \\ \phi_{hh}^t[N_w - 1] & \phi_{hh}^t[N_w - 2] & \cdots & \phi_{hh}^t[0] \end{bmatrix}, \tag{4.48}$$

where σ_h^2 is the variance of the channel and $\phi_{hh}^t[\kappa]$, $k \in \{0, 1, \ldots, N_w - 1\}$, is the autocorrelation function of the channel states in the time domain, which is stated in Equation 4.32.

4.4.1 Maximum-Likelihood MSDD

In non-coherent receivers, where no channel coding has been applied, the performance of HIHO MSDDs will be equivalent to the performance of SISO MSDDs, provided that the legitimate symbols are transmitted with equal probability, but the required complexity is smaller. In HIHO MSDDs, the detection is performed by finding that particular multi-level symbol estimate $\hat{\mathbf{x}}$ of Equation 4.38, or, equivalently, $\hat{\mathbf{s}}$ of Equation 4.37, which minimizes a specific metric, thus transforming the problem into a "shortest-vector" problem [166]. More specifically, the ML MSDD detects that particular symbol vector $\hat{\mathbf{s}}$, which maximizes the probability of $\hat{\mathbf{s}}$ having been transmitted, given that the symbol matrix $\mathbf{Y}$ has been received, or, in other words

$$\hat{\mathbf{s}}_{ML} = \arg\max_{\mathbf{s}\in\mathcal{M}^{N_w}} \left(P(\mathbf{s}|\mathbf{Y})\right) \tag{4.49}$$

$$= \arg\max_{\mathbf{s}\in\mathcal{M}^{N_w}} \left(\frac{p(\mathbf{Y}|\mathbf{s})\cdot P(\mathbf{s})}{p(\mathbf{Y})},\right) \tag{4.50}$$

where the Bayes' theorem [173, 174] was applied. Still referring to Equation 4.50, $p(\mathbf{Y}|\mathbf{s})$ is the conditional probability of having received the symbol matrix $\mathbf{Y}$, given that $\mathbf{s}$ was transmitted as in Equation 4.39, $P(\mathbf{s})$ is the *a priori* probability of the symbol vector $\mathbf{s}$ to have been transmitted and $p(\mathbf{Y})$ is termed as the system model probability, which represents the probability of having received $\mathbf{Y}$. Considering that a HIHO receiver is non-iterative and that the transmitter generated the source bits equiprobably, the values of $p(\mathbf{Y})$ and $P(\mathbf{s})$ are the same for every legitimate $\mathbf{s}$.

The conditional PDF $p(\mathbf{Y}|\mathbf{s})$ in Equation 4.39 is the ML metric of the HIHO MSDD. Therefore, based on Equation 4.50, the detected symbol vector $\hat{\mathbf{s}}$ will be the vector that satisfies

$$\hat{\mathbf{s}}_{ML} = \arg\max_{\mathbf{s}\in\mathcal{M}^{N_w}} \left(p(\mathbf{Y}|\mathbf{s})\right) \tag{4.51}$$

$$= \arg\min_{\mathbf{s}\in\mathcal{M}^{N_w}} \left(Tr\left\{\mathbf{Y}^H \Psi^{-1} \mathbf{Y}\right\}\right) \tag{4.52}$$

$$= \arg\min_{\mathbf{s}\in\mathcal{M}^{N_w}} \left(Tr\left\{\mathbf{Y}^H \,\mathrm{diag}(\mathbf{s})\, \mathbf{C}^{-1}\, \mathrm{diag}(\mathbf{s})^H\, \mathbf{Y}\right\}\right) \tag{4.53}$$

$$= \arg\min_{\mathbf{s}\in\mathcal{M}^{N_w}} \sum_{p=1}^{P} \left(\mathbf{s}^H \cdot \mathrm{diag}(\mathbf{y}_p) \cdot \mathbf{C}^{-1} \cdot \mathrm{diag}(\mathbf{y}_p)^H \cdot \mathbf{s}\right) \tag{4.54}$$

$$= \arg\min_{\mathbf{s}\in\mathcal{M}^{N_w}} \sum_{p=1}^{P} \left(\mathbf{s}^H \cdot \mathrm{diag}(\mathbf{y}_p) \cdot \mathbf{F}^H \cdot \mathbf{F} \cdot \mathrm{diag}(\mathbf{y}_p)^H \cdot \mathbf{s}\right), \tag{4.55}$$

where Equation 4.46 and Equation 4.44 were used and $\mathbf{F}$ is an upper-triangular matrix obtained by the Cholesky factorization of $\mathbf{C}^{-1}$ and satisfies

$$\mathbf{C}^{-1} = \mathbf{F}^H \mathbf{F}. \tag{4.56}$$

By defining the upper-triangular matrix $\mathbf{U}_p$ for $p = 1, 2, \ldots, P$ as

$$\mathbf{U}_p \triangleq \mathbf{F}\,\mathrm{diag}(\mathbf{y}_p)^H \tag{4.57}$$

$$= \mathbf{F}\,\mathrm{diag}(\mathbf{y}_p)^* \tag{4.58}$$

and substituting it in Equation 4.55 we obtain

$$\hat{\mathbf{s}}_{ML} = \arg\min_{\mathbf{s}\in\mathcal{M}^{N_w}} \sum_{p=1}^{P} \left(\mathbf{s}^H \cdot \mathbf{U}_p^H \cdot \mathbf{U}_p \cdot \mathbf{s}\right) \tag{4.59}$$

$$= \arg\min_{\mathbf{s}\in\mathcal{M}^{N_w}} \sum_{p=1}^{P} \left(\| \mathbf{U}_p \cdot \mathbf{s} \|_2^2\right). \tag{4.60}$$

The ML MSDD performs optimally by exhaustively searching the entire set $\mathcal{M}^{N_w-1}$ for the symbol vector $\mathbf{s}$ that satisfies Equation 4.60. Therefore, the Cost Function (CF) of the HIHO MSDD is

$$f_{MSDD}^{HIHO}(\mathbf{s}) = \sum_{p=1}^{P} \left(\| \mathbf{U}_p \cdot \mathbf{s} \|_2^2\right). \tag{4.61}$$

The MSDSD [166] is also based on the metric in Equation 4.60 and approaches the detection of $\hat{\mathbf{s}}$ by disassembling Equation 4.60 into a symbol-by-symbol decision. The performance of the MSDSD is near-optimal and its complexity is lower than that of the ML MSDD [21, 167].

4.4.2 Dürr-Høyer Algorithm-Based QMSDD

The DHA may be used for performing HIHO QMSDD. The DHA was detailed in Section 2.4.3. The ML MSDD evaluates the CF in Equation 4.61 for every legitimate symbol vector $\mathbf{s}$ in $\mathcal{M}^{N_w}$ with the first element of $\mathbf{s}$ being fixed to the reference symbol. Therefore, the effective search space is $\mathcal{M}^{N_w-1}$ and hence the complexity of the ML MSDD increases exponentially with the size of the detection window $2 \leq N_w \leq T_h$, requiring $\mathcal{M}^{N_w-1}$ CFEs. The DHA QMSDD replaces the U_f in the Oracle circuit in Figure 2.12 with the CF of the HIHO MSDD described in Equation 4.61. With the HIHO MSDD's CF operating in the Oracle, the DHA QMSDD succeeds in finding the specific symbol vector $\mathbf{s}$ that minimizes the CF in Equation 4.61 at a complexity of $O\left(\sqrt{M^{N_w-1}}\right)$ CFEs. Since no *a priori* knowledge is provided about a specific value for the symbol vector $\mathbf{s}$ as in the coherent MUD, where the MMSE detector could provide an initial estimate, the DHA QMSDD is randomly initialized.

Let us proceed by comparing the DHA QMSDD to both the ML MSDD and to the CDD in our DSS/SSCH SDMA-OFDM system characterized in Table 4.1 and Table 4.2. The size of the detection window N_w is chosen to be $N_w = 5$ or $N_w = 7$, where $N_w = 2$ corresponds to an MSDD equivalent to the CDD. The symbol detected by the MSDDs at the N_wth position of $\mathbf{s}$ is the reference symbol of the subsequent MSDD procedure.

Figure 4.7 depicts the BER performance of both the DHA QMSDD, as well as of

Table 4.3: Computational complexity in terms of the number of CFEs / bit in Figure 4.7

	$N_w = 5$	$N_w = 7$
ML MSDD	32 CFEs / bit	341.33 CFEs / bit
DHA MSDD	12.77 CFEs / bit	43.6 CFEs / bit

the ML MSDD and of the CDD in our system scenario. Additionally, we have included the performance of the equivalent coherent system for reference, where the channel states have been perfectly estimated at the BS. We may observe that the DHA QMSDD has an equivalent performance to that of the ML MSDD, for both values of N_w. At the same time, the computational complexity of the DHA QMSDD was only 55% and 12.77% of the corresponding complexities of the ML MSDD for $N_w = 5$ and $N_w = 7$, respectively, as presented in Table 4.3. Furthermore, the ML MSDD and the DHA QMSDD perform better than the CDD by approximately 0.6 dB for $N_w = 7$. Naturally, the BER versus Signal to Noise Ratio (SNR) improvement is achieved at an increased complexity, since the complexity of the CDD is 2 CFEs / bit. The BER improvement between the scenario where $N_w = 7$ was used and the one where $N_w = 5$ was selected is 0.2 dB. This is mainly due to the fact that since we have $T_h = 13$, there are two and three detection windows when $N_w = 7$ and $N_w = 5$, respectively, resulting in a similar performance. The expected 3 dB difference between the coherent ML detection and the MSDDs is indeed present in Figure 4.7 and it becomes higher upon increasing E_b/N_0 due to the channel coding having a more beneficial effect on coherent systems [21].

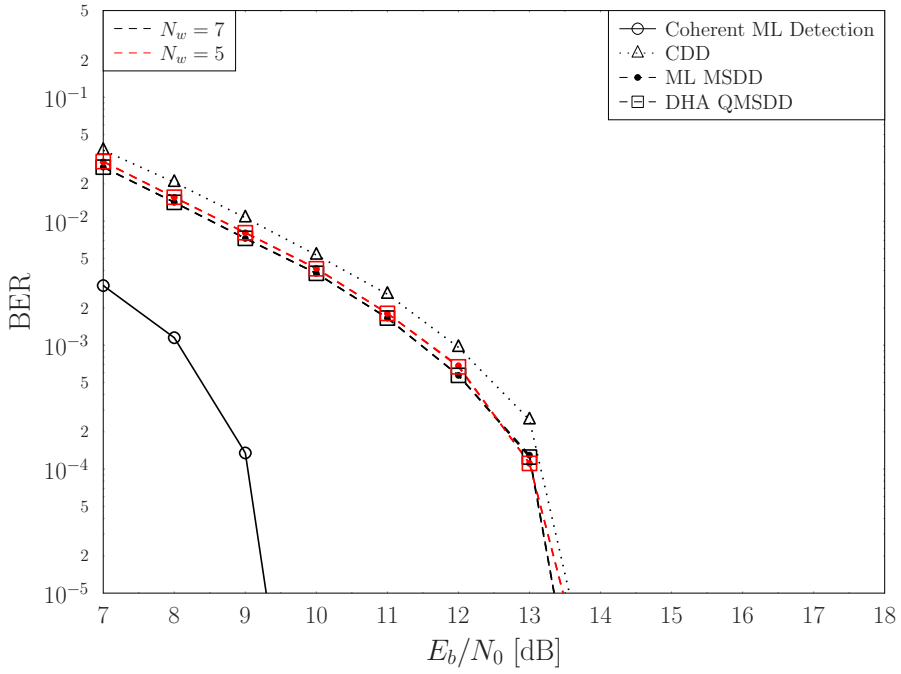

Figure 4.7: BER performance of the DHA QMSDD, the ML MSDD and the CDD in the coded example DSS/SSCH SDMA-OFDM system of Figure 4.2, using the parameters of Table 4.1 and the EPA channel model of Table 4.2. The BER performance of the coherent detection of the same example is also included for terms of comparison.

4.4.3 Early-Stopping Aided Dürr-Høyer Algorithm-Based QMSDD

The ES-DHA was presented in Section 2.4.4. Based on the acquired statistics of the required number of CFEs of off-line searches using the DHA, the ES-DHA may be able to reduce the necessary complexity of the QMSDD. In more detail, when the randomly-initialised or the deterministically-initialised DHA finds the symbol vector $\hat{\mathbf{s}}_{ML}$ of Equation 4.60 after a number of BBHT iterations, it does not realize this success until another BBHT iteration yields a symbol vector $\mathbf{s}$, which has a higher CF value than that of the already found $\hat{\mathbf{s}}_{ML}$. By simulating a large number of DHA searches in an off-line fashion for the same search space size as our system's search space, we may gather statistics concerning the number of CFEs that were required for the DHA to find the solution $\hat{\mathbf{s}}_{ML}$, rather than to realize that the solution has already been found [2]. By carefully interpreting these statistics, we are able to perform optimal MSDD at a reduced complexity, or allow a suboptimal performance, if we operate under a strict complexity-budget in terms of the number of CFEs.

For our scenario, the CDF curves of the number of CFEs performed both in the CD and the QD, as well as the total number of CFEs carried out in both domains during the DHA searches are plotted in Figure 4.8a for $N_w = 7$ and $E_b/N_0 = 13.5$. Since the initial DHA input is selected to be random, the value of the E_b/N_0 does not affect the resultant PDF and CDF curves [2]. We simulated the DHA in our system scenario for $12 \cdot 10^6$ independent instances. Figure 4.8a shows that in 99% of the DHA instances, the search was completed in fewer than 787 CFEs, or performing less than $787/4096 \cdot 100\% = 19.2\%$ of the number of CFEs required by the ML QMSDD. Similarly, 80% of the DHA searches were completed after evaluating the CF of Equation 4.60 at most 605 times, which forms 14.8% of the number of CFEs per multi-level MSDD symbol vector performed in the ML MSDDs. It should be noted at this point that the statistics do not take into consideration the success of the search, but only the complexity required for the search to be completed. However, the DHA has a success probability of ∼100%, hence in most of the instances the search is indeed successful. By exploiting the CDF curves of Figure 4.8 we may stop the DHA in our scenario after 787 CFEs and expect a ∼99% success probability in our search for $\hat{\mathbf{s}}_{ML}$.

By observing Figure 4.8a we are also able to infer that the minimum number of total CFEs required by the DHA to complete its actions is 313, which forms 7.6% of the CFEs in the ML MSDD. This is the minimum number of CFEs that the DHA required out of $12 \cdot 10^6$ instances for realizing that it had already found $\hat{\mathbf{s}}_{ML}$ and this corresponds to the scenario, where the random initial DHA input was equal to $\hat{\mathbf{s}}_{ML}$ and the minimum number of CFEs both in the CD and the QD were performed. The probability of the random initial DHA input to be equal to the optimal symbol index and at the same time the DHA to require exactly $4.5\sqrt{M^{N_w-1}} = 288$ CFEs in the QD for finding it turned out to be equal to $1.4 \cdot 10^{-5}$ based on the CDF seen in Figure 4.8b. Furthermore, the minimum number of CFEs performed in the CD was equal to 25 CFEs with a probability of occurrence equal to $9 \cdot 10^{-6}$ according to the CDF in Figure 4.8c. In total, the scenario associated with the lowest complexity is the one, where the random initial DHA input is equal to the optimal symbol index and the DHA performs 288 CFEs in the QD and 25 CFEs in the CD, resulting

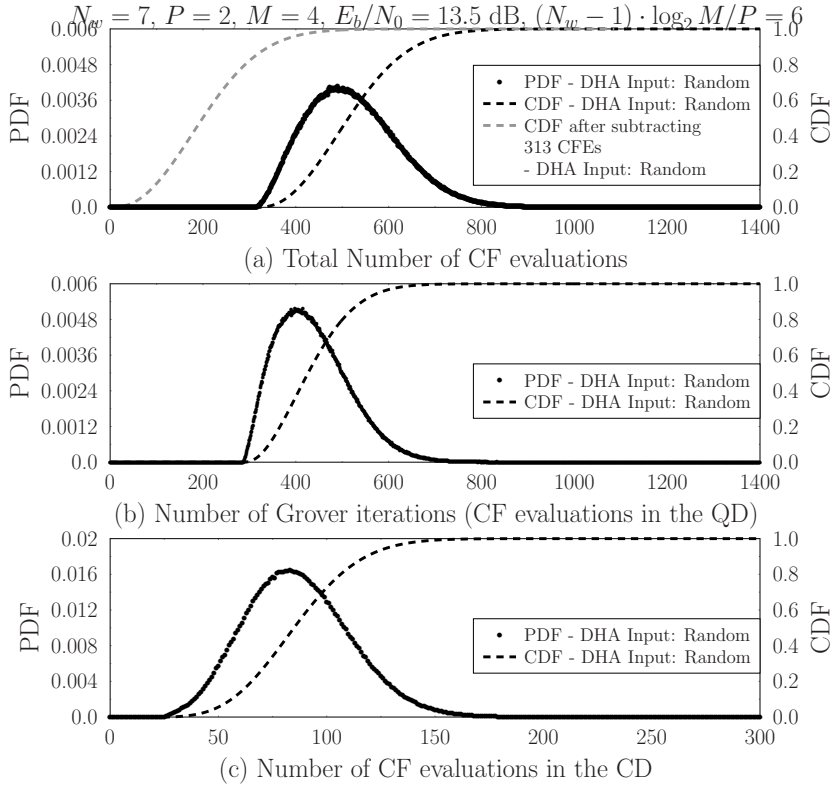

Figure 4.8: PDF and CDF curves of the DHA in the system scenario of Figure 4.2, described in Table 4.1 and Table 4.2 after $12 \cdot 10^6$ number of independent DHA instances, before and after subtracting the minimum total number of CFEs, equal to 314 CFEs, required by the DHA to realize that the solution has already been found.

in a total of 313 CFEs. In our simulation instances this incident occurred with a probability of $3 \cdot 10^{-6}$.

These 313 CFEs did not impact the output, since the initial DHA input was already equal to the desired output. Therefore, the ES-DHA QMSDD considers this amount of 313 CFEs as unnecessary complexity and always subtracts it from the affordable number of CFEs of the DHA, without altering the success probability indicated by the CDF curves. In other words, if we allow the DHA to run in our system scenario for 787 CFEs and for $787 - 313 = 474$ CFEs, which form only 11.6% of the number of CFEs performed in the ML MSDD, we should expect a ∼99% success probability in both scenarios. This non-intuitive phenomenon may be logically interpreted as the difference between the number of CFEs the DHA requires to find the solution and the number of CFEs the DHA requires to realize that it has already found the solution. In the first case, the DHA will naturally terminate its own operation 99% of the time while having found the solution. By contrast, in the second case the DHA will naturally stop on its own 34.4% of the time but it will again have found the solution 99% of the time, assuming a 100% success ratio. Figure 4.8a also presents the CDF curve after 313 CFEs have been subtracted.

The BER performance of the ES-DHA QMSDD is illustrated in Figure 4.9, where it is compared to the DHA QMSDD of Section 4.4.2 for various early stopping points based on the gray CDF curve in Figure 4.8a and $N_w = 7$. According to Figure 4.9, the BER

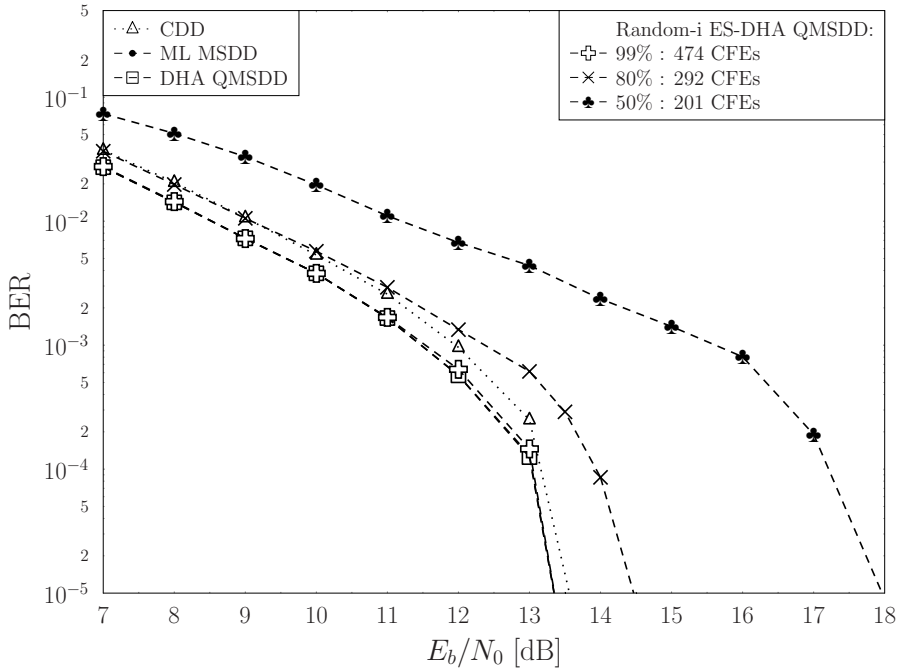

Figure 4.9: BER performance of the ES-DHA QMSDD for the 99%, 80% and 50% points of the CDF curve in Figure 4.8, corresponding to a maximum of 474, 292 and 201 CFEs, respectively, in the DSS/SSCH SDMA-OFDM system scenario of Figure 4.2, using the parameters summarized in Table 4.1 for $N_w = 7$ in the EPA channel of Table 4.2.

Table 4.4: Computational complexity in terms of the number of CFEs / bit in Figure 4.9

MSDD / QMSDD	Number of CFEs per bit		
CDD	2		
ML	341.33		
DHA	43.6		
ES-DHA	CDF %	CDF at $E_b/N_0 = 13.5$ dB	Number of CFEs per bit
	99%	474	37.9
	80%	292	24.33
	50%	201	16.75

performance of the ES-DHA QMSDD when the 474 CFEs corresponding to the 99% point of the CDF are chosen as the maximum affordable number of CFEs is equivalent to that of the DHA QMSDD and the ML MSDD. The computational complexity of the ES-DHA-99% QMSDD is equal to 37.9 CFEs per bit, compared to the complexity of the DHA QMSDD, which requires 43.6 CFEs per bit, according to Table 4.4. Moreover, when the 80% point of the CDF is selected, the ES-DHA QMSDD's performance is equivalent to that of the CDD until the $E_b/N_0 = 9$ dB point, after which it becomes worse. It seems that in this system scenario, the CDD finds the optimal solution more often than 80% of the time. This might have been expected, since the power gain of the MSDD when compared to the CDD is only 0.5 dB. Similarly, the performance of the ES-DHA QMSDD when the 50% point of the CDF in Figure 4.8 is chosen is worse than that of the CDD by $2-3$ dB. The reason for this is that the 201 CFEs in the ES-DHA QMSDD, which correspond to the

50% CDF point, are insufficient for achieving an acceptable performance. Furthermore, the fact that the ES-DHA is randomly-initialized contributes to the fact of experiencing a worse performance than the CDD, when the number of maximum affordable CFEs is not sufficiently high. We will propose a method for circumventing this problem in Section 4.6.

4.5 Soft-Input Soft-Output Multiple-Symbol Differential Detectors

When channel coding is used, the decoding procedure yields improved estimates of the source's bits, especially, when the inputs of the decoder are soft estimates of the encoded bits. Therefore, the MSDDs should provide the decoder these soft estimates by generating extrinsic bit-based or symbol-based LLRs. Moreover, the BER performance of the system is further improved, if information is allowed to be transferred from the decoder to the MSDD, resulting in iterations between the MSDD and the decoder. In this case, the MSDD should be capable of accepting soft inputs in terms of the *a priori* LLRs of the encoded bits. The *a priori* LLRs provided by the decoder affect the calculation of the extrinsic LLR.

4.5.1 Maximum *A Posteriori* Probability MSDD

Based on Equation 4.39, Equation 4.55 and Equation 4.60, the *a posteriori* LLR of the tth symbol's mth bit, with $t \in \{2, 3, \ldots, N_w\}$ and $m \in \{1, 2, \ldots, \log_2(M)\}$, at the output of the MAP MSDD is [21]

$$L_{MSDD,apo}\left(b_t^{(m)}\right) = \ln \frac{P\left(b_t^{(m)} = 0 \mid \mathbf{Y}\right)}{P\left(b_t^{(m)} = 1 \mid \mathbf{Y}\right)} \tag{4.62}$$

$$= \ln \frac{p\left(\mathbf{Y} \mid b_t^{(m)} = 0\right) \cdot P\left(b_t^{(m)} = 0\right) / P(\mathbf{Y})}{p\left(\mathbf{Y} \mid b_t^{(m)} = 1\right) \cdot P\left(b_t^{(m)} = 1\right) / P(\mathbf{Y})} \tag{4.63}$$

$$= \ln \frac{\sum\limits_{\mathbf{x} \in \chi(t,m,0)} p(\mathbf{Y} \mid \mathbf{x}) \cdot P(\mathbf{x})}{\sum\limits_{\mathbf{x} \in \chi(t,m,1)} p(\mathbf{Y} \mid \mathbf{x}) \cdot P(\mathbf{x})} \tag{4.64}$$

$$= \ln \frac{\sum\limits_{\mathbf{x} \in \chi(t,m,0)} \exp\left(-Tr\left\{\mathbf{Y}^H \Psi^{-1} \mathbf{Y}\right\}\right) \cdot P(\mathbf{x}) / \left(\det\left\{\pi\Psi\right\}\right)^P}{\sum\limits_{\mathbf{x} \in \chi(t,m,1)} \exp\left(-Tr\left\{\mathbf{Y}^H \Psi^{-1} \mathbf{Y}\right\}\right) \cdot P(\mathbf{x}) / \left(\det\left\{\pi\Psi\right\}\right)^P} \tag{4.65}$$

$$= \ln \frac{\sum\limits_{\mathbf{x} \in \chi(t,m,0)} \exp\left(-Tr\left\{\mathbf{Y}^H \Psi^{-1} \mathbf{Y}\right\} + \ln\left(P(\mathbf{x})\right)\right)}{\sum\limits_{\mathbf{x} \in \chi(t,m,1)} \exp\left(-Tr\left\{\mathbf{Y}^H \Psi^{-1} \mathbf{Y}\right\} + \ln\left(P(\mathbf{x})\right)\right)} \tag{4.66}$$

$$= \ln \frac{\sum\limits_{\mathbf{x}\in\chi(t,m,0)} \exp\left(-\sum\limits_{p=1}^{P} \left(\| \mathbf{U}_p \cdot \mathbf{s} \|_2^2 \right) + \ln\left(P(\mathbf{x})\right) \right)}{\sum\limits_{\mathbf{x}\in\chi(t,m,1)} \exp\left(-\sum\limits_{p=1}^{P} \left(\| \mathbf{U}_p \cdot \mathbf{s} \|_2^2 \right) + \ln\left(P(\mathbf{x})\right) \right)}, \tag{4.67}$$

where $\chi(n,m,v) = \left\{ \mathcal{M}^{N_w} \mid b_t^{(m)} = v \right\}$ is the set that includes the specific multi-level symbols of $\mathcal{M}^{N_w}$ of which the $(n \cdot \log_2(M) + m)$th bit is equal to v. Furthermore, assuming that the bits of a symbol are independent, the symbol-based *a priori* LLR $P(\mathbf{x})$ is equal to

$$P(\mathbf{x}) = P\left(b_2^{(1)}\right) \cdots P\left(b_2^{(\log_2(M))}\right) \cdot P\left(b_3^{(1)}\right) \cdots P\left(b_{N_w}^{(\log_2(M))}\right) \tag{4.68}$$

The extrinsic LLR of the tth symbol's mth bit is calculated by removing the contribution of the bit-based *a priori* LLR that corresponds to $b_t^{(m)}$, as in

$$L_{MSDD,ex}\left(b_t^{(m)}\right) = L_{MSDD,apo}\left(b_t^{(m)}\right) - \ln\left(\frac{P\left(b_t^{(m)}=0\right)}{P\left(b_t^{(m)}=1\right)}\right). \tag{4.69}$$

The MAP MSDD calculates every additive term in both the numerator and denominator of Equation 4.66 that takes part in the computation of the extrinsic LLR [21]. The CF in the SISO MSDD is similar to that of the HIHO MSDD and it is extracted from Equation 4.66 as in

$$f_{MSDD}^{SISO}(\mathbf{x}) = -Tr\left\{\mathbf{Y}^H \Psi^{-1} \mathbf{Y}\right\} + \ln\left(P(\mathbf{x})\right) \tag{4.70}$$

Therefore, when an M-ary modulation scheme is employed and the detection window of the MSDD has a size of N_w symbols, the complexity of the MAP MSDD is equal to

$$\mathcal{C}_{MAP} = \frac{M^{N_w-1}}{(N_w-1)\log_2(M)}, \tag{4.71}$$

where (N_w-1) was used instead of N_w, since the reference symbol is known at the receiver.

During the first MSDD-DEC iteration, where all the multi-level symbols have equal *a priori* probability, the two multi-level symbols $\mathbf{x}$ that minimize the CF in Equation 4.66 in the numerator and the denominator, respectively, of Equation 4.66 are the two multi-level symbols with the highest impact in the calculation of that bit's LLR. The MSDSD makes a careful selection of the legitimate $\mathbf{x}$ and creates a subset both for the numerator and for the denominator of Equation 4.66, which are used for the computation of the extrinsic LLRs. After the extrinsic LLRs of the MSDD are fed to the decoder, the updated decoder's extrinsic LLRs at its output return to the MSDD as the new *a priori* LLRs.

4.5.2 Dürr-Høyer Algorithm-based QMSDD with Maximum Approximation

As in the MAP MSDD analysis, let us focus our discussions on the calculation of the tth differentially encoded symbol's mth bit. The methodology of the DHA-based detector relying on the MAximum Approximation (DHA-MAA) is described in detail in Section 3.5.1. In this section we will apply the DHA-MAA algorithm for performing HISO QMSDD. The DHA-MAA QMSDD calculates the bit-based or symbol-based LLRs by using only a reduced subset of the legitimate multi-level MSDD symbol vectors in the MAP MSDD.

The DHA-MAA QMSDD invokes the DHA for finding the symbol vector $\hat{\mathbf{x}}_{\min}$ that satisfies

$$\hat{\mathbf{x}}_{\min} = \underset{\mathbf{x}\in\mathcal{M}^{N_w-1}}{\arg\max} \left\{ \exp\left(-Tr\left\{\mathbf{Y}^H \Psi^{-1} \mathbf{Y}\right\} + \ln\left(P(\mathbf{x})\right)\right)\right\} \tag{4.72}$$

$$= \underset{\mathbf{x}\in\mathcal{M}^{N_w-1}}{\arg\min} \left\{ \sum_{p=1}^{P} \left(\| \mathbf{U}_p \cdot \mathbf{s} \|_2^2 \right) - \ln\left(P(\mathbf{x})\right) \right\}, \tag{4.73}$$

$$= \underset{\mathbf{x}\in\mathcal{M}^{N_w-1}}{\arg\min} \left\{ f_{MSDD}^{SISO-DHA}(\mathbf{x}) \right\} \tag{4.74}$$

where the connection between $\mathbf{s}$ and $\mathbf{x}$ is stated in Equation 4.1 and its CF is given by:

$$f_{MSDD}^{SISO-DHA}(\mathbf{x}) = \sum_{p=1}^{P} \left(\| \mathbf{U}_p \cdot \mathbf{s} \|_2^2 \right) - \ln\left(P(\mathbf{x})\right). \tag{4.75}$$

The DHA will search through the entire legitimate search space $\mathcal{M}^{N_w-1}$, where the first symbol in the MSDD symbol vector $\mathbf{x}$ is fixed to its known value, since it corresponds to the reference symbol. During the search for $\hat{\mathbf{x}}$, the DHA evaluates the CF value of Equation 4.75 for many other multi-level symbols, which may be stored and exploited for the calculation of the LLRs. More precisely, once the search is completed, the best symbol found for the numerator and the best symbol found for the denominator of each bit's LLR are used for its calculation. Let us redefine a number of sets for assisting us in the analysis of the DHA-MAA QMSDD. The set $\mathcal{X}$ includes the unique symbols that were evaluated during the DHA search. From that set $\mathcal{X}$, we may then create two sets for each bit, based on the bit's specific value. For example, $\mathcal{X}^{t,m,\mathrm{v}}$ is that particular set, which contains all the symbols in $\mathcal{X}$, where the value of the tth transmitted symbol's mth bit is equal to v. By using the decimal representation x for indexing the corresponding symbol vector $\mathbf{x}$ as in Section 2.4, we have

$$x \in \mathcal{X}^{t,m,\mathrm{v}} \Leftrightarrow x \in \mathcal{X} \wedge \mathbf{x} \in \chi(t, m, \mathrm{v}). \tag{4.76}$$

In other words, $\mathcal{X}^{t,m,\mathrm{v}}$ includes all the unique symbols that the DHA search encountered, which have the $(t \cdot \log_2 M + m)$th bit of their binary representation equal to v. Hence, the

LLR calculated by the DHA-MAA is equal to

$$L_{DHA-MAA,apo}\left(b_t^{(m)}\right) = \ln \frac{\max\left(\exp\left(-f_{MSDD}^{SISO-DHA}(x)\right) \mid x \in \mathcal{X}^{t,m,0}\right)}{\max\left(\exp\left(-f_{MSDD}^{SISO-DHA}(x)\right) \mid x \in \mathcal{X}^{t,m,1}\right)}. \tag{4.77}$$

According to Equation 4.77, the globally optimal symbol $\hat{\mathbf{x}}$ that is found during the DHA search, will be used for the calculation of every bit's LLR, either in its numerator or in its denominator, since there is no symbol with a higher $\exp\left(-f_{MSDD}^{SISO-DHA}(x)\right)$ value than $\hat{x}_{\min}$. Hence, the signs of the LLRs calculated by the DHA-MAA QMSDD always match the signs of the LLRs calculated by the MAP MSDD. The difference between the two MSDDs' LLRs is in the magnitude of the LLRs, with the DHA-MAA QMSDD tending to output LLRs having a higher confidence than they actually have [3]. This occurs due to the fact that the optimal multi-level symbol of a set is used for the calculation of either the numerator or the denominator, while in some cases a sub-optimal symbol is used for the calculation of the denominator or the numerator, respectively.

In the case when a set $\mathcal{X}^{t,m,\mathrm{v}}$ is empty for a specific $\{t, m, \mathrm{v}\}$ set, the DHA is called again to search for the specific multi-level symbol $\hat{\mathbf{x}}_{\min}^{t,m,v} \in \chi(t, m, \mathrm{v})$ that minimizes the CF in Equation 4.73 [3]. By employing another DHA search, we can ensure that the optimal symbol of that set is found with ∼100% probability and considering that the globally optimal symbol was found during the initial DHA search, the value of the $(t \cdot \log_2 M + m)$th bit's LLR calculated by the DHA-MAA QMSDD will be close to that of the MAP MSDD. However, the additional complexity imposed by the extra DHA search is added to the total complexity of the DHA-MAA QMSDD. For this reason, we have proposed in [3] a solution that we termed as the Neighbour Exploitation (NE) technique.

Briefly, according to the NE technique, if the set $\mathcal{X}^{t,m,\mathrm{v}}$ is empty after the initial DHA search, then the neighbour of the globally optimal symbol $\hat{\mathbf{x}}$ that was found at the $(t \cdot \log_2 M + m)$th position becomes the sole member of $\mathcal{X}^{t,m,\mathrm{v}}$. More specifically, if the set $\mathcal{X}^{t,m,\mathrm{v}}$ is empty, then the set $\mathcal{X}^{t,m,\mathrm{v}\oplus 1}$ includes $\hat{\mathbf{x}}$. At the price of an additional CFE, we may use the globally optimal symbol $\hat{\mathbf{x}}$ and the corresponding neighbour of $\hat{\mathbf{x}}$ for the calculation of the tth symbol's mth bit's LLR.

As stated in Section 3.5.1, the minimum complexity per bit quantified in terms of the number of CFEs of the DHA-MAA QMSDD then becomes

$$\mathcal{C}_{DHA-MAA}^{\min} = \frac{4.5\sqrt{M^{(N_w-1)}} + L_{DHA}^{CD,\min}}{(N_w - 1) \cdot \log_2 M}, \tag{4.78}$$

where $L_{DHA}^{CD,\min}$ is the minimum possible number of CFEs performed in the classical domain during the initial DHA search, which is described in Equation 2.50. By contrast, the minimum number of CFEs of the DHA-MAA-NE QMSDD is equal to [3]

$$\mathcal{C}_{DHA-MAA-NE}^{\min} = \frac{4.5\sqrt{M^{(N_w-1)}} + L_{DHA}^{CD,\min}}{(N_w - 1) \cdot \log_2 M} + 1, \tag{4.79}$$

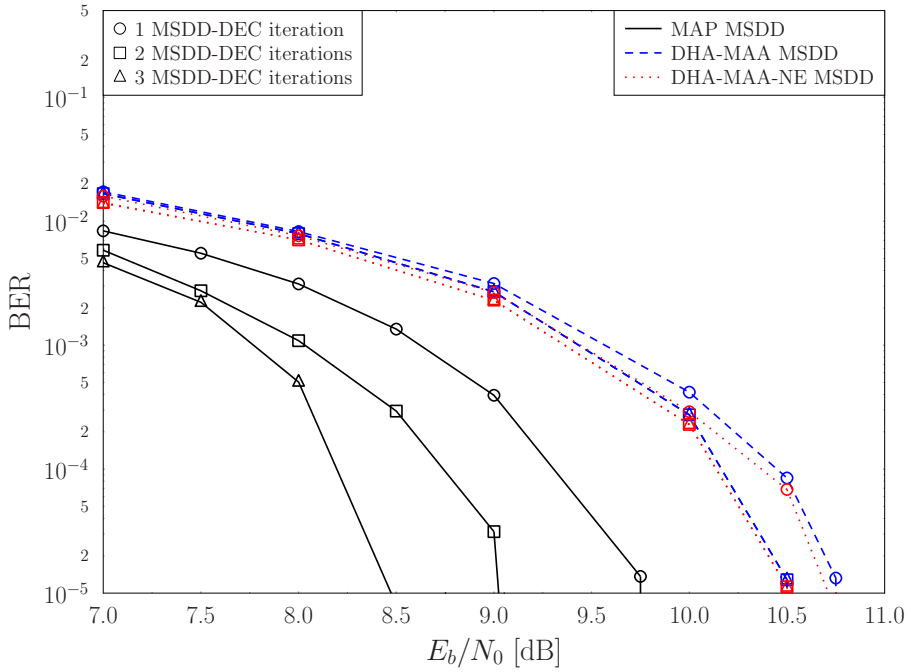

Figure 4.10: BER performance of the DHA-MAA QMSDDs and the MAP MSDD in the DSS/SSCH SDMA-OFDM system scenario of Figure 4.2, using the parameters summarized in Table 4.1 for $N_w = 7$ in the EPA channel of Table 4.2.

which is only a single CFE higher than the minimum complexity of the DHA-MAA QMSDD in Equation 4.78 due to the requirements of the NE technique.

In Figure 4.10 we compare the BER performances of the MAP MSDD and the DHA-MAA QMSDD both with and without the NE technique, when used in the DSS/SSCH SDMA-OFDM system scenario of Figure 4.2 relying on the parameters of Table 4.1 involving $J = 3$ iterations between the MSDD and the channel decoder. We may observe that there is an 1 dB loss between the MAP MSDD and the DHA-MAA QMSDD with 1 MSDD-DEC iteration. Additionally, the DHA-MAA-NE QMSDD offers a slightly better BER performance, when compared to that of the DHA-MAA QMSDD. When the number of iterations between the MSDDs and the decoders is increased, the performance of the MAP MSDD is improved, but those of the DHA-MAA QMSDD and the DHA-MAA-NE QMSDD essentially remain the same, hence resulting in a power loss of approximately 2 dB for the latter pair after $J = 3$ MSDD-DEC iterations between the MAP MSDD and the DHA-MAA QMSDDs.

The computational complexities of the MSDDs quantified in terms of the number of CFEs per bit are summarized in Table 4.5, where again the CF is given in Equation 4.75. We make the conclusive assumption that all the CF values obtained by the MAP MSDD during the first MSDD-DEC iteration are stored and reused during any subsequent iterations, which reduces the complexity. Therefore, the complexity of the MAP MSDD is assumed to be independent of the number of MSDD-DEC iterations, when quantified in terms of the number of CFEs. On the other hand, we assume that the DHA-MAA QMSDD is performed during every MSDD-DEC iteration. In this way, the comparison of the complexities of the classical and quantum MSDDs has the smallest difference possible and corresponds to the

Table 4.5: Complexity in terms of the number of CFEs / bit in Figure 4.10

MSDD / QMSDD	$E_b/N_0 = 10.5$ dB		
	Number of MSDD-DEC iterations		
	1	2	3
MAP	341.33	341.33	341.33
DHA-MAA	43.70	44.13	44.57
DHA-MAA-NE	44.62	45.95	46.26
MSDD / QMSDD	$E_b/N_0 = 5$ dB		
	Number of MSDD-DEC iterations		
	1	2	3
MAP	341.33	341.33	341.33
DHA-MAA	43.70	88.53	128.05
DHA-MAA-NE	44.62	88.34	130.73

worst-case-scenario for the QMSDDs.

According to Table 4.5, the complexities of the DHA-MAA and DHA-MAA QMSDDs are lower than that of the MAP MSDD. When operating at $E_b/N_0 = 10.5$ dB the complexity of the QMSDDs does not increase dramatically with the number of MSDD-DEC iterations, because most of the time the entire frame was correctly decoded during the first iteration. Therefore, the small number of additional CFEs, which may be as low as a single CFE per bit, when $J = 2$ MSDD-DEC iterations are performed, provides a modest gain of 0.25 dB as observed in Figure 4.10, when we compare the QMSDDs using $J = 1$ MSDD-DEC iteration and that using $J = 2$ MSDD-DEC iterations. Similarly, when $J = 3$ iterations are allowed between the MSDDs and the channel decoders, the complexities of the QMSDDs are only slightly increased at $E_b/N_0 = 10.5$ dB. However, the BER performance remains essentially the same as in the case, where $J = 2$ MSDD-DEC iterations were performed. When we have $E_b/N_0 = 5$ dB, the complexities of the DHA-MAA QMSDDs combined with multiple MSDD-DEC iterations may be deemed to be the corresponding multiples of the complexities required for a single MSDD-DEC iteration. For example, in the case of the DHA-MAA-NE QMSDD, 44.62 CFEs are required for a single MSDD-DEC iteration, while almost three times more are necessitated for the scenario where $J = 3$ MSDD-DEC iterations are performed. Observe in Figure 4.10 this increased complexity fails to achieve any substantial BER performance improvement for the system. The reason for the increase in complexity is that none of the frames are correctly decoded during any of the previous iterations.

Therefore, based on Figure 4.10, despite increasing the receiver-complexity by allowing iterations between the MSDD and the channel decoder, the performance of the DHA-MAA QMSDDs is not improved. In the context of the DHA-MAA QMSDD, the MSDD-DEC iterations translate into updated values of the *a priori* symbol-based probabilities $P(\mathbf{x})$ in Equation 4.66 and Equation 4.73. By calculating the LLR as in Equation 4.77, the

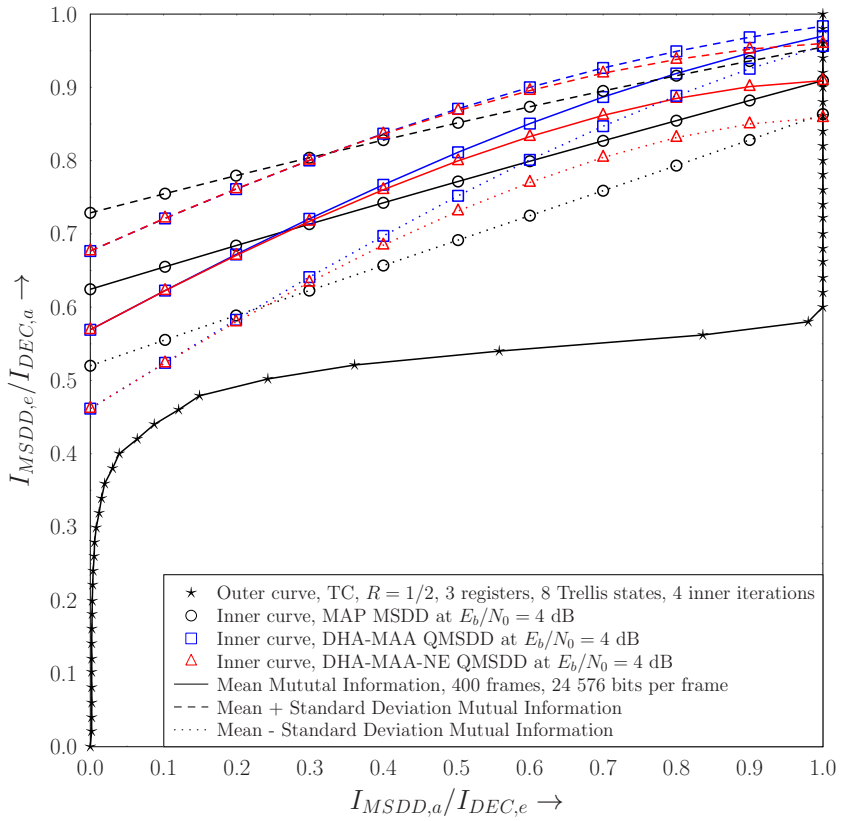

Figure 4.11: EXIT chart of the DHA-MAA QMSDDs in the DSS/SSCH SDMA-OFDM system scenario of Figure 4.2, using the parameters summarized in Table 4.1 with $N_w = 7$ in the EPA channel of Table 4.2. The inner and outer average EXIT curves of the mutual information are presented, along with the EXIT inner curves that take into consideration the standard deviation.

DHA-MAA QMSDD essentially ignores other symbols, although they would be expected to improve the resultant LLR value. Moreover, since the DHA-MAA QMSDD does not always use the optimal symbols for the calculation of both the numerator and the denominator of each bit's LLR, the excessive value of the resultant LLRs, which actually represent an undue confidence, have a negative effect on the channel decoder by misinforming it. This is verified by observing the EXIT chart of our system scenario in Figure 4.11, where the inner decoder's curves corresponding to the MSDDs and the outer decoder's curve corresponding to the Turbo Convolutional Codes (TCC) employed are depicted. All the EXIT curves in this treatise have been generated by using the histogram-based method [21], which provides more accurate predictions of the soft-information PDFs than the Gaussian approximation. The EXIT inner curves of our system are sensitive to the specific snapshot that they are calculated for, since we have a multi-carrier system with subcarrier hopping and a user may experience deep fading during one transmitted frame and a flat channel during the subsequent frame. The presented EXIT curves correspond to the mutual information of all the users combined. For this reason, we have also provided two additional EXIT inner curves for each MSDD, where the standard deviation of the acquired data of the mutual information at the output of the MSDDs is taken into account and the gap of approximately 0.1 at $I_{MSDD,e} = 0$ verifies the time-related sensitivity of our system.

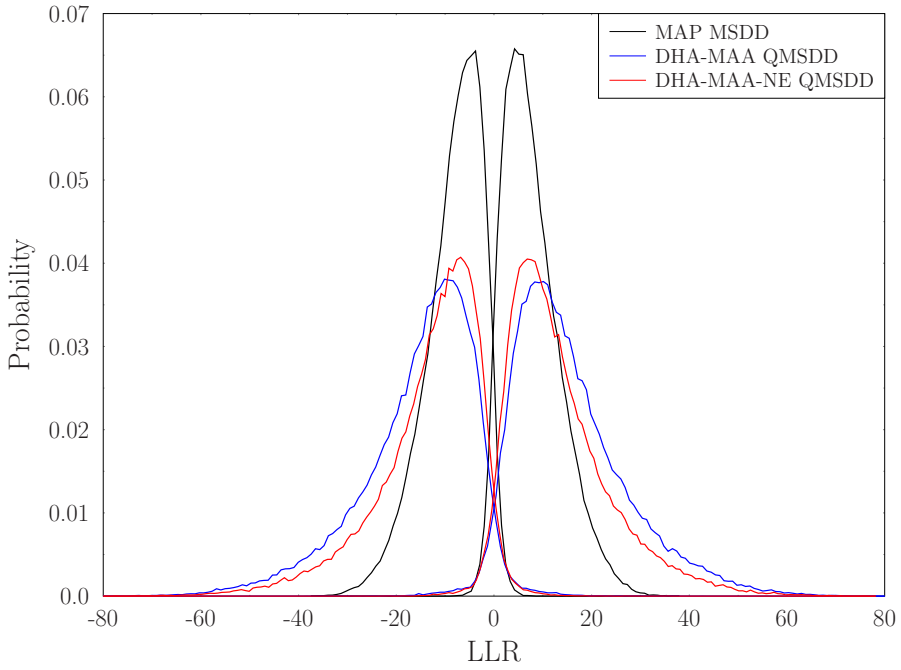

Figure 4.12: Histogram of the output LLRs of the MAP MSDD, the DHA-MAA QMSDD and the DHA-MAA-NE QMSDD at $I_{MSDD,a} = 0.5$ of a single frame of 24 576 bits per user in our system scenario of Figure 4.2, using the parameters summarized in Table 4.1 with $N_w = 7$ in the EPA channel of Table 4.2. The histograms which have their main peak at a positive LLR value correspond to the LLRs of a bit equal to 1, while those who have their main peak at a negative LLR value correspond to the LLRs of a bit equal to 0.

According to Figure 4.11, the DHA-MAA and DHA-MAA-NE QMSDDs initially output a lower MI than the MAP MSDD, but upon iterating they eventually become higher than that of the MAP MSDD, yielding a higher MI at their output. This fact does not represent the reality, yet, it was expected. The DHA-MAA and DHA-MAA-NE QMSDD always generate extrinsic LLRs, which have the same polarity as the ones the MAP MSDD generates. Due to the fact that the two QMSDDs generate their LLRs according to Equation 4.77 and that most of the times they do not use the optimal symbols for both the numerator and the denominator, we expect to obtain LLR values having the correct polarity, but higher values than they should truly have. Therefore, their inner decoder EXIT curves erroneously represent the belief that the QMSDDs surpass the performance of the MAP MSDD. All the EXIT curves seen in Figure 4.11 have been generated using Gaussian-distributed LLRs as their inputs. In practice, this is used because the outputs of the MSDDs and the channel decoders obey the Gaussian distribution, provided that their input is also Gaussianly distributed. Since the initial input of the MSDD is the Gaussian distribution with zero mean and zero standard deviation, that corresponds to the $I_{MSDD,a} = 0$ point. Hence, the generation of EXIT curves using input LLRs with Gaussian distribution is accurate. The QMSDDs employed also approximate the Gaussian distribution, but their confidence is higher than that of the MAP MSDD, as it may be observed in Figure 4.12. More precisely, for $I_{MSDD,a} = 0.5$ and for Gaussian distributed LLRs at the input of the MSDDs, the probability of obtaining an LLR with an absolute value equal to or higher than $|L_{MSDD,e}| \geq 20$ is 56.1% for the DHA-MAA QMSDD, 42.7% for the DHA-MAA-NE QMSDD and only

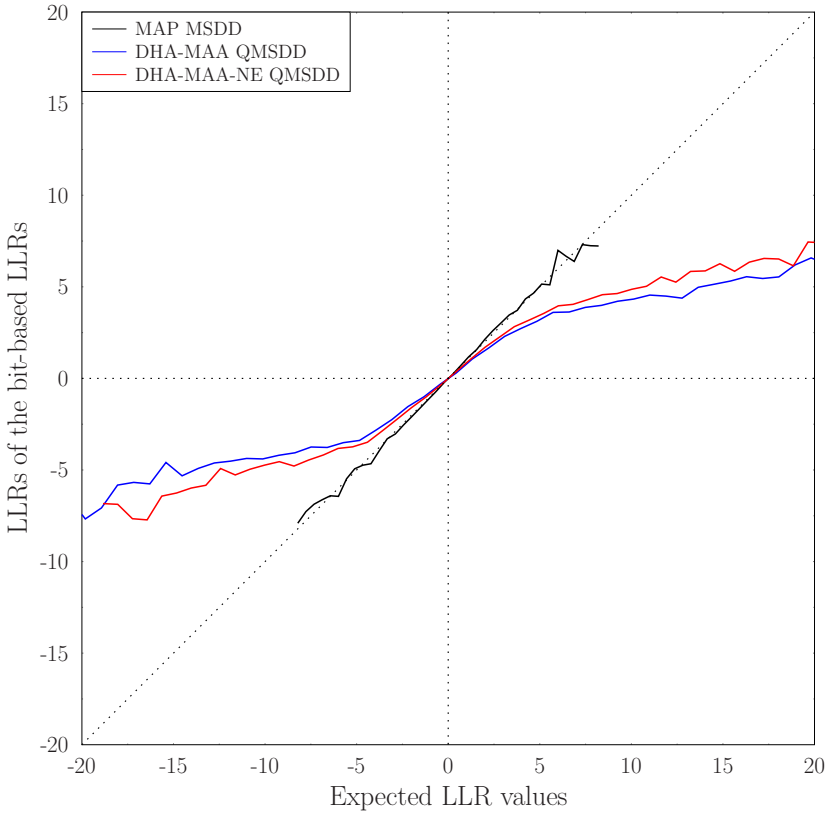

Figure 4.13: LLR values obtained by the MSDDs with respect to the expected LLR values based on the histograms in Figure 4.12 in the DSS/SSCH SDMA-OFDM system of Figure 4.2, using the parameters of Table 4.1 with $N_w = 7$ in the EPA channel of Table 4.2. The consistency condition for iterative detection for a particular MSDD is satisfied if its corresponding curve is close to the main diagonal line. The frame length of each user is equal to 24 576 bits.

7.8% for the MAP MSDD, indicating an inflated confidence of the DHA-MAA QMSDDs' outputs.

Figure 4.13 plots Equation 3.125 when the PDF of the MAP MSDD's, of the DHA-MAA QMSDD's and of the DHA-MAA-NE QMSDD's LLR values presented in Figure 4.12 are substituted into the right-hand term of Equation 3.125. The MAP MSDD satisfies the consistency condition, since its curve follows the main diagonal of Figure 4.13. This was expected, since the MAP MSDD does not use any approximations for computing the extrinsic LLRs and the only reason that its corresponding curve in Figure 4.13 does not exactly follow the diagonal curve is the finite length of the frame, which is equal to 24 576 bits for each user. On the other hand, the DHA-MAA QMSDD and the DHA-MAA-NE QMSDD do not satisfy the consistency condition, since the log-likelihood ratios of the probabilities of the bit-based LLRs $L(L_{m,e}(b))$ are not equal to those specific bit-based LLR values $L_{m,e}(b)$. The DHA-MAA-NE QMSDD's curve is closer to the diagonal, verifying its slightly better performance than that of the DHA-MAA QMSDD. Based on Figure 4.13 the DHA-MAA and the DHA-MAA-NE QMSDDs are not suitable for iterative decoding, which explains their slightly improved BER curves over multiple MSDD-DEC iterations.

The unsuitability of the DHA-MAA QMSDD and of the DHA-MAA-NE QMSDD for

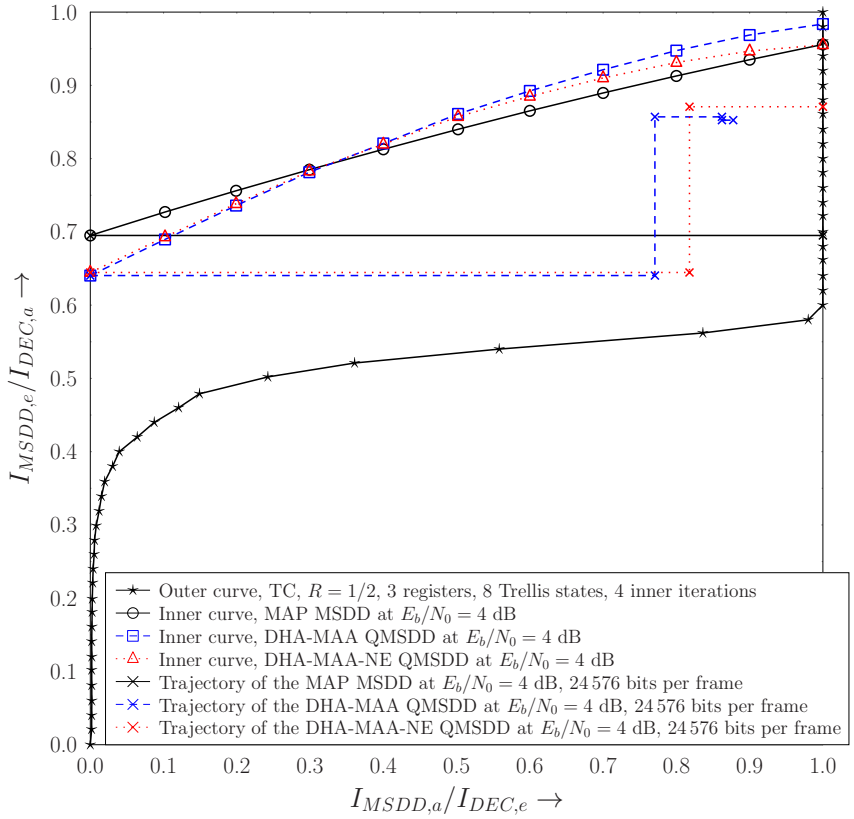

Figure 4.14: EXIT chart of the DHA-MAA and DHA-MAA-NE QMSDDs, as well as the MAP MSDD in the DSS/SSCH SDMA-OFDM system scenario of Figure 4.2, using the parameters of Table 4.1 with $N_w = 7$ in the EPA channel of Table 4.2, using a single snapshot for the inner EXIT curve which corresponds to the MSDDs.

iterative differential detection may be observed in Figure 4.14, where a single snapshot of their inner decoder EXIT curves and their corresponding trajectories are plotted for a single transmitted frame of 24 576 bits for each user. As a result of this Gaussian approximation, the decoding trajectories of the QMSDDs reach their respective inner decoder curve at $I_{MSDD,a} = 0$, but beyond this point they do not match with their respective EXIT curves. More specifically, the decoding trajectory of the DHA-MAA QMSDD fails to reach the $I_{DEC,e} = 1$ line of perfect convergence to a vanishingly low BER, when the inner and outer decoders are serially connected as in our scenario. The reasons for the behaviour of this trajectory is that the DHA-MAA and DHA-MAA-NE QMSDDs do not satisfy the consistency condition [147], which implies that they provide excessive, overconfident LLR values, which is partly attributable to the fact that their interleaver length is limited to 24 576 bits for each user. Again, the inner and outer decoder EXIT curves have been simulated assuming LLR inputs following the normal distribution. However, in reality the extrinsic LLRs at the outputs of the DHA-MAA and DHA-MAA-NE QMSDDs obey the distributions presented in Figure 4.12.

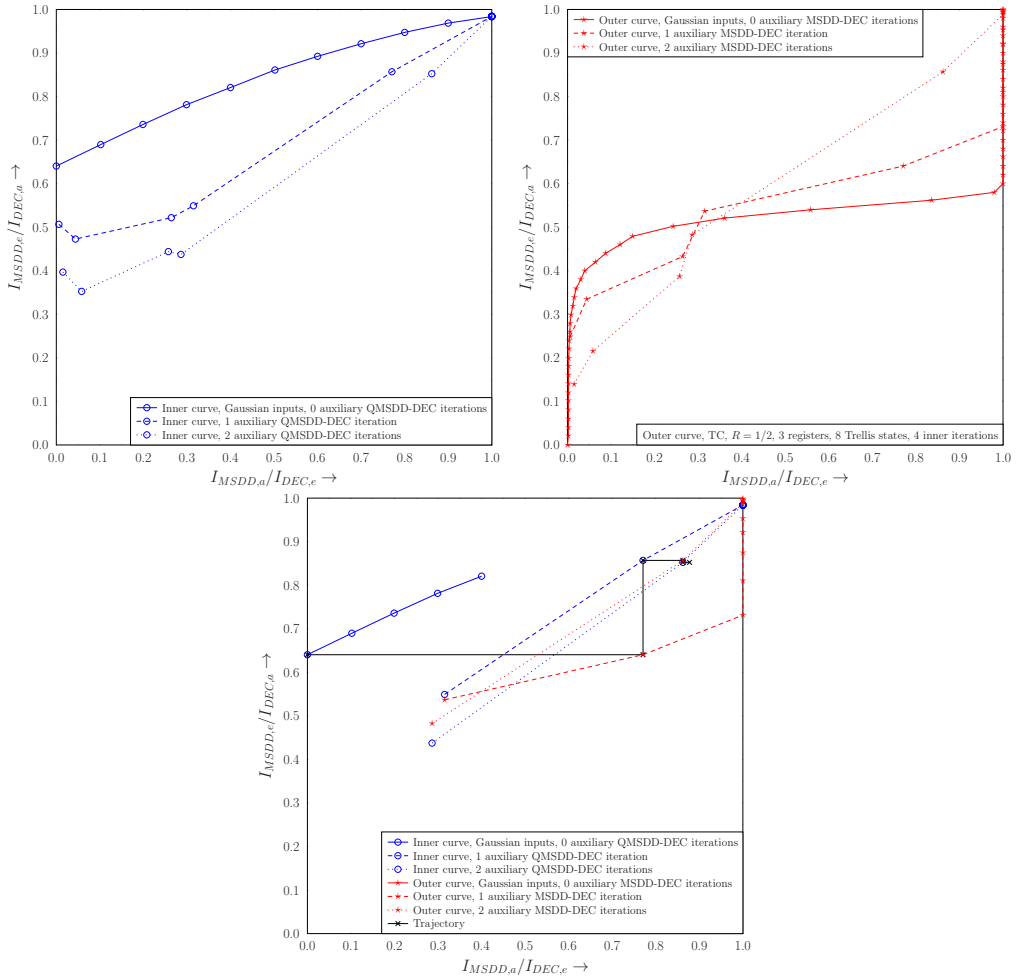

Figure 4.15: EXIT chart of the DHA-MAA QMSDD in the DSS/SSCH SDMA-OFDM system scenario of Figure 4.2, using the parameters of Table 4.1 with $N_w = 7$ in the EPA channel of Table 4.2 using 0, 1 and 2 auxiliary QMSDD-DEC iterations for the generation of the inner and outer EXIT curves for $E_b/N_0 = 4$ dB and $(E_b/N_0)^* = 0, 1, \ldots, 10$ dB. Top left: Inner EXIT curves. Top right: Outer EXIT curves Bottom: EXIT chart with inner and outer EXIT curves and the decoding trajectory.

4.5.2.1 EXIT Charts of the DHA-MAA QMSDDs without Gaussian Assumptions

For clarifying the behaviour of the DHA-MAA and DHA-MAA-NE QMSDDs, we generated the inner and outer decoder EXIT curves of our system with the input LLRs following their non-Gaussian distributions, as inspired by [144].

The inner and outer decoder EXIT curves of the DHA-MAA QMSDD with none, a single and two auxiliary MSDD-DEC iterations are plotted for $E_b/N_0 = 4$ dB in Figure 4.15, while those of the DHA-MAA-NE QMSDD are presented in Figure 4.16. The non-Gaussian inner and outer decoder EXIT curves were generated for $(E_b/N_0)^* = 0, 1, \ldots, 10$ dB. By observing the inner decoder EXIT curve in the top left EXIT chart of both Figure 4.15 and Figure 4.16, we may conclude that for a fixed value for $I_{MSDD,a}$, the output mutual information of the DHA-MAA and DHA-MAA-NE QMSDDs becomes lower upon increas-

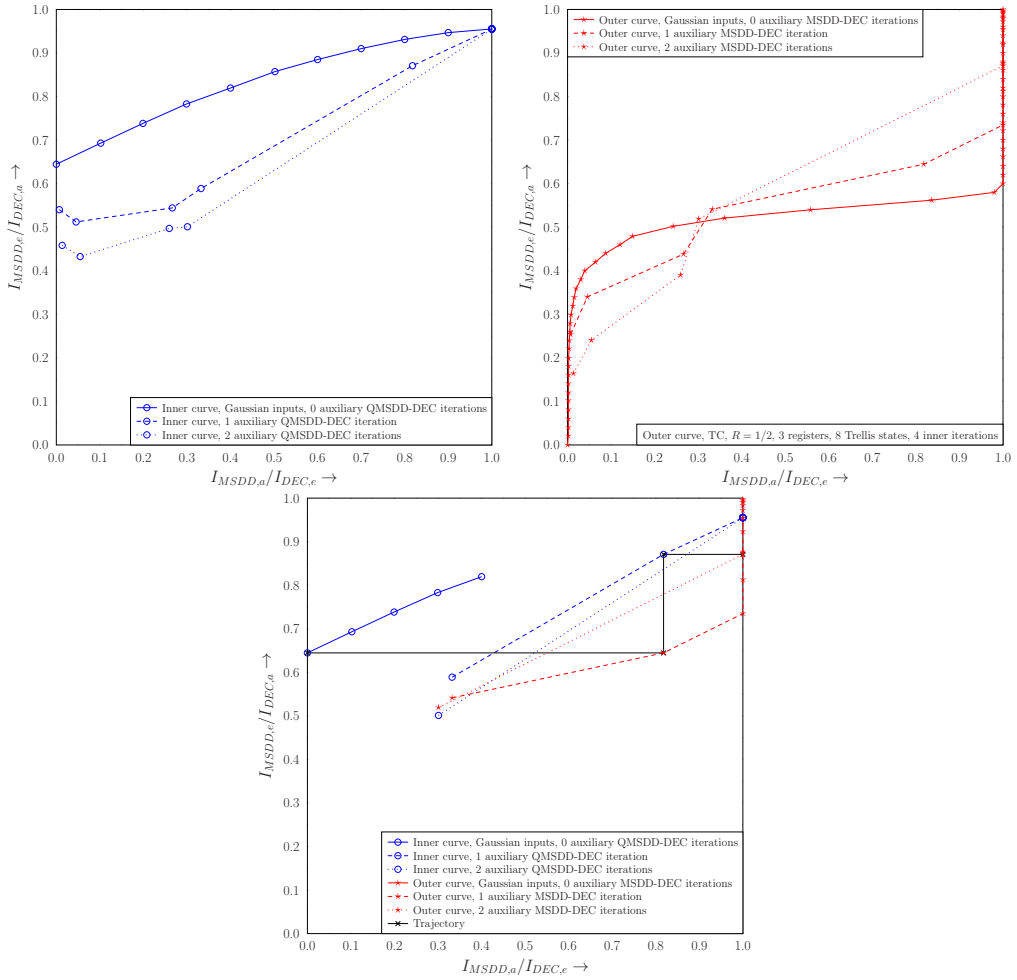

Figure 4.16: EXIT chart of the DHA-MAA-NE QMSDD in the DSS/SSCH SDMA-OFDM system scenario of Figure 4.2, using the parameters of Table 4.1 with $N_w = 7$ in the EPA channel of Table 4.2 using 0, 1 and 2 auxiliary QMSDD-DEC iterations for the generation of the inner and outer EXIT curves for $E_b/N_0 = 4$ dB and $(E_b/N_0)^* = 0, 1, \ldots, 10$ dB. Top left: Inner EXIT curves. Top right: Outer EXIT curves Bottom: EXIT chart with inner and outer EXIT curves and the decoding trajectory.

ing the number of MSDD / DEC iterations due to the output/input LLRs, which do not follow the Gaussian distribution. Similarly, the top right EXIT chart of the same figures verifies that the channel decoder is also affected by the non-Gaussian LLR inputs. More specifically, the channel decoder "loses" its turbo effect and provides lower $I_{DEC,e}$ for the same $I_{DEC,a}$ upon increasing the number of MSDD-DEC iterations, when the DHA-MAA and the DHA-MAA-NE QMSDDs are used. Finally, the bottom EXIT charts of Figure 4.15 and Figure 4.16 combine the two EXIT charts of their respective top row and present the decoding trajectories for the DHA-MAA QMSDD and the DHA-MAA-NE QMSDD, respectively. As expected for the DHA-MAA QMSDD, the outer decoder EXIT curve after two MSDD-DEC iterations at $I_{DEC,a} = 0.857$ has a higher output value for the mutual information $I_{DEC,e} = 0.862$, than the output of the MSDD after two auxiliary MSDD-DEC iterations at $I_{MSDD,a} = I_{DEC,e} = 0.862$ which has a value of $I_{MSDD,e} = 0.853$. In other words, at $I_{MSDD,a} = I_{DEC,e} = 0.862$, the outer decoder EXIT curve is higher than the

inner decoder EXIT curve, essentially closing the trajectory's tunnel. On the other hand, the specific trajectory of the DHA-MAA-NE shown in Figure 4.16 still experiences an open tunnel after two iterations and reaches the $I_{DEC,e} = 1$ line.

The employment of non-Gaussian EXIT charts helps in explaining the exact behaviour of practical receivers, where approximations have been applied at the multi-level symbol detectors or the decoders. EXIT curves with even more auxiliary iterations may also be generated, but since the aim of the design of an EXIT chart is to simplify that of a receiver, we chose to use the non-Gaussian EXIT charts only for explaining the non-intuitive behaviour of our QMSDDs, where the inner EXIT curve was higher than that of the optimal MAP MSDD.

4.5.3 Dürr-Høyer Algorithm-based QMSDD with Multi-Input Approximation

The Dürr-Høyer algorithm-based MUD with MUA was analysed in Section 3.5.2. The same principles are followed here for the creation of the DHA-MUA QMSDD. The DHA-MUA QMSDD starts by performing a single DHA search for finding the optimal multi-level MSDD symbol vector that belongs to the numerator of the first bit's LLR and another single DHA search for finding the optimal multi-level symbol that belongs to the denominator of the first bit's LLR. Therefore, the search space of each of the first two DHA searches has M^{N_w-2} entries. The CF used for determining the optimality of the symbols is the one formulated in Equation 4.75.

When we randomly initialize the DHA-MUA QMSDD, if the randomly selected initial symbol belongs to the numerator of the first bit's LLR, we firstly perform the DHA search for that numerator. Similarly, we commence with the denominator of the first bit's LLR, provided that the random initial symbol belongs to it. Let us assume that we start by performing the DHA for the numerator. After we find the optimal symbol $\hat{\mathbf{x}}_{\min}^{1,1,0}$ in the $\mathcal{X}^{1,1,0}$ set, we initialize the DHA search for the denominator using the neighbour of $\hat{\mathbf{x}}_{\min}^{t,m,0}$ in the first bit position. Once both searches have been completed, we compare the two optimal symbols $\hat{\mathbf{x}}_{\min}^{1,1,0}$ and $\hat{\mathbf{x}}_{\min}^{1,1,1}$ for determining the globally optimal symbol $\hat{\mathbf{x}}_{\min}$ with the aid of:

$$\hat{\mathbf{x}}_{\min} = \begin{cases} \hat{\mathbf{x}}_{\min}^{1,1,0} & \text{if } f_{DHA}\left(\hat{\mathbf{x}}_{\min}^{1,1,0}\right) < f_{DHA}\left(\hat{\mathbf{x}}_{\min}^{1,1,1}\right) \\ \hat{\mathbf{x}}_{\min}^{1,1,1} & \text{if } f_{DHA}\left(\hat{\mathbf{x}}_{\min}^{1,1,0}\right) > f_{DHA}\left(\hat{\mathbf{x}}_{\min}^{1,1,1}\right) \end{cases} . \tag{4.80}$$

For the calculation of the LLRs of the subsequent bits, we only perform a single DHA search per bit. More specifically, if the globally optimal symbol $\hat{\mathbf{x}}_{\min}$ belongs to the numerator of a bit's LLR, then we perform a DHA search for the specific search space that corresponds to the denominator of that bit's LLR, and vice versa. At the end, every set $\mathcal{X}^{t,m,\mathrm{v}}$ for $t \in \{1, 2, \ldots, N_w - 1\}$, $m \in \{1, 2, \ldots, \log_2 M\}$ and $\mathrm{v} \in \{0, 1\}$ will contain at least one symbol. Let us assume without loss of generality that the symbols both in $\mathcal{X}^{t,m,0}$ and $\mathcal{X}^{t,m,1}$ are stored in a descending order based on their CF values. The pair of knowledge transfer techniques that were investigated in [3] in the context of MUDs, namely the

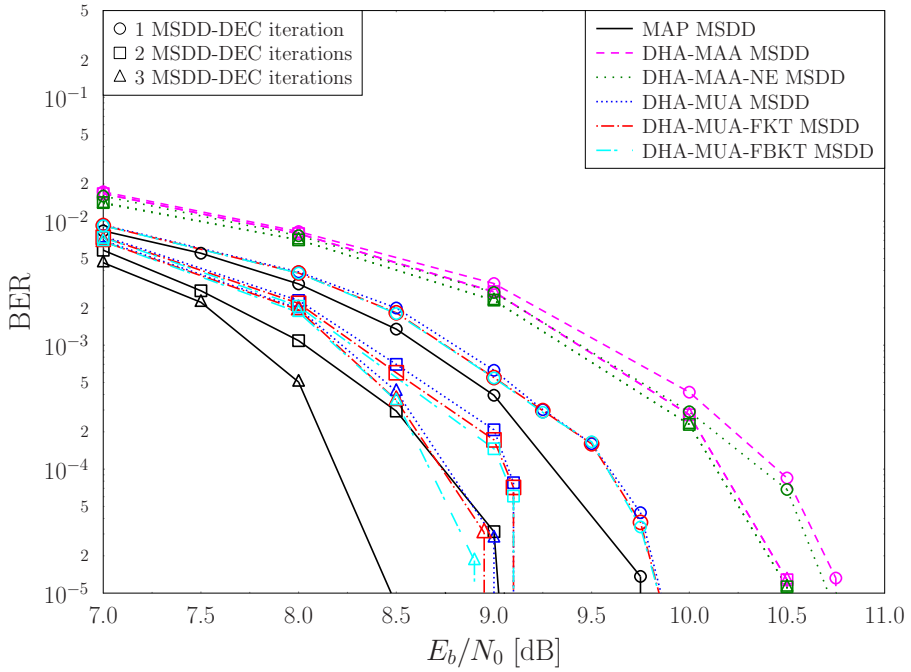

Figure 4.17: BER performance of the family of DHA-MUA QMSDDs and the MAP MSDD in the DSS/SSCH SDMA-OFDM system scenario of Figure 4.2, using the parameters of Table 4.1 with $N_w = 7$ in the EPA channel of Table 4.2.

Forward Knowledge Transfer (FKT)[1] of Section 3.5.2.2 and the Forward and Backward Knowledge Transfer (FBKT)[2] of Section 3.5.2.3, may be readily applied in the context of the QMSDD for the creation of the sets $\mathcal{X}^{t,m,\mathrm{v}}$. The NE technique is also applicable in the DHA-MUA QMSDD.

Moreover, let us assume that $\mathcal{X}^{t,m,1}$ contains more symbols than $\mathcal{X}^{t,m,0}$, i.e. we have that $\left|\mathcal{X}^{t,m,1}\right| > \left|\mathcal{X}^{t,m,0}\right|$. Then, the sets $\bar{\mathcal{X}}^{t,m,0}$ and $\bar{\mathcal{X}}^{t,m,1}$ are created by trimming the last symbols in $\mathcal{X}^{t,m,1}$ with the lowest CF values, so that the resultant set $\bar{\mathcal{X}}^{t,m,1}$ has the same size as $\bar{\mathcal{X}}^{t,m,0} = \mathcal{X}^{t,m,0}$. Let us also define the sign variable $\varsigma_{t,m}$, which is equal to $+1$ if the globally optimal symbol $\hat{\mathbf{x}}_{\min}$ belongs to $\bar{\mathcal{X}}^{t,m,0}$, otherwise it is -1.

Afterwards, we calculate the difference between the CF values of the respective last symbols in the sorted $\bar{\mathcal{X}}^{t,m,0}$ and $\bar{\mathcal{X}}^{t,m,1}$ sets. If the sign of the result does not match the value of $\varsigma_{t,m}$, both symbols are deleted from their respective sets and we continue this process with the rest of the symbol pairs until we reach the first elements of each set. If the sign of the difference matches the value of $\varsigma_{t,m}$, no action is taken and we proceed with

[1] In the DHA-MUA QMSDD, the search results obtained for the $[(u-1)\cdot\log_2(M)+m]$th bit of a multi-level QMSDD symbol vector on the qth subcarrier are stored in $\mathcal{X}_q^{u,m,0}$ and $\mathcal{X}_q^{u,m,1}$. These search results are used only for calculating the LLR of the $[(u-1)\cdot\log_2(M)+m]$th bit. When the Forward Knowledge Transfer modification is employed, the search results of the DHA related to the $[(u-1)\cdot\log_2(M)+m]$th bit are also used for the calculation of the LLRs of the subsequent bits $b_{[(u-1)\cdot\log_2(M)+m+1]}, b_{[(u-1)\cdot\log_2(M)+m+2]}, \ldots, b_{[U\cdot\log_2(M)]}$ of the multi-level symbol, by being stored in their corresponding sets $\mathcal{X}_q^{u,m+1,0}, \mathcal{X}_q^{u,m+1,1}, \ldots, \mathcal{X}_q^{U,\log_2(M),0}, \mathcal{X}_q^{U,\log_2(M),1}$.

[2] Similarly to the Forward Knowledge Transfer modification, when the Forward & Backward Knowledge Transfer modification is employed, the search results of the DHA related to the $[(u-1)\cdot\log_2(M)+m]$th bit of a multi-level QMSDD symbol vector are also used for the calculation of the LLRs of all the bits $b_1, b_2, \ldots, b_{[U\cdot\log_2(M)]}$ of the multi-level symbol, by being stored in their corresponding sets $\mathcal{X}_q^{1,1,0}, \mathcal{X}_q^{1,1,1}, \ldots, \mathcal{X}_q^{U,\log_2(M),0}, \mathcal{X}_q^{U,\log_2(M),1}$.

Table 4.6: Complexity in terms of the number of CFEs / bit in Figure 4.17

MSDD / QMSDD	$E_b/N_0 = 8$ dB		
	Number of MSDD-DEC iterations		
	1	2	3
MAP	341.33	341.33	341.33
DHA-MUA	392.17	466.73	501.15
DHA-MUA-FKT	316.72	374.51	401.11
DHA-MUA-FBKT	316.72	374.51	401.11
MSDD / QMSDD	$E_b/N_0 = 4$ dB		
	Number of MSDD-DEC iterations		
	1	2	3
MAP	341.33	341.33	341.33
DHA-MUA	394.06	689.93	962.78
DHA-MUA-FKT	317.87	585.44	820.46
DHA-MUA-FBKT	317.87	585.44	820.46

the next symbol pairs. The newly formed sets are described by $\hat{\mathcal{X}}^{t,m,0}$ and $\hat{\mathcal{X}}^{t,m,1}$. By performing this procedure, we ensure that the resultant LLR's polarity is the same as in the MAP MSDD.

The LLR of the tth symbol's mth bit is calculated as in

$$L_{DHA-MUA,apo}\left(b_t^{(m)}\right) = \ln \frac{\sum\limits_{x\in\hat{\mathcal{X}}^{t,m,0}} \exp\left(-f_{MSDD}^{SISO-DHA}(x)\right)}{\sum\limits_{x\in\hat{\mathcal{X}}^{t,m,1}} \exp\left(-f_{MSDD}^{SISO-DHA}(x)\right)}. \tag{4.81}$$

In this treatise we will only consider the scenario, where the DHA-MUA QMSDDs adopt the NE technique having a total minimum complexity of

$$\mathcal{C}_{DHA-MUA-NE}^{\min} = \left(4.5\sqrt{M^{N_w-1}/2} + L_{DHA}^{CD,\min}\right)\left(1 + \frac{1}{(N_w-1)\cdot\log_2 M}\right) + 1 \tag{4.82}$$

The BER performances of the DHA-MUA QMSDD are illustrated in Figure 4.17 for our system scenario associated with $N_w = 7$, where they are compared to the DHA-MAA QMSDD, DHA-MAA-NE QMSDD and the MAP MSDD. In the same figure we have also plotted the BER curves, when different knowledge transfer techniques are exploited. If we allow a single iteration between the MSDDs and the channel decoders, the performance of the DHA-MUA, DHA-MUA-FKT and DHA-MUA-FBKT QMSDDs is near optimal, with those of the DHA-MUA-FBKT and DHA-MUA-FKT QMSDDs being slightly better than that of the DHA-MUA QMSDD and only 0.12 dB away from that of the optimal MAP MSDD, due to their more intelligent knowledge transfer technique. When we calculate the BER at the output of the decoders after two MSDD-DEC iterations, there is a 0.35 dB

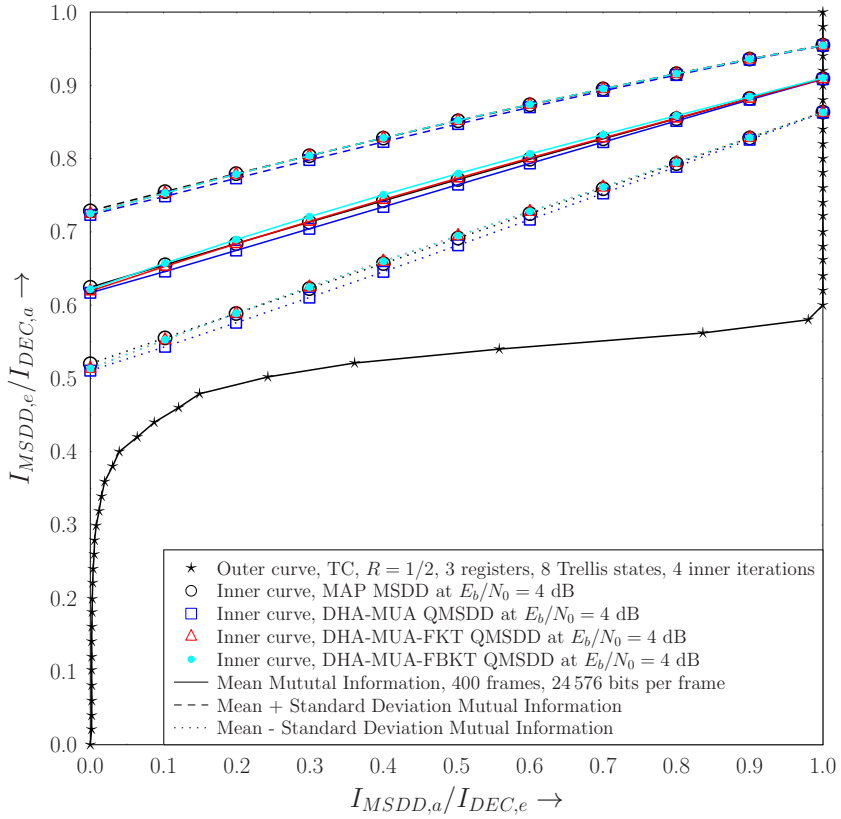

Figure 4.18: EXIT chart of the family of DHA-MUA QMSDDs in the DSS/SSCH SDMA-OFDM system scenario of Figure 4.2, using the parameters of Table 4.1 for $N_w = 7$ in the EPA channel of Table 4.2. The inner and outer average EXIT curves of the mutual information are presented, along with the EXIT inner curves that take into consideration the standard deviation.

loss between the DHA-MUA-FBKT QMSDD and the MAP MSDD. The reason for this increased loss when multiple iterations are performed is the specific nature of the approximations that have been adopted for the QMSDDs, when considering the calculation of the LLRs. During the first MSDD-DEC iteration, the *a priori* LLRs are all-zero, hence they are the same for the MAP MSDD and the QMSDDs. During the second iteration, the *a priori* LLRs of the QMSDDs become different from those of the MAP MSDD, hence eroding the performance. Nonetheless, only 0.1 dB extra transmission power is required for the DHA-MUA-FBKT QMSDD to achieve the same performance as the MAP MSDD. Finally, when $J = 3$ MSDD-DEC iterations are performed, the performance of the QMSDDs becomes similar to their respective performance, when assuming that $J = 2$ MSDD-DEC iterations were allowed, provided that we have $E_b/N_0 < 8$ dB. The gain of allowing a third MSDD-DEC iteration appears so late due to the finite frame length of 24 576 bits per user and owing to the simplifications applied by the QMSDDs. The power loss between the DHA-MUA-FBKT QMSDD and the MAP MSDD is 0.45 dB at BER $= 10^{-5}$.

The complexities of the QMSDDs are summarized in Table 4.6 and, once again, the complexities of the QMSDDs at multiple MSDD-DEC iterations rely on the E_b/N_0 value. In our scenario we may see that the complexities of the DHA-MUA QMSDDs approach that of the MAP MSDD. Therefore, the family of DHA-MUA QMSDDs is more suitable

for non-coherent receivers, where N_w and M are high, for the sake of achieving a higher complexity gain compared to the MAP MSDD, as we will see in Section 4.8. Since the complexity of the DHA-MUA QMSDD decreases upon increasing the SNR and a typical system is desired to operate around BER $= 10^{-5}$, we expect that the top half of Table 4.6 will be more applicable in practice. It should also be noted that the complexity of the DHA-MUA QMSDD encountered in our scenario is higher than that of the MAP MSDD even during the first MSDD-DEC iteration, while the complexities of the DHA-MUA-FKT and DHA-MUA-FBKT QMSDDs become higher than that of the MAP MSDD during the second MSDD-DEC iteration. The DHA-MUA-FKT and DHA-MUA-FBKT QMSDDs require more memory than the DHA-MUA, DHA-MAA and DHA-MAA-NE due to the associated knowledge transfer, but their required memory is still smaller than that of the MAP MSDD. Furthermore, the FBKT technique imposes delay on the system, due to the backward knowledge transfer, but once again, the delay is lower than that of the MAP MSDD, where all the bits have to wait for all the CFEs to be performed.

The DHA-MUA QMSDDs are eligible for employment in an iterative receiver, by updating the values of the *a priori* symbol probabilities in Equation 4.73 and restarting the DHA searches. The inner decoder EXIT curves of the DHA-MUA, DHA-MUA-FKT and DHA-MUA-FBKT QMSDDs in our system scenario of Table 4.1 and the EPA channel of Table 4.2 are given in Figure 4.18 for $E_b/N_0 = 4$ dB. The inner EXIT curves of the DHA-MUA-FKT and DHA-MUA-FBKT QMSDDs match that of the MAP MSDD, with the

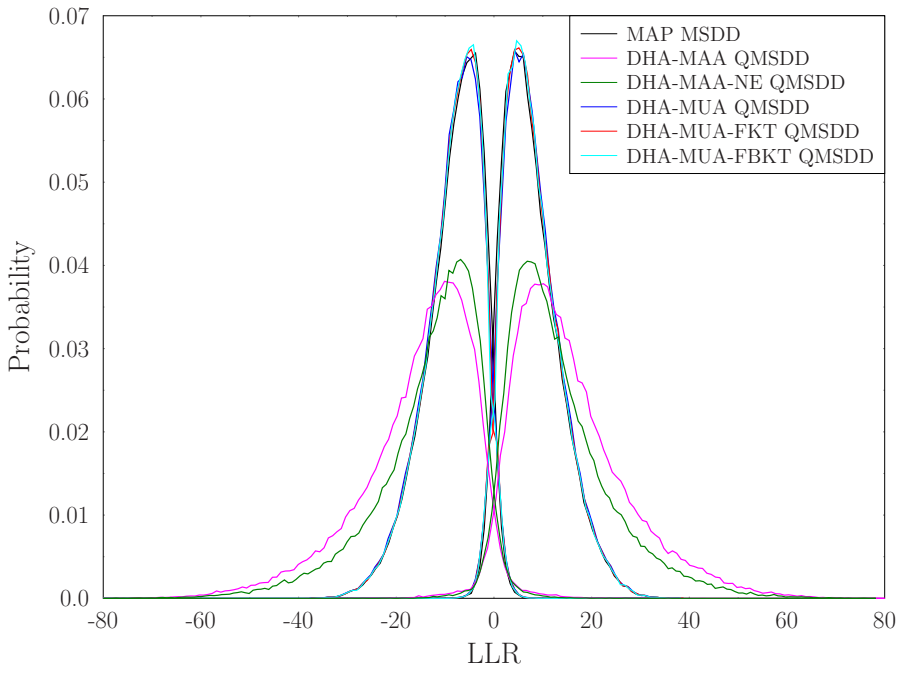

Figure 4.19: Histograms of the output LLRs of the MAP MSDD, the DHA-MUA, DHA-MUA-FKT and DHA-MUA-FBKT QMSDDs at $I_{MSDD,a} = 0.5$ of a single frame of 24 576 bits per user in our system scenario described in Figure 4.2, using the parameters of Table 4.1 with $N_w = 7$ in the EPA channel of Table 4.2. The histograms which have their main peak at a positive LLR value correspond to the LLRs of a bit equal to 1, while those who have their main peak at a negative LLR value correspond to the LLRs of a bit equal to 0.

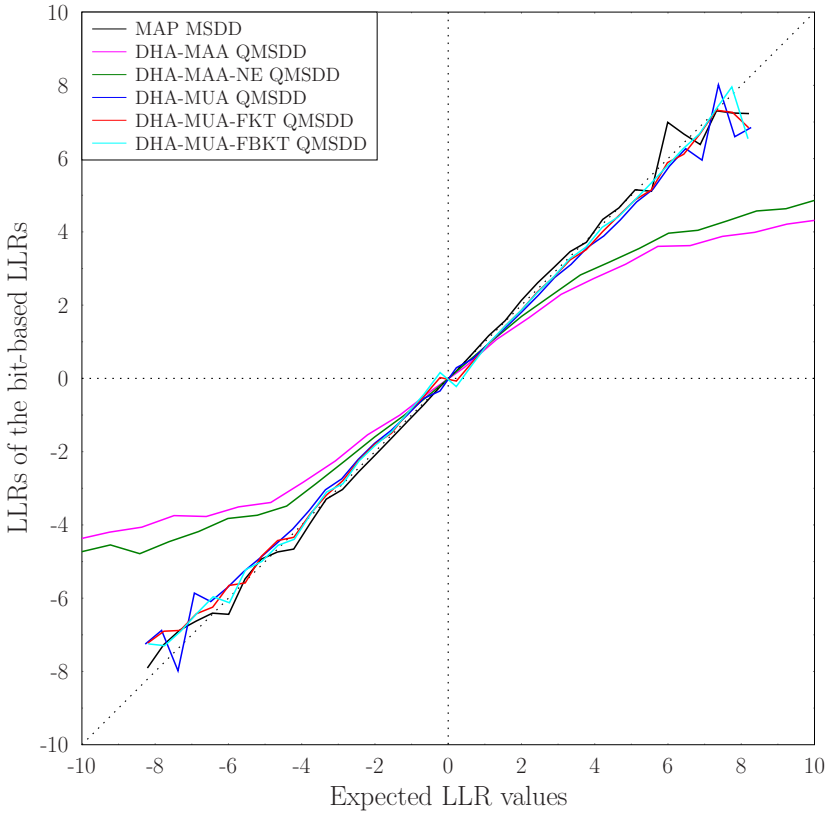

Figure 4.20: LLR values obtained by the MSDDs with respect to the expected LLR values based on the histograms in Figure 4.19. The consistency condition for iterative detection for a particular MSDD is satisfied if its corresponding curve is close to the main diagonal line. The frame length of each user is equal to 24 576 bits.

inner decoder EXIT curves of the DHA-MUA being a little lower than those of the rest. The fact that the inner decoder EXIT curves of the DHA-MUA-FKT and DHA-MUA-FBKT QMSDDs are slightly higher than that of the MAP MSDD at $I_{MSDD,A} = 0.5$ is due to the simplifications made by the MUA and the visualisation relying on EXIT charts assuming to have Gaussian inputs, similarly to the MAA case. In systems associated with larger search spaces, the difference is expected to be more obvious, since the approximations of the QMSDDs will have a larger impact on the performance.

4.5.3.1 Consistency Condition of the DHA-MUA QMSDDs

The PDF curves of the DHA-MUA QMSDDs' LLRs are presented in Figure 4.19, where they are compared to those of the MAP MSDD. Based on Figure 4.19 we may conclude that the behaviour of the family of DHA-MUA QMSDDs recorded for our system scenario is adequate, since their PDF curves of the bit-based LLRs are close to those of the MAP MSDD. In addition, Figure 4.20 visualises the consistency condition for the DHA-MUA QMSDDs and verifies the expectations of the DHA-MUA QMSDDs to be eligible to operate in an iterative receiver, since their corresponding curves are close to the main diagonal line and hence satisfy the consistency condition of Equation 3.124.

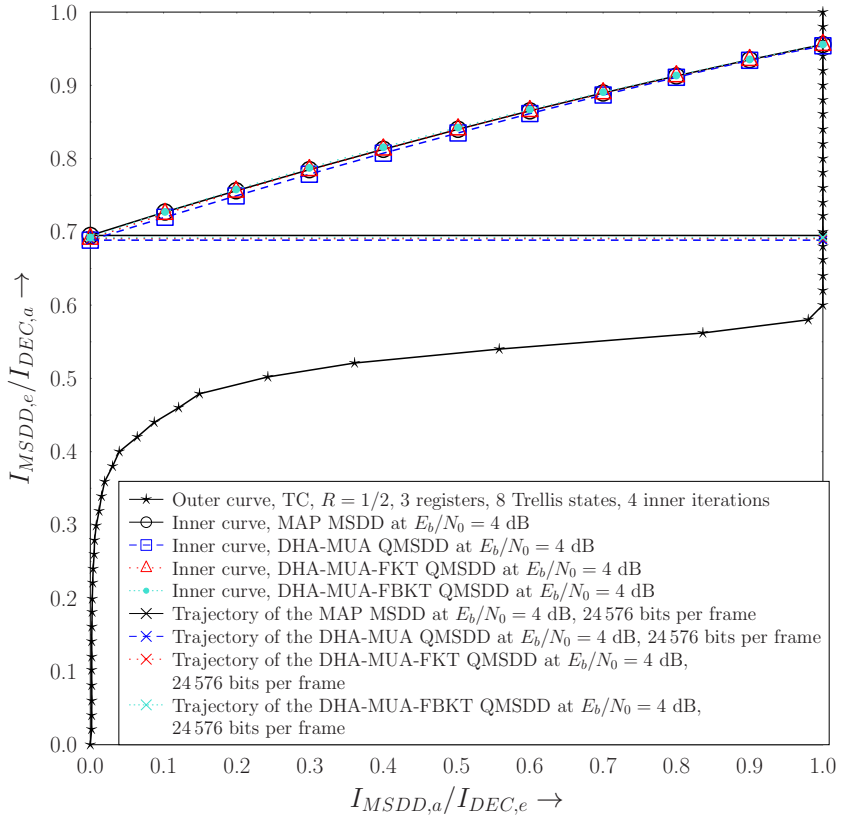

Figure 4.21: EXIT chart of the DHA-MUA, DHA-MUA-FKT and DHA-MUA-FBKT QMSDDs, as well as the MAP MSDD in the DSS/SSCH SDMA-OFDM system scenario of Figure 4.2, using the parameters of Table 4.1 with $N_w = 7$ in the EPA channel of Table 4.2, using a single snapshot for the inner EXIT curve which corresponds to the MSDDs.

4.5.3.2 EXIT Charts of the DHA-MAA QMSDDs without Gaussian Assumptions

Let us proceed by invoking EXIT charts for the family of DHA-MUA QMSDDs. Figure 4.21 shows snapshots of the inner decoder EXIT curves of the DHA-MUA QMSDDs and their respective decoding trajectories for the same transmitted frames as in Figure 4.14, where we have $E_b/N_0 = 4$ dB and the transmit frame of each user includes 24 576 bits. We may observe that in Figure 4.21 all the decoding trajectories reach the $I_{DEC,e} = 1$ line after a single MSDD-DEC iteration.

The effects of the simplifications applied by the DHA-MUA QMSDDs may become more intuitive, if we examine their EXIT charts, where no Gaussian assumptions are made for the input extrinsic LLRs. Similar to Figure 4.15 and Figure 4.16 recorded for the DHA-MAA QMSDDs, Figure 4.22, Figure 4.23 and Figure 4.24 present the inner and outer EXIT curves of the DHA-MUA QMSDD, DHA-MUA-FKT QMSDD and DHA-MUA-FBKT QMSDD, along with their respective trajectories, after one and two auxiliary QMSDD-DEC iterations, following the methodologies described in Section 3.9.1 and Figure 3.39. By comparing the top left EXIT charts of the DHA-MUA, DHA-MUA-FKT and DHA-MUA-FBKT QMSDDs in Figure 4.22, Figure 4.23, Figure 4.24 to those of the DHA-MAA and DHA-MAA-NE

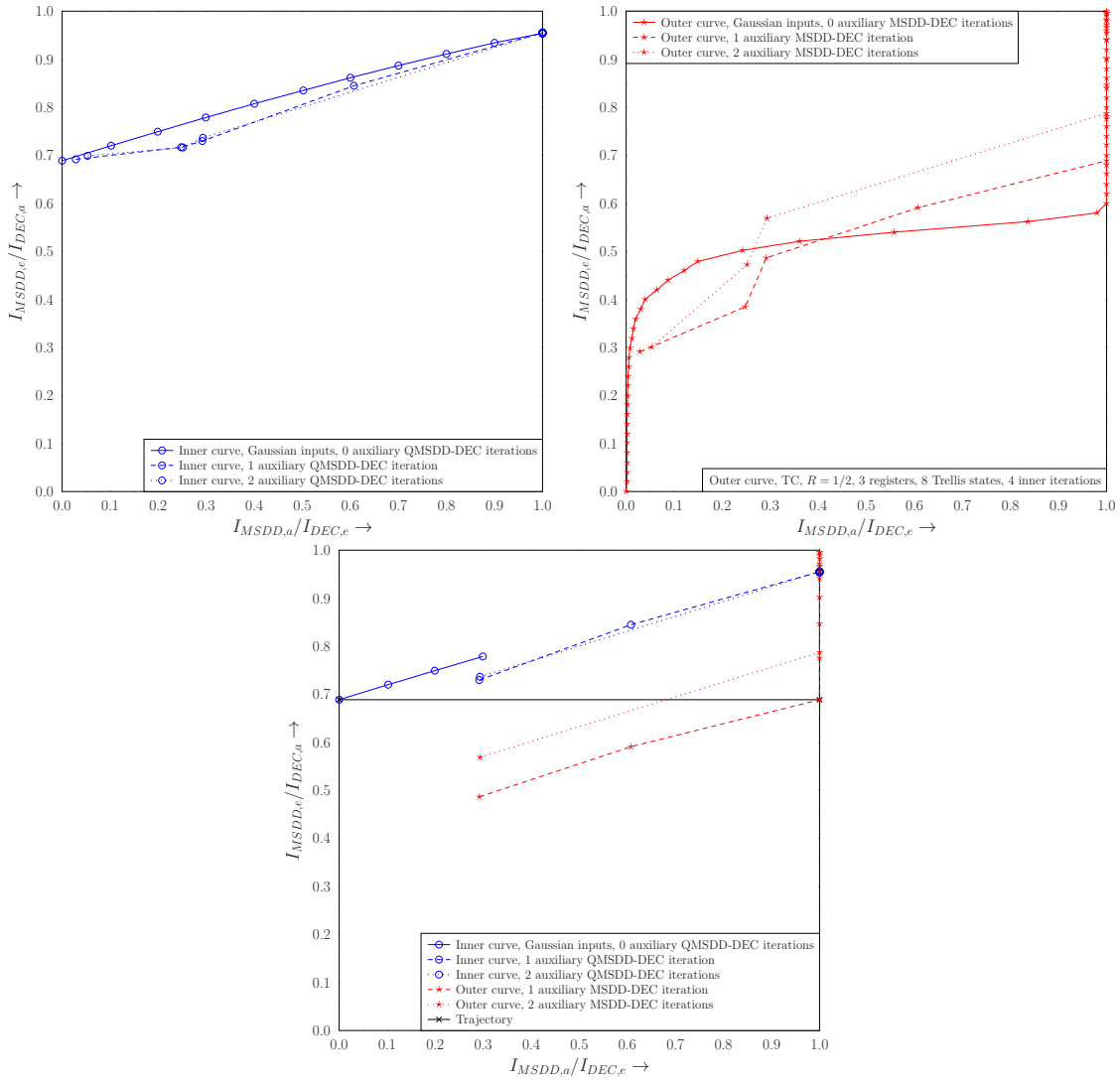

Figure 4.22: EXIT chart of the DHA-MUA QMSDD in the DSS/SSCH SDMA-OFDM system scenario of Figure 4.2, using the parameters of Table 4.1 for $N_w = 7$ in the EPA channel of Table 4.2 using 0, 1 and 2 auxiliary QMSDD-DEC iterations for the generation of the inner and outer EXIT curves for $E_b/N_0 = 4$ dB and $(E_b/N_0)^* = 0, 1, \ldots, 10$ dB. Top left: Inner EXIT curves. Top right: Outer EXIT curves Bottom: EXIT chart with inner and outer EXIT curves and the decoding trajectory.

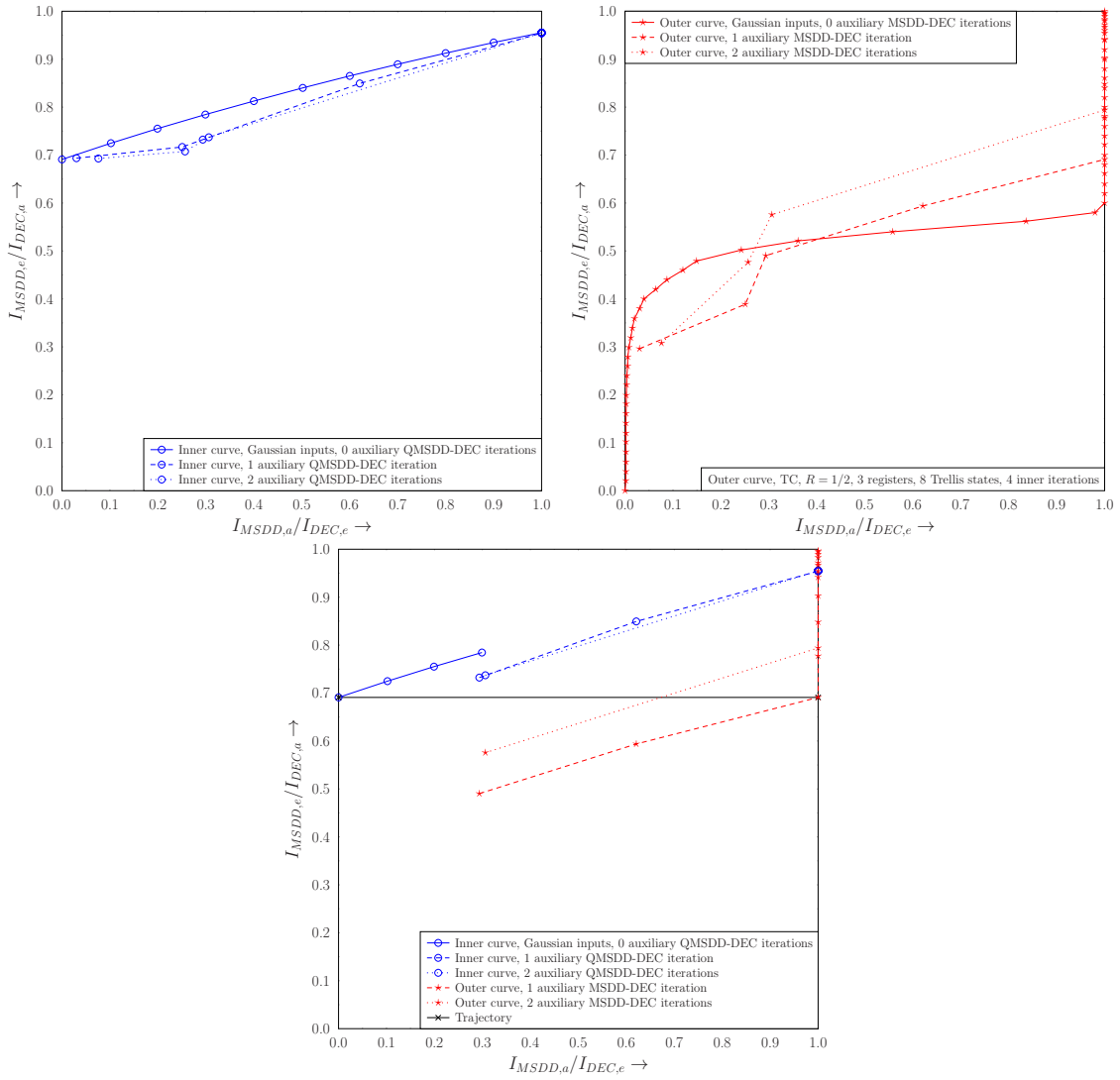

Figure 4.23: EXIT chart of the DHA-MUA-FKT QMSDD in the DSS/SSCH SDMA-OFDM system scenario of Figure 4.2, using the parameters Table 4.1 with $N_w = 7$ in the EPA channel of Table 4.2 using 0, 1 and 2 auxiliary QMSDD-DEC iterations for the generation of the inner and outer EXIT curves for $E_b/N_0 = 4$ dB and $(E_b/N_0)^* = 0, 1, \ldots, 10$ dB. Top left: Inner EXIT curves. Top right: Outer EXIT curves Bottom: EXIT chart with inner and outer EXIT curves and the decoding trajectory.

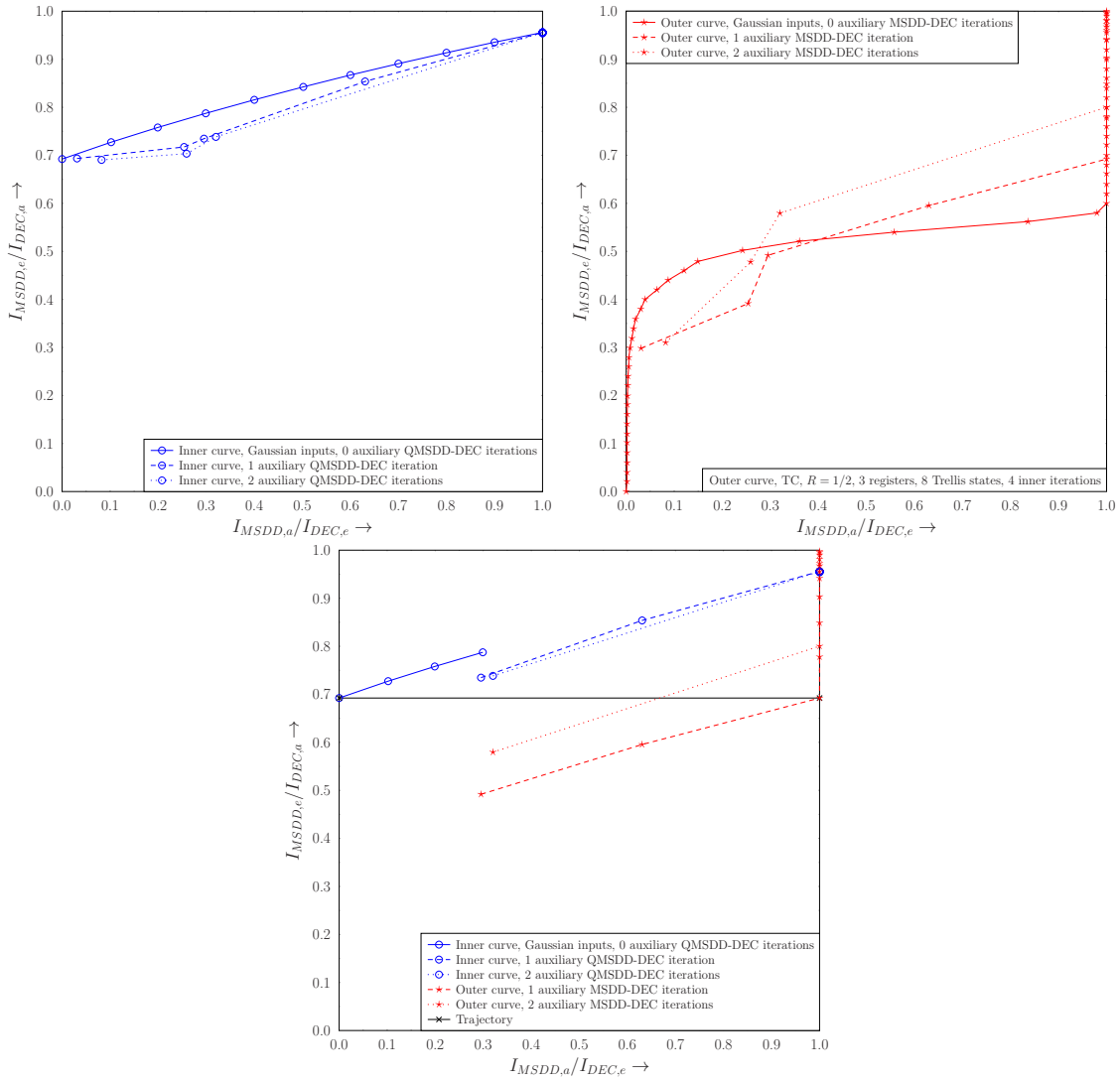

Figure 4.24: EXIT chart of the DHA-MUA-FBKT QMSDD in the DSS/SSCH SDMA-OFDM system scenario of Figure 4.2, using the parameters of Table 4.1 for $N_w = 7$ in the EPA channel of Table 4.2 using 0, 1 and 2 auxiliary QMSDD-DEC iterations for the generation of the inner and outer EXIT curves for $E_b/N_0 = 4$ dB and $(E_b/N_0)^* = 0, 1, \ldots, 10$ dB. Top left: Inner EXIT curves. Top right: Outer EXIT curves Bottom: EXIT chart with inner and outer EXIT curves and the decoding trajectory.

QMSDDs in Figure 4.15 and Figure 4.16, we observe that the family of DHA-MUA QMSDDs offer a better behaviour over multiple MSDD-DEC iterations, since their inner EXIT curves after one and two auxiliary MSDD-DEC iterations do not differ much from the inner decoder EXIT curves generated by Gaussian inputs. Similarly, the outer decoder EXIT curves shown at the top right EXIT charts of the aforementioned figures verify that the DHA-MUA QMSDDs have a better performance, due to satisfying the consistency condition, which is translated in the LLRs' PDF curves becoming more Gaussian-like. The finite interleaver length of 24 576 bits per frame per user does not succeed in completely eliminating the correlation between the bits, hence also contributing to the shaping of the inner and outer decoder EXIT curves.

4.5.4 Quantum Weighted Sum Algorithm-based QMSDD

The QWSA described in Section 3.4 may be used for performing non-coherent MSDD. The QWSA estimates the weighted sum of a function at a precision, which depends on the number l_{QWSA} of qubits employed in its Quantum Control Register (QCR). The more qubits are used in the QCR, the higher the estimation accuracy becomes, but at the same time, the computational complexity of the QWSA is increased. The detailed analysis of the QWSA is given in Section 3.4. In our MSDD applications, we use the *a priori* bit-based LLRs of the MSDD, associated with the *a priori* bit probabilities as the weights of the QWSA. At the same time, the function to be estimated by the weighted sum is the normalized CF of the MSDD presented in Equation 4.61 as in

$$f_{QWSA}(\mathbf{s}) = \frac{\sum_{p=1}^{P} \left(\| \mathbf{U}_p \cdot \mathbf{s} \|_2^2 \right)}{\sum_{p=1}^{P} \left(\| \mathbf{U}_p \cdot \mathbf{s}_{\max} \|_2^2 \right)}, \tag{4.83}$$

where $\mathbf{s}_{\max}$ is the legitimate multi-level symbol that maximizes the CF of the MSDD in Equation 4.61. The QWSA only accepts functions that obey $f : \{0, 1, \ldots, N-1\} \rightarrow [0, 1]$. The reason for including the denominator of Equation 4.83 for normalizing the CF of the QWSA is ensuring that the CF values remains limited to its legitimate value range.

Any search algorithm may be used for finding $\mathbf{s}_{\max}$, which is suitable for calculating the denominator in Equation 4.83. These are exemplified by the brute force search, ant colony optimization and genetic algorithm-based search. However, suboptimal search methods may output an $\mathbf{s}_{\max}$ value that is different from the true one, in which case the CF value of the true $\mathbf{s}_{\max}$ will have a value higher than 1, hence forcing the QWSA to output erroneous results. In this treatise, the DHA is employed for finding $\mathbf{s}_{\max}$, since we may achieve a $\sim$100% probability of success at a low complexity. The total computational complexity of the DHA-aided QWSA QMSDD expressed in terms of the number of CFEs per bit depends

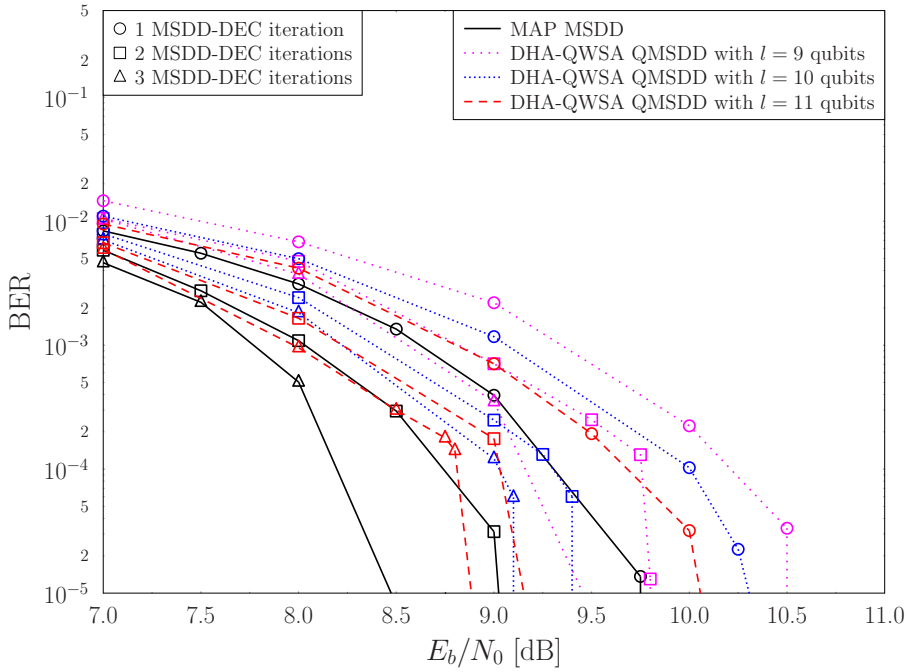

Figure 4.25: BER performance of the DHA-aided QWSA QMSDD and the MAP MSDD in the DSS/SSCH SDMA-OFDM system scenario of Figure 4.2, using the parameters of Table 4.1 with $N_w = 7$ in the EPA channel of Table 4.2, when using $l = 9, 10, 11$ control qubits in the QWSA.

on both the DHA as well as the QWSA and it is in the range of

$$\mathcal{C}_{DHA-QWSA} = 2^{l+3} + \begin{cases} 22.5\sqrt{M^{N_w-1}}/\left[(N_w-1)\log_2(M)\right] & \text{upper bound} \\ 4.5\sqrt{M^{N_w-1}}/\left[(N_w-1)\log_2(M)\right] & \text{lower bound} \end{cases}. \quad (4.84)$$

According to [1], the DHA-QWSA and hence the DHA-QWSA QMSDD may also be employed in large-scale systems, since its effect can only be evident there. However, we will focus our attention on small-scale systems, due to the practical constraints in our simulation time and memory requirements. Let us employ the DHA-QWSA QMSDD in our system scenario described in Table 4.1 for the EPA channel of Table 4.2. The BER performance of the DHA-QWSA QMSDD for $l_{QWSA} = 9, 10, 11$ qubits is compared to that of the optimal classical MAP MSDD in Figure 4.25. We may verify that by increasing the number of control qubits l_{QWSA} in the QWSA, we improve the system's performance, at the cost of increasing the complexity required to achieve it. For $l_{QWSA} = 10$ qubits, we may achieve a loss of 0.5 dB, when compared to the MAP MSDD, while if $l_{QWSA} = 11$ qubits are used in the QCR of the QWSA, we have a 0.22 dB loss, when $J = 3$ MSDD-DEC iterations are affordable. The total number of CFEs of the DHA-QWSA QMSDDs in Figure 4.25 are given in Table 4.7. Since the complexity of the DHA-QWSA QMSDD is higher than that of the MAP MSDD in every instance of our scenario, it is worth noting once again that the DHA-QWSA QMSDD is suitable for large-scale systems, as are most of the quantum detectors advocated in this treatise. Based on Table 4.7 we may observe

Table 4.7: Complexity in terms of the number of CFEs / bit in Figure 4.25

MSDD / QMSDD		$E_b/N_0 = 8$ dB		
		Number of MSDD-DEC iterations		
		1	2	3
MAP		341.33	341.33	341.33
QWSA	$l = 9$	4139.65	5266.92	6004.28
	$l = 10$	8235.71	10 100.34	10 919.02
	$l = 11$	16 427.67	19 849.57	21 323.38
MSDD / QMSDD		$E_b/N_0 = 4$ dB		
		Number of MSDD-DEC iterations		
		1	2	3
MAP		341.33	341.33	341.33
QWSA	$l = 9$	4139.66	8235.68	12 331.66
	$l = 10$	8235.80	16 427.73	24 619.80
	$l = 11$	16 427.80	32 811.80	49 195.80

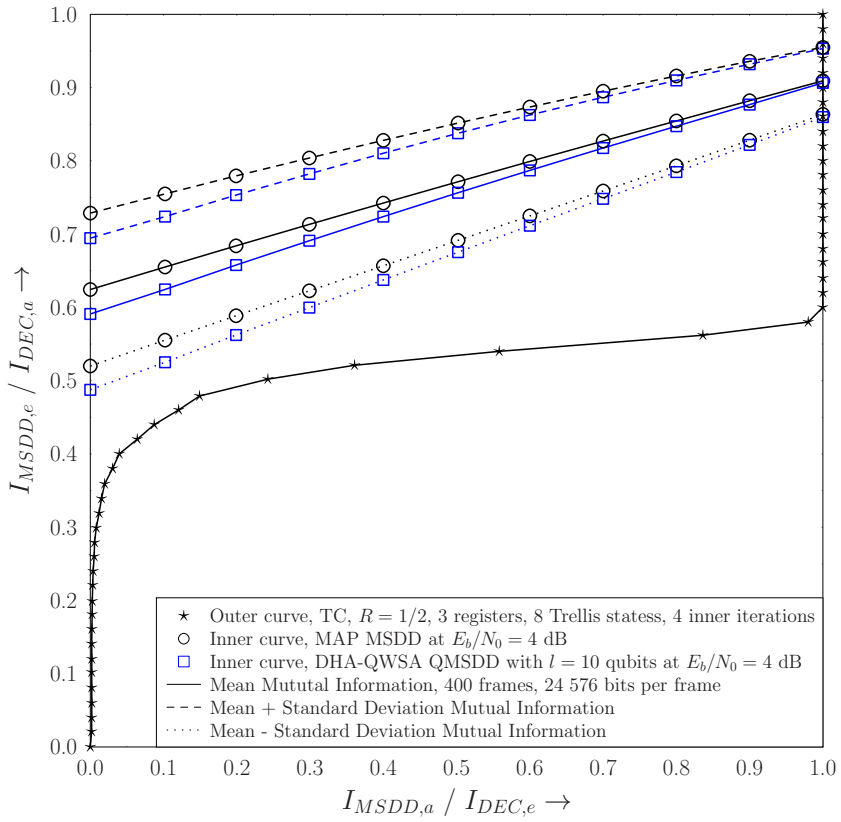

Figure 4.26: EXIT chart of the DHA-QWSA QMSDD with $l = 10$ qubits in the DSS/SSCH SDMA-OFDM system scenario of Figure 4.2, using the parameters of Table 4.1 in the EPA channel of Table 4.2. The inner and outer average EXIT curves of the mutual information are presented, along with the EXIT inner curves that take into consideration the standard deviation.

that the performance of the DHA-QWSA QMSDD is almost independent of the power during the first MSDD-DEC iteration, since the number of CFEs per bit is similar for both $E_b/N_0 = 4$ dB and $E_b/N_0 = 8$ dB. On the other hand, when we can afford multiple MSDD-DEC iterations, the complexity becomes lower, when the power is increased, which is due to the fact that a second or a third MSDD-DEC iteration is required less often, because the frame is perfectly decoded during the first or second MSDD-DEC iteration.

The average inner EXIT curves of the DHA-aided QWSA QMSDD, along with the statistically acquired standard deviation, are depicted for $E_b/N_0 = 4$ dB and $l = 10$ in Figure 4.26 for our scenario of Table 4.1 and for the EPA channel of Table 4.2. As expected, the inner EXIT curves of the DHA-QWSA QMSDD closely match those of the MAP MSDD and an open tunnel exists between the inner and outer decoder EXIT curves.

4.5.4.1 Consistency Condition of the DHA-QWSA QMSDD

Figure 4.27 shows the PDF curves of the bit-based LLRs of a single frame averaged over the four supported users in our system of Table 4.1 when $I_{MSDD,a} = 0.5$. The quantization of

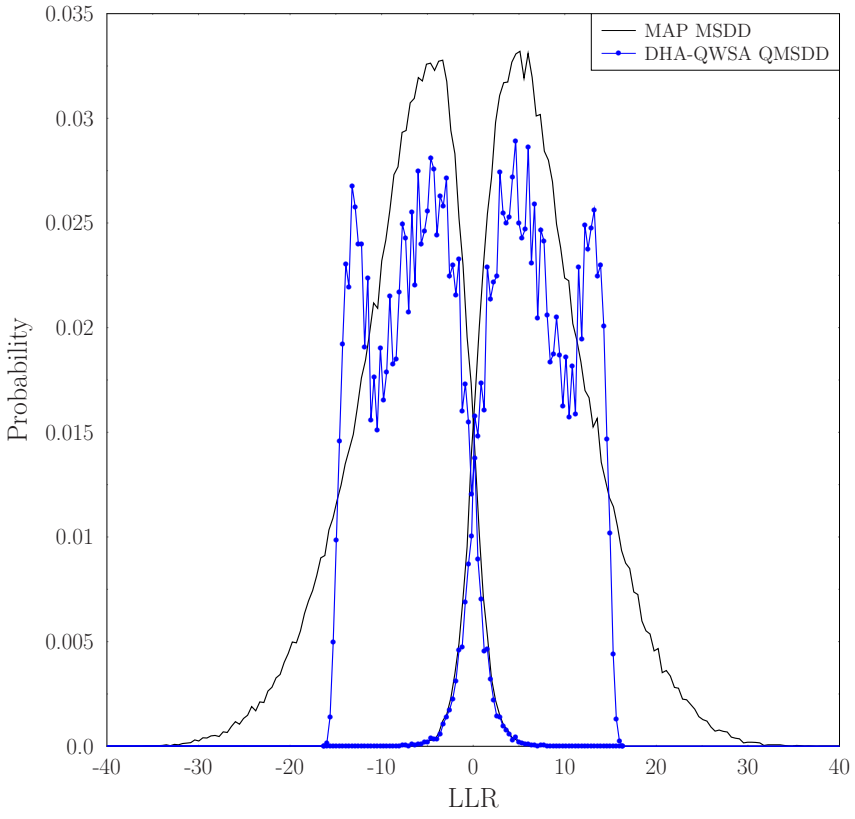

Figure 4.27: Histograms of the output LLRs of the MAP MSDD and the DHA-QWSA QMSDD with $l = 10$ qubits at $I_{MSDD,a} = 0.5$ of a single frame of 24 576 bits per user in our system scenario described in Figure 4.2, using the parameters of Table 4.1 for $N_w = 7$ in the EPA channel of Table 4.2. The histograms which have their main peak at a positive LLR value correspond to the LLRs of a bit equal to 1, while those who have their main peak at a negative LLR value correspond to the LLRs of a bit equal to 0.

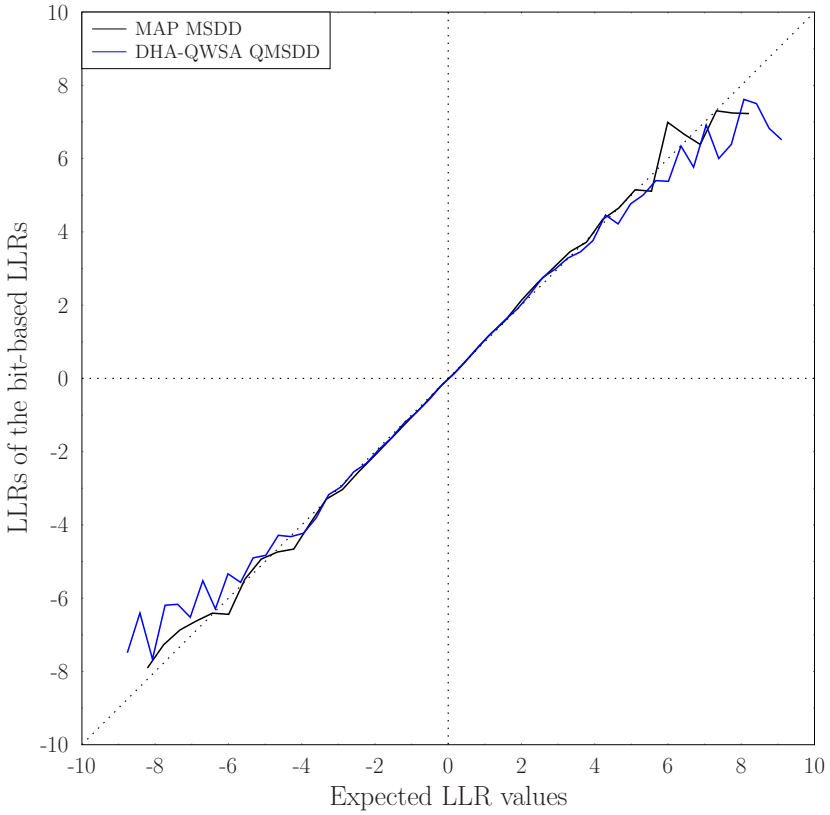

Figure 4.28: LLR values obtained by the MSDDs with respect to the expected LLR values based on the histograms in Figure 4.27. The consistency condition for iterative detection for a particular MSDD is satisfied if its corresponding curve is close to the main diagonal line. The frame length of each user is equal to 24 576 bits.

the numerator and the denominator of the LLR calculation in Equation 4.66 naturally leads to a quantization of the LLR values, explaining the appearance of spikes in the PDF curves in Figure 4.27. Furthermore, the presence of "cliffs" at LLR $= \pm 16$ is due to the selected minimum value at the output of the QWSA. As described in Section 3.4, the minimum sum value that the QWSA can output while using l number of control qubits is equal to $a_{QWSA,\,\min} = 0$. Furthermore, the minimum non-zero sum value is equal to

$$a_{QWSA,\,nz,\min} = \sin^2\left(\pi/2^l\right). \tag{4.85}$$

Therefore, when the sum in the numerator or the denominator of an LLR is smaller than $a_{QWSA,\,nz,\min}/2$, it is most likely to be mapped to $a_{QWSA,\,\min} = 0$, resulting in an LLR of plus or minus infinity, respectively. For avoiding this issue, we have decided to map these sums that are initially equal to $a_{QWSA,\,\min} = 0$ to the value of

$$a_{QWSA,\,\min} = \sin^2\left(0.1 \cdot \pi/2^l\right), \tag{4.86}$$

which depends on the number of control qubits l, scaling it to the rest of the legitimate values. If we opted for an even lower positive number for $a_{QWSA,\,\min}$, the resultant LLR range would become larger, since the upper and lower limits of the LLR values with the

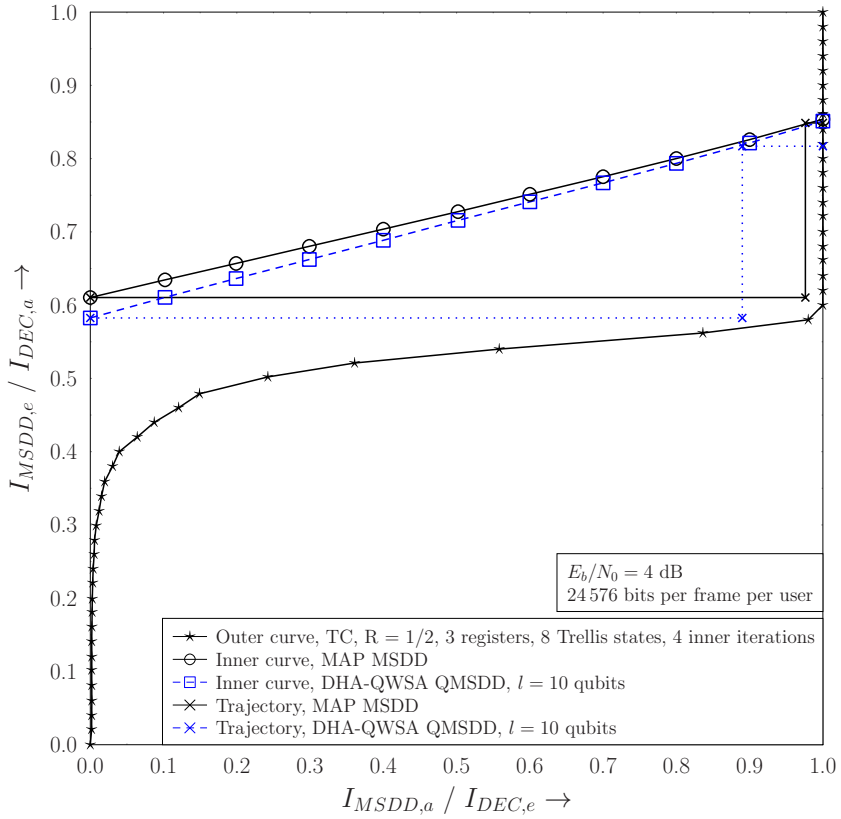

Figure 4.29: EXIT chart of the QWSA QMSDD with $l = 10$ qubits, as well as the MAP MSDD in the DSS/SSCH SDMA-OFDM system scenario of Figure 4.2, using the parameters of Table 4.1 and the EPA channel of Table 4.2, using a single snapshot for the inner EXIT curve which corresponds to the MSDDs.

aforementioned modification become

$$L_{\max} = \ln \frac{\sin^2\left(2^{l-1} \cdot \pi/2^l\right)}{\sin^2\left(0.1 \cdot \pi/2^l\right)} \tag{4.87}$$

$$= \ln \frac{\sin^2\left(\pi/2\right)}{\sin^2\left(0.1 \cdot \pi/2^l\right)} \tag{4.88}$$

$$= \ln \frac{1}{\sin^2\left(0.1 \cdot \pi/2^l\right)} \tag{4.89}$$

$$= -\ln\left(\sin^2\left(0.1 \cdot \pi/2^l\right)\right) \tag{4.90}$$

$$L_{\min} = \ln\left(\sin^2\left(0.1 \cdot \pi/2^l\right)\right), \tag{4.91}$$

respectively, where the upper limit $L_{\max}$ corresponds to the case, when the numerator is equal to the highest legitimate value of 1 and the denominator is equal to $a_{QWSA,\min}$, while the opposite is true for the lower limit. For our scenario of $l = 10$ qubits, we have $a_{QWSA,\min} = 9.412 \cdot 10^{-8}$, resulting in $L_{\min} = -16.179$ and $L_{\max} = 16.179$ as verified in Figure 4.27. Still referring to Figure 4.27, we should note that the main peaks of the PDF curves match those of the MAP MSDD, while the secondary peaks are formed due to the range limitation we introduced in conjunction with $a_{QWSA,\min} = 9.412 \cdot 10^{-8}$.

The consistency condition of the DHA-QWSA QMSDD is tested in Figure 4.28. By

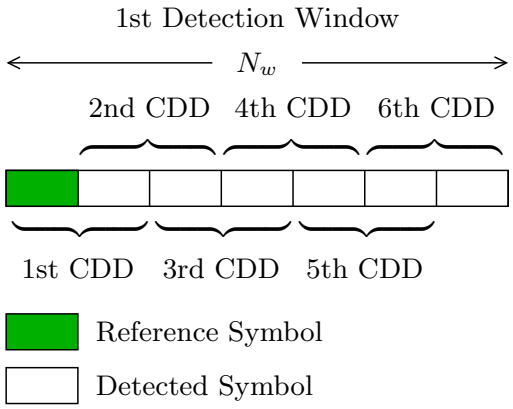

Figure 4.30: Exploitation of the CDD for initializing the DHA searches in the first detection window of the QMSDDs, resulting in reduced complexity and same performance.

observing Figure 4.28 we may conclude that the DHA-aided QWSA QMSDD is eligible for integration in an iterative receiver, since its curve matches that of the MAP MSDD. Figure 4.29 presents the EXIT chart of our scenario for a single frame transmitted by each user at $E_b/N_0 = 4$ dB. According to Figure 4.29, the frame length of 24 576 bits per frame per user was not sufficient for the specific Monte-Carlo decoding trajectory to be fully decoded by the MAP MSDD after one iteration. Both the MAP MSDD and the DHA-QWSA QMSDD successfully reach the $I_{DEC,E} = 1$ point after two MSDD-DEC iterations. By observing Figure 4.29 we may conclude that the DHA-aided QWSA QMSDD may be beneficially incorporated into an iterative receiver, since its inner decoder EXIT curve matches that of the MAP MSDD.

4.6 Exploitation of the Conventional Differential Detector

All the MSDDs that detect the transmitted symbols over an N_w-long symbol window require the reception of N_w signals. In our discussions presented in the previous sections, we have assumed having a random initial input to the DHA, since we have no *a priori* information about the transmitted multi-level symbol. When we used coherent multi-user detection in Chapter 2 and Chapter 3, we initialized the DHA searches with the output symbol of either the MF, ZF or the MMSE detectors.

By assuming that the signals arrive in the same sequence as they were transmitted, we may be able to perform CDD for every consecutively formed received signal pair in each N_w-long symbol window, while waiting for all the N_w signals to be received. Once all the signals are received and the QMSDD procedure can be initiated, the combined outputs of the $(N_w - 1)$ CDDs may be used as the initial input of the corresponding DHA search. Therefore, no additional delay is imposed on the QMSDD and there is only a modest increase in complexity, since the $(N_w - 1)$-fold increase of the CDD applications is compensated by the lower complexity required by a deterministically-initialized DHA. By exploiting the CDD in our scenario described in Table 4.1, the resultant procedure is described in Figure 4.30, where the first detection window is presented.

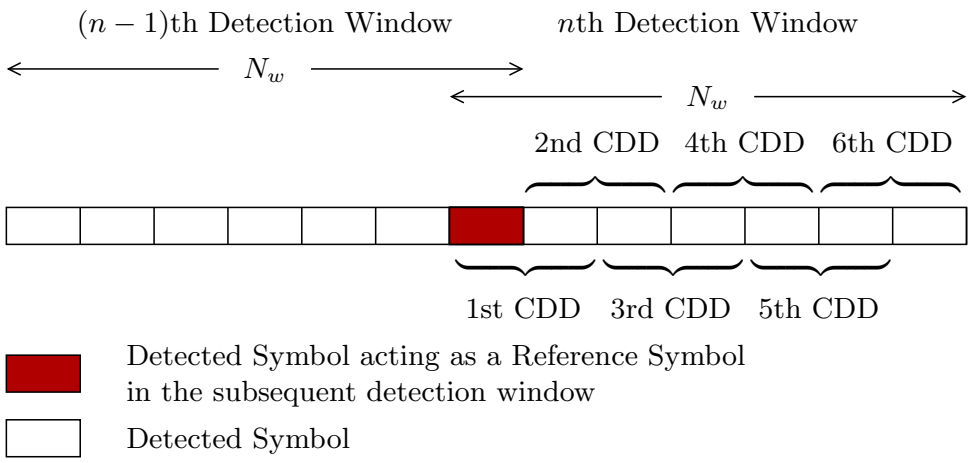

Figure 4.31: Exploitation of the CDD for initializing the DHA searches in the nth detection window of the QMSDDs, resulting in reduced complexity and same performance.

More specifically, we firstly receive the reference signal, which is buffered. When the second signal is received, we perform the CDD on the first two received signals, obtaining the symbol index output $x_{CDD,1} \in \{0, 1, \ldots, M-1\}$. Both received signals remain buffered. After the third signal has arrived, the CDD is applied for the detection window formed by the second and third signal, where the second signal acts as the reference, which is equal to $x_{CDD,1}$. The output of the second CDD is $x_{CDD,2} \in \{0, 1, \ldots, M-1\}$. The same process is repeated, until all N_w signals have been received and (N_w-1) CDDs have been performed, obtaining $x_{CDD,k}$, $k = 1, 2, \ldots, N_w-1$. Finally, we are ready to combine the CDD outputs for the sake of obtaining a multi-level symbol index, which may be the initial symbol of the DHA in the QMSDD employed. The initial multi-level symbol index is equal to

$$x_{init} = \sum_{k=1}^{N_w-1} x_{CDD,k} \cdot M^{N_w-1-k}. \tag{4.92}$$

During the second detection window, the procedure ensues similarly to the one analysed during the first detection window, with the slight difference that instead of a reference symbol, the output of the QMSDD generated for the last symbol of the previous detection window is used. The visual representation of the CDD activation for the nth detection window is depicted in Figure 4.31. By using the CDD initialization, we essentially perform a CDD for every unknown symbol. Therefore, the additional complexity of the CDD initialization imposed to the overall detection complexity in terms of number of CFEs per bit is equal to

$$\mathcal{C}_{CDD,init} = \frac{M}{\log_2(M)}. \tag{4.93}$$

4.6.1 Hard-Output CDD-initialized Quantum Multiple-Symbol Differential Detection

The impact of the deterministic CDD initialization of the DHA is more apparent, when we use the DHA QMSDD of Section 4.4.2. Figure 4.32 shows the PDF and CDF curves

of our system scenario presented in Table 4.1 for the EPA channel of Table 4.2, when we either initialize the DHA using the CDD outputs or randomly. In the same figure, we may observe that the DHA finds the solution sooner, when it is initialized by the CDD instead of being randomly initialized. This is indeed expected, since the closer we start the search to the optimal symbol, the faster the optimal symbol will be found and the search will be concluded. It is reasonable to expect that the DHA search is completed sooner when the initial symbol is the optimal one. Based on the CDF curves seen in Figure 4.8 we may also invoke the "CDD-initialized" ES-DHA for achieving a near-optimal performance at an even lower complexity. For example, if we stop the CDD-initialized ES-DHA QMSDD of Figure 4.8 in Section 4.4.3 after $363 - 313 = 50$ CFEs, we will have found the optimal multi-level symbol with a success probability of 90%, where in our scenario 313 is the minimum number of CFEs that the DHA needs for realizing that the solution has indeed been found in our scenario. On the other hand, we will require $656 - 313 = 343$ CFEs to achieve the same probability of success with a randomly-initialized ES-DHA QMSDD. It is reasonable to conclude that achieving a good performance by the CDD is vital for the sake of attaining a substantial complexity reduction by the CDD-initialized DHA QMSDD. According to Figure 4.7, the BER performance of the CDD was 0.5 dB away from that of the ML MSDD, therefore its outputs were identical to the optimal symbol most of the time, as it can also be inferred from the shape of the CDD-initialized DHA QMSDD's

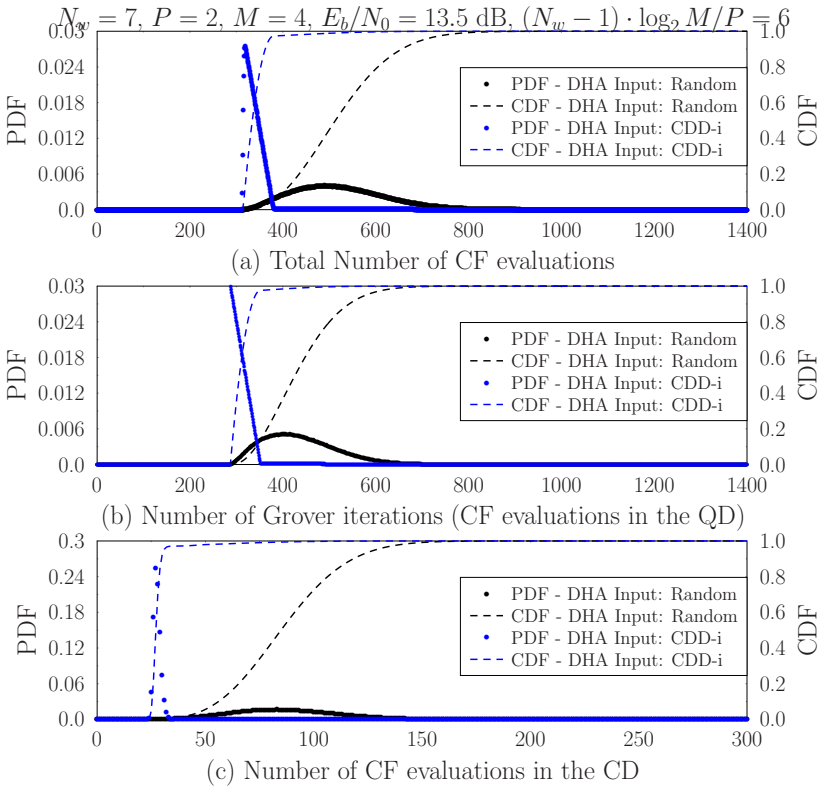

Figure 4.32: PDF and CDF curves of the DHA in the DSS/SSCH SDMA-OFDM scenario of Figure 4.2, using the parameters of Table 4.1 for $N_w = 7$ in Table 4.2 after $12 \cdot 10^6$ number of independent DHA instances, when the DHA searches are initialized by using the pre-calculated CDD outputs or by using a random symbol index.

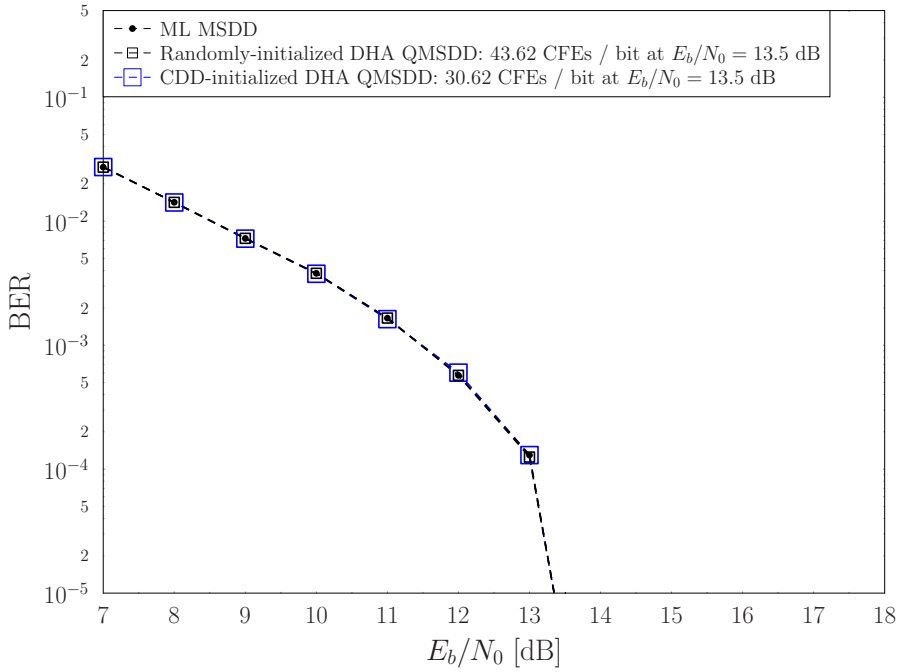

Figure 4.33: BER performance of the randomly-initialized and CDD-initialized DHA QMSDD in the DSS/SSCH SDMA-OFDM system scenario of Figure 4.2, using the parameters of Table 4.1 for $N_w = 7$ in the EPA channel of Table 4.2.

PDF curve portrayed in Figure 4.32a. The BER performance of the CDD-initialized DHA QMSDD is expected to be equivalent to that of the randomly-initialized DHA QMSDD. This is indeed verified in Figure 4.33, where we may observe that the CDD-initialized DHA QMSDD performs equivalently both to the random-initialized DHA QMSDD and to the ML MSDD.

4.6.2 Soft-Input Soft-Output CDD-initialized Quantum Multiple-Symbol Differential Detection

The initialization of the DHA searches with the aid of the CDD outputs may also be used in the SISO DHA-aided QMSDDs of Figure 4.17 in Section 4.5.3. The effect of the CDD-aided initialization of the DHA search in the SISO QMSDDs is not as straightforward as in the hard-output QMSDDs, since the goal is not only to find the optimal multi-level symbol, but also to create a set of the best symbols found. By commencing the search closer to the optimal multi-level symbol, we may exclude a number of near-optimal symbols that would have been found, if the randomly-initialized search was used instead.

In addition to the CDD-aided initialization of the DHA searches, in the iterative QMSDDs we may also use the optimal multi-level symbol found during the first MSDD-DEC iteration as the initial input of the DHA search during the second MSDD-DEC iteration. Similarly, the best symbol found during the second MSDD-DEC iteration may initialize the DHA search of the same detection window during the third MSDD-DEC iteration and so on. In this way, the CDD is performed only during the first MSDD-DEC iteration and no additional complexity is imposed by initializing the DHA search during the subsequent

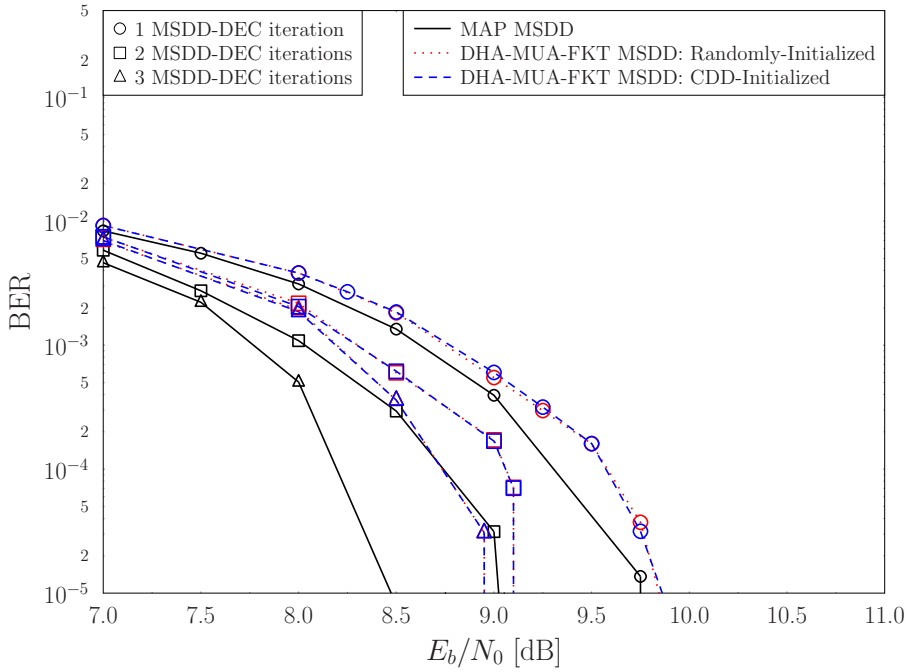

Figure 4.34: BER performance of the randomly-initialized and CDD-initialized DHA-MUA-FKT QMSDD in the DSS/SSCH SDMA-OFDM system scenario of Figure 4.2, using the parameters of Table 4.1 for $N_w = 7$ in the EPA channel of Table 4.2. The CDD-initialized DHA-MUA-FKT QMSDD also employs deterministic DHA initialization during the second and third MSDD-DEC iterations by using the optimal symbol of each detection window found during the previous MSDD-DEC iteration.

MSDD-DEC iterations. Let us use the term *deterministic initialization* in the context of the SISO QMSDD, when we employ the CDD-based initialization for the DHA searches during the first QMSDD-DEC iteration and we use the best found symbols for initializing the DHA searches of the subsequent QMSDD-DEC iterations.

The BER performance of the deterministically-initialized DHA-MUA-FKT QMSDD is compared in Figure 4.34 both to that of the randomly-initialized DHA-MUA-FKT QMSDD of Figure 4.17 as well as to that of the MAP MSDD of Figure 4.17, while their respective computational complexities are given in Table 4.8. Based on Figure 4.34, the performance of the CDD-initialized DHA-MUA-FKT QMSDD is seen to be equivalent to that of the randomly-initialized DHA-MUA-FKT QMSDD. According to Table 4.8, the complexity of the deterministically-initialized DHA-MUA-FKT QMSDD is higher than that of the randomly-initialized DHA-MUA-FKT QMSDD during the first QMSDD-DEC iteration and it becomes lower during the second and third QMSDD-DEC iteration. The reason that the deterministically-initialized DHA-MUA-FKT QMSDD of Figure 4.34 has a higher complexity lies in its nature, where multiple DHA searches take place. For example, let us focus our attention on the nth detection window. The two DHA searches of the multi-level symbol's first bit will be concluded sooner in the deterministically-initialized DHA-MUA-FKT QMSDD than in the randomly-initialized DHA-MUA-FKT QMSDD, as it was also shown in the case of the hard-output DHA QMSDD of Section 4.6.1. Therefore, it is expected for the resultant sets $\mathcal{X}^{1,1,0}$ and $\mathcal{X}^{1,1,1}$ of the deterministically-initialized DHA-MUA-FKT QMSDD to contain fewer elements. According to the methodology followed

Table 4.8: Computational complexity in terms of the number of CFEs / bit in Figure 4.34

MSDD / QMSDD	Number of CFEs per bit at $E_b/N_0 = 8$ dB		
	1 MSDD-DEC iteration	2 MSDD-DEC iterations	3 MSDD-DEC iterations
MAP	341.33	341.33	341.33
DHA-MUA-FKT			
Random Initialization	316.72	374.51	401.11
Deterministic Initialization	317.74	374.11	399.94
Random Initialization & **Iteration memory**	316.72	373.07	398.86
DHA-MUA			
Random Initialization	392.17	466.73	501.15
Deterministic Initialization	384.29	455.13	487.74
MSDD / QMSDD	Number of CFEs per bit at $E_b/N_0 = 4$ dB		
	1 MSDD-DEC iteration	2 MSDD-DEC iterations	3 MSDD-DEC iterations
MAP	341.33	341.33	341.33
DHA-MUA-FKT			
Random Initialization	317.87	585.44	820.46
Determinstic Initialization	318.75	581.18	810.12
Random Initialization & **Iteration memory**	317.87	580.30	809.16
DHA-MUA			
Random Initialization	394.06	689.93	962.78
Deterministic Initialization	387.25	673.33	926.09

by the DHA-MUA-FKT QMSDD, the subsequent DHA searches of the rest of the bits in the multi-level symbols are initialized either based on the best already found symbols during the previous DHA searches due to the forward knowledge transfer, or based on the neighbours of the globally optimal symbol. Therefore, the more elements are included in the sets $\mathcal{X}^{1,1,0}$ and $\mathcal{X}^{1,1,1}$, the higher the probability of initializing the DHA search of the second bit closer to its optimal symbol. Hence, the randomly-initialized DHA-MUA-FKT QMSDD has the edge over the deterministically-initialized DHA-MUA-FKT QMSDD during this part due to the size of its initial sets $\mathcal{X}^{1,1,0}$ and $\mathcal{X}^{1,1,1}$, effectively mitigating the complexity imposed during the first bit's first DHA search. After the DHA searches of the first few bits have been completed, the deterministically-initialized DHA-MUA-FKT QMSDD of Figure 4.34 has also increased its sets' size and the complexity of the DHA searches conducted for the rest of the bits in the multi-level symbol is similar to that in its randomly-initialized counterpart. It should be noted that in the DHA-MUA QMSDD, where there is no knowledge transfer, the deterministically-initialized DHA-MUA QMSDD will have a lower complexity than its randomly-initialized counterpart, as portrayed in

Table 4.8.

During the subsequent QMSDD-DEC iterations, the initial advantage of the deterministically initialized DHA-MUA-FKT QMSDD of Figure 4.34 becomes more dominant, since the initialization of the first bit's first DHA is the best found symbol during the previous QMSDD-DEC iteration and it often remains the optimal symbol of the specific detection window during the rest of the QMSDD-DEC iterations. This results in the deterministically-initialized DHA-MUA-FKT QMSDD essentially initializing the first bit's DHA search with its solution. The deterministically-initialized DHA-MUA-FKT is expected to have fewer elements in the $\mathcal{X}_q^{t,m,\mathrm{v}}$ sets than its randomly-initialized counterpart, since it will reach the optimal multi-level MSDD symbol vector after fewer CFEs, which, in turn leads to fewer unique CF values found. The problem of the smaller set size arrived at after the first two DHA searches also persists for the deterministically-initialized DHA-MUA-FKT QMSDD, but the difference in complexity reduction is not mitigated sufficiently rapidly by the randomly-initialized DHA-MUA-FKT QMSDD of Figure 4.34.

In Table 4.8 we also characterize the randomly-initialized DHA-MUA-FKT QMSDD with iteration memory, which uses a randomly selected initial input for the DHA searches during the first MSDD-DEC iteration and then later employs the globally optimal multi-level symbol found during the previous iteration for the subsequent MSDD-DEC iterations. The randomly-initialized DHA-MUA-FKT QMSDD associated with an iteration memory uses a random initial input only during the $J = 1$st MSDD-DEC iteration. For the subsequent $J \geq 2$ MSDD-DEC iterations the best symbol found during the previous MSDD-DEC iteration is used instead for the sake of initializing the DHA. This hybrid semi-deterministically-initialized DHA-MUA-FKT QMSDD has a complexity, which is identical to that of the randomly-initialized DHA-MUA-FKT QMSDD during the first iteration, while its complexity during the rest of the iterations is similar to that of ts deterministically-initialized counterpart.

4.7 Employment of the QMSDD every IpS QMSDD-DEC Iterations

In case of coherent detection, when we use the MAP MUD we may assume that improved channel estimates become available during the subsequent MUD-DEC iterations, therefore the MAP MUD should re-evaluate the CF for all the legitimate multi-level symbols during each MUD-DEC iteration, which, inevitably increases its complexity upon each additional iteration. By contrast, in case of non-coherent detection, the MAP MSDD is only employed during the first MSDD-DEC iteration and the hitherto computed complete set of CFEs is reused during the subsequent MSDD-DEC iterations. In this treatise, we assume that the reuse of the same hitherto found CFE set is granted without any additional computational complexity, since our metric is selected to be the number of CFEs performed by an MSDD. This may have been observed in Table 4.5, Table 4.6, Table 4.7 and Table 4.8, where the complexity of the MAP MSDD remains constant over the three MSDD-DEC iterations.

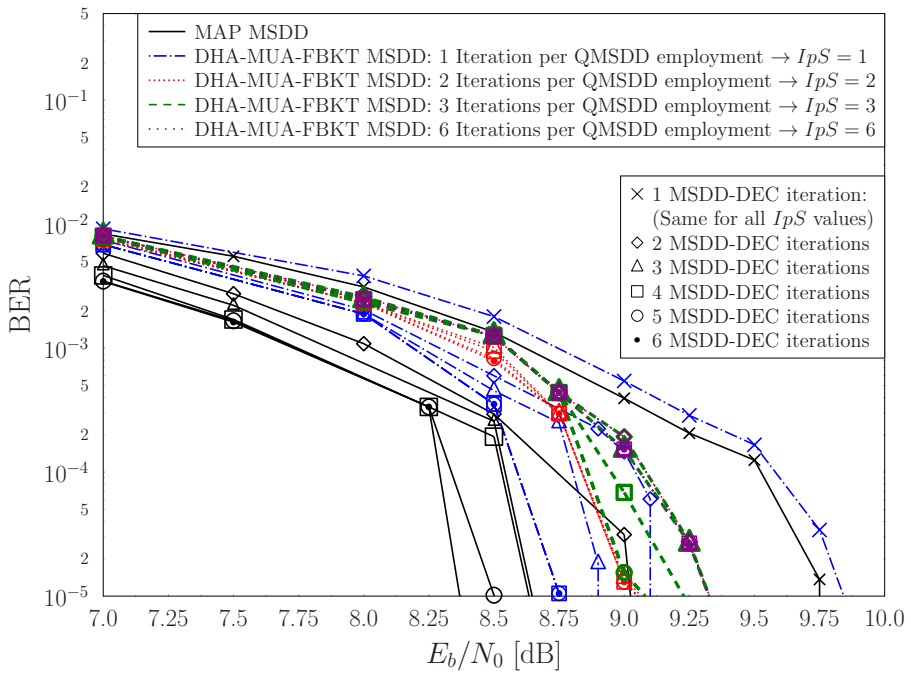

Figure 4.35: BER performance of the randomly-initialized DHA-MUA-FBKT QMSDD with iteration memory in the DSS/SSCH SDMA-OFDM system of Figure 4.2, using the parameters summarized in Table 4.1 for $N_w = 7$ in the EPA channel of Table 4.2 for $IpS \in \{1, 2, 3, 6\}$.

However, we have employed our QMSDDs during each QMSDD-DEC iteration, taking into consideration the fact that there is a possibility that during the second QMSDD-DEC iteration the globally optimal symbol may be a symbol that was not found during the first QMSDD-DEC iteration. This may occur, since the proposed QMSDDs find a suitable subset of symbols used for calculating the bit-based LLRs, instead of calculating the CFE corresponding to every legitimate multi-level symbol, as in the MAP MSDD.

In this section we investigate the effect of actively not employing the DHA-MUA-FBKT QMSDD during every QMSDD-DEC iteration in our scenario presented in Table 4.1 for the EPA channel of Table 4.2 in the interest of reducing the complexity imposed. During the specific QMSDD-DEC iterations which dispense with employing the QMSDD, the LLRs are calculated based on the most recently found CFE set and the newly obtained *a priori* probabilities gleaned from the channel decoder. Hence, the CF that is used when the QMSDD is employed does not include the *a priori* probabilities, which is in contrast to Equation 4.75 and it becomes

$$f_{MSDD,IpS}^{SISO-DHA}(\mathbf{x}) = \sum_{p=1}^{P} \left(\| \mathbf{U}_p \cdot \mathbf{s} \|_2^2 \right), \tag{4.94}$$

where the relationship between $\mathbf{s}$ and $\mathbf{x}$ is described in Equation 4.1. By dispensing with the employment of the QMSDD during each QMSDD-DEC iteration and by exploiting both the previously found symbol as well as the CFE sets we expect an even lower complexity, albeit at the cost of a BER performance degradation. It should be noted that the entire CFE set that was found during the most recent QMSDD-DEC iteration, where the QMSDD was

Table 4.9: Computational complexity in terms of the number of CFEs / bit in Figure 4.35

MSDD / QMSDD	Number of CFEs per bit at $E_b/N_0 = 8$ dB		
	1 MSDD-DEC iteration	2 MSDD-DEC iterations	3 MSDD-DEC iterations
MAP	341.33	341.33	341.33
DHA-MUA-FBKT			
$IpS = 1$	316.72	374.51	401.11
$IpS = 2$	316.72	316.72	346.97
$IpS = 3$	316.72	316.72	316.72
$IpS = 6$	316.72	316.72	316.72
MSDD / QMSDD	4 MSDD-DEC iterations	5 MSDD-DEC iterations	6 MSDD-DEC iterations
MAP	341.33	341.33	341.33
DHA-MUA-FBKT			
$IpS = 1$	412.99	426.07	439.15
$IpS = 2$	346.97	368.65	368.65
$IpS = 3$	342.73	342.73	342.73
$IpS = 6$	316.72	316.72	316.72

used will be exploited for the calculation of the LLRs during the QMSDD-DEC iterations, where the QSMDD is not used, by substituting the CF values in Equation 4.66, along with the updated *a priori* probabilities.

Figure 4.35 presents the BER performance of the randomly-initialized DHA-MUA-FBKT QMSDD of Section 4.5.3 relying on having an iteration memory in our scenario as portrayed in Section 4.6.2, when it is employed during every QMSDD-DEC iteration. In other words, this corresponds to an Iterations per Search (IpS) ratio of $IpS = 1$. Furthermore, the scenarios of $IpS = 2, 3$ and 6 are also presented in Figure 4.35. We may observe that the BER performance is worse, when we employ the QMSDD less frequently. However, the complexity reduction attained by reusing the same, previously obtained sets diminishes upon increasing the number of QMSDD-DEC iterations. Observe in Figure 4.35 that there is a trade-off between the performance gain and the decoding complexity obtained by a QMSDD-DEC iteration, where the previously found symbol set is used.

Based on Figure 4.35 we observe that as expected, the gain achieved during an additional iteration, when the QMSDD is employed is higher than that when the previously obtained CFE set is used. However, the performance degradation may not be severe, whilst the attainable complexity reduction is substantial. For example, the performance of the DHA-MUA-FBKT QMSDD associated with $IpS = 3$ after $J = 3$ MSDD-DEC iterations is 0.25 dB away from that of its counterpart relying on $IpS = 1$ at BER $= 10^{-5}$. In other words, in this scenario if we employ the DHA-MUA-FBKT QMSDD only during the first MSDD-DEC iteration, similarly to the MAP MSDD, we would need 0.25 dB more power

for achieving the same performance as in the case, where we employed $J = 3$ MSDD-DEC iterations. The complexities of the systems investigated are summarized in Table 4.9. It should be noted that similarly to the MAP MSDD, the complexity of the QMSDD relying on the previously found sets being reused remains the same.

4.8 Detection Window Length and Frequency of Subcarrier Hopping

In non-coherent multiple-symbol differential detection, extending the length of the detection window N_w has a beneficial impact on the system's performance, which however has to be traded-off against the detector's complexity. Explicitly, the MAP MSDD's complexity increases exponentially with the detection window's size, but the BER performance is improved. This is illustrated in Figure 4.36, where we investigate the system specified in Table 4.1 for the EPA channel of Table 4.2 with the slight difference that 10 752 bits are transmitted by each of the 4 users in each frame, when we have $N_w = 8$ and $N_w = 4$ and when QPSK modulation associated with $M = 4$ is used, resulting in a search space of $M^{N_w-1} = 16\,384$ and 64 legitimate multi-level symbols, respectively. We may observe that fewer bit errors occur at the end of the channel decoding procedure, for $N_w = 8$ than in the case of $N_w = 4$ for the same E_b/N_0 value. More specifically, the performance gap between the $N_w = 8$ system and the $N_w = 4$ system is approximately 0.3 dB, when a single MSDD-DEC iteration is performed and 0.5 dB when we allow 2 or 3 MSDD-DEC iterations. However, the complexity of the $N_w = 8$ MAP MSDD quantified in terms of the number of CFEs per bit is 109.68 times higher than that of the MAP MSDD, which uses $N_w = 4$. In more detail, according to Equation 4.71, the complexity of the MAP MSDD associated with $N_w = 8$ is equal to 1170.3 CFEs per bit, while only 10.67 CFEs per bit are required by the MAP MSDD for $N_w = 4$.

It should be noted that in both systems characterized in Figure 4.36 the same value was used for the period of subcarrier hopping T_h. The reason T_h was kept the same is that of providing a fair comparison between the MSDDs having different detection window lengths. In fact, even by keeping the value of T_h the same, there is a difference in the operation of the MAP MSDDs using $N_w = 8$ and $N_w = 4$, since the former one has to detect the signal of $(T_h - 1)/(N_w - 1) = 21/7 = 3$ windows after the most recent reception of a reference symbol and before a new reference symbol arrives on a different subcarrier, while the MAP MSDD associated with $N_w = 4$ has to detect the signals gleaned from $(T_h - 1)/(N_w - 1) = 21/3 = 7$ windows during the same period. Naturally, the difference in the number of detection windows affects the system's performance in the case, where the last symbol of a detection window which is subsequently used as the reference symbol of the next detection window has been erroneously detected. That scenario occurs more frequently, when we have a shorter window length N_w and a longer subcarrier hopping period T_h.

When we increase the subcarrier hopping period T_h, we require the transmission of

fewer reference symbols, since each user transmits on the same slow-fading subcarrier for a longer period of time, therefore increasing the system's throughput. At the same time however, we do not allocate the resources to the users in a fair manner, since in the scenario of a user operating in a deeply-fading channel, that user will have to continue to have to suffer for the duration of T_h symbols. A trade-off between the throughput and quality of service has to be struck in the SSCH multi-carrier systems.

In our QMSDD application, the value of T_h may have an additional impact in the performance of the system. Explicitly, when we increase the subcarrier hopping period T_h, the number of consecutive detection windows with only the first symbol of the first detection window of that chain being a reference symbol is also increased. Intuitively, this would lead to a worse BER performance than when the subcarrier hopping period T_h is equal to the detection window's length N_w and hence a reference symbol is transmitted for each detection window. In Figure 4.37, we show the BER performance of our system, when we use the MAP MSDD associated with $[N_w, T_h] \in \{[8,8],[8,22],[4,4],[4,22]\}$. We may conclude that the value of T_h has an impact on the BER performance, even though the gain achieved is relatively modest and should be considered in the light of the associated system throughput reduction. Interestingly, in the case of $N_w = 4$, the performance improves, when we increase T_h in the BER$= 10^{-2} - 10^{-4}$ range, but when operating at BER$= 10^{-5}$, the performance of the two MAP MSDDs remains essentially the same.

For comparison, in Figure 4.37 we have also included the BER curves of the MAP MSDD associated with $[N_w = 7, T_h = 13]$, where each user transmits 12 288 bits per frame. The objective of this comparison is that of determining the impact of the detection window's length N_w, when contrasted to an increased interleaver length and hence a commensurately

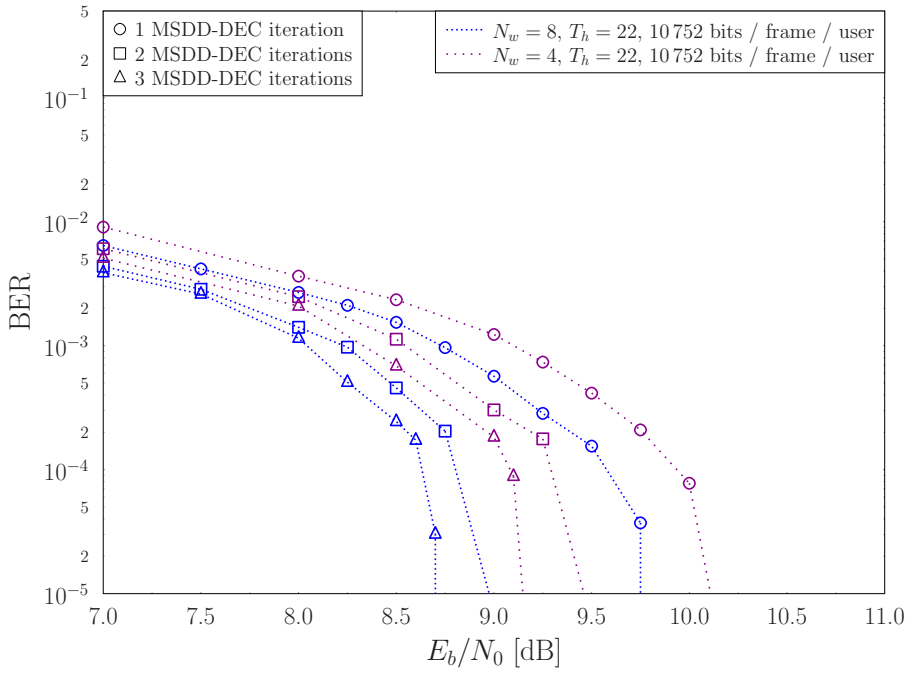

Figure 4.36: BER performance of the MAP MSDD in the DSS/SSCH SDMA-OFDM system described in Figure 4.2, using the parameters of Table 4.1 in the EPA channel of Table 4.2 for 10 752 bits per frame per user and $N_w \in \{4, 8\}$.

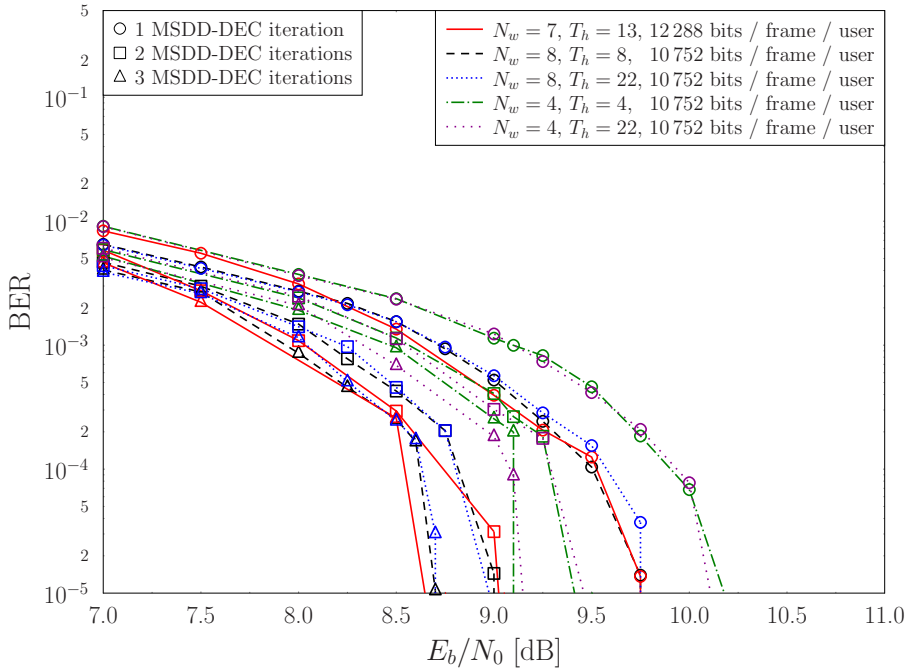

Figure 4.37: BER performance of the MAP MSDD in the DSS/SSCH SDMA-OFDM system of Figure 4.2, using the parameters of Table 4.1 in the EPA channel of Table 4.2 for 10 752 bits per frame per user and $[N_w, T_h] \in \{[8,8],[8,22],[4,4],[4,22]\}$.

Table 4.10: Computational complexity in terms of the number of CFEs / bit of the QMSDDs that use $N_w = 8$ in Figure 4.37, Figure 4.38, Figure 4.39 and Figure 4.40

MSDD / QMSDD	Number of CFEs per bit at $E_b/N_0 = 9$ dB		
	1 MSDD-DEC iteration	2 MSDD-DEC iterations	3 MSDD-DEC iterations
MAP	1170.30	1170.30	1170.30
DHA-MUA	739.82	775.47	781.79
DHA-MUA-FKT	604.95	639.17	645.11
DHA-MUA-FBKT	604.95	639.17	645.11

improved channel decoding performance. Based on Figure 4.37, the BER performance of the MAP MSDD using $[N_w = 8, T_h = 8]$ when 10 752 bits per frame per user are transmitted is equivalent to that of the MAP MSDD associated with $[N_w = 7, T_h = 13]$ when 12 288 bits per frame per user are used. Therefore, the interleavers' length and the value of the detection window's length N_w have the most substantial impact on a system, while that of the subcarrier hopping period T_h is significantly lower.

In Figure 4.38, Figure 4.39 and Figure 4.40 we present the BER performance with respect to the E_b/N_0 values of the deterministically-initialized DHA-MUA QMSDD, DHA-MUA-FKT QMSDD and DHA-MUA-FBKT QMSDD, respectively, all equipped with an iteration memory for the sake of updating the initial guess of the DHA searches. In the same figures, we have replotted the BER performance of the MAP MSDD associated with $[N_w = 8, T_h = 8]$ for comparison. As expected, the QMSDDs using $[N_w = 8, T_h = 8]$ performs

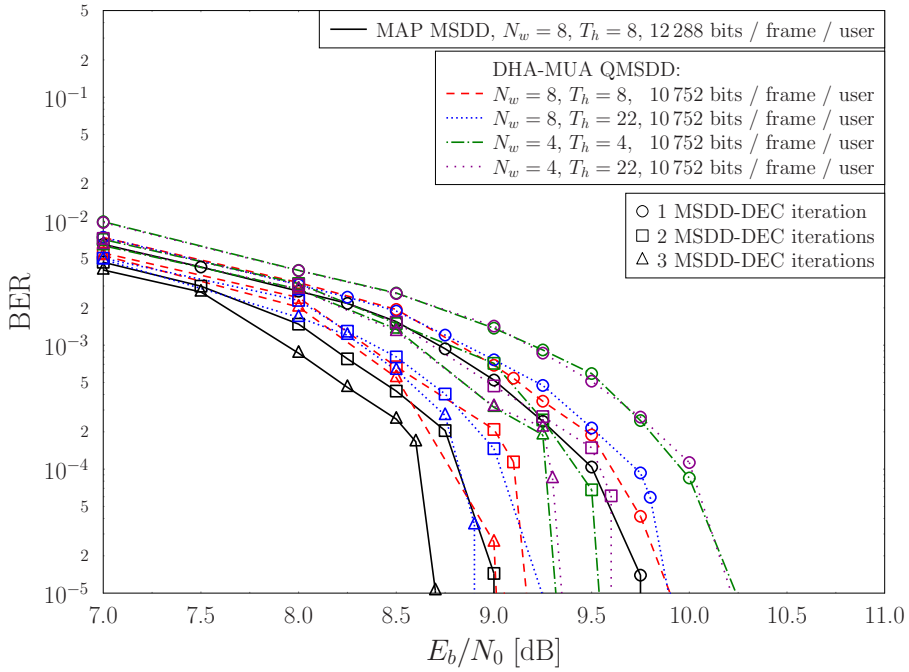

Figure 4.38: BER performance of the deterministically-initialized DHA-MUA QMSDD with iteration memory in the DSS/SSCH SDMA-OFDM system of Figure 4.2, using the parameters of Table 4.1 in the EPA channel of Table 4.2 for 10 752 bits per frame per user and $[N_w, T_h] \in \{[8,8],[8,22],[4,4],[4,22]\}$.

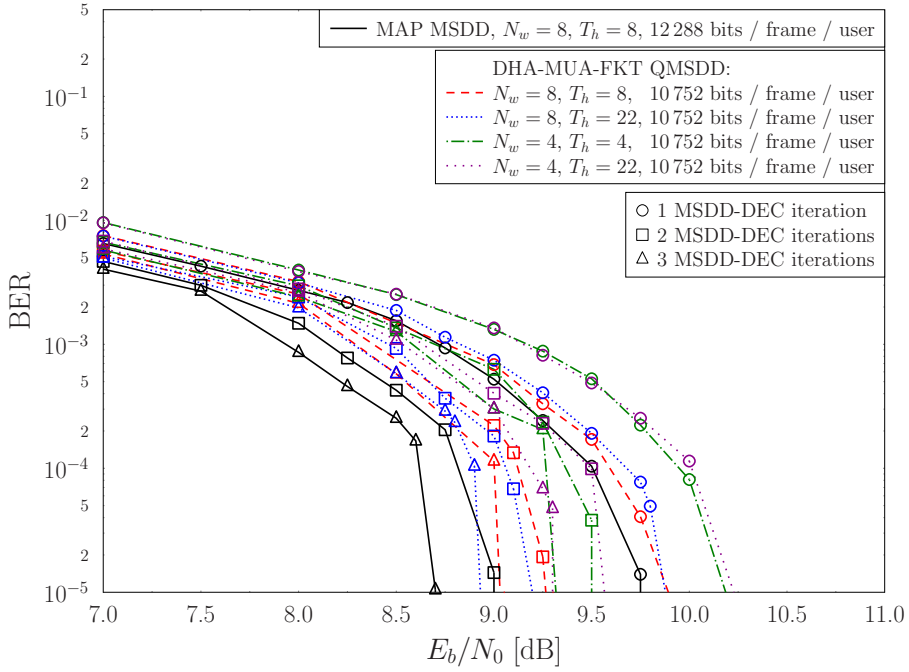

Figure 4.39: BER performance of the deterministically-initialized DHA-MUA-FKT QMSDD with iteration memory in the DSS/SSCH SDMA-OFDM system of Figure 4.2, using the parameters of Table 4.1 in the EPA channel of Table 4.2 for 10 752 bits per frame per user and $[N_w, T_h] \in \{[8,8],[8,22],[4,4],[4,22]\}$.

close to the optimal MAP MSDD. Once again, the effect of T_h is not very pronounced, since systems having the same detection window length N_w perform equally well. On the other hand, by increasing N_w we achieve an improved BER performance at the cost of a

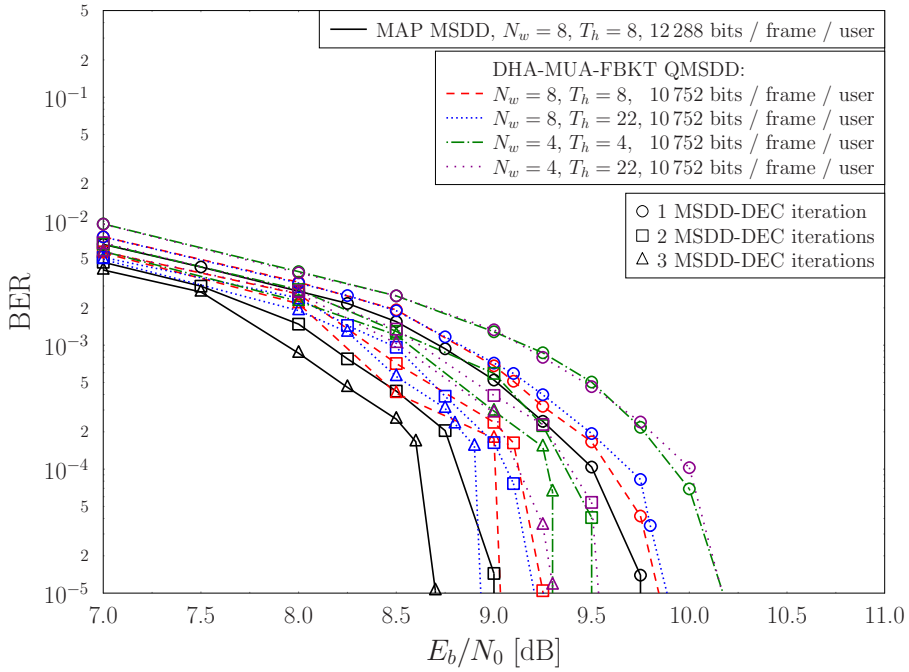

Figure 4.40: BER performance of the deterministically-initialized DHA-MUA-FBKT QMSDD with iteration memory in the DSS/SSCH SDMA-OFDM system of Figure 4.2, using the parameters of Table 4.1 in the EPA channel of Table 4.2 for 10 752 bits per frame per user and $[N_w, T_h] \in \{[8, 8], [8, 22], [4, 4], [4, 22]\}$.

concomitant increase in complexity, as stated in Table 4.10, where only the complexities of the QMSDDs that employ $N_w = 8$ are stated, since their complexity recorded for $N_w = 4$ is higher than that of the respective MAP MSDD associated with $N_w = 4$. It should be noted that the value of T_h does not affect the complexity of the QMSDD, therefore the same QMSDDs that employ $[N_w = 8, T_h = 8]$ and $[N_w = 8, T_h = 22]$ have an identical complexity in terms of the CFEs. Based on Table 4.10, the QMSDDs have lower complexities than the MAP MSDD, even after $J = 3$ MSDD-DEC iterations. A comparison between the complexities stated in Table 4.6 and Table 4.10, which characterize the same QMSDDs associated with $N_w = 7$ and $N_w = 8$, respectively, demonstrates the scaling of the QMSDDs' complexities with respect to that of the MAP MSDD. The reason for the associated slight increase of the number of CFEs per bit required in the QMSDDs when adding an extra QMSDD-DEC iteration is that due to the relatively high value of $E_b/N_0 = 9$ dB, most of the frames were successfully decoded during the previous iterations. Therefore, only the erroneously detected frames will participate in the subsequent MSDD-DEC iteration. When the value of E_b/N_0 is lower, the complexity of the QMSDDs seen in Table 4.10 becomes higher, while that of the MAP MSDD will remain the same. However, since typically it is required for the systems to operate at BER $= 10^{-5}$ or even lower, the choice of $E_b/N_0 = 9$ dB satisfies the QMSDDs associated with $J = 3$ QMSDD-DEC iterations.

4.9 Conclusions

In this chapter we answered a number of design dilemmas. More explicitly, we argued in favour of the family of non-coherent receivers, which do not require channel estimates, in contrast to their higher-complexity coherent receiver counterparts, which rely on the accuracy of the channel estimation. Therefore, the complexity of the non-coherent receivers is lower, but their BER performance is degraded, when compared to that of a coherent receiver provided with perfect channel estimates. Furthermore, we showed that the MSDD performs better than the CDD, by performing detection over an extended window of several symbols. Based on the complexity reduction achieved by the quantum algorithms over their classical counterparts, we opted for exploiting them in the context of MSDD in non-coherent receivers, whilst achieving a near-optimal performance at a reduced complexity.

We introduced a number of quantum-assisted multi-symbol differential detectors. More specifically, we investigated the HIHO DHA QMSDD and ES-DHA QMSDD in Section 4.4.2 and Section 4.4.3, respectively, as well as the SO DHA-MAA QMSDD and DHA-MAA-NE QMSDD in Section 4.5.2. Furthermore, we presented the SISO DHA-MUA QMSDD, DHA-MUA-FKT QMSDD, DHA-MUA-FBKT QMSDD in Section 4.5.3 and the DHA-aided QWSA QMSDD in Section 4.5.4.

In Figure 4.7 we showed that the DHA QMSDD offers an equivalent performance to the ML MSDD, while requiring fewer CFEs per bit. The ES-DHA QMSDD provides a tunable performance based on the affordable complexity budget, as demonstrated in Figure 4.9. We showed in Figure 4.10 and Figure 4.14 that the DHA-MAA and the DHA-MAA-NE QMSDDs are unsuitable for integration with iterative receivers, but they provide a near-optimal performance at a low complexity during the first MSDD-DEC iteration. The family of DHA-MUA QMSDDs may be used in a receiver, as presented in Figure 4.21, where iterations are carried out between the MSDD and the DEC, hence achieving a BER performance, which is less than 1 dB away from that of the optimal MAP MSDD's performance, as depicted in Figure 4.17. Figure 4.41 depicts the performance of the best SISO and HIHO QMSDDs with respect to the classic optimal SISO MAP MSDD and HIHO ML MSDD, for the parameters summarized in Table 4.1 and for the EPA channel of Table 4.2.

Moreover, in Section 4.6 we proposed a methodology for deterministically initializing the DHA searches of the QMSDDs, by employing the CDD, while waiting for the signals that participate in a detection window to arrive and hence acquiring an early estimate of the optimal symbol. In the scenarios, when the CDD estimate turns out to be the same as the MSDD's estimate, or close to it in terms of its Hamming distance, the complexity reduction achieved is higher. As seen in Figure 4.32 and Table 4.8, the impact of the CDD initialization on the complexity is more apparent in the HIHO DHA and ES-DHA QMSDDs, where the objective is to simply find the globally optimal multi-level symbol. Table 4.11 summarizes both the performance and the complexity of the HIHO QMSDDs designed for the DSS/SSCH SDMA-OFDM system of Table 4.1 and the EPA channel of Table 4.2. We may note that the CDD-initialized DHA QMSDD performs better than the Randomly-initialized ES-DHA QMSDD operating at the 99% point of its CDF of Figure 4.8,

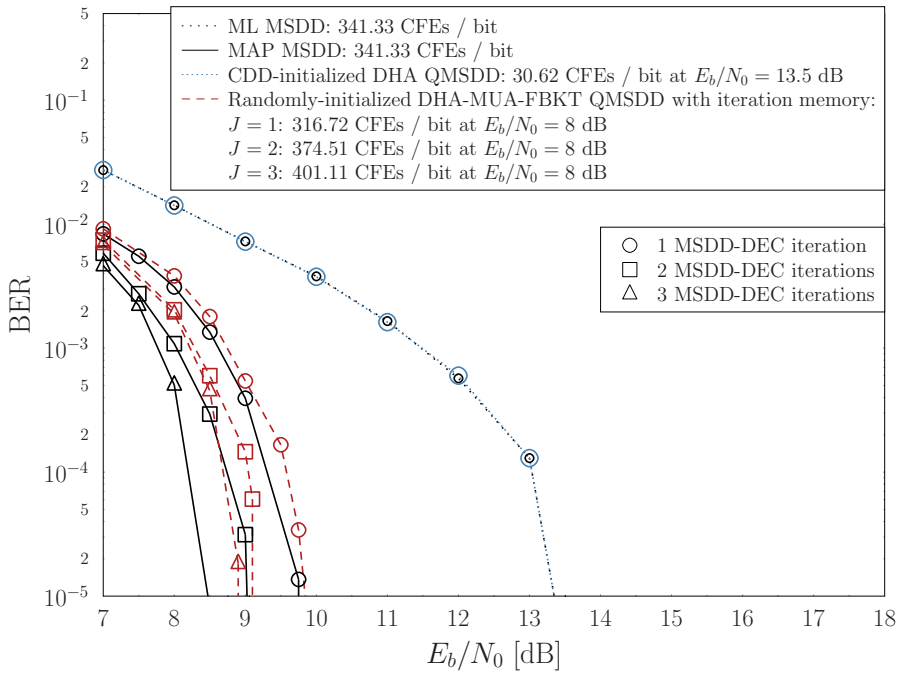

Figure 4.41: BER performance of the deterministically-initialized SISO DHA-MUA-FBKT and HIHO DHA QMSDDs in the DSS/SSCH SDMA-OFDM system of Figure 4.2, using the parameters of Table 4.1 in the EPA channel of Table 4.2.

Table 4.11: Summary of the presented HIHO QMSDDs for the DSS/SSCH SDMA-OFDM system of Table 4.1 in the EPA channel of Table 4.2

MSDD	Complexity (CFEs / bit)	% complexity of the ML MSDD	E_b/N_0 (dB)	E_b/N_0 difference from the ML MSDD (dB)	BER Figure
Random-i ES-DHA (50% CDF)	16.75	4.9%	18	4.65	4.9
Random-i ES-DHA (80% CDF)	24.33	7.2%	14.46	1.11	4.9
CDD-i DHA	30.62	9%	13.35	0	4.33
Random-i ES-DHA (99% CDF)	37.9	11.1%	13.35	0	4.9
Random-i DHA	43.6	12.8%	13.35	0	4.9, 4.33
ML	341.33	100%	13.35	0	4.9, 4.33

while requiring fewer CFEs per bit. In the case of the SISO DHA-based QMSDDs, the CDD-initialized QMSDDs require approximately the same complexity as the randomly-initialized QMSDDs, due to their more complex methodology. For this reason, we proposed the *iteration memory* concept of Section 4.6.2 for the SISO QMSDDs, where the globally optimal symbol found during a single MSDD-DEC iteration is used for initializing the DHA searches of the next MSDD-DEC iteration, hence further reducing the complexity.

Table 4.12: Summary of the presented QMSDDs for the DSS/SSCH SDMA-OFDM system of Table 4.1 in the EPA channel of Table 4.2 at BER = 10^{-5}

MSDD	MSDD-DEC iterations	Complexity (CFEs / bit)	% complexity of the MAP MSDD	E_b/N_0 (dB)	E_b/N_0 difference from the MAP MSDD (dB)	BER Figure
Random-i DHA-MAA	1	43.7	12.8%	10.75	1	4.10
	2	44.13	12.9%	10.5	1.48	
	3	44.57	13.1%	10.5	2.03	
Random-i DHA-MAA-NE	1	44.62	13.1%	10.71	0.96	4.10
	2	45.95	13.5%	10.5	1.48	
	3	46.26	13.6%	10.5	2.03	
CDD-i DHA-MUA	1	384.29	112.6%	9.855	0.105	4.17
	2	455.13	133.3%	9.1	0.08	
	3	487.74	142.9%	9	0.53	
Random-i DHA-MUA-FKT iteration memory	1	316.72	92.8%	9.845	0.095	4.34
	2	373.07	109.3%	9.1	0.08	
	3	398.86	116.9%	8.95	0.48	
Random-i DHA-MUA-FBKT	1	316.72	92.8%	9.84	0.09	4.17
	2	374.51	109.72%	9.1	0.08	
	3	401.11	117.51%	8.9	0.43	
DHA-QWSA	1	8235.71	2412.8%	10.3	0.55	4.25
	2	10100.34	2959.1%	9.4	0.38	
	3	10919.02	3199%	9.1	0.63	
MAP	1	341.33	100%	9.75	0	4.10, 4.17, 4.25
	2	341.33	100%	9.02	0	
	3	341.33	100%	8.47	0	

A summary of the SISO QMSDDs that were employed in the DSS/SSCH SDMA-OFDM system of Figure 4.2, using the parameters of Table 4.1 in the EPA channel of Table 4.2 is given in Table 4.12.

Furthermore, motivated by our quest for low-complexity QMSDDs, we proposed the reuse of the symbol set created by the SISO DHA-based QMSDDs during a single QMSDD-DEC iteration in $(IpS-1)$ of the subsequent QMSDD-DEC iterations, hence reducing the complexity, since the QMSDD was not employed in those iterations. We found that the system performance associated with $IpS > 1$ was close to that of the scenario, where the QMSDD is employed during every QMSDD-DEC iteration, albeit the corresponding complexity was lower for $IpS > 1$.

Finally, in Figure 4.37, Figure 4.38, Figure 4.39 and Figure 4.40 we investigated the effect of the detection window length N_w, of the subcarrier-hopping period T_h and of the

interleaver length on the system's performance. The parameters having the highest impact were the interleaver length and the detection window length N_w, with the subcarrier-hopping period T_h having a much lower effect on the system's BER.

Chapter 5

Conclusions and Future Work

Based on quantum computing, in this treatise we have proposed a number of optimal and near-optimal hard-input hard-output (HIHO), as well as soft-input soft-output (SISO) quantum-assisted multi-user detectors (QMUD) for coherent receivers and quantum-assisted multiple symbol differential detectors (QMSDD) conceived for non-coherent receivers. We have demonstrated that the performance of the HIHO quantum-assisted detectors used in DS-CDMA and SDMA communication systems matches that of the ML detectors, despite its substantial computational complexity reduction. Similarly, the SISO quantum-assisted detectors were employed in both DSS/SSCH SDMA-OFDM and MC-IDMA communication systems and were shown to provide a performance equivalent to that of the optimal Maximum *A posteriori* Probability (MAP) detector. Most of the proposed quantum-assisted detectors rely on the Dürr-Høyer algorithm (DHA). The DHA performs a search in an N-element, unsorted database and succeeds to find the specific index that corresponds to the minimum entry of the database after $O(\sqrt{N})$ queries to the database, while the optimal, serial search requires $O(N)$ queries.

The novel fixed-complexity early-stopping-aided DHA based multiple-symbol detector [2] of Section 2.4.4 succeeds in performing similarly to the optimal ML MUD in Chapter 2, while having a reduced complexity with respect to the optimal DHA QMUD [2] of Section 2.4.3. The ES-aided DHA QMUD of Section 2.4.4 is also tunable in terms of its complexity, albeit at a sub-optimal performance. The ES-aided DHA QMUD relies on the pre-computed CDF curves of the optimal DHA QMUD and exploits their statistics in order to predict the probability of succeeding in estimating the transmitted multi-level symbols.

Additionally, in Chapter 3 we have conceived a quantum algorithm termed as the quantum weighted sum algorithm (QWSA) [1], which is based on the quantum mean algorithm presented in [62]. By using the QWSA of Section 3.4 in combination with the DHA of Section 2.4.3 we were able to formulate a soft-input soft-output quantum-assisted multiple-symbol detector [1], which may be integrated with receivers for performing iterative detection with at least a quadratic reduction in the computational complexity of the MAP detector.

The DHA was also used for the provision of soft bit-based log likelihood ratios (LLR), which are required for performing iterative detection at the receiver. Iterative detection was achieved by employing the ES-DHA QMUD once for the numerator and once for the denominator of each bit of the multi-level symbol for computing the bit-based LLRs. More specifically, by using the maximum approximation (MAA) [13] and the multi-input approximation (MUA) [63], the DHA-MAA detector of Section 3.5.1 and the DHA-MUA SISO detector of Section 3.5.2 were created [3]. It was shown that the DHA-MUA detector performs better than the DHA-MAA detector, even though it has a higher complexity. The performance of the DHA-MUA detector of Section 3.5.2 was demonstrated to be closer to that of the MAP detector than to that of the DHA-QWSA detector of Section 3.4.5, while having a lower complexity than both the MAP detector and the DHA-QWSA detector, always with respect to the number of cost function evaluations. The DHA-MAA detector of Section 3.5.1 was found to be more suitable for soft-output detection, rather than iterative detection. In Section 3.7 the soft-output detectors were also compared to the soft-output ant colony optimization (ACO) detectors of Section 3.6 proposed in [13, 63].

By using the output of a conventional detector, such as the MF or MMSE detector, as the initial guesses for the minimum entry in the DHA search, we were able to further reduce the complexity. This may not be the case in highly rank-deficient systems, where the conventional detector's performance is so poor that it may be considered random. Furthermore, the neighbour exploitation (NE) modification of Section 3.5.1.1 was proposed for the soft DHA detectors. By using the neighbour exploitation modification, we may achieve an improved BER performance at essentially the same complexity.

The forward knowledge transfer (FKT) methodology of Section 3.5.2.2 and the forward and backward knowledge transfer (FBKT) methodology of Section 3.5.2.3 were also investigated and applied to the DHA-MUA detectors of Section 3.5.2. It was shown that by exploiting knowledge about the cost function values to be transferred between a multi-level symbol's bits we are able to greatly improve the performance, while reducing the complexity imposed.

The iterative detection capabilities of the proposed quantum-assisted detectors were evaluated in Section 3.9 with the aid of Gaussian extrinsic information transfer (EXIT) charts [21], as well as non-Gaussian EXIT charts [144]. The mutual information in the non-Gaussian EXIT charts was created by exploiting a number of auxiliary decoding iterations prior to the main decoding iteration. By using non-Gaussian EXIT charts we may visualise the actual nature of the detection and decoding algorithms employed and their true capabilities when employed in iterative receivers. However, the Gaussian EXIT charts are less complex to create and they have similar results to the non-Gaussian EXIT charts, when the decoding components are suitable for iterative detection.

The non-coherent systems of Chapter 4 were shown to have a degraded performance with respect to the coherent systems, but they do not require any knowledge about the channel states. In future wireless communications, where lastge-scale MIMO and mm-Wave systems are expected to be the norm, the estimation of hundreds of channel states may become unrealistic, due to the high complexity required for channel estimation. The HIHO

and SISO quantum-assisted detectors were also applied in non-coherent receivers, achieving a near-optimal performance.

Apart from the challenges of near-optimal non-coherent detection at a low complexity, there is a number of open problems in wireless systems that may be efficiently tackled by quantum computing and quantum search algorithms. Our future work will be focused on:

1. Creating a joint quantum MUD and decoder, by incorporating the forward error correction metric into the multiple-stream detection metric.

2. Moreover, quantum-assisted turbo synchronization and channel estimation may prove less complex than the existing algorithms, while the Minimum BER (MBER) criterion may be adopted for performing quantum-assisted turbo synchronization, channel estimation and detection [175, 176].

3. A study, which benchmarks the quantum-assisted solutions against the best known bio-inspired algorithms [11, 21, 23, 177, 178] may also prove beneficial.

4. Quantum search algorithms may also be used in the context of network coding [179, 180].

5. Furthermore, the quantum search algorithms employed in this treatise are assumed to operate in an error-free environment. In practice, based on the imperfections of the materials that will be used to create the quantum gates, the qubits may have a non-zero probability of changing their states [43, 44], leading to undesirable search outcomes. Modelling the effects of specific materials as a quantum channel, we may be able to use quantum error correction codes [67, 181] for stabilizing the quantum states in the quantum circuits.

6. The proposed quantum-assisted detectors may be employed in visible light communication systems, providing a better detection performance than the state-of-art iterative, parallel interference cancellation detectors [182, 183].

7. Quantum-assisted solutions may also be used in mm-Wave systems [17] for achieving low-complexity search and detection.

8. The consideration of SDMA scenarios where each user is assigned a Relay Node (RN) for conveying to the BS the information of the primary user. In a scenario where each user cooperates with a unique RN, the size of the transmitters is doubled and hence low-complexity MUDs such as our proposed QMUDs are required.

9. The cooperative scenario may be extended to a multi-cell system where the BSs are linked by optical fibre allowing them to cooperate [184]. Once again, low-complexity QMUDs may be employed for operating at the ML MUD's limit.

List of Abbreviations

ACO	Ant Colony Optimization
ACS	Add-Compare-Select
AE	Antenna Element
APP	*A Posteriori* Probability
AWGN	Additive White Gaussian-distributed Noise
BBHT	Boyer-Brassard-Høyer-Tapp
BER	Bit Error Ratio
BICM	Bit-Interleaved Coded Modulation
BPSK	Binary Phase Shift Keying
BS	Base Station
CC	Convolutional Code
CDD	Conventional Differential Detector
CDF	Cumulative Density Function
CF	Cost Function
CFE	Cost Function Evaluation
CIR	Channel Impulse Response
COMP	Cooperative Multi-cell Processing
CP	Cyclic Prefix
CSI	Channel State Information
DEC	Decoder
DFDD	Decision-Feedback Differential Detectors

DHA	Dürr-Høyer Algorithm
DPSK	Differential Phase Shift Keying
DS-CDMA	Direct-Sequence Code Division Multiple Access
DSS	Direct Sequence Spreading
EPR	Einstein-Podolsky-Rosen
ES	Early Stopping
ETU	Extended Typical Urban
EVA	Extended Vehicular A
EXIT	Extrinsic Information Transfer
FBKT	Forward and Backward Knowledge Transfer
FCSD	Fixed-Complexity Sphere Decoder
FD	Frequency Domain
FD-CHTF	Frequency-Domain Channel Transfer Function
FFT	Fast Fourier Transform
FKT	Forward Knowledge Transfer
FW	Free Will
GA	Genetic Algorithm
HIHO	Hard-Input Hard-Output
HIHO	Hard-Input Hard-Output
HISO	Hard-Input Soft-Output
ID	Iterative Detection
IDMA	Interleave Division Multiple Access
IFFT	Inverse Fast Fourier Transform
IpS	Iterations per Search
IQFT	Inverse Quantum Fourier Transform
LBER	Least Bit Error Ratio
LLR	Log-Likelihood Ratio
LTE	Long Term Evolution

MAA	MAximum Approximation
MAP	Maximum *A Posteriori* Probability
MBER	Minimum Bit Error Ratio
MBER	Minimum Bit Error Ratio
MC	Multi-Carrier
MC-CDMA	Multi-Carrier Code Division Multiple Access
MC-IDMA	Multi-Carrier Interleave Division Multiple Access
MF	Matched Filter
MFAA	Multi-Functional Antenna Array
MIMO	Multiple-Input Multiple-Output
ML	Maximum Likelihood
ML	Maximum Likelihood
MMSE	Minimum Mean Square Error
MSDD	Multiple Symbol Differential Detector
MSDSD	Multiple Symbol Differential Sphere Detector
MSE	Mean Square Error
MU	Multi-User
MUA	MUlti-input Approximation
MUD	Multi-User Detection
MUD	Multi-User Detection
MUI	Multi-User Interference
NE	Neighbour Exploitation
NE	Neighbour Exploitation
NSCC	Non-Systematic Convolutional Code
OFDM	Orthogonal Frequency-Division Multiplexing
PDF	Probability Density Function
PEA	Phase Estimation Algorithm
PSAM	Pilot Symbol Assisted Modulation

PSO	Particle Swarm Optimization
QAA	Quantum Amplitude Amplification
QAE	Quantum Amplitude Estimation
QAM	Quadrature Amplitude Modulation
QBSC	Quantum Bit String Comparator
QCA	Quantum Counting Algorithm
QCR	Quantum Control Register
QD	Quantum Domain
QET	Quantum Existence Testing
QFT	Quantum Fourier Transform
QGOA	Quantum Genetic Optimization Algorithm
QIR	Quantum Index Register
QMA	Quantum Mean Algorithm
QMSDD	Quantum-assisted Multiple Symbol Differential Detector
QMUD	Quantum Multi-User Detection
QoS	Quality of Service
QR	Quantum Register
QSA	Quantum Search Algorithm
QWSA	Quantum Weighted Sum Algorithm
RN	Relay Node
RSSCH	Random Slow Subcarrier Hopping
SDM	Space Division Multiplexing
SDMA	Spatial Division Multiple Access
SF	Spreading Factor
SFH	Slow Frequency Hopping
SISO	Soft-Input Soft-Output
SM	Spatial Multiplexing
SNR	Signal to Noise Ratio

SO	Soft-Output
SSCH	Slow Subcarrier Hopping
TCC	Turbo Convolutional Code
TD	Time Domain
USSCH	Uniform Slow SubCarrier Hopping
UWB	Ultra-Wide Band
WH	Walsh-Hadamard
ZF	Zero Forcing

Bibliography

[1] Botsinis, P. and Ng, S.X. and Hanzo, L., "Quantum Search Algorithms, Quantum Wireless, and a Low-Complexity Maximum Likelihood Iterative Quantum Multi-User Detector Design," *IEEE Access*, vol. 1, pp. 94–122, 2013.

[2] Botsinis, P., Ng, S.X. and Hanzo, L., "Fixed-Complexity Quantum-Assisted Multi-User Detection for CDMA and SDMA," *IEEE Transactions on Communications*, vol. 62, pp. 990–1000, March 2014.

[3] Botsinis, P. and Alanis, D. and Ng, S.X. and Hanzo, L., "Low-Complexity Soft-Output Quantum-Assisted Multiuser Detection for Direct-Sequence Spreading and Slow Subcarrier-Hopping Aided SDMA-OFDM Systems," *IEEE Access*, vol. 2, pp. 451–472, May 2014.

[4] Botsinis, P. and Soon Xin Ng and Hanzo, L., "Low-Complexity Iterative Quantum Multi-User Detection in SDMA Systems," in *IEEE International Conference on Communications*, pp. 5592–5597, June 2014.

[5] P. Botsinis, D. Alanis, Z. Babar, S.X. Ng, and L. Hanzo, "Iterative Quantum-Assisted Multi-User Detection for Multi-Carrier Interleave Division Multiple Access Systems," *IEEE Transactions on Communications*, vol. pp, p. pp, 2015.

[6] P. Botsinis, D. Alanis, Z. Babar, S.X. Ng, and L. Hanzo, "Non-Coherent Quantum Multiple Symbol Differential Detection for Wireless Systems," *IEEE Access*, vol. pp, p. pp, 2015.

[7] Hanzo, L. and El-Hajjar, M. and Alamri, O., "Near-Capacity Wireless Transceivers and Cooperative Communications in the MIMO Era: Evolution of Standards, Waveform Design, and Future Perspectives," *Proceedings of the IEEE*, vol. 99, no. 8, pp. 1343 – 1385, 2011.

[8] Hanzo, L. and Haas, H. and Imre, S. and O'Brien, D. and Rupp, M. and Gyongyosi, L., "Wireless Myths, Realities, and Futures: From 3G/4G to Optical and Quantum Wireless," *Proceedings of the IEEE*, vol. 100, pp. 1853–1888, 13 2012.

[9] Hanzo, L. and Alamri, O. and El-Hajjar, M. and Wu, N., *Near-Capacity Multi-Functional MIMO Systems: Sphere-Packing, Iterative Detection and Cooperation.* Chichester, UK: John Wiley & Sons, IEEE Press, May 2009.

[10] Lajos Hanzo and T. H. Liew and Bee Yeap and R. Y. S. Tee and S. X. Ng, *Turbo Coding, Turbo Equalisation and Space-Time Coding: EXIT-Chart Aided Near-Capacity Designs for Wireless Channels.* John Wiley & Sons, 2010.

[11] Lajos Hanzo and Lie-Liang Yang and E-L. Kuan and K. Yen, *Single and Multi-Carrier DS-CDMA: Multi-User Detection, Space-Time Spreading, Synchronisation, Networking, and Standards.* John Wiley & Sons, 2003.

[12] Zemen, T. and Mecklenbrauker, C.F. and Wehinger, J. and Muller, R.R., "Iterative Joint Time-Variant Channel Estimation and Multi-User Detection for MC-CDMA," *IEEE Transactions on Wireless Communications*, vol. 5, pp. 1469–1478, June 2006.

[13] Chong Xu and Bin Hu and Lie-Liang Yang and Hanzo, L., "Ant-Colony-Based Multiuser Detection for Multifunctional-Antenna-Array-Assisted MC DS-CDMA Systems," *IEEE Transactions on Vehicular Technology*, vol. 57, pp. 658–663, January 2008.

[14] Sheng Chen and Hanzo, L. and Livingstone, A., "MBER Space-Time Decision Feedback Equalization Assisted Multiuser Detection for Multiple Antenna Aided SDMA Systems," *IEEE Transactions on Signal Processing*, vol. 54, no. 8, pp. 3090–3098, 2006.

[15] C.Y. Wei and J. Akhtman and S.X. Ng and L. Hanzo, "Iterative Near-Maximum-Likelihood Detection in Rank-Deficient Downlink SDMA Systems," *IEEE Transactions on Vehicular Technology*, vol. 57, pp. 653–657, January 2008.

[16] Chun-Yi Wei and Li Wang and Hanzo, L., "Iterative Irregular Sphere Detection in High-Rate Downlink SDMA Systems," *IEEE Transactions on Vehicular Technology*, vol. 58, no. 7, pp. 3855–3861, 2009.

[17] Rappaport, T.S. and Shu Sun and Mayzus, R. and Hang Zhao and Azar, Y. and Wang, K. and Wong, G.N. and Schulz, J.K. and Samimi, M. and Gutierrez, F., "Millimeter Wave Mobile Communications for 5G Cellular: It Will Work!," *IEEE Access*, vol. 1, pp. 335–349, 2013.

[18] Li Ping and Lihai Liu and Keying Wu and Leung, W. K., "Interleave Division Multiple-Access," *IEEE Transactions on Wireless Communications*, vol. 5, pp. 938–947, April 2006.

[19] Rong Zhang and Lajos Hanzo, "Three Design Aspects of Multicarrier Interleave Division Multiple Access," *IEEE Transactions on Vehicular Technology*, vol. 57, pp. 3607–3617, November 2008.

[20] Rong Zhang and Lei Xu and Sheng Chen and Hanzo, L., "EXIT-Chart-Aided Hybrid Multiuser Detector for Multicarrier Interleave-Division Multiple Access," *IEEE Transactions on Vehicular Technology*, vol. 59, pp. 1563–1567, March 2010.

[21] Lajos Hanzo and Yosef Akhtman and Ming Jiang and Li Wang, *MIMO-OFDM for LTE, WIFI and WIMAX: Coherent versus Non-Coherent and Cooperative Turbo-Transceivers*. John Wiley & Sons, 2010.

[22] Ye Li and Winters, J.H. and Sollenberger, N.R., "MIMO-OFDM for Wireless Communications: Signal Detection with Enhanced Channel Estimation," *IEEE Transactions on Communications*, vol. 50, no. 9, pp. 1471–1477, 2002.

[23] Ming Jiang and Hanzo, L., "Multiuser MIMO-OFDM for Next-Generation Wireless Systems," *Proceedings of the IEEE*, vol. 95, no. 7, pp. 1430–1469, 2007.

[24] Botella, C. and Pinero, G. and Gonzalez, A. and De Diego, M., "Coordination in a Multi-Cell Multi-Antenna Multi-User W-CDMA System: A Beamforming Approach," *IEEE Transactions on Wireless Communications*, vol. 7, no. 11, pp. 4479–4485, 2008.

[25] Pischella, M. and Belfiore, J. -C, "Distributed Resource Allocation for Rate-Constrained Users in Multi-Cell OFDMA Networks," *Communications Letters, IEEE*, vol. 12, no. 4, pp. 250–252, 2008.

[26] Chunyuan Liu and Chungui Liu and Yonghong Hou and Han Zhou, "Power Allocation of Multi-Users Based on Optimal Power Allocation Algorithm in Uplink Base Stations Cooperative System," in *7th International Conference on Wireless Communications, Networking and Mobile Computing (WiCOM)*, pp. 1–5, 2011.

[27] Jeong Gon Kim and Won Seok Choi, "Joint ZF and Partial ML Detection for Uplink Cellular Base Station Cooperation," in *International Conference on ICT Convergence (ICTC)*, pp. 321–326, 2011.

[28] Sugiura, S. and Sheng Chen and Hanzo, L., "Coherent and Differential Space-Time Shift Keying: A Dispersion Matrix Approach," *IEEE Transactions on Communications*, vol. 58, pp. 3219–3230, November 2010.

[29] Li Wang and Li Li and Chao Xu and Dandan Liang and Soon Xin Ng and Hanzo, L., "Multiple-Symbol Joint Signal Processing for Differentially Encoded Single- and Multi-Carrier Communications: Principles, Designs and Applications," *IEEE Communications Surveys Tutorials*, vol. 16, pp. 689–712, February 2014.

[30] Alanis, D. and Botsinis, P. and Soon Xin Ng and Hanzo, L., "Quantum-Assisted Routing Optimization for Self-Organizing Networks," *IEEE Access*, vol. 2, pp. 614–632, June 2014.

[31] Yong Yuan and Zhihai He and Min Chen, "Virtual MIMO-Based Cross-Layer Design for Wireless Sensor Networks," *IEEE Transactions on Vehicular Technology*, vol. 55, no. 3, pp. 856–864, 2006.

[32] Hui Wang and Yuhang Yang and Maode Ma and Jianhua He and Xiaomin Wang, "Network Lifetime Maximization with Cross-Layer Design in Wireless Sensor Networks," *IEEE Transactions on Wireless Communications*, vol. 7, no. 10, pp. 3759–3768, 2008.

[33] Hui Wang and Agoulmine, N. and Maode Ma and Yanliang Jin, "Network Lifetime Optimization in Wireless Sensor Networks," *IEEE Journal on Selected Areas in Communications*, vol. 28, no. 7, pp. 1127–1137, 2010.

[34] Shirazi, G. and Lampe, L., "Lifetime Maximization in UWB Sensor Networks for Event Detection," *IEEE Transactions on Signal Processing*, vol. 59, no. 9, pp. 4411–4423, 2011.

[35] Ying Lin and Jun Zhang and Chung, H.S.-H. and Wai Hung Ip and Yun Li and Yu-hui Shi, "An Ant Colony Optimization Approach for Maximizing the Lifetime of Heterogeneous Wireless Sensor Networks," *IEEE Transactions on Systems, Man, and Cybernetics, Part C: Applications and Reviews*, vol. 42, no. 3, pp. 408–420, 2012.

[36] Zukang Shen and Andrews, J.G. and Evans, B.L., "Adaptive Resource Allocation in Multiuser OFDM Systems with Proportional Rate Constraints," *IEEE Transactions on Wireless Communications*, vol. 4, no. 6, pp. 2726–2737, 2005.

[37] Jianwei Huang and Subramanian, V.G. and Agrawal, R. and Berry, R., "Joint Scheduling and Resource Allocation in Uplink OFDM Systems for Broadband Wireless Access Networks," *IEEE Journal on Selected Areas in Communications*, vol. 27, no. 2, pp. 226–234, 2009.

[38] Lan Zhang and Ying-Chang Liang and Yan Xin, "Joint Beamforming and Power Allocation for Multiple Access Channels in Cognitive Radio Networks," *IEEE Journal on Selected Areas in Communications*, vol. 26, no. 1, pp. 38–51, 2008.

[39] Ngo, D.T. and Tellambura, C. and Nguyen, H.H., "Resource Allocation for OFDMA-Based Cognitive Radio Multicast Networks With Primary User Activity Consideration," *IEEE Transactions on Vehicular Technology*, vol. 59, no. 4, pp. 1668–1679, 2010.

[40] Zhang, P. and Chen, S. and Hanzo, L., "Differential Space-Time Shift Keying Aided Successive Relaying Assisted Cooperative Multi-User CDMA," *IEEE Transactions on Vehicular Technology*, vol. 62, pp. 2156–2169, June 2013.

[41] Shinya Sugiura and Sheng Chen and Lajos Hanzo, "MIMO-Aided Near-Capacity Turbo Transceivers: Taxonomy and Performance Versus Complexity," *IEEE Communications Surveys & Tutorials*, vol. 14, pp. 421–442, May 2012.

[42] Hoydis, J. and ten Brink, S. and Debbah, M., "Massive MIMO in the UL/DL of Cellular Networks: How Many Antennas Do We Need?," *IEEE Journal on Selected Areas in Communications*, vol. 31, no. 2, pp. 160–171, 2013.

[43] Nielsen, M. A. and I. L. Chuang, *Quantum Computation and Quantum Information*. Cambridge University Press, 2000.

[44] Sándor Imre and Ferenc Balázs, *Quantum Computing and Communications: An Engineering Approach*. John Wiley & Sons, 2005.

[45] Marinescu, Dan C., *Classical and Quantum Information*. Academic Press, 1st ed., 2011.

[46] Sándor Imre and Laszlo Gyongyosi, *Advanced Quantum Communications: An Engineering Approach*. John Wiley & Sons, 2013.

[47] S. Barz, J. F. Fitzsimons, E. Kashefi, P. Walther, "Experimental Verification of Quantum Computation," *Nature Physics*, vol. 9, pp. 727–731, November 2013.

[48] G. Brassard, P. Høyer, M. Mosca, A. Tapp , "Quantum Amplitude Amplification and Estimation," *eprint arXiv:quant-ph/0005055*, May 2000.

[49] L. K. Grover, "A Fast Quantum Mechanical Algorithm for Database Search," *Proceedings, 28th Annual ACM Symposium on the Theory of Computing*, pp. 212–219, May 1996.

[50] Grover, Lov K., "Quantum Mechanics Helps in Searching for a Needle in a Haystack," *Physical Review Letters*, vol. 79, pp. 325–328, July 1997.

[51] Boyer, Michel and Brassard, Gilles and Høyer, Peter and Tapp, Alain, "Tight Bounds on Quantum Searching," *Fortschritte der Physik*, vol. 46, pp. 493–506, 1998.

[52] C. Durr, P. Høyer, "A Quantum Algorithm for Finding the Minimum," *eprint arXiv:quant-ph/9607014*, July 1996.

[53] P. W. Shor, "Scheme for reducing Decoherence in Quantum Computer Memory," *Physical Review A*, vol. 52, no. 4, pp. 2493–2496, 1995.

[54] Calderbank, A.R. and Rains, E.M. and Shor, P.M. and Sloane, N.J.A., "Quantum Error Correction via Codes over GF(4)," *IEEE Transactions on Information Theory*, vol. 44, pp. 1369–1387, July 1998.

[55] Hughes, Richard and Nordholt, Jane, "Refining Quantum Cryptography," *Science*, vol. 333, no. 6049, pp. 1584–1586, 2011.

[56] Razavi, M., "Multiple-Access Quantum Key Distribution Networks," *IEEE Transactions on Communications*, vol. 60, pp. 3071–3079, October 2012.

[57] Imre, S. and Balázs, F., "Non-Coherent Multi-user Detection Based on Quantum Search," in *IEEE International Conference on Communications*, vol. 1, pp. 283–287, 2002.

[58] Imre, S. and Balazs, F., "Performance Evaluation of Quantum based Multi-User Detector," in *IEEE Seventh International Symposium on Spread Spectrum Techniques and Applications*, vol. 3, pp. 722–725, 2002.

[59] G. Brassard, P. Høyer, A. Tapp, "Quantum Counting," *eprint arXiv:quant-ph/9805082*, May 1998.

[60] R. Cleve, A. Ekert, C. Macchiavello, M. Mosca, "Quantum Algorithms Revisited," *Royal Society of London Proceedings Series A*, vol. 454, pp. 339–357, January 1998.

[61] X.-Q. Zhou, P. Kalasuwan, T. C. Ralph, J. L. O'Brien, "Calculating Unknown Eigenvalues with a Quantum Algorithm," *Nature Photonics*, vol. 7, pp. 223–228, March 2013.

[62] G. Brassard, F. Dupuis, S. Gambs, A. Tapp, "An Optimal Quantum Algorithm to Approximate the Mean and its Application for Approximating the Median of a Set of Points Over an Arbitrary Distance," *eprint arXiv:quant-ph/1106.4267v1*, June 2011.

[63] Chong Xu and Maunder, R.G. and Lie-Liang Yang and Hanzo, L., "Near-Optimum Multiuser Detectors Using Soft-Output Ant-Colony-Optimization for the DS-CDMA Uplink," *IEEE Signal Processing Letters*, vol. 16, pp. 137–140, February 2009.

[64] Nan Zhao and Zhilu Wu and Yaqin Zhao and Taifan Quan, "A Population Declining Mutated Ant Colony Optimization Multiuser Detector for MC-CDMA," *IEEE Communications Letters*, vol. 14, pp. 497–499, June 2010.

[65] ten Brink, S., "Convergence Behavior of Iteratively Decoded Parallel Concatenated Codes," *IEEE Transactions on Communications*, vol. 49, pp. 1727–1737, October 2001.

[66] El-Hajjar, M. and Hanzo, L., "EXIT Charts for System Design and Analysis," *IEEE Communications Surveys & Tutorials*, vol. 16, pp. 127–153, January 2014.

[67] Babar, Z. and Ng, S.X. and Hanzo, L., "EXIT-Chart Aided Near-Capacity Quantum Turbo Code Design," *IEEE Transactions on Vehicular Technology*, vol. PP, no. 99, pp. 1–1, 2014.

[68] Feynman, Richard, "Simulating Physics with Computers," *International Journal of Theoretical Physics*, vol. 21, pp. 467–488, June 1982.

[69] Benioff, Paul, "Quantum Mechanical Hamiltonian Models of Turing Machines," *Journal of Statistical Physics*, vol. 29, pp. 515–546, 1982. 10.1007/BF01342185.

[70] Wimmel, H., *Quantum Physics & Observed Reality: A Critical Interpretation of Quantum Mechanics*. World Scientific, 1992.

[71] Everett, Hugh, "Relative State Formulation of Quantum Mechanics," *Reviews of Modern Physics*, vol. 29, pp. 454–462, July 1957.

[72] Deutsch, D., "Quantum Theory, the Church-Turing Principle and the Universal Quantum Computer," *Proceedings of the Royal Society of London. Series A, Mathematical and Physical Sciences*, vol. 400, no. 1818, pp. 97–117, 1985.

[73] Deutsch, David and Jozsa, Richard, "Rapid Solution of Problems by Quantum Computation," *Proceedings: Mathematical and Physical Sciences*, vol. 439, pp. 553–558, December 1992.

[74] Shor, P.W., "Algorithms for Quantum Computation: Discrete Logarithms and Factoring," in *35th Annual Symposium on Foundations of Computer Science, Proceedings*, pp. 124–134, November 1994.

[75] Shor, P., "Polynomial-Time Algorithms for Prime Factorization and Discrete Logarithms on a Quantum Computer," *SIAM Journal on Computing*, vol. 26, no. 5, pp. 1484–1509, 1997.

[76] Bell, John S., "On the Problem of Hidden Variables in Quantum Mechanics," *Reviews of Modern Physics*, vol. 38, pp. 447–452, July 1966.

[77] Einstein, A. and Podolsky, B. and Rosen, N., "Can Quantum-Mechanical Description of Physical Reality Be Considered Complete?," *Physical Reviews*, vol. 47, pp. 777–780, May 1935.

[78] E. Martín-López, A. Laing, T. Lawson, R. Alvarez, X.-Q. Zhou, J. L. O'Brien, "Experimental Realization of Shor's Quantum Factoring Algorithm Using Qubit Recycling," *Nature Photonics*, vol. 6, pp. 773–776, November 2012.

[79] Xu, Nanyang and Zhu, Jing and Lu, Dawei and Zhou, Xianyi and Peng, Xinhua and Du, Jiangfeng, "Quantum Factorization of 143 on a Dipolar-Coupling Nuclear Magnetic Resonance System," *Physical Review Letters*, vol. 108, p. 130501, Mar 2012.

[80] Daniel R. Simon, "On the Power of Quantum Computation," *SIAM Journal on Computing*, vol. 26, pp. 116–123, 1994.

[81] Holevo, A.S., "The Capacity of the Quantum Channel With General Signal States," *IEEE Transactions on Information Theory*, vol. 44, pp. 269–273, January 1998.

[82] Concha, J.I. and Poor, H.V., "Multiaccess Quantum Channels," *IEEE Transactions on Information Theory*, vol. 50, pp. 725–747, May 2004.

[83] Min-Hsiu Hsieh and Wilde, M.M., "Entanglement-Assisted Communication of Classical and Quantum Information," *IEEE Transactions on Information Theory*, vol. 56, pp. 4682–4704, September 2010.

[84] Xu Wang and Wada, N. and Miyazaki, T. and Cincotti, G. and Kitayama, K.-i., "Asynchronous Multiuser Coherent OCDMA System With Code-Shift-Keying and Balanced Detection," *IEEE Journal of Selected Topics in Quantum Electronics*, vol. 13, pp. 1463–1470, September - October 2007.

[85] Gyongyosi, L. and Imre, S., "Information Geometrical Analysis of Additivity of Optical Quantum Channels," *IEEE/OSA Journal of Optical Communications and Networking*, vol. 3, pp. 48–55, January 2011.

[86] Bennett, Charles H. and Bernstein, Ethan and Brassard, Gilles and Vazirani, Umesh, "Strengths and Weaknesses of Quantum Computing," *SIAM J.Sci.Statist.Comput.*, 1996.

[87] Zalka, Christof, "Grover's Quantum Searching Algorithm is Optimal," *Physical Review A*, vol. 60, pp. 2746–2751, Oct 1999.

[88] D. Ventura, and T. Martinez, , "Quantum Associative Memory," *eprint arXiv:quant-ph/9807053*, July 1998.

[89] Gui Lu Long and Yan Song Li and Wei Lin Zhang and Li Niu, "Phase Matching in Quantum Searching," *Physics Letters A*, vol. 262, pp. 27–34, October 1999.

[90] A. Ahuja, S. Kapoor, "A Quantum Algorithm for finding the Maximum," *eprint arXiv:quant-ph/9911082*, Nov. 1999.

[91] Hogg, Tad, "Quantum Search Heuristics," *Physical Review A*, vol. 61, p. 052311, Apr 2000.

[92] Shenvi, Neil and Kempe, Julia and Whaley, K. Birgitta, "Quantum Random-Walk Search Algorithm," *Physical Review A*, vol. 67, p. 052307, May 2003.

[93] Imre, S. and Balázs, F., "The Generalized Quantum Database Search Algorithm," *Computing*, vol. 73, no. 3, pp. 245–269, 2004.

[94] S. M. Zhao and Jia Yao and B. Y. Zheng, "Multiuser Detection Based on Grover's Algorithm," in *IEEE International Symposium on Circuits and Systems, 2006. ISCAS 2006. Proceedings, 2006*, pp. 4735–4738, May 2006.

[95] Imre, S., "Quantum Existence Testing and Its Application for Finding Extreme Values in Unsorted Databases," *IEEE Transactions on Computers*, vol. 56, pp. 706–710, May 2007.

[96] Malossini, A. and Blanzieri, E. and Calarco, T., "Quantum Genetic Optimization," *IEEE Transactions on Evolutionary Computation*, vol. 12, pp. 231–241, April 2008.

[97] Fei Li and Lizhi Zhou and Li Liu and Haibo Li, "A Quantum Search Based Signal Detection for MIMO-OFDM Systems," in *18th International Conference on Telecommunications (ICT)*, pp. 276–281, May 2011.

[98] Tad Hogg and Dmitriy Portnov, "Quantum Optimization," *Information Sciences*, vol. 128, no. 34, pp. 181–197, 2000.

[99] Garcia-Escartin, J.C. and Chamorro-Posada, P., "Quantum Spread Spectrum Multiple Access," *IEEE Journal of Selected Topics in Quantum Electronics*, vol. 21, pp. 1–7, May 2015.

[100] Dirac, P. A. M., *The Principles of Quantum Mechanics*. Oxford University Press, USA, 4 ed., February 1982.

[101] Brassard, Gilles, "Searching a Quantum Phone Book," *Science*, vol. 275, no. 5300, pp. 627–628, 1997.

[102] Einstein, Albert and Born, Max and Born, Hedwig , *The Born-Einstein Letters: Correspondence between Albert Einstein and Max and Hedwig Born from 1916-1955, with Commentaries by Max Born ; Translated from the German by Irene Born* . London : Macmillan, 1971. Translation of briefwechsel 1916-1955.

[103] Verdu, Sergio, *Multiuser Detection*. New York, NY, USA: Cambridge University Press, 1st ed., 1998.

[104] Shimon Moshavi, "Multi-User Detection for DS-CDMA Communications," *IEEE Communnications Magazine*, pp. 124–136, October 1996.

[105] Byonghyo Shim and Jun Won Choi and Insung Kang, "Towards the Performance of ML and the Complexity of MMSE: A Hybrid Approach for Multiuser Detection," *IEEE Transactions on Wireless Communications*, vol. 11, pp. 2508–2519, July 2012.

[106] Kai Li and Xiaodong Wang, "EXIT Chart Analysis of Turbo Multiuser Detection," *IEEE Transactions on Wireless Communications*, vol. 4, pp. 300–311, January 2005.

[107] Xiaodong Wang and Poor, H.V., "Space-Time Multiuser Detection in Multipath CDMA Channels," *IEEE Transactions on Signal Processing*, vol. 47, pp. 2356–2374, September 1999.

[108] Sheng Chen and Samingan, A.K. and Mulgrew, B. and Hanzo, L., "Adaptive Minimum-BER Linear Multiuser Detection for DS-CDMA Signals in Multipath Channels," *IEEE Transactions on Signal Processing*, vol. 49, pp. 1240–1247, June 2001.

[109] Sheng Chen and Livingstone, A. and Hanzo, L., "Minimum Bit-Error Rate Design for Space-Time Equalization-Based Multiuser Detection," *IEEE Transactions on Communications*, vol. 54, pp. 824–832, May 2006.

[110] Shuang Tan and Sheng Chen and Hanzo, L., "On Multi-User EXIT Chart Analysis Aided Turbo-Detected MBER Beamformer Designs," *IEEE Transactions on Wireless Communications*, vol. 7, pp. 314–323, January 2008.

[111] Jiang, M. and Akhtman, J. and Hanzo, L., "Iterative Joint Channel Estimation and Multi-User Detection for Multiple-Antenna Aided OFDM Systems," *IEEE Transactions on Wireless Communications*, vol. 6, pp. 2904–2914, August 2007.

[112] Klein, A. and Baier, P., "Linear Unbiased Data Estimation in Mobile Radio Systems Applying CDMA," *IEEE Journal on Selected Areas in Communications*, vol. 11, no. 7, pp. 1058–1066, 1993.

[113] Wautelet, X. and Dejonghe, A. and Vandendorpe, L., "MMSE-based Fractional Turbo Receiver for Space-Time BICM Over Frequency-Selective MIMO Fading Channels," *IEEE Transactions on Signal Processing*, vol. 52, no. 6, pp. 1804–1809, 2004.

[114] Chen, S. and Ahmad, N. N. and Hanzo, L., "Adaptive Minimum Bit-Error Rate Beamforming," *IEEE Transactions on Wireless Communications*, vol. 4, no. 2, pp. 341–348, 2005.

[115] Damen, O. and Chkeif, A. and Belfiore, J. -C, "Lattice Code Decoder for Space-Time Codes," *IEEE Communications Letters*, vol. 4, no. 5, pp. 161–163, 2000.

[116] Li Wang and Alamri, O. and Hanzo, L., "Sphere Packing Modulation in the SDMA Uplink Using K -Best Sphere Detection," *IEEE Signal Processing Letters*, vol. 16, no. 4, pp. 291–294, 2009.

[117] Agrell, E. and Eriksson, T. and Vardy, A. and Zeger, K., "Closest Point Search in Lattices," *IEEE Transactions on Information Theory*, vol. 48, no. 8, pp. 2201–2214, 2002.

[118] Chengwei Zheng and Xuezheng Chu and McAllister, J. and Woods, R., "Real-Valued Fixed-Complexity Sphere Decoder for High Dimensional QAM-MIMO Systems," *IEEE Transactions on Signal Processing*, vol. 59, no. 9, pp. 4493–4499, 2011.

[119] Ergun, C. and Hacioglu, K., "Multiuser Detection Using a Genetic Algorithm in CDMA Communications Systems," *IEEE Transactions on Communications*, vol. 48, pp. 1374–1383, August 2000.

[120] Alias, M.Y. and Sheng Chen and Hanzo, L., "Multiple-Antenna-Aided OFDM Employing Genetic-Algorithm-Assisted Minimum Bit Error Rate Multiuser Detection," *IEEE Transactions on Vehicular Technology*, vol. 54, pp. 1713–1721, September 2005.

[121] Yen, K. and Hanzo, L., "Antenna-Diversity-Assisted Genetic-Algorithm-Based Multiuser Detection Schemes for Synchronous CDMA Systems," *IEEE Transactions on Communications*, vol. 51, pp. 366–370, March 2003.

[122] Babich, F. and Crismani, A. and Driusso, M. and Hanzo, L., "Design Criteria and Genetic Algorithm Aided Optimization of Three-Stage-Concatenated Space-Time Shift Keying Systems," *IEEE Signal Processing Letters*, vol. 19, no. 8, pp. 543–546, 2012.

[123] Soo, K.K. and Siu, Y.M. and Chan, W.S. and Yang, L. and Chen, R.S., "Particle-Swarm-Optimization-Based Multiuser Detector for CDMA Communications," *IEEE Transactions on Vehicular Technology*, vol. 56, pp. 3006–3013, September 2007.

[124] Hongwu Liu and Ji Li, "A Particle Swarm Optimization-Based Multiuser Detection for Receive-Diversity-Aided STBC Systems," *IEEE Signal Processing Letters*, vol. 15, pp. 29–32, 2008.

[125] Ying Zhao and Junli Zheng, "Particle Swarm Optimization Algorithm in Signal Detection and Blind Extraction," in *7th International Symposium on Parallel Architectures, Algorithms and Networks, 2004. Proceedings.*, pp. 37–41, May 2004.

[126] Vishnu Vardhan, K. and Mohammed, S.K. and Chockalingam, A. and Sundar Rajan, B., "A Low-Complexity Detector for Large MIMO Systems and Multicarrier CDMA

Systems," *IEEE Journal on Selected Areas in Communications*, vol. 26, pp. 473–485, April 2008.

[127] Heng Siong Lim and Venkatesh, B., "An Efficient Local Search Heuristics for Asynchronous Multiuser Detection," *IEEE Communications Letters*, vol. 7, pp. 299–301, July 2003.

[128] Shuyuan Yang and Min Wang and Licheng Jiao, "A Novel Quantum Evolutionary Algorithm and its Application," in *Congress on Evolutionary Computation, CEC2004*, vol. 1, pp. 820–826, June 2004.

[129] de Oliveira, L.D. and Ciriaco, F. and Abrao, T. and Jeszensky, P.J.E., "Particle Swarm and Quantum Particle Swarm Optimization Applied to DS/CDMA Multiuser Detection in Flat Rayleigh Channels," in *IEEE Ninth International Symposium on Spread Spectrum Techniques and Applications, 2006*, pp. 133–137, August 2006.

[130] Hongyuan Gao and Ming Diao, "Quantum Particle Swarm Optimization for MC-CDMA Multiuser Detection," in *International Conference on Artificial Intelligence and Computational Intelligence, 2009, AICI '09*, vol. 2, pp. 132–136, November 2009.

[131] Hongwu Liu and Gaojun Song, "A Multiuser Detection Based on Quantum PSO with Pareto Optimality for STBC-MC-CDMA System," in *IEEE International Conference on Communications Technology and Applications*, pp. 652–655, October 2009.

[132] Fei Li and Min Zhou and Haibo Li, "A Novel Neural Network Optimized by Quantum Genetic Algorithm for Signal Detection in MIMO-OFDM Systems," in *IEEE Symposium on Computational Intelligence in Control and Automation (CICA), 2011*, pp. 170–177, April 2011.

[133] Ajit Narayanan and Mark Moore, "Quantum-Inspired Genetic Algorithms," in *Proceedings of the 1996 IEEE International Conference on Evolutionary Computation (ICEC96)*, pp. 61–66, Press, 1995.

[134] Fei Li and Liang Hong and Baoyu Zheng, "Quantum Genetic Algorithm and its Application to Multi-User Detection," in *9th International Conference on Signal Processing, ICSP*, pp. 1951–1954, October 2008.

[135] Rusek, F. and Persson, D. and Buon Kiong Lau and Larsson, E.G. and Marzetta, T.L. and Edfors, O. and Tufvesson, F., "Scaling Up MIMO: Opportunities and Challenges with Very Large Arrays," *IEEE Signal Processing Magazine*, vol. 30, no. 1, pp. 40–60, 2013.

[136] Srinidhi, N. and Datta, T. and Chockalingam, A. and Rajan, B.S., "Layered Tabu Search Algorithm for Large-MIMO Detection and a Lower Bound on ML Performance," *IEEE Transactions on Communications*, vol. 59, no. 11, pp. 2955–2963, 2011.

[137] Mohammed, S.K. and Larsson, E.G., "Per-Antenna Constant Envelope Precoding for Large Multi-User MIMO Systems," *IEEE Transactions on Communications*, vol. 61, no. 3, pp. 1059–1071, 2013.

[138] C.Radhakrishna Rao and Haruo Yanai, "Generalized Inverse of Linear Transformations: A Geometric Approach," *Linear Algebra and its Applications*, vol. 66, pp. 87–98, 1985.

[139] Oliveira, D.S. and Melo de Sousa, P.B. and Ramos, R.V., "Quantum Search Algorithm Using Quantum Bit String Comparator," in *IEEE International Telecommunications Symposium*, pp. 582–585, September 2006.

[140] Li Ping, "Interleave-Division Multiple Access and Chip-by-Chip Iterative Multi-User Detection," *IEEE Communications Magazine*, vol. 43, pp. S19–S23, June 2005.

[141] Cristea, B. and Roviras, D. and Escrig, B., "Turbo Receivers for Interleave-Division Multiple-Access Systems," *IEEE Transactions on Communications*, vol. 57, pp. 2090–2097, July 2009.

[142] Hao-Hsiang Chung and Yung-Chih Tsai and Mao-Chao Lin, "IDMA Using Non-Gray Labelled Modulation," *IEEE Transactions on Communications*, vol. 59, pp. 2492–2501, September 2011.

[143] Jian Dang and Wenshu Zhang and Liuqing Yang and Zaichen Zhang, "OFDM-IDMA with User Grouping," *IEEE Transactions on Communications*, vol. 61, pp. 1947–1955, May 2013.

[144] Yen-Ming Chen and Yeong-Luh Ueng and Hau-Jung Shiau, "An EXIT-Based Design Method for LDPC-Coded Schemes without Gaussian Assumptions," *IEEE Communications Letters*, vol. 17, pp. 1648–1651, August 2013.

[145] Dorigo, M. and Gambardella, L.M., "Ant Colony System: A Cooperative Learning Approach to the Traveling Salesman Problem," *IEEE Transactions on Evolutionary Computation*, vol. 1, pp. 53–66, April 1997.

[146] Sesia, Stefania and Toufik, Issam and Baker, Matthew, *LTE, The UMTS Long Term Evolution: From Theory to Practice*. Wiley Publishing, 2009.

[147] Joachim Hagenauer, "The EXIT Chart - Introduction to Extrinsic Information Transfer," in *12th European Signal Processing Conf (EUSIPCO) in Iterative Processing,*, pp. 1541–1548, 2004.

[148] Li Wang and Hanzo, L., "Dispensing with Channel Estimation: Differentially Modulated Cooperative Wireless Communications," *IEEE Communications Surveys Tutorials*, vol. 14, pp. 836–857, March 2012.

[149] Dong, Min and Lang Tong, "Optimal Design and Placement of Pilot Symbols for Channel Estimation," *IEEE Transactions on Signal Processing*, vol. 50, pp. 3055–3069, December 2002.

[150] Vosoughi, A and Scaglione, A, "Everything You Always Wanted to Know About Training: Guidelines Derived Using the Affine Precoding Framework and the CRB," *IEEE Transactions on Signal Processing*, vol. 54, pp. 940–954, March 2006.

[151] Buchoux, V. and Cappe, O. and Moulines, E. and Gorokhov, A, "On the Performance of Semi-Blind Subspace-Based Channel Estimation," *IEEE Transactions on Signal Processing*, vol. 48, pp. 1750–1759, June 2000.

[152] de Carvalho, E. and Slock, D. T M, "Blind and Semi-Blind FIR Multichannel Estimation: (Global) Identifiability Conditions," *IEEE Transactions on Signal Processing*, vol. 52, pp. 1053–1064, April 2004.

[153] Lang Tong and Liu, R. and Soon, V.C. and Yih-Fang Huang, "Indeterminacy and Identifiability of Blind Identification," *IEEE Transactions on Circuits and Systems*, vol. 38, pp. 499–509, May 1991.

[154] Lang Tong and Perreau, S., "Multichannel Blind Identification: From Subspace To Maximum Likelihood Methods," *Proceedings of the IEEE*, vol. 86, pp. 1951–1968, October 1998.

[155] Necker, M.C. and Stuber, G.L., "Totally Blind Channel Estimation For OFDM On Fast Varying Mobile Radio Channels," *IEEE Transactions on Wireless Communications*, vol. 3, pp. 1514–1525, September 2004.

[156] Cavers, J.K., "An Analysis of Pilot Symbol Assisted Modulation for Rayleigh Fading Channels [Mobile Radio]," *IEEE Transactions on Vehicular Technology*, vol. 40, pp. 686–693, November 1991.

[157] Divsalar, D. and Simon, Marvin K., "Multiple-Symbol Differential Detection of MPSK," *IEEE Transactions on Communications*, vol. 38, pp. 300–308, March 1990.

[158] Adachi, F. and Sawahashi, M., "Decision Feedback Multiple-Symbol Differential Detection for M-ary DPSK," *Electronics Letters*, vol. 29, pp. 1385–1387, July 1993.

[159] Mackenthun, K., Jr., "A Fast Algorithm for Multiple-Symbol Differential Detection of MPSK," *IEEE Transactions on Communications*, vol. 42, pp. 1471–1474, February 1994.

[160] Peleg, M. and Shamai, S., "Iterative Decoding of Coded and Interleaved Noncoherent Multiple Symbol Detected DPSK," *Electronics Letters*, vol. 33, pp. 1018–1020, June 1997.

[161] Divsalar, D. and Simon, Marvin K., "Maximum-Likelihood Differential Detection of Uncoded and Trellis Coded Amplitude Phase Modulation Over AWGN and Fading Channels-Metrics and Performance," *IEEE Transactions on Communications*, vol. 42, pp. 76–89, January 1994.

[162] Ho, P. and Fung, D., "Error Performance of Multiple-Symbol Differential Detection of PSK Signals Transmitted Over Correlated Rayleigh Fading Channels," *IEEE Transactions on Communications*, vol. 40, pp. 1566–1569, October 1992.

[163] Schober, R. and Gerstacker, W.H. and Huber, J.B., "Decision-Feedback Differential Detection of MDPSK for Flat Rayleigh Fading Channels," *IEEE Transactions on Communications*, vol. 47, pp. 1025–1035, July 1999.

[164] Leib, H., "Data-Aided Noncoherent Demodulation of DPSK," *IEEE Transactions on Communications*, vol. 43, pp. 722–725, February 1995.

[165] Schober, R. and Gerstacker, W.H., "Decision-Feedback Differential Detection Based On Linear Prediction For MDPSK Signals Transmitted Over Ricean Fading Channels," *IEEE Journal on Selected Areas in Communications*, vol. 18, pp. 391–402, March 2000.

[166] Lampe, L. and Schober, R. and Pauli, V. and Windpassinger, C., "Multiple-Symbol Differential Sphere Decoding," *IEEE Transactions on Communications*, vol. 53, pp. 1981–1985, December 2005.

[167] Chao Xu and Sugiura, S. and Soon Xin Ng and Hanzo, L., "Reduced-Complexity Noncoherently Detected Differential Space-Time Shift Keying," *IEEE Signal Processing Letters*, vol. 18, pp. 153–156, March 2011.

[168] Chao Xu and Li Wang and Soon Xin Ng and Hanzo, L., "Multiple-Symbol Differential Sphere Detection Aided Differential Space-Time Block Codes Using QAM Constellations," *IEEE Signal Processing Letters*, vol. 18, pp. 497–500, September 2011.

[169] Lampe, L. H-J and Schober, R., "Low-Complexity Iterative Demodulation For Noncoherent Coded Transmission Over Ricean-Fading Channels," *IEEE Transactions on Vehicular Technology*, vol. 50, pp. 1481–1496, November 2001.

[170] Lampe, L. H-J and Schober, R., "Iterative Decision-Feedback Differential Demodulation of Bit-Interleaved Coded MDPSK for Flat Rayleigh Fading Channels," *IEEE Transactions on Communications*, vol. 49, pp. 1176–1184, July 2001.

[171] Hoeher, P. and Lodge, J., ""Turbo DPSK": Iterative Differential PSK Demodulation and Channel Decoding," *IEEE Transactions on Communications*, vol. 47, pp. 837–843, June 1999.

[172] Pauli, V. and Lampe, L. and Schober, R., ""Turbo DPSK" Using Soft Multiple-Symbol Differential Sphere Decoding," *IEEE Transactions on Information Theory*, vol. 52, pp. 1385–1398, April 2006.

[173] John G. Proakis, *Digital Communications*. McGraw-Hill, fourth ed., 2001.

[174] Lajos Hanzo and M. Münster and B. Choi and T. Keller, *OFDM and MC-CDMA for Broadband Multi-User Communications, WLANs and Broadcasting*. John Wiley & Sons, 2003.

[175] Dutta, A.K. and Hari, K.V.S. and Hanzo, L., "Channel Estimation Relying on the Minimum Bit-Error Ratio Criterion for BPSK and QPSK Signals," *IET Communications*, vol. 8, pp. 69–76, January 2014.

[176] Dutta, A. and Hari, K. and Hanzo, L., "Minimum-Error-Probability CFO Estimation for Muti-User MIMO OFDM Systems," *IEEE Transactions on Vehicular Technology*, vol. PP, no. 99, pp. 1–1, 2014.

[177] Ng, S. X. and Yen, K. and Hanzo, L., "M-ary Coded Modulation Assisted Genetic Algorithm Based Multiuser Detection for CDMA Systems," in *IEEE Wireless Communications and Networking Conference*, vol. 2, pp. 779–783 vol.2, March 2003.

[178] Ming Jiang and Soon Xin Ng and Hanzo, L., "Hybrid Iterative Multiuser Detection For Channel Coded Space Division Multiple Access OFDM Systems," *IEEE Transactions on Vehicular Technology*, vol. 55, pp. 115–s127, Jan 2006.

[179] Wei Chen and Hanzo, L. and Zhigang Cao, "Network Coded Modulation for Two-Way Relaying," in *IEEE Wireless Communications and Networking Conference*, pp. 1765–1770, March 2011.

[180] Wei Chen and Zhigang Cao and Hanzo, L., "Maximum Euclidean Distance Network Coded Modulation for Asymmetric Decode-And-Forward Two-Way Relaying," *IET Communications*, vol. 7, pp. 988–998, July 2013.

[181] Babar, Z. and Soon Xin Ng and Hanzo, L., "Near-Capacity Code Design for Entanglement-Assisted Classical Communication over Quantum Depolarizing Channels," *IEEE Transactions on Communications*, vol. 61, pp. 4801–4807, December 2013.

[182] Xiaolin Zhou and Dingchen Zhang and Rong Zhang and Lajos Hanzo, "A Photon-Counting Spatial-Diversity-and-Multiplexing MIMO Scheme for Poisson Atmospheric Channels Relying on Q-ary PPM," *Optics Express*, vol. 20, pp. 26379–26393, November 2012.

[183] Lingbin Li and Xiaolin Zhou and Rong Zhang and Dingchen Zhang and Lajos Hanzo, "Performance and Capacity Analysis of Poisson Photon-Counting based Iter-PIC OCDMA Systems," *Optics Express*, vol. 21, pp. 25954–25967, November 2013.

[184] Xinyi Xu and Rong Zhang and Ghafoor, Salman and Hanzo, L., "Imperfect Digital-Fiber-Optic-Link-Based Cooperative Distributed Antennas With Fractional Frequency Reuse in Multicell Multiuser Networks," *IEEE Transactions on Vehicular Technology*, vol. 60, no. 9, pp. 4439–4449, 2011.

Index

W

Z

Author Index

I

J

K

L

X

Y

Z